

# Stark Structure of the Spectrum and Decay Kinetics of the Er<sup>3+</sup> Photoluminescence in Pseudoamorphous *a*-nc-GaN Films

A. A. Andreev

*Ioffe Physicotechnical Institute, Russian Academy of Sciences,  
Politekhnikeskaya ul. 26, St. Petersburg, 194021 Russia*

Received April 29, 2003

**Abstract**—Amorphous films containing nanocrystalline inclusions, *a*-nc-GaN, were codoped with Er in the course of magnetron sputtering. Intense intracenter emission of Er<sup>3+</sup> ions in the wavelength region  $\lambda = 1510$ – $1550$  nm was obtained only after multistage annealing at temperatures of 650–770°C. The intracenter emission was excited indirectly through electron–hole pair generation in the *a*-nc-GaN matrix by a pulsed nitrogen laser. Subsequent recombination via a number of localized states in the band gap transferred the excitation energy to the Er<sup>3+</sup> ions. Measurements of photoluminescence (PL) spectra carried out with time resolution in various annealing stages at different temperatures in the range 77–500 K and in the course of decay permitted us to establish the Stark nature of the PL spectrum and to reveal the dynamic and nonequilibrium character of redistribution of the intracenter emission energy among the Stark modes in the course of the excitation pulse relaxation. The information thus obtained was used to interpret the dominant hot-mode contribution and the complex decay kinetics. © 2004 MAIK “Nauka/Interperiodica”.

## 1. INTRODUCTION

The interest in studies of the luminescence of trivalent erbium ions in various semiconductor matrices stems primarily from the possibility of developing narrow band, thermally stable emitters for the wavelength (1535 nm) corresponding to minimum losses in quartz fiber waveguides [1]. This subject is also of fundamental significance, because many attendant issues still remain unsolved. In particular, the specific features of erbium photoluminescence (PL) at high concentrations of optically active ions ( $\geq 10^{20}$  cm<sup>-3</sup>), the mechanism of energy transfer from the pumped matrix to erbium ions, and the PL dynamics at high pulsed pump power levels on the order of 100 kW/cm<sup>2</sup>, i.e., in the conditions close to the superluminescence threshold [2], are very poorly understood.

While the present study deals to a certain extent with these issues, it does not claim to have solved them and should be considered rather as a step in this direction. This study includes two new elements, namely, (1) the choice of an amorphous *a*-nc-GaN matrix for Er<sup>3+</sup> ions, which allows erbium doping to high concentrations (up to  $5 \times 10^{20}$  cm<sup>-3</sup>) [3], and (2) the use of a pulsed nitrogen laser with a pulse power of 1.6 kW to excite the matrix–erbium ions system. The laser radiation does not coincide in energy ( $\hbar\nu = 3.68$  eV) with any of the  $4f^{11}$  erbium ion shell levels and, therefore, cannot be transferred to the erbium ion through direct resonance absorption of a photon. Thus, the erbium ions can be excited only indirectly, through dissipation of the

energy of the electron–hole pairs created in the matrix with  $E_g = 3.4$  eV. In the course of interband recombination involving a broad spectrum of localized states, the energy of the pairs is transferred to the erbium ions nonresonantly via the GaN lattice–Er<sup>3+</sup> bonds; this accounts for the multitude of intracenter transitions, of which we are interested only in the transition connecting the first excited state of the ion to the ground state, i.e., the  $^4I_{13/2} \rightarrow ^4I_{15/2}$  transition at the wavelength  $\lambda \cong 1535$  nm. The nonresonant mechanism of energy transfer to the ion is very poorly understood, but it undoubtedly has specific features and should affect the Er<sup>3+</sup> PL pattern. Furthermore, the high excitation density reached in a pulse makes the population of the  $^4I_{13/2}$  Stark states a nonequilibrium process, a factor that substantially modifies the PL decay kinetics.

## 2. EXPERIMENTAL

Films of amorphous *a*-GaN measuring 4–7 nm with a fairly uniform distribution of nc-GaN nanocrystallites of hexagonal symmetry were prepared by magnetron sputtering of metallic Ga in a reactive gas mixture Ar + N<sub>2</sub>. The critical parameter for the process is the substrate temperature  $T_s$ , which was found to be optimal around 300–350°C. It was established that, at higher values of  $T_s$  approaching 500°C, films tend toward uncontrollable crystallization under subsequent annealing. The erbium ion PL in such films is unstable.

Codoping with erbium was achieved in the course of film growth by placing small Er-metal platelets of calibrated area into the magnetron discharge. The concentration thus introduced was varied in the range  $(1-10) \times 10^{20} \text{ cm}^{-3}$ . The maximum intensity was achieved at an Er concentration of  $5 \times 10^{20} \text{ cm}^{-3}$ . A further increase in the concentration resulted in a strong decrease in the PL lifetime.

Structural characterization of the films was done by means of x-ray diffraction, Raman spectral measurements, and direct HRTEM observation of the microstructure. The HRTEM method permitted us to detect inclusions of nanocrystals and their belonging to the *c*-GaN hexagonal phase and determine their dimensions (5–7 nm), the fractional volume of the phase ( $\approx 10\%$ ), and its variation under annealing, namely, the increase in the volume fraction of the nanocrystals without an increase in their size [4, 5]. The HRTEM data were kindly provided by Prof. H.P. Strunk (Erlangen, Germany). While the vibrational mode structure in the Raman spectra obtained by V.Yu. Davydov (Ioffe Institute, Russian Academy of Sciences, St. Petersburg) is fairly diffuse, the maxima of the  $A_1(\text{TO}) + E_1 + E_2$  and  $A_1(\text{LO}) + E_1(\text{LO})$  modes nevertheless coincide in position with those for the *c*-GaN. The Raman spectrum of the films sharpens with annealing, which is evidence there is a growing contribution from the nanocrystalline fraction, and is in agreement with the HRTEM data. Despite this trend, the *a*-nc-GaN films retain their two-phase (*a* + nc) microstructure up to at least 775°C, demonstrating also high adhesion to such substrates as *c*-Si and fused quartz.

Directly after deposition, Er-doped films do not exhibit the characteristic erbium PL at  $\lambda \approx 1535 \text{ nm}$ . To obtain this emission, one has to optically activate the erbium ions, a process consisting in a series of high-temperature anneals with  $T_{\text{ann}}$  in the range 650–770°C. To achieve the maximum  $\text{Er}^{3+}$  PL intensity, several cycles with  $T_{\text{ann}}$  increased judiciously in each subsequent cycle will suffice. Annealing at a temperature in excess of the maximum  $T_{\text{ann}}$ , 775°C, initiates a clearly pronounced macrocrystallization, which brings about film turbidity and a complete or partial disappearance of the erbium PL.

PL measurements were carried out with an optical resolution of 5 nm. The InGaAs-based photodiode with a sensitivity of 25  $\mu\text{V}/\text{mW}$  provided by L.B. Karlina (Ioffe Institute, RAS, St. Petersburg) had a low internal resistance, which favored reaching a low level of electromagnetic noise induction from the pulsed-laser power supply and permitted us to reach high instrument sensitivity over a broad enough dynamic range of variation of the signal amplitude (up to two orders of magnitude). Time-resolved spectra were obtained with a gate width of down to  $(3-5) \times 10^{-2}$  of the PL decay time. Decay curves were recorded directly with an oscillograph.

### 3. RESULTS AND DISCUSSION

#### 3.1. Changes in the $\text{Er}^{3+}$ Spectra in the Course of Optical Activation

It is known [1, 3, 6] that the mechanism of optical activation consists in the formation of a local atomic environment around the erbium ion, generating a crystal field of electrostatic nature without inversion symmetry. Such a crystal field results in Stark splitting of the erbium  $4f^{11}$  multiplets. In addition, because there is no inversion site symmetry, the allowed *f*-*d* transitions become admixed to the *f*-*f* transitions forbidden by selection rules, thus making the *f*-*f* intracenter transitions possible, although with a low probability, and this manifests itself, as will be seen from what follows, in the low PL decay rate.

The most efficient crystal field is generated by atoms of highly electronegative elements, such as nitrogen and oxygen. The absence of any experimentally observable optical activity of the erbium ion in as-prepared films implies that nitrogen does not create the required configuration in the  $\text{Er}^{3+}$  ion environment. Such a configuration does not form even though there is an excess of chemically active nitrogen in the form of plasma ions during the film growth. Our experiment shows that optical activity appears only at temperatures favoring the generation of nitrogen vacancies in the GaN structural network [7]. This takes place in the temperature interval 650–770°C. This allows two alternatives, namely, either the released nitrogen becomes chemically bonded to  $\text{Er}^{3+}$  or the process of nitrogen generation is conducive to the diffusion of residual oxygen (which is always present in the matrix in dissolved form) to the erbium ions. This residual oxygen is gettered efficiently by the erbium to form the  $\text{ErO}_x$  complex, whose erbium ion is acted upon by the field of negative oxygen charges. Irrespective of the way in which this process evolves, one can be confident that it does not occur quickly and is extended both in time and temperature. By measuring the  $\text{Er}^{3+}$  PL spectra in different stages of optical activation, one can follow the mechanism of crystal field formation, as well as draw some conclusions concerning the field symmetry and, hence, understand the nature of the  $\text{Er}^{3+}$  PL spectra.

The first anneal ( $T_{\text{ann}} = 650^\circ\text{C}$ ) gives rise to a very weak  $\text{Er}^{3+}$  PL signal with a fine structure consisting of a set of narrow, well-resolved peaks. Curve 1 in Fig. 1 displays this spectrum, obtained by S.B. Aldabergenova on a high-resolution double monochromator (0.85-m Spex 1404). After the next anneal ( $T_{\text{ann}} = 700^\circ\text{C}$ ), the intensity increases by a factor of 2–3, the spectral lines broaden, and the line structure still persists. Only in the last stage ( $T_{\text{ann}} = 750-770^\circ\text{C}$ ) is there a significant growth in intensity of up to one-hundredfold the initial level and does the fine structure in the spectrum disappear (curve 2, Fig. 1).

The PL displayed in Fig. 1 (curve 1) is obviously a Stark spectrum. It is specific in that the Stark manifold

consists of “hot” transitions only, i.e., of transitions from the Stark levels of the  $^4I_{13/2}$  manifold to the  $^4I_{15/2}$  ground state. Only the weak line at 1598 nm can be assigned to “cold” transitions, i.e., transitions from the lowest  $^4I_{13/2}$  state to the  $^4I_{15/2}$  Stark manifold.

The spectrum obtained in the final stage of optical activation (curve 2) is fairly diffuse and does not contain distinct Stark lines. Nevertheless, taking into account the dynamics of the transformation of spectrum 1 to spectrum 2, as well as a certain similarity in the distribution of averaged intensity (which also manifests itself in the dominant contribution of the high-energy wing), one can assume the final-state spectrum to derive from a sum of Stark transitions. The Stark peaks should be broadened compared to the ones in curve 1, because they originate from the considerably higher density of elementary emitters, which have an inherent configurational diffuseness [8]. To verify the possibility itself of assigning the spectrum to Stark transitions, we performed a numerical modeling by fitting the radiation originating from the Stark levels by Gaussians. In this procedure, the positions of the Stark levels for the high-energy wing of the experimental spectrum were prescribed in accordance with those in Fig. 1 (curve 1). As for the low-energy wing, it appeared reasonable to assume an averaged distribution of Stark levels spaced about 10 nm apart. This simplification does not introduce fundamental errors, because, first, the difference in the Stark level distribution between the major types of crystal field symmetries is of the order of or less than this quantity and, second, the tendency of ions of rare-earth metals (REM) to form multipole positions at high densities [9], i.e., positions with symmetries alternating from one site to another, inevitably brings about an averaging of the spectrum. Figure 1 presents a modeled Stark spectrum (curve 3) and its envelope (open circles on the experimental curve 2). We readily see that a Stark representation of the diffuse spectrum is reasonable. Subsequently, we will consider additional arguments for the Stark nature of the broad and diffuse experimental spectrum of the  $\text{Er}^{3+}$  ions. It would be appropriate to make a few comments here.

(1) At first glance, the narrowness of the Stark lines in the initial annealing stage might seem strange. This observation can, however, be accounted for by the weak interaction of the erbium ion and its nearest environment (to be more precise, the oxygen ions) with the amorphous network of the matrix. The strong chemical bonding of the  $\text{ErO}_x$  complex governs its structure, and the weaker external interaction with the matrix does not affect the structure of this complex noticeably. This results in the formation of a set of structurally identical emitting centers, which do not interact with one another because of their low concentration. This is what accounts for the fine structure of the spectrum. This idea is argued for by the fact that a nearly identical Stark spectrum of  $\text{Er}^{3+}$  was obtained by us earlier on *a*-

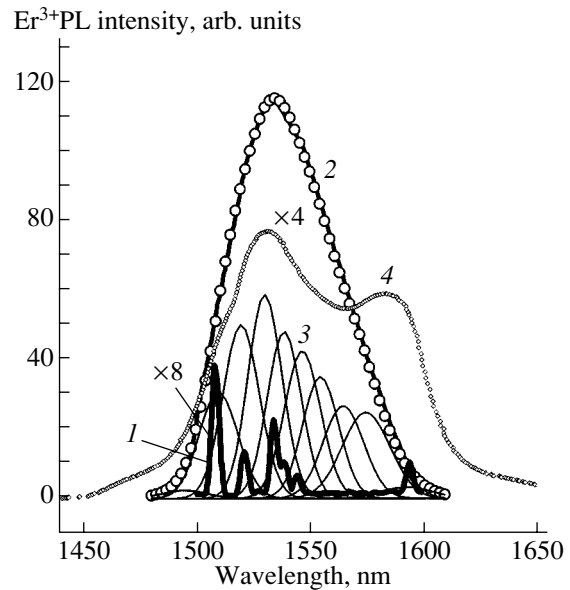


**Fig. 1.** Photoluminescence spectra of  $\text{Er}^{3+}$  ions in the *a*-nc-GaN pseudoamorphous matrix: (1) initial stage of optical activation following annealing at 650°C, (2) spectrum of the maximum intensity reached after multistage annealing with a final temperature of 770°C (solid line), (3) manifold of Stark emitters whose total spectrum is depicted by open circles on curve 2, and (4) spectrum obtained at the onset of macrocrystallization.

Si : H amorphous silicon, which contains no nitrogen at all [10]. This suggests that it is the  $\text{ErO}_x$  oxygen complex that produces the emission spectrum. The matrix plays a secondary role, which is easy to understand physically. Because it is inherently labile, it adjusts itself, as it were, to the rigid  $\text{ErO}_x$  complex.

(2) The above observations and conclusions (see the previous comment) give rise to the legitimate question of the structure of the  $\text{ErO}_x$  complex, which was raised more than once before. It was found that the complex contains six oxygen atoms making up a somewhat deformed octahedron, on whose *C* axis the erbium atom is located in a slightly off-center position, and this is what accounts for there being no center of inversion [11, 12]. This complex has a  $C_{4v}$ -type tetragonal symmetry. Some authors, however, tend to believe that the erbium site has a lower symmetry and that the ion features have, accordingly, a lower oxygen coordination [13, 14]. We compared an experimental set of Stark lines (for hot transitions) with the calculations available for two crystal field symmetry types, namely, the highest cubic symmetry  $T_d$  and the lower rhombohedral symmetry  $C_{3v}$ . No one-to-one correspondence was found for either symmetry group. The only thing one can maintain is that the experimental spectrum contains elements of both symmetries simultaneously. In principle, this is possible, because the  $C_{3v}$  configuration, just as  $C_{4v}$  is actually the result of a deformation of cubic symmetry along the (111) and (001) directions. If we

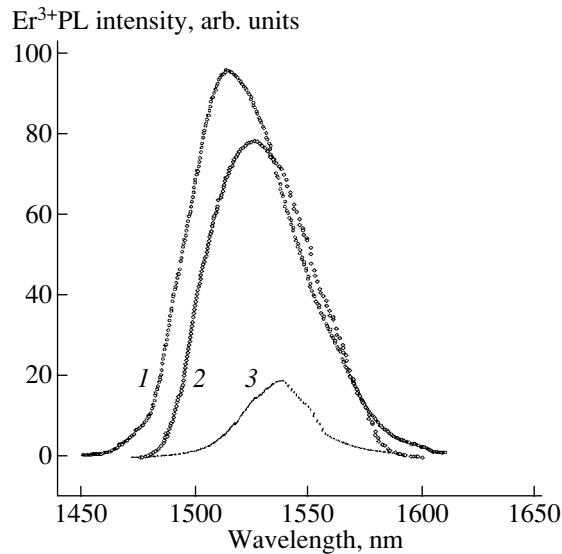


**Fig. 2.** Time-resolved spectra obtained at 300 K under pulsed excitation by a nitrogen laser with a pulse power of  $\approx 100 \text{ kW/cm}^2$  for time delay (1)  $\approx 5$ , (2)  $\approx 150$ , and (3)  $\approx 450 \mu\text{s}$ .

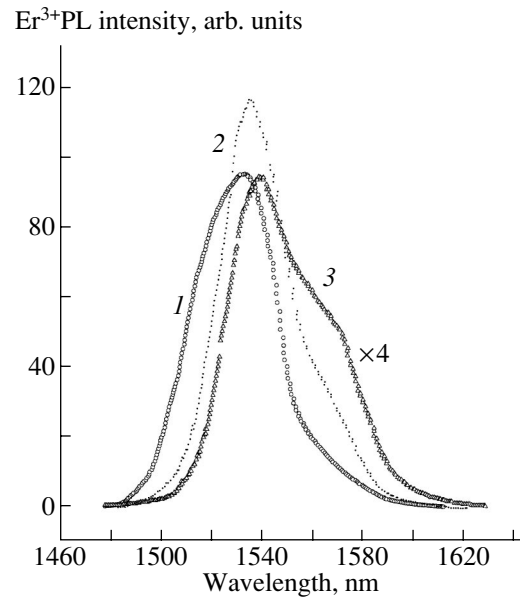


**Fig. 3.** Time-resolved spectra obtained at 77 K. The notation is the same as that in Fig. 2.

allow now that the extent of this deformation varies from one emitting center to another, we come to the multipole configuration of the erbium centers and, accordingly, to a structure of the spectrum that does not lend itself to unambiguous assignment.

(3) Curve 4 in Fig. 1 presents the spectrum of a sample that was not properly annealed to perform optical activation; more specifically, the sample was overannealed, which led to macrocrystallization. In addition to the overall weakening of the PL intensity, one observes an additional spectral broadening and a noticeable contribution from the Stark line at  $\approx 1695 \text{ nm}$ . The weakening of the PL intensity is most probably due to a sizable fraction of the erbium ions being expelled to intergrain voids, followed by their precipitation. The broadening of the spectrum should be assigned to the impact of the rigid crystalline matrix environment, which is capable of straining the  $\text{ErO}_x$  complexes that became incorporated in the GaN microcrystals.

### 3.2. $\text{Er}^{3+}$ Photoluminescence in *a-nc-GaN* as Derived from Its Time-Resolved Spectra and Decay Kinetics

The pulsed excitation technique offers the possibility of studying the  $\text{Er}^{3+}$  emission kinetics. We obtained both PL spectra at various gate delays  $\Delta$  after the termination of the pump pulse and PL decay curves at a number of emission wavelengths. This series of measurements was carried out on samples with the highest PL intensity. The PL decay in such samples lasted as long as 500–800  $\mu\text{s}$ . The time-resolved spectra were taken by properly delaying the 20- $\mu\text{s}$ -wide gate to fixed times  $\Delta = 5, 150, \text{ and } 450 \mu\text{s}$ . The results obtained for 300 K

are displayed in Fig. 2, and for 77 K, in Fig. 3. Measurements were also performed at 473 K. The relations recorded did not reveal any qualitative differences; for this reason, the data for 473 K are omitted. Nevertheless, to illustrate the pattern of the temperature behavior, Fig. 4 presents integral spectra, i.e., spectra measured without gating, for the three temperatures. As for the temperature dependence of the amplitude of the

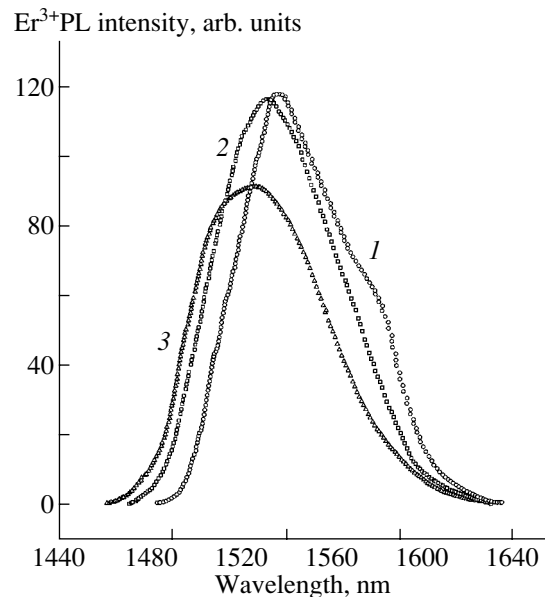


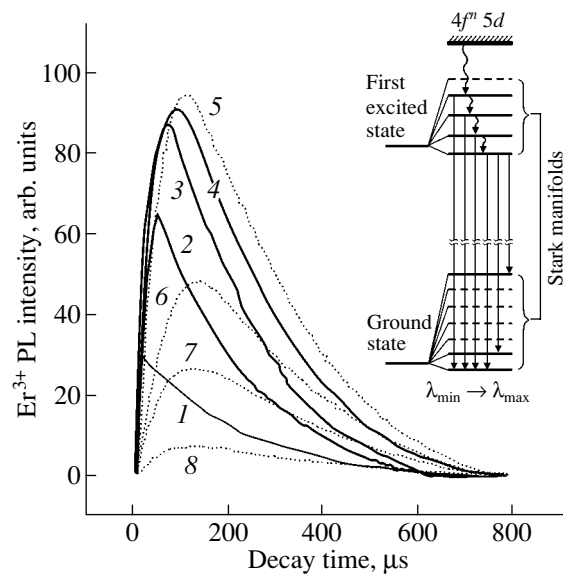
**Fig. 4.** Erbium photoluminescence spectra obtained at temperatures of (1) 77, (2) 300, and (3) 473 K.

intensity, it is seen to be practically absent over the range 77–300 K.

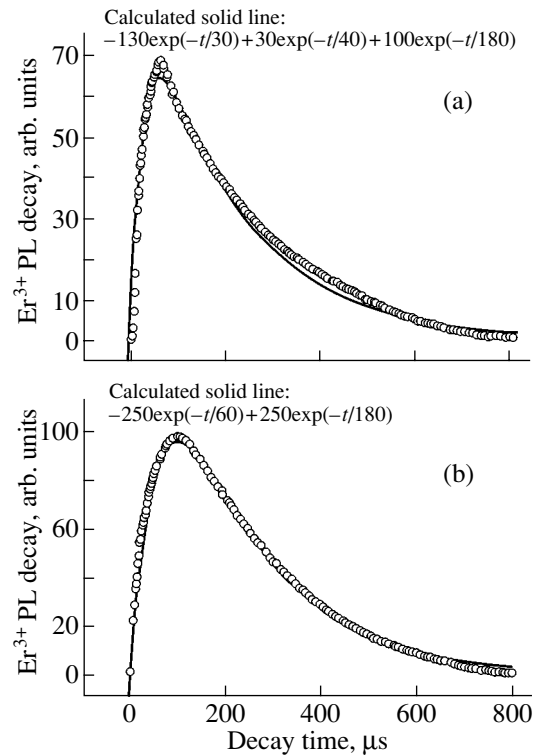
The main and most essential finding that follows from the above data is that the peak of maximum emission intensity shifts toward higher energies with both a decrease in the delay time and an increase in temperature. The magnitude of the shift amounts to 10 nm. Because the position of the emission lines of REM ions and, specifically, of  $\text{Er}^{3+}$  does not depend on the method of measurement or temperature, one may conclude that the observed shift is only apparent and is due to a redistribution of intensity between the emission peaks in the manifold of the Stark modes. This conclusion offers an additional and compelling argument for the validity of the earlier model, following which the broad PL spectrum is represented by a set of narrower band emitters (the Stark states).

Figure 5 displays the PL decay kinetics measured for different wavelengths at 300 K. The curves obtained at 77 and 473 K do not differ radically from the data collected for 300 K and, therefore, are omitted in the figure. Figure 5 reveals the presence of two competing processes, namely, a rise in intensity and a decay, which occur with different characteristic times  $\tau$ . The intensity rise and decay curves can be approximated generally by a sum of three exponentials,  $-A_1 \exp(-t/\tau_1) + A_2 \exp(-t/\tau_2) + A_3 \exp(-t/\tau_3)$ , where  $\tau_1$  is the time of the rise in intensity and  $\tau_2$  and  $\tau_3$  are the decay times. Figures 6a and 6b illustrate the fitting of experimental curves with three and two exponentials, respectively. The first case applies always to decay curves obtained at wavelengths of the high-energy wing of the spectrum, and the second case, to all other wavelengths. As follows from an analysis of the complete set of data obtained for the decay curves, the characteristic times vary, depending on the actual wavelength and temperature, within the following limits:  $\tau_1 \approx 10\text{--}30 \mu\text{s}$ ,  $\tau_2 \approx 10\text{--}60 \mu\text{s}$ , and  $\tau_3 \approx 70\text{--}200 \mu\text{s}$ . For  $\lambda \approx 1535 \text{ nm}$  (the wavelength corresponding to emission from the lowest  $^4I_{13/2}$  state), the times of the intensity rise,  $\tau_1$ , and decay,  $\tau_3$ , reach maximum values of 60 and 200  $\mu\text{s}$ , respectively. We can add that the decay kinetics follows a monomolecular law, as should be expected for intracenter emission.

The totality of the experimental data available on the PL decay kinetics and on the emission peak shift as a function of delay time  $\Delta$  can be understood in terms of the Stark splitting scheme of the  $^4I_{13/2}$  and  $^4I_{15/2}$  states proposed earlier. Consider the relaxation of the externally excited matrix–optically active erbium center system. The electron–hole pairs created by the laser undergo thermalization to the conduction band edge, their energy being transferred subsequently to the localized-state distribution in the conduction band tail. The dominant role played by localized states in the energy transfer to the erbium ions is supported by measurements of the PL excitation (PLE) function in the



**Fig. 5.** Erbium photoluminescence decay curves obtained at room temperature and various values of wavelength  $\lambda$ : (1) 1490, (2) 1500, (3) 1510, (4) 1520, (5) 1535, (6) 1550, (7) 1575, and (8) 1595 nm. Inset: diagram illustrating the radiative and nonradiative transitions between the Stark manifold states.



**Fig. 6.** Modeling of the intensity rise and decay curves by (a) a sum of three exponentials for hot transitions at  $\lambda \approx 1500 \text{ nm}$  and (b) a sum of two exponentials for transitions at  $\lambda \approx 1535 \text{ nm}$ .

${}^4I_{13/2} \longrightarrow {}^4I_{15/2}$  transitions. These measurements performed on *c*-GaN [15] show that the PLE function contains not only the resonance peaks originating from direct resonance photon absorption by the  $4f^{11}$  multiplet states but also an exponentially decaying tail, which extends from the edge of the conduction band deep into the band gap. This tail is due to nonresonant energy transfer to ions, apparently through *d*-*f* hybridization and excitation thermalization in the *f*-multiplet system. Rather than trying to delve into the physics underlying this process, which remains largely unknown theoretically, we stress only the point of most interest for the present study, namely, that the energy received by the matrix reaches the first excited state  ${}^4I_{13/2}$  and dissipates subsequently in radiative transitions to the ground state. In the crystal field, the first excited state  ${}^4I_{13/2}$  represents a manifold of Stark levels; hence, the excitation energy is absorbed by these levels. Moreover, if the energy dissipates through thermalization, the first to be reached by excitation are the upper Stark levels. If we accept this scenario, the appreciable contribution from the hot Stark transitions to the PL spectra observed by us, as well as the dominant part played by them in time-resolved spectra for  $\Delta \longrightarrow 0$ , become clear; namely, this is the result of a nonsteady-state process in which the population of the upper Stark states immediately after the termination of the pump pulse is nonequilibrium and approaches equilibrium only as the excitation undergoes thermalization over the Stark manifold of the  ${}^4I_{13/2}$  state. Thus, immediately after the termination of the excitation pulse, two competing processes occur simultaneously, namely, radiative transitions from the  ${}^4I_{13/2}$  Stark states to the  ${}^4I_{15/2}$  ground state and nonradiative transitions from the upper  ${}^4I_{13/2}$  Stark states to lower lying levels of the  ${}^4I_{13/2}$  Stark manifold.

The inset to Fig. 5 shows a simplified scheme of these transitions. This scheme offers the following explanation for the complex rise in PL intensity and decay kinetics observed at various wavelengths. For the shortest wavelengths in the high-energy wing of the spectrum, 1500–1520 nm, the intensity rise and decay process can be described by a sum of three exponentials. The first of them, with a characteristic time  $\tau_1$ , reflects the transfer of excitation energy to the erbium ion, including thermalization of the excitation over the *f* shell to the  ${}^4I_{13/2}$  Stark states. The second exponential, with characteristic time  $\tau_2$ , describes thermalization of the pump energy over the system of  ${}^4I_{13/2}$  Stark levels through successive nonradiative transitions from the uppermost Stark level of this manifold to a lower lying one, down to the lowest  ${}^4I_{13/2}$  state. The third exponential, with characteristic time  $\tau_3$ , describes the radiative process itself. The second term in the sum is actually responsible for the apparent acceleration of decay in the initial stage of the PL decay caused by the decrease in the population of the upper Stark levels resulting from nonradiative transitions. This mechanism remains oper-

ative until the population of the upper Stark levels decreases to the equilibrium value determined by the Boltzmann distribution. Now, considering emission kinetics from lower energy Stark states and, in the limit, from the lowest  ${}^4I_{13/2}$  state, we note that these states receive excitation energy in the nonsteady-state and nonequilibrium process in the course of its nonradiative relaxation from the upper Stark levels. Because this energy is transferred in a multistage pattern, the population of the lower levels slows down and  $\tau_1$  should increase, accordingly, by a factor of 2–4, exactly what is observed experimentally. Furthermore, the lowest  ${}^4I_{13/2}$  state is no longer capable of transferring the energy in a nonradiative manner. This results in the loss of the second term in the sum of the exponentials, so the emission process is now described by one characteristic constant only,  $\tau_3$ . Note that the values of  $\tau_3$  are approximately the same for all the  ${}^4I_{13/2}$  Stark levels. It should be stressed that the peak of emission from the lowest state is located at  $\approx 1535$  nm and is seen as the narrowest line with a half-width of  $\approx 25$  nm. Considered within our model, this comes as no surprise, because emission from the lowest  ${}^4I_{13/2}$  state corresponds to the conditions closest to equilibrium, in which the contribution of the hot transitions is minimal. We may also add that the emission spectra measured with long delay times are very close to those observed under stationary and equilibrium conditions realized under continuous low-power excitation ( $\approx 20$ – $50$  mW).

The temperature behavior of both the time-resolved spectra and the decay kinetics also agrees with the above scenario. As the temperature increases, the process of nonequilibrium occupation of the upper Stark levels is paralleled by an increase in the population of these levels through thermal excitation. Combined action of these two mechanisms gives rise to an increase in the intensity of the high-energy PL wing.

#### 4. CONCLUSIONS

(1) The main emission line of  $\text{Er}^{3+}$  ( ${}^4I_{13/2} \longrightarrow {}^4I_{15/2}$ ) in the *a*-nc-GaN matrix has been shown to be of Stark nature.

(2) The relaxation of pulsed excitation energy for a pulse power of  $100 \text{ kW/cm}^2$  was established to be a nonequilibrium process for times of at least up to  $100 \mu\text{s}$ .

(3) The PL intensity rise and decay process occurring in nonequilibrium conditions is described, in a first approximation, by three exponentials, the first of which characterizes the mechanism of excitation transfer; the second, the mechanism of nonradiative energy relaxation from the upper to lower Stark levels; and the third, the radiative process itself.

The characteristic time of the radiative process for optimized samples can be as long as  $\approx 200 \mu\text{s}$ .

## REFERENCES

1. A. Polman, *J. Appl. Phys.* **82** (1), 1 (1997).
2. M. S. Bresler, O. B. Gusev, E. I. Terukov, I. N. Yassievich, B. P. Zakharchenya, V. I. Emel'yanov, B. V. Kamenev, P. K. Kashkarov, E. A. Konstantinova, and V. Yu. Timoshenko, *Mater. Sci. Eng. B* **81**, 52 (2001).
3. A. A. Andreev, *Fiz. Tverd. Tela (St. Petersburg)* **44** (2), 239 (2002) [*Phys. Solid State* **44**, 248 (2002)].
4. S. B. Aldabergenova, M. Albrecht, A. A. Andreev, C. Inglefield, J. Viner, V. Yu. Davydov, P. C. Taylor, and H. P. Strunk, *J. Non-Cryst. Solids* **283** (1–3), 173 (2001).
5. A. A. Andreev, *Fiz. Tverd. Tela (St. Petersburg)* **45** (3), 395 (2003) [*Phys. Solid State* **45**, 419 (2003)].
6. A. Terrasi, G. Franzo, S. Coffa, F. Priolo, F. D. Acapito, and S. Mobilio, *Appl. Phys. Lett.* **70** (13), 1712 (1997).
7. S. Nakamura and G. Fasol, *The Blue Laser Diode. GaN-Based Light Emitters and Lasers* (Springer, Berlin, 1997), p. 129.
8. A. A. Kaminskiĭ, *Laser Crystals* (Nauka, Moscow, 1975), pp. 25–27.
9. S. Kim, S. J. Rhee, D. A. Turnbull, E. E. Reuter, X. Li, J. J. Coleman, and S. G. Bishop, *Appl. Phys. Lett.* **71** (2), 231 (1997).
10. S. B. Aldabergenova, M. Albrecht, H. P. Strunk, J. Viner, P. C. Taylor, and A. A. Andreev, *Mater. Sci. Eng. B* **81** (1–3), 29 (2001).
11. M. Ishii, Y. Tanaka, I. Ishikawa, S. Komuro, T. Morikawa, and Y. Aoyagi, *Appl. Phys. Lett.* **78** (2), 183 (2001).
12. M. Ishio and Y. Komukai, *Appl. Phys. Lett.* **97** (7), 934 (2001).
13. H. Przybylinska, W. Jantsch, Yu. Suprun-Belevitch, M. Stepikhova, L. Palmetshofer, G. Hendorfer, A. Kozanecki, R. J. Wilson, and B. J. Sealy, *Phys. Rev. B* **54** (4), 2532 (1996).
14. D. E. Wortman, C. A. Morrison, and J. L. Bradshaw, *J. Appl. Phys.* **82** (5), 2580 (1997).
15. Myo Thaik, U. Hommerich, R. N. Schwartz, R. G. Wilson, and J. M. Zavada, *Appl. Phys. Lett.* **71** (18), 2641 (1997).

*Translated by G. Skrebtsov*

---

**SEMICONDUCTORS  
AND DIELECTRICS**

---

## Frequency Dispersion of Dielectric Coefficients of Layered TlGaS<sub>2</sub> Single Crystals

S. N. Mustafaeva

*Institute of Physics, National Academy of Sciences of Azerbaijan, pr. Narimanova 33, Baku, 1143 Azerbaijan*  
*e-mail: itpcht@itpcht.ab.az*

Received June 30, 2003

**Abstract**—Frequency dependence of the dissipation factor  $\tan\delta$ , the permittivity  $\epsilon$ , and the ac conductivity  $\sigma_{ac}$  across the layers in the frequency range  $f = 5 \times 10^4$ – $3 \times 10^7$  Hz was studied in layered TlGaS<sub>2</sub> single crystals. A significant dispersion in  $\tan\delta$  was observed in the frequency range  $10^6$ – $3 \times 10^7$  Hz. In the range of frequencies studied, the permittivity of TlGaS<sub>2</sub> samples varied from 26 to 30. In the frequency range  $5 \times 10^4$ – $10^6$  Hz, the ac conductivity obeyed the  $f^{0.8}$  law, whereas for  $f > 10^6$  Hz  $\sigma_{ac}$  was proportional to  $f^2$ . It was established that the mechanism of the ac charge transport across the layers in TlGaS<sub>2</sub> single crystals in the frequency range  $5 \times 10^4$ – $10^6$  Hz is hopping over localized states near the Fermi level. Estimations yielded the following values of the parameters: the density of states at the Fermi level  $N_F = 2.1 \times 10^{18}$  eV<sup>-1</sup> cm<sup>-3</sup>, the average time of charge carrier hopping between localized states  $\tau = 2$   $\mu$ s, and the average hopping distance  $R = 103$  Å. © 2004 MAIK “Nauka/Interperiodica”.

### 1. INTRODUCTION

TlGaS<sub>2</sub> single crystals are typical representatives of layered semiconductors and attract a lot of attention due to their interesting physical properties. These properties include strong anisotropy of the electronic parameters related to special features in the crystalline structure. Layered crystals usually contain structural defects, such as vacancies and dislocations. The presence of these defects results in a high density of localized states near the Fermi level. The states localized in the band gap are responsible for most electronic processes occurring in semiconductors. Both dc and ac charge transport proceeds via these localized states. In [1], it was experimentally established that, in layered TlGaS<sub>2</sub> single crystals at temperatures  $T \leq 200$  K, the dc conductivity both along and across the natural layers have variable-range hopping over localized states near the Fermi level. Using the experimental results on the dc conductivity of TlGaS<sub>2</sub> single crystals along and across the layers, the density of states at the Fermi level  $N_F$  was estimated to be  $2.5 \times 10^{18}$  and  $2.0 \times 10^{18}$  eV<sup>-1</sup> cm<sup>-3</sup>, respectively; i.e., the density of states is rather high. From this point of view, TlGaS<sub>2</sub> single crystals are interesting objects for study in ac electric fields. Experimental data on the frequency-dependent conductivity of TlGaS<sub>2</sub> single crystals have been reported in the literature [2, 3]. In [2], a value of  $9.0 \times 10^{18}$  eV<sup>-1</sup> cm<sup>-3</sup> was obtained for  $N_F$ , which exceeds the value of  $N_F$  that we found by measuring  $\sigma_{dc}$  across the TlGaS<sub>2</sub> layers [1]. In [4], the results of permittivity measurements for a TlGaS<sub>2</sub> single crystal at a frequency of  $10^5$  Hz were

described. Quite recently, observations of the dispersion of the permittivity and conductivity of TlGaS<sub>2</sub> crystals measured at frequencies of  $10^2$ ,  $10^3$ ,  $10^4$ , and  $10^6$  Hz were reported [5]. Whereas in [2] the TlGaS<sub>2</sub> ac conductivity measured in the frequency range  $10^5$ – $10^7$  Hz was described by a power law ( $f^{0.8}$ ), the  $\sigma_{ac}(f)$  dependence measured in [5] in the frequency range  $10^2$ – $10^6$  Hz was rather weak. In view of these inconsistencies, we experimentally studied the frequency-dependent dielectric parameters of layered TlGaS<sub>2</sub> single crystals and the mechanisms of ac charge transport.

The layered TlGaS<sub>2</sub> single crystals studied had a rather high electrical resistance  $\rho$  at room temperature. The value of  $\rho$  was  $2 \times 10^7$   $\Omega$  cm along the natural layers and  $\rho = 7 \times 10^9$   $\Omega$  cm across the layers.

### 2. EXPERIMENTAL TECHNIQUES

Measurements of the dielectric coefficients of TlGaS<sub>2</sub> single crystals were performed at fixed frequencies in the range  $5 \times 10^4$ – $3 \times 10^7$  Hz by the resonant method using a TESLA BM560  $Q$  meter. TlGaS<sub>2</sub> samples formed flat capacitors whose plane was perpendicular to the crystalline  $C$  axis. The thickness of a TlGaS<sub>2</sub> single crystalline layer was 0.05–0.06 cm, and the capacitor plate area was 0.5–0.7 cm<sup>2</sup>. For electrical measurements, the samples were placed in a specially constructed screened cell. An ac electric field was applied across the natural layers of TlGaS<sub>2</sub> single crystals. The amplitude of the applied field corresponded to the Ohmic region of the current–voltage characteristics



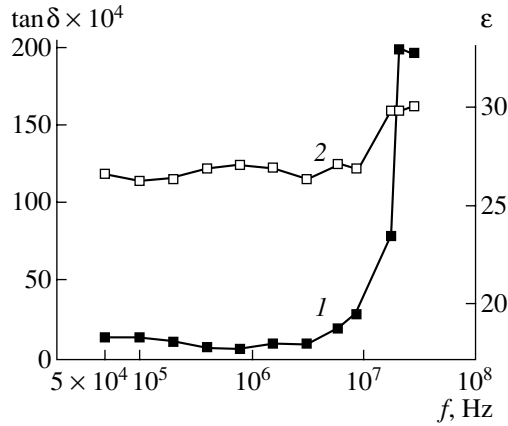


**Fig. 1.** Frequency dependences of (1) the dissipation factor and (2) the permittivity of a TiGaS<sub>2</sub> single crystal at  $T = 300$  K.

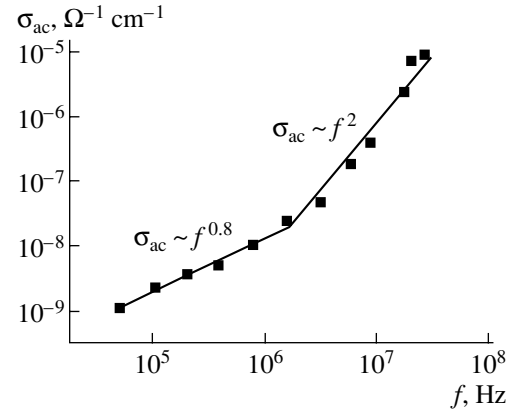


**Fig. 2.** Frequency dependence of the ac conductivity of a TiGaS<sub>2</sub> single crystal at  $T = 300$  K.

of TiGaS<sub>2</sub> samples. All measurements were performed at  $T = 300$  K. The accuracy in determining the resonance capacitance and the quality factor  $Q = 1/\tan\delta$  of the measuring circuit was limited by errors related to the resolution of the device readings. The accuracy of the capacitor graduation was  $\pm 0.1$  pF. The reproducibility of the resonance position was  $\pm 0.2$  pF in capacitance and  $\pm(1.0-1.5)$  scale divisions in quality factor.

### 3. EXPERIMENTAL RESULTS AND DISCUSSION

Figure 1 shows the experimental frequency dependence of the dissipation factor  $\tan\delta$  for a TiGaS<sub>2</sub> single crystal (curve 1). The  $\tan\delta(f)$  curve has two branches: a steadily descending one (in the frequency range  $5 \times 10^4-10^6$  Hz) and a rising one at  $f > 10^6$  Hz. A significant dispersion in  $\tan\delta$  is observed for  $f > 10^7$  Hz. At room temperature, where TiGaS<sub>2</sub> single crystals exhibit appreciable ac conductivity, conductivity loss becomes the main dielectric loss mechanism.

We also measured the electric capacitance of TiGaS<sub>2</sub> samples in the frequency range  $5 \times 10^4-3 \times 10^7$  Hz; the capacitances were 21–24 pF. The maximum capacitance of TiGaS<sub>2</sub> samples corresponded to a frequency of  $\sim 3 \times 10^7$  Hz. Using the measured capacities of TiGaS<sub>2</sub> samples, we calculated the permittivity  $\epsilon$  at different frequencies; the permittivity varied from 26 to 30 (curve 2 in Fig. 1); i.e., no appreciable dispersion of  $\epsilon$  was observed in the whole frequency range investigated.

It was shown in [2] that the permittivity of TiGaS<sub>2</sub> samples is frequency-independent in the interval  $10^4-10^7$  Hz,  $\epsilon = 22 \pm 2$ . In [4], the TiGaS<sub>2</sub> permittivity at a frequency of  $10^5$  Hz was found to be  $\epsilon = 25$ . In [5], the TiGaS<sub>2</sub> permittivity varied in the limits  $\epsilon \approx 20-38$  in the frequency range  $10^2-10^6$  Hz; the dispersion of  $\epsilon$  was observed in the range  $10^2-10^4$  Hz, whereas for  $f >$

$10^4$  Hz the permittivity  $\epsilon$  was practically frequency-independent.

Figure 2 shows the experimentally measured frequency dependence of the ac conductivity of a TiGaS<sub>2</sub> single crystal at  $T = 300$  K. The ac conductivity  $\sigma_{ac}$  varies as  $f^{0.8}$  in the frequency range  $5 \times 10^4-10^6$  Hz and follows a quadratic law  $\sigma_{ac} \sim f^2$  in the range  $f = 10^6-3 \times 10^7$  Hz. The  $\sigma_{ac} \sim f^{0.8}$  dependence indicates that the mechanism of charge transport is hopping over localized states near the Fermi level [6]. The magnitude of this conductivity is much greater than that of the dc hopping conductivity of TiGaS<sub>2</sub> [1]. This charge transport mechanism is characterized by the following expression obtained in [7]:

$$\sigma_{ac}(f) = (\pi^3/96)e^2kTN_F^2a^5f[\ln(v_{ph}/f)]^4, \quad (1)$$

where  $e$  is the elementary charge,  $k$  is the Boltzmann constant,  $N_F$  is the density of localized states at the Fermi level,  $a = 1/\alpha$  is the localization length,  $\alpha$  is the decay parameter of the wave function of a localized charge carrier,  $\Psi \sim e^{-\alpha r}$ , and  $v_{ph}$  is the phonon frequency. Using expression (1), we can calculate the density of states at the Fermi level from the measured values of the conductivity  $\sigma_{ac}(f)$ . For  $T = 300$  K,  $v_{ph} = 10^{12}$  Hz, and  $f = 10^6$  Hz, we obtain from Eq. (1) the following relation:

$$N_F^2 = 2.1 \times 10^{50} \sigma_{ac}(f) a^{-5}, \quad (2)$$

where the localization length is measured in angstroms,  $\sigma_{ac}$  in  $\Omega^{-1} \text{ cm}^{-1}$ , and  $N_F$  in  $\text{eV}^{-1} \text{ cm}^{-3}$ . The quantity  $N_F$  for TiGaS<sub>2</sub> calculated using Eq. (2) is  $2.1 \times 10^{18} \text{ eV}^{-1} \text{ cm}^{-3}$  with the localization radius chosen as  $14 \text{ \AA}$ , in analogy with the GaS single crystal [8], which is a double analog of TiGaS<sub>2</sub>. This value of  $N_F$  agrees well with the value  $N_F = 2 \times 10^{18} \text{ eV}^{-1} \text{ cm}^{-3}$  found in experiments on the dc conductivity across the TiGaS<sub>2</sub> layers [1].

The theory of ac hopping conductivity provides an opportunity to determine the average time  $\tau$  of charge carrier hopping from one localized state to another using the formula [6]

$$\tau^{-1} = v_{\text{ph}} \exp(-2R\alpha), \quad (3)$$

where  $R$  is the average hopping distance. Using the experimental  $\sigma_{\text{ac}}(f)$  dependence,  $\tau^{-1}$  is found to be  $5 \times 10^5$  Hz ( $\tau^{-1}$  is defined as the average frequency for which  $\sigma_{\text{ac}}$  obeys the  $f^{0.8}$  law). This corresponds to the average hopping time  $\tau = 2$   $\mu\text{s}$ . The average hopping distance calculated by the formula

$$R = (1/2\alpha) \ln(v_{\text{ph}}/f) \quad (4)$$

is  $R = 103$   $\text{\AA}$ , which is approximately seven times greater than the average distance between localization centers. From the measurements of the TlGaS<sub>2</sub> dc conductivity, the average value of  $R$  was found to be 108  $\text{\AA}$  [1].

In contrast to the results from [2], where  $\sigma_{\text{ac}}$  follows the  $f^{0.8}$  law in the whole frequency range  $10^5$ – $10^7$  Hz investigated, in our experiments, as indicated above, the quadratic dependence  $\sigma_{\text{ac}} \sim f^2$  was observed for  $f > 10^6$  Hz (Fig. 2). It was shown in [6] that the conductivity proportional to  $f^2$  is related to optical transitions in semiconductors and is dominant at high frequencies. Previously, we also observed the quadratic law  $\sigma_{\text{ac}} \sim f^2$  in TlInS<sub>2</sub> single crystals for  $f > 10^6$  Hz [9].

#### 4. CONCLUSIONS

Thus, the results of the study of the dc [1] and ac conductivities across the TlGaS<sub>2</sub> layers are in good agreement. The dc conductivity at  $T \leq 200$  K and the ac conductivity for  $f \leq 10^6$  Hz are both due to charge carrier hopping over localized states near the Fermi level

( $N_{\text{F}} = 2.0 \times 10^{18}$  eV<sup>-1</sup> cm<sup>-3</sup>). The average hopping distances are 108 and 103  $\text{\AA}$  for  $\sigma_{\text{dc}}$  and  $\sigma_{\text{ac}}$ , respectively. The values of the TlGaS<sub>2</sub> permittivity agree with the results from [2, 4, 5], and the frequency dependences  $\sigma_{\text{ac}} \sim f^{0.8}$  and  $\sigma_{\text{ac}} \sim f^2$  observed for TlGaS<sub>2</sub> in the ranges  $f = 5 \times 10^4$ – $10^6$  Hz and  $f > 10^6$  Hz, respectively, are similar to those obtained for the isostructural TlInS<sub>2</sub> compound in [9].

#### REFERENCES

1. S. N. Mustafaeva, V. A. Aliev, and M. M. Asadov, Fiz. Tverd. Tela (St. Petersburg) **40** (4), 612 (1998) [Phys. Solid State **40**, 561 (1998)].
2. A. M. Darvish, A. É. Bakhyshev, and V. I. Tagirov, Fiz. Tekh. Poluprovodn. (Leningrad) **11** (4), 780 (1977) [Sov. Phys. Semicond. **11**, 458 (1977)].
3. A. É. Bakhyshev, R. S. Samedov, S. Bules, and V. I. Tagirov, Fiz. Tekh. Poluprovodn. (Leningrad) **16** (1), 161 (1982) [Sov. Phys. Semicond. **16**, 98 (1982)].
4. R. A. Aliev, K. R. Allakhverdiev, A. I. Baranov, N. R. Ivanov, and R. M. Sardarly, Fiz. Tverd. Tela (Leningrad) **26** (5), 1271 (1984) [Sov. Phys. Solid State **26**, 775 (1984)].
5. A. U. Sheleg, K. V. Iodkovskaya, and N. F. Kurilovich, Fiz. Tverd. Tela (St. Petersburg) **45** (1), 68 (2003) [Phys. Solid State **45**, 69 (2003)].
6. N. F. Mott and E. A. Davis, *Electronic Processes in Non-Crystalline Materials* (Clarendon, Oxford, 1971; Mir, Moscow, 1974).
7. M. Pollak, Philos. Mag. **23**, 519 (1971).
8. V. Augelli, C. Manfredotti, R. Murri, R. Piccolo, and L. Vasanelli, Nuovo Cimento B **38** (2), 327 (1977).
9. S. N. Mustafaeva, M. M. Asadov, and V. A. Ramazan-zade, Fiz. Tverd. Tela (St. Petersburg) **38** (1), 14 (1996) [Phys. Solid State **38**, 7 (1996)].

Translated by I. Zvyagin

---

SEMICONDUCTORS  
AND DIELECTRICS

---

# New Data on RC Radiation Centers Obtained from a Photoluminescence Study of Cubic Boron Nitride Irradiated with Electrons of Near-Threshold Energies

E. M. Shishonok\* and J. W. Steeds\*\*

\**Institute of Solid State and Semiconductor Physics, Belarussian Academy of Sciences,  
ul. Brovki 17, Minsk, 220072 Belarus  
e-mail: shishonok@ifttp.bas-net.by*

\*\**Bristol University, Bristol, Great Britain*

Received October 28, 2003

**Abstract**—New data on radiation centers of the RC series are obtained by studying the photoluminescence of boron nitride cubic crystals irradiated with electrons of energies of 150 to 300 eV and annealed in vacuum at temperatures of 400 to 800°C. Changes in the fine structure of no-phonon lines from these centers were observed as the electron energy reached the “threshold” value or after annealing. These changes are likely to be associated with the response of a vacancy (which is a structural element of RC defects) to differently directed uniaxial stresses. The fine structure of the no-phonon line from the RC3 center is less sensitive to threshold effects and relaxes more easily during annealing in comparison with those from the RC1 and RC2 centers. New data are obtained on the fine structure of phonon replicas of no-phonon lines from RC centers; this structure is due to interaction of the corresponding electron transitions with lattice phonons of energies of 0.1 to 0.125 eV. © 2004 MAIK “Nauka/Interperiodica”.

## 1. INTRODUCTION

Cubic boron nitride (cBN) is well known as a wide-band-gap semiconductor; this compound is similar to diamond but excels it in many characteristics, such as chemical resistance and ability to emit electrons and to form materials exhibiting both types of electrical conductivity. Cubic boron nitride offers higher resistance to radiation than does diamond; therefore, it can be used for devices operating under high-radiation conditions. Unfortunately, the properties of this compound have not been adequately studied.

Studies into the effect of irradiation with 4.5-MeV electrons,  $\gamma$  rays, and ions on the defect structure of cubic boron nitride were performed in [1, 2]. Cathodoluminescence (CL) spectra of irradiated samples revealed the presence of a series of luminescence centers (irrespective of the quality of the samples) characterized by no-phonon lines at 545 (RC1), 577 (RC2), and 624 nm (RC3). These centers were found to be Frenkel pairs differing in the mutual orientation of nitrogen vacancies and nitrogen interstitials. The temperatures of annealing after which the RC lines in CL spectra of cBN samples irradiated with ions and electrons disappeared completely were different. For samples irradiated with electrons, the annealing temperature was approximately 1000 K. It was also shown in [1, 2] that all no-phonon lines of RC centers in samples irradiated with ions can be only doublets. The experimental profiles of these doublets were most closely fit-

ted by three Gaussians. The reason for no-phonon line splitting was associated with the Jahn–Teller effect.

Another luminescence center, RC4, was observed in CL spectra of cBN only after irradiation of samples with ions and was not included in the RC series mentioned above.

The RC2 and RC2–RC3 centers were detected in CL spectra of polycrystals [3] and (111) faces of cBN single crystals [4] after the samples were subjected to a pressure of up to 3.5 GPa.

The effect of irradiation with electrons of near-threshold energies (150–300 keV) on the photoluminescence (PL) of single-crystal cubic boron nitride was studied in [5], and a new radiation-induced (apparently interstitial) defect, BN1, was detected. This defect was characterized by a no-phonon luminescence line at 376.5 nm [5], and its total photoluminescence spectrum was similar in structure to the CL band of the center observed at 3.188 eV in diamond [6]. The formation of BN1 defects in cBN was observed to occur after the samples were irradiated with electrons with an energy of 230 keV, which is equal to the threshold energy for displacements of intrinsic atoms.

In this work, we studied the photoluminescence of cubic boron nitride irradiated with electrons of near-threshold energies. New data are obtained on the structure of the luminescence spectra of RC centers in cBN, which are of both fundamental and experimental interest. Particular attention is given to the differences in the defect structure between cBN samples irradiated with

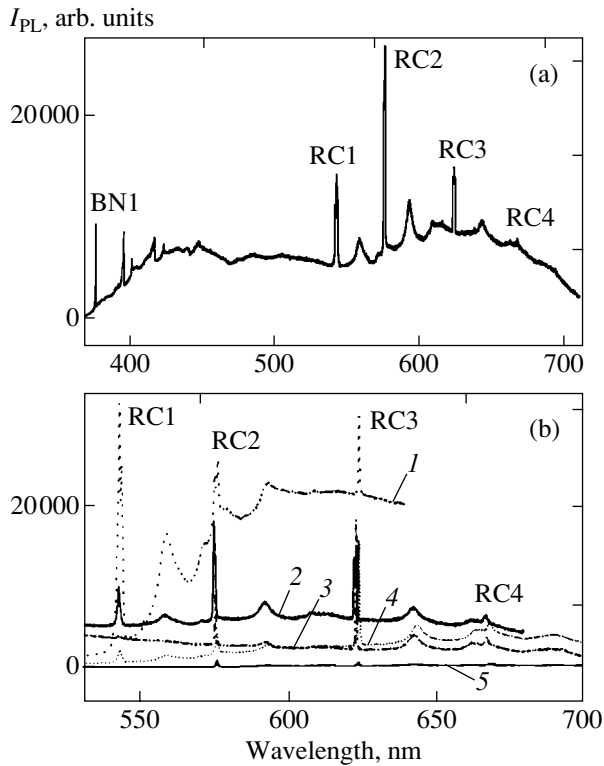


**Fig. 1.** (a) PL spectrum obtained from a region of a cubic boron nitride single crystal irradiated with 230-keV electrons and (b) the lines of RC centers in PL spectra obtained from different regions of a cBN crystal irradiated with electrons with energies of (1) 300, (2) 230, (3) 200, (4) 170, and (5) 150 keV.

electrons of low (150–300 keV) and high (4.5 MeV) energies.

## 2. EXPERIMENTAL

PL spectra of samples of cubic boron nitride were recorded with a Renishaw-1000 spectrometer at temperature  $T = 6$  K using a helium cryostat and a laser operating at a wavelength of 488 nm. The surface of a crystal was scanned in the discrete mode to form a map and in the line-scan mode along directions crossing the irradiated and unirradiated areas of the surface, which made it possible to study the irradiated and nonirradiated materials simultaneously.

Optically transparent cBN single crystals 200 to 400  $\mu\text{m}$  in size were studied. The crystals were synthesized from hexagonal boron nitride (hBN) at high pressures and temperatures using catalysts that ensured an excess of boron or nitrogen in the crystals (light smoky gray or light yellow in color, respectively). Different areas of the single-crystal surfaces were irradiated with electrons (directly in a Philips EM430 TEM electron microscope) of different energies in a single experiment (300, 230, 200, 170, 150 keV) [5] at room and liquid-helium temperatures (only at 230 keV), and then

the samples were annealed in vacuum at temperatures of 400 to 800°C.

## 3. RESULTS AND DISCUSSION

It was established that cubic boron nitride crystals irradiated with electrons of near-threshold and high energies differed not only in the luminescence centers formed but also in the influence of irradiation on the parameters of no-phonon lines of RC centers, including the energy position of the maxima and the structure of the lines.

### 3.1. The Formation of RC Defects

It was found in [5] that irradiation of nitrogen-enriched cBN single crystals with low-energy electrons does not bring about the formation of RC defects. This fact can be explained by radiation-induced defects being compensated for by the defects that were in cBN (due to departures from stoichiometry) before the irradiation. An analogous phenomenon was observed in electron-irradiated diamond; more specifically, the GR-1 luminescence center was observed in CL spectra of diamond [7] only after a critical radiation dose was reached or after the electron energy was increased in order to increase the defect production rate. For example, RC defects were observed in all cBN samples irrespective of their quality when the electron energy was increased up to 4.5 MeV.

All centers of the RC series (RC1, RC2, RC3, and RC4, corresponding to PL lines at 543.9, 576.8, 623.1, and 667.3 nm, respectively) were represented in PL spectra from five regions of a boron-enriched crystal irradiated with electrons of various energies (150, 170, 200, 250, 300 keV; dose of  $2 \times 10^{20} \text{ cm}^{-2}$ ); however, the intensity distributions of no-phonon lines of these centers and their energy positions were different in these regions (Fig. 1).

The association between the formation of RC defects and the stoichiometry of cBN substantiates the assumption (made in [1, 2, 5]) that these defects are intrinsic.

Figure 1a shows a typical PL spectrum from a transparent boron-enriched cBN single crystal irradiated with 230-keV electrons at room temperature. No-phonon lines and their phonon replicas corresponding to the BN1, RC1, RC2, RC3, and RC4 centers are observed in the spectrum.

In this study, the RC4 center was observed to appear in the PL spectrum only after cubic boron nitride was irradiated with electrons of energies of 150 to 230 keV at room temperature, which contradicts the CL data [2]. This center was not observed in PL spectra of cBN samples irradiated with low-energy electrons at liquid-helium temperatures and with 300-keV electrons at room temperature, which can be due to differences in structure and stability between the RC1–RC3 and RC4

defects. We note that the latter center is represented by a weak no-phonon line.

### 3.2. The Structure of Phonon Replicas of No-Phonon Lines of the RC Centers

The Renishaw-1000 spectrometer enabled us to resolve and analyze the structure of the PL spectra of RC centers in more detail than that of the CL spectra obtained earlier.

It was found [2] that electron transitions in the RC1–RC4 centers involve phonons with an energy of 64 meV presumably localized on a nitrogen vacancy. In this study, we established that phonon replicas of the no-phonon lines of all RC centers are similar in structure; however, their structure was found to be more complex than assumed earlier. Each of the four no-phonon lines is accompanied by a phonon wing consisting of two wide bands, which also have a structure (see, e.g., the PL spectrum of the RC2 center in Fig. 2). It was found that the structure of the first band of each of the four phonon wings is associated not only with a phonon with an energy of 64 meV but also with RC phonons with energies of 47–48 and 71–75 meV, whose interaction with electron transitions is less strong. Note that electron transitions occurring in the GC-1 and GC-2 centers (nitrogen and boron vacancies bound to identical defects of unknown nature [8]) interact not only with phonons with energies of 64 and 56 meV, respectively, but also with phonons with an energy of 48 meV.

The second band in the phonon wings of the no-phonon lines of all RC centers has a fine structure, whose resolution depends on the sample. In addition to the PL spectrum of the RC2 center, Fig. 2 shows the no-phonon line and its phonon wing (the first phonon replica) for the BN1 center [5], with the energy measured from the maximum of the no-phonon line of the corresponding center. It can be seen that the fine structures of the phonon wings correlate well with each other in the range 0.1–0.125 eV.

It is likely that the high-energy part of the phonon wing of the BN1 no-phonon line reproduces the phonon density of states of cubic boron nitride, with the features of the fine structure corresponding to singular points of the phonon spectrum, as was the case for an analog of the BN1 center in the luminescence spectrum of diamond (at 3.188 eV) [6]. Therefore, electron transitions in the RC centers strongly interact with phonons with energies of 100 to 125 meV, which are very likely lattice phonons.

Annealing of the single crystals at temperatures of 400 to 800°C did not change the structure of the phonon wings of the RC center no-phonon lines.

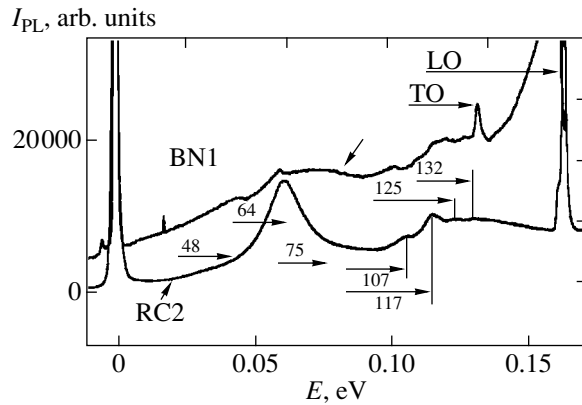


**Fig. 2.** PL spectra of the BN1 (first phonon replica) and RC2 centers in which the energy (in millielectronvolts) is reckoned from the position of the maximum of the no-phonon line.

### 3.3. The Structure of the No-Phonon Lines of RC Centers

In this study, we established that the structure of the no-phonon lines of RC centers in electron-irradiated cBN is sensitive to the electron energy and annealing temperature.

The no-phonon lines of RC centers are observed in the form of doublets in PL spectra of cBN, in contrast to CL spectra, after cBN is irradiated with electrons of even near-threshold energies, which is likely due to the differences in the conditions of excitation of PL and CL, as was the case with the GR-1 center in diamond [9]. However, there is a relation between the splitting of a no-phonon line and the electron energy in the energy range under study (Fig. 3). As the electron energy increases from 150 to 200 keV (in this range, BN1 defects form in small proportion or do not form at all), the no-phonon lines of the RC2, RC3, and RC4 centers (in the form of singlets) shift to higher energies by 2.3 (RC2) and 2.2 meV (RC3). Irradiation with 230-keV electrons (producing BN1 defects in quantity) causes a higher energy (wider) component to split off from the no-phonon lines of the RC2 and RC3 centers by 2.1 meV. The no-phonon line of the RC1 center does not shift noticeably, but a component splits off from it by  $\Delta = 1.9$  meV at the same electron energy. As the electron energy is increased up to 300 keV (where BN1 defects no longer form), the no-phonon lines of all RC centers tend to shift to lower energies. A 400°C annealing of a cBN single crystal irradiated with electrons of threshold energy (230 keV) causes broadening of all no-phonon lines and smoothes their structure but does not change the energy position of the maxima of their components. Subsequent heat treatment at 650°C makes the no-phonon lines narrower than their initial profiles by decreasing the distance between the energy positions of their components. Annealing at 800°C increases the distance between the components of the no-phonon line of the RC1 center, and this line splits;

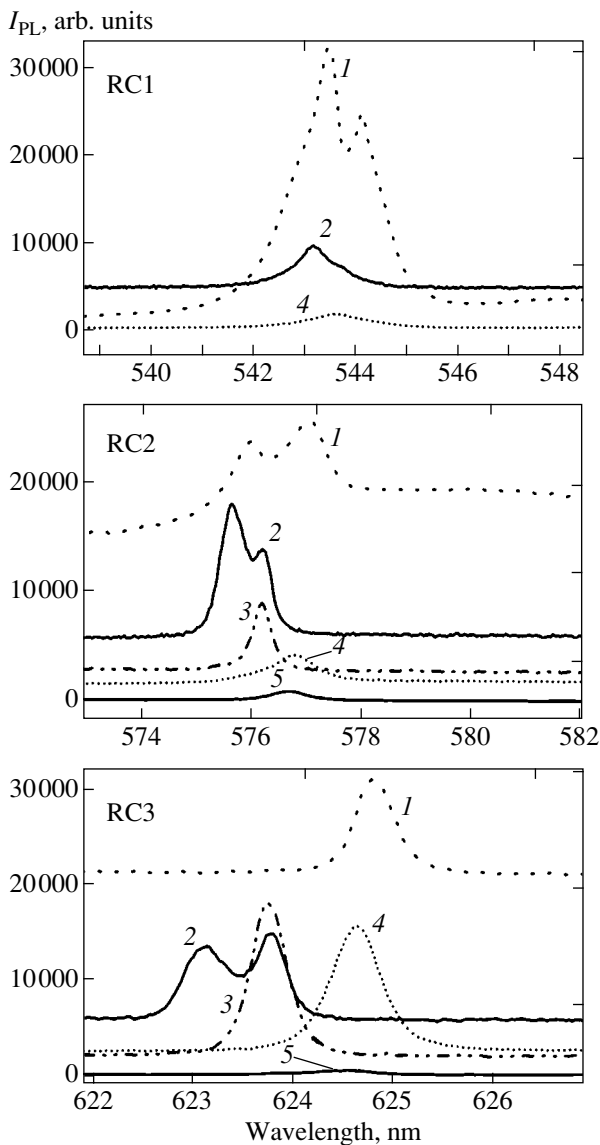


**Fig. 3.** No-phonon lines of the RC1–RC3 centers in PL spectra obtained from different regions of a cBN single crystal irradiated with electrons with energies of (1) 300, (2) 230, (3) 200, (4) 170, and (5) 150 keV.

the low-energy components of the no-phonon lines of the RC2 and RC3 centers increase in intensity, whereas the high-energy components decrease in intensity (as an example, Fig. 4 shows the no-phonon line of the RC3 center). In contrast to an earlier report, annealing at 850°C does not cause a noticeable decrease in the intensity of the no-phonon lines of any RC centers.

Note that the case where only low-energy components are observed in the structure of no-phonon lines (RC2, RC3) is characteristic of the crystal regions irradiated with electrons of energies below or above the threshold value (i.e., in the absence of BN1 defects) and of crystals annealed at 800°C.

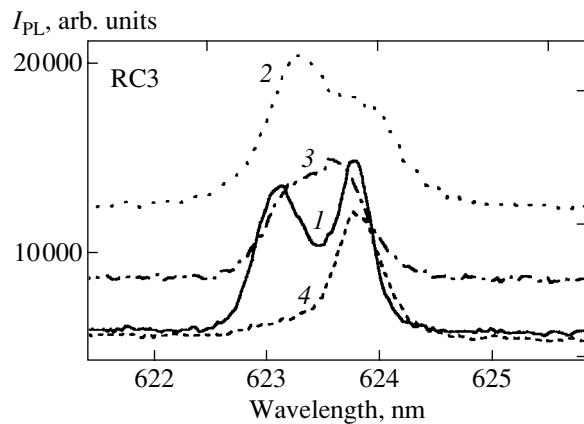


**Fig. 4.** No-phonon line of the RC3 center in PL spectra obtained from a region of a cBN single crystal (1) irradiated with electrons with an energy of 230 keV and then annealed at temperatures of (2) 400, (3) 650, and (4) 800°C.

Since the no-phonon lines of all RC centers were asymmetric, we not only considered their doublet structure but also performed a thorough analysis of their fine structures by decomposing them into components using the ORIGIN-5 software package. The optimal decomposition corresponded to the minimal error  $\Delta I$  in fitting the experimental no-phonon line profile and to the minimum possible number of components used for the given line profile.

The number of components used to fit the no-phonon lines of RC centers (6, 4, 3, 2) depended on the RC center, electron energy, and annealing temperature (Fig. 5). Six components were used to decompose the no-phonon line of the RC1 center observed in PL spectra after irradiation with electrons with energies of 300 and 230 keV, and three components, for electron energies of 170 and 150 keV or after annealing at 650–800°C. After irradiation with electrons with energies of 300, 230, and 170 keV, the no-phonon line of the RC2 center was decomposed into 4, 4, and 3 components, respectively, and after annealing at  $T = 400, 650,$  or  $800^\circ\text{C}$ , into 3, 2, and 2 components, respectively. The number of components used to decompose the no-phonon line of the RC3 center was 3, 2, and 2 after irradiation with electrons with energies of 230, 200, and 170 keV, respectively. For samples irradiated with electrons with an energy of 230 keV and then annealed at 400, 650, or 800°C, the fine structure of the no-phonon line of the RC3 center was decomposed into 3, 3, and 2 components, respectively.

#### 4. DISCUSSION

The symmetry of defects can be lower than the symmetry of their position in the perfect crystal, e.g., because of a spontaneous distortion lowering the symmetry and resulting in a more stable configuration of a defect (the Jahn–Teller effect). The symmetry group of

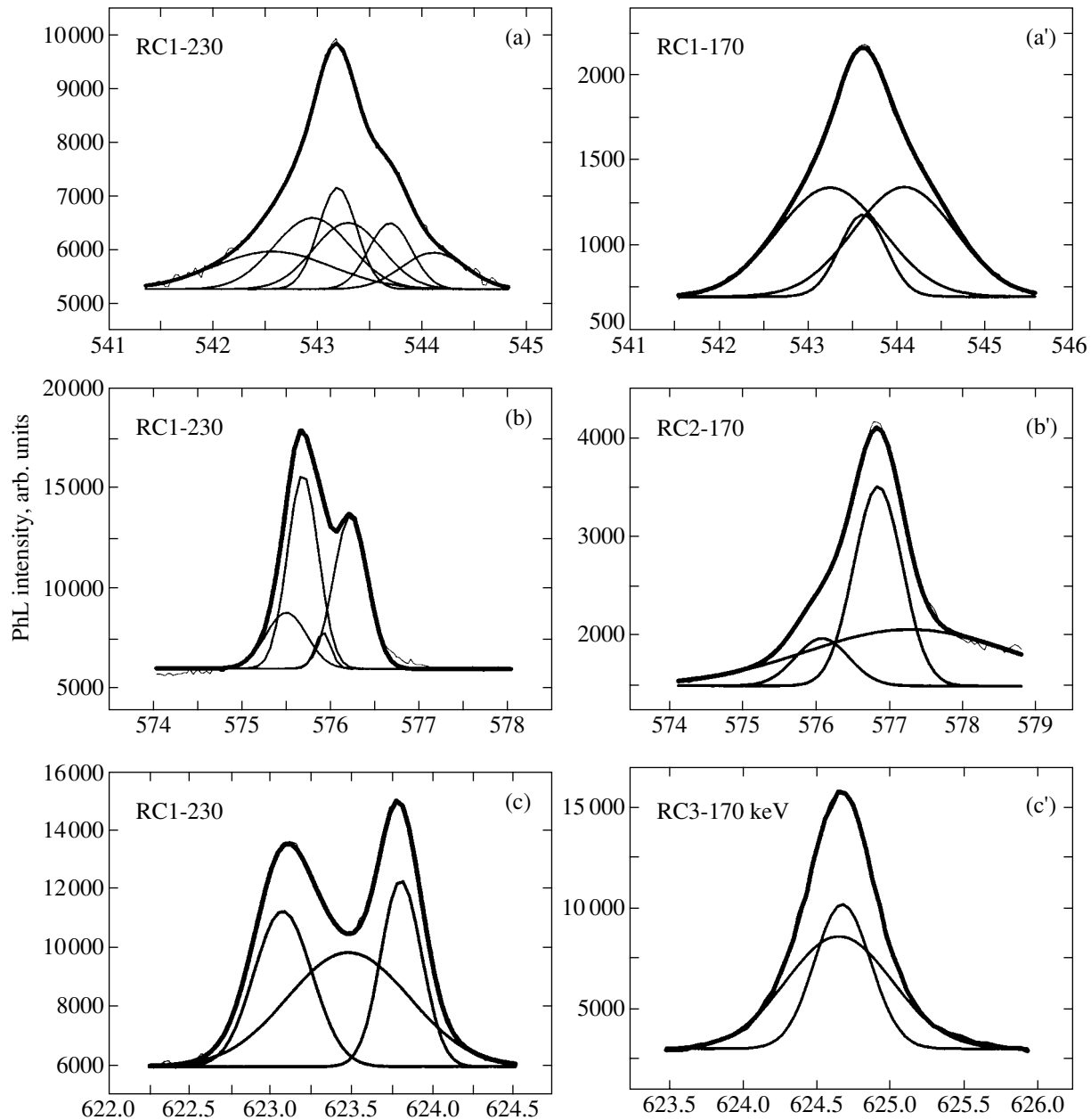


**Fig. 5.** Experimental and calculated shapes of the no-phonon lines of (a, a') the RC1, (b, b') RC2, and (c, c') RC3 centers in PL spectra obtained from regions of a cBN single crystal irradiated with electrons with energies of (a, c) 230 and (a', c') 170 keV. The Gaussians into which the spectral lines were decomposed are shown by thin lines.

a distorted configuration is a subgroup of the original group. For example, in the case of diamond, the  $T_d$  group (vacancy GR1) can reduce to its (tetragonal)  $D_{2d}$ , (orthorhombic)  $C_{2v}$ , and (trigonal)  $C_{3v}$  subgroups. A distortion causes a splitting of degenerate electronic states of the defect (depending on the character of the distortion) or a shift of the corresponding energy levels. The magnitude of the shift is a measure of the amount of distortion [10].

The splittings of energy levels of a defect of symmetry  $T_d$  caused by tetragonal, trigonal, and orthorhombic distortions can be obtained by applying uniaxial stresses to the defect along the  $\langle 100 \rangle$ ,  $\langle 111 \rangle$ , and  $\langle 110 \rangle$  directions, respectively.

Each of the subgroups mentioned above is characterized by electronic states that are different from the ground and excited states corresponding to the  $T_d$  group. For example, in the case of an orthorhombic dis-

tortion of the GR1 vacancy, the ground state  $E$  is doubly degenerate and the excited state  $T_2$  is triply degenerate, while in the case of tetragonal and trigonal distortions the excited state  $T_2$  is doubly degenerate [11]. In the former case, the fine structure of the no-phonon line (GC1) consists of a sextuplet of lines, while in the latter case it consists of a quadruplet, as observed in the absorption and cathodoluminescence spectra of diamond [9, 11].

In addition to the Jahn–Teller effect, the state of a defect can be affected by other defects randomly distributed over the lattice. In this case, the no-phonon line associated with electron transitions between the degenerate (unsplit) ground and excited states of a defect belonging, say, to the  $T_d$  group should be broadened. This conclusion is supported by the fact that the no-phonon line of the RC3 center consists of two components centered at the same energy and having different half-widths (Fig. 5c') and that all no-phonon lines in the PL spectrum are highly broadened after annealing of  $c$ BN single crystals at 400°C (curve 2 in Fig. 4).

Based on the results of the analysis of the structure of the no-phonon lines of vacancy-type RC centers, the known data on the vacancy defect  $V^\circ$  (GR1) in irradiated diamond, and the similarity between crystal lattices of diamond and cubic boron nitride, the following conclusions can be drawn regarding radiation-induced centers in cubic boron nitride.

The fine structure of the no-phonon lines of RC centers changes after irradiation with electrons of the threshold energy for atomic displacement from their lattice sites over a distance smaller than the lattice parameter of  $c$ BN. Vacancies that are located at sites of  $T_d$  symmetry and belong to RC defects are affected differently (depending, in particular, on the charge state) by directed and uniaxial stresses arising in the  $c$ BN lattice, which can be considered a manifestation of different types of distortion of the vacancies (or other defects substituting for them) [10]. As in the case of diamond [11], the RC1 no-phonon line can split into six lines when the vacancy is located along a  $\langle 110 \rangle$  direction with respect to the source of its distortion and reduces its symmetry to orthorhombic. The RC2 no-phonon line can split into four components when the vacancy is located along the  $\langle 100 \rangle$  or  $\langle 111 \rangle$  directions relative to the source of its distortion and reduces its  $T_d$  symmetry to tetragonal and trigonal, respectively. The source of distortion that reduces the symmetry of a vacancy belonging to an RC defect can be another element of the structure of the defect situated near the vacancy.

The no-phonon lines corresponding to unperturbed vacancies of  $T_d$  symmetry should be single lines. The triplet structure of the no-phonon lines of the RC1 and RC2 centers (observed after irradiation of  $c$ BN with electrons of energies below the threshold value) and of the RC3 center (observed when the electron energy is equal to the threshold value) indicates that the doubly degenerate ground states of defects with  $T_d$  symmetry

split and that the defect centers are affected by stresses randomly distributed over  $c$ BN. The changes in the fine structure of no-phonon lines caused by “threshold” effects characterize the end effect of directed stresses on the vacancies belonging to RC defects. Judging from the number of components into which the no-phonon lines were decomposed, the vacancy belonging to the RC3 center is affected by threshold and subthreshold stresses to a smaller extent than the vacancies in other RC centers.

Annealing at temperatures of 650 to 800°C causes RC centers in the “threshold” state to relax to the “subthreshold” state, the RC3 center being more mobile in this respect (Fig. 4).

After irradiation with electrons with an energy of 4.5 MeV, stresses are randomly distributed over the material due to secondary displacements, with the consequence that all RC defects can be in the unperturbed states for which the no-phonon lines are in the low-energy position. These lines are either unsplit or their profiles can be closely fitted by three Gaussians [2].

## 5. CONCLUSIONS

(1) The RC1–RC4 centers can be produced in  $c$ BN by irradiating a sample with electrons of near-threshold energies (cathodoluminescence spectra reveal RC4 centers only after irradiating a sample with ions).

(2) The no-phonon lines of RC centers in PL spectra of  $c$ BN irradiated with electrons of near-threshold energies can be doublets, in contrast to CL spectra, where the no-phonon lines are not doublets.

(3) The electron energy during irradiation affects the position of the no-phonon lines of the RC1–RC4 centers; lines with the longest wavelength are observed after irradiation by electrons with energies above the threshold value.

(4) Electron transitions in RC centers strongly interact with the 64-meV phonon and lattice phonons with energies of 0.1 to 0.125 eV and weakly interact with the 48- and 75-meV phonons.

(5) The no-phonon lines of the RC1–RC3 centers have a fine structure, which changes as the electron energy reaches a threshold value; it is likely that, at this threshold energy, the symmetry of the vacancies belonging to RC defects is reduced to orthorhombic symmetry with the axis along  $\langle 110 \rangle$  (for the RC1 center) and to tetragonal or trigonal symmetry with the axis along  $\langle 100 \rangle$  and  $\langle 111 \rangle$ , respectively (for the RC2, RC3 centers); this change in the vacancy symmetry is due to directed stresses, which can be caused by an element of the RC defect structure situated near the vacancy. These conjectures can be useful in modeling the structure of RC defects.

(6) For samples of cubic boron nitride irradiated by electrons with threshold energies, annealing at temperatures of 650 to 800°C causes relaxation of the defect



structure and the structure of the RC center no-phonon lines to their "subthreshold" state.

(7) The fine structure of the no-phonon line of the RC3 center is less sensitive to threshold and subthreshold effects and relaxes more easily during annealing than do the structures of the RC1 and RC2 no-phonon lines.

#### ACKNOWLEDGMENTS

This study was supported by the Royal Society Fellowship (2001).

#### REFERENCES

1. A. M. Zaitsev, A. A. Melnikov, E. M. Shishonok, and V. B. Shipilo, *Phys. Status Solidi A* **94**, 125 (1985).
2. A. M. Zaitsev, Doctoral Dissertation (Belorus. Gos. Univ., Minsk, 1992).
3. V. B. Shipilo, E. M. Shishonok, A. M. Zaitsev, A. A. Malnikov, and A. I. Olekhnovich, *Phys. Status Solidi A* **108**, 431 (1988).
4. V. B. Shipilo, E. M. Shishonok, A. M. Zaitsev, N. G. Anichenko, and L. S. Unyarkha, *Neorg. Mater.* **26** (8), 1651 (1990).
5. E. M. Shishonok and J. W. Steeds, *Diamond Relat. Mater.* **11** (10), 1774 (2002).
6. A. M. Zaitsev, *Phys. Rev. B* **61** (19), 12909 (2000).
7. C. D. Clark and J. Walker, *Proc. R. Soc. London, Ser. A* **334**, 241 (1973).
8. V. B. Shipilo, A. M. Zaitsev, E. M. Shishonok, and A. A. Mel'nikov, *Zh. Prikl. Spektrosk.* **45** (4), 601 (1986).
9. A. T. Collins, *J. Phys. C: Solid State Phys.* **20** (13), 2027 (1978).
10. M. Lanno and J. Bourgoin, *Point Defects in Semiconductors, Experimental Aspects* (Springer, New York, 1981; Mir, Moscow, 1985).
11. G. Davies, *Proc. R. Soc. London, Ser. A* **36**, 507 (1974).

*Translated by Yu. Epifanov*

---

---

SEMICONDUCTORS  
AND DIELECTRICS

---

---

## Silicon Dioxide Modification by an Electron Beam

L. A. Bakaleinikov, M. V. Zamoryanskaya, E. V. Kolesnikova,  
V. I. Sokolov, and E. Yu. Flegontova

*Ioffe Physicotechnical Institute, Russian Academy of Sciences,  
Politekhnicheskaya ul. 26, St. Petersburg, 194021 Russia*

*e-mail: zam@mail.ioffe.ru*

Received October 13, 2003

**Abstract**—The overheating temperature of a microvolume of silicon dioxide produced by bombardment by a high specific-power electron beam has been estimated. Calculations showed that the maximum temperature to which a microvolume of silicon dioxide is overheated can be as high as 1200°C for an electron beam current of 100 nA. The variation in the cathodoluminescence characteristics of amorphous silica with different contents of hydroxyl groups was studied for various electron beam specific-power levels. The impact of a high specific-power electron beam was shown to create additional lattice defects up to the formation of silicon clusters.  
© 2004 MAIK “Nauka/Interperiodica”.

### 1. INTRODUCTION

The SiO<sub>2</sub>/Si structure is a basic system currently employed in the development of modern microelectronics, and it is unlikely to be replaced by a different system in the near future.

To achieve a higher efficiency of SiO<sub>2</sub>/Si systems in optoelectronics, various methods of their fabrication are currently being tried. The radiative properties of this system depend on the structural features and geometric parameters of its components. Such systems can be produced by a variety of means, for instance, by deposition of off-stoichiometric silicon dioxide films, oxidation of porous silicon, etc. Among these techniques is modification of silicon dioxide by a high-energy electron beam of a high specific power [1]. In this case, silicon clusters are produced from silicon dioxide irradiated by electrons. Silicon clusters form as a result of irradiation and local heating of silicon dioxide by the electron beam, which brings about a variation in the cathodoluminescence (CL) characteristics of the microvolume.

This communication reports on a study of the variation in the CL properties of amorphous silica bombarded by a high-energy electron beam at different specific-power levels.

CL spectra of impurity-free amorphous silicon dioxide contain bands related to structural defects, such as the non-bridging oxygen atom and the twofold-coordinated silicon atom. The non-bridging oxygen atom produces a luminescence band peaking at 1.9 eV, which corresponds to the absorption bands at 4.75 and 2.0 eV [2, 3]. The other intrinsic defect in silicon dioxide is responsible for the 4.3- and 2.65-eV luminescence bands, which are excited at 5.0 eV. The most probable model of this defect is a silicon atom with only two

neighboring oxygen atoms, i.e., a twofold-coordinated silicon atom [4, 5]. These emission bands are excited in a CL spectrum, because the electron beam energy (1–30 keV) is many times larger than the band-gap width of silicon dioxide.

The CL properties of the SiO<sub>2</sub>/Si system vary strongly in the presence of silicon clusters. Silicon is an indirect-gap semiconductor with weak luminescence. It emits in the IR region at 1.1 eV, but silicon microcrystals with linear dimensions on the order of a few nanometers produce luminescence bands from 1.4 to 1.8 eV [6]. The reason for this lies in the fact that the band gap width of silicon depends on the geometric size of the silicon crystals [6]. The presence of silicon clusters in silicon dioxide is always accompanied by a strong variation in the luminescence properties and the appearance of an intense emission in the green region of the spectrum with a maximum at 2.2–2.3 eV [7].

In CL studies, one can vary the electron beam diameter and electron current over a broad range. This enables one to vary the specific power of the electron beam to within several orders of magnitude. If the specific power of the electron beam is high enough, the sample microvolume heats. Heating can produce additional structural defects in the irradiated microvolume.

Investigation of the temperature fields generated by an electron beam in various samples provides information of value for interpreting experimental data obtained in CL studies. Because the experiments were performed at the maximum attainable focusing of the electron beam (the beam diameter did not exceed 0.1 μm), the region of heat release was small, which makes experimental measurement of the overheating temperature a very difficult problem. This necessitated a theoretical estimation of the silicon dioxide overheating temperature under electron beam impact.

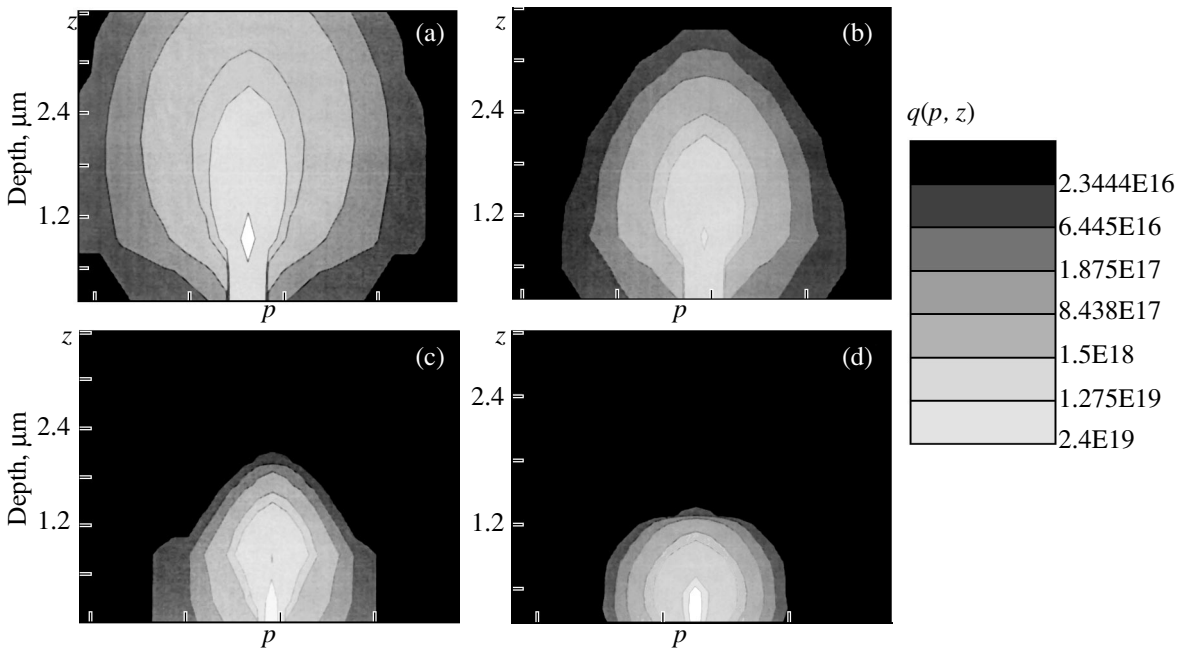


**Fig. 1.** Monte Carlo calculation of the spatial stationary energy loss distribution in silica for various beam energies: (a) 20, (b) 15, (c) 10, and (d) 5 keV. The energy loss densities are in units of J/(m<sup>3</sup> s K).

## 2. THEORETICAL ESTIMATION OF TEMPERATURE FIELDS IN SILICON DIOXIDE

To estimate the effect of sample heating under electron beam irradiation, we calculated the temperature distribution in silicon dioxide by the technique proposed in [8, 9]. The distribution of the energy loss density per electron was calculated by the Monte Carlo method in terms of the single-scattering model. For the differential cross section of elastic scattering, the Mott cross section was taken [10], while the inelastic interaction was computed based on optical data with the algorithm proposed in [11].<sup>1</sup>

The code followed the trajectories of only the primary electrons, which resulted in a certain error in the distribution of the energy loss but did not affect its total value. The simulation took into account the carbon layer present on the sample surface.

We made use of the technique proposed in [9] to obtain the spatial distribution of the energy loss density  $q(\rho, z)$  (here,  $z$  is the depth, and  $\rho$  is the radius) for an electron beam current of 100 nA and beam energies  $E_0 = 5, 10, 15,$  and  $20$  keV (Fig. 1).

By approximating the shape of the heat generation region with a half-ellipsoid, one can take into account the differences between the lateral and longitudinal source dimensions. While the real shape naturally does not coincide with this approximation, this approach

provides an estimate for the maximum overheating temperature [9].

We considered the problem of uniform heat generation in the volume of a half-ellipsoid with semi-axes  $a$  and  $b$ . The temperature field is given by the equation

$$\Delta T = -q/\kappa, \tag{1}$$

where  $\Delta$  is the Laplace operator,  $\kappa$  is the thermal conductivity coefficient, and  $q$  is the energy loss density (Fig. 1),

$$q = \begin{cases} q_0, & \frac{\rho^2}{b^2} + \frac{z^2}{a^2} \leq 1 \\ 0, & \frac{\rho^2}{b^2} + \frac{z^2}{a^2} > 1. \end{cases} \tag{2}$$

The semi-axes  $a$  and  $b$  were twice the half-widths  $\sigma_z$  and  $\sigma_\rho$ , respectively, of the Gaussian distribution  $A \exp(-z^2/\sigma^2 - \rho^2/\sigma_\rho^2)$  approximating the energy loss density distribution.

We obtained estimates for the maximum overheating temperature for the case of heat generated in a prolate ellipsoid of revolution ( $a > b$ ),

$$T_{\max} = \frac{q_0}{4k} \frac{ab^2}{\sqrt{a^2 - b^2}} \ln \frac{a + \sqrt{a^2 - b^2}}{a - \sqrt{a^2 - b^2}} \tag{3}$$

<sup>1</sup>The data on the differential electron scattering cross sections computed by the present authors can be found at [www.ioffe.ru/ES](http://www.ioffe.ru/ES).

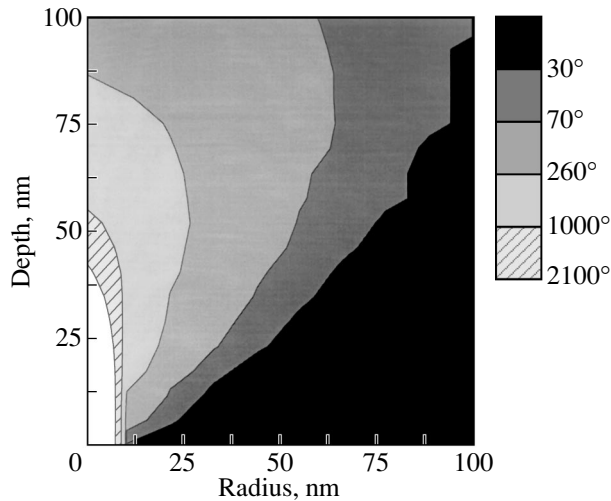


**Fig. 2.** Temperature field isotherms for sources of semielliptical shape. The figures at the isotherms are the overheating temperatures relative to the sample temperature that were reached in interaction with an electron beam with an energy of 5 eV and with a current of 100 nA.

and in an oblate ellipsoid of revolution ( $a < b$ ),

$$T_{\max} = \frac{q_0}{2k} \frac{ab^2}{\sqrt{b^2 - a^2}} \operatorname{arccot} \frac{a}{\sqrt{b^2 - a^2}}. \quad (4)$$

Figure 2 shows the spatial distribution of the overheating temperature for a focused beam with an electron energy of 5 keV and a beam current of 100 nA. We readily see that, at the point of electron beam impact on the sample, the temperature rises 2100°C above the sample temperature. We calculated the overheating temperature taking into account the finite beam diameter (0.1  $\mu\text{m}$ ); it was found to be 1200°C for a region about 40 nm in diameter. Indeed, as the electron beam current is increased to 100 nA, the optical microscope reveals irreversible surface changes in the silicon dioxide sample. A crater forms in the region of electron interaction with the sample. It is known that, for silicon islands to form, it is sufficient to heat silicon oxide in vacuum to 400–600°C [12]. It thus follows that, at an electron current of 100 nA bombarding silicon oxide, defects associated with oxygen deficiency should form in it up to the creation of silicon clusters.

Since the overheating temperature depends linearly, in a first approximation, on the probing electron current (the relation of Castaing [13]), it may be conjectured that the structure of silicon oxide should not undergo pronounced modification at currents on the order of 10–15 nA, because the overheating temperature would not be in excess of 200°C.

In this connection, we studied primarily the CL spectra of silicon dioxide obtained at electron beam currents of 15 nA, which contained emission lines of weakly modified silicon dioxide. The next in line were the changes in the CL spectra observed with currents of

100 nA. We also studied the dependence of the intensity of the main CL bands on exposure time to a 100-nA electron beam.

### 3. EXPERIMENTAL TECHNIQUE

The effect produced by a focused electron beam incident on silica was studied with a Camebax electron microprobe analyzer equipped with two optical spectrometers [14].

To broaden the range of probing the CL properties of a sample, measurements were conducted in various operational regimes of the analyzer:

(1) stationary regime, in which a beam bombards the sample continuously to obtain an emission spectrum;

(2) time-resolved mode, in which two spectra are measured at each point of the sample, with the first spectrum being obtained under irradiation of the sample by an electron beam and the second, with a given time delay (0.5  $\mu\text{s}$  to a few seconds) after the deflection of the beam;

(3) study of the emission band decay dynamics; this mode permits measurement of the emission band intensity versus time following the termination of the excitation;

(4) measuring the dependence of luminescence band intensity on the sample exposure time to the electron beam.

The stationary and band decay dynamics spectra were obtained at an electron energy of 15 keV and a beam current of 100 nA. The dependence of the luminescence band intensity on exposure time was studied at the same electron energy and beam current. The time resolved spectra were taken at an electron energy of 15 keV and beam current of 15 nA at a gating delay of 200  $\mu\text{s}$ .

We studied CL spectra of two types of  $\text{SiO}_2$  glasses containing different amounts of the hydroxyl group OH: KU with an OH content of 2400–3000 ppm and KI with an OH content of 1–2 ppm.

The content of other impurities in the glasses studied was below 3 ppm. Before the measurements, the glass samples were polished and a carbon layer about 200  $\text{\AA}$  thick was applied to them to improve the sample conductivity.

### 4. MAIN RESULTS AND DISCUSSION

Characteristics of the CL emission bands were obtained for the KU glass. Figure 3 presents typical time-resolved CL spectra of amorphous silica measured at an electron beam current of 15 nA and energy of 15 keV with a time delay of 200  $\mu\text{s}$ .

The CL spectra of the sample exhibit bands characteristic of such defects as the non-bridging oxygen atom [the (1.90  $\pm$  0.05) eV band] and the twofold-coordinated silicon atom [the (2.65  $\pm$  0.05) eV band]. The

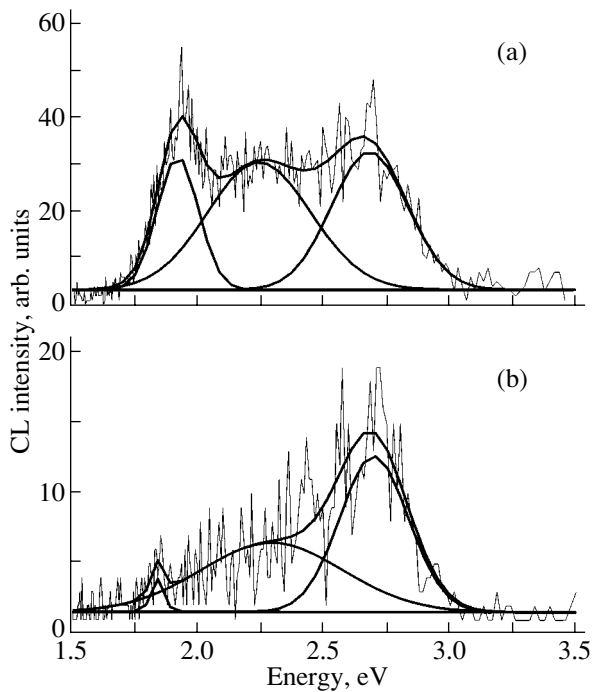


**Fig. 3.** Time-resolved CL spectra of KU-type glass: (a) spectrum obtained under sample irradiation with an electron beam and (b) spectrum measured with a delay of 200  $\mu$ s after termination of the sample excitation.

spectrum also has a shoulder in the green region. To derive the spectral characteristics of the bands, the CL spectrum was unfolded into three constituent bands using the ORIGIN code. The observed bands were assumed to have Gaussian shape. Such a deconvolution allows us to interpret the green shoulder as a band peaking at  $(2.20 \pm 0.05)$  eV and having a half-width of 0.4 eV. The spectrum taken with a time delay of 200  $\mu$ s clearly reveals a band at 2.65 eV and a shoulder in the green region. Deconvolution of this spectrum showed that this shoulder can also be traced to a band with a maximum at 2.2 eV. The 1.9-eV band in this spectrum is not observed. This implies that this band decays in a time shorter than the gate delay time. The strongest band, peaking at 2.65 eV, has the longest decay time; therefore, its intensity in the delayed spectrum is maximum.

These conclusions were supported by measurements of the decay time dynamics of the bands observed in the spectrum. As seen from Fig. 4, the band decay dynamics has an exponential character,  $I = I_0 \exp(-t/\tau)$ , where  $I_0$  is the band intensity during the sample irradiation by the electron beam,  $t$  is the time elapsed from the instant the beam deflects from the sample, and  $\tau$  is the decay time of the luminescence band.

Thus, we obtained the following spectral characteristics of the main CL bands for amorphous silicon dioxide. For the 1.9-eV band, the decay time is  $(28 \pm 1)$   $\mu$ s

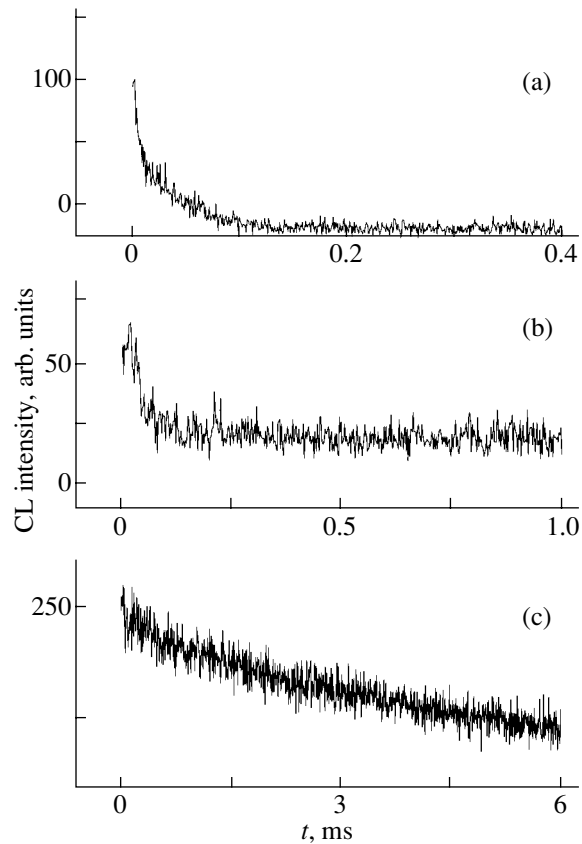


**Fig. 4.** Intensity decay dynamics obtained for some bands in the CL spectrum of KU-type glass: (a) band at 1.9 eV, (b) band at 2.3 eV, and (c) band at 2.65 eV.

and its half-width is  $(0.13 \pm 0.04)$  eV. For the 2.2-eV band, these parameters are  $(59 \pm 3)$   $\mu$ s and  $(0.40 \pm 0.05)$  eV. The band at 2.65 eV is comparatively the longest lived; its decay time was found to be  $(4.9 \pm 0.2)$  ms and its half-width,  $(0.30 \pm 0.05)$  eV. Because the half-widths and decay times for different bands are different, this can only mean that they are due to different defects.

Increasing the specific excitation power brings about a noticeable change in the CL spectra. We raised the excitation power in this study by increasing the electron beam current by an order of magnitude. Figure 5 displays spectra of two types of glass obtained at an electron current of 100 nA and an energy of 15 keV. A comparison of the spectra taken at 15 and 100 nA reveals that an increase in beam current results in a substantial growth in the intensity of the 2.2-eV band relative to the other bands. Comparing CL spectra of glasses of different types shows that the KU glass (OH group content 2400–3000 ppm) produces a stronger luminescence than does the KI glass, which indicates that the number of defects is larger in  $\text{SiO}_2$  with a higher concentration of OH groups. This accounts for

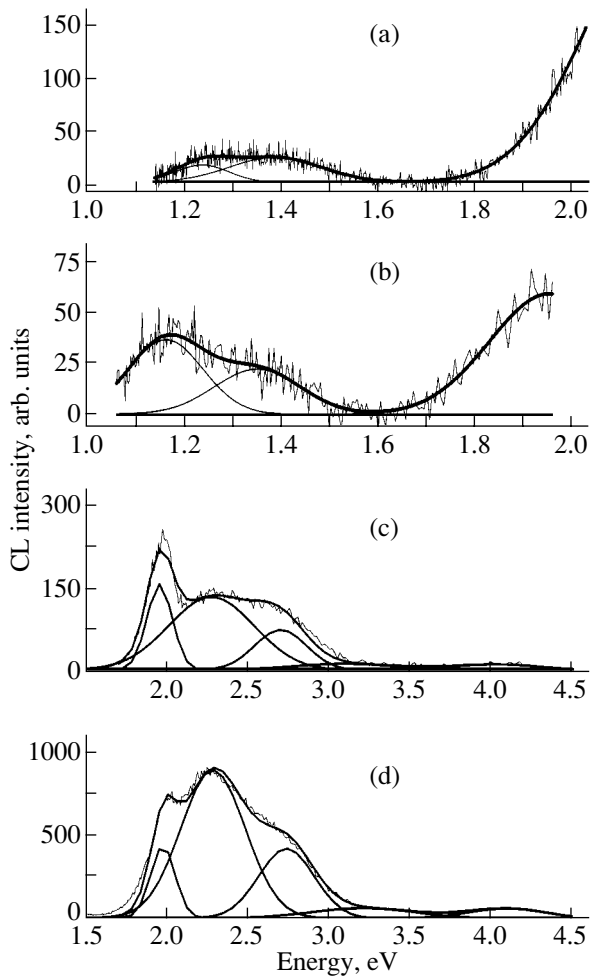


**Fig. 5.** CL spectra of glasses obtained in the IR and visible regions: (a) KI glass, IR spectrum; (b) KU glass, IR spectrum; (c) KI glass, visible spectrum; and (d) KU glass, visible spectrum.

the lower intensity of the KI glass, because its structure contains less defects.

The spectral changes are the most pronounced in the IR region of glass emission. At low specific-excitation powers, no emission bands appear in the IR range (1.0–1.8 eV). As the electron current is increased, weak emission bands peaking at 1.1 and 1.35 eV emerge in the spectra. The positions of the maxima were found by unfolding the spectra into two constituent bands. The shoulder with the maximum at 1.35 eV may be due either to the emission of amorphous silicon or to the formation of silicon clusters [15].

Figure 6 presents the dependences of the CL band intensity on the sample exposure time to the electron beam. The 1.9- and 2.65-eV bands in the KI glass (with a low OH group content) reach maximum intensity 200 s after the modification begins, thus indicating an increase in the number of defects in the volume under study. The next to attain maximum intensity are the

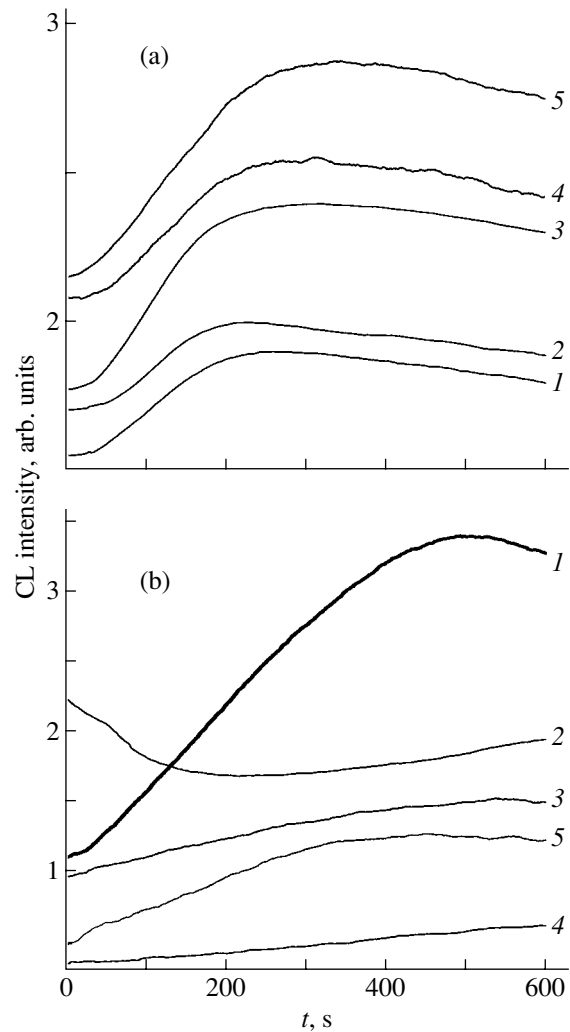


**Fig. 6.** CL intensity plotted vs. exposure time to an electron beam for (a) KI glass and (b) KU glass: (1) band peaking at 2.65 eV, (2) 1.9 eV, (3) 2.2 eV, (4) 1.4 eV, and (5) 1.1 eV.

bands at 1.35 and 2.3 eV (after 300 s). This can be attributed to the formation of crystalline or amorphous silicon clusters of small size. The last band to reach maximum intensity (in 350 s) is the one at 1.1 eV, which signals the formation of silicon clusters of a fairly large size.

The pattern is different for the KU glass with a high OH content. All bands grow in intensity with increasing electron irradiation time in the same way, except for the band at 1.9 eV. However, for all bands, it takes a longer time to reach the maximum than in the case of the silicon dioxide with a low OH group content. The intensity of the 1.9-eV band decreases and comes to a minimum 200 s after the modification begins. This may mean that first the defects associated with the high OH content are healed and only after that do new defects form. The band at 1.1 eV attains a maximum 400 s after the modification begins.

## 5. CONCLUSIONS

We thus see that, when exposed to a high-power electron beam, glass with a low hydroxyl group content passes through three stages of modification [16, 17]:

(1) an increase in the fraction of intrinsic defects associated with either a deficiency or excess of oxygen, which is caused by the rupture of the oxygen–silicon bonds in the glass;

(2) a fast rise in the intensity of the band with a maximum at 2.2–2.3 eV, which originates from the formation of intrinsic oxygen-deficient defects, as well as the appearance and growth in intensity of the 1.4-eV band associated with silicon nanoclusters or islands of amorphous silicon;

(3) appearance and growth in intensity of the band peaking at 1.1 eV, which should be assigned to the formation of relatively large islands of crystalline silicon.

Interaction of an electron beam with KU-type glass brings about, first of all, a decrease in the fraction of intrinsic defects associated with an oxygen excess. The formation of islands or clusters of silicon takes more time.

## ACKNOWLEDGMENTS

This study was supported by the Russian Foundation for Basic Research, project no. 03-02-16621.

## REFERENCES

1. G. Allan, C. Delerue, and M. Lannoo, *Phys. Rev. Lett.* **78** (16), 3161 (1997).
2. L. N. Skula and A. R. Silin, *Phys. Status Solidi A* **70**, 43 (1982).
3. C. Delerue, G. Allan, and M. Lannoo, *J. Lumin.* **80**, 65 (1999).
4. H.-G. Fitting, T. Barflies, A. N. Trukhin, B. Schmidt, A. Gulans, and A. von Czarnowsky, *J. Non-Cryst. Solids* **303**, 218 (2002).
5. L. N. Skuja, A. N. Streletsky, and A. B. Pakovich, *Solid State Commun.* **50** (12), 1069 (1984).
6. M. S. Bresler and I. N. Yassievich, *Fiz. Tekh. Poluprovodn. (St. Petersburg)* **27** (5), 873 (1993) [*Semiconductors* **27**, 475 (1993)].
7. M. Takeguchi, K. Furuya, and K. Yoshinara, *Jpn. J. Appl. Phys., Part 1* **38** (12B), 7140 (1999).
8. S. K. Obyden, G. A. Perlovskii, G. V. Saporin, and S. I. Popov, *Izv. Akad. Nauk SSSR, Ser. Fiz.* **48** (12), 2374 (1984).
9. L. A. Bakaleĭnikov, E. V. Galaktionov, V. V. Tret'yakov, and É. A. Tropp, *Fiz. Tverd. Tela (St. Petersburg)* **43** (5), 779 (2001) [*Phys. Solid State* **43**, 811 (2001)].
10. E. D. Palik, *Handbook of Optical Constants of Solids II* (Academic, New York, 1991).
11. Z.-J. Ding and R. Shimizu, *Surf. Sci.* **222**, 313 (1989).
12. N. A. Kolobov and M. M. Samokhvalov, *Diffusion and Oxidation in Semiconductors* (Metallurgiya, Moscow, 1975).
13. R. Castaing, Thesis (Univ. de Paris, 1951).
14. M. V. Zamoryanskaya, A. N. Zamoryanskiĭ, and I. A. Vaĭnshenker, *Prib. Tekh. Éksp.*, No. 4, 192 (1987).
15. M. V. Zamoryanskaya and V. I. Sokolov, *Mater. Res. Soc. Symp. Proc.* **737**, F3.40 (2003).
16. M. V. Zamoryanskaya, V. I. Sokolov, and A. A. Sytnikova, *Solid State Phenom.* **78–79**, 349 (2001).
17. M. V. Zamoryanskaya, V. N. Bogomolov, S. A. Gurevich, V. I. Sokolov, A. A. Sitnikova, and I. Smirnova, *Fiz. Tverd. Tela (St. Petersburg)* **43** (2), 357 (2001) [*Phys. Solid State* **43**, 373 (2001)].

*Translated by G. Skrebtsov*

SEMICONDUCTORS  
AND DIELECTRICS

## Optical Phonons in $\text{Rb}_2\text{TeBr}_6$ and $\text{Cs}_2\text{TeBr}_6$ Crystals

V. A. Stefanovich, L. M. Suslikov, Z. P. Gad'mashi, E. Yu. Peresh, V. I. Sideř,  
O. V. Zubaka, and I. V. Galagovets

Uzhgorod National University, Uzhgorod, 88000 Ukraine

e-mail: [vostef@univ.uzhgorod.ua](mailto:vostef@univ.uzhgorod.ua)

Received October 28, 2003

**Abstract**—Raman scattering in  $\text{Rb}_2\text{TeBr}_6$  and  $\text{Cs}_2\text{TeBr}_6$  crystals is studied. The phonon spectra of the crystals are calculated using the factor group method. The number of Raman-active modes, their symmetries, and selection rules are found. Observed Raman spectrum lines are identified with atomic vibration modes of the crystal. © 2004 MAIK "Nauka/Interperiodica".

Crystals of alkali metal chalcogenides  $A_2^I B^{VI} C_6^{VII}$  (where  $A^I$  is K, Rb, or Cs;  $B^{VI}$  is S, Se, or Te;  $C^{VII}$  is Cl, Br, or I) represent a vast class of semiconductors whose physical properties are virtually unexplored [1–3]. X-ray structure analysis shows that alkali metal chalcogenides crystallize into a cubic lattice with space group  $O_h^5-Fm3m$  (except  $\text{K}_2\text{TeBr}_6$ ) [4, 5]. Therefore, these materials are promising for use in optical modulation and scanning devices [6, 7] and comprehensive study of their optical properties is of considerable interest.

In this paper, the phonon spectra of  $\text{Rb}_2\text{TeBr}_6$  and  $\text{Cs}_2\text{TeBr}_6$  crystals is studied by means of Raman spectroscopy. In addition to independent determination of the crystal structure of the materials, this technique provides valuable information about interactions of atoms in the crystal and about the nature of their chemical bonding. Our experiments were performed at room temperature.

$\text{Rb}_2\text{TeBr}_6$  and  $\text{Cs}_2\text{TeBr}_6$  single crystals were grown using the directional solidification method (Bridgman technique). The solidification front velocity was 0.1–0.3 mm/h, and the temperature gradient in the solidification zone was 2–4 K/mm. Crystals were annealed at a temperature of 473 K for three days and then cooled to room temperature at a rate of 30 K/h. The  $\text{Rb}_2\text{TeBr}_6$  and  $\text{Cs}_2\text{TeBr}_6$  single crystals thus obtained were 25 to 55 mm long and 15 to 22 mm in diameter.

The phonon spectra of the crystals under study were calculated beforehand using the positional symmetry method [8, 9]. As mentioned above,  $\text{Rb}_2\text{TeBr}_6$  and  $\text{Cs}_2\text{TeBr}_6$  compounds have cubic structure (space group  $O_h^5-Fm3m$ ) and contain four formula units per unit cell. Atoms occupy sites as follows: 8 Rb (Cs) atoms are in position  $d$  (0, 1/2, 1/4), 4 Te atoms are in position  $a$  (0, 0, 0), 8 Br atoms are in position  $e$  (0, 0, 0.2509), and 16 Br atoms are in position  $h$  (0.2341, 0.2756, 0). The lattice constant  $a$  is 10.918 Å for  $\text{Cs}_2\text{TeBr}_6$  and

10.713 Å for  $\text{Rb}_2\text{TeBr}_6$ . The primitive unit cell contains nine atoms (fcc Bravais lattice). The space group  $O_h^5$  is characterized by the following types of atomic positions:  $2O_h(1)$ ,  $T_d(2)$ ,  $D_{2h}(6)$ ,  $C_{4v}(6)$  (6),  $C_{3v}(8)$ ,  $3C_{2v}(12)$ ,  $2C_s(24)$ , and  $C_1(48)$ . X-ray analysis reveals that Rb and Cs atoms occupy sites with point symmetry group  $T_d$ , Te atoms occupy sites with symmetry  $O_h$ , and Br atoms occupy sites with symmetry  $C_{4v}$ . The results of factor group analysis of vibration spectra of  $\text{Rb}_2\text{TeBr}_6$  and  $\text{Cs}_2\text{TeBr}_6$  crystals based on these data are presented in Table 1.

It follows from this table that lattice vibrations of the crystals under study are distributed over irreducible representations of the factor group  $O_h$  of the crystal at the center of the Brillouin zone in the following way:

$$\Gamma = A_{1g} + E_g + F_{1g} + 2F_{2g} + 4F_{1u} + F_{2u}.$$

Acoustic modes have symmetry  $\Gamma_{ac} = F_{1u}$ ; therefore,

$$\Gamma_{opt}(k=0) = A_{1g}(R) + E_g(R) + 2F_{2g}(R) + 3F_{1u}(IR).$$

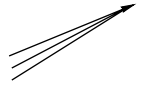
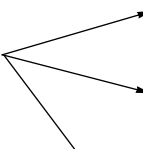


Here, R stands for Raman scattering and IR, for infrared reflection.

Because the crystals under study have a center of inversion, there are selection rules according to which the Raman spectra contain only four vibrational modes: one  $A_{1g}$  mode, one  $E_g$  mode, and two  $F_{2g}$  modes.

The experimental studies of the Raman spectra were performed on a Raman spectrometer DFS-24 with two identical diffraction gratings (replicas) serving as dispersive elements. The gratings had 1200 lines per millimeter and worked in the first order. A photomultiplier FÉU-79 was used as a detector of light. The instantaneous light intensity (averaged over the specified characteristic time) was measured using electronic circuit and registered with a PDA-1 chart recorder. The spectra obtained were processed on computer.



**Table 1.** Factor group analysis of lattice vibrations of Rb<sub>2</sub>TeBr<sub>6</sub> and Cs<sub>2</sub>TeBr<sub>6</sub> crystals

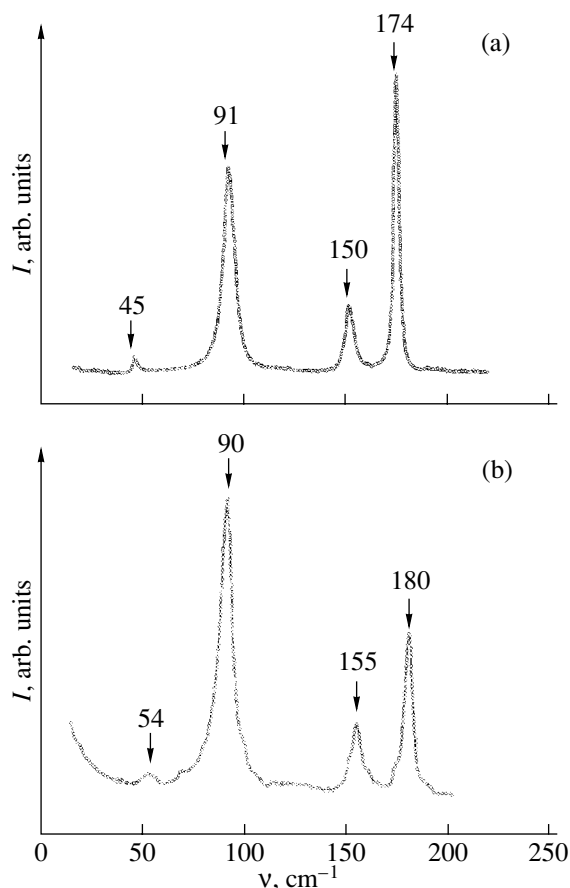
Number and type of atoms	Site symmetry with inclusion of translation (groups $C_{4v}$ , $T_d$ , $O_h$ )	Correlation 	Factor group $O_h$	Number of modes	Symmetry	Activity
6Br	$A_1$		$A_{1g}$	1	$\alpha_{xx} + \alpha_{yy} + \alpha_{zz}$	R
			$E_g$	1	$\alpha_{xx} + \alpha_{yy} - 2\alpha_{zz}$ $\alpha_{xx} - \alpha_{yy}$	R
2Cs	$E$		$F_{1g}$	1	$\alpha_{xy}$ , $\alpha_{yz}$ , $\alpha_{zx}$	R
			$F_{2g}$	2		
Te	$F_{2u}$		$F_{1u}$	4	$\mu_x$ , $\mu_y$ , $\mu_z$	IR
			$F_{2u}$	1		

An LGN-215 He–Ne laser ( $\lambda = 0.6328 \mu\text{m}$ ,  $W = 50 \text{ mW}$ ) working in a single-mode regime was used to excite Raman spectra. We utilized the  $90^\circ$  scattering geometry, which provides for maximal collections of scattered light. This geometry offers the best reduction of parasitic Tyndall and Rayleigh scattering. A polarizing prism was used to check the polarization of the scattered light. The spectral resolution was  $1 \text{ cm}^{-1}$ . The relative error in measuring the intensity for the maxima of spectral lines and of their half-width distortion in comparison to the true half-width of the spectral lines did not exceed 1%. We used single crystals of good optical quality oriented along the  $\{100\}$  planes. Because of the cubic symmetry of the crystals and the small number of lines in the Raman spectra, it is possible to identify observed vibrations correctly by means of unpolarized light measurements.

The experimental Raman spectra of Rb<sub>2</sub>TeBr<sub>6</sub> and Cs<sub>2</sub>TeBr<sub>6</sub> crystals are presented in Fig. 1, and the symmetries and frequencies of all observed modes are listed in Table 2. The experimental results agree with theoretical calculations; the Raman spectra do have four vibrational modes, in contrast to those reported in [10], where only three modes were observed. Vibrations with the  $F_{1u}$  symmetry could be observed in the IR-transmission (reflection) spectra only. Hence, Raman spectroscopy data confirm the structure of Rb<sub>2</sub>TeBr<sub>6</sub> and Cs<sub>2</sub>TeBr<sub>6</sub> crystals established previously.

Our interpretation of the experimental results is based on the features of the crystal structure. The lattices of these compounds consist of closely packed  $\{\text{Rb}(\text{Cs})\text{Br}_3\}$  layers, with half of the  $[\text{Br}_6]$  octahedral voids filled with Te atoms. Hence, it is possible to single out an isolated group of atoms TeBr<sub>6</sub> with an octahedral symmetry  $O_h$ . The vibrational spectrum of the crystal can be considered to consist of internal vibrations of these atomic complexes and their external oscillations relative to Rb(Cs) atoms. Normal modes of the free octahedral molecule are shown in Fig. 2 [11].

The Raman spectrum of this molecule contains two stretching vibrations  $\nu_1$  and  $\nu_2$  with  $A_{1g}$  and  $E_g$  symmetries and one bending vibration  $\nu_5$  with  $F_{2g}$  symmetry. Frequencies of these modes were measured for  $\text{TeBr}_6^{2-}$  ions in a water solution:  $\nu_1 = 166$ ,  $\nu_2 = 151$ , and  $\nu_5 =$

**Fig. 1.** Raman spectra of (a) Cs<sub>2</sub>TeBr<sub>6</sub> and (b) Rb<sub>2</sub>TeBr<sub>6</sub> crystals.

**Table 2.** Raman-active modes of  $\text{Rb}_2\text{TeBr}_6$  and  $\text{Cs}_2\text{TeBr}_6$  crystals

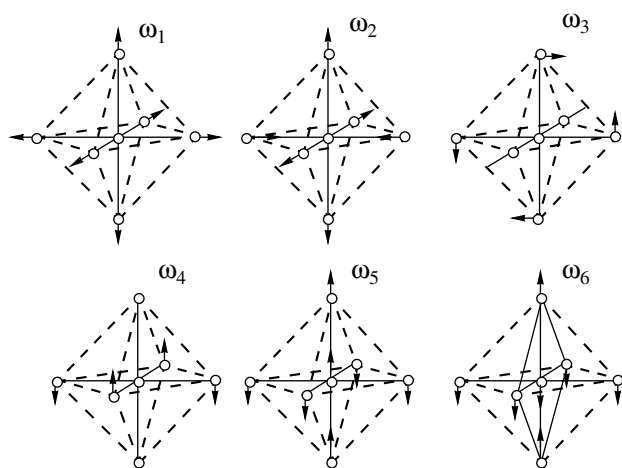
Symmetry	Frequency, $\text{cm}^{-1}$	
	$\text{Rb}_2\text{TeBr}_6$	$\text{Cs}_2\text{TeBr}_6$
$A_{1g}$	180	174
$E_g$	155	150
$F_{2g}$	90	91
$F_{2g}$	54	45

$74 \text{ cm}^{-1}$  [11, 12]. Because the  $\text{TeBr}_6^{2-}$  ion and crystals under study are similar in structure, we can assume that the crystal field does not cause significant distortion of the  $\text{TeBr}_6^{2-}$  ion and does not break the selection rules for its vibrational spectrum. The crystal field can give rise to an insignificant frequency shift of the modes, and this is actually observed experimentally. Hence, for the  $\text{Rb}_2\text{TeBr}_6$  and  $\text{Cs}_2\text{TeBr}_6$  crystals, the vibrational modes at 180 and  $174 \text{ cm}^{-1}$ , respectively, could be attributed to the fully symmetric  $A_{1g}$  stretching vibration of bromine atoms; the modes at 155 and  $150 \text{ cm}^{-1}$ , respectively, to the antisymmetric  $E_g$  stretching vibration; and the modes at 90 and  $91 \text{ cm}^{-1}$ , respectively, to the triply degenerate  $F_{2g}$  bending vibration of the  $\text{TeBr}_6$  group. The Raman spectrum of the free  $\text{TeBr}_6$  molecule has only one  $F_{2g}$  mode. In  $\text{Rb}_2\text{TeBr}_6$  and  $\text{Cs}_2\text{TeBr}_6$  compounds, another Raman active  $F_{2g}$  mode arises because of the presence of the alkali atoms and the appearance of a crystal field (Table 1). It is natural to attribute this

mode to external oscillations of the  $\text{TeBr}_6$  complex relative to the Rb and Cs atoms situated in the octahedral voids. The frequency of these vibrations is  $45 \text{ cm}^{-1}$  for the  $\text{Cs}_2\text{TeBr}_6$  crystal and  $54 \text{ cm}^{-1}$  for the  $\text{Rb}_2\text{TeBr}_6$  crystal (Fig. 1, Table 2). The minor difference in electronegativity between the Te and Br atoms indicates the covalent nature of the Te–Br bond. This feature is the cause of noticeable changes in polarizability during relative oscillations of these atoms and of the considerable intensity of the Raman scattering lines corresponding to these oscillations (Fig. 1). At the same time, the Rb–( $\text{TeBr}_6$ ) bond has a pronounced ionic nature and the Raman scattering line corresponding to this stretching vibration has a low intensity. Note that the replacement of Rb atoms in these crystals by the heavier Cs atom has only a slight effect both on the frequencies of the phonon modes at the center of the Brillouin zone (Table 2) and on the intensities of the corresponding Raman spectral lines.

## REFERENCES

1. V. A. Grin'ko, V. V. Safonov, V. I. Ksenzenko, and B. G. Korshunov, *Zh. Neorg. Khim.* **17** (6), 1755 (1972).
2. G. M. Serebryannikova, V. V. Safonov, G. R. Allakhverdov, V. A. Grin'ko, B. D. Stepin, and V. I. Ksenzenko, *Zh. Neorg. Khim.* **18** (1), 155 (1973).
3. V. V. Safonov, T. V. Kuzina, L. G. Titov, and V. G. Korshunov, *Zh. Neorg. Khim.* **21** (4), 585 (1976).
4. A. K. Das and I. D. Brown, *Can. J. Chem.* **44** (7), 939 (1966).
5. W. Abriel and J. Ihringer, *J. Solid State Chem.* **52** (2), 274 (1984).
6. Yu. K. Rebrin, *Controlling of an Optical Beam in Space* (Sovetskoe Radio, Moscow, 1977).
7. E. R. Mustel' and V. N. Parygin, *Methods of Light Modulation and Scanning* (Nauka, Moscow, 1970).
8. A. I. Grigor'ev, *Introduction to Oscillation Spectroscopy of Inorganic Compounds* (Mosk. Gos. Univ., Moscow, 1977).
9. G. N. Zhizhin, B. N. Mavrin, and V. F. Shabanov, *Optical Oscillation Spectra of Crystals* (Nauka, Moscow, 1984).
10. K. I. Petrov, A. V. Konov, Yu. M. Golovin, V. A. Grin'ko, V. V. Sazonov, and V. I. Ksenzenko, *Zh. Neorg. Khim.* **19** (1), 82 (1974).
11. K. W. F. Kohlrausch, in *Hand- und Jahrbuch der Chemischen Physik* (Edwards, Ann Arbor, 1944), Vol. 9, Part 6 [*Raman Scattering Spectra* (Inostrannaya Literatura, Moscow, 1952)].
12. *The Raman Effect*, Vol. 2: *Application*, Ed. by A. Andersen (Marcel Dekker, New York, 1973; Mir, Moscow, 1977).

**Fig. 2.** Normal modes of the  $\text{TeBr}_6$  octahedral molecule.

*Translated by G. Tsydynzhapov*

## Electrical Conductivity and Permittivity of the One-Dimensional Superionic Conductor $\text{LiCuVO}_4$

L. S. Parfen'eva\*, A. I. Shelykh\*, I. A. Smirnov\*, A. V. Prokof'ev\*\*, and W. Assmus\*\*

\**Ioffe Physicotechnical Institute, Russian Academy of Sciences, Politekhnikeskaya ul. 26, St. Petersburg, 194021 Russia*  
e-mail: igor.smirnov@pop.ioffe.rssi.ru

\*\**Institute of Physics, Goethe University, Frankfurt am Main, 60054 Germany*

Received October 24, 2003

**Abstract**—The electrical conductivity  $\sigma^a$  and permittivities  $\epsilon^a$ ,  $\epsilon^b$ , and  $\epsilon^c$  of a  $\text{LiCuVO}_4$  single crystal have been measured along the  $a$ ,  $b$ , and  $c$  crystallographic axes, respectively, in the temperature range 300–390 K at a frequency of  $10^3$  Hz. The temperature dependences  $\sigma(T)$  and  $\epsilon(T)$  were found to be typical for superionics. © 2004 MAIK “Nauka/Interperiodica”.

Measurements of the electrical conductivity  $\sigma$  of  $\text{LiCuVO}_4$  performed in the temperature interval 300–500 K and the anomalous behavior of thermal conductivity in the range 100–300 K led to the conclusion [1] that this compound is a quasi-one-dimensional superionic.

When the temperature is increased, superionic conductors exhibit, in addition to an exponential growth in electrical conductivity, an exponential increase in the permittivity  $\epsilon$ , which can reach fairly large values at high enough temperatures [2, 3]. For instance,  $\epsilon$  of the  $\text{Li}_2\text{B}_4\text{O}_7$  quasi-one-dimensional lithium superionic [2] (which belongs to materials with the  $4mm$  tetragonal symmetry) measured along the polar  $c$  axis of the crystal at  $\sim 10^2$  Hz increases from 20 at 300 K to 4200 at 500 K.

The present study was aimed primarily at measuring  $\epsilon(T)$  for  $\text{LiCuVO}_4$  in order to verify the conclusion from [1] that this material is a fairly good superionic.

$\text{LiCuVO}_4$  crystallizes in an orthorhombic distorted inverted spinel structure, in which the nonmagnetic  $\text{V}^{5+}$  ions occupy tetrahedral voids and the nonmagnetic  $\text{Li}^+$  and magnetic  $\text{Cu}^{2+}$  ( $S = 1/2$ ) ions are arranged in an ordered manner in octahedral voids of the anion sublattice [4, 5]. The  $\text{CuO}_6$ - and  $\text{LiO}_6$ -octahedra make up “magnetic” and “nonmagnetic” chains, respectively, aligned in  $\text{LiCuVO}_4$  with the  $b$  and  $a$  crystallographic directions (see inset to Fig. 1).

The  $\text{LiCuVO}_4$  single crystals intended for permittivity and electrical conductivity measurements were grown using the technique described in [6]. They were grown from solution in a  $\text{LiVO}_3$  melt under slow cooling in the range 650–580°C. Such crystals are conventionally called [1] “high-temperature”  $\text{LiCuVO}_4$  single crystals.

A chemical analysis of a large set of such high-temperature  $\text{LiCuVO}_4$  single crystals revealed, despite a certain scatter of data, that their average composition is  $\text{Li}_{0.92}\text{Cu}_{1.03}\text{VO}_4$ , i.e., that they are off-stoichiometric

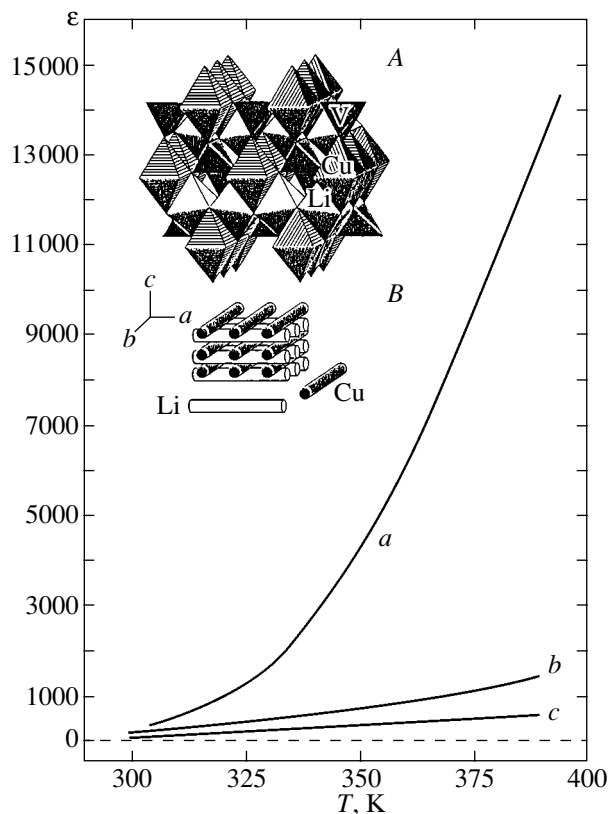


**Fig. 1.** Temperature behavior of the permittivity of a  $\text{LiCuVO}_4$  single crystal in the  $a$ ,  $b$ , and  $c$  crystallographic directions. Inset shows (A) the crystal structure [4] and (B) the rod model [5] proposed for  $\text{LiCuVO}_4$ . The mutually perpendicular Li and Cu rod layers alternate.

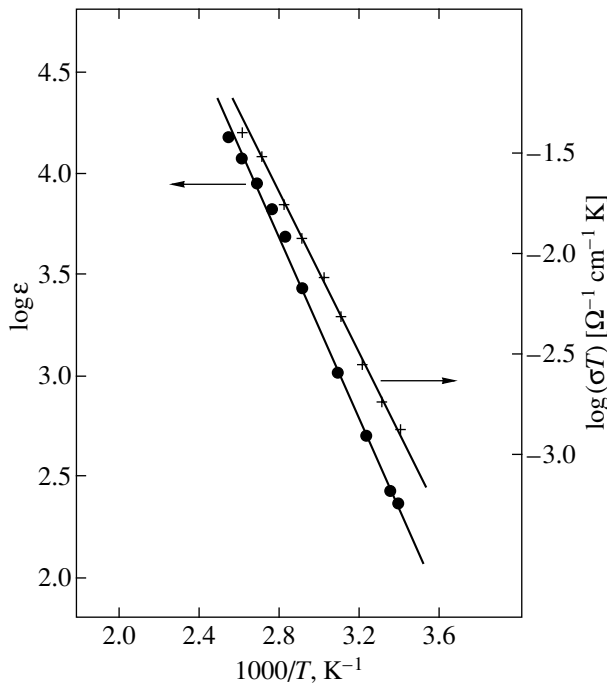


**Fig. 2.** Temperature dependences of the electrical conductivity and permittivity of a  $\text{LiCuVO}_4$  single crystal measured along the  $a$  crystallographic direction.

both in lithium and in copper [1]. The main type of defects in these crystals is, however, vacancies on the lithium sublattice.

The electrical conductivity  $\sigma^a(T)$  and the permittivity  $\epsilon^a(T)$ ,  $\epsilon^b(T)$ , and  $\epsilon^c(T)$  were measured in the range 300–390 K at a frequency  $\omega \sim 10^3$  Hz. The experimental data obtained on  $\sigma^a(T)$  and  $\epsilon^{a,b,c}(T)$  for  $\text{LiCuVO}_4$  are presented graphically in Figs. 1 and 2.

Consider the results obtained on  $\sigma^a(T)$ . As is evident from Fig. 2, the experimental points fall on a straight line, which is described, in the case of ionic conduction, by the Arrhenius relation [7, 8]

$$\sigma T = \sigma_0 \exp(-\Delta H^a/kT), \quad (1)$$

where  $\Delta H^a$  is the activation enthalpy for electrical conduction.

$\Delta H^a$  for  $\text{LiCuVO}_4$  was found to be  $\sim 0.40$  eV, which is in good agreement with the values of  $\Delta H$  quoted for lithium-based superionics [8].

Because the  $\text{LiCuVO}_4$  single crystals at our disposal were fairly small, the values of  $\sigma^a$  may have been determined with some error, but the slope of the  $\log(\sigma^a) = f(10^3/T)$  straight line was found with good accuracy.

The increase in  $\sigma^a(T)$  with temperature should be assigned primarily to the diffusion of Li ions over vacancies on the lithium sublattice in  $\text{LiCuVO}_4$ .

Consider the data obtained on  $\epsilon^a(T)$ ,  $\epsilon^b(T)$ , and  $\epsilon^c(T)$  (Figs. 1, 2). As in the case of the  $\text{Li}_2\text{B}_4\text{O}_7$  quasi-one-

dimensional superionic [2],  $\text{LiCuVO}_4$  exhibits exponential growth in  $\epsilon$  with increasing temperature. The increase in the permittivity is the strongest for  $\epsilon^a(T)$  (Fig. 2); it scales with temperature as  $\epsilon^a(T) \sim \exp(-\Delta E^a/kT)$  with  $\Delta E^a \sim 0.46$  eV, a figure close in magnitude to the value of  $\Delta H^a$  obtained for  $\sigma^a(T)$  (Fig. 2).

$\epsilon^b(T)$  and  $\epsilon^c(T)$  also grow with temperature but not as strongly as  $\epsilon^a(T)$  does (Fig. 1). This behavior of  $\epsilon^{a,b,c}(T)$  can apparently be explained by the observation that ionic conduction is realized most easily over the defected lithium sublattice in  $\text{LiCuVO}_4$ , i.e., along the  $a$  axis. This conclusion is corroborated by our measurements of  $\sigma(T)$  in  $\text{LiCuVO}_4$  performed with an ac current at  $\sim 10^3$  Hz at 390 K in the  $a$ ,  $b$ , and  $c$  directions, for which we obtained the following values:  $1.5 \times 10^{-4}$ ,  $7 \times 10^{-6}$ , and  $4.5 \times 10^{-6} \Omega^{-1} \text{cm}^{-1}$ , respectively.

The permittivity of  $\text{LiCuVO}_4$  in the region 2–300 K was extracted earlier [9] for the  $a(\epsilon^a)$  and  $b(\epsilon^b)$  crystallographic directions from optical high-frequency measurements in the IR region;  $\epsilon^a$  varied from 10.9 at 2 K to 11.4 at 300 K, while  $\epsilon^b$  remained practically constant in the same temperature region (10.4 at 2 K and 10.6 at 300 K).

Analysis of experimental data on  $\sigma(T)$ ,  $\epsilon(T)$ , and other kinetic coefficients in materials with ionic conduction is complicated by the need to take into account and evaluate parameters that are determined not only by the volume of the material but also by its near-electrode regions [7, 8]. Applying an external voltage may bring about the formation of a space charge region to a depth  $d_0 \sim 10^{-4}$  cm near one of the electrodes in this material [7], and it is this region which will govern the magnitude of the capacitance  $C$  and electrical conductivity being measured. In a uniform dielectric (with no near-contact charged layer present),  $\epsilon$  is determined uniquely by the measured capacitance of the material filling the space between the electrodes (a distance  $d$  apart). Therefore, the error in determining  $\epsilon$ , with a near-contact space-charge layer  $d_0 \sim 10^{-4}$  cm thick and for sample thicknesses  $d \sim 0.2$  cm, would constitute  $d/d_0 \sim 10^3$ , which may result in an overestimated magnitude of  $\epsilon$  calculated under the assumption of the absence of a near-contact space-charge layer in the sample under study.

We attempted several experimental approaches to answering the question of whether such a near-contact charged layer does indeed form in our case in the measurement of  $\epsilon(T)$  and  $\sigma(T)$  in  $\text{LiCuVO}_4$ .

(1) A near-contact space-charge layer should have made the dependence of the voltage drop along the layer thickness  $d$  nonlinear. We observed no such effect on the samples studied.

(2) The voltage on the samples on which the capacitance and electrical conductivity were measured with an ac current ( $\omega \sim 10^3$  Hz) was 4.3 V. We also per-

formed measurements in which an additional dc voltage of 20 V was applied simultaneously across the sample, which could have produced a noticeable impact on both the magnitude and distribution of the near-electrode potential and affected the capacitance and electrical conductivity measurements. We did not observe any differences between the measurements of  $C(T)$  and  $\sigma(T)$  with and without the dc bias applied.

(3) The concentration of the electric field ( $E_0$ ) in a thin near-contact layer of the material should have generated a field  $E_0 \sim 10^4\text{--}10^5$  V/cm capable of causing electric breakdown in the near-contact region or current instability. No such effect was observed by us experimentally.

Thus, the above experiments permit the conclusion that, most likely, no thin near-contact layer was present in  $\text{LiCuVO}_4$  in the  $\epsilon(T)$  and  $\sigma(T)$  measurements.

Not all factors capable of affecting the behavior of  $\epsilon(T)$  in the  $\text{LiCuVO}_4$  superionic were, however, taken into account by us (we disregarded the effect of the contact material, the existence of electronic conduction, etc.). It would therefore be more prudent to call the  $\epsilon(T)$  obtained by us experimentally the “effective permittivity” of  $\text{LiCuVO}_4$ .

We emphasize in conclusion that in carrying out this study we were not interested in the question of why  $\epsilon^{a,b,c}(T)$  in  $\text{LiCuVO}_4$  have such high values or of whether these values could be assigned to the existence of a near-contact space-charge region, thus invalidating our calculation of  $\epsilon(T)$ . The only thing we can be confident of is that  $\text{LiCuVO}_4$  features ionic conduction, because  $\epsilon$  grows markedly with temperature. Furnishing supportive evidence for this conclusion was the main purpose of this experiment.

## ACKNOWLEDGMENTS

This study was supported by the Russian Foundation for Basic Research (project no. 02-02-17657) within the framework of a bilateral agreement between the Russian Academy of Sciences and Deutsche Forschungsgemeinschaft.

## REFERENCES

1. L. S. Parfen'eva, A. I. Shelykh, I. A. Smirnov, A. V. Prokof'ev, W. Assmus, H. Misiorek, J. Mucha, A. Jezowski, and I. G. Vasil'eva, *Fiz. Tverd. Tela (St. Petersburg)* **45** (11), 1991 (2003) [*Phys. Solid State* **45**, 2093 (2003)].
2. A. É. Aliev, Ya. V. Burak, and I. T. Lyseïko, *Neorg. Mater.* **26**, 1991 (1990).
3. A. A. Abramovich, A. Sh. Akramov, A. É. Aliev, and L. N. Fershtat, *Fiz. Tverd. Tela (Leningrad)* **29** (8), 2479 (1987) [*Sov. Phys. Solid State* **29**, 1426 (1987)].
4. M. A. Lafontaine, M. Leblanc, and G. Ferey, *Acta Crystallogr. C* **45**, 1205 (1989).
5. M. O. Keefe and S. Andersson, *Acta Crystallogr. A* **33**, 914 (1977).
6. A. V. Prokofiev, D. Wichert, and W. Assmus, *J. Cryst. Growth* **220**, 345 (2000).
7. A. B. Lidiard, in *Handbuch der Physik*, Ed. by S. Flugge (Springer, Berlin, 1957; *Inostrannaya Literatura*, Moscow, 1962), p. 246.
8. A. K. Ivanov-Shits and I. V. Murin, *Ionics of Solids (S.-Peterb. Gos. Univ., St. Petersburg, 2000)*, Vol. 1.
9. B. Gorshunov, P. Haas, M. Dressel, V. I. Torgashev, V. B. Shirokov, A. V. Prokofiev, and W. Assmus, *Eur. Phys. J. B* **23**, 427 (2001).

*Translated by G. Skrebtsov*

SEMICONDUCTORS  
AND DIELECTRICS

## Optical Absorption by $\text{Nd}^{3+}$ and $\text{Gd}^{3+}$ Ions in Epitaxial Films Grown on $\text{Gd}_3\text{Ga}_5\text{O}_{12}$ Substrates from a Lead-Containing Solution Melt

V. V. Randoshkin\*, N. V. Vasil'eva\*, V. G. Plotnichenko\*\*, Yu. N. Pyrkov\*\*, S. V. Lavrishchev\*\*,  
M. A. Ivanov\*, A. A. Kiryukhin\*<sup>†</sup>, A. M. Saletskii\*\*\*, and N. N. Sysoev\*\*\*

\* Institute of General Physics, Russian Academy of Sciences, ul. Vavilova 38, Moscow, 119991 Russia

\*\* Research Center of Fiber Optics, Institute of General Physics, Russian Academy of Sciences,  
ul. Vavilova 38, Moscow, 119991 Russia

\*\*\* Moscow State University, Vorob'evy gory, Moscow, 119992 Russia

e-mail: antony@aha.ru

Received July 15, 2003; in final form, November 4, 2003

**Abstract**—Epitaxial films of composition  $(\text{Gd},\text{Nd})_3\text{Ga}_5\text{O}_{12}$  or  $(\text{Gd},\text{Y},\text{Nd})_3\text{Ga}_5\text{O}_{12}$  with a neodymium content varying from 0.3 to 15 at. % are grown by liquid-phase epitaxy from a supercooled  $\text{PbO}-\text{B}_2\text{O}_3$ -based solution melt on  $\text{Gd}_3\text{Ga}_5\text{O}_{12}(111)$  substrates. The optical absorption spectra of the epitaxial films grown are measured in the wavelength range 0.2–1.0  $\mu\text{m}$ . The results of interpreting the absorption bands observed in the spectra are used to construct the energy level diagrams of  $\text{Nd}^{3+}$  and  $\text{Gd}^{3+}$  ions in the matrices of the epitaxial films.  
© 2004 MAIK “Nauka/Interperiodica”.

### 1. INTRODUCTION

Neodymium-doped lasers with various solid matrices, especially with those made up of single-crystal garnets (for example, gadolinium gallium garnet  $\text{Gd}_3\text{Ga}_5\text{O}_{12}$ ), have been extensively used in quantum electronics [1]. The basic problem of increasing the efficiency of these lasers is associated with the impossibility of growing optically homogeneous crystals with a high concentration of doping rare-earth ions, in particular,  $\text{Nd}^{3+}$  ions, whose distribution coefficient is considerably less than that for the ions replacing them in the matrix [2]. As a result, the concentration of doping rare-earth elements changes significantly along the axis of the growing single crystal.

The above disadvantage can often be eliminated upon changing over to single-crystal films grown by liquid-phase epitaxy from a supercooled solution melt. In this case, the difference between the distribution coefficients of the rare-earth elements introduced into the epitaxial film can be decreased through appropriate choice of the ratio between garnet-forming components in the solution melt. Since only an insignificant amount of these components passes from the solution melt into the film, the concentration of rare-earth elements in the bulk of the film remains almost unchanged over the film thickness.

The first mention of a thin-film single-crystal laser based on an  $\text{Y}_{1.25}\text{Ho}_{0.1}\text{Er}_{0.55}\text{Tm}_{0.5}\text{Yb}_{0.6}\text{Al}_5\text{O}_{12}$  garnet film grown on an  $\text{Y}_3\text{Al}_5\text{O}_{12}$  substrate was made in 1972

by van der Ziel *et al.* [3]. In 1973, Bonner [4] succeeded in generating stimulated emission at a wavelength of 1.06  $\mu\text{m}$  at 300 K in  $\text{Y}_3\text{Al}_5\text{O}_{12}$  epitaxial films containing 2 at. %  $\text{Nd}^{3+}$ .

In this work, we investigated the optical absorption in the wavelength range 0.2–1.0  $\mu\text{m}$  in neodymium-containing single-crystal garnet films grown on  $\text{Gd}_3\text{Ga}_5\text{O}_{12}(111)$  substrates through liquid-phase epitaxy from a supercooled  $\text{PbO}-\text{B}_2\text{O}_3$ -based solution melt.

### 2. THE GROWTH OF FILMS

Epitaxial single-crystal gallium garnet films with a neodymium content  $C(\text{Nd})$  ranging from 0.3 to 15 at. % were grown through liquid-phase epitaxy from a supercooled  $\text{PbO}-\text{B}_2\text{O}_3$ -based solution melt [5]. For a neodymium content  $C(\text{Nd}) \geq 1.7$  at. %, yttrium was introduced into the epitaxial single-crystal films with the aim of matching the lattice parameters of the film and the substrate. The composition of the batch was characterized by the following molar ratios ( $R_1, R_2, R_3$ ):

$$R_1 = [\text{Ga}_2\text{O}_3]/(\Sigma[\text{Ln}_2\text{O}_3]) \approx 14.4,$$

$$R_2 = [\text{PbO}]/[\text{B}_2\text{O}_3] \approx 16.0,$$

$$R_3 = (\Sigma[\text{Ln}_2\text{O}_3] + [\text{Ga}_2\text{O}_3]) / (\Sigma[\text{Ln}_2\text{O}_3] + [\text{Ga}_2\text{O}_3] + [\text{PbO}] + [\text{B}_2\text{O}_3]) \approx 0.08,$$

<sup>†</sup> Deceased.

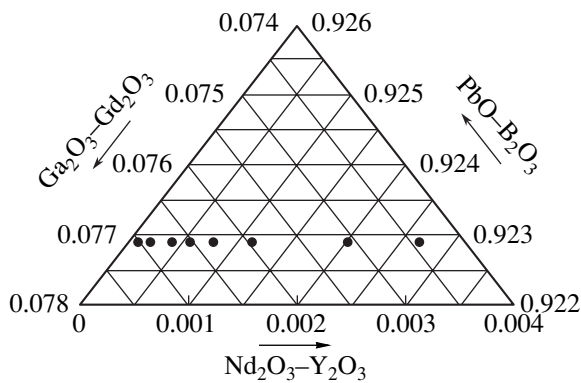


**Fig. 1.** Fragment of the concentration triangle of the  $(\text{Nd}_2\text{O}_3\text{-Y}_2\text{O}_3)\text{-}(\text{Gd}_2\text{O}_3\text{-Ga}_2\text{O}_3)\text{-}(\text{PbO-B}_2\text{O}_3)$  pseudoternary system. Mole fractions of oxides contained in the batch are plotted along the sides of the triangle. Closed circles indicate the compositions of the solution melts used to grow epitaxial single-crystal films of gallium garnets with a neodymium content ranging from 0.3 to 15 at. % (parameters of the films are given in Table 1).

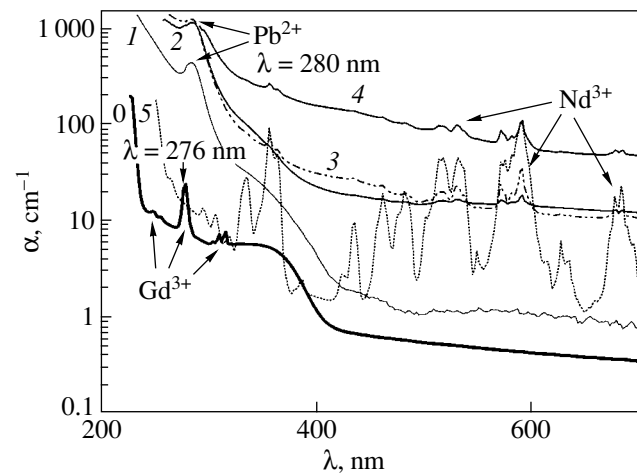


**Fig. 2.** Optical absorption spectra  $\alpha(\lambda)$  for (0) the  $\text{Gd}_3\text{Ga}_5\text{O}_{12}$  substrate; (1) the neodymium-free  $\text{Gd}_3\text{Ga}_5\text{O}_{12}$  film; (2–4)  $\text{Gd}_3\text{Ga}_5\text{O}_{12}$  epitaxial film samples (2) **5**, (3) **7**, and (4) **10** with different neodymium contents; and (5) the  $\text{Nd}_3\text{Ga}_5\text{O}_{12}$  single crystal. The numbering of the films is the same as in Table 1.

where  $\Sigma[\text{Ln}_2\text{O}_3] = [\text{Gd}_2\text{O}_3] + [\text{Nd}_2\text{O}_3] + [\text{Y}_2\text{O}_3]$  and brackets designate the oxide content in the batch in mole percent.

The growth experiments are illustrated in Fig. 1, which shows a fragment of the concentration triangle of the  $(\text{Nd}_2\text{O}_3\text{-Y}_2\text{O}_3)\text{-}(\text{Gd}_2\text{O}_3\text{-Ga}_2\text{O}_3)\text{-}(\text{PbO-B}_2\text{O}_3)$  system. In order to prepare an epitaxial single-crystal film of the specified composition, the ratio between rare-earth oxides in the batch was determined with due regard for the known distribution coefficients of the rare-earth elements [2]. Epitaxial films were grown under supercooling conditions ensuring the absence of additional absorption associated with the intervalence pair transitions of  $\text{Pb}^{2+}$  and  $\text{Pb}^{4+}$  impurity ions [6, 7]. The epitaxial single-crystal films thus grown were col-

orless and optically homogeneous, except the films with a neodymium content  $C(\text{Nd}) \approx 15$  at. %, which were yellowish brown and had microcracks.

The solution melt was homogenized in a platinum crucible at a temperature  $T = 1100^\circ\text{C}$  for 4 h. Then, the temperature was reduced step-by-step to the crystallization temperature of the solution melt. At each temperature step (i.e., at the growth temperature  $T_g = \text{const}$ ), we carried out the growth of the films. As the neodymium content increased, the temperature of saturation  $T_s$  of the solution melt decreased from 1030 to  $920^\circ\text{C}$ . The maximum thickness of the epitaxial films grown amounted to  $50\ \mu\text{m}$ . Thick films with a thickness  $h \geq 25\ \mu\text{m}$  were grown after an additional homogenization of the solution melt.

**Table 1.** Characteristics of  $(\text{Gd,Y,Nd})_3\text{Ga}_5\text{O}_{12}$  epitaxial single-crystal films

Sample no.	$C(\text{Nd})$ , at. %	$T_g$ , $^\circ\text{C}$	$2h$ , $\mu\text{m}$	$f_g$ , $\mu\text{m}/\text{min}$	$\alpha_{806.9}$ , $\text{cm}^{-1}$	$\Delta\lambda$ , nm
<b>1</b>	0.3	999	105.0	0.44	3.8	0.84
<b>2</b>	0.9	979	76.8	1.28	13.7	0.86
<b>3</b>	0.9	976	33.4	0.56	16.7	0.87
<b>4</b>	1.7	950	95.8	0.40	–	–
<b>5</b>	2.3	964	73.8	0.37	30.6	0.92
<b>6</b>	3.3	950	53.8	0.90	47.8	0.92
<b>7</b>	5.0	930	67.9	0.28	76.2	0.92
<b>8</b>	10.0	944	12.0	0.20	125.0	0.96
<b>9</b>	10.0	935	68.7	0.19	123.0	0.96
<b>10</b>	15.0	887	99.8	0.16	176.3	1.01

Note:  $T_g$  is the growth temperature,  $\alpha_{806.9}$  is the absorption coefficient without regard for scattering at the maximum of the spectral line, and  $\Delta\lambda$  is the half-width of the spectral line at a wavelength of 806.9 nm.

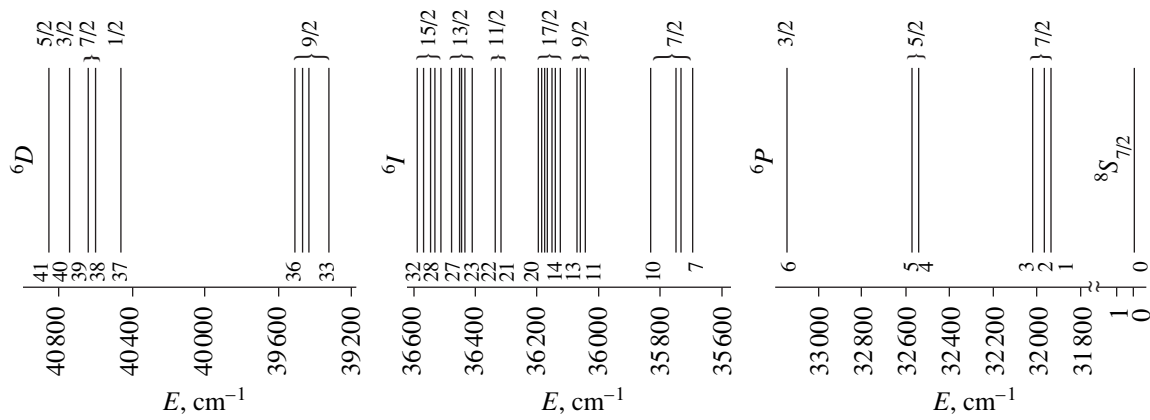


**Fig. 3.** Diagram of Stark levels of the  $Gd^{3+}$  ion in the  $Gd_3Ga_5O_{12}$  single crystal at room temperature.

For the above ratio of components in the batch, the growth of films on the surface of the solution melt and platinum auxiliaries was accompanied by spontaneous crystallization of garnet single crystals in the form of tetragonal trioctahedra with  $\{211\}$  facets.

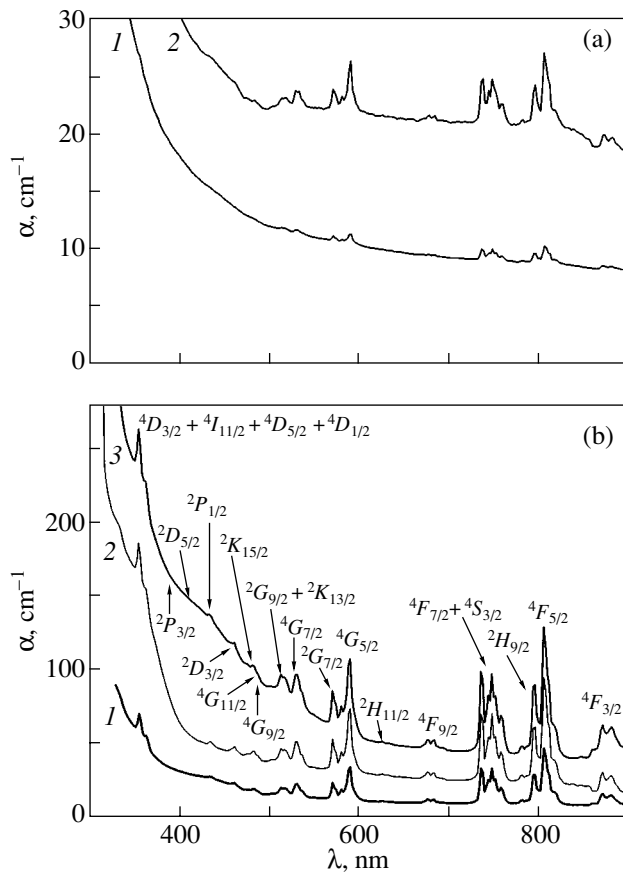


**Fig. 4.** Optical absorption spectra  $\alpha(\lambda)$  for  $Gd_3Ga_5O_{12}$  epitaxial films with different neodymium contents  $C(Nd)$ : (a) (1) 0.3 and (2) 0.9; and (b) (1) 5, (2) 10, and (3) 15 at. %.

### 3. EXPERIMENTAL TECHNIQUE

The total thickness  $2h$  of the films grown on both sides of the substrate and the growth rate  $f_g$  of these films (Table 1) were determined by weighing the substrate prior to the epitaxial growth and the film-substrate-film structure after the growth. In this case, we ignored the difference in the quantitative compositions of the film and the substrate.

The transmission spectra of the films were measured on a Lambda 900 (Perkin-Elmer) spectrophotometer in the wavelength range  $\lambda = 0.2-1.0 \mu m$  in steps of 2 nm at room temperature.

The absorption spectra of the films were calculated from the transmission spectra as follows. Initially, the transmission spectrum of the substrate, which was measured prior to the growth, was divided by the transmission spectrum of the substrate with the grown films. Then, the natural logarithm of this ratio was divided by the total thickness of the films grown on both sides of the substrate.

### 4. RESULTS AND DISCUSSION

Figure 2 shows the optical absorption spectra  $\alpha(\lambda)$  for the  $Gd_3Ga_5O_{12}$  substrate (curve 0), the neodymium-free  $Gd_3Ga_5O_{12}$  epitaxial film (curve 1),  $Gd_3Ga_5O_{12}$  epitaxial films with different neodymium contents (curves 2-4), and the  $Nd_3Ga_5O_{12}$  single crystal (curve 5) grown by the Czochralski technique. As can be seen from Fig. 2, the optical absorption spectra of neodymium-containing films exhibit absorption bands associated with  $Nd^{3+}$  ions that are characteristic of  $Nd_3Ga_5O_{12}$  single crystals (curve 5). Moreover, these spectra contain an absorption band with a maximum at a wavelength of 280 nm, which, as in the case of  $Gd_3Ga_5O_{12}$  epitaxial films (Fig. 2, curve 1) [6], is attributed to the  $(6s^2) ^1S_0 \rightarrow ^3P_1$  transition of the  $Pb^{2+}$  ions [8]. It should be noted that all absorption bands of neodymium ions that are characteristic of the



**Table 2.** Stark levels of the  $Gd^{3+}$  ion in the  $Gd_3Ga_5O_{12}$  crystal at 300 K

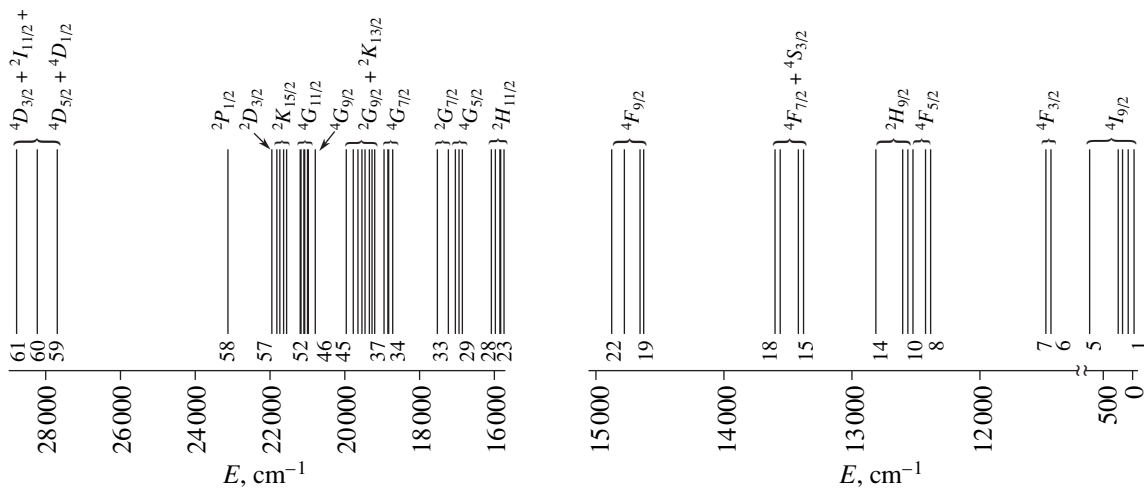
Term	Nos. of Stark levels in the term (Fig. 4)	Positions of Stark levels in the term, $cm^{-1}$	Number of Stark components				$\Delta E$ , $cm^{-1}$
			theory	experiment	[10] YAG : $Gd^{3+}$	[11] $GdCl_3 \cdot 6H_2O$	
$^8S_{7/2}$	0	0	4	–	–	–	–
$^6P_{7/2}$	1–3	31942, 31972, 32020	4	3	4	4	78
$^6P_{5/2}$	4, 5	32545, 32575	3	2	3	3	30
$^6P_{3/2}$	6	33150	2	1	2	2	
$^6I_{7/2}$	7–10	35694, 35731, 35748, 35834	4	4	4	4	140
$^6I_{9/2}$	11–13	36044, 36061, 36071	5	3	5	5	27
$^6I_{17/2}$	14–20	36125, 36140, 36150, 36166, 36177, 36184, 36194	7	7	3	7	69
$^6I_{11/2}$	21, 22	36320, 36335	6	2	3	5	15
$^6I_{13/2}$	23–27	36413, 36438, 36448, 36456, 36482	7	5	–	7	69
$^6I_{15/2}$	28–32	36515, 36534, 36549, 36569, 36594	8	5	–	8	79
$^6D_{9/2}$	33–36	39320, 39425, 39464, 39505	5	4	–	5	185
$^6D_{1/2}$	37	40465	1	1	–	1	–
$^6D_{7/2}$	38, 39	40602, 40645	4	2	–	2	43
$^6D_{3/2}$	40	40748	2	1	–	2	–
$^6D_{5/2}$	41	40860	3	1	–	3	–

$Nd_3Ga_5O_{12}$  single crystal are observed in the absorption spectra of neodymium-containing films.

The optical absorption spectrum of the substrate (Fig. 2, curve 0) exhibits narrow bands in the wavelength range 244–314 nm due to the presence of  $Gd^{3+}$  ions in the substrate. In this range, the transmission spectra were additionally measured in steps of 0.1 nm with a spectral resolution of 0.1 nm. As a result, we revealed 41 maxima in the absorption bands of the spectra. Figure 3 shows the energy level diagram of the  $Gd^{3+}$  ion in the  $Gd_3Ga_5O_{12}$  single crystal, which was constructed taking into account the data available in the literature [9–11]. Although Hellwege *et al.* [11] studied  $GdCl_3 \cdot 6H_2O$  and  $Y(Gd)Cl_3 \cdot 6H_2O$  matrices with a nongarnet structure, we used their data for the interpretation of our experimental results. This is explained by the fact that those authors obtained more complete information as compared to Azamatov *et al.* [10], who investigated the  $Y_{2.95}Gd_{0.05}Al_5O_{12}$  matrix (YAG :  $Gd^{3+}$ ). However, our results of the measurements of the wavelengths at the maxima of the absorption bands proved to be in closer agreement with the data obtained in [10]. Note also that the diagram of the  $^6I_{17/2}$  and  $^6I_{11/2}$  electron terms obtained in [11] (and, consequently, in our work) differs from that proposed in [10]. The Stark levels shown in Fig. 3 are numerated sequentially starting from the fundamental term  $^8S_{7/2}$ . The level positions and

complete splittings  $\Delta E$  of the electron terms of the  $Gd^{3+}$  ion in the  $Gd_3Ga_5O_{12}$  single crystal at room temperature are listed in Table 2. Since the ground state of the  $Gd^{3+}$  ion at room temperature corresponds to a single level (level 0 in Fig. 3), the absorption spectrum of the  $Gd_3Ga_5O_{12}$  single crystal contains bands associated with the transitions from the ground state to excited states of the  $Gd^{3+}$  ion.

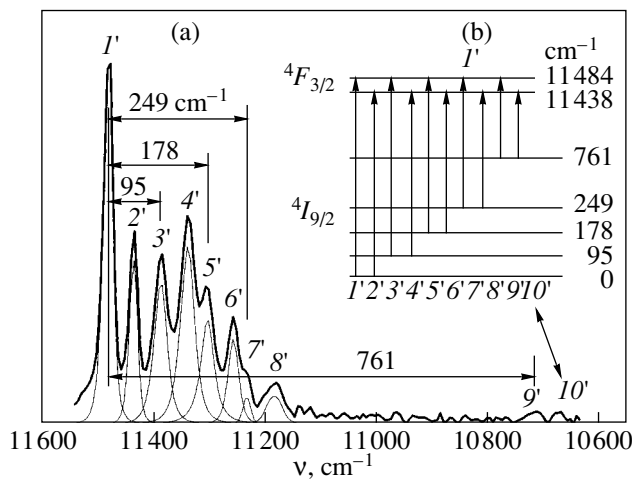
Moreover, we revealed that the short-wavelength edge of the absorption band of  $Gd^{3+}$  ions in the  $Gd_3Ga_5O_{12}$  epitaxial films with a neodymium content of 15 at. % is shifted by 0.014 nm toward the longer wavelength range with respect to the absorption band of the  $Gd^{3+}$  ion in the substrate. In order to determine this shift, we measured the absorption bands associated with the substrate and films in the wavelength range from 270 to 285 nm with a step of 0.2 nm and a spectral resolution of 0.05 nm. This shift can be attributed to the distortion of the crystal lattice at a high neodymium content, which is confirmed by the formation of microcracks in the epitaxial films at  $C(Nd) = 15$  at. %. Therefore, we can state that the energy level diagram of the  $Gd^{3+}$  ion in the grown films differs from that of the  $Gd^{3+}$  ion in the  $Gd_3Ga_5O_{12}$  single crystal (Fig. 3) in terms of the magnitude of the aforementioned shift. For epitaxial films with a lower neodymium content, these energy levels coincide with each other.



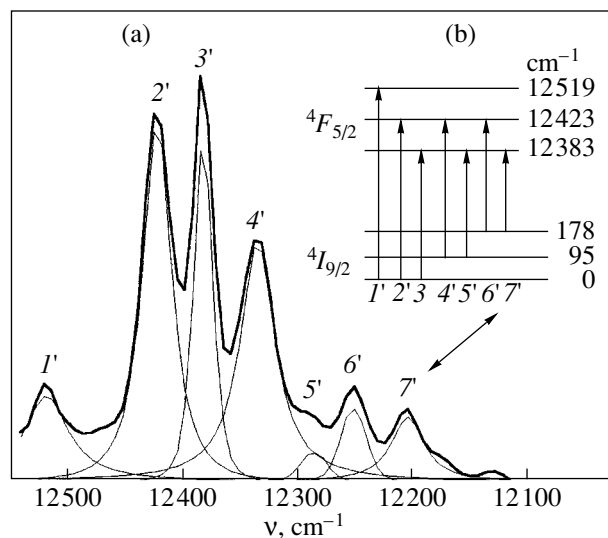
**Fig. 5.** Diagram of Stark levels of the Nd<sup>3+</sup> ion in the Gd<sub>3</sub>Ga<sub>5</sub>O<sub>12</sub> : Nd epitaxial film at room temperature.

Figure 4 shows the absorption bands associated with the presence of neodymium in the epitaxial films and the conventional notation for electron terms of the Nd<sup>3+</sup> ion (Fig. 4b) [12, 13]. It turned out that the positions of these bands are independent of the neodymium content and completely coincide with those in the optical absorption spectrum of the Nd<sub>3</sub>Ga<sub>5</sub>O<sub>12</sub> single crystal (Fig. 2). In the general case, both the intensity of each absorption peak and the intensity of absorption at any wavelength in the range under investigation increase in proportion to the neodymium content C(Nd).

The energy level diagram of the Nd<sup>3+</sup> ion in the Gd<sub>3</sub>Ga<sub>5</sub>O<sub>12</sub> : Nd film is depicted in Fig. 5. The experimental data on the position of the Stark levels and the complete splitting  $\Delta E$  of the electron terms of the Nd<sup>3+</sup> ion in the Gd<sub>3</sub>Ga<sub>5</sub>O<sub>12</sub> : Nd film at a temperature of 300 K are presented in Table 3. In this case, the transmission spectra of the epitaxial films were additionally measured with a step of 0.5 nm and a spectral resolution of 0.5 nm in the wavelength range from 200 to 950 nm. As a result, we revealed 61 maxima of the absorption bands. For the purpose of determining the positions of the Stark levels more exactly, the spectral lines were



**Fig. 6.** (a) Optical absorption spectrum of the  $4I_{9/2} \rightarrow 4F_{3/2}$  transition and the curves of decomposition into components and (b) diagram of the crystalline splitting of the  $4I_{9/2}$  and  $4F_{3/2}$  terms of the Nd<sup>3+</sup> ion in the Gd<sub>3</sub>Ga<sub>5</sub>O<sub>12</sub> : Nd film at room temperature.



**Fig. 7.** (a) Optical absorption spectrum of the  $4I_{9/2} \rightarrow 4F_{5/2}$  transition and the curves of decomposition into components and (b) diagram of the crystalline splitting of the  $4I_{9/2}$  and  $4F_{5/2}$  terms of the Nd<sup>3+</sup> ion in the Gd<sub>3</sub>Ga<sub>5</sub>O<sub>12</sub> : Nd film at room temperature.

**Table 3.** Stark levels of the Nd<sup>3+</sup> ion in the Gd<sub>3</sub>Ga<sub>5</sub>O<sub>12</sub> : Nd film at 300 K

Term	Nos. of Stark levels in the term (Fig. 5)	Positions of Stark levels in the term, cm <sup>-1</sup>	Number of Stark components				$\Delta E$ , cm <sup>-1</sup>
			theory	experiment	[12] Nd : YGaG	[13] Nd : Gd <sub>3</sub> Ga <sub>5</sub> O <sub>2</sub>	
<sup>4</sup> I <sub>9/2</sub>	1–5	0, 95, 178, 249, 761	5	5	4	5	761
<sup>4</sup> F <sub>3/2</sub>	6, 7	11438, 11484	2	2	2	2	46
<sup>4</sup> F <sub>5/2</sub>	8–10	12383, 12423, 12519	3	3	3	3	136
<sup>2</sup> H <sub>9/2</sub>	11–14	12565, 12596, 12598, 12810, ...	5	4	5	5	–
<sup>4</sup> F <sub>7/2</sub> + <sup>4</sup> S <sub>3/2</sub>	15–18	13375, 13415, ..., 13560, 13597, ...	6	4	5	6	–
<sup>4</sup> F <sub>9/2</sub>	19–22	14638, 14661, 14785, 14884, ...	5	4	4	4	–
<sup>2</sup> H <sub>11/2</sub>	23–28	15779, 15840, 15883, 15993, 16088, 16095	6	6	6	6	316
<sup>4</sup> G <sub>5/2</sub>	29–31	16888, 16991, 17053	3	3	3	3	165
<sup>2</sup> G <sub>7/2</sub>	32, 33	..., 17266, ..., 17551	4	2	4	4	–
<sup>4</sup> G <sub>7/2</sub>	34–37	18771, 18828, 18872, 18986	4	4	4	4	215
<sup>2</sup> G <sub>9/2</sub> + <sup>2</sup> K <sub>13/2</sub>	38–45	19248, 19324, 19383, 19494, 19570, 19692, 19821, 19991	12	8	10	10	743
<sup>4</sup> G <sub>9/2</sub>	46, 47	..., ..., 20813, 20825	5	2	3	4	–
<sup>4</sup> G <sub>11/2</sub>	48–52	21012, ..., 21089, 21116, 21171, 21190	6	5	5	6	178
<sup>2</sup> K <sub>15/2</sub>	53–56	21602, 21679, ..., ..., 21768, 21867	8	4	6	6	265
<sup>2</sup> D <sub>3/2</sub>	57	21978	2	1	–	1	–
<sup>2</sup> P <sub>1/2</sub>	58	23172	1	1	1	1	–
<sup>2</sup> D <sub>5/2</sub>	–	–	3	–	3	3	–
<sup>2</sup> P <sub>3/2</sub>	–	–	2	–	2	–	–
<sup>4</sup> D <sub>3/2</sub> + <sup>2</sup> I <sub>11/2</sub> + <sup>4</sup> D <sub>5/2</sub> + <sup>4</sup> D <sub>1/2</sub>	59–61	27718*, 28270*, 28854*	12	3	–	–	–

Note: The ellipsis ... indicates the position of the Stark levels, which we failed to determine in the grown films. The level positions marked by an asterisk require further refinement.

decomposed into components with the use of a specially developed program. The results of this decomposition with numbering of the maxima of the absorption bands are presented in Figs. 6a–8a. The diagrams of the crystalline splitting of the electron terms of the Nd<sup>3+</sup> ion in the Gd<sub>3</sub>Ga<sub>5</sub>O<sub>12</sub> : Nd film are depicted in Figs. 6b–8b.

In order to determine the absorption coefficient at the maximum of the absorption band at a wavelength of 806.9 nm (Table 1), we additionally measured the transmission spectra for the films and substrates in the wavelength range from 770 to 860 nm with a step of 0.1 nm and a spectral resolution of 0.1 nm. As the neodymium content increases, the absorption coefficient in the absence of scattering increases from 3.8 cm<sup>-1</sup> at C(Nd) = 0.3 at. % to 176.3 cm<sup>-1</sup> at C(Nd) = 15 at. %. The half-width (the full width at half-maximum) of this band also increases from 0.84 to 1.01 nm, respectively. For calcium niobium gallium garnet

(CNGG) and calcium lithium niobium gallium garnet (CLNGG) crystals doped with neodymium ions at C(Nd) = 1 at. %, the full width at half-maximum is equal to 4 nm. For yttrium aluminum garnet (YAG) crystals with the same neodymium content, the full width at half-maximum is approximately equal to 1 nm. The absorption coefficient at a wavelength of 807.5 nm is equal to 4 cm<sup>-1</sup> for CNGG and CLNGG and 12 cm<sup>-1</sup> for YAG [14].

It should be noted that, during double passage of a semiconductor diode laser at pumping wavelengths of 805 and 808 nm, epitaxial films with a neodymium content C(Nd) = 1.7–3.3 at. % absorb approximately 1/3 of the power. Therefore, these films can be used in cross-beam lasers. Moreover, epitaxial films with a neodymium content up to 3.3 at. %, for which the luminescence lifetime can be as long as 60 μs [5], hold promise for lasing.

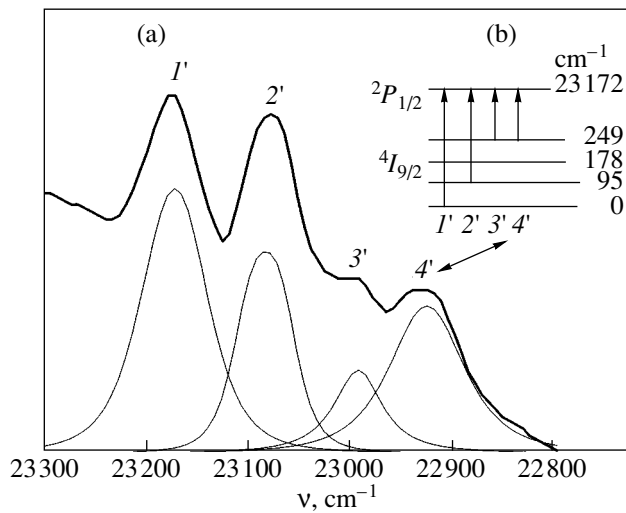


**Fig. 8.** (a) Optical absorption spectrum of the  ${}^4I_{9/2} \rightarrow {}^4P_{1/2}$  transition and curves of the decomposition into components and (b) diagram of the crystalline splitting of the  ${}^4I_{9/2}$  and  ${}^4P_{1/2}$  terms of the  $\text{Nd}^{3+}$  ion in the  $\text{Gd}_3\text{Ga}_5\text{O}_{12} : \text{Nd}$  film at room temperature.

## 5. CONCLUSIONS

In this work, we obtained the following results.

(i) Neodymium-containing single-crystal gallium garnet films with a neodymium content varying from 0.3 to 15 at. % were grown by liquid-phase epitaxy from a supercooled  $\text{PbO-B}_2\text{O}_3$ -based solution melt on  $\text{Gd}_3\text{Ga}_5\text{O}_{12}(111)$  substrates.

(ii) The energy diagram of Stark levels was constructed for different electron terms of the  $\text{Gd}^{3+}$  ion in  $\text{Gd}_3\text{Ga}_5\text{O}_{12}$  at room temperature.

(iii) It was found that the short-wavelength edge of the absorption band of  $\text{Gd}^{3+}$  ions in epitaxial films at a neodymium content of 15 at. % is shifted by 0.014 nm with respect to that in the substrate.

(iv) The positions of the Stark levels of the  $\text{Nd}^{3+}$  ion were determined for  $(\text{Gd},\text{Nd})_3\text{Ga}_5\text{O}_{12}$  and  $(\text{Gd},\text{Y},\text{Nd})_3\text{Ga}_5\text{O}_{12}$  epitaxial films at room temperature.

## ACKNOWLEDGMENTS

We would like to thank M.I. Belovolov, A.V. Vasil'ev, V.F. Lebedev, and S.N. Ushakov for their assistance in performing this work and participation in helpful discussions.

## REFERENCES

1. *A Handbook on Lasers*, Ed. by A. M. Prokhorov (Sovetskoe Radio, Moscow, 1978), Vol. 1, p. 237.
2. V. V. Randoshkin, V. I. Chani, and A. A. Tsvetkova, *Pis'ma Zh. Tekh. Fiz.* **13** (4), 839 (1987) [*Sov. Tech. Phys. Lett.* **13**, 348 (1987)].
3. J. P. van der Ziel, W. A. Bonner, L. Kopf, and L. G. van Uitert, *Phys. Lett. A* **42A** (1), 105 (1972).
4. W. A. Bonner, *J. Electron. Mater.* **3** (1), 193 (1974).
5. V. V. Randoshkin, M. I. Belovolov, N. V. Vasil'eva, K. A. Zykov-Myzin, A. M. Saletskii, N. N. Sysoev, and A. N. Churkin, *Kvantovaya Élektron. (Moscow)* **31** (9), 799 (2001).
6. V. V. Randoshkin, N. V. Vasil'eva, A. V. Vasil'ev, V. G. Plotnichenko, S. V. Lavrishchev, A. M. Saletskii, K. V. Stashun, N. N. Sysoev, and A. N. Churkin, *Fiz. Tverd. Tela (St. Petersburg)* **43** (9), 1594 (2001) [*Phys. Solid State* **43**, 1659 (2001)].
7. V. V. Randoshkin, N. V. Vasil'eva, A. M. Saletskii, K. V. Stashun, N. N. Sysoev, and A. N. Churkin, *Fiz. Mysl' Ross.*, No. 2, 27 (2000).
8. G. B. Scott and J. L. Page, *J. Appl. Phys.* **48** (3), 1342 (1977).
9. A. A. Kaminskiï, *Laser Crystals* (Nauka, Moscow, 1975).
10. Z. T. Azamatov, P. A. Arsen'ev, and M. V. Chukichev, *Opt. Spektrosk.* **28** (2), 289 (1970).
11. K. H. Hellwege, S. Hufner, and H. Schmidt, *Z. Phys.* **172** (4), 460 (1963).
12. J. A. Koningstein, *J. Chem. Phys.* **44** (10), 3957 (1966).
13. Kh. S. Bagdasarov, G. A. Bogomolova, M. M. Gritsenko, A. A. Kaminskiï, A. M. Kevorkov, A. M. Prokhorov, and S. É. Sarkisov, *Dokl. Akad. Nauk SSSR* **216** (5), 1018 (1974) [*Sov. Phys. Dokl.* **19**, 353 (1974)].
14. Yu. K. Voron'ko, N. A. Es'kov, A. S. Podstavkin, P. A. Ryabochkina, A. A. Sobol', and S. N. Ushakov, *Kvantovaya Élektron. (Moscow)* **31** (6), 531 (2001).

*Translated by N. Korovin*

---

## DEFECTS, DISLOCATIONS, AND PHYSICS OF STRENGTH

---

# Effect of Isolated Defects and Defect Pairs on the Spectrum of the Edge Luminescence of Solids

K. D. Glinchuk and A. V. Prokhorovich

Institute of Semiconductor Physics, National Academy of Sciences of Ukraine, pr. Nauki 45, Kiev, 03028 Ukraine  
e-mail: ria@isp.kiev.ua

Received May 5, 2003; in final form, August 26, 2003

**Abstract**—Expressions for the intensities of bands in the edge luminescence spectrum of a solid containing both isolated defects (shallow acceptors and donors) and defect pairs are given. Conditions under which the contribution of defects to the edge luminescence bands is negligible or dominant are found. Analysis of the edge luminescence spectrum of semi-insulating GaAs shows that situations in which the intensities of the edge luminescence bands are determined by the states of isolated shallow acceptors and donors and donor–acceptor pairs are quite probable. © 2004 MAIK “Nauka/Interperiodica”.

### 1. INTRODUCTION

It is known that, in the luminescence spectra of solids, intense edge (impurity and exciton–impurity) bands are observed; their appearance is due to recombination of electrons and holes at defects (shallow acceptors and donors) and annihilation of excitons bound to defects. When calculating the intensities of edge luminescence bands, it is usually assumed that a solid contains isolated defects (shallow acceptors and donors; we call them acceptors and donors in what follows) [1–5] or acceptors and donors forming donor–acceptor pairs [1, 6, 7]. However, it is obvious that there are both isolated acceptors and donors and donor–acceptor pairs. In this study, we calculate the intensities of near-edge luminescence bands in solids containing both isolated defects (shallow acceptors and donors) and defect pairs. We show that, in this case (in contrast to existing concepts), the contribution of isolated impurities and pairs to the edge luminescence spectra is not always determined only by the relationship between their concentrations. In particular, situations are quite probable in which isolated impurities and impurity pairs give substantially different contributions to the intensities of edge luminescence bands even if their concentrations are of the same order of magnitude. The relationships obtained are used to clarify the role of isolated impurities and impurity pairs in forming the edge luminescence spectrum of semi-insulating gallium arsenide crystals.

### 2. MODEL AND BASIC ASSUMPTIONS

We consider a solid at low temperatures, where there are no thermally stimulated processes and the conductivity is determined by uniformly distributed photoelectrons (with concentration  $\delta n$ ) and photoholes (with concentration  $\delta p$ ). Let the concentrations of isolated

acceptors and donors be  $N_{A1}$  and  $N_{D1}$  and the concentrations of acceptors and donors in the pairs be  $N_{A2}$  and  $N_{D2}$ , respectively (the total acceptor concentration is  $N_A = N_{A1} + N_{A2}$ , and the total donor concentration is  $N_D = N_{D1} + N_{D2}$ ). We denote by  $c_{nA}^0$  and  $c_{nD}^+$  the capture coefficients of free electrons by acceptors and donors, respectively, and by  $c_{pA}^-$  and  $c_{pD}^0$  the capture coefficients of free holes by acceptors and donors, respectively. Let the average coefficient of interimpurity recombination be  $c_n^*$ . The probabilities of occupation of the acceptors in the pairs (at low interimpurity transition rates) and isolated acceptors by holes are  $\varphi_{A^0} = c_{pA}^- \delta p / (c_{pA}^- \delta p + c_{nA}^0 \delta n)$ , the probability of donors filling by electrons is  $\varphi_{D^0} = c_{nD}^+ \delta n / (c_{nD}^+ \delta n + c_{pD}^0 \delta p)$ , and the probability of donors filling by holes is  $1 - \varphi_{D^0} = c_{pD}^0 \delta p / (c_{nD}^+ \delta n + c_{pD}^0 \delta p)$  [5, 7]. Free X excitons (with concentration  $n_X$ ) can be bound to neutral acceptors  $A^0$  and ionized  $D^+$  and neutral  $D^0$  donors forming exciton–impurity complexes  $A^0X$ ,  $D^+X$ , and  $D^0X$  (the binding coefficients are  $b_{A^0X}$ ,  $b_{D^+X}$ ,  $b_{D^0X}$ , and the probabilities are  $b_{A^0X} N_{A^0}$ ,  $b_{D^+X} N_{D^+}$ ,  $b_{D^0X} N_{D^0}$ , respectively). Below, we write expressions for intensities of edge luminescence bands corresponding to free-electron (e) transitions to neutral acceptors ( $I_{eA^0}$ ), free-hole (h) transitions to neutral donors ( $I_{hd^0}$ ), donor–acceptor transitions ( $I_{D^0A^0}$ ), and annihilation of bound excitons  $A^0X$ ,  $D^+X$ , and  $D^0X$  ( $I_{A^0X}$ ,  $I_{D^+X}$ , and  $I_{D^0X}$ , respectively) (see Fig. 1) under the assumption that recombination transi-

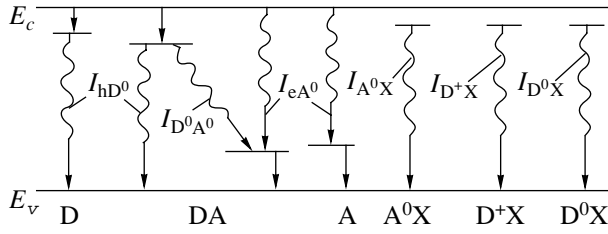


**Fig. 1.** Radiative (wavy lines) and nonradiative (straight lines) transitions to isolated donors D and acceptors A, transitions in donor–acceptor pairs DA, and bound exciton transitions  $A^0X$ ,  $D^+X$ , and  $D^0X$ .

tions are mainly radiative. Moreover, the intensities of the edge spectrum bands are usually determined using the most probable relationships between the quantities  $c_{nD}^+ N_{D2} \delta n = b$  and  $c_{pA}^- N_{A2} \delta p = d$  ( $b \gg d$  or  $d \gg b$ ) and for the case of low  $[c_n^*(b + d) \gg (c_{nD}^+ \delta n + c_{pD}^0 \delta p)(c_{pA}^- \delta p + c_{nA}^0 \delta n) = a]$  and high  $[a \gg c_n^*(b + d)]$  values of  $\delta p$  and  $\delta n$ . The reason for this is that one can obtain convenient analytical expressions for the concentrations of acceptors and donors in pairs in different charge states only in these cases [5, 7].

### 3. THEORETICAL EXPRESSIONS FOR THE INTENSITIES OF EDGE LUMINESCENCE BANDS IN SEMICONDUCTORS CONTAINING BOTH ISOLATED IMPURITIES AND DONOR–ACCEPTOR PAIRS

#### 3.1. General Relationships

Obviously, in the case under study, the spectrum of edge luminescence is formed by electron–hole transitions both to isolated acceptors and donors and to donor–acceptor pairs and also by annihilation of bound excitons (Fig. 1). The band intensities are determined by the concentrations of neutral acceptors and ionized and neutral donors both that are isolated ( $N_{A^0_1}$ ,  $N_{D^+1}$ , and  $N_{D^0_1}$ , respectively) and form pairs ( $N_{A^0_2}$ ,  $N_{D^+2}$ , and  $N_{D^0_2}$ , respectively; we have  $N_{D^+1} + N_{D^0_1} = N_{D1}$  and  $N_{D^+2} + N_{D^0_2} = N_{D2}$ ), as well as by the concentrations of photoelectrons, photoholes, and free excitons ( $\delta n$ ,  $\delta p$ , and  $n_X$ , respectively, which are possibly dependent on  $N_A$  and  $N_D$ ). The intensities are given by (see Fig. 1)<sup>1</sup>

$$I_{eA^0} = c_{nA}^0 (N_{A^0_1} + N_{A^0_2}) \delta n, \quad (1)$$

<sup>1</sup>When writing expressions (4)–(6), we assumed that only a small number of neutral acceptors and ionized and neutral donors are occupied by bound excitons.

$$I_{hD^0} = c_{pD}^0 (N_{D^0_1} + N_{D^0_2}) \delta p, \quad (2)$$

$$I_{D^0A^0} = c_n^* N_{D^0_2} N_{A^0_2}, \quad (3)$$

$$I_{A^0X} = b_{A^0X} (N_{A^0_1} + N_{A^0_2}) n_X, \quad (4)$$

$$I_{D^+X} = b_{D^+X} (N_{D^+1} + N_{D^+2}) n_X, \quad (5)$$

$$I_{D^0X} = b_{D^0X} (N_{D^0_1} + N_{D^0_2}) n_X. \quad (6)$$

It follows from Eqs. (1)–(6) that the relative effects of isolated acceptors and donors and of donor–acceptor pairs on the intensities of edge luminescence bands depend on the relationship between the values of  $N_{A^0_1}$  and  $N_{A^0_2}$ ,  $N_{D^+1}$  and  $N_{D^+2}$ , and  $N_{D^0_1}$  and  $N_{D^0_2}$  (the intensities are determined by isolated acceptors and donors if  $N_{A^0_1} \gg N_{A^0_2}$ ,  $N_{D^+1} \gg N_{D^+2}$ , and  $N_{D^0_1} \gg N_{D^0_2}$  and by donor–acceptor pairs if  $N_{A^0_2} \gg N_{A^0_1}$ ,  $N_{D^+2} \gg N_{D^+1}$ , and  $N_{D^0_2} \gg N_{D^0_1}$ ). It also follows from Eqs. (1)–(6) that the intensities  $I_{eA^0}$  and  $I_{A^0X}$  are related to the same state of acceptors (isolated if  $N_{A^0_1} \gg N_{A^0_2}$  and belonging to pairs if  $N_{A^0_2} \gg N_{A^0_1}$ ) and that the intensities  $I_{hD^0}$  and  $I_{D^0X}$  are determined by the same state of donors (isolated if  $N_{D^0_1} \gg N_{D^0_2}$  and belonging to pairs if  $N_{D^0_2} \gg N_{D^0_1}$ ).

In what follows, we use expressions (1)–(6) to define the intensities of edge luminescence bands in semiconductors containing both isolated acceptors and donors and donor–acceptor pairs at low and high concentrations of photoholes and photoelectrons (the quantities  $N_{A^0_{1,2}}$ ,  $N_{D^+_{1,2}}$ , and  $N_{D^0_{1,2}}$  in these expressions are given in [5, 7] for different relationships between  $b$  and  $d$  and for low and high values of  $\delta p$  and  $\delta n$ ).

We represent each of the above expressions for  $I_{eA^0}$ ,  $I_{hD^0}$ ,  $I_{A^0X}$ ,  $I_{D^+X}$ , and  $I_{D^0X}$  as the sum of two terms, one of which describes the contribution of isolated acceptors and donors to the intensities of edge luminescence bands and the second represents the contribution from donor–acceptor pairs.

#### 3.2. Low Values of $\delta p$ and $\delta n$

For simplicity, we restrict ourselves to the typical cases  $c_{nD}^+ N_{D2} \delta n \gg c_{pA}^- N_{A2} \delta p$  and  $c_{pA}^- N_{A2} \delta p \gg c_{nD}^+ N_{D2} \delta n$ .

**3.2.1.**  $c_{nD}^+ N_{D2} \delta n \gg c_{pA}^- N_{A2} \delta p$ . If this condition on the recombination parameters of shallow defects is sat-

ified, then the intensities of the impurity, interimpurity, and exciton luminescence are given by

$$I_{eA^0} = c_{nA}^0 \left( \varphi_{A0} N_{A1} + \frac{c_{pA}^- \delta p}{c_n^* \varphi_{D^0} N_{D2}} N_{A2} \right) \delta n, \quad (7)$$

$$I_{hd^0} = c_{pD}^0 \varphi_{D^0} (N_{D1} + N_{D2}) \delta p, \quad (8)$$

$$I_{D^0A^0} = c_{pA} N_{A2} \delta p, \quad (9)$$

$$I_{A^0X} = b_{A^0X} \left( \varphi_{A^0} N_{A1} + \frac{c_{pA}^- \delta p}{c_n^* \varphi_{D^0} N_{D2}} N_{A2} \right) n_X, \quad (10)$$

$$I_{D^+X} = b_{D^+X} \left\{ (1 - \varphi_{D^0}) N_{D1} + \left[ (1 - \varphi_{D^0}) N_{D2} + \frac{c_{pA}^- N_{A2} \delta p}{c_{nD}^+ \delta n + c_{pD}^0 \delta p} \right] \right\} n_X, \quad (11)$$

$$I_{D^0X} = b_{D^0X} \varphi_{D^0} (N_{D1} + N_{D2}) n_X \quad (12)$$

(here, obviously,  $c_{pA}^- \delta p / c_n^* \varphi_{D^0} N_{D2} \ll 1$ ,  $c_{pA}^- N_{A2} \delta p / (c_{nD}^+ \delta n + c_{pD}^0 \delta p) \ll N_{D2}$ , and  $N_{D1} + N_{D2} = N_D$ ).

In this case, we have the following:<sup>2</sup>

(1)  $I_{eA^0}/I_{D^0A^0} = c_{nA}^0 \varphi_{A^0} N_{A1} \delta n / c_{pA}^- N_{A2} \delta p$  if  $I_{eA^0}$  is determined by isolated acceptors [therefore,  $I_{eA^0} \ll I_{D^0A^0}$  if  $N_{A2} \geq N_{A1}$  and  $\varphi_{A^0} \approx 1$ ;  $I_{eA^0}/I_{D^0A^0} = N_{A1}/N_{A2}$  ( $I_{eA^0} > I_{D^0A^0}$  for  $N_{A1} > N_{A2}$ , and  $I_{eA^0} < I_{D^0A^0}$  for  $N_{A1} < N_{A2}$ ) if  $\varphi_{A^0} \ll 1$ ], and  $I_{eA^0}/I_{D^0A^0} = c_{nA}^0 \delta n / c_n^* \varphi_{D^0} N_{D2} \ll 1$  if  $I_{eA^0}$  is determined by acceptors of the pairs;

(2)  $I_{hd^0}/I_{D^0A^0} = c_{pD}^0 \varphi_{D^0} N_{D1} / c_{pA}^- N_{A2}$  if  $I_{hd^0}$  is determined by isolated donors, and  $I_{hd^0}/I_{D^0A^0} = c_{pD}^0 \varphi_{D^0} N_{D2} / c_{pA}^- N_{A2}$  if  $I_{hd^0}$  is determined by donors of the pairs (typically,  $I_{hd^0} \ll I_{D^0A^0}$ , since one might expect that  $c_{pD}^0 \ll c_{pA}^-$ );

<sup>2</sup> Obviously,  $\varphi_{A^0} \approx 1$  if  $c_{pA}^- \delta p \gg c_{nA}^0 \delta n$ ;  $\varphi_{A^0} = c_{pA}^- \delta p / c_{nA}^0 \delta n \ll 1$  if  $c_{pA}^- \delta p \ll c_{nA}^0 \delta n$ ;  $\varphi_{D^0} \approx 1$  if  $c_{nD}^+ \delta n \gg c_{pD}^0 \delta p$  (then  $1 - \varphi_{D^0} = c_{pD}^0 \delta p / c_{nD}^+ \delta n \ll 1$ ); and  $\varphi_{D^0} = c_{nD}^+ \delta n / c_{pD}^0 \delta p \ll 1$  if  $c_{nD}^+ \delta n \ll c_{pD}^0 \delta p$ . Of course,  $\varphi_{A^0}, 1 - \varphi_{D^0}, \varphi_{D^0} \neq (\delta n, \delta p)$  if  $\delta p \sim \delta n$ .

(3)  $I_{eA^0} \sim \varphi_{A^0} \delta n$  and  $I_{A^0X} \sim \varphi_{A^0} n_X$  if the radiation is due to isolated acceptors (then  $I_{eA^0} \sim \delta p$  and  $I_{A^0X} \sim (\delta p / \delta n) n_X$  if  $\varphi_{A^0} \ll 1$ ), and  $I_{eA^0} \sim \delta p \delta n / \varphi_{D^0}$  and  $I_{A^0X} \sim n_X \delta p / \varphi_{D^0}$  if the radiation is due to acceptors of the pairs (then  $I_{eA^0} \sim \delta p^2$  and  $I_{A^0X} \sim (\delta p^2 / \delta n) n_X$  if  $\varphi_{D^0} \ll 1$ );

(4)  $I_{hd^0} \sim \varphi_{D^0} \delta p$ ,  $I_{D^+X} \sim (1 - \varphi_{D^0}) n_X$ , and  $I_{D^0X} \sim \varphi_{D^0} n_X$  if the radiation is due to isolated donors or to acceptors and donors of the pairs [then  $I_{D^+X} \sim (\delta p / \delta n) n_X$  if  $\varphi_{D^0} \approx 1$  and  $I_{hd^0} \sim \delta n$  and  $I_{D^0X} \sim (\delta n / \delta p) n_X$  if  $\varphi_{D^0} \ll 1$ ].

**3.2.2.**  $c_{pA}^- N_{A2} \delta p \gg c_{nD}^+ N_{D2} \delta n$ . If this inequality is satisfied, then the intensities of edge luminescence bands are determined by

$$I_{eA^0} = c_{nA}^0 \varphi_{A^0} (N_{A1} + N_{A2}) \delta n, \quad (13)$$

$$I_{hd^0} = c_{pD}^0 \left( \varphi_{D^0} N_{D1} + \frac{c_{nD}^+ \delta n}{c_n^* \varphi_{A^0} N_{A2}} N_{D2} \right) \delta p, \quad (14)$$

$$I_{D^0A^0} = c_{nD}^+ N_{D2} \delta n, \quad (15)$$

$$I_{A^0X} = b_{A^0X} \varphi_{A^0} (N_{A1} + N_{A2}) n_X, \quad (16)$$

$$I_{D^+X} = b_{D^+X} [(1 - \varphi_{D^0}) N_{D1} + N_{D2}] n_X, \quad (17)$$

$$I_{D^0X} = b_{D^0X} \left( \varphi_{D^0} N_{D1} + \frac{c_{nD}^+ \delta n}{c_n^* \varphi_{A^0} N_{A2}} N_{D2} \right) n_X \quad (18)$$

(here, obviously,  $c_{nD}^+ \delta n / c_n^* \varphi_{A^0} N_{A2} \ll 1$  and  $N_{A1} + N_{A2} = N_A$ ). In this case, we have the following:

(1)  $I_{eA^0}/I_{D^0A^0} = c_{nA}^0 \varphi_{A^0} N_{A1} / c_{nD}^+ N_{D2}$  if  $I_{eA^0}$  is determined by isolated acceptors, and  $I_{eA^0}/I_{D^0A^0} = c_{nA}^0 \varphi_{A^0} N_{A2} / c_{nD}^+ N_{D2}$  if  $I_{eA^0}$  is determined by acceptors of the pairs (typically,  $I_{eA^0} \ll I_{D^0A^0}$ , since one might expect that  $c_{nA}^0 \ll c_{nD}^+$ );

(2)  $I_{hd^0}/I_{D^0A^0} = c_{pD}^0 \varphi_{D^0} N_{D1} \delta p / c_{nD}^+ N_{A2} \delta n$  if  $I_{hd^0}$  is determined by isolated donors [then  $I_{hd^0} \ll I_{D^0A^0}$  if  $N_{D2} \geq N_{D1}$  and  $\varphi_{D^0} \approx 1$  and  $I_{hd^0}/I_{D^0A^0} = N_{D1}/N_{D2}$  (i.e.,  $I_{hd^0} > I_{D^0A^0}$  for  $N_{D1} > N_{D2}$  and  $I_{hd^0} < I_{D^0A^0}$  for  $N_{D1} <$

$N_{D2}$ ) if  $\varphi_{D^0} \ll 1$ ], and  $I_{hd^0}/I_{D^0A^0} = c_{pD}^0 \delta p / c_n^* \varphi_{A^0} N_{A2} \ll 1$  if  $I_{hd^0}$  is determined by donors of the pairs;

(3)  $I_{eA^0} \sim \varphi_{A^0} \delta n$  and  $I_{A^0X} \sim \varphi_{A^0} n_X$  if the radiation is due to isolated acceptors or acceptors of the pairs [then  $I_{eA^0} \sim \delta p$  and  $I_{A^0X} \sim (\delta p / \delta n) n_X$  if  $\varphi_{A^0} \ll 1$ ];

(4)  $I_{hd^0} \sim \varphi_{D^0} \delta p$ ,  $I_{D^+X} \sim (1 - \varphi_{D^0}) n_X$ , and  $I_{D^0X} \sim \varphi_{D^0} n_X$  if the radiation is due to isolated donors [then  $I_{D^+X} \sim (\delta p / \delta n) n_X$  if  $\varphi_{D^0} \approx 1$  and  $I_{hd^0} \sim \delta n$  and  $I_{D^0X} \sim (\delta n / \delta p) n_X$  if  $\varphi_{D^0} \ll 1$ ], and  $I_{hd^0} \sim \delta p \delta n / \varphi_{A^0}$ ,  $I_{D^+X} \sim n_X$ , and  $I_{D^0X} \sim n_X \delta n / \varphi_{A^0}$  if the radiation is due to donors of the pairs [then  $I_{hd^0} \sim \delta n^2$  and  $I_{D^0X} \sim (\delta n^2 / \delta p) n_X$  if  $\varphi_{A^0} \ll 1$ ].

### 3.3. High Values of $\delta n$ and $\delta p$

Obviously, at high  $\delta n$  and  $\delta p$ , the intensities of edge luminescence bands are

$$I_{eA^0} = c_{nA}^0 \varphi_{A^0} (N_{A1} + N_{A2}) \delta n, \quad (19)$$

$$I_{hd^0} = c_{pD}^0 \varphi_{D^0} (N_{D1} + N_{D2}) \delta p, \quad (20)$$

$$I_{D^0A^0} = c_n^* N_{A2} N_{D2}, \quad (21)$$

$$I_{A^0X} = b_{A^0X} \varphi_{A^0} (N_{A1} + N_{A2}) n_X, \quad (22)$$

$$I_{D^+X} = b_{D^+X} (1 - \varphi_{D^0}) (N_{D1} + N_{D2}) n_X, \quad (23)$$

$$I_{D^0X} = b_{D^0X} \varphi_{D^0} (N_{D1} + N_{D2}) n_X, \quad (24)$$

where, as noted above,  $N_{A1} + N_{A2} = N_A$  and  $N_{D1} + N_{D2} = N_D$ .<sup>3</sup>

In this case, (1)  $I_{eA^0}, I_{hd^0} \gg I_{D^0A^0}$  and (2) the form of the dependences  $I_{eA^0}, I_{hd^0}, I_{A^0X}, I_{D^+X}$ , and  $I_{D^0X}$  on  $\delta p$  and  $\delta n$  is the same for the cases where the radiation is related to isolated acceptors and donors and to donor–acceptor pairs [ $I_{D^+X} \sim (\delta p / \delta n)$  for  $\varphi_{D^0} \approx 1$ ;  $I_{eA^0} \sim \delta p$  and  $I_{A^0X} \sim (\delta p / \delta n) n_X$  for  $\varphi_{A^0} \ll 1$ ; and  $I_{hd^0} \sim \delta n$  and  $I_{D^0X} \sim (\delta n / \delta p) n_X$  for  $\varphi_{D^0} \ll 1$ ].

<sup>3</sup> In Eq. (23) for  $I_{D^+X}$ , we took into account that  $N_{D^+2} \approx (1 - \varphi_{D^0}) N_{D2}$  at high  $\delta p$  and  $\delta n$  [7]. As follows from the general expression for  $dN_{D^+2}/dt = -dN_{D^02}/dt = 0$  (see [7, Eq. (2)]), this is justified for  $c_{pD}^0 \delta p \gg c_n^* N_{A^02} \approx c_n^* \varphi_{A^0} N_{A2}$ , i.e., for high  $\delta p$ .

### 3.4. Discussion

**3.4.1. Low values of  $\delta p$  and  $\delta n$ .** When analyzing the above expressions for the intensities of edge luminescence bands at low photohole and photoelectron concentrations, we can make the following comments. Only in certain cases do the contributions from isolated acceptors and donors and from donor–acceptor pairs to the intensities of edge luminescence bands of a semiconductor depend only on the relative concentrations (they are proportional to the concentrations if  $\delta n, \delta p$ , and  $n_X$  are independent of  $N_A$  and  $N_D$ ). These cases correspond to the situation in which the quantities  $N_{A^02}, N_{D^+2}$ , and  $N_{D^02}$  are only slightly affected by interimpurity transitions, i.e.,  $N_{A^02}, N_{D^+2}$ , and  $N_{D^02} \neq \varphi(c_n^*)$ . In these cases, the edge luminescence spectrum is determined by isolated acceptors and donors if  $N_{A1} \gg N_{A2}$  and  $N_{D1} \gg N_{D2}$ , and, on the contrary, by acceptors and donors of the pairs if  $N_{A2} \gg N_{A1}$  and  $N_{D2} \gg N_{D1}$ . For  $b \gg d$ , this statement refers to the intensities  $I_{hd^0}$  and  $I_{D^0X}$ , and for  $d \gg b$ , to the intensities  $I_{eA^0}, I_{A^0X}$ , and  $I_{D^+X}$  [see Eqs. (8), (12), (13), (16), (17)]. However, in most cases (where interimpurity transitions essentially affect the quantities  $N_{A^01}, N_{D^+2}$ , and  $N_{D^02}$ ), the contributions from isolated acceptors and donors and from donor–acceptor pairs to the intensities of the edge luminescence bands of the semiconductor depend not only on their relative concentrations but also on the recombination characteristics. Thus, for  $\varphi_{A^0} N_{A1} \gg (c_{pA}^- \delta p / c_n^* \varphi_{D^0} N_{D2}) N_{A2}$  and  $\varphi_{D^0} N_{D1} \gg (c_{nD}^+ \delta n / c_n^* \varphi_{A^0} N_{A2}) N_{D2}$ , the luminescence intensities  $I_{eA^0}$  and  $I_{A^0X}$  (for  $b \gg d$ ) and  $I_{hd^0}$  and  $I_{D^0X}$  (for  $d \gg b$ ) can be determined by isolated acceptors and donors even if their concentrations  $N_{A1}$  and  $N_{D1}$  are much lower than the concentrations of acceptors  $N_{A2}$  and donors  $N_{D2}$  in the pairs [see Eqs. (7), (10), (14), (18)]. At the same time, the intensity of exciton luminescence  $I_{D^+X}$  can be determined by acceptors of the pairs (for  $b \gg d$ ) even if their concentration  $N_{A2}$  is lower than the donor concentration  $N_D$  [for  $c_{pA}^- N_{A2} \gg c_{pD}^0 N_D$ , see Eq. (11)] and by donors of the pairs (for  $d \gg b$ ) even if their concentration  $N_{D2}$  is much lower than the concentration of isolated donors  $N_{D1}$  [this is the case for  $N_{D2} \gg (1 - \varphi_{D^0}) N_{D1}$ ; see Eq. (17)]. Obviously, the intensity of interimpurity luminescence is determined only by acceptors and donors of the pairs [see Eqs. (9), (15)].

Typically, under the conditions considered, we have  $I_{eA^0}, I_{hd^0} \ll I_{D^0A^0}$  (see Subsection 3.2). Only in certain



cases (if the intensities  $I_{eA^0}$  and  $I_{hd^0}$  are determined by isolated acceptors and donors,  $N_{A1} > N_{A2}$ ,  $\varphi_{A^0} \ll 1$ , and  $N_{D1} > N_{D2}$ ,  $\varphi_{D^0} \ll 1$ ) can the inequalities  $I_{eA^0}, I_{hd^0} > I_{D^0A^0}$  be satisfied.

Of course, at low photohole and photoelectron concentrations, the illumination–brightness characteristics for the intensities  $I_{eA^0}$  and  $I_{hd^0}$  and for  $I_{A^0X}$ ,  $I_{D^+X}$ , and  $I_{D^0X}$  coincide ( $I_{eA^0}, I_{hd^0} \sim \delta n$  or  $\delta p$ , and  $I_{A^0X}, I_{D^+X}, I_{D^0X} \sim n_X$ ) if they correspond to isolated acceptors and donors and  $\delta p \sim \delta n$  [i.e.,  $\varphi_{A^0}, \varphi_{D^0} \neq \varphi(\delta p, \delta n)$ ] (see Subsection 3.2). At the same time, the illumination–brightness characteristics for the intensities  $I_{eA^0}$  and  $I_{hd^0}$  or for  $I_{A^0X}$  and  $I_{D^0X}$  are substantially different if they are determined by acceptors and donors of the pairs.

**3.4.2. High  $\delta p$  and  $\delta n$ .** Clearly, at high photohole and photoelectron concentrations, the contributions of isolated acceptors and donors and of donor–acceptor pairs to the intensities of edge bands of impurity and exciton luminescence of a semiconductor depend only on their relative concentrations (the intensities are proportional to the concentrations if  $\delta n$ ,  $\delta p$ , and  $n_X$  do not depend on  $N_A$  and  $N_D$ ) [see Eqs. (19), (20), (22)–(24)]. Obviously, the intensity of interimpurity luminescence in this case, as well for low values of  $\delta p$  and  $\delta n$ , is determined only by donor–acceptor pairs [see Eq. (21)]. In the case considered, the illumination–brightness characteristics for the intensities  $I_{eA^0}$  and  $I_{hd^0}$  or for  $I_{A^0X}$ ,  $I_{D^+X}$ , and  $I_{D^0X}$  coincide ( $I_{eA^0}, I_{hd^0} \sim \delta n$  or  $\delta p$ , and  $I_{A^0X}, I_{D^+X}, I_{D^0X} \sim n_X$ ) irrespective of their being determined by isolated acceptors and donors or by donor–acceptor pairs and  $\delta p \sim \delta n$  [i.e.,  $\varphi_{A^0}, \varphi_{D^0} \neq \varphi(\delta p, \delta n)$ ] (see Subsection 3.3).

#### 4. ANALYSIS OF THE SPECTRUM OF EDGE LUMINESCENCE OF SEMI-INSULATING GaAs

Figure 2 shows the spectrum of edge luminescence and the dependence of the spectral-band intensities on the excitation intensity  $L$  measured for undoped semi-insulating gallium arsenide at 4.2 K at low  $\delta p$  and  $\delta n$  (the luminescence was excited by He–Ne laser radiation,  $\lambda = 632.8$  nm,  $h\nu = 1.96$  eV; the conductivity was controlled by excess holes and electrons,  $\delta p, \delta n \sim L$ ). The shape of the edge luminescence spectrum and intensities of spectral bands are determined by (a) radiative transitions in the donor–acceptor pairs (luminescence band  $I_{D^0A^0}$ ), (b) radiative recombination due to transitions of free electrons to isolated acceptors (band  $I_{eA^0}$ ) and radiative annihilation of excitons bound to

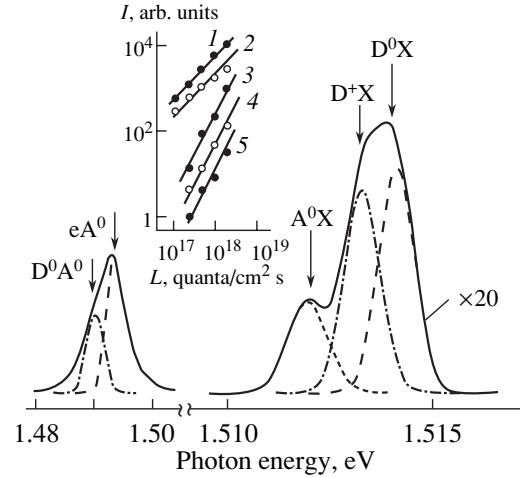


**Fig. 2.** The spectrum of edge luminescence of semi-insulating gallium arsenide (different dashed lines correspond to the decomposition of the spectrum into elementary components). The inset shows the dependence of the intensities of edge luminescence bands (1)  $I_{D^0A^0}$ , (2)  $I_{eA^0}$ , (3)  $I_{A^0X}$ , (4)  $I_{D^+X}$ , and (5)  $I_{D^0X}$  on the excitation intensity (the ratios of the band intensities are arbitrary; the actual relations between the band intensities can be seen from the spectrum). Measurements were performed at  $T = 4.2$  K for low values of  $\delta p$  and  $\delta n$ ; the spectrum was recorded at  $L = 10^{18}$  quanta/cm<sup>2</sup> s.

isolated acceptors (band  $I_{A^0X}$ ), and (c) radiative annihilation of excitons bound to isolated donors (bands  $I_{D^+X}$  and  $I_{D^0X}$ ). The intensities  $I_{A^0X}$ ,  $I_{D^+X}$ , and  $I_{D^0X}$  depend on the excitation intensity  $L$  in a similar way; namely,  $I_{A^0X}, I_{D^+X}, I_{D^0X} \sim L^2$  (see Fig. 2 and Subsection 3.4); this is possible if  $\delta p \sim \delta n$ . The similar excitation intensity dependence indicates the dominant role of isolated acceptors and donors in forming the corresponding luminescence bands. The dominant contribution of isolated acceptors to the band intensity  $I_{eA^0}$  is confirmed by the fact that the defects responsible for the band intensity  $I_{A^0X}$  were established to be isolated acceptors (as noted in Subsection 3.1, the bands with intensities  $I_{eA^0}$  and  $I_{A^0X}$  are related to the same acceptor state). This conclusion is also confirmed by the close values of the intensities  $I_{eA^0}$  and  $I_{D^0A^0}$  at any value of  $L$  ( $I_{eA^0}, I_{D^0A^0} \sim L$ ; i.e., the ratio  $I_{eA^0}/I_{D^0A^0}$  does not depend on  $L$ ) (see Fig. 2 and Subsection 3.4). Therefore, both isolated acceptors and donors and donor–acceptor pairs contribute to the spectrum of edge luminescence in semi-insulating gallium arsenide.

## 5. CONCLUSIONS

The contribution from shallow isolated defects and defect pairs to the intensities of low-temperature edge luminescence bands can be both additive (depending only on the relative defect concentrations) and nonadditive (depending both on the relative concentrations and on the recombination characteristics of the defects, as well as on the photoelectron and photohole concentrations in a solid). This conclusion is based on the fact that the filling of shallow defects by electrons and holes, i.e., the values  $N_{A^{0_2}}$ ,  $N_{D^{+2}}$ , and  $N_{D^{0_2}}$ , is affected differently by interimpurity transitions. The above relations between the intensities of impurity, interimpurity, and exciton radiation bands, as well as the dependence of the intensities of edge luminescence bands on the excitation level, enable one to experimentally establish the contributions of shallow isolated defects and defect pairs to the spectrum of edge luminescence in solids.

## REFERENCES

1. A. A. Bergh and P. J. Dean, *Light-Emitting Diodes* (Clarendon, Oxford, 1976, Mir, Moscow, 1979).
2. O. Brandt, J. Ringling, and K. H. Ploog, *Phys. Rev. B* **58** (24), R15977 (1998).
3. S. Seto, K. Suzuki, M. Adachi, and K. Inabe, *Physica B* (Amsterdam) **302–303**, 307 (2000).
4. I. Brousell, J. A. H. Stotz, and M. L. W. Thewalt, *J. Appl. Phys.* **92** (10), 5913 (2002).
5. K. D. Glinchuk and A. V. Prokhorovich, *Fiz. Tekh. Poluprovodn. (St. Petersburg)* **36** (5), 519 (2002) [*Semiconductors* **36**, 487 (2002)].
6. T. Schmidt, K. Lischka, and W. Zulehner, *Phys. Rev. B* **45** (16), 8989 (1992).
7. K. D. Glinchuk and A. V. Prokhorovich, *Fiz. Tekh. Poluprovodn. (St. Petersburg)* **37** (2), 159 (2003) [*Semiconductors* **37**, 148 (2003)].

*Translated by I. Zvyagin*

---

---

**DEFECTS, DISLOCATIONS,  
AND PHYSICS OF STRENGTH**

---

---

## Study of the IR Photoionization Spectrum of Electronic States Generated under Plastic Deformation of Colored NaCl Crystals

**E. V. Korovkin**

*Institute of Solid-State Physics, Russian Academy of Sciences, Chernogolovka, Moscow oblast, 142432 Russia*

*e-mail: korovkin@issp.ac.ru*

Received June 6, 2003; in final form, October 13, 2003

**Abstract**—This paper reports on the results of an experimental study of IR photoconductivity induced in NaCl single crystals colored under gamma irradiation and subjected to plastic deformation after preliminary exposure to *F*-center exciting light. The IR photoconductivity spectrum is decomposed into main components, among which the broad band observed in the range 0.64–2.20 eV upon plastic deformation is of special interest. The assumption is made that this band can be caused by photoionization of electrons in the dislocation band and deeper localized electronic states associated with the dislocation. © 2004 MAIK “Nauka/Interperiodica”.

1. The electronic properties of dislocations in semiconductors have been intensively studied in recent years (see, for example, [1, 2]). Similar investigations in dielectrics, in particular, alkali halide crystals, are also of great interest. These investigations go back to the discovery of the phenomenon of luminescence in colored alkali halide crystals under deformation [3–5]. More recently, it was found that luminescence is also observed under plastic deformation of alkali halide crystal samples without fracture of the material. These findings provided a basis for the development of model concepts regarding the existence of a dislocation electronic level (band) [6–13] (see also references in [13]). A considerable contribution to the elaboration of the model concepts was made by the discovery of IR quenching of the photoplastic effect in alkali halide crystals [14]. Ermakov and Nadgornyi [14] interpreted the measured IR quenching spectrum in terms of the photoionization spectrum of electrons in a dislocation level (band). Subsequent investigations of the photoplastic effect in alkali halide crystals have actually proved not only the participation of “dislocation” electrons in the photoplastic effect itself and in its manifestations (such as IR quenching, aftereffect, photoplastic memory) but also the motion of electrons along a dislocation (i.e., the existence of dislocation-induced electron bands in alkali halide crystals) and with a dislocation [15, 16] (see also references in [16]).

Infrared photoconductivity induced after exposure of a sample to *F*-center exciting light (*F*-induced IR photoconductivity) is an efficient tool for studying electronic levels in colored alkali halide crystals. Electrons released from *F* centers under exposure to *F* light occupy electron traps, including the dislocation level. The observed IR quenching of the photoplastic effect at room temperature [16] indicates that dislocation elec-

trons have a long lifetime at room temperature and remain stable at low temperatures. Therefore, the exposure of a sample to light at a specific wavelength (according to [14], IR light) should lead to photoionization of dislocation electrons and, consequently, the possibility of observing IR photoconductivity. Our first attempts to carry out such experiments enabled us to detect an intense signal due to polaron-type electronic states at liquid-helium temperatures (see [17] and references therein). These experimental investigations revealed that polaron states in NaCl disappear at temperatures  $T > 90$ – $100$  K. On the other hand, according to our data, the deformation of NaCl crystals brings about the formation of a large number of defects that have a dipole moment and are responsible for the strong signal detected at  $T > 180$  K. In our more recent work [18], these findings were taken into account when choosing the temperature of the sample and the experiments were performed in the temperature range from 110 to 120 K. It was found that, upon plastic deformation of NaCl crystals colored under gamma irradiation, the spectrum of IR photoconductivity induced by *F* light contains a broad band with two sharp maxima at photon energies of 0.74 and 0.88 eV. It is known that plastic deformation leads to the formation of a large number of point defects and their complexes in the sample; part of these defects can capture electrons from the conduction band and thus initiate a signal of IR conductivity induced by *F* light. Therefore, it can be assumed that the observed band consists of individual peaks (forming the aforementioned two sharp maxima) corresponding to electron traps of different types. Since the position of the maximum at 0.74 eV is close to the position of the maximum at 0.7 eV in the IR quenching spectrum [14], we can also assume that the former maximum is attributed to the photoionization of dislocation

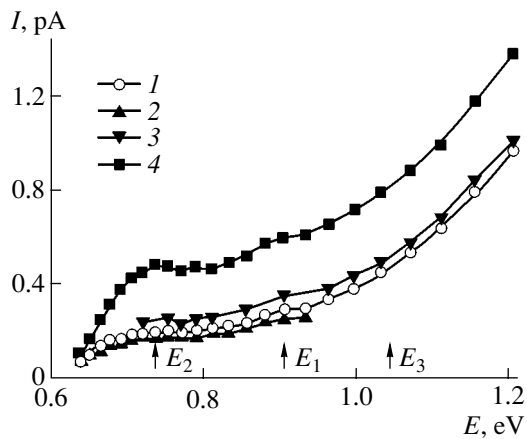


**Fig. 1.** IR photoconductivity spectra induced by  $F$  light for plastically strained NaCl crystals (1–3) with and (4) without additional exposure to monochromatic light at photon energies (1)  $E_1 = 0.91$  eV, (2)  $E_2 = 0.74$  eV, and (3)  $E_3 = 1.07$  eV (indicated by arrows  $E_1$ – $E_3$ ).

electrons. In the present work, an attempt was made to decompose the  $F$ -induced photoconductivity spectra of plastically strained NaCl samples into its main components with the aim of separating and analyzing the contribution from a signal caused by the photoionization of dislocation electrons. For this purpose, prior to each measurement, the sample was additionally exposed to monochromatic light at a specific wavelength. After subtracting the spectrum of the sample subjected to additional exposure to monochromatic light from the spectrum of this sample measured prior to additional exposure, we obtained the spectrum of electronic states sensitive only to the additional monochromatic treatment (which effectively depletes these states). By varying the wavelength of monochromatic light used in additional treatment, it is possible to reveal the main components of the spectrum under consideration.

2. The experiments were performed with NaCl crystal samples  $2 \times 2 \times 12$  mm in size. The NaCl crystal samples were irradiated with gamma rays at a dose of  $10^7$  rad and were then subjected to plastic deformation at a rate of  $1.8 \times 10^{-5} \text{ s}^{-1}$  to a strain of 12–14% at room temperature. The experimental technique and conditions for measuring the IR photoconductivity induced by  $F$ -center exciting light were described in our previous work [18]. Initially, the sample was exposed to light at wavelengths in the range 450–800 nm (SI-8 lamp, S3S25 optical filters) for 30 s in order to excite centers ( $F$ ,  $M$ , etc.) donating electrons to the conduction band and to deplete “undesirable” traps (see [18]) in the range 600–800 nm. Then, these traps were further depleted for 20 s with the use of an OS14 optical filter (without excitation of the  $F$  and  $M$  centers) added to the S3S25 filters. Thereafter, if required, the sample was additionally exposed to monochromatic light from an IKS-21 spectrometer. Finally, the IR photoconductivity was measured under exposure to monochromatic light

from the same spectrometer. This cycle was repeated two times at different polarities of the voltage applied to the sample for the purpose of preventing electrical polarization. Then, the measurements were carried out at the next point of the IR photoconductivity spectrum.

Figure 1 shows the spectra measured in one of these experiments (test experiment; strain of the sample, 12.65%;  $T = 113$  K). Initially, the IR photoconductivity spectrum was measured for the sample without additional exposure to monochromatic light (Fig. 1, curve 4). Then, the time of additional monochromatic treatment was chosen so that the intensity of the signal at a wavelength corresponding to the monochromatic light used in this treatment was approximately halved (the time required to accomplish the additional monochromatic treatment turned out to be 10 s). The same procedure was performed when measuring the other spectra with additional exposure of the sample to the monochromatic light. Thereafter, we measured first the IR photoconductivity spectrum for the sample additionally exposed to monochromatic light with photon energy  $E_1 = 0.91$  eV (Fig. 1, curve 1) and then the spectrum for the sample subjected to additional exposure to monochromatic light with photon energy  $E_2 = 0.74$  eV (Fig. 1, curve 2). As can be seen, spectrum 2 coincides, to within a constant factor, with spectrum 1 over the entire range of measurements, including the range between the photon energies  $E_1$  and  $E_2$ . In the range  $E_2$ – $E_1$ , the difference between these spectra, if it exists, should be the most pronounced. Therefore, spectrum 2 was not measured at  $E > E_1$  (in this range, the spectra should be all the more identical to each other). Moreover, it should be noted that the decrease in the number of measurements was dictated by the necessity of reducing the bleaching of the crystal as much as possible (for the recording of each point of the spectrum, the sample was twice exposed to  $F$  light for 30 s). For the same reason, all the spectra were measured with a relatively large step. Then, we measured the IR photoconductivity spectrum for the sample additionally exposed to monochromatic light with photon energy  $E_3 = 1.07$  eV (Fig. 1, curve 3).

3. The processing of the measured spectra was performed as follows. The spectra recorded for different additional monochromatic treatments were sequentially subtracted from the total spectrum (Fig. 1, curve 4). As a result, we obtained, to within a constant factor, the spectra of electronic states destroyed upon these additional treatments and then compared them with each other. The calculated spectra are shown in Fig. 2. The difference between spectra 4 and 1 in Fig. 1 is represented by spectrum 1 in Fig. 2. The difference between spectra 4 and 2 in Fig. 1 was multiplied by 0.9 and also depicted in Fig. 2 (spectrum 2). As can be seen from Fig. 2, spectra 1 and 2 virtually coincide with each other. The difference between spectra 4 and 3 in Fig. 1 (multiplied by 1.23) is represented by spectrum 3 in Fig. 2. It is seen from Fig. 2 that spectrum 3 almost

coincides with spectra 1 and 2 in the range between  $E_1$  and  $E_2$  but deviates from them at  $E > E_1$ . The difference between spectra 3 and 1 (or 2) in Fig. 2 is depicted by curve 4. From analyzing the results obtained, we can make the inference that, in the plastically strained NaCl crystal, there exist single-type electron traps, for which the photoionization spectrum is represented by curve 1 in Fig. 2. This spectrum remains unchanged with variations in the photon energy in the range 0.74–1.07 eV; i.e., it cannot be further decomposed into components by the method employed. Moreover, the plastically strained NaCl crystal contains electron traps of another type, for which the photoionization spectrum is represented by spectrum 4 in Fig. 2. This spectrum most likely corresponds either to the low-energy tail of the peak located at  $E > 1.2$  eV or to the sum of similar peaks. Furthermore, this spectrum can be associated with the electronic states that remained destroyed under additional exposure of the sample to nonmonochromatic light (orange light; see [18]). A comparison of spectrum 1 in Fig. 2 with the spectra obtained in [18] allowed us to draw the conclusion that the electronic states responsible for spectrum 1 are absent in the unstrained samples and appear in the strained samples. The spectrum of these states extends to photon energies  $E > 1.2$  eV, which cannot be measured with our experimental setup.

Spectra 1 and 4 in Fig. 2 are the spectra of electronic states that are effectively destroyed under additional exposure of the sample to the monochromatic light used. If the spectrum of these states is subtracted from the total spectrum (Fig. 1, curve 4), we obtain the spectrum of electronic states that are not destroyed upon the monochromatic treatments with a pulse duration of 10 s. The latter states are responsible for the IR photoconductivity signal and, hence, are destroyed by IR light; however, they remain undestroyed in our experiment. This situation occurs only with  $F$  and  $M$  centers. Their concentration is too high to be changed significantly by the action of a short IR light pulse (under exposure to  $F$  light from the same source for 1 h, the intensity of the  $F$  band decreases by only 10–20%). In this case, only the long-wavelength tails of the spectra of the electronic states under consideration lie in the IR range. It should be noted that the photoconductivity induced by a light pulse with an intensity identical to the intensity of IR light used in the additional monochromatic treatment, but with a wavelength 475 nm ( $F$  light), is at least four orders of magnitude higher than the photoconductivity observed in the above experiments. Thus, the high concentration of these centers and the high sensitivity of the equipment make it possible to observe their photoionization under exposure to IR light without a noticeable decrease in the concentration.

Figure 3 depicts the total spectrum (curve 1 is similar to curve 4 in Fig. 1), the spectrum of electronic states destroyed upon additional monochromatic treat-

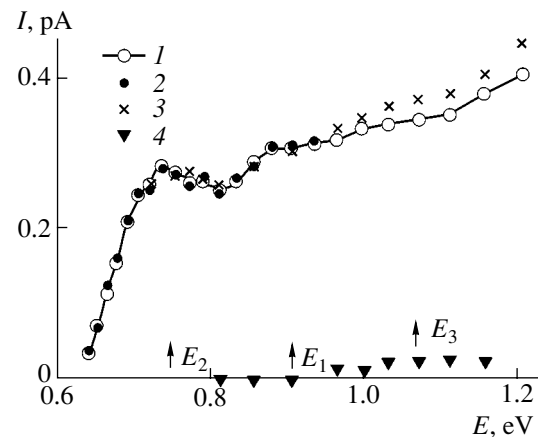


**Fig. 2.** Photoionization spectra of electronic states destroyed under additional exposure of the samples to monochromatic light at photon energies (1)  $E_1 = 0.91$  eV, (2)  $E_2 = 0.74$  eV, and (3)  $E_3 = 1.07$  eV. (4) Photoionization spectrum of electronic states destroyed under additional exposure to monochromatic light at photon energy  $E_3$  and electronic states not destroyed at photon energies  $E_1$  and  $E_2$ .

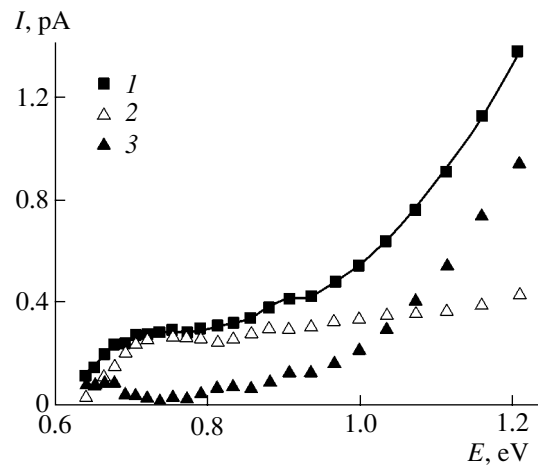


**Fig. 3.** (1) Total IR photoconductivity spectrum of the strained NaCl crystal and photoionization spectra of electronic states (2) destroyed and (3) undestroyed under additional exposure to monochromatic light.

ments (curve 2 is the sum of spectra 1 and 4 in Fig. 2), and their difference (curve 3). As expected, the spectrum of undestroyed states consists predominantly of long-wavelength tails whose maxima are located in the visible range. Moreover, there is one more signal at  $E = 0.67$  eV. Since this signal is absent at  $E > E_2$ , it cannot be destroyed under exposure to monochromatic light at any energy. It is not surprising, then, that the electronic states responsible for this signal appear to be undestroyed in our experiment. The above signal can be associated with any traps (not necessarily generated under plastic deformation).

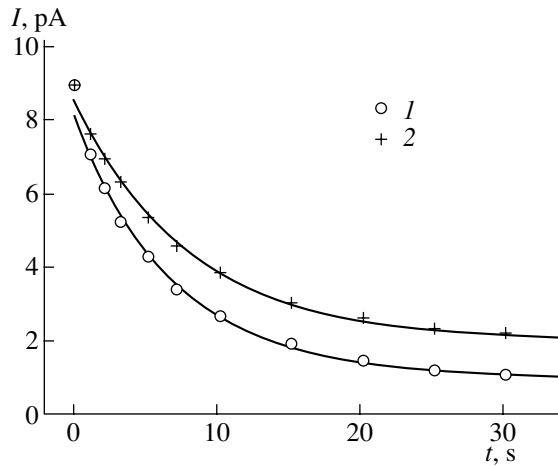


**Fig. 4.** Dependences of the intensity of the IR photoconductivity signal induced by IR light at a photon energy of 0.74 eV on the time of additional exposure to monochromatic light at wavelengths of (1) 1000 and (2) 562 nm. The fitted curves represent exponential functions plus constants.

As can be seen from Fig. 3, the IR photoconductivity signal at  $E = 0.74$  eV is almost completely provided by the electronic states generated under deformation of the sample and characterized by a spectrum in the form of a broad band (spectrum 1 in Fig. 2 will be referred to hereafter as the broad spectrum). Therefore, the signal at  $E = 0.74$  eV can serve as a measure of concentration of these states.

In the next (second) experiment, this signal was used to determine the high-energy edge of the broad spectrum. The wavelength of the monochromatic light used in the additional treatment varied in the range 1000–562 nm (1.2–2.2 eV, SI-8 lamp, interference filters). The rate of depletion of the electronic states responsible for the broad spectrum upon exposure to monochromatic light can be estimated from the intensity of the IR photoconductivity signal induced by IR light at a photon energy of 0.74 eV, which, in turn, makes it possible to determine the high-energy edge of the broad spectrum.

It was assumed that the broad spectrum does not extend to wavelengths longer than 700 to 800 nm. Otherwise, the states under consideration would also be destroyed upon depletion of undesirable states with orange light. However, it turned out that even the light at a wavelength of 562 nm (2.2 eV) effectively depletes the former states. The dependences of the intensity of the IR photoconductivity signal on the time of additional exposure to monochromatic light at wavelengths of 1000 and 562 nm are plotted in Fig. 4. It can be seen that, in both cases, the electronic states are depleted according to an exponential law, however not to zero but to a particular level (differing for different filters).

A similar dependence was observed in our earlier work [15] concerned with the destruction of photostoppers (electron traps that can interact with a dislocation

through different mechanisms depending on whether or not they capture an electron) located at immobile dislocations under exposure to light. This dependence can be explained by a complex mechanism of the action of the light used. On the one hand, the exposure to the light corresponding to the photosensitivity spectrum of traps results in their depletion. On the other hand, the light excites  $F$  centers (possibly, also  $M$  centers) donating electrons for the filling of traps, expels electrons from them, and thus provides repeated filling of the traps under consideration. Consequently, there is a limit below which traps cannot be destroyed. Since the light wavelength of 562 nm is closer to the light wavelength of the  $F$  band (475 nm) as compared to the light wavelength of 1000 nm, the regenerating effect of the light at a wavelength of 562 nm is more pronounced (see Fig. 4), which provides a higher equilibrium concentration of filled traps.

Thus, the above experiment showed that the spectrum of electron traps created under plastic deformation (Fig. 2, curve 1) extends from 0.64 eV to photon energies of no less than 2 eV. It is difficult to perceive the origin of such a broad spectrum that cannot be decomposed into individual components. The photoionization spectra of electron traps produced by point defects and their simple complexes, as a rule, have a smaller width.

Such a broad photoionization spectrum can be attributed to electrons in a sufficiently narrow dislocation band. In this case, the mass  $m_d$  of a dislocation electron should be considerably greater than the mass  $m_c$  of an electron in the conduction band. As a result, the substantial difference between the slopes of their parabolic dispersion curves leads to a large width  $H$  of the photoionization spectrum:  $H = \Delta E(m_d/m_c)$ , where  $\Delta E \approx (1-2)kT$  is the energy width of the band of filled states in the dislocation band.

Moreover, the results of the second experiment can be explained in another way that does not require extending the spectrum to an energy of 2 eV or higher. Actually, localized electronic levels of defects located in the vicinity of dislocations, for example, photostoppers (see [15]) with a maximum in the photoionization spectrum at approximately 620 nm, can be associated with the dislocations. The transfer of electrons from these levels to the conduction band under exposure to light will initially lead not to a decrease in the number of electrons in these levels but to a decrease in the number of electrons in the dislocation band. Indeed, the electrons lost by defects will be immediately compensated for by dislocation electrons. Only after depleting the dislocation band will the levels of these defects begin to lose their electrons.

Consequently, the width of the photoionization spectrum can be little more than 1 eV. In our case, we have  $\Delta E \approx 0.01$  eV and the above width of the spectrum will be observed for dislocation electrons with a mass  $m_d \approx (100-150)m_c$ . The following factors can be responsible for this large mass of dislocation electrons.

(i) The distance between equivalent sites in an edge dislocation is larger than the analogous distance in an ideal NaCl lattice by a factor of  $\sqrt{2}$ . This leads to a threefold or fourfold decrease in the overlap integral.

(ii) The structure factor, i.e., the number of equivalent sites surrounding a given site in the NaCl lattice, is six times larger than that in the dislocation (twelve and two, respectively). As a result, the probability of the dislocation electron leaving the occupied site is six times less than the same probability for the electron in the conduction band, all other factors being equal.

(iii) In an edge dislocation, a negative chlorine ion is located between two equivalent sites (sodium ions). This affects the electron wave function and drastically decreases the overlap integral.

If the above hypothesis explaining the large width of the photoionization spectrum holds true, the width of the spectrum should substantially depend on the temperature. This offers possibilities for experimentally verifying the hypothesis, even though low-temperature investigations involve problems due to the presence of a strong IR signal caused by the bound polaron states (studied in our earlier work [17]) at temperatures  $T < 78$  K. It should also be noted that the real situation is much more complex, because the electron captured by the dislocation is most likely to be a dislocation polaron than a dislocation electron.

#### ACKNOWLEDGMENTS

I would like to thank V.Ya. Kravchenko for his participation in discussions of the results and for helpful remarks.

#### REFERENCES

1. H. F. Matare, *Defect Electronics in Semiconductors* (Wiley, New York, 1971; Mir, Moscow, 1974).
2. *Electronic Properties of Dislocations in Semiconductors*, Ed. by Yu. A. Osip'yan (Editorial URSS, Moscow, 2000).
3. J. Trinks, *Sitzungsber. Akad. Wiss. Wien, Math.-Naturwiss. Kl., Abt. 2A* **147**, 217 (1938).
4. F. J. Metz, R. N. Schweiner, H. R. Leider, and G. A. Girifalco, *J. Phys. Chem.* **61**, 86 (1957).
5. C. T. Butler, *Phys. Rev.* **141** (2), 750 (1966).
6. V. V. Korshunov, F. D. Senchukov, and S. Z. Shmurak, *Pis'ma Zh. Éksp. Teor. Fiz.* **13**, 289 (1971).
7. M. I. Molotskiĭ, *Fiz. Tverd. Tela (Leningrad)* **26** (4), 1204 (1984) [*Sov. Phys. Solid State* **26**, 731 (1984)].
8. V. A. Zakrevskiĭ and A. V. Shul'diner, *Fiz. Tverd. Tela (Leningrad)* **27** (10), 3042 (1985) [*Sov. Phys. Solid State* **27**, 1826 (1985)].
9. A. A. Kusov, M. I. Klinger, and V. A. Zakrevskiĭ, *Fiz. Tverd. Tela (Leningrad)* **31** (7), 67 (1989) [*Sov. Phys. Solid State* **31**, 1136 (1989)].
10. M. V. Gol'dfarb, M. I. Molotskiĭ, and S. Z. Shmurak, *Fiz. Tverd. Tela (Leningrad)* **32** (8), 2398 (1990) [*Sov. Phys. Solid State* **32**, 1392 (1990)].
11. V. A. Zakrevskiĭ, T. S. Orlova, and A. V. Shul'diner, *Fiz. Tverd. Tela (St. Petersburg)* **37** (3), 675 (1995) [*Phys. Solid State* **37**, 367 (1995)].
12. V. A. Zakrevskiĭ and A. V. Shul'diner, *Fiz. Tverd. Tela (St. Petersburg)* **42** (2), 263 (2000) [*Phys. Solid State* **42**, 270 (2000)].
13. M. I. Molotskii and S. Z. Shmurak, *Phys. Lett. A* **166** (3–4), 286 (1992).
14. G. A. Ermakov and É. M. Nadgornyi, *Pis'ma Zh. Éksp. Teor. Fiz.* **14**, 45 (1971) [*JETP Lett.* **14**, 29 (1971)].
15. G. A. Ermakov, E. V. Korovkin, and Ya. M. Soĭfer, *Fiz. Tverd. Tela (Leningrad)* **16** (3), 697 (1974) [*Sov. Phys. Solid State* **16**, 457 (1974)].
16. E. V. Korovkin, *Fiz. Tverd. Tela (Leningrad)* **24** (2), 524 (1982) [*Sov. Phys. Solid State* **24**, 294 (1982)].
17. E. V. Korovkin and T. A. Lebedkina, *Fiz. Tverd. Tela (St. Petersburg)* **42** (8), 1412 (2000) [*Phys. Solid State* **42**, 1451 (2000)].
18. E. V. Korovkin and T. A. Lebedkina, *Fiz. Tverd. Tela (St. Petersburg)* **44** (12), 2155 (2002) [*Phys. Solid State* **44**, 2257 (2002)].

*Translated by O. Borovik-Romanova*

---

**DEFECTS, DISLOCATIONS,  
AND PHYSICS OF STRENGTH**

---

## Polygonization in High-Purity Rolled (001)[110] Tungsten Single Crystals

L. N. Pronina, I. M. Aristova, and A. A. Mazilkin

*Institute of Solid-State Physics, Russian Academy of Sciences, Chernogolovka, Moscow oblast, 142432 Russia*

*e-mail: pronina@issp.ac.ru, aristova@issp.ac.ru, mazilkin@issp.ac.ru*

Received October 14, 2003

**Abstract**—Electron microscopy is used to study changes in the dislocation structure of high-purity rolled (001)[110] tungsten single crystals during short-term high-temperature annealings. The effects of the annealing temperature and time on the formation of low-angle boundaries are investigated. Local defects, which are similar to those detected earlier upon annealing in the structure of molybdenum single-crystal ribbons, are found to form and dissociate upon annealing. These defects are concluded to have a dislocation nature. © 2004 MAIK “Nauka/Interperiodica”.

### 1. INTRODUCTION

It was shown in [1, 2] that, under certain conditions, oriented rolling of refractory bcc single crystals can produce single-crystal ribbons of metals, such as Mo, W, and Nb. Upon long-term high-temperature annealing (at temperatures above  $0.8T_m$ , where  $T_m$  is the melting temperature), the single-crystal ribbons produced do not recrystallize and retain the orientations of the initial single crystals.

The evolution of rolled and annealed single crystals has a number of peculiar features. For example, a detailed electron-microscopic study of polygonization in (001)[110] single-crystal ribbons of molybdenum having different degrees of purity (with the resistivity ratio  $RRR = \rho_{273\text{ K}}/\rho_{4.2\text{ K}} = 1000$  and 140000) showed that a stable dislocation structure forms in several

stages, which includes the formation and dissociation of the so-called “local” defects [3] located in dislocation lines and at subgrain-boundary dislocation nodes.

It is of interest to compare the data on the formation and dissociation of local defects in molybdenum single-crystal ribbons with analogous data for other refractory metals, in particular, tungsten.

### 2. EXPERIMENTAL

As the initial materials for our investigations, we used cylindrical [110] tungsten single crystals grown by electron-beam zone melting. The purity of the material was characterized by the residual resistivity ratio  $RRR = \rho_{273\text{ K}}/\rho_{4.2\text{ K}}$ , which was 50000 and 200000 for the single crystals under study. Single-crystal ribbons were fabricated by rolling along the (001) plane in the

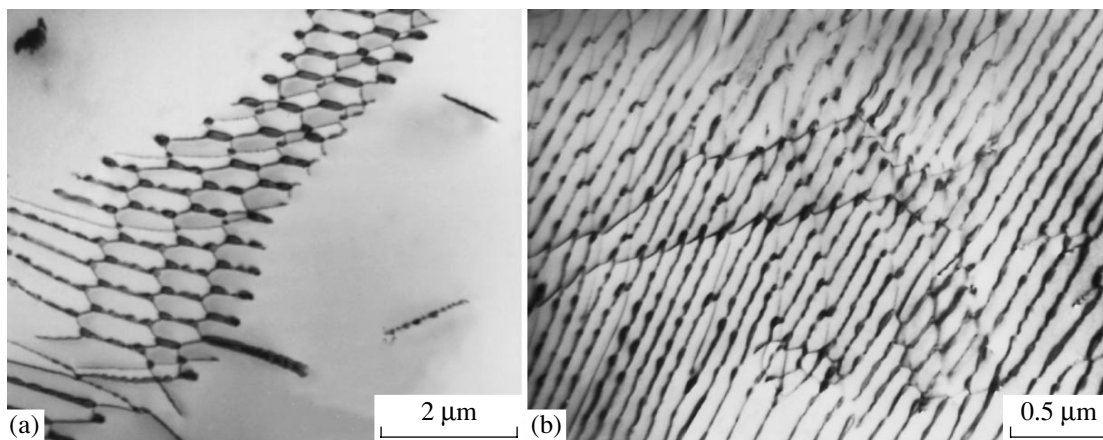


**Fig. 1.** Local defects in subgrain boundaries in tungsten single crystals with  $RRR = 50000$  after annealing at  $2200^\circ\text{C}$  for 10 s: (a) hexagonal network consisting of two families of  $(a/2)\langle 111 \rangle$  dislocations (dislocations with Burgers vector  $a[001]$  form at the points of intersection of these families) and (b) vertical wall of  $a[001]$  edge dislocations.



[110] direction. High-temperature annealings of various duration were performed by passing an electric current through the ribbons in an USU-4 vacuum device in an oil-free vacuum of  $10^{-6}$  Torr at temperatures varied from 2000 to 2300°C. Electron-microscopic studies were carried out on JEM-100CX, JEM-1000, and JEM-2000FX electron microscopes.

### 3. RESULTS

Local defects in the structure of tungsten single crystals with  $RRR = 50000$  are detected after annealing at 2200°C for 10 s. This annealing results in the formation of subgrain boundaries; some of the boundaries are dislocation networks. Figure 1a shows a hexagonal network consisting of two families of  $(a/2)\langle 111 \rangle$  dislocations; at the points of intersection of these families, dislocations with the Burgers vector  $a[001]$  are formed. Figure 1b shows a subgrain boundary, which is a vertical wall of  $a[001]$  edge dislocations. As seen from Fig. 1, local defects form in dislocations with  $\mathbf{b} = a[001]$  and in the nodes of dislocation networks. These defects are also visible after annealing at the same temperature for 20 s and disappear when the annealing time increases to 40 s. After 60 s of annealing, the structure is made up predominantly of walls of edge dislocations with  $\mathbf{b} = a[001]$  almost without dislocation networks (Fig. 2). This structure is stable; it does not change as the holding time increases at this annealing temperature.

It should be noted that the diffraction contrast of local defects is extremely complex and cannot be interpreted unambiguously; the presence of these defects does not cause any additional reflections in the electron diffraction pattern.

The tungsten single crystals with  $RRR = 200000$  have no local defects upon annealing at 2200°C for even the shortest time (3 s). However, by decreasing the annealing temperature, we could find that local defects appear in these crystals in subgrain boundaries upon annealing at 2000°C for 10 s (Fig. 3) and disappear when the annealing time at this temperature exceeds 30 s.

### 4. DISCUSSION OF THE RESULTS

It was shown in [3] that the local defects forming in molybdenum have a dislocation nature. It was assumed that they can form by the mechanism proposed by Cottrell and Beilby for bcc crystals [4]. According to this mechanism, part of a perfect lattice dislocation can split into two partial dislocations, one of which is a sessile dislocation and the other is a glide dislocation. The region between the two partials is a twin stacking fault. The cross slip of a partial dislocation leads to the formation of new stacking faults lying in the plane of motion. One partial dislocation can turn around a pole dislocation to form a spiral. The result of the dislocation restructuring is likely to be visible as local defects.

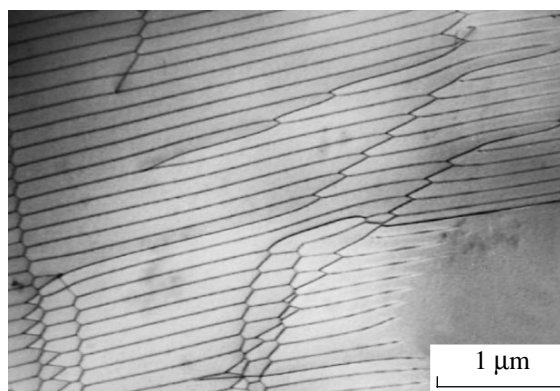


**Fig. 2.** Structure of the tungsten with  $RRR = 50000$  after annealing at 2200°C for 60 s.

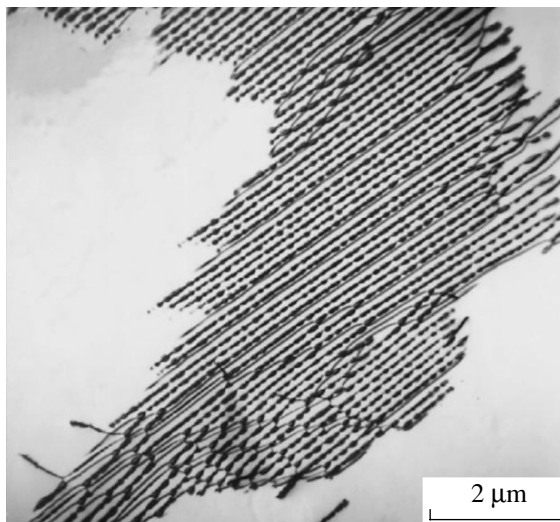


**Fig. 3.** Local defects in subgrain boundaries in the tungsten single crystals with  $RRR = 200000$  after annealing at 2000°C for 10 s.

The stacking fault energy for refractory bcc metals is very high, 0.3 J/m<sup>2</sup> in molybdenum [5] and 0.5 J/m<sup>2</sup> in tungsten [6]. However, it should be taken into account that a large number of excess vacancies (as compared to the equilibrium concentration) are present in the material under study due to the high degrees of deformation. If the velocity of vacancies moving to dislocations is higher than the rate of their disappearance at dislocation jogs, Cottrell vacancy clouds can form around a dislocation [7]. The high concentration of point defects can result in a significant decrease in the stacking fault energy and make the Cottrell–Beilby mechanism operative.

When the vacancy concentration decreases with increasing annealing time, the reverse process occurs:

partials transfer into perfect dislocations, which are more stable for bcc crystals. This process is accompanied by the disappearance of stacking faults.

This explanation implies that the rate of the dislocation restructuring should noticeably depend on the stacking fault energy. Pronina *et al.* [8] showed that annealing of tungsten single crystals at 2300°C did not cause the formation of local defects in subgrain boundaries. However, annealing of molybdenum at the same homologous temperature brought about the formation of local defects about 0.1  $\mu\text{m}$  in size, which existed for a time that was sufficient for their detection and observation.

These parameters should also strongly depend on the presence of impurities, which can also decrease the stacking fault energy; the rate of the process in a pure material might be expected to be higher.

A significant increase in the purity of tungsten (to  $RRR = 200\,000$ ) leads to an increase in the rate of the dislocation restructuring such that we can detect local defects only at low annealing temperatures (as low as 2000°C).

Thus, our experiments support the assumption [3] that the aggregates termed local defects have a dislocation nature.

## REFERENCES

1. L. N. Pronina, M. V. Bayazitova, and A. A. Mazilkin, *Fiz. Tverd. Tela (St. Petersburg)* **38** (3), 441 (1996) [*Phys. Solid State* **38**, 437 (1996)].
2. L. N. Pronina, I. M. Aristova, and A. A. Mazilkin, *Materiavedenie*, No. 4, 7 (1999).
3. L. N. Pronina and I. M. Aristova, *Fiz. Tverd. Tela (St. Petersburg)* **35** (10), 2701 (1993) [*Phys. Solid State* **35**, 1336 (1993)].
4. J. P. Hirth and J. Lothe, *Theory of Dislocations* (McGraw-Hill, New York, 1967; Atomizdat, Moscow, 1972).
5. Ya. D. Vishnyakov, *Stacking Faults in Crystalline Structure* (Metallurgiya, Moscow, 1970).
6. C. S. Hartley, *Acta Met.* **14** (9), 1193 (1966).
7. P. Coulomb and J. Friedel, in *Dislocation and Mechanical Properties of Crystals* (Wiley, New York, 1957; Inostrannaya Literatura, Moscow, 1960).
8. L. N. Pronina, A. A. Mazilkin, and I. M. Aristova, *Fiz. Tverd. Tela (St. Petersburg)* **40** (3), 498 (1998) [*Phys. Solid State* **40**, 458 (1998)].

*Translated by K. Shakhlevich*

## DEFECTS, DISLOCATIONS, AND PHYSICS OF STRENGTH

# Kinetic Interpretation of the Structural-Time Criterion for Fracture

P. A. Glebovskii and Yu. V. Petrov

St. Petersburg State University, Petrodvorets, 198504 Russia

e-mail: [pietr@mail.ru](mailto:pietr@mail.ru), [yp@yp1004.spb.edu](mailto:yp@yp1004.spb.edu)

Received September 19, 2003

**Abstract**—The incubation-period-based criterion for fracture is considered in terms of the Zhurkov kinetic model of fracture. Within the kinetic model, fracture is treated as a continuously developing process, which starts immediately after the application of a tensile load to a sample and consists in breaking of the interatomic bonds and gradual accumulation of broken bonds in the material in the course of a fracture test. For certain materials, the inclusion of the thermal-fluctuation mechanism for fracture in the incubation-period-based criterion significantly affects the position of the static branch of the time dependence of strength. Time dependences of strength are calculated for a number of materials. The experimental data are analyzed using the structural-time criterion for fracture, which allows one to obtain a unified time dependence of strength for quasi-static and high-rate short-term loadings. The temperature dependence of the incubation period (latent time) is calculated analytically, and a relation is found between the latent fracture time and the thermal vibration frequency of atoms. © 2004 MAIK “Nauka/Interperiodica”.

In classical criteria, it is assumed that the energy and momentum that go into forming new surfaces and fracture regions are expended continuously. Allowance for the discreteness of the process of dynamic fracture leads to a dynamic generalization of the linear mechanics of fracture.

In particular, in [1–4], a structural-time approach is developed in which the pulse characteristics of the stress field and the structural features of materials are taken into account. The structure is considered on both space and time scales [1, 2]. The corresponding time scale  $\tau$  is referred to as the latent (structural) time of fracture.

It is assumed that fracture occurs when the impulse of a force acting over time  $\tau$  reaches a critical value,  $J(t) \leq J_c$ . In terms of the continuum mechanics, we can write

$$\int_{t-\tau}^t \sigma(t') dt' \leq \sigma_c \tau, \quad (1)$$

where  $\sigma_c$  is the ultimate stress for the defect-free material, i.e., a material that does not contain intentionally produced defects and concentrators, such as cracks and sharp notches.

Applying a stress  $\sigma_c$  is not enough to destroy an element; the critical stress must act over a certain period of time. The time  $\tau$  is defined as the minimum time necessary for fracture of a material subjected to a critical stress  $\sigma_c$ . It is shown in [3–5] that, in the case of defect-free materials, the experimental data on high-rate fracture (chipping-off) can be adequately explained under

the assumption that  $\tau = d/c$ , where  $c$  is the maximum velocity of elastic waves and  $d = \frac{2K_{Ic}^2}{\pi\sigma_c^2}$  is a length char-

acterizing an elementary fracture cell on the given scale ( $K_{Ic}$  is the toughness of the material). At the present time, the physical meaning of the length  $d$  is not clearly understood. The problem of interpreting  $d$  is discussed in [6, 7].

It is shown in [4] that  $\tau$  can be interpreted as the minimum time introduced in [8]. Within this approach, the parameters  $\sigma_c$  and  $\tau$  describe the strength of the defect-free material. The structural fracture time  $\tau$  characterizes the dynamic features of brittle fracture and should be determined experimentally for each material. As for  $\sigma_c$ , the physical meaning of this parameter needs clarification and can be determined using the approach developed by Zhurkov and coworkers. The present paper is devoted to this problem.

Studies of the physical basis of strength of solids have shown that there are universal features characterizing the temperature and time dependences of strength. It was established in [9] that the time  $t_*$  elapsing between the application of a tensile breaking stress  $\sigma$  and fracture of the test sample is described well by the formula

$$t_* = t_0 \exp[(U_0 - \gamma\sigma)/kT], \quad (2)$$

where  $T$  is the absolute temperature and  $U_0$ ,  $t_0$ , and  $\gamma$  are constants characterizing the strength properties of the material:  $U_0$  is closely related to the energy for interatomic bond breaking and characterizes the activation

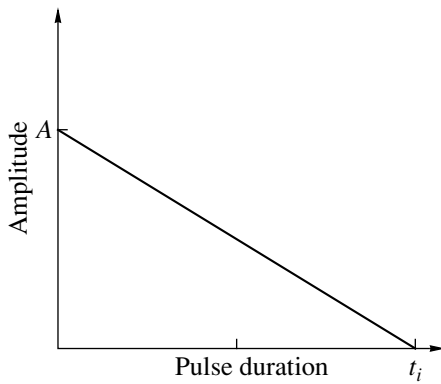


Fig. 1. Tensile stress pulse.

energy for fracture,  $t_0 = 10^{-13}$  s is a fundamental characteristic of the material coinciding with the period of thermal oscillations of atoms, and  $\gamma$  is a coefficient that is proportional to the excess stress applied to interatomic bonds (relative to the average stress in the sample).

According to the kinetic model developed in [9–11], fracture is a process that starts immediately after the application of a load to the sample and continuously develops in time. This process consists in the breaking of interatomic bonds and the gradual accumulation of broken bonds in the material subjected to a fracture load. It was shown in [9] that the time factor is a fundamental characteristic of strength. One cannot gain a deep insight into the phenomenon of strength without considering the time taken by fracture. Equation (2) shows that tensile breaking is an activation process whose rate is determined by the mean thermal fluctuation frequency (or waiting time) and that there is an energy barrier  $U_0$  that must be overcome in order to break the bonds responsible for the strength of the material. This barrier depends on the nature of these bonds, and, according to Eq. (2), a certain mechanism operates that decreases the initial barrier  $U_0$  by  $\gamma\sigma$  when tensile stresses are applied.

Let us analyze the fracture of a defect-free material. The one-dimensional problem of fracture of an elastic rod subjected to a tensile stress pulse triangular in shape (Fig. 1) was solved in [12] using the incubation-period-based criterion (1).

Let us consider the reflection of a compressive stress pulse that is triangular in shape from the free end of a semi-infinite rod aligned with the  $x$  axis and located in the region  $x > 0$ . The incident pulse is written as  $\sigma_- = -A(1 - t/t_i - x/ct_i)[H(ct + x) - H(ct + x - ct_i)]$ , where  $A$  is the amplitude of the pulse,  $t_i$  is its duration,  $H(t)$  is the Heaviside step function, and  $c$  is the maximum velocity of acoustic waves. The rise time of the pulse is zero. The pulse reflected from the free end of the rod is  $\sigma_+ = A(1 - t/t_i + x/ct_i)[H(ct - x) - H(ct - x - ct_i)]$ . The total stress is  $\sigma = \sigma_- + \sigma_+$ .

The tensile-stress maximum first arises at the point  $x = ct_i/2$ . The minimum amplitude  $A_*$  at which fracture occurs for a given pulse duration  $t_i$  can be found from the condition  $\max I = \sigma_c$ , where  $I = \frac{1}{\tau} \int_{(t-\tau)}^t \sigma(t') dt'$ .

As a result, we obtain the following expression describing the time dependence of strength for any loading duration with allowance for the latent fracture time:

$$A_* = \begin{cases} \frac{\sigma_c}{1 - \frac{\tau}{2t_i}}, & t_i \geq \tau \\ \frac{2\sigma_c\tau}{t_i}, & t_i \leq \tau. \end{cases} \quad (3)$$

The time  $t_*$  elapsing between the application of a stress and fracture is given by

$$t_* = \tau + \frac{t_i}{2},$$

where  $\tau$  is the structural fracture time,  $\sigma_c$  is the static strength,  $t_i$  is the stress pulse duration, and  $A_*$  is the threshold amplitude.

Since the static tensile strength  $\sigma_c$  is defined ambiguously and has no clear physical interpretation [9], we transform Eq. (3) using the Zhurkov formula (2) and obtain the time dependence of strength (Fig. 2). The fracture of a material subjected to external forces is not a purely mechanical phenomenon; thermal fluctuations are of fundamental importance here, and tensile stresses only favor the fluctuation process by lowering the energy barrier and making the fracture more probable. Let us represent Eq. (2) in the form

$$\sigma = (U_0 - kT \ln(t_*/t_0))/\gamma. \quad (4)$$

Substituting Eq. (4) into Eq. (3) gives

$$A_* = \begin{cases} \frac{U_0 - kT \ln(t_*/t_0)}{\left(1 - \frac{\tau}{2t_i}\right)/\gamma}, & t_i \geq \tau \\ \frac{2(U_0 - kT \ln(t_*/t_0))\tau}{t_i\gamma}, & t_i \leq \tau. \end{cases} \quad (5)$$

The parameters  $t_0$ ,  $U_0$ , and  $\gamma$  can be determined experimentally and are listed in the table. All calculations are performed for the same temperature, equal to 300 K. For comparison, Fig. 2 also shows the results obtained without regard for the Zhurkov correction (dashed lines). The experimental data are taken from [15], where brittle fracture of solids subjected to tensile stress waves was studied using transverse impacts of a plate-shaped target and a parallel striking plate.

It should be noted that earlier attempts have also been made to analyze the kinetic nature of strength. For

instance, the kinetics of fracture was discussed in [16] in terms of the Bailey criterion. However, this approach cannot be extended to the case of high-rate pulse tests. Using the incubation-period-based criterion with correction (4) makes it possible to describe the entire range of loading durations (covering both quasi-static and dynamic tests). It can also be seen from Fig. 2 that the substitution of Eq. (4) for  $\sigma_c$  has a significant effect on the position of the static branch of the strength time dependence. The kinetic model of fracture describes the experimental data more adequately. However, using Eq. (2) has no effect on the dynamic branch, whose position is mainly determined by the incubation period of fracture.

Let us show that, in the limiting case, the latent time can be expressed in terms of  $t_0$ . This condition must be satisfied, because the parameters of the structural–time criterion should be chosen so that the results obtained within the kinetic model of fracture are reproduced in the limiting case. Therefore, we will analyze the strength in structural-time terms within the kinetic model in the transient region of the time dependence of strength, i.e., for loading pulse durations  $t_i \geq \tau$  and  $t_i \sim \tau$ , where the effect of the incubation period is significant. For this purpose, we use Eq. (3), which corresponds to the period of time before fracture characterized by the time  $t_*$ . Using Eq. (2), the latent (structural) time is found to be

$$\tau = t_0 \exp[(U_0 - \gamma\sigma)/kT] - \frac{t_i}{2},$$

where  $t_0$  is associated with the period of thermal oscillations of atoms and  $\sigma$  is determined by Eq. (5) or is chosen as the stress corresponding to the given pulse duration in the strength–time curve. By introducing the notation  $t_i = n\tau$ , the latent time can be written as

$$\tau = t_0 \exp[(U_0 - \gamma\sigma)/kT] / (1 + n/2). \quad (6)$$

The dependence of the latent time on the stress pulse duration is shown in Fig. 3. The time  $\tau$  is seen to be constant over almost the entire range of pulse durations. Therefore, the latent time is independent of the loading parameters and can be considered a parameter of the material.

According to Eq. (6),  $\tau$  can be expressed in terms of the parameter  $t_0$  as  $\tau \equiv \lambda t_0$ , where  $\lambda = \exp[(U_0 - \gamma\sigma)/kT] / (1 + n/2)$ . This equation can be used to analyze the temperature dependence of the latent time.

Thus, the following conclusions can be made:

(1) In the case of slow loadings, the structural-time criterion given by Eq. (1) in which the static strength is calculated from the Zhurkov formula (2) allows one to obtain a more correct unified time dependence of strength [in comparison with that calculated without regard for Eq. (2)].

(2) Taking into account the thermal-fluctuation mechanism for fracture and using the incubation period

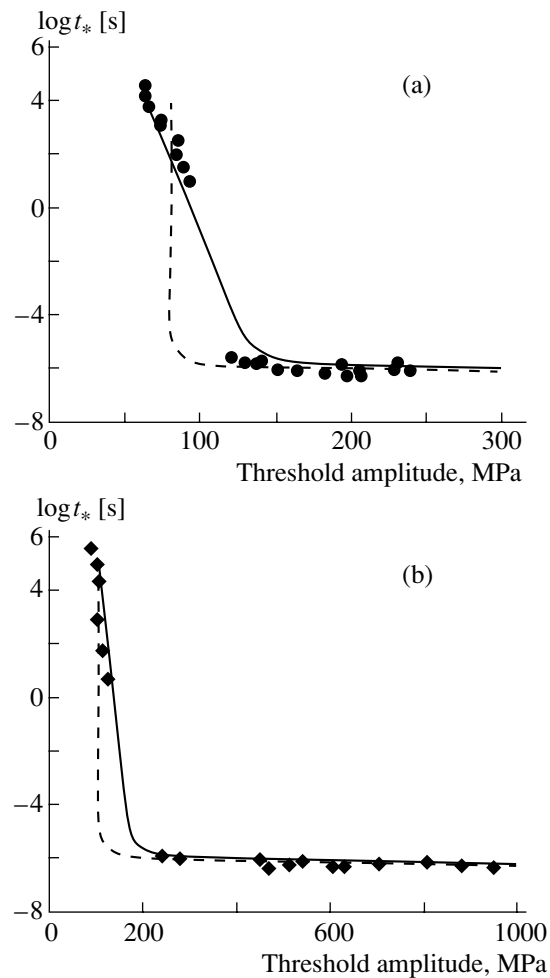


Fig. 2. Relation between the fracture time and strength for (a) PMMA and (b) aluminum calculated with (solid lines) and without (dashed lines) regard for the Zhurkov formula. Points are experimental data [16].

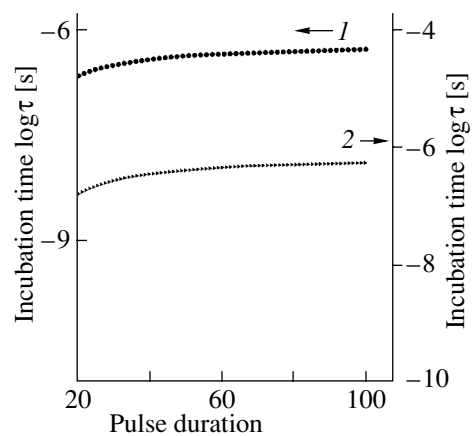


Fig. 3. Dependence of the latent fracture time at a constant temperature on the relative duration of a threshold pulse calculated with allowance for the Zhurkov formula for (1) aluminum and (2) PMMA.

Parameters for calculating the time dependence of strength

Material	$U_0$ , kJ/mol	$\gamma$ , $10^{-28}$ m <sup>3</sup>	$t_0$ , s	$\tau$ , $\mu$ s [6]
Al [13]	195	14.7	$10^{-13}$	0.75
PMMA [14]	150	13.2	$10^{-13}$	0.65

model makes it possible to more correctly determine the breaking load in dynamic fracture tests.

(3) A relation is found between the latent time and the thermal oscillation period.

(4) Allowance for the kinetic nature of fracture makes it possible to find the temperature dependence of the latent fracture time, which can be used in further analysis of the fracture of materials.

#### ACKNOWLEDGMENTS

This work was supported by the Russian Foundation for Basic Research (project nos. 03-01-39010, 02-01-01035) and the Ministry of Education (project no. A03-2.10-270).

#### REFERENCES

1. Yu. V. Petrov, Preprint No. 139 (Inst. of Problems in Machine Science, Russian Academy of Sciences, St. Petersburg, 1996).
2. N. F. Morozov and Yu. V. Petrov, *Problems of the Fracture Dynamics of Solids* (S.-Peterb. Gos. Univ., St. Petersburg, 1997).
3. N. F. Morozov, Yu. V. Petrov, and A. A. Utkin, Dokl. Akad. Nauk SSSR **313** (2), 276 (1990) [Sov. Phys. Dokl. **35**, 646 (1990)].
4. N. F. Morozov and Yu. V. Petrov, Dokl. Akad. Nauk **324** (5), 964 (1992) [Sov. Phys. Dokl. **37**, 285 (1992)].
5. Y. V. Petrov and N. F. Morozov, ASME Trans. J. Appl. Mech. **61**, 710 (1994).
6. N. V. Morozov and Yu. V. Petrov, *Dynamics of Fracture* (Springer, Berlin, 2000).
7. R. V. Gol'dshteĭn and N. M. Osipenko, Dokl. Akad. Nauk SSSR **240** (4), 829 (1978) [Sov. Phys. Dokl. **23**, 421 (1978)].
8. J. F. Kalthoff and D. A. Shockey, J. Appl. Phys. **48** (3), 986 (1977).
9. S. N. Zhurkov and S. A. Abbasov, Vysokomol. Soedin. **3** (3), 450 (1961).
10. S. N. Zhurkov, V. I. Betekhtin, and A. N. Bakhitbaev, Fiz. Tverd. Tela (Leningrad) **11** (3), 690 (1969) [Sov. Phys. Solid State **11**, 553 (1969)].
11. S. N. Zhurkov, Izv. Akad. Nauk SSSR, Neorg. Mater. **3** (10), 1767 (1967).
12. N. F. Morozov, Yu. V. Petrov, and A. A. Utkin, Dokl. Akad. Nauk SSSR **40** (4), 1233 (1991).
13. A. M. Molodets and A. N. Dremin, Fiz. Goreniya Vzryva, No. 5, 154 (1983).
14. B. Tsoĭ, É. M. Kartashov, and V. V. Shevelev, *Strength and Fracture of Polymer Films and Fibers* (Khimiya, Moscow, 1999).
15. É. N. Bellendir, Candidate's Dissertation (Physicotechnical Inst., USSR Academy of Sciences, Leningrad, 1990).
16. V. R. Regel', A. I. Slutsker, and É. E. Tomashevskiĭ, *Kinetic Nature of the Strength of Solids* (Nauka, Moscow, 1974).

Translated by Yu. Epifanov

---

## DEFECTS, DISLOCATIONS, AND PHYSICS OF STRENGTH

---

# Molecular Dynamics Simulation of Plastic Effects upon Spalling

A. M. Krivtsov

Institute for Problems in Mechanical Engineering, Russian Academy of Sciences, Vasil'evskii Ostrov,  
Bol'shoi pr. 61, St. Petersburg, 199178 Russia

e-mail: krivtsov@AK5744.spb.edu

Received June 2, 2003; in final form, September 26, 2003

**Abstract**—The molecular dynamics method is applied to simulate spalling during the plane shock interaction between plates. The effect of lattice defects in a material on the propagation of a shock wave and the process of spalling is studied. The plastic effects are described using a model of imperfect particle packing with defects (vacancies). The model proposed can describe the separation of the shock-wave front into an elastic precursor and a plastic front and give velocity profiles for the free target surface close to the experimental profiles. © 2004 MAIK “Nauka/Interperiodica”.

## 1. INTRODUCTION

In the last decades, the molecular dynamics (MD) method has been widely used to simulate the deformation and fracture of solids [1–5]; the representation of a material as a set of interacting particles allows one to describe its mechanical properties at both the micro- and macrolevel [6, 7]. To construct computer models for high-strain-rate fracture of materials, it is convenient to use the results of full-scale spalling tests, in which extremely high loads are created in a material under the conditions of uniaxial deformation [8–10]. In most works dealing with the MD simulation of spalling, ideal single-crystal particle packing was studied [11–13]. However, the mechanical properties of materials are rather sensitive to structural defects [14, 15]. Moreover, in many processes where real materials exhibit plastic properties, single crystals behave elastically until fracture. Although plastic behavior manifests itself upon MD simulation of the propagation of shock waves in single crystals [16], it differs substantially from the plastic deformation of real materials. In particular, in full-scale tests, a shock wave is clearly divided into an elastic precursor and a plastic front, whereas this division is weak or even absent in ideal single crystals. To solve this problem and describe the phenomena mentioned above, we propose a model of a crystalline material with artificially introduced structural defects (vacancies).

## 2. SIMULATION PROCEDURE

The simulation procedure applied in this work is identical to that used in [13, 17] and is described in detail in [18]. The material is represented by a set of

particles interacting through a pair potential  $\Pi(r)$ . The equations of particle motion have the form

$$m\ddot{\mathbf{r}}_k = \sum_{n=1}^N \frac{f(|\mathbf{r}_k - \mathbf{r}_n|)}{|\mathbf{r}_k - \mathbf{r}_n|} (\mathbf{r}_k - \mathbf{r}_n), \quad (1)$$

where  $\mathbf{r}_k$  is the radius vector of the  $k$ th particle,  $m$  is the particle mass,  $N$  is the total number of particles, and  $f(r) = -\Pi'(r)$  is the interparticle interaction force. Contrary to [13], dissipative forces do not act in this system. We use the following notation:  $a$  is the equilibrium distance between two particles,  $f(a) \equiv 0$ ,  $C$  is the stiffness of the interatomic bond in equilibrium, and  $T_0$  is the period of vibrations of the mass  $m$  under the action of a linear force with stiffness  $C$ :

$$C = \Pi''(a) \equiv -f'(a), \quad T_0 = 2\pi\sqrt{m/C}. \quad (2)$$

We will use the quantities  $a$  and  $T_0$  as microscopic distance and time scales.

For a particle of mass  $m$  that is in equilibrium in the potential field  $\Pi(r)$  to be at infinity, its minimum velocity (dissociation velocity) must be equal to

$$v_d = \sqrt{2D/m}, \quad (3)$$

where  $D = \Pi(a)$  is the binding energy. The velocity of propagation of long-wavelength waves in an infinite chain is determined by the formula

$$v_0 = \sqrt{a^2 C/m}. \quad (4)$$

In this work, we analyze a two-dimensional material. In the case where particles are packed to form an ideal tri-

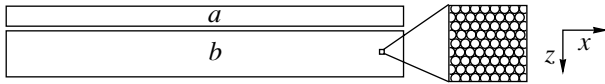


**Fig. 1.** Setup of the computer experiment: (a) impactor and (b) target.

angular (close-packed) crystal lattice, the velocity  $v_l$  of propagation of long longitudinal waves is

$$v_l = \sqrt{\frac{9}{8}} v_0 \approx 1.06 v_0. \quad (5)$$

We will illustrate these formulas for the case of the classical Lennard–Jones potential:

$$\Pi(r) = D \left[ \left( \frac{a}{r} \right)^{12} - 2 \left( \frac{a}{r} \right)^6 \right], \quad (6)$$

where  $D$  and  $a$  are the binding energy and equilibrium interatomic distances introduced earlier, respectively. The corresponding interaction force  $f(r) = -\Pi'(r)$  has the form

$$f(r) = \frac{12D}{a} \left[ \left( \frac{a}{r} \right)^{13} - \left( \frac{a}{r} \right)^7 \right]. \quad (7)$$

In the case of the Lennard–Jones potential, the stiffness  $C$  and binding energy  $D$  obey the relation  $C = 72D/a^2$ ; therefore, the velocity of propagation of long waves and the dissociation velocity are connected by the simple relation  $v_0 = 6v_d$ . The Lennard–Jones potential is the simplest potential that allows one to take into account the general properties of interatomic interaction: repulsion of particles that approach each other, attraction of

particles moving away from each other, and the absence of interaction at large distances between them. In this work, we study the principal possibility of describing the plastic effects upon spalling rather than simulate the behavior of a certain material; therefore, we will use only the Lennard–Jones potential. Our results can easily be extended to more complex potentials describing the properties of materials more exactly.

### 3. SIMULATION OF SPALLING

Figure 1 shows the setup of the computer experiment. Particles form two rectangles lying in the  $xz$  plane; they simulate the sections of an impactor ( $a$ ) and a target ( $b$ ). The impactor and target consist of the same particles, whose interaction is described by Eq. (6). The particles are ordered to form a triangular lattice, which is identical for the impactor and target; the lattice is oriented so that one of its basis vectors is directed along the  $x$  axis. Free boundary conditions are used at all outer boundaries. The lattice parameter  $a_e$  in the initial configuration is chosen so as to ensure the absence of internal stresses at a cutoff radius of  $2.1a$  [18].<sup>1</sup>

Initially, the target has a zero velocity and the impactor velocity is directed along the  $z$  axis toward the target. Moreover, at the initial instant of time, each particle in the impactor and target is given an additional random velocity that is chosen from a two-dimensional uniform random distribution with a given variance  $\sigma$ , defined as

$$\sigma = \frac{1}{n} \sum_{k=1}^n (V_k - \bar{V})^2, \quad \bar{V} = \frac{1}{n} \sum_{k=1}^n V_k. \quad (8)$$

Here,  $V_k$  is the projection of the velocity of the  $k$ th particle along the shock direction and  $k$  runs over the values specifying a certain set of particles that enters the total system of particles to be analyzed in the experiment. We also use the standard deviation of the particle velocities  $\Delta V = \sqrt{\sigma}$ .

The states of the impactor and target after simulation are shown in Fig. 2. A spalling crack formed in the target is clearly visible. However, the interface between the impactor and target is invisible because of the ideal coincidence of the contacting surfaces (matching of the crystal lattices in the impactor and target). The parameter values for this case are given in the table (experi-

<sup>1</sup>  $a_e = 0.9917496a$ .

#### Calculation parameters

Parameter	Experiment		
	A	B	C
Approximate number of particles $N$	100000	500000	1000000
Impactor velocity $v_{\text{imp}}$	$1.05v_d$	$v_d$	$1.1v_d$
Particle-velocity deviation $\Delta V_0$	$0.001v_d$	0	0
Vacancy concentration $p$ , %	0	6	1
Cutoff radius $a_{\text{cut}}$	$2.1a$	$2.1a$	$2.1a$
Impactor (target) width $w$	$708a$	$1584a$	$2238a$
Impactor thickness $h_1$	$35a$	$78a$	$111a$
Target thickness $h_2$	$88a$	$196a$	$277a$
Number of particle layers $N_z$	142	319	450
Integration step $\Delta t$	$0.03T_0$	$0.03T_0$	$0.03T_0$
Calculation time $t_{\text{max}}$	$3t_s$	$3t_s$	$3t_s$



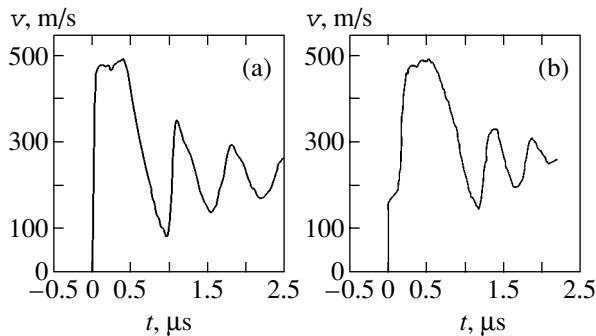


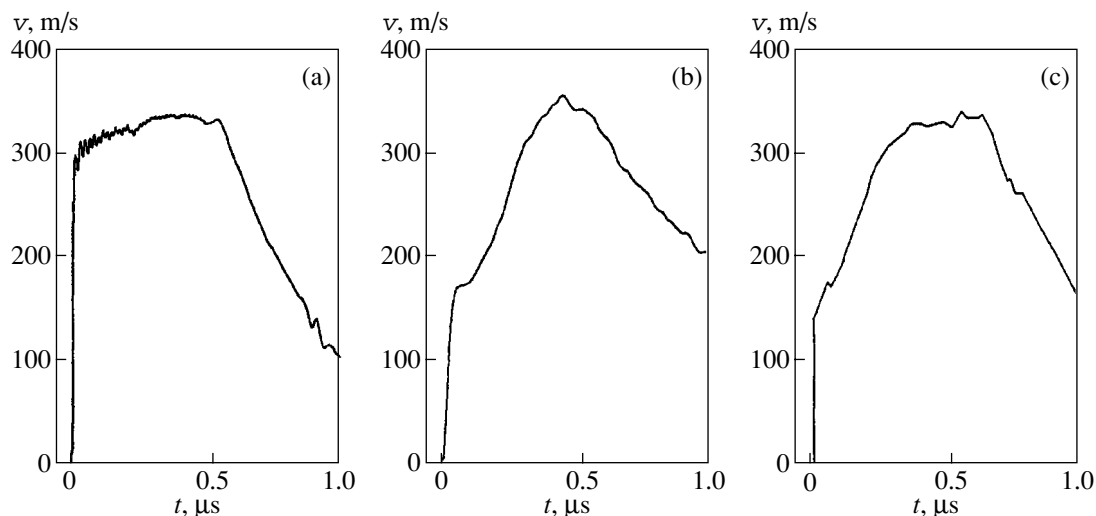
**Fig. 3.** Time dependence of the velocity of the free target surface for (a) single crystal (calculation) and (b) titanium alloy (experiment).

ment A). Computer experiments show that the minimum impactor velocity at which spalling begins is approximately equal to the dissociation velocity  $v_d$ ; therefore, it is worthwhile to compare the velocities used in the calculation with this value (see table). The dimensions of the impactor and target in this computer experiment are such that  $h_1/w \approx 1/20$  and  $h_1/h_2 \approx 2/5$ . The spalling time  $t_s$  can be estimated from the formula  $t_s = (h_1 + h_2)/v_l$ , where  $h_1$  and  $h_2$  are the thicknesses of the impactor and target, respectively, and  $v_l$  is determined from Eq. (5). In this case,  $t_s = 18.4T_0$ . Of course, this estimation is very rough, since  $v_l$  is the velocity of longitudinal waves according to linear theory; i.e., this velocity corresponds to small-amplitude waves. According to nonlinear theory, the larger the amplitude of waves in a single crystal, the higher their velocity. However, in a crystalline material with defects, the wave velocity can be lower than  $v_l$ . Moreover, a wave has a certain extent in space, which can also introduce error in the spalling time. Nevertheless, it is convenient

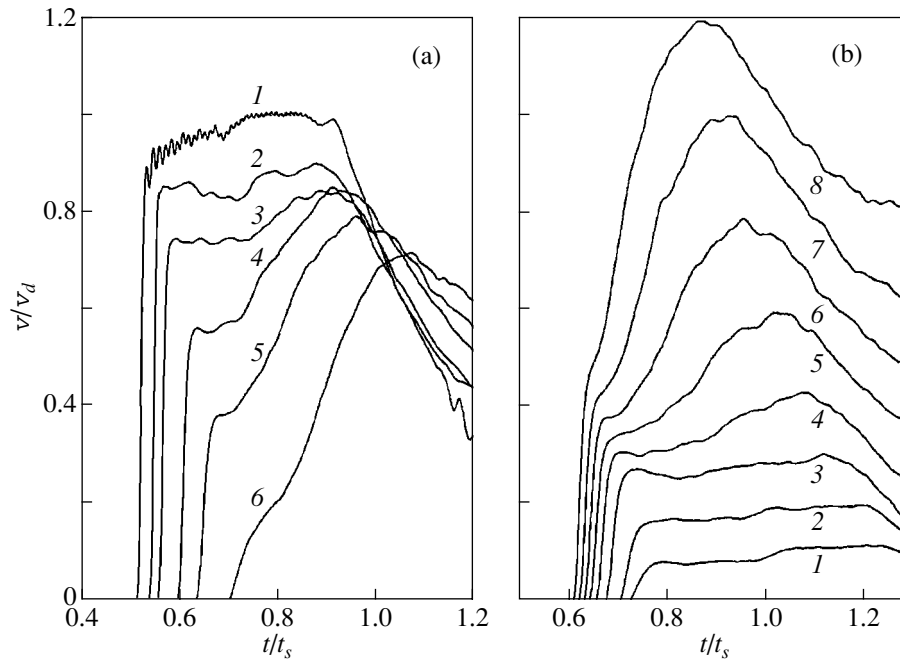
to use the time  $t_s$  as a time scale, since it has a clear physical meaning and can easily be determined. The quantity  $N_z$  in the table is equal to the total number of particle layers (in the impactor + target system) along the shock direction.

Figure 3a shows the simulated time dependence of the velocity of the free target surface. To measure the velocity of the free surface, we used two lower particle layers, more specifically, only the central part of these layers of width  $w_0 = w - 2(h_1 + h_2)$ , to eliminate edge effects. The dependence obtained was averaged over time to exclude high-frequency vibrations. For comparison, Fig. 3b shows an analogous experimental dependence obtained during a full-scale spalling test of a titanium alloy at an impactor velocity of 602 m/s [9]. The time and velocity scales in Fig. 3a are chosen according to the full-scale experiment. The shapes of the curves are seen to be similar: the main maximum corresponding to the instant at which the shock wave reaches the free surface and vibrations in the target are clearly defined in both dependences. However, there are substantial differences. First, the shapes of the shock-wave fronts are different. In the full-scale experiment, the shock front is clearly divided into an elastic precursor and the subsequent plastic front, whereas this division is absent in the simulation. In the latter case, only the elastic component of the front exists and the plastic front is virtually absent; this behavior is caused by the ideal (defect-free) structure of the model single crystal.

To simulate plastic deformation at the shock front, we consider a crystalline material with lattice defects. As the initial material, we choose the single crystal mentioned above. To produce an imperfect material, we randomly remove atoms from the initial material to achieve the required defect (vacancy) concentration, which is calculated as the percentage ratio of the num-



**Fig. 4.** Time dependence of the velocity of the free target surface for (a) a perfect single crystal (calculation), (b) a single crystal with defects (calculation), and (c) VT-20 titanium alloy (experiment).



**Fig. 5.** Velocity profiles for the free target surface (simulation): (a) at  $v_{\text{imp}} = v_d$  and a vacancy fraction of (1) 0, (2) 1, (3) 2, (4) 4, (5) 6, and (6) 9%; (b) at a vacancy fraction of 6% and  $v_{\text{imp}}/v_d$  equal to (1) 0.1, (2) 0.2, (3) 0.4, (4) 0.6, (5) 0.8, (6) 1.0, (7) 1.2, and (8) 1.4.

ber of removed atoms to the initial number of atoms. When a shock wave moves in such a material, vacancies initiate irreversible changes in its structure, which lead to plastic deformation of the medium.

The initial values of the parameters are given in the table (experiment B). The model contains  $\sim 5 \times 10^5$  particles, with the ratios of the impactor and target dimensions remaining as before. Figures 4a and 4b show the time dependences of the velocity of the free surface when the shock wave reaches the surfaces of the perfect single crystal and the imperfect material (vacancy fraction 6%), respectively. For comparison, Fig. 4c shows the experimental curve recorded during a full-scale spalling test of a VT-20 titanium alloy at an impactor velocity of 365 m/s [9]. The time and velocity scales in Figs. 4a and 4b are chosen according to the experimental scales. In Fig. 4a, the shock-wave front is virtually vertical and carries only elastic deformation. In contrast, Figs. 4b and 4c demonstrate a pronounced elastic precursor followed by a plastic front.

The relation between the amplitudes of the elastic and plastic fronts depends on the defect concentration and the impactor velocity, which is illustrated in Figs. 5a and 5b. Figure 5a shows the velocity profiles of the target free surface simulated at the same parameters as those in Fig. 3b but at different defect concentrations. The time and velocity are measured in units of the calculated spalling time  $t_s$  and the dissociation velocity  $v_d$ . As the defect concentration increases, the elastic-precursor amplitude decreases significantly faster than

the plastic-front amplitude, which leads to their distinct separation. Figure 5b shows the results of analogous simulations at the same defect concentration (6%) and various values of the impactor velocity  $v_{\text{imp}}$ . At low  $v_{\text{imp}}$  values ( $v_{\text{imp}} \leq 0.2v_d$ ), the shock-wave front contains only an elastic component. However, as the impactor velocity increases, a plastic component appears, which increases much faster than the elastic component with a further increase in  $v_{\text{imp}}$ .

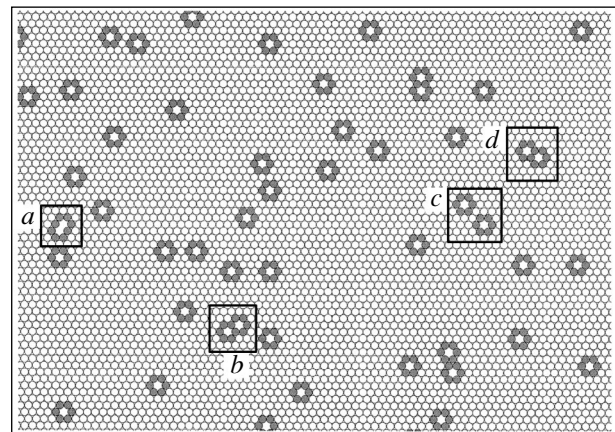


**Fig. 6.** Structure of the model material before passing a shock wave: (a) microvoid and (b–d) pairs of vacancies. The particles that have less than six neighbors at a distance of  $1.1a$  are dark.

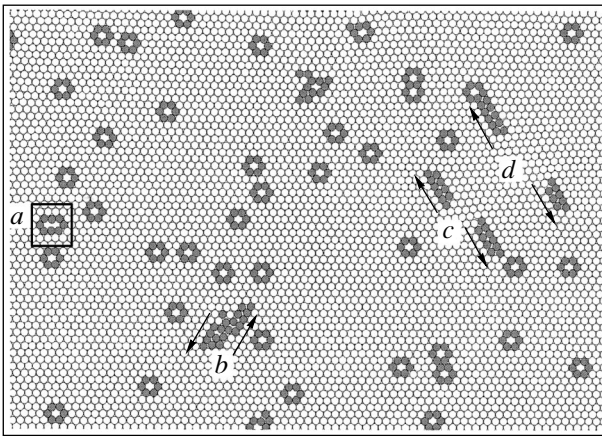


**Fig. 7.** Changes in the material structure upon passing a shock wave: (a) microvoid, (b) dislocation nucleation, and (c, d) decomposition of pairs of vacancies into dislocation pairs.

#### 4. DISCUSSION OF THE RESULTS

To elucidate the behavior of defects at the shock-wave front, we consider an element of the model material before and after passing a shock wave (Figs. 6, 7). These pictures are obtained as a result of simulating spalling at the parameters given in the table (experiment C). The material element shown in Figs. 6 and 7 contains about 4800 particles, which is less than 0.5% of the total volume to be simulated. To study the behavior of defects, we analyzed the total volume; this element is shown only for illustration. In Figs. 6 and 7, the particles located near lattice defects are dark.<sup>2</sup> In the undeformed material (Fig. 6), the defects are vacancies. However, due to their random distribution, some of them are in immediate vicinity to each other and some vacancies combine to form microvoids (Fig. 6a). Let us choose several closely spaced vacancies (Figs. 6, vacancies *a–d*) and follow their evolution upon passing a shock wave (Fig. 7, vacancies *a–d*). Microvoid *a* in Fig. 7 is seen to change its orientation under the effect of the shock wave. As for the other chosen vacancy groups, they decompose into pairs of moving dislocations (Fig. 7, groups *c, d*; the arrows show the directions of dislocation motion). The shock front in Fig. 7 moves from the top down; therefore, different stages of the decomposition of the vacancy groups are visible in Fig. 7 (groups *b–d*): nucleation of dislocations (Fig. 7, group *b*) and their recession (Fig. 7, groups *c, d*). A comparison of single vacancies in Figs. 6 and 7 shows that a shock wave of the given intensity cannot cause their migration or transformation into dislocations. Thus, plasticity in the imperfect material under study occurs mainly via the decomposition of closely spaced vacancies to form dislocation-like defects, which

<sup>2</sup> Specifically, the particles that have less than six neighbors at a distance of  $1.1a$  are dark (in the ideal triangular lattice, the number of neighbors for each atom is equal to six).

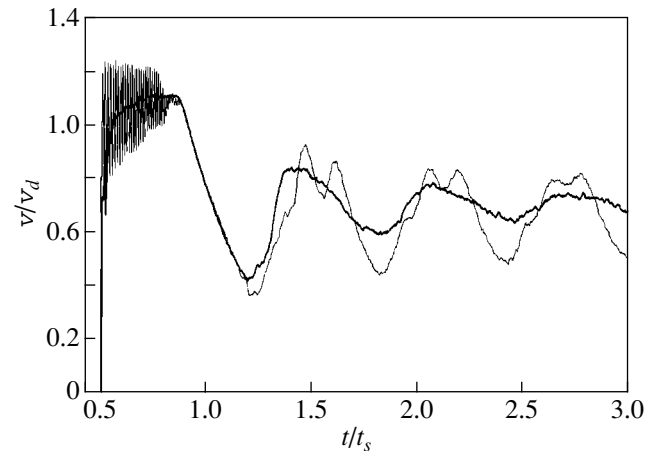


**Fig. 8.** Velocity profiles of the free target surface for the vacancy concentrations of 0 (thin line) and 0.1% (heavy line).

causes shear strains at the shock front upon defect motion.

Note that even an insignificant number of defects results in a significant change in the velocity profile of the free surface. Figure 8 illustrates the results of simulating a perfect single crystal and a similar crystal where one atom per one thousand atoms is removed (the defect concentration is 0.1%). The impactor velocity is  $v_{\text{imp}} = 1.1 v_d$ , and the values of the other parameters correspond to experiment B (see table). For illustration, the curves were not averaged over time. Therefore, the profile of the perfect single crystal demonstrates clearly visible high-frequency vibrations (induced by the discreteness of the MD representation) at the shock front. These vibrations virtually disappear in the material with defects. Moreover, the vibrations in the target strongly change in character and the rate of their damping increases significantly. At the low defect concentration used in the simulation, the elastic and plastic fronts cannot be separated. However, these fronts will likely be separated in this material as the crystal thickness along the shock direction increases.

#### 5. CONCLUSIONS

Thus, when loaded with a shock wave, a single crystal consisting of particles that interact through the Lennard–Jones potential and containing a sufficient concentration of lattice defects demonstrates pronounced plastic effects, such as separation of the shock-wave front into elastic and plastic components. As a result, we could obtain time dependences of the velocity of the free target surface very close to the experimental curves, in particular, to the curves recorded upon spalling of titanium alloys.

## ACKNOWLEDGMENTS

The author is grateful to Yu.I. Meshcheryakov for experimental data and useful discussions.

This work was supported by the Ministry of Education of the Russian Federation, project no. E02-4.0-33.

## REFERENCES

1. B. L. Holian, *Shock Waves* **5** (3), 149 (1995).
2. A. I. Lobastov, V. E. Shudegov, and V. G. Chudinov, *Zh. Tekh. Fiz.* **70** (4), 123 (2000) [*Tech. Phys.* **45**, 501 (2000)].
3. V. A. Lagunov and A. B. Sinani, *Fiz. Tverd. Tela* (St. Petersburg) **43** (4), 644 (2001) [*Phys. Solid State* **43**, 670 (2001)].
4. F. F. Abraham, R. Walkup, H. Gao, M. Duchaineau, T. D. De La Rubia, and M. Seager, *Proc. Natl. Acad. Sci. USA* **99** (9), 5783 (2002).
5. A. M. Krivtsov, in *Problems in Mechanics of Deformed Solids* (S.-Peterb. Gos. Univ., St. Petersburg, 2002), pp. 173–178.
6. A. M. Krivtsov and N. F. Morozov, *Dokl. Akad. Nauk* **381** (3), 825 (2001) [*Dokl. Phys.* **46**, 825 (2001)].
7. A. M. Krivtsov and N. F. Morozov, *Fiz. Tverd. Tela* (St. Petersburg) **44** (12), 2158 (2002) [*Phys. Solid State* **44**, 2260 (2002)].
8. A. M. Rajendran and D. J. Grove, *Int. J. Impact Eng.* **18** (6), 611 (1996).
9. Yu. I. Mescheryakov, A. K. Divakov, and N. I. Zhigacheva, *Shock Waves* **10**, 43 (2000).
10. G. I. Kanel', S. V. Razorenov, and V. E. Fortov, in *Problems in Mechanics of Deformed Solids* (S.-Peterb. Gos. Univ., St. Petersburg, 2002), pp. 159–165.
11. N. J. Wagner, B. L. Holian, and A. F. Voter, *Phys. Rev. A* **45** (12), 8457 (1992).
12. W. C. Morrey and L. T. Wille, *Comput. Mater. Sci.* **10** (1–4), 432 (1998).
13. A. M. Krivtsov, *Int. J. Impact Eng.* **23** (1), 466 (1999).
14. S. P. Nikanorov and B. K. Kardashev, *Elasticity and Dislocation Inelasticity of Crystals* (Nauka, Moscow, 1985).
15. V. A. Lagunov and A. B. Sinani, *Fiz. Tverd. Tela* (St. Petersburg) **45** (3), 542 (2003) [*Phys. Solid State* **45**, 573 (2003)].
16. B. L. Holian and P. S. Lomdahl, *Science* **280** (5372), 2085 (1998).
17. A. M. Krivtsov and Y. I. Mescheryakov, *Proc. SPIE* **3687**, 205 (1999).
18. A. M. Krivtsov and N. V. Krivtsova, *Dal'nevost. Mat. Zh.* **3** (2), 254 (2002).

*Translated by K. Shakhlevich*

---

## MAGNETISM AND FERROELECTRICITY

---

# Refraction of Surface Spin Waves in Spatially Inhomogeneous Ferroelectrics with Biaxial Magnetic Anisotropy

S. A. Reshetnyak

*Institute of Magnetism, National Academy of Sciences of Ukraine, Kiev, 03142 Ukraine*

*e-mail: rsa@users.ntu-kpi.kiev.ua*

Received August 13, 2003

**Abstract**—The refractive index of surface spin waves propagating in a ferromagnetic medium with a nonuniform distribution of the parameters of uniaxial and orthorhombic magnetic anisotropies and exchange coupling is determined within the spin-density formalism. The coefficients of reflection and transmission of spin waves at the interface between two homogeneous magnets with different constants of uniaxial and orthorhombic magnetic anisotropies, exchange coupling, and saturation magnetization are calculated. The dependences of the intensity of a reflected wave and the refractive index on the wave frequency and the strength of an external dc homogeneous magnetic field are determined. © 2004 MAIK “Nauka/Interperiodica”.

### 1. INTRODUCTION

Considerable progress achieved in the field of nanotechnologies and nanoelectronics over the last decade has brought to the fore the necessity of designing new materials and devices based on the use of unique properties of high-frequency waves. In this respect, it is of interest to investigate the specific features of surface spin waves from the practical standpoint.

A theoretical description of the features of propagation of spin waves, as a rule, has been performed within the wave approach, which, for example, has been successfully used to determine the spectral characteristics of magnetic materials [1–5].

In this work, the behavior of surface spin waves propagating in a ferromagnetic medium with a nonuniform distribution of magnetic parameters was described using mathematical tools of geometrical optics. Within this approach, the required change in the direction of propagation of surface spin waves (in particular, focusing) can be achieved both through the creation of artificial inhomogeneities of the magnetic parameters of a medium of the specified configuration and by varying the strength of an external magnetic field.

Earlier [6, 7], we calculated the refractive indices of bulk and surface spin-wave rays and investigated their behavior at the interface between two homogeneous magnets with different parameters of exchange coupling and uniaxial magnetic anisotropy. The purpose of the present work was to analyze (i) the case of a continuous distribution of the aforementioned parameters of exchange coupling and uniaxial magnetic anisotropy and (ii) the case of a continuous distribution of the parameter of orthorhombic anisotropy in a magnetically biaxial medium. Moreover, I calculated the refractive index and the intensity of reflection of a surface

spin wave from the interface between two homogeneous ferromagnets with different constants of uniaxial and orthorhombic magnetic anisotropies, exchange coupling, and saturation magnetization.

### 2. EQUATIONS OF MAGNETIZATION DYNAMICS

Let us consider an infinite ferromagnet consisting of two semi-infinite parts that are in contact along the  $yOz$  plane. In the corresponding half-spaces, these parts of the ferromagnet are characterized by the saturation magnetizations  $M_{01}$  and  $M_{02}$ , as well as by continuously (or piecewise continuously) and slowly varying parameters of exchange coupling ( $\alpha_1, \alpha_2$ ), uniaxial magnetic anisotropy ( $\beta_1, \beta_2$ ), and orthorhombic magnetic anisotropy ( $\rho_1, \rho_2$ ). The easy magnetization axis of the ferromagnet and the external dc magnetic field are directed parallel to the  $Oz$  axis.

For a magnet of the above configuration, the energy density in the exchange approximation has the form

$$w = \sum_{j=1}^2 \Theta[(-1)^j x] w_j + A \delta(x) \mathbf{M}_1 \mathbf{M}_2. \quad (1)$$

Here,

$$w_j = \frac{\alpha}{2} \left( \frac{\partial m_j}{\partial x_k} \right)^2 + \frac{\beta}{2} (m_{jx}^2 + m_{jy}^2) + \rho m_{jx}^2 - H_0 M_{jz}, \quad (2)$$

$\Theta(x)$  is the Heaviside step function,  $A$  is the parameter characterizing the exchange coupling between the half-spaces at  $x = 0$ , and  $\mathbf{M}_j = M_{0j} \mathbf{m}_j$  (where  $\mathbf{m}_j$  are the unit vectors aligned parallel to the magnetization vector and  $j = 1, 2$ ).

In the framework of the spin-density formalism [8], the magnetization can be represented in the form

$$\mathbf{M}_j(\mathbf{r}, t) = M_{0j}\Psi_j^+(\mathbf{r}, t)\boldsymbol{\sigma}\Psi_j(\mathbf{r}, t), \quad j = 1, 2, \quad (3)$$

where  $\Psi_j$  are the quasi-classical wave functions, which play the role of an order parameter of the spin density;  $\mathbf{r}$  is the radius vector in the Cartesian coordinate system;  $t$  is the time; and  $\boldsymbol{\sigma}$  is the Pauli matrix.

The Lagrange equations for the quasi-classical wave functions  $\Psi_j$  take the form

$$i\hbar\frac{\partial\Psi_j(\mathbf{r}, t)}{\partial t} = -\mu_0\mathbf{H}_{ej}(\mathbf{r}, t)\boldsymbol{\sigma}\Psi_j(\mathbf{r}, t), \quad (4)$$

where  $\mu_0$  is the Bohr magneton and  $\mathbf{H}_{ej} = -\frac{\partial w_j}{\partial \mathbf{M}_j} + \frac{\partial}{\partial x_k}\frac{\partial w_j}{\partial(\partial \mathbf{M}_j/\partial x_k)}$ .

Making allowance for the fact that, in the ground state, the material is magnetized parallel to the vector  $\mathbf{e}_z$  and assuming that  $M_j^2(\mathbf{r}, t) = \text{const}$  in each half-space, we will seek the solution to the Lagrange equations (4) in the following form:

$$\Psi_j(\mathbf{r}, t) = \exp(i\mu_0 H_0 t/\hbar)\left(\chi_j(\mathbf{r}, t)\right), \quad (5)$$

where  $\chi_j(\mathbf{r}, t)$  is a small addition accounting for the deviation of the magnetization from the ground state. After linearization of the Lagrange equations (4) with due regard for expression (5), we obtain

$$\begin{aligned} & \frac{i\hbar}{2\mu_0 M_{0j}} \frac{\partial \chi_j(\mathbf{r}, t)}{\partial t} \\ &= \left( \alpha(\mathbf{r})\Delta - \beta(\mathbf{r}) - \frac{\rho(\mathbf{r})}{2} - \tilde{H}_{0j} \right) \chi_j(\mathbf{r}, t) - \frac{\rho(\mathbf{r})}{2} \chi_j^*(\mathbf{r}, t), \end{aligned} \quad (6)$$

$$\frac{i\hbar}{2\mu_0 M_{0j}} \frac{\partial \chi_j^*(\mathbf{r}, t)}{\partial t}$$

$$= \left( \alpha(\mathbf{r})\Delta - \beta(\mathbf{r}) - \frac{\rho(\mathbf{r})}{2} - \tilde{H}_{0j} \right) \chi_j^*(\mathbf{r}, t) - \frac{\rho(\mathbf{r})}{2} \chi_j(\mathbf{r}, t),$$

where  $\tilde{H}_{0j} = H_0/M_{0j}$  and  $j = 1, 2$ .

By separating out the quantity  $\chi_j^*(\mathbf{r}, t)$  from one of the equations in system (6) and substituting it into the other equation of this system, we derive the equation of magnetization dynamics:

$$\begin{aligned} -\frac{\hbar^2}{(2\mu_0 M_{0j})^2} \frac{\partial^2 \chi_j(\mathbf{r}, t)}{\partial t^2} &= \left[ \alpha^2 \Delta^2 - 2\alpha \left( \beta + \frac{\rho}{2} + \tilde{H}_{0j} \right) \Delta \right. \\ &\quad \left. + (\beta + \tilde{H}_{0j})(\beta + \rho + \tilde{H}_{0j}) \right] \chi_j(\mathbf{r}, t). \end{aligned} \quad (7)$$

In this case, the boundary condition satisfied at the surface  $z = 0$  can be written in the form [9]

$$\frac{\partial \chi_j}{\partial z}(x, y, 0, t) - L_j \chi_j(x, y, 0, t) = 0, \quad (8)$$

where  $L_j$  is a parameter characterizing the spin pinning on the surface of the magnet. After the Fourier transformation, we obtain the dispersion relation for the exponential damping of a surface spin wave along the  $Oz$  axis of a homogeneous uniaxial magnetic material [7]:

$$\begin{aligned} \Omega_j^2 &= [\alpha(\mathbf{r}_\perp)k_\perp^2(\mathbf{r}_\perp) + \beta(\mathbf{r}_\perp) + \tilde{H}_{0j} - \alpha(\mathbf{r}_\perp)L_j^2] \\ &\times [\alpha(\mathbf{r}_\perp)k_\perp^2(\mathbf{r}_\perp) + \rho(\mathbf{r}_\perp) + \beta(\mathbf{r}_\perp) + \tilde{H}_{0j} - \alpha(\mathbf{r}_\perp)L_j^2], \end{aligned} \quad (9)$$

where  $\Omega_j = \omega\hbar/2\mu_0 M_{0j}$ ,  $\omega$  is the frequency,  $\mathbf{k} = (\mathbf{k}_\perp, k_z)$  is the wave vector, and  $\mathbf{r}_\perp = (x, y)$ .

### 3. GEOMETRICAL-OPTICS APPROXIMATION

Now, we will attempt to simplify the equation of magnetization dynamics (7). For this purpose, we will use the Wentzel–Kramers–Brillouin method described in [10, 11].

In the equation of magnetization dynamics (7), we introduce the function  $\chi_j(\mathbf{r}_\perp, t) = C \exp[i(k_0 s_j(\mathbf{r}_\perp) - \omega t)]$ , where  $k_0$  is the magnitude of the wave vector of the surface wave, for example, at an infinitely large distance from the boundary  $x = 0$  as viewed from the incident wave [the precise definition of this quantity, as will be shown below, is necessary only for the relative measurement of the wave vector  $\mathbf{k}(\mathbf{r}_\perp)$  when determining the refractive index] and  $C$  is the slowly varying amplitude. From the dispersion relation (9), we obtain

$$\begin{aligned} \alpha(\mathbf{r}_\perp)k_\perp^2(\mathbf{r}_\perp) &= \alpha(\mathbf{r}_\perp)L_j^2 - \rho(\mathbf{r}_\perp)/2 - \beta(\mathbf{r}_\perp) \\ &\quad - \tilde{H}_{0j} \pm \sqrt{\Omega_j^2 + \rho^2(\mathbf{r}_\perp)}/4. \end{aligned}$$

Next, we assume that the length of a spin wave  $\lambda$  satisfies the geometrical-optics condition:

$$\lambda \ll a, \quad (10)$$

where  $a$  is the characteristic size of inhomogeneities involved in the medium. Then, from the equation of magnetization dynamics (7), we deduced an equation analogous to the classical Hamilton–Jacobi equation, that is,

$$(\nabla_\perp s_j(\mathbf{r}_\perp))^2 = n_j^2(\mathbf{r}_\perp), \quad (11)$$

where

$$\nabla_\perp = \mathbf{e}_x \frac{\partial}{\partial x} + \mathbf{e}_y \frac{\partial}{\partial y}, \quad (12)$$

$$n_j^2(\mathbf{r}_\perp) = k_j^2(\mathbf{r}_\perp)/k_0^2.$$

As has been done in optics [12], we assume that the right-hand side of expression (11) is the square of the refractive index,

$$n_j^\pm(\mathbf{r}_\perp) = \frac{1}{k_0} [(\alpha(\mathbf{r}_\perp)L_j^2 - \rho(\mathbf{r}_\perp)/2 - \beta(\mathbf{r}_\perp) - \tilde{H}_{0j} \pm [\Omega_j^2 + \rho^2(\mathbf{r}_\perp)/4]^{1/2})/\alpha(\mathbf{r}_\perp)]^{1/2}, \quad (13)$$

because the ratio between the magnitudes of the wave vectors at two different points of the space characterizes the change in the direction of the propagation of the spin wave.

Therefore, the pinning of spins on the surface of a magnetic material makes it possible to observe the effect of birefringence of a surface spin wave. It should be noted that, for bulk spin waves propagating in a magnetic material, there exists only one branch that corresponds to the positive sign in expression (13), as is the case in the absence of spin pinning on the surface. If the value of  $\alpha(\mathbf{r}_\perp)L_j^2$  is relatively large, there appears another branch that corresponds to the negative sign in expression (13).

Equation (11) can be represented in the form

$$H = \frac{1}{2}[\mathbf{p}^2 - n^2(\mathbf{r}_\perp)] = 0,$$

where  $\mathbf{p} = \nabla_\perp s$ . From this relation, we derive the equations describing the ray path in the Hamiltonian form:

$$\begin{aligned} \dot{\mathbf{r}} &= \mathbf{p}, \\ \dot{\mathbf{p}} &= \frac{1}{2}\nabla_\perp n^2(\mathbf{r}_\perp). \end{aligned}$$

Hence, it follows from expression (11) that  $|\nabla_\perp s_\perp(\mathbf{r}_\perp)| = ds(\mathbf{r}_\perp)/d\tau = n(\mathbf{r}_\perp)$ , where  $d\tau = \sqrt{dx^2 - dy^2}$  is the element of the ray path. Therefore, the function  $s$  can be determined as the curvilinear integral taken along the ray path; that is,

$$s = \int_A^B n d\tau. \quad (14)$$

Minimizing the curvilinear integral (14) with the use of Fermat's principle [13], we deduce the following equation of the ray path [10]:

$$\frac{d}{d\tau}\left(n\frac{d\mathbf{r}_\perp}{d\tau}\right) = \nabla_\perp n.$$

#### 4. REFRACTION OF A SPIN-WAVE RAY AT THE INTERFACE BETWEEN TWO HOMOGENEOUS MAGNETS

Formula (14) can be applied to the case of a semi-infinite magnet composed of two contacting homogeneous parts.

We will consider the situation where a spin wave is incident on the interface between two homogeneous magnets that are in contact along the  $yz$  plane and are characterized by the parameters  $\alpha_1, \beta_1, \rho_1, M_{01}$ , and  $L_1$  and  $\alpha_2, \beta_2, \rho_2, M_{02}$ , and  $L_2$ , respectively. Note that the spin wave is incident on the interface as viewed from the first magnet. A spin-wave ray propagates from the point  $(x_1, y_1, z_1)$  located in medium **1** with a refractive index  $n_0 = 1$  to the point  $(x_2, y_2, z_2)$  in medium **2** with a refractive index  $n^\pm$ , which, according to expression (13), can be written in the form

$$n^\pm = \frac{\alpha_1 \alpha_2 L_2^2 - \beta_2 - \rho_2/2 - \tilde{H}_{02} \pm \sqrt{\Omega_2^2 + \rho_2^2/4}}{\sqrt{\alpha_2 \alpha_1 L_1^2 - \beta_1 - \rho_1/2 - \tilde{H}_{01} \pm \sqrt{\Omega_1^2 + \rho_1^2/4}}}.$$

The spin-wave ray passes through the interface at the point  $(0, y, z)$ . In this case, from the extremum conditions of the function  $s$ , we have

$$\frac{\sin\theta_1^\pm}{\sin\theta_2^\pm} = \frac{k_2^\pm}{k_0^\pm}$$

$$= \frac{\alpha_1 \alpha_2 L_2^2 - \beta_2 - \rho_2/2 - \tilde{H}_{02} \pm \sqrt{\Omega_2^2 + \rho_2^2/4}}{\sqrt{\alpha_2 \alpha_1 L_1^2 - \beta_1 - \rho_1/2 - \tilde{H}_{01} \pm \sqrt{\Omega_1^2 + \rho_1^2/4}}} = n^\pm, \quad (15)$$

where  $\theta_1^\pm$  is the angle of incidence and  $\theta_2^\pm$  is the angle of refraction.

The same result can also be obtained from other considerations. In the equation of magnetization dynamics (7), we introduce the following designations:

$$\chi_I = \exp(i(\mathbf{k}_0 \mathbf{r} - \omega t)) \quad (16)$$

for an incident wave,

$$\chi_R = R \exp(i(\mathbf{k}_1 \mathbf{r} - \omega t)) \quad (17)$$

for a reflected wave, and

$$\chi_D = D \exp(i(\mathbf{k}_2 \mathbf{r} - \omega t)) \quad (18)$$

for a transmitted wave.

In expressions (16)–(18),  $R$  is the complex amplitude of reflection of the spin wave from the interface;  $D$  is the transmission amplitude; and  $\mathbf{k}_0, \mathbf{k}_1$ , and  $\mathbf{k}_2$  are the wave vectors of the incident, reflected, and transmitted waves, respectively.

Taking into account the boundary condition (8), we can write the following relations:

$$\begin{aligned} (k_0^\pm)^2 &= (k_1^\pm)^2 \\ &= (\alpha_1 L_1^2 - \beta_1 - \rho_1/2 - \tilde{H}_{01} \pm \sqrt{\Omega_1^2 + \rho_1^2/4})/\alpha_1, \\ (k_2^\pm)^2 &= (\alpha_2 L_2^2 - \beta_2 - \rho_2/2 - \tilde{H}_{02} \pm \sqrt{\Omega_2^2 + \rho_2^2/4})/\alpha_2. \end{aligned}$$

Here,

$$k_{1x} = -\sqrt{(k_{1\perp})^2 - k_{1y}^2},$$

$$k_{2x} = \sqrt{(k_{2\perp})^2 - k_{2y}^2},$$

where the sign “-” in the expression for  $k_{1x}$  corresponds to a spin wave propagating from the interface and  $k_{0y} = k_{1y} = k_{2y}$  are the magnitudes of the wave vectors at the interface. It follows from these equations that the incident, reflected, and transmitted waves, as well as the normal to the surface at the point of incidence, lie in the same plane. In this case, the angle of incidence is equal to the angle of reflection (by analogy with the law of reflection of light waves in optics [12]).

For real values of  $k_{2x}$ , i.e., under the condition

$$(k_{2\perp})^2 > k_{2y}^2,$$

which is equivalent to the condition

$$\frac{\alpha_1 \alpha_2 L_2^2 - \beta_2 - \rho_2/2 - \tilde{H}_{02} \pm \sqrt{\Omega_2^2 + \rho_2^2/4}}{\alpha_2 \alpha_2 L_2^2 - \beta_1 - \rho_1/2 - \tilde{H}_{01} \pm \sqrt{\Omega_1^2 + \rho_1^2/4}} > \sin^2 \theta_1^{\pm},$$

we obtain formula (15).

If the condition  $(k_{2\perp})^2 < k_{2y}^2$  ( $k_1^2 > 0$ ,  $k_2^2 < 0$ ) is satisfied, we have

$$k_{2x} = -i\sqrt{k_{1y}^2 - (k_{2\perp})^2} = -i/2h,$$

$$\chi_D(\mathbf{r}_{\perp}, t) = D \exp(-x/2h) \exp(i(k_{2y}t - \omega t)).$$

This means that the quantity  $h$  is the depth of penetration of the spin wave into the second material:

$$h^{\pm} = \frac{1}{(k_0^{\pm})_{\perp} \sqrt{\sin^2 \theta_1^{\pm} - (n^{\pm})^2}}.$$

## 6. ESTIMATION OF THE PARAMETERS OF SPIN LENSES AND MIRRORS

Now, we estimate the parameters of a material of a thin lens in the case when the angles of incidence of spin-wave rays with respect to the optical axis of the lens are small and ensure the required transparency of

The critical angle of total reflection of the spin wave is determined from the expression

$$\sin \theta_0^{\pm} = \left( \frac{\alpha_1 \alpha_2 L_2^2 - \beta_2 - \rho_2/2 - \tilde{H}_{02} \pm \sqrt{\Omega_2^2 + \rho_2^2/4}}{\alpha_2 \alpha_2 L_2^2 - \beta_1 - \rho_1/2 - \tilde{H}_{01} \pm \sqrt{\Omega_1^2 + \rho_1^2/4}} \right)^{1/2}.$$

## 5. REFLECTION OF SPIN WAVES FROM THE INTERFACE BETWEEN TWO HOMOGENEOUS MEDIA

In all cases where waves of arbitrary nature undergo reflection and refraction, it is necessary to estimate the intensity ratio of the transmitted and reflected waves. If the intensity of the reflected wave is substantially higher than the intensity of the transmitted wave, the structure under investigation can be used for designing mirrors of different types (for example, plane, convex, or concave mirrors of spherical or cylindrical type). Otherwise, when the intensity of the reflected wave is considerably lower than the intensity of the transmitted wave, the studied structure can be used for fabricating lenses with specified parameters.

Let us derive appropriate expressions for the amplitudes of reflection and transmission of a spin wave. For this purpose, we will use the boundary conditions for  $\chi(\mathbf{r}, t)$  at the interface, which follow from formulas (1) and (2):

$$[A\gamma(\chi_2 - \chi_1) + \alpha_1 \chi_1']_{x=0} = 0, \quad (19)$$

$$[A(\chi_1 - \chi_2) - \gamma \alpha_2 \chi_2']_{x=0} = 0,$$

where  $\gamma = M_{02}/M_{01}$ .

Upon substituting the functions  $\chi(\mathbf{r}, t)$  in the exponential form [see formulas (16)–(18)] into the system of equations (19), we obtain the following expressions for the amplitudes of reflection and transmission of a spin wave (for simplicity, the signs “±” are omitted from the formulas):

$$R = \frac{k_0 \alpha_1 \alpha_2 \gamma \cos \theta_1 \sqrt{n^2 - \sin^2 \theta_1} - iA(\alpha_1 \cos \theta_1 - \alpha_2 \gamma^2 \sqrt{n^2 - \sin^2 \theta_1})}{k_0 \alpha_1 \alpha_2 \gamma \cos \theta_1 \sqrt{n^2 - \sin^2 \theta_1} - iA(\alpha_1 \cos \theta_1 + \alpha_2 \gamma^2 \sqrt{n^2 - \sin^2 \theta_1})}, \quad (20)$$

$$D = \frac{-2iA \alpha_1 \cos \theta_1}{k_0 \alpha_1 \alpha_2 \gamma \cos \theta_1 \sqrt{n^2 - \sin^2 \theta_1} - iA(\alpha_1 \cos \theta_1 + \alpha_2 \gamma^2 \sqrt{n^2 - \sin^2 \theta_1})}.$$

the lens. Recall that the intensity of a reflected wave is determined by the square of the reflection amplitude and, as follows from expression (20),  $|R|^2 \approx [(\alpha_1 - \alpha_2 \gamma^2 n)/(\alpha_1 + \alpha_2 \gamma^2 n)]^2$  (for small angles of incidence and  $A \rightarrow \infty$ ). On this basis, under the condition  $|R|^2 < \eta$  (where  $\eta$  is a parameter specifying the required degree



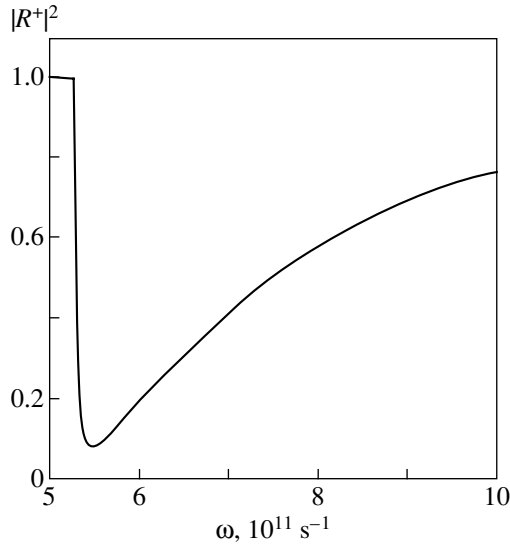


**Fig. 1.** Dependence of the reflection coefficient  $|R^+|^2$  on the frequency  $\omega$  of a surface spin wave for the following parameters:  $\alpha_1 = 10^{-7} \text{ cm}^2$ ,  $\alpha_2 = 2 \times 10^{-7} \text{ cm}^2$ ,  $\beta_1 = 50$ ,  $\beta_2 = 100$ ,  $\rho_1 = 10$ ,  $\rho_2 = 20$ ,  $L_1 = L_2 = 10^4 \text{ cm}^{-1}$ ,  $M_{01} = 100 \text{ G}$ ,  $M_{02} = 125 \text{ G}$ ,  $A = 100$ ,  $\theta_1 = \pi/80$ , and  $H_0 = 1870 \text{ Oe}$ .

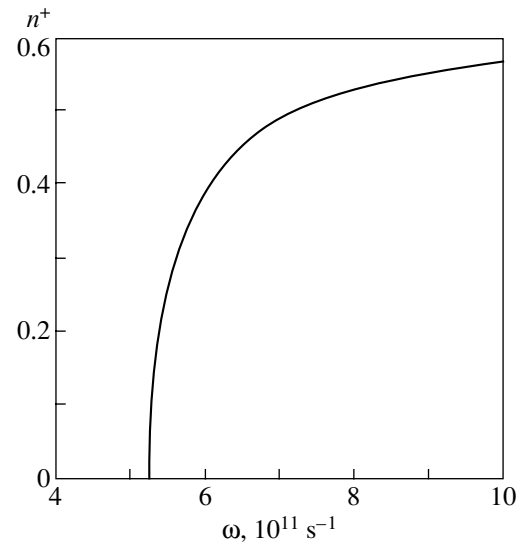


**Fig. 2.** Dependence of the refractive index  $n^+$  on the frequency  $\omega$  of a surface spin wave for the following parameters:  $\alpha_1 = 10^{-7} \text{ cm}^2$ ,  $\alpha_2 = 2 \times 10^{-7} \text{ cm}^2$ ,  $\beta_1 = 50$ ,  $\beta_2 = 100$ ,  $\rho_1 = 10$ ,  $\rho_2 = 20$ ,  $L_1 = L_2 = 10^4 \text{ cm}^{-1}$ ,  $M_{01} = 100 \text{ G}$ ,  $M_{02} = 125 \text{ G}$ , and  $H_0 = 1870 \text{ Oe}$ .

of smallness of the reflection coefficient), we obtain the following restrictions on refractive index  $n$  and, consequently, on the parameters  $\alpha$ ,  $\beta$ ,  $\rho$ ,  $\omega$ ,  $L$ ,  $M_0$ , and  $H_0$ :

$$\frac{1 - \sqrt{\eta}}{1 + \sqrt{\eta}} < \frac{\alpha_2}{\alpha_1} n < \frac{1 + \sqrt{\eta}}{1 - \sqrt{\eta}}.$$

In particular, at  $\alpha_1 = \alpha_2$ ,  $M_{01} = M_{02}$ , and  $L_1 = L_2$ , the reflection coefficient does not exceed 10%, provided the refractive index falls in the range  $0.52 < n < 1.92$ . For a mirror, the restrictions are as follows:

$$\frac{\alpha_2}{\alpha_1} n < \frac{1 - \sqrt{\eta}}{1 + \sqrt{\eta}} \quad \text{or} \quad \frac{\alpha_2}{\alpha_1} n > \frac{1 + \sqrt{\eta}}{1 - \sqrt{\eta}}.$$

For example, the reflection amplitude squared  $|R|^2 > 0.9$  can be reached in the case when  $\alpha_1 = \alpha_2$ ,  $M_{01} = M_{02}$ , and  $L_1 = L_2$  at  $n < 0.03$  or  $n > 37.97$ .

The geometrical-optics condition (10) is satisfied when the thickness of the lens (or mirror) is limited by the inequality

$$a \geq 2\pi \sqrt{\alpha / (\alpha L^2 - \beta - \rho/2 - \tilde{H}_0 \pm \sqrt{\Omega^2 + \rho^2/4})}. \quad (21)$$

As can be seen from expressions (15), (20), and (21), the choice of the parameters for a lens or a mirror does not present any problems, even with a large variety of magnetic materials [14]. Specifically, in the case of garnet-type ferrites, from condition (21) for a thin lens, it follows that the characteristic size of inhomogeneities should fall in the range  $a > 10^{-4} - 10^{-6} \text{ cm}$ .

Figures 1 and 2 show the dependences of the reflected intensity  $I_{R^+} = |R^+|^2$  and the refractive index  $n^+$  on the frequency of a surface spin wave for characteristic parameters of the material [14]. It is clearly seen from these figures that, at a chosen frequency, the

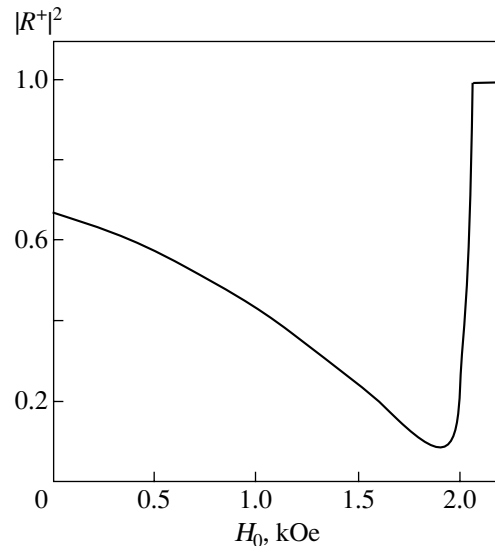


**Fig. 3.** Dependence of the reflection coefficient  $|R^+|^2$  on the external dc magnetic field  $H_0$  for the following parameters:  $\alpha_1 = 10^{-7} \text{ cm}^2$ ,  $\alpha_2 = 2 \times 10^{-7} \text{ cm}^2$ ,  $\beta_1 = 50$ ,  $\beta_2 = 100$ ,  $\rho_1 = 10$ ,  $\rho_2 = 20$ ,  $L_1 = L_2 = 10^4 \text{ cm}^{-1}$ ,  $M_{01} = 100 \text{ G}$ ,  $M_{02} = 125 \text{ G}$ ,  $A = 100$ ,  $\theta_1 = \pi/80$ , and  $\omega = 5.55 \times 10^{11} \text{ s}^{-1}$ .

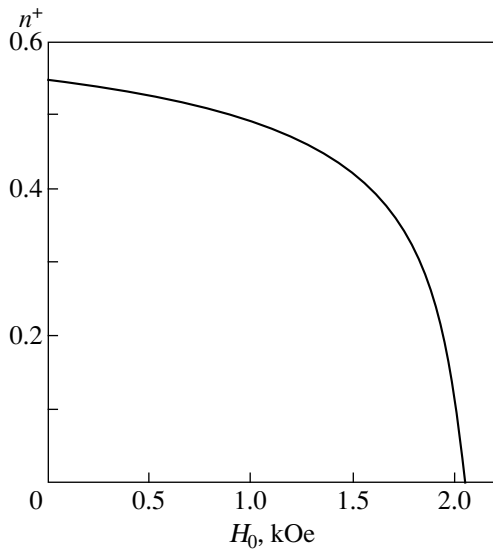


**Fig. 4.** Dependence of the refractive index  $n^+$  on the external homogeneous magnetic field  $H_0$  for the following parameters:  $\alpha_1 = 10^{-7} \text{ cm}^2$ ,  $\alpha_2 = 2 \times 10^{-7} \text{ cm}^2$ ,  $\beta_1 = 50$ ,  $\beta_2 = 100$ ,  $\rho_1 = 10$ ,  $\rho_2 = 20$ ,  $L_1 = L_2 = 10^4 \text{ cm}^{-1}$ ,  $M_{01} = 100 \text{ G}$ ,  $M_{02} = 125 \text{ G}$ , and  $\omega = 5.55 \times 10^{11} \text{ s}^{-1}$ .

required intensity ratio of the reflected and transmitted waves can be achieved by appropriately choosing the material parameters. Moreover, as can be seen from Fig. 3, the reflected intensity substantially depends on the strength of the external homogeneous magnetic field. Therefore, the intensity of a reflected wave can be controlled over a wide range by varying only the strength of the external magnetic field for constant parameters of the material. The corresponding dependence of the refractive index  $n^+$  on the external homogeneous magnetic field is depicted in Fig. 4.

Thus, the coefficient of reflection of spin waves from an inhomogeneous inclusion that plays the role of a lens or a mirror can be controlled by varying the strength of the external magnetic field. It should be noted that, in this case, the reflection coefficient can change significantly, even though the parameters of the medium remain constant. Consequently, the same inhomogeneities can be used both as lenses and as mirrors for the same parameters of the structure.

The dependences of the reflected intensity  $I_R = |R^-|^2$  and the refractive index  $n^-$  on the frequency of a surface spin wave and the strength of the external magnetic field for parameters of the material that allow for the existence of this branch of spin waves are shown in Figs. 5–8. It is worth noting that the refractive index becomes infinite in the ranges of spin-wave frequencies and external magnetic fields that correspond to the edge of the band gap in the first material (Figs. 6, 8). In Figs. 5 and 7, these ranges of spin-wave frequencies and external magnetic fields are indicated by conven-

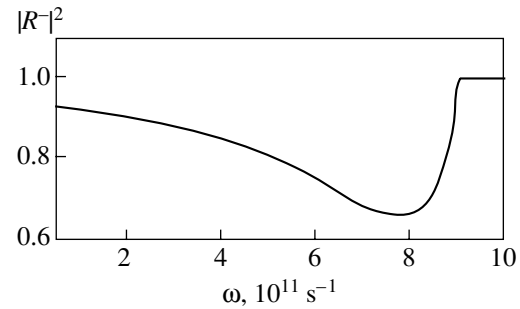


**Fig. 5.** Dependence of the reflection coefficient  $|R^-|^2$  on the frequency  $\omega$  of a surface spin wave for the following parameters:  $\alpha_1 = 10^{-7} \text{ cm}^2$ ,  $\alpha_2 = 2 \times 10^{-7} \text{ cm}^2$ ,  $\beta_1 = 50$ ,  $\beta_2 = 100$ ,  $\rho_1 = 10$ ,  $\rho_2 = 20$ ,  $L_1 = L_2 = 8 \times 10^4 \text{ cm}^{-1}$ ,  $M_{01} = 100 \text{ G}$ ,  $M_{02} = 125 \text{ G}$ ,  $A = 100$ ,  $\theta_1 = \pi/80$ , and  $H_0 = 750 \text{ Oe}$ .

tional lines of the total reflection, even though, in this case, the incident wave is actually absent because of the fast damping in the first material.

Furthermore, the material parameters, if required, can be chosen so that the spin waves corresponding to only one of the two branches will be transmitted through the interface between the two materials, whereas the waves of the second branch will be completely filtered out. Obviously, the material parameters can also be chosen so that a situation will occur in which the “negative” branch of spin waves will correspond to the forbidden band of the second material with an increase in the frequency (or in the external mag-

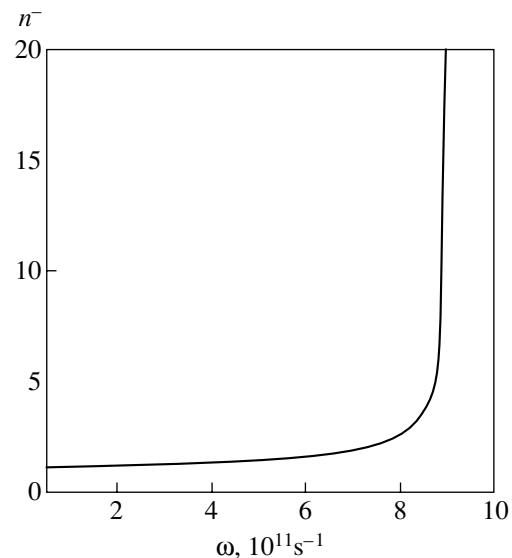


**Fig. 6.** Dependence of the refractive index  $n^-$  on the frequency  $\omega$  of a surface spin wave for the following parameters:  $\alpha_1 = 10^{-7} \text{ cm}^2$ ,  $\alpha_2 = 2 \times 10^{-7} \text{ cm}^2$ ,  $\beta_1 = 50$ ,  $\beta_2 = 100$ ,  $\rho_1 = 10$ ,  $\rho_2 = 20$ ,  $L_1 = L_2 = 8 \times 10^4 \text{ cm}^{-1}$ ,  $M_{01} = 100 \text{ G}$ ,  $M_{02} = 125 \text{ G}$ , and  $H_0 = 750 \text{ Oe}$ .

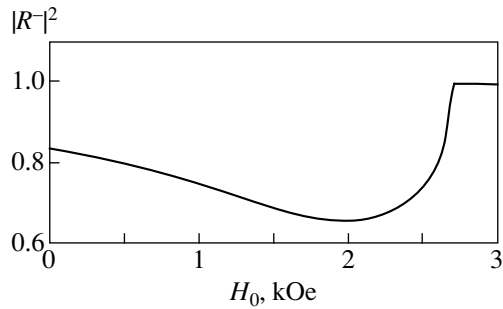


**Fig. 7.** Dependence of the reflection coefficient  $|R|^{-2}$  on the external dc magnetic field  $H_0$  for the following parameters:  $\alpha_1 = 10^{-7} \text{ cm}^2$ ,  $\alpha_2 = 2 \times 10^{-7} \text{ cm}^2$ ,  $\beta_1 = 50$ ,  $\beta_2 = 100$ ,  $\rho_1 = 10$ ,  $\rho_2 = 20$ ,  $L_1 = L_2 = 8 \times 10^4 \text{ cm}^{-1}$ ,  $M_{01} = 100 \text{ G}$ ,  $M_{02} = 125 \text{ G}$ ,  $A = 100$ ,  $\theta_1 = \pi/80$ , and  $\omega = 5.55 \times 10^{11} \text{ s}^{-1}$ .

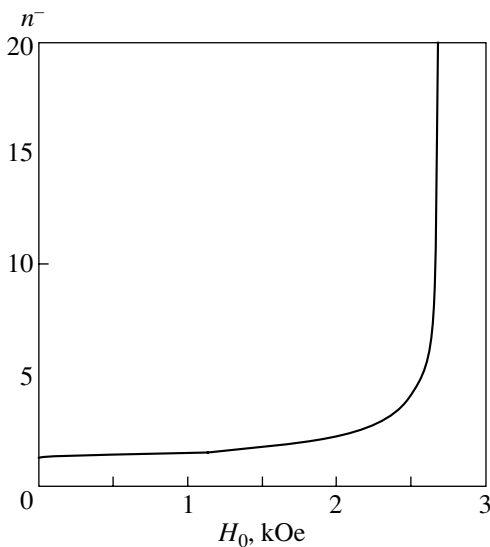


**Fig. 8.** Dependence of the refractive index  $n^-$  on the external homogeneous magnetic field  $H_0$  for the following parameters:  $\alpha_1 = 10^{-7} \text{ cm}^2$ ,  $\alpha_2 = 2 \times 10^{-7} \text{ cm}^2$ ,  $\beta_1 = 50$ ,  $\beta_2 = 100$ ,  $\rho_1 = 10$ ,  $\rho_2 = 20$ ,  $L_1 = L_2 = 8 \times 10^4 \text{ cm}^{-1}$ ,  $M_{01} = 100 \text{ G}$ ,  $M_{02} = 125 \text{ G}$ , and  $\omega = 5.55 \times 10^{11} \text{ s}^{-1}$ .

netic field), whereas the relevant band of the first material will remain allowed. It is this situation that actually arises with the total reflection of spin waves from the interface.

## 7. CONCLUSIONS

Thus, the geometrical-optics approximation, as applied to the case of propagation of surface spin waves in biaxial ferromagnets, made it possible to determine the restrictions imposed on the material parameters at which the spin waves possess properties specific to rays. It was demonstrated that the refraction of a surface spin wave at the interface between two homoge-

neous media is accompanied by birefringence due to the pinning of spins on the surface of the material. In this situation, each of the two branches is characterized by a specific dependence of the coefficient of reflection of a spin wave from the interface between these two media. Consequently, it becomes possible to control the ratio between the intensities of the waves transmitted through the interface between two materials and corresponding to different branches. This ratio can be changed to the extent that one of the branches will be eliminated completely. The regularities revealed in this work can be used in designing devices for spin-wave microelectronics, including filters and spin-wave analogs of optical devices.

## ACKNOWLEDGMENTS

The author would like to thank Yu.I. Gorobets for his participation in discussions of the results and helpful remarks.

This work was supported by the National Academy of Sciences of Ukraine and the Ministry of Education and Science of Ukraine.

## REFERENCES

1. A. L. Sukstanskii, E. P. Stefanovskii, S. A. Reshetnyak, and V. N. Varyukhin, *Phys. Rev. B* **61** (13), 8843 (2000).
2. J. Y. Gan, F. C. Zhang, and Z. B. Su, *Phys. Rev. B* **67** (14), 4427 (2003).
3. M. Buchmeier, B. K. Kuanr, R. R. Gareev, D. E. Bürgler, and P. Grünberg, *Phys. Rev. B* **67** (18), 4404 (2003).
4. J. Fransson, E. Holmström, O. Eriksson, and I. Sandalov, *Phys. Rev. B* **67** (20), 5210 (2003).
5. V. P. Antropov, *J. Magn. Magn. Mater.* **262** (2), L192 (2003).
6. Yu. I. Gorobets and S. A. Reshetnyak, *Zh. Tekh. Fiz.* **68** (2), 60 (1998) [*Tech. Phys.* **43**, 188 (1998)].
7. Yu. I. Gorobets and S. A. Reshetnyak, in *Proceedings of International School–Seminar on New Magnetic Materials in Microelectronics* (Moscow, 2002), p. 175.
8. V. G. Bar'yakhtar and Yu. I. Gorobets, *Bubble Domains and Their Lattices* (Naukova Dumka, Kiev, 1988).
9. A. I. Akhiezer, V. G. Bar'yakhtar, and S. V. Peletminskii, *Spin Waves* (Nauka, Moscow, 1967; North-Holland, Amsterdam, 1968).
10. Yu. A. Kravtsov and Yu. I. Orlov, *Geometrical Optics of Inhomogeneous Media* (Nauka, Moscow, 1980).
11. P. M. Morse and H. Feshbach, *Methods of Theoretical Physics* (McGraw-Hill, New York, 1953; Inostrannaya Literatura, Moscow, 1960), Vol. 2.
12. M. Born and E. Wolf, *Principles of Optics*, 4th ed. (Pergamon, Oxford, 1969; Nauka, Moscow, 1973).
13. R. Courant, *Partielle Differentialgleichungen* (Göttingen, 1932; Mir, Moscow, 1964).
14. A. H. Eschenferder, *Magnetic Bubble Technology*, 2nd ed. (Springer, Berlin, 1980; Mir, Moscow, 1983).

*Translated by O. Borovik-Romanova*

## MAGNETISM AND FERROELECTRICITY

# Hall Effect in the $\text{Fe}_x\text{Mn}_{1-x}\text{S}$ Magnetic Semiconductors

L. I. Ryabinkina, G. M. Abramova, O. B. Romanova, and N. I. Kiselev

*Kirensky Institute of Physics, Siberian Division, Russian Academy of Sciences,  
Akademgorodok, Krasnoyarsk, 660036 Russia*

*e-mail: lir@iph.krasn.ru*

Received July 16, 2003

**Abstract**—The electrical properties and the Hall effect in the  $\text{Fe}_x\text{Mn}_{1-x}\text{S}$  magnetic semiconductors ( $0 < x \leq 0.5$ ) have been experimentally studied in the range 77–300 K in magnetic fields of up to 15 kOe. The cation-substituted sulfides with  $0.25 \leq x \leq 0.3$  possessing colossal magnetoresistance (CMR) were established to be narrow-gap semiconductors with carrier concentrations  $n \sim 10^{11}$ – $10^{15}$   $\text{cm}^{-3}$  and high carrier mobilities  $\mu \sim 10^2$ – $10^4$   $\text{cm}^2 \text{V}^{-1} \text{s}^{-1}$ . It is believed that the CMR effect in these sulfides can be explained in terms of the model of magnetic and electron phase separation, which is analogous to the percolation theory in the case of heavily doped semiconductors. © 2004 MAIK “Nauka/Interperiodica”.

### 1. INTRODUCTION

Despite an impressive number of experimental and theoretical studies into the colossal magnetoresistance effect (CMR) [1–5], clear understanding of its mechanism is still lacking and the criteria governing the realization of this effect in a substance are unknown. An efficient method to gain insight into the mechanisms of conduction is based on investigating the Hall effect; this approach makes it possible to determine the type, concentration, and mobility of charge carriers. Combined study of the Hall effect and the magnetoresistance may help us to understand the mechanism of CMR in magnetic semiconductors [6–8].

### 2. SAMPLES AND EXPERIMENTAL TECHNIQUES

The present communication reports on the results of a study on the electrical and galvanomagnetic properties of solid solutions in the  $\text{Fe}_x\text{Mn}_{1-x}\text{S}$  sulfide system ( $0 < x \leq 0.5$ ). The technology of synthesized polycrystalline  $\text{Fe}_x\text{Mn}_{1-x}\text{S}$  samples and the results of their x-ray characterization are described elsewhere [2, 3]. X-ray diffraction analysis showed the  $\text{Fe}_x\text{Mn}_{1-x}\text{S}$  samples prepared from  $\alpha$ -MnS by cation substitution to have a NaCl-type fcc lattice deformed slightly in the region  $\sim 150$  K. Experimental studies on the electrical and galvanomagnetic properties of the samples were carried out using the standard four-probe dc method at temperatures of 77 to 300 K in magnetic fields  $H = 5, 10,$  and 15 kOe oriented normal to the sample plane. To avoid possible side effects, the Hall voltages were measured for two field and current directions in a sample [9]. The samples prepared for measurements were  $3 \times 5 \times 10$  mm parallelepipeds pelletized from the starting powder material and annealed at 1000°C for 2 h.

### 3. EXPERIMENTAL RESULTS

At room temperature, manganese monosulfide is a *p*-type semiconductor with carrier concentration  $n = 10^{18}$   $\text{cm}^{-3}$  and carrier mobility  $\mu = 0.065$   $\text{cm}^2 \text{V}^{-1} \text{s}^{-1}$  [10]. When in the paramagnetic phase, the conduction activation energy of manganese monosulfide is 0.3 eV in the range 150–300 K. Below the Néel temperature ( $T_N \sim 150$  K), conduction has a practically nonactivated character (similar to  $\text{LaMnO}_3$  [1]).

Increasing the cation substitution  $x$  in the  $\text{Fe}_x\text{Mn}_{1-x}\text{S}$  sulfide compounds prepared from  $\alpha$ -MnS changes the type of magnetic order from antiferromagnetic to ferromagnetic [2], as occurs in manganese oxide compounds synthesized from  $\text{LaMnO}_3$  and possessing CMR [1]. Similar to the  $\text{LaMnO}_3$ -based cation-substituted systems, the  $\text{Fe}_x\text{Mn}_{1-x}\text{S}$  sulfides exhibit CMR for some concentrations  $x$  [2].

Figure 1 plots the temperature dependences of the electrical resistivity  $\rho$  of the cation-substituted  $\text{Fe}_x\text{Mn}_{1-x}\text{S}$  sulfides ( $0 < x \leq 0.5$ ) measured with no magnetic field applied. As the cation substitution  $x$  increases, the electrical resistivity of the  $\text{Fe}_x\text{Mn}_{1-x}\text{S}$  sulfides changes behavior with temperature in the range 77–300 K. One observes a decrease in the electrical resistivity and activation energy for conduction (the slope of the  $\log \rho$  vs.  $1/T$  curves), a feature characteristic of the Anderson-type concentration transitions [11]. The critical concentration at which the  $\text{Fe}_x\text{Mn}_{1-x}\text{S}$  sulfides switch from the semiconductor to semimetal state is  $x_c \sim 0.4$  [12].

Figure 2 displays the temperature dependences of the electrical resistivity measured for the compositions with  $x \sim 0.29$  and  $\sim 0.3$  in magnetic fields of up to 30 kOe. The variation in the electrical resistivity in the temperature interval from 4.2 to 300 K with magnetic field (for a given composition  $x$ ) is similar in character

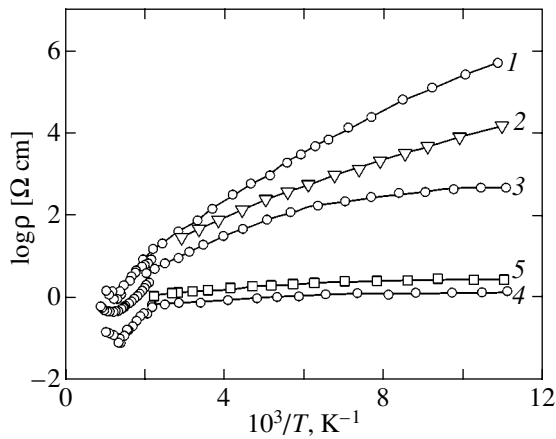
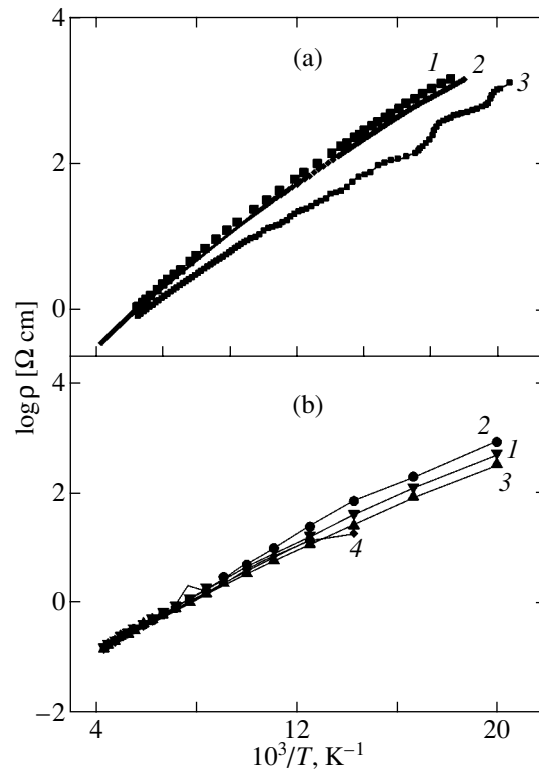


**Fig. 1.** Temperature dependences of the electrical resistivity of samples of the  $\text{Fe}_x\text{Mn}_{1-x}\text{S}$  sulfide system obtained for compositions with (1)  $x = 0.3$ , (2) 0.33, (3) 0.36, (4) 0.4, and (5) 0.5 in zero magnetic field.

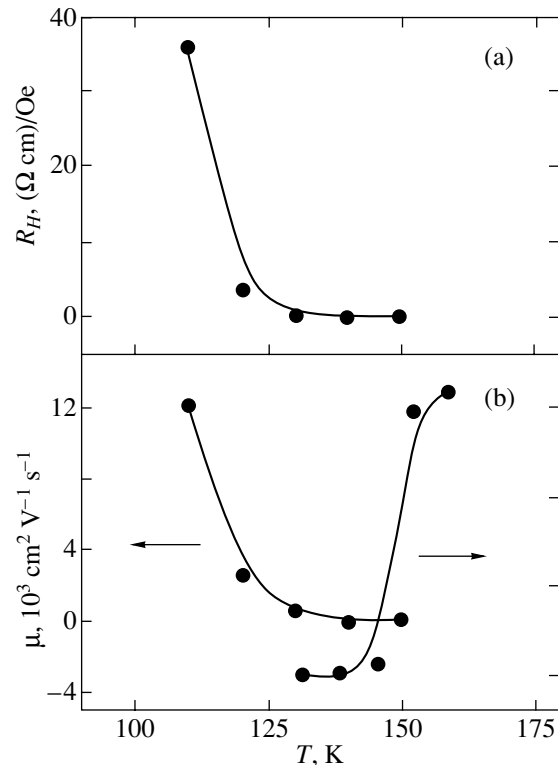
to the variation in  $\rho(T)$  observed in  $\text{Fe}_x\text{Mn}_{1-x}\text{S}$  with increasing cation substitution  $x$  without a magnetic field; in other words, application of a magnetic field brings about a simultaneous decrease in the electrical resistivity and conduction activation energy, as is seen as the substitution concentration  $x$  increases. Negative magnetoresistance  $\delta_H = (R(H \neq 0) - R(H = 0))/R(H \neq 0) \times 100\%$  is observed in the  $\text{Fe}_x\text{Mn}_{1-x}\text{S}$  sulfide system in ferromagnetic compositions in the range  $0.25 \leq x \leq 0.4$ . The value of the magnetoresistance depends on the concentration  $x$  and reaches a maximum for the composition  $x \sim 0.29$  ( $\delta_H = -450\%$  in a magnetic field of 30 kOe at a temperature of 50 K) [2, 3]).

Figure 3 shows temperature dependences of the Hall constant, carrier concentration, and mobility obtained for  $x \sim 0.25$  in a magnetic field of 10 kOe. The Hall constant  $R_H$  grows with decreasing temperature and is positive. When measured at temperature  $T = 110$  K in a field of 10 kOe, the carrier concentration and mobility for  $x \sim 0.25$  are  $n = 0.32 \times 10^{11} \text{ cm}^{-3}$  and  $\mu = 1.2 \times 10^4 \text{ cm}^2 \text{ V}^{-1} \text{ s}^{-1}$ .

Figure 4 presents graphs of the temperature dependences of the Hall constant, carrier mobility, and concentration measured in different magnetic fields on the  $\text{Fe}_x\text{Mn}_{1-x}\text{S}$  sulfide with  $x \sim 0.29$ , the composition with maximum magnetoresistance. In magnetic fields  $H = 5$  and 10 kOe at temperatures of 77–300 K, our sulfide samples with  $x \sim 0.29$  are  $p$ -type semiconductors, which is illustrated by the positive sign of the Hall constant  $R_H$  (Fig. 4a). The Hall constant changed in sign to negative in a magnetic field of 15 kOe for  $T < 180$  K, with electrons becoming the majority carriers in this temperature region. For a given field  $H = 5$  kOe, the mobility of the  $p$ -type carriers in this sample increases and their concentration decreases with decreasing temperature, similar to the way this occurs in the  $x \sim 0.25$  composition in a field of 10 kOe. An increase in mag-



**Fig. 2.** Temperature dependences of the electrical resistivity of  $\text{Fe}_x\text{Mn}_{1-x}\text{S}$  samples obtained in different magnetic fields: (a)  $x \sim 0.29$  and (1)  $H = 0$ , (2) 5, and (3) 30 kOe; (b)  $x \sim 0.3$  and (1)  $H = 3$ , (2) 7, (3) 8, and (4) 14 kOe.



**Fig. 3.** Temperature dependences of (a) the Hall constant and (b) carrier concentration and mobility for  $\text{Fe}_x\text{Mn}_{1-x}\text{S}$  ( $x \sim 0.25$ ) obtained in a field  $H = 10$  kOe.

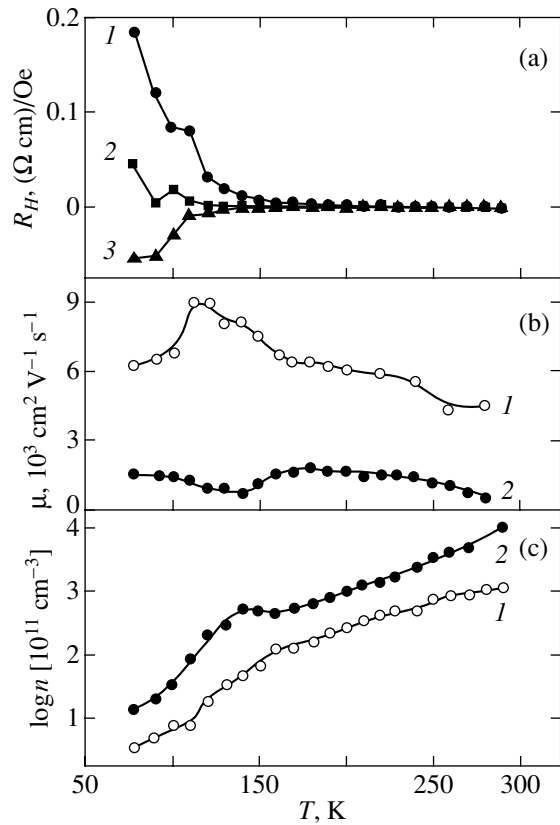


**Fig. 4.** Temperature dependences of (a) the Hall constant and (b) carrier mobility and (c) concentration for  $\text{Fe}_x\text{Mn}_{1-x}\text{S}$  ( $x \sim 0.29$ ) obtained in different magnetic fields  $H$ : (1) 5, (2) 10, and (3) 15 kOe.

netic field (up to 10 kOe) brings about a decrease in the mobility of  $p$  carriers and lead to a weak temperature dependence in the sample with  $x \sim 0.29$  (Fig. 4b). The  $p$ -carrier concentration increases (Fig. 4c). For  $T = 110$  K and  $H = 10$  kOe, the carrier concentrations and mobilities in the sample with  $x \sim 0.29$  are  $n = 8.6 \times 10^{12} \text{ cm}^{-3}$  and  $\mu = 1.3 \times 10^3 \text{ cm}^2 \text{ V}^{-1} \text{ s}^{-1}$ .

Figure 5 illustrates the temperature behavior of the Hall constant and carrier concentration in different magnetic fields studied for the composition with  $x \sim 0.3$ . The majority carriers in this sulfide are negatively charged particles, electrons. In a magnetic field of 5 kOe, the temperature dependence of  $n(T)$  is similar to that for the  $x \sim 0.25$  composition (Fig. 3b), with the temperature at which  $n(T)$  undergoes a sharp change shifting toward high temperatures with increasing field. At  $T = 110$  K and  $H = 10$  kOe, the carrier concentration and mobility for the sample with  $x \sim 0.3$  are  $n = 6.94 \times 10^{13} \text{ cm}^{-3}$  and  $\mu = 1.92 \times 10^2 \text{ cm}^2 \text{ V}^{-1} \text{ s}^{-1}$ . As the magnetic field is increased to 15 kOe, the carrier concentration increases to  $n \sim 10^{15} \text{ cm}^{-3}$ . The carrier mobility for this composition depends only weakly on temperature and was measured to be  $\sim 10^2 \text{ cm}^2 \text{ V}^{-1} \text{ s}^{-1}$ .

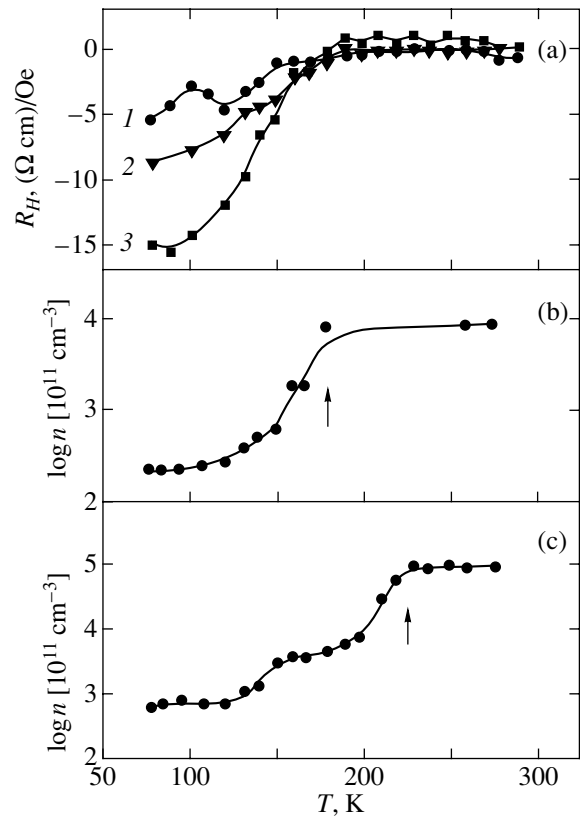


**Fig. 5.** Temperature dependences (a) of the Hall constant in magnetic fields  $H$  (1) 5, (2) 10, and (3) 15 kOe and (b, c) of the carrier concentration in magnetic fields  $H$  (b) 5 and (c) 15 kOe for  $\text{Fe}_x\text{Mn}_{1-x}\text{S}$  ( $x \sim 0.3$ ).

Figure 6 shows field dependences of the electrical resistivity, carrier concentration, and magnetization for the  $x \sim 0.29$  composition measured at 160 K. We see that the decrease in the electrical resistivity and the growth in the magnetization are related to the increasing carrier concentration.

#### 4. DISCUSSION OF THE RESULTS

The CMR effect was first discovered in NaCl-type fcc magnetic semiconductors (such as europium chalcogenides EuSe [13]), which are isostructural to manganese monosulfide. Just as in the europium chalcogenides, the magnetic transition from the paramagnetic to antiferromagnetic state in manganese monosulfide is accompanied by a rhombohedral-type lattice deformation caused by the exchange–striction mechanisms [14]. The antiferromagnetic transition in the cation-substituted sulfides  $\text{Fe}_x\text{Mn}_{1-x}\text{S}$  is apparently of the same nature. As the cation substitution in  $\text{Fe}_x\text{Mn}_{1-x}\text{S}$  increases from  $x = 0$  to  $\sim 0.3$ , the Néel temperature increases from 150 K ( $x = 0$ ) to 230 K ( $x \sim 0.3$ ) [2, 3], which indicates expansion of the temperature region in which the antiferromagnetic state exists. As follows from Hall effect data, the concentration of the  $p$  carriers

decreases and their mobility increases. This suggests that the nature of the antiferromagnetic transition in the  $\text{Fe}_x\text{Mn}_{1-x}\text{S}$  solid solutions is related to a decrease in the  $p$ -carrier concentration and an increase in their mobility.

Many researchers relate the origin of the CMR in magnetic semiconductors (for instance, in  $\text{EuSe}$ ,  $\text{CdCr}_2\text{Se}_4$ ,  $\text{HgCr}_2\text{Se}_4$ ) to a red shift of the conduction band bottom and carrier localization in ferron-type impurity states [6]. The dependence of the carrier concentration and mobility on magnetic field observed in these compounds is assigned to the delocalization of electrons in the ferron states, which gives rise to a reversal of the carrier sign and an increase in the electron concentration and mobility.

The above results obtained in an experimental study of the galvanomagnetic properties of the  $\text{Fe}_x\text{Mn}_{1-x}\text{S}$  sulfides permit us to conclude that, in magnetic fields  $H \leq 10$  kOe at temperatures from 77 to 300 K, the  $\text{Fe}_x\text{Mn}_{1-x}\text{S}$  sulfides ( $x \leq 0.29$ ) are  $p$ -type semiconductors, similar to manganese monosulfide. As  $x$  is increased from 0 to  $\sim 0.29$ , the  $p$ -carrier concentration decreases by five orders of magnitude and their mobility rises by the same factor (relative to  $\alpha$ - $\text{MnS}$ ,  $x = 0$ ). In the composition region of  $x \sim 0.3$ , the carriers reverse sign, with  $n$ -type carriers becoming the majority species. The conduction activation energy  $E_a \sim 10^{-1}$  eV, the carrier concentration  $n \sim 10^{11} - 10^{15} \text{ cm}^{-3}$ , and the mobility  $\mu \sim 10^3 \text{ cm}^2 \text{ V}^{-1} \text{ s}^{-1}$  found for the  $\text{Fe}_x\text{Mn}_{1-x}\text{S}$  sulfides in the range  $0.25 \leq x \leq 0.3$  are typical of semiconductors with narrow-band gaps and small ( $m^*/m \sim 10^{-2}$ ) effective carrier masses (for instance,  $\text{PbS}$ ,  $\text{Ge}$ ,  $\text{Si}$ ) [11].

The Hall resistivity in magnetic semiconductors is defined as  $\rho_H = R_0 B + R_s M$ , where  $R_0$  and  $R_s$  are the normal and anomalous (spontaneous) Hall coefficients,  $B$  is the induction in the sample, and  $M$  is the magnetization. For a sample geometry with a demagnetizing factor of unity, we have  $B = H$ . Studies of the Hall effect in manganese monosulfide [10] showed that the Hall constant  $R_0$  in the range 77–300 K is so small that it lies within the experimental error. Our studies demonstrated a similar situation to exist in a  $\text{Fe}_x\text{Mn}_{1-x}\text{S}$  sample with  $x \sim 0.25$  at temperatures of  $\sim 200$ –300 K. Below 200 K, the Hall constant in the antiferromagnetic phase grows sharply (Fig. 3a). In ferromagnetic samples with  $x \sim 0.29$  and  $\sim 0.3$ , the Hall effect is observed throughout the temperature range 77–300 K. It may be conjectured that the Hall constant observed in the interval from 200 to 300 K is actually the anomalous component  $R_s$ . It has positive sign for the composition  $x \sim 0.29$  and negative sign for  $x \sim 0.3$ . The reversal of the carrier sign from the hole to the electronic sign in manganese monosulfide ( $x = 0$ ) is observed to occur above  $\sim 480$  K [10]. In view of this observation and the results of studies into the Hall effect in cation-substituted sulfides, the compounds investigated by us could be assigned to semiconductors with mixed con-

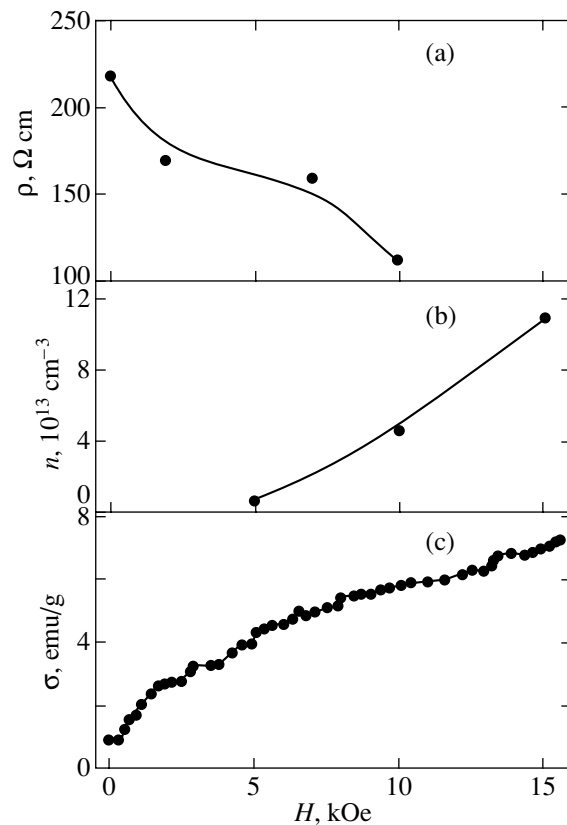


Fig. 6. Magnetic field dependences of (a) the electrical resistivity, (b) carrier concentration, and (c) magnetization for the  $x \sim 0.29$  composition measured at  $T = 160$  K.

duction character, where both holes and electrons act as carriers. The ratio of the electron to hole concentrations determines the type of the carrier, which varies depending on the temperature and composition. A magnetic field apparently exerts a similar impact on the  $x \sim 0.29$  composition in the range 77–200 K, where CMR and the coexistence of the antiferromagnetic and ferromagnetic phases are observed [15]. The sharp rise in the  $p$ -type carrier mobility as the degree of cation substitution  $x$  in the  $\text{Fe}_x\text{Mn}_{1-x}\text{S}$  sulfides is increased compared to the starting manganese monosulfide indicates either the formation of a light-carrier impurity band or a weakening of the polaron or ferron effects, as is the case with the magnetic semiconductors  $\text{La}_{1-x}\text{Sr}_x\text{MnO}_3$  and  $\text{HgCr}_2\text{Se}_4$  [6–8].

To explain the concentration-driven transition from an antiferromagnetic semiconductor to a ferromagnetic metal occurring in  $\text{Fe}_x\text{Mn}_{1-x}\text{S}$  for zero magnetic field, an electronic level diagram was proposed, which includes a  $p$ - $d$  hybridized valence band  $E_1$  and a narrow impurity band  $E_2$  [16]. It was shown that as  $x$  is increased, an Anderson transition takes place in  $\text{Fe}_x\text{Mn}_{1-x}\text{S}$  through a shift of the mobility edge  $E_c$  and crossing of the Fermi level  $E_F$ . The similarity observed in the behavior of the electrical resistivity as a function

of concentration  $x$  (Fig. 1) and of magnetic field  $H$  (Fig. 2) suggests that the mechanism of the concentration transition and the decrease in the electrical resistivity in a magnetic field (the negative CMR effect) have the same (percolation) character. This conjecture fits the model of electronic and magnetic phase separation [1], which is analogous to the theory of percolation in heavily doped semiconductors [17].

#### ACKNOWLEDGMENTS

This study was supported, in part, jointly by the Russian Foundation for Basic Research and Krasnoyarsk Krai Science Foundation, project no. 02-02-97702 “r 2002 Enisei a.”

#### REFERENCES

1. É. L. Nagaev, *Usp. Fiz. Nauk* **166** (8), 833 (1996) [*Phys. Usp.* **39**, 781 (1996)].
2. G. A. Petrakovskii, L. I. Ryabinkina, G. M. Abramova, N. I. Kiselev, D. A. Velikanov, and A. F. Bovina, *Pis'ma Zh. Éksp. Teor. Fiz.* **69** (12), 895 (1999) [*JETP Lett.* **69**, 949 (1999)].
3. G. A. Petrakovskii, L. I. Ryabinkina, G. M. Abramova, A. D. Balaev, D. A. Balaev, and A. F. Bovina, *Pis'ma Zh. Éksp. Teor. Fiz.* **72** (2), 99 (2000) [*JETP Lett.* **72**, 70 (2000)].
4. P. Chen and Y. W. Du, *J. Phys. Soc. Jpn.* **71** (1), 209 (2001).
5. G. A. Petrakovskii, L. I. Ryabinkina, G. M. Abramova, N. I. Kiselev, D. A. Balaev, O. B. Romanova, G. I. Makovetskii, K. I. Yanushkevich, A. I. Galyas, and O. F. Demidenko, *Phys. Met. Metallogr.* **93** (1), 82 (2002).
6. N. I. Solin and N. M. Chebotaev, *Fiz. Tverd. Tela* (St. Petersburg) **39** (5), 848 (1997) [*Phys. Solid State* **39**, 754 (1997)].
7. R. I. Zaïnullina, N. G. Bebenin, V. V. Mashkautsan, V. V. Ustinov, V. G. Vasil'ev, and B. V. Slobodin, *Fiz. Tverd. Tela* (St. Petersburg) **40** (11), 2085 (1998) [*Phys. Solid State* **40**, 1889 (1998)].
8. V. V. Mashkautsan, R. I. Zaïnullina, N. G. Bebenin, V. V. Ustinov, and Ya. M. Mukovskii, *Fiz. Tverd. Tela* (St. Petersburg) **45** (3), 468 (2003) [*Phys. Solid State* **45**, 494 (2003)].
9. V. V. Chechernikov, *Magnetic Measurements* (Mosk. Gos. Univ., Moscow, 1969).
10. H. Heikens, C. F. van Bruggen, and C. Haas, *J. Phys. Chem. Solids* **39** (8), 833 (1978).
11. N. F. Mott and E. A. Davis, *Electron Processes in Non-Crystalline Materials*, 2nd ed. (Clarendon, Oxford, 1979; Mir, Moscow, 1982), Vol. 2.
12. L. I. Ryabinkina, Candidate's Dissertation (Inst. of Physics, Siberian Division, Russian Academy of Sciences, Krasnoyarsk, 1993).
13. Y. Shapira, S. Foner, and T. B. Reed, *Phys. Rev. B* **8** (5), 2299 (1973).
14. B. Morosin, *Phys. Rev. B* **1** (1), 236 (1970).
15. G. Petrakovskii, B. Roessli, L. Ryabinkina, G. Abramova, D. Balaev, and O. Romanova, in *Book of Abstracts: Moscow International Symposium on Magnetism* (Moscow, 2002), p. 167.
16. G. V. Loseva, L. I. Ryabinkina, and S. G. Ovchinnikov, *Fiz. Tverd. Tela* (Leningrad) **33** (11), 3420 (1991) [*Sov. Phys. Solid State* **33**, 1929 (1991)].
17. B. I. Shklovskii and A. L. Éfros, *Electronic Properties of Doped Semiconductors* (Nauka, Moscow, 1979; Springer, New York, 1984).

*Translated by G. Skrebtsov*



---

**MAGNETISM  
AND FERROELECTRICITY**

---

# High-Frequency Susceptibility and Ferromagnetic Resonance in Multidomain Thin Films of the Yttrium–Iron Garnet Type

V. F. Shkar'\*, E. I. Nikolaev\*, V. N. Sayapin\*, and V. D. Poïmanov\*\*

\* Donetsk Physicotechnical Institute, National Academy of Sciences of Ukraine, Donetsk, 83114 Ukraine

\*\* Donetsk National University, Universitetskaya ul. 24, Donetsk, 83114 Ukraine

e-mail: shkar@donapex.net.ua, nikol@donapex.net.ua

Received May 26, 2003; in final form, October 13, 2003

**Abstract**—The field dependence of the high-frequency susceptibility and the ferromagnetic resonance were experimentally studied in a thin ( $d \approx 0.1 \mu\text{m}$ ) (111)-oriented single-crystal film of substituted yttrium–iron garnet with the factor  $q \ll 1$ . It was shown that the anomaly in the high-frequency susceptibility observed in a magnetic field  $\mathbf{H}$  parallel to the normal to the film surface in the magnetization saturation region ( $H \approx H_s$ ) has a dual nature; more specifically, this anomaly is associated with an abrupt collapse of the stripe domain structure and a ferromagnetic resonance in the experimental configuration  $\mathbf{H} \parallel [111]$  and  $\mathbf{h} \perp \mathbf{H}$ . In this case, the film transition from the inhomogeneous multidomain state to the homogeneous (single-domain) state at the point  $H \approx H_s$  has no indications of a second-order phase transition. The experimental frequency–field dependence of ferromagnetic resonance (FMR) in the sample under study, having a characteristic minimum at the point  $\omega_0 = 5 \text{ MHz}$  and  $H_{\text{FMR}} = H_s$ , agrees qualitatively and quantitatively with calculations. The influence of the cubic magnetic anisotropy and the film thickness on the FMR spectrum and the orientation of the spontaneous magnetization in domains with respect to the film plane in the zero field  $H$  was theoretically studied. © 2004 MAIK “Nauka/Interperiodica”.

## 1. INTRODUCTION

Thin films of yttrium–iron garnet (YIG) with partial rare-earth substitution and diamagnetic dilution and an in-plane magnetic moment were previously used as thin underlayers controlling the domain-wall structure in the above-lying magnetically uniaxial garnet ferrite layer of a two-layer garnet structure [1, 2]. Recently, significant attention has been given to the domain structure (DS) of the thinnest YIG films due to new possibilities for their application. In particular, they can be a component of the layered periodic structure of photonic crystals containing a stripe DS with a period of the order of the light wavelength [3, 4]. Since the Faraday rotation is small in such a film, it is not feasible to study DSs using conventional magneto-optical methods.

Previous studies [5, 6] of the spin-wave interactions in the above-mentioned two-layer garnet ferrite structures suggest that the ferromagnetic resonance (FMR) method used in combination with high-frequency magnetic susceptibility (HFMS) makes it possible not only to detect specific dynamic effects in ultrathin YIG films but also to obtain certain information on the “hidden” DS. In this study, the HFMS and FMR spectra are measured in an ultrathin ( $d \approx 0.1 \mu\text{m}$  thick) single-crystal YIG-type film with a DS and theoretical estimates are made.

Interest in this study was stimulated in some respects by paper [7], where it was reported that two

second-order orientational phase transitions (OPT-2) were observed in a similar film at room temperature. This result seems to be unique, since well-established OPTs were observed exclusively in the low-temperature range (mostly at  $T = 4\text{--}150 \text{ K}$ ) in long-term studies of both spontaneous and field-induced OPTs in crystals and films of rare-earth–iron garnets [8–10]. The experiments in [7] cast doubt on the interpretation of the results obtained and the validity of the corresponding conclusions. With thin films similar to those studied in [7], we carried out experimental and theoretical studies; the results are considered below.

## 2. EXPERIMENTAL

### 2.1. Sample under Study and Experimental Technique

Experimental studies were performed using a single-crystal garnet film of composition  $(\text{YLaGd})_3(\text{FeGa})_5\text{O}_{12}$  with a thickness  $d \approx 0.1 \mu\text{m}$  grown on a single-crystal  $\text{Gd}_3\text{Ga}_5\text{O}_{12}$  substrate oriented in the (111) plane such that the [111] crystallographic axis of the film was parallel to the normal  $\mathbf{n}$  to the surface. To grow such a thin film, we used modified liquid-phase epitaxy from a wetting melt-solution layer [11]. According to the original destination of such films, their composition was selected with the intent to minimize the growth-induced magnetic anisotropy along the normal to the surface. In the demagnetized state,

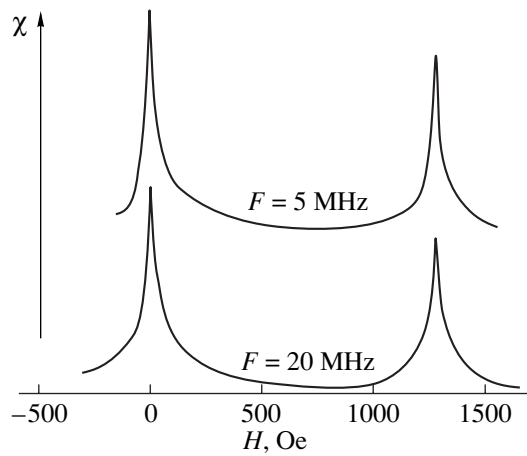


**Fig. 1.** High-frequency susceptibility of a (111)-oriented garnet ferrite film in a field  $\mathbf{H} \parallel [111]$  at frequencies of 5 and 20 MHz.

such a film should contain a stripe DS. The orientation of the spontaneous magnetic moment vector  $\mathbf{M}$  in either of the two types of oppositely polarized magnetic domains in such a film is mainly controlled by the competition between the demagnetization field, which tends to align the vectors  $\mathbf{M}$  in the film plane, and the cubic magnetic anisotropy field, which tends to deflect the vectors  $\mathbf{M}$  from the film plane toward one of the easy magnetization axes of the [111] type, three of which form an angle of  $19^\circ 30'$  with the film surface.

The magnetic characteristics of the film were determined by measuring the FMR parameters. The effective uniaxial anisotropy, which is equal to  $4\pi M_s$  in this case (since there is almost no growth- and stress-induced uniaxial magnetic anisotropy in the sample), was determined according to [12]; more specifically, the experimental and theoretical dependences of resonant fields were constructed for the (110) plane perpendicular to the film plane and, by setting various values of  $4\pi M_s$ , these dependences were brought into coincidence. The gyromagnetic ratio  $\gamma$  was determined from the slope of the frequency–field dependence (straight line) for the field direction perpendicular to the sample plane [13]. The cubic anisotropy field  $H_A$  was determined from the angular (azimuthal) dependence of the resonant field for a fixed polar angle  $\theta \approx 52^\circ$ , which is the most accurate method for determining  $H_A$  in a (111) film. The values determined are  $\gamma = 1.76 \times 10^7 \text{ Oe}^{-1} \text{ s}^{-1}$ ,  $H_A = 45 \text{ Oe}$ , and  $4\pi M_s = 1350 \text{ Oe}$ .

The HFMS was studied using the autodyne technique. The sample under consideration was placed on a rotator in a high-frequency (HF) magnetic field  $h$  induced by high-frequency Helmholtz coils incorporated in a drive circuit of an autodyne oscillator, whose frequency was set between 5 and 30 MHz. The external dc magnetic field  $\mathbf{H}$  was induced by an electromagnet placed on an independent rotator. The electromagnet was power-supplied from a stabilized dc source. The

field  $H$  could be varied within 0–2000 Oe. The two rotators made it possible to rotate the sample about the normal  $\mathbf{n}$  to its surface and to rotate the field  $\mathbf{H}$  in the vertical plane with respect to the sample from the position  $\mathbf{H} \perp \mathbf{n}$  to  $\mathbf{H} \parallel \mathbf{n}$ . The drive circuit voltage varied with the HF power absorbed by the sample. A change in this voltage was amplified and applied to the Y input terminals of an X–Y recorder. A voltage proportional to the external magnetic field was applied to the X input terminals.

The FMR parameters were determined using a reflection-mode setup allowing study in the frequency range 0.005–10 GHz with magnetic field modulation. As a measuring cell (sensitive element), a copper microstrip 0.1 mm wide and 6 mm long was used at the first stage (operation at frequencies above 1 GHz); at the second stage, a copper meander on a polycore substrate was used (operation in the range 0.005–1 GHz).

A sample 6 mm in diameter was glued to the end of a brass axis of the rotator and was densely tightened to the meander by a spring. The rotation axes of the sample and magnet were mutually perpendicular, which allowed us to apply the external field along a required direction.

## 2.2. High-Frequency Susceptibility

The studies presented in this paper were initiated by the observation of a significant change in the HFMS of an YIG-based thin film in a quasi-static magnetic field  $\mathbf{H} \parallel \mathbf{n}$  in the vicinity of the point  $\mathbf{H} = H_s$  ( $H_s$  is the magnetization saturation field of the film, generally defined as a characteristic point (region) in the magnetization curve). Figure 1 shows the dependence of the sample HFMS on the field  $\mathbf{H} \parallel \mathbf{n}$  at frequencies of 5 and 20 MHz. We can see that the first and second susceptibility jumps are observed near the points  $\mathbf{H} = 0$  and  $\mathbf{H} \approx H_s$ , respectively. The second jump is reliably observed only in the case of exact orientation of the external field  $\mathbf{H}$  along the [111] axis of the film and corresponds to the film transition from the inhomogeneous multidomain to a homogeneous single-domain state. Based on published experimental data, we analyze whether or not a causal relation exists between these phenomena.

Studies of the static susceptibility of garnet ferrite films [14] have shown that the DS plays a part in the formation of the sample response to an external field. It is clear that the HFMS of YIG-type multidomain films should also differ from the HF susceptibility of single-domain samples [15]. However, the question arises of how sharply the DS rearrangement or disappearance occurs. In this regard, study [16] is worth noting as it dealt with the field dependence of the YIG film HFMS in an external magnetic field oriented in the film (111) plane (i.e.,  $\mathbf{H} \perp [111]$ ). It was shown that an HFMS jump occurs only in the case of sharp DS rearrangement in the narrow range of values of the field strength  $H$

where distinctive features in the film magnetization curve are observed. No susceptibility anomalies at the point  $H \approx H_s$  were detected during magnetization reversal of the film along either the easy ( $H_s = 30$  Oe) or hard ( $H_s = 50$  Oe) axes.

A similar feature should presumably also be observed in the experimental configuration  $\mathbf{H} \parallel [111]$  if the magnetization reversal in a sample proceeds as was assumed in [7], i.e., via gradual rotation of the spontaneous magnetization vectors  $\mathbf{M}$  toward the field  $\mathbf{H}$  in oppositely polarized stripe domains separated by  $180^\circ$  walls. However, near the field  $H = H_s$ , these vectors are almost aligned along the field  $H$  and domain walls are spread; therefore, such a film state (in terms of energy) differs only very slightly from the single-domain state. This means that no sharp rearrangement of the film DS occurs in the vicinity of  $H = H_s$ ; hence, there is no cause for the HFMS anomaly.

In this case, a question arises concerning the cause of the HFMS jump near  $H \approx H_s$  in Fig. 1. According to [7], as mentioned above, an OPT-2 takes place at  $\mathbf{H} \parallel [111]$  at the point  $H = H_s$  in the sample under study. However, in this case, for  $H \approx H_s$ , there is a critical point passage through which should be accompanied by a set of characteristic features. Such features, observed in spin-orientational transitions in rare-earth magnets, are anomalies in the static magnetic susceptibility, specific heat, Young's modulus, thermal expansion, magnetostriction, and others [8, 9]. However, in the case of a very thin film, measurement of many static characteristics is complicated in practice. It is more convenient to observe critical dynamic phenomena, which should take place during an OPT-2 in cubic ferrimagnets, for example, the critical spin dynamics that is observed in a YIG single crystal at the Curie temperature  $T_C$  (where a typical second-order phase transition occurs) and manifests itself in a characteristic change in the relaxation rate of uniform magnetization precession (spin diffusion) [17]. This relaxation rate can be determined from the measured linewidth  $\Delta H_{\text{FMR}}$ .

The field dependence of  $\Delta H_{\text{FMR}}$  for  $\mathbf{H} \parallel [111]$  was experimentally studied in the vicinity of the point  $H \approx H_s$ . The quantity  $\Delta H_{\text{FMR}}$  has been repeatedly measured in the resonance frequency range 5–180 MHz. The  $\Delta H_{\text{FMR}}$  measurement accuracy was 0.1 Oe. The average value of this quantity was 15 Oe, with the spread being  $\pm 1.5$  Oe, whereas the change in  $\Delta H$  near  $T_C$  in the YIG crystal was tens of oersteds [17]. As follows from these data, the critical spin dynamics was not observed experimentally.

The situation that arose in the above-described study of HFMS called for additional analysis (see below).

### 2.3. Ferromagnetic Resonance

The first stage of this study was carried out using an FMR setup before it was modernized as described

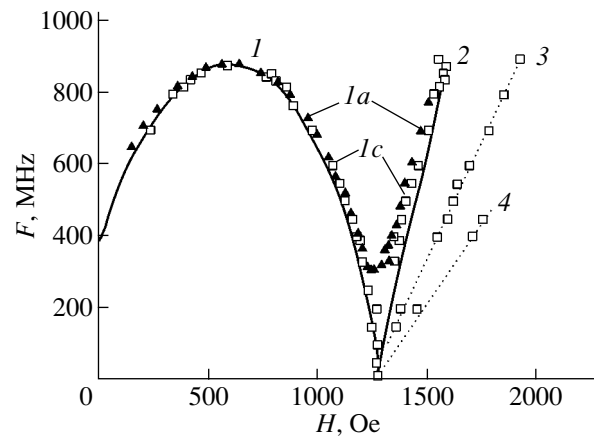


**Fig. 2.** Frequency–field dependences of FMR in a (111)-oriented garnet ferrite film for field  $\mathbf{H} \parallel [111]$ : (1) curve calculated for transverse ( $\mathbf{h} \perp \mathbf{H}$ ) FMR in a multidomain film, (1a, 1c) FMR observed (1a) before and (1c) after modernization of the setup, (2) uniform FMR, and (3, 4) presumably nonuniform FMR in the saturated state of the sample.

below. Figure 2 shows the experimental frequency–field dependence of the FMR (curve 1a) in the sample under study in a field  $\mathbf{H} \parallel [111]$  at  $\mathbf{h} \perp \mathbf{H}$ . Solid lines represent the theoretical dependence of the FMR corresponding to the type of oscillations excited in the sample. The calculation of these dependences is described in Section 4. As follows from Fig. 2, there is good agreement between the experimental (curve 1a) and calculated (curve 1c) data, except in the region of  $H \approx H_s$ . In this region, the resonance frequency does not vanish, in contrast to the prediction from the theory, which results in a “gap”  $\sim 200$  MHz wide in the experimental curve; this gap is similar to that described in [7]. The fact that the FMR frequency  $\omega_0 = \gamma H_{\text{eff}}$  in the sample must vanish in the field  $H \approx H_s$  follows from general considerations. With no external field  $\mathbf{H}$ , the magnetic moment in an anisotropic ferromagnet is subject to the resulting anisotropy field, which, in general, is due to the uniaxial, cubic, orthorhombic, and other types of crystallographic anisotropy, as well as the shape anisotropy of the sample and domains. This field is the effective field  $H_{\text{eff}}$  that controls the frequency  $\omega_0$  at the point  $\mathbf{H} = 0$  in the FMR spectrum. As an external field  $\mathbf{H}$  is applied along a hard magnetization axis of the sample, the magnetic moment begins to rotate from the easy magnetization direction to the hard magnetization axis. This rotation lasts until the external magnetic field  $\mathbf{H}$  become equal to the anisotropy field. At this point, the effective magnetic field  $H_{\text{eff}}$  (acting on the magnetic moment) becomes zero and the FMR frequency  $\omega_0$  vanishes. In the sample at hand, any direction in the (111) plane is easy, while the [111] axis, parallel to the normal  $\mathbf{n}$  to the film surface, is the hard direction along which the external field  $\mathbf{H}$  is applied. When the magnetic moments cease to rotate in domains and become directed along  $\mathbf{n} \parallel [111]$ , the field  $\mathbf{H}$  is the saturation

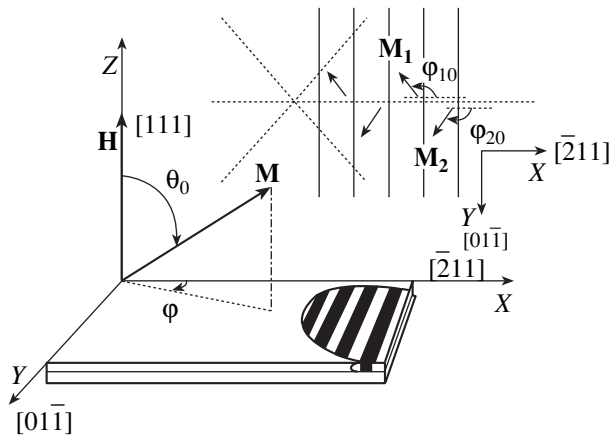


**Fig. 3.** Coordinate system and (inset) the domain structure (schematic) accepted in the theoretical consideration of the problem.

field  $H_s$  exactly equal to the resulting anisotropy field  $H_k$ , which (in the absence of uniaxial anisotropy) is given by  $H_k = 4\pi M - (4/3)K/M$ , where  $4\pi M$  is the demagnetizing field (shape anisotropy) for an unbounded film and  $K$  is the first cubic anisotropy constant. Taking into account that the first term is an order of magnitude greater than the second for the sample at hand, we can write  $H_s \approx 4\pi M_s$ . Hence, when the field magnetizing the sample along the hard magnetization axis varies from zero to a value above the magnetization saturation field, the FMR frequency must pass through zero as the external field becomes equal to this anisotropy field. If the magnetic field  $\mathbf{H}$  is not directed strictly along the hard magnetization axis, only the projection of the anisotropy field onto the external field direction (rather than the total anisotropy field) will be compensated. In this case, the magnetic moment continues to be in a certain nonzero field  $H_{\text{eff}}$  and the FMR frequency will not reach zero. Another cause for the FMR frequency not reaching zero can be the difference in the symmetry of the components of the effective anisotropy or insufficient sensitivity of the microstrip sensor at frequencies close to zero.

Taking into account the above factors, we modernized the FMR setup as follows.

(i) The electromagnet rotator was equipped with an optical laser device for orienting the external magnetic field with an accuracy of several arc minutes with respect to the normal  $\mathbf{n}$  to the film surface.

(ii) The 6-mm-long microstrip used as a measuring cell was replaced with a copper meander grown by photolithography on a polycore substrate (for operation in the range 0.005–1 GHz). The meander dimensions were as follows: the width and thickness of a strip were 0.1 and 0.05 mm, respectively, and the distance between the strips was 0.1 mm. The total strip length in the meander was 180 mm. For the range 1–10 GHz, the distance between strips was chosen to be 2 mm. This

modernization significantly improved the sensitivity of the measuring cell.

The frequency–field dependence of FMR in the sample under study, measured using the modernized radio spectrometer, is shown in Fig. 2 (curve 1c). We can see that the FMR frequency almost vanishes in the saturation field, in full agreement with theory.

### 3. Theory and Calculations

Let us study the factors determining the shape of the experimental frequency–field dependence of FMR shown in Fig. 2. To this end, we calculate the theoretical curve with allowance for the magnetic properties, domain structure, and shape of the sample under study.

(i) We now consider an infinite plate of the cubic YIG single crystal with a negative anisotropy constant  $K$ . The [111] easy magnetization axis coincides with the normal to the plate. The external magnetic field is also perpendicular to the film plane. Under these conditions, saturation in such a sample takes place in the field  $H_s = 4\pi M - (4/3)|H_A|$ , where  $H_A = K/M$ . At  $H > H_s$ , the sample is saturated and the FMR frequency can be determined immediately from the Smith–Suhl equations

$$\dot{\theta} = -\frac{\gamma}{M \sin \theta} \frac{\partial U}{\partial \varphi}, \quad \dot{\varphi} = \frac{\gamma}{M \sin \theta} \frac{\partial U}{\partial \theta}, \quad (1)$$

where  $\theta$  and  $\varphi$  are the polar and azimuthal angles of the magnetization vector, respectively. The energy density for such a structure is given by

$$U = U_H + U_M + U_A = -MH \cos \theta + 2\pi M^2 \cos^2 \theta - |K| \left( \frac{\sin^4 \theta}{4} + \frac{\cos^4 \theta}{3} + \frac{\sqrt{2}}{3} \sin^3 \theta \cos \theta \cos 3\varphi \right), \quad (2)$$

where  $U_H$ ,  $U_M$ , and  $U_A$  are the energy densities of the magnetization  $M$  in the external field and of the demagnetizing and anisotropy fields of the plate, respectively [13]. Substituting expression (2) into the second equation of set (1) and setting  $\theta = 0$ , we immediately derive the FMR frequency

$$\omega = \dot{\varphi} = \gamma \left( H - 4\pi M + \frac{4}{3}|H_A| \right). \quad (3)$$

The fact that  $\theta$  is positive means that the absence of domains is possible if  $H > H_s$ .

(ii) Let us consider the case where the external field  $\mathbf{H}$  is directed along the normal to the film plane and is weaker than the saturation field,  $H < H_s$ . We assume that the sample contains two domain groups forming a periodic stripe DS oriented along the  $Y$  axis, as shown in Fig. 3 (the dashed lines indicate the projections of the three other triad axes onto the film plane).

Following [12, 13], we write the Lagrangian function for such a structure. With allowance for the energy

of domain wall oscillations, the Lagrangian takes on the form

$$L = T - U - \delta U, \quad (4)$$

where

$$T = 4\pi M^2 \left[ \frac{\beta \dot{v}^2}{2} - \frac{1}{\omega_0} (v \cos \theta_1 \dot{\phi}_1 + (1-v) \cos \theta_2 \dot{\phi}_2) \right] \quad (5)$$

is the kinetic energy density and

$$\begin{aligned} U = & 4\pi M^2 [-(v \cos \theta_1 + (1-v) \cos \theta_2)] \tilde{H} \\ & + \frac{1}{2} (v \cos \theta_1 + (1-v) \cos \theta_2)^2 \\ & + q \frac{v(1-v)}{2} (\sin \theta_1 \cos \phi_1 - \sin \theta_2 \cos \phi_2)^2 \\ & - d \left[ v \left( \frac{\sin^4 \theta_1}{4} + \frac{\cos^4 \theta_1}{3} + \frac{\sqrt{2}}{3} \sin^3 \theta_1 \cos \theta_1 \cos 3\phi_1 \right) \right. \\ & \left. + (1-v) \left( \frac{\sin^4 \theta_2}{4} + \frac{\cos^4 \theta_2}{3} + \frac{\sqrt{2}}{3} \sin^3 \theta_2 \cos \theta_2 \cos 3\phi_2 \right) \right] \end{aligned} \quad (6)$$

is the potential energy density, consisting of the energy densities of the magnetization  $M$  in the external field and of the demagnetizing and anisotropy fields of the plate, as well as the energy density of domain walls (the third term). Subscripts 1 and 2 indicate two domain groups,  $\theta_i$  and  $\phi_i$  are the polar and azimuthal angles of the magnetization vector in each domain, vis the relative domain size,  $\omega_0 = 4\pi M \gamma$ , and  $\beta = m_r b / 4\pi M^2$  ( $m_r$  is the domain wall mass and  $b$  is the average thickness of a domain). Here, we introduced the dimensionless anisotropy constant  $d = |H_A| / 4\pi M$  and the dimensionless external field  $\tilde{H} = H / 4\pi M$ . The parameter  $q$  (depending on the film thickness) defines the contribution from the domain demagnetizing field to the total energy and should be determined experimentally (for an indefinitely thin domain, this parameter is equal to zero, which means that the stripe structure half-period is much larger than the film thickness). The energy density of the ac field is given by

$$\begin{aligned} \delta U = & 4\pi M^2 \tilde{h} [v (\sin \theta_h \sin \theta_1 \cos(\phi_1 - \phi_h) \\ & + \cos \theta_h \cos \theta_1)] + (1-v) (\sin \theta_h \sin \theta_2 \cos(\phi_2 - \phi_h) \\ & + \cos \theta_h \cos \theta_2), \end{aligned} \quad (7)$$

where  $\tilde{h} = h / 4\pi M$ . With no perturbation  $\delta U$ , the equilibrium orientation of the magnetization vectors can be determined from the equilibrium conditions

$$U_{\theta_1} = U_{\theta_2} = U_{\phi_1} = U_{\phi_2} = U_v = 0, \quad (8)$$

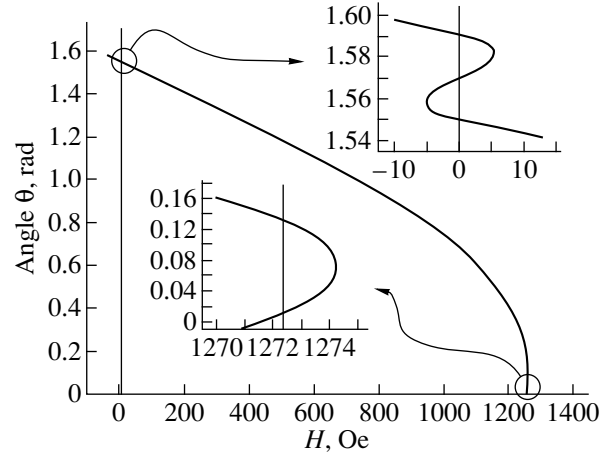


**Fig. 4.** Dependence of the polar angle  $\theta$  on the field  $H$ . There are positive-slope portions in the curves near zero field and the magnetization saturation field, which cause the features in the magnetization curve and peaks in the magnetic susceptibility curve.

from which, by differentiating Eq. (6), we immediately obtain

$$v_0 = \frac{1}{2}, \quad \phi_{10} = -\phi_{20} = \frac{2\pi}{3}, \quad \theta_{10} = \theta_{20} = \theta_0 \quad (9)$$

(see Fig. 3 for the angle  $\phi$  in domains). The equilibrium angle  $\theta_0$  is related to the external field as

$$\begin{aligned} \tilde{H} = & \cos \theta_0 + d \left[ \cos \theta_0 \left( 1 - \frac{7}{3} \cos^2 \theta_0 \right) \right. \\ & \left. + \sqrt{2} \sin \theta_0 \left( 1 - \frac{4}{3} \sin^2 \theta_0 \right) \right]. \end{aligned} \quad (10)$$

The corresponding dependence is shown in Fig. 4. We can see that the equilibrium angle of the deviation of the vectors  $\mathbf{M}_1$  and  $\mathbf{M}_2$  from the film plane is greater than one degree in a zero field. We one can also see that the sample transfers to the saturation state in a jump, since the derivative of  $\theta_0(H)$  changes sign in the region of  $H \approx H_s$ . This jump is approximately  $3^\circ$ . These features in the  $\theta_0(H)$  dependence arise exclusively as a result of cubic magnetic anisotropy in the sample and are absent in the case  $H_A = 0$ .

Writing the Lagrange equations

$$\begin{aligned} \frac{d}{dt} \left( \frac{\partial L}{\partial (\cos \dot{\theta}_i)} \right) &= \frac{\partial L}{\partial (\cos \theta_i)}, \quad \frac{d}{dt} \left( \frac{\partial L}{\partial \dot{\phi}_i} \right) = \frac{\partial L}{\partial \phi_i}, \\ \frac{d}{dt} \left( \frac{\partial L}{\partial \dot{v}} \right) &= \frac{\partial L}{\partial v} \end{aligned} \quad (11)$$

for this system and expanding the derivatives near the equilibrium values (assuming the domain wall mass to be infinite, since the magnetization is changed due to

rotation processes), we solve Eqs. (11) and find the frequency–field dependences of FMR:

$$y_{1,2} = \frac{1}{2}(c_1 \pm \sqrt{c_1^2 - 4c_2}), \quad (12)$$

where  $y_1$  and  $y_2$  are expressed in terms of the FMR frequency and the equilibrium angle as

$$y_{1,2} = \left( \frac{\sin \theta_0 \omega_{1,2}}{2 \omega_0} \right)^2. \quad (13)$$

The coefficients  $c_1$  and  $c_2$  are given by

$$c_1 = u_{\theta+} u_{\varphi+} + u_{\theta-} u_{\varphi-}, \quad c_2 = u_{\theta+} u_{\varphi-} (u_{\theta-} u_{\varphi+} - 4u_{\theta\varphi}^2),$$

where

$$u_{\varphi\pm} = u_{\varphi\varphi} \pm u_{\varphi_1\varphi_2}, \quad u_{\theta\pm} = u_{\theta\theta} \pm u_{\theta_1\theta_2},$$

$$u_{\theta\theta} = \frac{1}{2} \left( \cos \theta_0 \tilde{H} + \frac{3}{2} \sin^2 \theta_0 - 1 + \frac{1}{8} q \sin^2 \theta_0 - d \left( 7 \sin^2 \theta_0 \cos^2 \theta_0 - \sin^4 \theta_0 - \frac{4}{3} \cos^4 \theta_0 + 2\sqrt{2} \sin \theta_0 \cos \theta_0 \left( 1 - \frac{8}{3} \sin^2 \theta_0 \right) \right) \right), \quad (14)$$

$$u_{\varphi\varphi} = \frac{3}{4} \sin \theta_0 \left( \frac{q}{4} + \sqrt{2} d \sin 2\theta_0 \right),$$

$$u_{\theta_1\theta_2} = \frac{1}{4} \left( \sin^2 \theta_0 - \frac{1}{4} q \cos^2 \theta_0 \right), \quad u_{\varphi_1\varphi_2} = \frac{3}{16} q \sin^2 \theta_0.$$

By substituting the previously determined constants ( $\gamma = 1.76 \times 10^7 \text{ Oe}^{-1} \text{ s}^{-1}$ ,  $H_A = 45 \text{ Oe}$ ,  $4\pi M = 1350 \text{ Oe}$ ) and setting  $q = 0.01$ , we can derive the frequency–field dependences shown for transverse oscillations in Fig. 2 (solid lines).

#### 4. DISCUSSION

Let us compare these results and the data obtained in other studies of YIG [16] and substituted YIG [7] films where the autodyne technique was used to study the HFMS and FMR, as in this work.

We recall that this technique makes it possible to observe variations in the HF energy absorption by a sample in the drive oscillatory circuit of an HF-power signal generator as the sample is exposed to a mutually perpendicular or parallel external dc magnetic field  $\mathbf{H}$  and HF field  $\mathbf{h}$ . The frequency  $\Omega$  of the field  $\mathbf{h}$  was set between 5 and 25 MHz [16] or was 5 MHz [7]. In both cases, the sensitive element of the measuring circuit, whether it be a Helmholtz coil or a planar multiturn coil, is the inductance in the oscillatory circuit, whose  $Q$  factor varies under the influence of the sample. These variations give rise to a change in the amplitude and to a frequency shift of HF oscillations of the signal generator. It makes no difference whether the signal propor-

tional to the amplitude or the frequency shift is measured. It is of no importance what processes cause a change in the magnetic state of the sample; this change will be measured only as a result of an increase in the HF power absorption (magnetic loss in the sample). Hence, identification of the processes initiated in the sample by the field  $\mathbf{H}$  calls for not only HFMS measurements but also additional studies (microscopic observation of the DS, construction of the magnetization curve, FMR parameter measurements, etc.).

If the condition  $\Omega = \omega_0 = \gamma H_{\text{eff}}$  is satisfied in the study of a YIG-type film using the scheme described above, these devices will measure a jump in the HF susceptibility; however, the jump will be caused in this case by resonant absorption of the HF power in the sample as a result of FMR, because FMR is the selective absorption (by the YIG film in this case) of the electromagnetic field energy at the frequency equal to the frequency  $\omega_0$  of precession of magnetic moments of the electronic system in the internal effective magnetic field  $H_{\text{eff}}$  [13].

In [16], the HFMS was studied in fields  $H < 100 \text{ Oe}$  in the frequency range  $\omega = 5\text{--}25 \text{ MHz}$ , which is much lower than the precession frequency  $\omega_0$  for a thick (5–7  $\mu\text{m}$ ) YIG film in such a field at any relative orientation of the vectors  $\mathbf{H}$  and  $\mathbf{h}$  and the [111] axis. For this reason, that experiment was free of side FMR effects (in terms of the objectives pursued in [16]). This circumstance allowed the authors of [16] to observe the anomalous HFMS caused only by the critical DS rearrangement in the YIG film under study. It was shown that the transition of the film from the multidomain to the single-domain (saturated) state at the point  $H \approx H_s$  is not in itself a critical process in the sense that it is not accompanied by an HFMS anomaly.

The experimentally observed resonant absorption of the HF power (5–20 MHz) at the point  $H \approx 1300 \text{ Oe}$  (Fig. 1) corresponds to the frequency range of uniform magnetization precession for the sample under study, as follows from Fig. 2; therefore, this absorption must be considered in connection with FMR.

As already noted, the above-mentioned HFMS anomaly was interpreted in [7] as a magnetic susceptibility jump due to the OPT-2. In this case, an important role in the arguments in favor of this version was assigned in [7] to the shape of the frequency–field dependence of the FMR, which corresponds to experimental curve  $Ia$  in Fig. 2 in this paper. Special attention was paid to distinct minima in weak fields and in a field of the order of 1300 Oe, i.e., at the starting (the first OPT) and ending point (the second OPT) of reorientation, and it was postulated that the observed spectrum corresponds to soft quasi-ferromagnetic modes, since they always have a minimum frequency at OPT-2 points. The energy gap in the region  $H \approx 1300 \text{ Oe}$  ( $\nu_0 \approx 200 \text{ MHz}$ ) is also interpreted in [7] in favor of the OPT version by analogy with rare-earth orthoferrites, in which such a gap is observed at the phase transition



point as “a result of the dynamic interaction of various oscillatory systems of a magnet.” Moreover, the results calculated in [7] agree with the experimental value  $\nu_0 \approx 200$  MHz.

Our counterarguments are based on the above results of the experimental and theoretical studies performed for an identical garnet ferrite film and are as follows.

(i) A number of factors were determined that possibly control the HFMS jumps observed in the garnet ferrite film under study regardless of the phase transition.

One of these factors is irreversible rotation [18] of the spontaneous magnetization vector  $\mathbf{M}$  in stripe domains in the region  $H \approx 1300$  Oe. As follows from the dependence of the polar angle  $\theta$  on the field  $\mathbf{H} \parallel [111]$  (Fig. 4), the gradual rotation of the vector  $\mathbf{M}$  toward the field  $\mathbf{H} \parallel [111]$  stops at the point  $H = H_s$ . As the field is further strengthened, the vector  $\mathbf{M}$  abruptly transfers to the position  $\mathbf{M} \parallel [111]$ . In [16], it was shown that such an abrupt DS rearrangement is always accompanied by an HFMS anomaly.

Another factor is FMR, which occurs, in particular, in an external field  $\mathbf{H} \parallel [111]$  for  $\mathbf{h} \perp \mathbf{H}$  at the point  $\omega = 5$  MHz and  $H \approx 1300$  Oe corresponding to the coordinates of the second HFMS jump for the sample under study (Figs. 1, 2). In this context, it should be noted that the autodyne technique dealing with electromagnetic oscillations with a frequency of 5 MHz is incorrectly interpreted in [7] to be a method of static magnetic susceptibility, whereas it is conventionally considered a method of HF susceptibility [16, 19]. Since such a purely dynamic effect as FMR is observed at this frequency, this cannot be static. However, even an anomaly in the static magnetic susceptibility is not an unambiguous attribute of the OPT, which is indicated, e.g., by the shape of the magnetization curve of magnetically uniaxial garnet ferrite films in the vicinity of the bubble domain collapse field, where the OPT is absent a priori [19].

The HFMS anomaly at the point  $\mathbf{H} \parallel [111] = 0$  also results from irreversible processes of magnetization rotation [18], which, in turn, is caused by cubic anisotropy.

(ii) It was shown that the critical spin dynamics, i.e., a characteristic change in the spin relaxation rate at the boundary of the second-order phase transition, does not manifest itself near the point  $H \approx H_s$  (see Subsection 2.2).

(iii) It was shown that the gap in the FMR spectrum of the sample is caused by incorrect measurement. In [7], measurements were carried out without precision orientation of the external field with respect to the [111] axis; a microstrip sensor was used whose sensitivity is insufficient for this film at frequencies below 200 MHz. A more sensitive sensor and an optical device for precise orientation of an electromagnet by a laser beam allowed us (for the same setup and an identical sample) to apply the external field accurately along the [111]

axis of the sample and to measure the actual FMR spectrum (containing no gap) at frequencies 5–200 MHz (Fig. 2, curve 1c). According to [7], the second OPT-2 occurs when the angle  $\theta$  between the vector  $\mathbf{H}$  and the [111] axis is zero: “at  $\theta \neq 0$ , the transition disappears.” As follows from Fig. 2, the gap in the FMR spectrum simply indicates the misorientation ( $\theta \neq 0$ ) at which (as argued in [7]) the OPT-2 does not take place. In this case, there is no reason to interpret the minimum at  $H \approx 1300$  Oe in the FMR spectrum as “softening ... of the soft mode at the end point of reorientation.”

(iv) It was shown that the existence of a minimum at  $H \approx 1300$  Oe in the FMR spectrum follows from the FMR theory as a result of the vanishing of the effective magnetic field, around whose direction the vector  $\mathbf{M}$  precesses (Section 4, Fig. 2). The existence of the minimum at  $H = 0$  is also substantiated by the FMR theory for a cubic ferromagnet with a nonzero cubic magnetic anisotropy energy (Fig. 2). The sample under study is similar to such a ferromagnet under the conditions of this experiment. The calculation carried out in [7] disregards the cubic magnetic anisotropy and the actual contribution from the demagnetizing fields of domains in such a thin film and disagrees with the experiment, which was incorrectly interpreted in [7] in favor of the occurrence of the OPT (namely, as the result of “softening ... of the soft mode at the start and end points of the reorientation” [7]).

(v) The first OPT-2 observed in the sample under study is interpreted in [7] as the transition from the state where the magnetization in domains lies strictly in the film plane (i.e.,  $\mathbf{M} \perp [111]$ ) at  $H = 0$  to the state where the magnetization makes an angle with the film plane at  $H \neq 0$ . In such a case, the initial phase  $\mathbf{M} \perp [111]$  has no domain of existence in the magnetic phase diagram for the field  $\mathbf{H} \parallel [111]$ , which should induce the OPT. This is impossible from the viewpoint of the Landau theory of phase transitions. Furthermore, the calculation we carried out with allowance for the experimentally measured cubic anisotropy constant shows that, even in the field  $H = 0$ , the magnetization  $\mathbf{M}$  in domains does not lie in the film plane and forms an angle  $\alpha \approx 1^\circ$  with it even in such a thin film (see the calculation performed in Section 4). In other words, the OPT-2 is absent at the point  $H = 0$  by definition.

(vi) The second OPT-2 is defined in [7] as the end of the transition from the state where the vector  $\mathbf{M}$  makes an angle with the film plane (at  $H < H_s$ ) to the state where  $\mathbf{M} \parallel \mathbf{H} \parallel [111]$  at  $H \approx H_s$ . Thus, it is assumed that the sample contains two magnetic phases, with  $\mathbf{M} \perp [111]$  and  $\mathbf{M} \parallel [111]$ , between which an induced orientational transition via a third phase takes place. We recall that, according to the phenomenological Landau theory, the phase transition is a transition between the magnetic phases possible in this crystal that correspond to the minimum of the thermodynamic potential [8, 9]. The question concerning the magnetic phases that can exist in cubic ferromagnets (among which is included

garnet ferrite with a paramagnetic rare-earth sublattice) was studied theoretically and experimentally in [20]. The results are as follows.

(1) Only three high-symmetry magnetic phases  $\mathbf{M} \parallel [100]$ ,  $\mathbf{M} \parallel [110]$ , and  $\mathbf{M} \parallel [111]$  can exist in this system; there are no equilibrium canted phases, i.e., states in which the magnetization direction does not coincide with these axes [8, 9].

(2) In an external magnetic field  $\mathbf{H} \parallel [111]$ , the transition to the phase  $\mathbf{M} \parallel [111]$  is possible only from the phase  $\mathbf{M} \parallel [100]$  or  $\mathbf{M} \parallel [110]$ ; both transitions are first-order OPTs. These conclusions were experimentally verified for rare-earth-iron garnets in a magnetic field by measuring the magnetization, susceptibility, and nuclear magnetic resonance [20].

Thus, the statement made by the authors of [7] about the occurrence of an OPT-2 in a thin garnet ferrite film seems to be theoretically and experimentally unfounded.

Some interesting results obtained in this study were not properly analyzed, because they are beyond the scope of this work. In particular, the experimental observation of magnetic-resonance modes corresponding to straight lines 3 and 4 in Fig. 2 should be the subject of a separate study. We can only conjecture that these modes are spin-wave resonances excited along the film surface by the inhomogeneous HF field of the microstrip meander.

#### REFERENCES

1. E. I. Nikolaev, A. I. Linnik, and V. N. Sayapin, Pis'ma Zh. Tekh. Fiz. **17** (17), 85 (1991) [Sov. Tech. Phys. Lett. **17**, 639 (1991)].
2. E. I. Nikolaev, A. I. Linnik, and V. N. Sayapin, Mikroelektronika **21** (6), 86 (1992).
3. M. Inoue, K. Arai, T. Fujii, and M. Abe, J. Appl. Phys. **83** (11), 6768 (1998).
4. I. L. Lyubchanskii, N. N. Dodoenkova, M. I. Lyubchanskii, E. A. Shapovalov, Th. Rasing, and A. Lakhtakia, Proc. SPIE **4806**, 302 (2002).
5. A. M. Grishin, V. S. Dellalov, V. F. Shkar, E. I. Nikolaev, and A. I. Linnik, Phys. Lett. A **140** (3), 133 (1989).
6. A. M. Grishin, V. S. Dellalov, E. I. Nikolaev, and V. F. Shkar', Zh. Éksp. Teor. Fiz. **104** (4), 3450 (1993) [JETP **77**, 636 (1993)].
7. V. D. Buchel'nikov, N. K. Dan'shin, A. I. Linnik, L. T. Tsymbal, and V. G. Shavrov, Zh. Éksp. Teor. Fiz. **122** (1), 122 (2002) [JETP **95**, 106 (2002)].
8. K. P. Belov, A. K. Zvezdin, A. M. Kadomtseva, and R. Z. Levitin, *Oriental Transitions in Rare-Earth Magnets* (Nauka, Moscow, 1979).
9. A. K. Zvezdin, V. M. Matveev, F. F. Mukhin, and F. I. Popov, *Rare-Earth Ions in Magnetically Ordered Crystals* (Nauka, Moscow, 1985).
10. T. N. Tarasenko, Candidate's Dissertation (Physicotechnical Inst., Donetsk, 1986).
11. E. I. Nikolaev and I. A. Krasin, Kristallografiya **33** (2), 478 (1988) [Sov. Phys. Crystallogr. **33**, 282 (1988)].
12. K. B. Vlasov and L. G. Onoprienko, Fiz. Met. Metall. **15** (1), 45 (1963).
13. A. G. Gurevich and G. A. Melkov, *Magnetic Oscillations and Waves* (Nauka, Moscow, 1994).
14. I. E. Dikshtein, F. V. Lisovskii, E. G. Mansvetova, and E. S. Chizhik, Zh. Éksp. Teor. Fiz. **90** (2), 614 (1986) [Sov. Phys. JETP **63**, 357 (1986)].
15. King-Ye Tang, J. Appl. Phys. **61** (8), 4259 (1987).
16. B. A. Belyaev, S. N. Kulinich, and V. V. Tyurnev, Preprint No. 556F, IF SO AN SSSR (Inst. of Physics, Siberian Division, USSR Academy of Sciences, Krasnoyarsk, 1989).
17. V. N. Berzhanskii and V. I. Ivanov, Preprint No. 405F, IF SO AN SSSR (Inst. of Physics, Siberian Division, USSR Academy of Sciences, Krasnoyarsk, 1986).
18. G. S. Krinchik, *Physics of Magnetic Phenomena* (Mosk. Gos. Univ., Moscow, 1985).
19. *Bubble Domains-Based Elements and Devices: Reference Book*, Ed. by N. N. Evtikhiev and B. N. Naumov (Radio i Svyaz', Moscow, 1987).
20. V. G. Bar'yakhtar, V. A. Borodin, and V. D. Doroshev, Zh. Éksp. Teor. Fiz. **74**, 600 (1978) [Sov. Phys. JETP **47**, 315 (1978)].

*Translated by A. Kazantsev*



## MAGNETISM AND FERROELECTRICITY

# Influence of a Magnetic Two-Phase State on the Magnetocaloric Effect in the $\text{La}_{1-x}\text{Sr}_x\text{MnO}_3$ Manganites

R. V. Demin and L. I. Koroleva

Lomonosov Moscow State University, Vorob'evy gory, Moscow, 119899 Russia

e-mail: koroleva@ofef343.phys.msu.su

Received June 3, 2003; in final form, October 31, 2003

**Abstract**—The magnetocaloric effect  $\Delta T_{\text{ex}}$  and the magnetization in  $\text{La}_{1-x}\text{Sr}_x\text{MnO}_3$  single crystals ( $x = 0.1, 0.125, 0.175, 0.3$ ) have been experimentally studied. The magnetic entropy and the magnetocaloric effect  $\Delta T_{\text{th}}$  were computed from magnetization curves. All the samples exhibited a maximum in the  $\Delta T_{\text{th}}(T)$  curve at  $T = T'_{\text{max}}$ . A step was observed on the  $\Delta T_{\text{ex}}(T)$  curve in the region of  $T'_{\text{max}}$ , with the value of  $\Delta T_{\text{ex}}$  on this step being substantially smaller than  $\Delta T_{\text{th}}$ . The step on the  $\Delta T_{\text{ex}}(T)$  curve was followed by a maximum, which appeared at a temperature 20–40 K above  $T'_{\text{max}}$ . This anomalous behavior of  $\Delta T_{\text{ex}}$  and  $\Delta T_{\text{th}}$  is assigned to the coexistence of two magnetic (ferro- and antiferromagnetic) phases in the crystal. The calculated value of  $\Delta T_{\text{th}}$  is determined primarily by the ferromagnetic part of the crystal and disregards the negative contribution from the antiferromagnetic part of the crystal to  $\Delta T_{\text{ex}}$ . © 2004 MAIK “Nauka/Interperiodica”.

Studies of perovskite-type manganese compounds  $R_{1-x}A_x\text{MnO}_3$  (here,  $R$  stands for rare-earth elements and  $A = \text{Ca}, \text{Sr}, \text{Ba}$ ) have been recently attracting considerable attention. The interest in these materials stems primarily from their colossal magnetoresistance (CMR), which is exhibited by some of them at room temperature. The giant volume magnetostriction found in [1] in the vicinity of the Curie point in some manganite compositions makes them promising materials for use in various magneto-mechanical devices. The above compounds also revealed a large change in magnetic entropy near the Curie point [2, 3]. For some compositions, this change is even larger than for Gd, for which the magnetocaloric effect reaches 5 K in a field of 2 T; therefore, they could be expected to feature a large magnetocaloric effect. However, there are almost no publications on direct measurement of the magnetocaloric effect in manganites.

An ever increasing number of researchers have been recently tending to believe that the CMR in manganites originates from the coexistence in them of two magnetic phases, ferro- and antiferromagnetic, caused by the strong  $s$ - $d$  exchange interaction [4, 5]. The magnetic two-phase state (MTPS) can be insulating at low doping levels, where ferromagnetic (FM) regions are embedded in an insulating antiferromagnetic (AFM) matrix, and conducting at higher doping levels, where insulating AFM regions are incorporated in a conducting ferromagnetic matrix. In the  $\text{La}_{1-x}\text{Sr}_x\text{MnO}_3$  system, the compounds with  $x = 0.1$  and 0.125 are semiconductors and the compounds with  $x = 0.175$  and 0.3 are metals [6]. Therefore, it may be conjectured that the insulating MTPS takes place in the former compounds and

the conductive MTPS takes place in the latter. The MTPS should become manifest in specific features of the magnetocaloric effect, because this effect is negative for antiferromagnets and positive for ferromagnets.

We report here on a study of the temperature dependence of the magnetocaloric effect and of the magnetization in  $\text{La}_{1-x}\text{Sr}_x\text{MnO}_3$  single crystals ( $x = 0.1, 0.125, 0.175, 0.3$ ). The single crystals were grown using the crucibleless zone melting technique. The magnetization was measured with a vibrating magnetometer. The magnetocaloric effect was studied with the use of a copper–constantan thermocouple, whose one junction was fitted tightly in the sample. The thermocouple EMF was measured with a microvoltmeter, thus providing sensitivity as high as 0.01 K.

According to classical thermodynamics, the change in the magnetic part of the entropy of a ferromagnet induced by the adiabatic application of a magnetic field can be written as

$$\Delta S_M = \int_0^H \left( \frac{dM}{dT} \right)_H dH, \quad (1)$$

where  $M$  is the magnetization. The magnetocaloric effect is calculated from the relation

$$\Delta T_{\text{th}} = \frac{C_H(T)}{T} \Delta S_M(T), \quad (2)$$

where  $C_H$  is the specific heat at constant field.

We calculated  $\Delta T_{\text{th}}$  from Eq. (2), with  $\Delta S_M$  determined with the use of Eq. (1) from magnetization measurements and with  $C_H$  taken from [6]. Numerical inte-

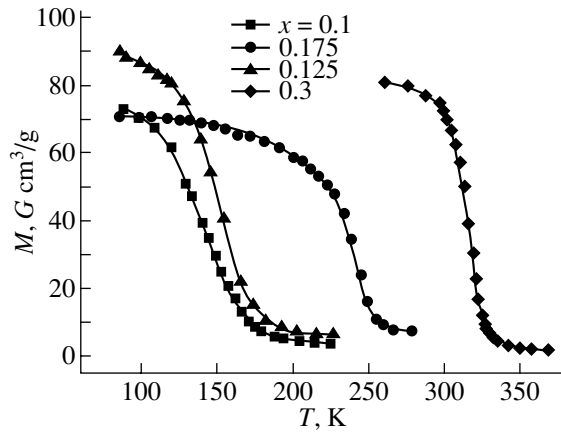


**Fig. 1.** Magnetization of  $\text{La}_{1-x}\text{Sr}_x\text{MnO}_3$  single crystals in a field of 8.2 kOe plotted vs. temperature.

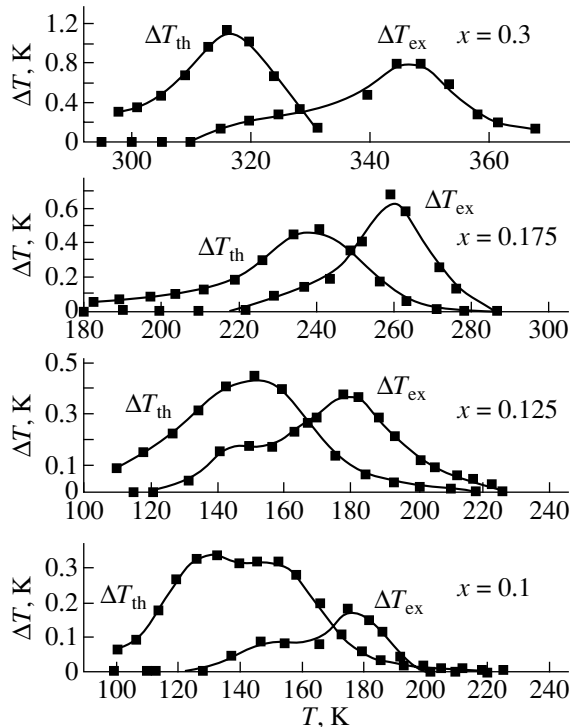


**Fig. 2.** Theoretical and experimental magnetocaloric effects obtained for  $\text{La}_{1-x}\text{Sr}_x\text{MnO}_3$  single crystals in a field of 8.2 kOe.

gration in Eq. (1) was performed following Simpson's method. The  $dM/dT$  derivative was found by interpolation through three points following numerical smoothing of the  $M(T)$  curves. Figure 1 plots the temperature dependences of the magnetization  $M$ , and Fig. 2, the  $\Delta T_{\text{ex}}(T)$  and  $\Delta T_{\text{th}}(T)$  curves obtained in a field  $H = 8.2$  kOe for all samples. As seen from Fig. 2, all the curves have maxima but differ in terms of the temperature positions: on the experimental curves, the maxima

lie 20–40 K higher than those obtained from Eq. (2). Interestingly, the  $\Delta T_{\text{ex}}(T)$  curves exhibit a step in the temperature region where the  $\Delta T_{\text{th}}(T)$  curves have a maximum. This observation, as well as the difference between the temperatures of the maxima on the  $\Delta T_{\text{ex}}(T)$  and  $\Delta T_{\text{th}}(T)$  curves, can be explained as being due to the coexistence of the FM and AFM phases in the samples. Invoking the entropy-based treatment [7], we write the condition of adiabaticity of the process assuming the magnet to consist of two subsystems, namely, a subsystem of magnetic moments with entropy  $S_M$  and a subsystem of lattice atoms with entropy  $S_C$ . The condition of adiabaticity of the process can be cast as

$$\Delta S_C + \Delta S_M = 0. \quad (3)$$

In the case where the sample is in the MTPS and the FM and AFM parts can be considered to be decoupled, one can roughly assume  $S_M$  to be the sum of two parts, the entropy of regions of ferromagnetically ordered magnetic atoms,  $S_{\text{FM}}$ , and the entropy of regions of antiferromagnetically ordered atoms  $S_{\text{AFM}}$ . In this case, the condition of adiabaticity of the process for the MTPS can be written in the form

$$\Delta S_C + \Delta S_{\text{AFM}} + \Delta S_{\text{FM}} = 0. \quad (4)$$

According to Eq. (4), the magnetocaloric effect can be considered approximately to be the sum of two parts,

$$\Delta T_{\text{ex}} = \Delta T_{\text{AFM}} + \Delta T_{\text{FM}}, \quad (5)$$

where  $\Delta T_{\text{AFM}}$  and  $\Delta T_{\text{FM}}$  are the changes in the sample temperature induced by a change in the magnetic order in the FM and AFM regions of the crystal, respectively. Obviously enough, the value of the magnetocaloric effect  $\Delta T_{\text{th}}$  calculated from Eq. (2) is determined primarily by the change in the temperature of the sample caused by the change in the magnetic order in the FM part of the sample, because the existence of the AFM part should only provide an insignificant contribution to  $\Delta S_M$  near the Curie point  $T_C$ . Therefore, if we subtract the magnetocaloric effect calculated from Eq. (2) from the experimental value, we obtain the contribution to  $\Delta T_{\text{ex}}(T)$  due to the AFM part of the crystal. The graph of the temperature dependence of this AFM contribution plotted in Fig. 3 has a shape characteristic of antiferromagnets [8, 9].

At the Néel point, the magnetocaloric effect vanishes, and above this point a positive magnetocaloric effect typical of paramagnets is observed. The above reasoning applies to compositions with  $x < 0.175$ , where the MTPS is either insulating ( $x = 0.1, 0.125$ ) or conducting ( $x = 0.175$ ) but the FM and AFM phases are comparable in volume. In the  $x = 0.3$  composition, however, the FM phase occupies nearly all of the sample volume at low temperatures when there is no magnetic field, although the contribution from the AFM part to  $\Delta T_{\text{ex}}$  is fairly large, as is evident from Fig. 3. This fact should apparently be assigned to the strong increase in

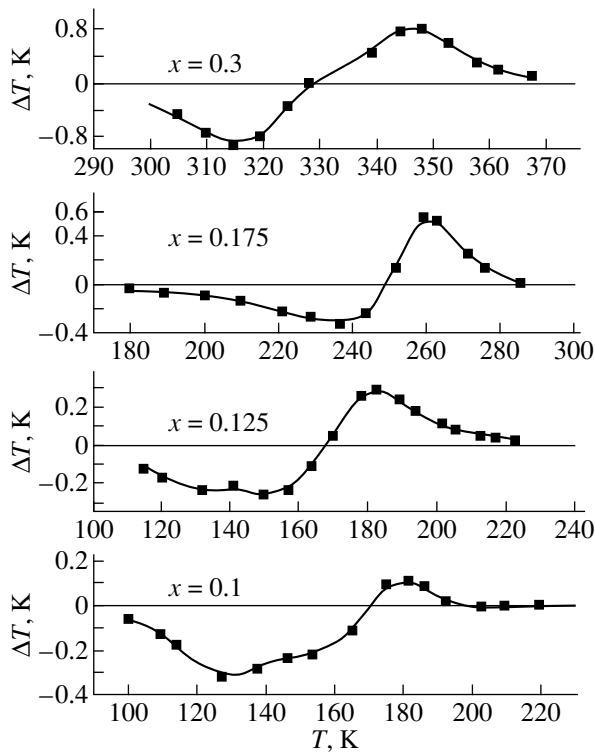


**Fig. 3.** Magnetocaloric effect induced by a change in magnetic order in antiferromagnetic regions of  $\text{La}_{1-x}\text{Sr}_x\text{MnO}_3$  single crystals.

the magnetic nonuniformity in this composition near  $T_C$ . Indeed, data obtained from neutron diffraction [10], EPR [11], absorption spectra [12], and other studies quoted in review [13] suggest the existence of a mixed FM–AFM state in compositions with  $0.17 < x < 0.3$  near  $T_C$ . Note that Eq. (4) does not take into account the entropy of the interface separating the FM and AFM regions. However, it was shown in [1] that the exchange interaction between the FM and AFM regions is substantially weaker than that within these regions; therefore, there should be practically no transition layer between them.

Thus, the existence of the MTPS can account for the anomalous behavior of the experimentally observed magnetocaloric effect. This is one more argument for the existence of the MTPS in the system under study. Earlier [1], we invoked the mixed FM–AFM phase state in  $\text{La}_{1-x}\text{Sr}_x\text{MnO}_3$  to explain the analogous behavior of the volume magnetostriction and magnetoresistance

and the displaced hysteresis loops of samples cooled in a magnetic field. Furthermore, the giant red shift  $\sim 0.4$  eV observed by us in this system and associated with the FM order implies that the energy of mobile holes decreases with increasing FM order, with the result that localization in the FM part of the crystal is preferable for the holes [14].

#### ACKNOWLEDGMENTS

The authors express their sincere gratitude to A.M. Balbashov for preparation of the samples and their characterization.

This study was supported by the Russian Foundation for Basic Research, project no. 03-02-16100.

#### REFERENCES

1. R. V. Demin, L. I. Koroleva, R. Szymczak, and H. Szymczak, *Pis'ma Zh. Éksp. Teor. Fiz.* **75**, 402 (2002) [JETP Lett. **75**, 331 (2002)].
2. Z. B. Guo, Y. W. Du, J. S. Zhu, H. Huang, W. P. Ding, and D. Feng, *Phys. Rev. Lett.* **78**, 1142 (1997).
3. X. Bohigwas, J. Tejada, E. del Barco, X. X. Zhang, and M. Sales, *Appl. Phys. Lett.* **73**, 390 (1998).
4. É. L. Nagaev, *Physics of Magnetic Semiconductors* (Nauka, Moscow, 1979).
5. É. L. Nagaev, *Usp. Fiz. Nauk* **166**, 833 (1996) [*Phys. Usp.* **39**, 781 (1996)].
6. G. L. Liu, J. S. Zhou, and J. B. Goodenough, *Phys. Rev. B* **64**, 144414 (2001).
7. K. P. Belov, *Thermomagnetic Phenomena in Rare-Earth Magnets* (Nauka, Moscow, 1990).
8. B. V. Znamenskiĭ and I. G. Fakidov, *Fiz. Met. Metall-oved.* **13**, 312 (1962).
9. R. Rawat and I. Das, *Phys. Rev. B* **64**, 52407 (2001).
10. M. Viret, H. Glattli, C. Fermon, A. M. Loen-Guevara, and A. M. Revcolevschi, *Europhys. Lett.* **42**, 301 (1998).
11. V. A. Ivashin, J. Deisenhofer, H.-A. Krug von Nidda, A. Loidl, A. A. Mukhin, A. M. Balbashov, and M. V. Eremin, *Phys. Rev. B* **61**, 6213 (2000).
12. A. Machida, Y. Moritomo, and A. Nakamura, *Phys. Rev. B* **58**, 12540 (1998).
13. E. Dagotto, T. Hotta, and A. Moreo, *Phys. Rep.* **344**, 1 (2001).
14. R. V. Demin, L. I. Koroleva, and A. M. Balbashov, *Pis'ma Zh. Éksp. Teor. Fiz.* **70**, 303 (1999) [JETP Lett. **70**, 314 (1999)].

*Translated by G. Skrebtsov*

---

## MAGNETISM AND FERROELECTRICITY

---

# Magnetic Anisotropy of Co/Cu/Co Films with Indirect Exchange Coupling

A. V. Ognev, A. S. Samardak, Yu. D. Vorob'ev, and L. A. Chebotkevich

Institute of Physics and Information Technology, Far-East State University, ul. Sukhanova 8, Vladivostok, 690600 Russia

e-mail: lchebot@lemoi.phys.dvgu.ru

Received November 4, 2003

**Abstract**—The effect of isothermal annealing on the magnetic anisotropy, bilinear and biquadratic exchange coupling energies, and domain structure of Co/Cu/Co trilayer films with  $d_{\text{Co}} = 6$  nm and  $d_{\text{Cu}} = 1.0$  and 2.1 nm prepared by magnetron sputtering has been studied. It is shown that, under isothermal annealing, the biquadratic coupling energy decreases by more than an order of magnitude in films with  $d_{\text{Cu}} = 1.0$  nm and increases in films with  $d_{\text{Cu}} = 2.1$  nm. The fourth-order magnetic anisotropy is shown to be related to the existence of biquadratic exchange energy. © 2004 MAIK “Nauka/Interperiodica”.

### 1. INTRODUCTION

Interlayer exchange coupling between ferromagnetic (FM) layers separated by nonmagnetic spacers plays a key role in many properties observed in multilayer films. For instance, the variation in the pattern of the magnetoresistance field dependence (or the magnetization curves) under rotation of the film about the film plane normal, considered together with the energy of indirect exchange coupling between the ferromagnetic layers, provides information about the order of the magnetic anisotropy of multilayer films [1]. Any multilayer structure in which the easy magnetization axes of layers are noncollinear and the magnetization direction changes from one layer to another has a high order of anisotropy. Two exchange-coupled films with identical thickness, magnetization, and anisotropy, whose easy magnetization axes are mutually perpendicular, reveal biaxial anisotropy of  $K_u/2E_b$  in weak magnetic fields, where  $E_b$  is the coupling energy [2]. In strong magnetic fields, the anisotropy decreases in proportion to  $1/H$ , with the system becoming gradually isotropic. Fields  $H \rightarrow 0$  give rise to biaxial and four-axial anisotropy, which is small for high coupling energies between ferromagnetic layers and decreases as  $1/H^3$  in strong fields [3, 4].

This communication reports on a study of the behavior of the biquadratic exchange coupling, magnetic anisotropy, and domain structure under isothermal annealing and the effect of biquadratic coupling energy on the magnetic anisotropy.

### 2. EXPERIMENTAL TECHNIQUES

Co/Cu/Co samples were prepared by dc magnetron sputtering in an Ar atmosphere ( $P_{\text{Ar}} = 5 \times 10^{-3}$  Torr). The films were applied to (111)Si single crystals at room temperature. The layer thickness was monitored

in relation to the deposition time. The rate of Co and Cu deposition was 0.1 and 0.08 nm/s, respectively. We studied Co/Cu/Co films with a Co layer thickness  $d_{\text{Co}} = 6$  nm and a copper spacer thickness  $d_{\text{Cu}} = 1.0$  and 2.1 nm. The film structure was probed by electron microscopy and electron diffraction techniques. The magnetoresistance was measured by the four-probe compensation method in magnetic fields varied from 0 to 10 kOe, and the magnetic hysteresis loops were recorded with a computerized vibrating-sample magnetometer. The isothermal annealing of the films was performed at  $T_{\text{ann}} = 250^\circ\text{C}$  in a vacuum of  $10^{-5}$  Torr.

### 3. RESULTS AND DISCUSSION

Electron microscope images showed all the films studied to be polycrystalline with a grain size of  $\sim 5$  nm. The magnetic anisotropy of the trilayers was extracted from magnetization curves obtained in one cycle of film rotation about the surface normal in a step of  $10^\circ$ . Figure 1 shows polar diagrams  $M/M_s = f(H, \varphi)$  of a trilayer film with  $d_{\text{Cu}} = 1.0$  nm (the first antiferromagnetic (AFM) maximum) obtained for several fixed values of the magnetic field. We readily see that, in magnetic fields  $H = 100$  and 250 Oe, the magnetization in the as-deposited film reaches the maximum value in all directions. In fields  $H = 20$  and 60 Oe, the  $M(H, \varphi)$  curves exhibit four maxima, which indicates the presence of biaxial anisotropy in the film. The pattern of the polar diagrams obtained in fields  $H = 100$  and 250 Oe does not change under isothermal annealing ( $T_{\text{ann}} = 250^\circ\text{C}$ ). By contrast, the diagrams measured in fields  $H = 20$  and 60 Oe vary substantially with annealing. A 30-min anneal reduces the two maxima in the diagram, with the polar diagram acquiring the shape of an elongated lobe. Increasing the annealing time to 230 min

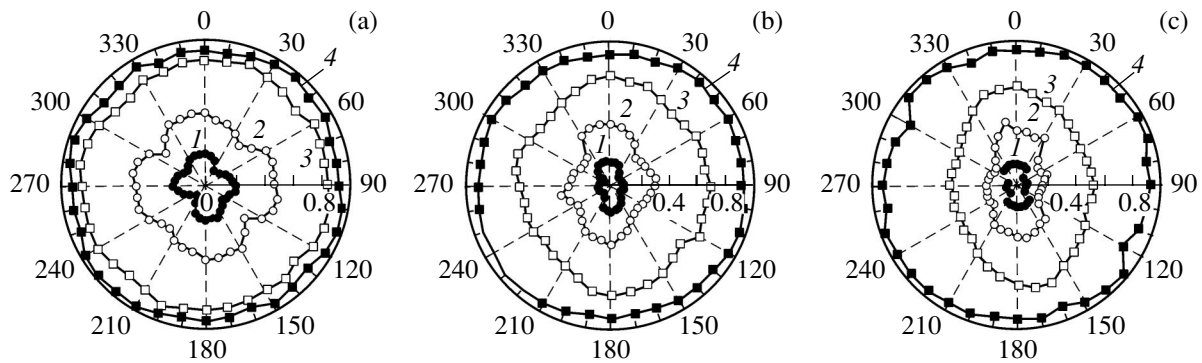


**Fig. 1.** Polar diagrams of the relative magnetization  $M/M_s$  of the Co/Cu(1 nm)/Co film for (1)  $H = 20$ , (2) 60, (3) 100, and (4) 250 Oe and various values of  $t_{\text{ann}}$ : (a) 0, (b) 30, and (c) 230 min.

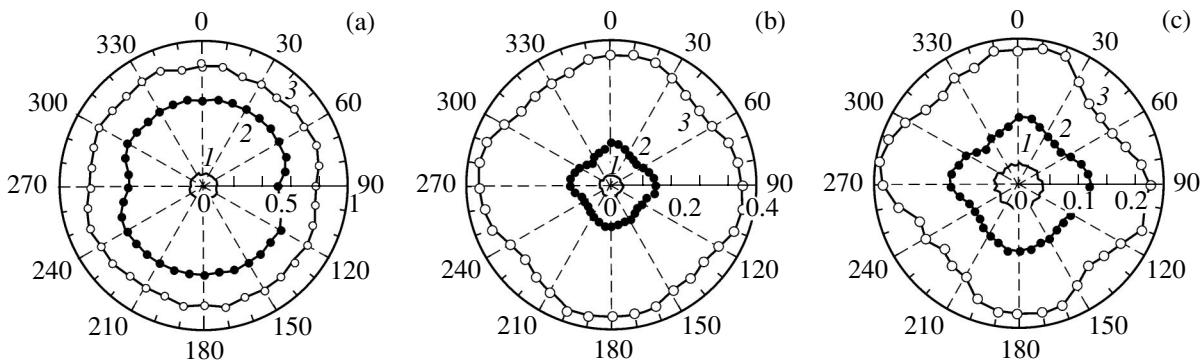


**Fig. 2.** Polar diagrams of the relative magnetization  $M/M_s$  of the Co/Cu(2.1 nm)/Co film for (1)  $H = 50$ , (2) 100, and (3) 150 Oe and various values of  $t_{\text{ann}}$ : (a) 0, (b) 30, and (c) 230 min.

makes the lobe shape more distinct, which indicates the onset of uniaxial in-plane magnetic anisotropy.

The polar diagrams of relative magnetization of the Co/(2.1 nm)Cu/Co film (the second AFM maximum), both as deposited and after annealing, are displayed in Fig. 2. In a field of 150 Oe, the polar diagram of the as-deposited film is isotropic. The diagram obtained at 100 Oe (curve 2), however, reveals a weak high-order anisotropy. The  $M/M_s = f(H, \varphi)$  curves measured in fields  $H = 100$  and 150 Oe after 30 min of isothermal annealing exhibit four clearly pronounced maxima, thus indicating the formation of in-plane fourth-order magnetic anisotropy, which becomes enhanced after an additional  $t_{\text{ann}} = 80$  min of annealing.

The parameters of the bilinear,  $J_1$ , and biquadratic,  $J_2$ , exchange coupling were found by fitting the theoretical magnetization curves to experimental data. It was revealed that the Co layers in the as-deposited films are coupled both bilinearly and biquadratically (see table). The bilinear coupling energy of the film with  $d_{\text{Cu}} = 1.0$  nm increases with increasing time of annealing, to reach saturation for  $t_{\text{ann}} = 80$  min. The biquadratic cou-

pling energy decreases gradually with increasing time of annealing, to reach  $J_2 = -0.003$  erg/cm<sup>2</sup> after 230 min of annealing.

The bilinear and biquadratic exchange coupling energies in the film with  $d_{\text{Cu}} = 2.1$  nm increased after isothermal annealing by a factor of 2.1 and 2.2, respectively (see table). The increase in the biquadratic coupling energy brought about a clearly pronounced fourth-order anisotropy.

Thus, films with biquadratically coupled Co layers are biaxial and those in which  $J_2 \rightarrow 0$  are uniaxial. Indirect exchange coupling appears to induce biaxial anisotropy in the upper Co layer during condensation (or under subsequent isothermal annealing), because the growth conditions of the bottom and top layers are different. The uniaxial anisotropy of the bottom Co layer is induced by the magnetron field. The anisotropy in the top Co layer is induced by the magnetostatic field of the bottom layer and the field of indirect exchange coupling of the bottom layer with the growing top Co layer through the Cu spacer.

## Magnetoresistance ratio and the bilinear and biquadratic coupling energies in isothermally annealed Co/Cu/Co films

$d_{\text{Cu}}$ , nm	$t_{\text{ann}}$ , min	$-J_1$ , erg/cm <sup>2</sup>	$-J_2$ , erg/cm <sup>2</sup>	$H_s$ , Oe	$K_u^{(2)}$ , 10 <sup>3</sup> erg/cm <sup>3</sup>	$K_u^{(1)}$ , 10 <sup>3</sup> erg/cm <sup>3</sup>	$\Delta\rho/\rho$ , %
1.0	0	0.05	0.017	550	60	10	1.4
	30	0.14	0.005	750	30	60	3.3
	80	0.14	0.04	790	25	110	3.4
	230	0.135	0.03	760	20	105	3.3
2.1	0	0.04	0.018	450	60	30	1.2
	30	0.075	0.043	570	70	25	2.2
	80	0.082	0.042	620	80	24	2.4
	230	0.085	0.04	630	85	22	2.4

Note:  $K_u^{(1)}$  and  $K_u^{(2)}$  are magnetic anisotropy constants of second and fourth order, respectively, derived by fitting theoretical relative magnetization  $M/M_s = f(H)$  and the magnetoresistance ratio  $\Delta\rho/\rho = f(H)$  curves to experimental data.

Annealing initiates an increase in effective indirect exchange coupling between the ferromagnetic layers  $H_s = 2|J_{\text{eff}}|/M_s d_{\text{Co}}$ , where  $J_{\text{eff}} = J_1 + 2J_2$  [4] and  $M_s$  is the saturation magnetization (see table), and of the magnetoresistance in both films, but the actual relation between the bilinear and biquadratic coupling components after annealing depends on the thickness of the Cu spacer. As seen from Figs. 1 and 2, isothermal annealing of the Co/(2.1 nm)Cu/Co film results in an increase in the biquadratic exchange coupling energy and a more pronounced fourth-order anisotropy, whereas in the Co/(1.0 nm)Cu/Co film the biquadratic exchange coupling energy decreases by an order of magnitude ( $J_2 \rightarrow 0$ ) and makes the film uniaxial.

Several mechanisms of biquadratic coupling between ferromagnetic layers in multilayer films have been proposed to date. These are the model of bilinear coupling fluctuations [5], the free-spin model based on the presence of impurity atoms in the nonmagnetic

spacer or of ferromagnetic atoms at the interface [6, 7], and the magnetic dipole mechanism related to interface roughness [7]. In fine-grained polycrystalline trilayers, it is the latter two mechanisms that are apparently realized. Biquadratic indirect exchange coupling between ferromagnetic layers in a film can result in noncollinear magnetic order only under the condition  $J_2 < -|J_1|/2$  [8]. For our films with  $d_{\text{Cu}} = 1$  and 2.1 nm annealed at  $T_{\text{ann}} = 250^\circ\text{C}$ , the conditions  $J_1 - 2J_2 < 0$  and  $J_1 < 0$  are satisfied. This shows that the equilibrium state for  $H = 0$  can be identified with antiferromagnetic ordering of magnetic moments in adjacent Co layers.

The difference in the behavior of biquadratic coupling observed to occur as a result of isothermal annealing between films with  $d_{\text{Cu}} = 1$  and 2.1 nm should possibly be assigned to the impurity mechanism of biquadratic coupling. Annealing of films at  $T_{\text{ann}} = 250^\circ\text{C}$  is accompanied by a growth in the size of grains (up to 10 nm) and impurity diffusion toward sinks, which are grain boundaries in polycrystalline films. It may be conjectured that, in films with a thinner spacer, impurity atoms escape faster from the spacer at the given temperature of isothermal annealing, which results in a faster decrease in the  $J_2/J_1$  ratio in the film with  $d_{\text{Cu}} = 1$  nm. This conjecture is corroborated by the calculated diffusion coefficients  $D$ . If we accept the approximation proposed for multilayer structures [9, 10], we can derive the diffusion coefficient from the relation  $D = -(\Lambda^2/8\pi^2)d\ln(\rho_t/\rho_0)/dt$ , where  $\rho_0$  is the initial electrical resistivity,  $\rho_t$  is the electrical resistivity after isothermal annealing for a time  $t$ , and  $\Lambda = d_{\text{Co}} + d_{\text{Cu}}$ . For this purpose, we derived a relation connecting the logarithm of the relative electrical resistivity with the time of annealing (Fig. 3). The behavior of the  $\ln(\rho_t/\rho_0) = f(t)$  relation suggests that diffusion in multilayer Co/Cu films can occur at two rates, depending on the isothermal annealing time. Within region 1 in Fig. 3, the diffusion rate is  $D_1 = 7 \times 10^{-22}$  m<sup>2</sup>/s, and within region 2,  $D_2 = 0.2 \times 10^{-22}$  m<sup>2</sup>/s. The relaxation processes are characterized

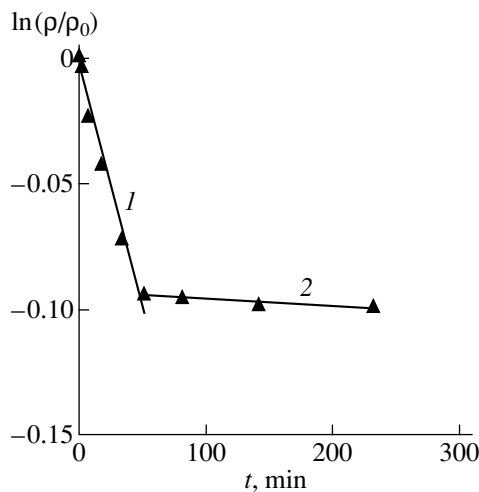
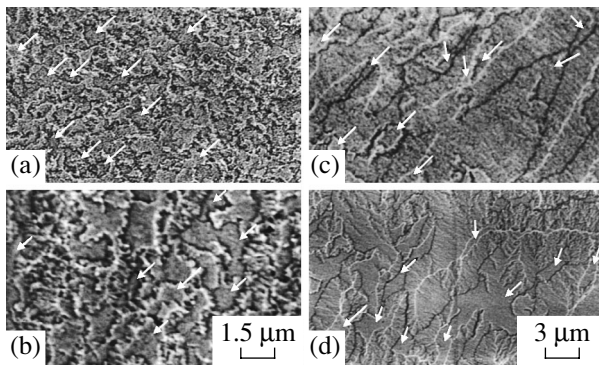


Fig. 3. Logarithm of the relative electrical resistivity vs. annealing time for a multilayer Co/Cu film.



**Fig. 4.** Domain structure of Co/Cu/Co films with (a, b)  $d_{\text{Cu}} = 1$  nm and (c, d)  $d_{\text{Cu}} = 2.1$  nm; (a, c) as-deposited, (b, d) after annealing. Arrows identify regions in which the Co layers are antiferromagnetically coupled.

by an activation energy  $Q = 0.15$  eV, a figure typical of point defect annealing and internal stress relaxation.

To be able to observe the domains, domain walls, and magnetization ripple simultaneously, the domain structure of films with  $d_{\text{Cu}} = 1$  and 2.1 nm was studied by Lorentz microscopy. As seen from images of the domain structure, the films have partially antiferromagnetic and partially ferromagnetic coupling (Fig. 4). Figure 4 reveals the presence of coupled Néel walls in the films. The Néel walls in the top and bottom Co layers are displaced with respect to one another. In the photographs, the AFM regions are identified by arrows. We readily see that the annealing-induced change in magnetic anisotropy is accompanied by rearrangement of the domain structure. The as-deposited film with  $d_{\text{Cu}} = 1$  nm (Fig. 4a), whose polar diagram exhibits biaxial anisotropy, has a complex domain structure; namely, the domain wall arrangement lacks geometric regularity, there are regions with closed domain walls, and the domains themselves are small ( $\sim 0.43$   $\mu\text{m}$ ). Such a domain structure is characteristic of films with strong indirect exchange coupling between the ferromagnetic layers. The complex domain structure persists in the annealed film, as seen from the image shown in Fig. 4b. However, the domain size increased nearly twofold (average domain dimension  $\sim 0.83$   $\mu\text{m}$ ) and the domain walls became more extended.

In the film with  $d_{\text{Cu}} = 2.1$  nm (where the polar diagram reveals high-order anisotropy), the domain structure is larger (average domain size  $\sim 3$   $\mu\text{m}$ ) and the domain walls are more extended (Fig. 4c). The overall pattern of the domain structure suggests the presence of a certain preferential magnetization orientation in the film. The film features regions with AFM and FM coupling between Co layers. After the annealing, the film exhibits a clearly pronounced biaxial anisotropy (Fig. 2b) and the domain structure changes; more spe-

cifically, the domain walls are no longer preferentially oriented and become more twisted and the average domain size decreases to 1.8  $\mu\text{m}$  (Fig. 4d).

#### 4. CONCLUSIONS

Studies of fine-grained, polycrystalline Co/Cu/Co trilayer films have shown the fourth-order magnetic anisotropy to be due to the presence of biquadratic exchange coupling between the ferromagnetic Co layers; the effect of isothermal low-temperature annealing on the energy of the bilinear and biquadratic exchange coupling between the Co layers depends on the thickness of the nonmagnetic spacer. Films with fourth-order magnetic anisotropy feature a complex domain structure with no geometric regularity in the domain wall arrangement and whose domain walls are closed and domains small.

#### ACKNOWLEDGMENTS

This study was supported by the federal research program “Studies in Topical Areas of Science and Technology for Civilian Use” of the Ministry of Industry, Science, and Technology of the Russian Federation (project no. 3-02/DVGU under state contract no. 40.012.1.1.1151) and by the Ministry of Education of the Russian Federation (project no. RD 02-1.2-50).

#### REFERENCES

1. V. V. Ustinov, M. A. Milyaev, L. N. Romashev, T. P. Krinitsina, and E. A. Kravtsov, *J. Magn. Magn. Mater.* **226–230**, 1811 (2001).
2. A. Yelon, in *Physics of Thin Films: Advances in Research and Development*, Ed. by M. H. Francombe and R. W. Hoffman (Academic, New York, 1971; Mir, Moscow, 1973), p. 392.
3. A. Yelon, *J. Appl. Phys.* **35**, 770 (1964).
4. C. H. Marrows, B. J. Hickey, M. Herrmann, S. McVitie, J. N. Chapman, M. Ormston, A. K. Petford-Long, N. P. A. Hase, and B. K. Tanner, *Phys. Rev. B* **61**, 4131 (2000).
5. J. C. Slonczewski, *Phys. Rev. Lett.* **67**, 3172 (1991).
6. J. C. Slonczewski, *J. Magn. Magn. Mater.* **150**, 13 (1995).
7. S. O. Demokritov, E. Tsymbal, P. Grunberg, W. Zinn, and I. K. Schuller, *Phys. Rev. B* **49**, 720 (1994).
8. V. V. Ustinov, N. G. Bebenin, L. N. Romashev, V. I. Minin, M. A. Milyaev, A. R. Del, and A. V. Semerikov, *Phys. Rev. B* **54** (2), 15958 (1996).
9. P. M. Levy, *J. Appl. Phys.* **67** (9), 5914 (1990).
10. A. V. Boltushkin, V. M. Fedosyuk, and O. I. Kasyutich, *Fiz. Met. Metalloved.* **75** (6), 58 (1993).

*Translated by G. Skrebtsov*

## MAGNETISM AND FERROELECTRICITY

# Mössbauer Effect Study in $\text{Fe}_{1-x}\text{V}_x\text{BO}_3$ Solid Solutions

O. A. Bayukov\*, M. M. Abd-Elmeguid\*\*, N. B. Ivanova\*\*\*, N. V. Kazak\*,  
S. G. Ovchinnikov\*, and V. V. Rudenko\*

\*Kirensky Institute of Physics, Siberian Division, Russian Academy of Sciences,  
Akademgorodok, Krasnoyarsk, 660036 Russia

\*\*Physikalisches Institut, Universität zu Köln, Köln, 50937 Germany

\*\*\*Krasnoyarsk State Technical University, Krasnoyarsk, 660074 Russia

Received September 16, 2003; in final form, November 13, 2003

**Abstract**—The Mössbauer effect in the  $\text{Fe}_{1-x}\text{V}_x\text{BO}_3$  solid solutions has been measured at 130 and 300 K. The  $\text{Fe}_{0.05}\text{V}_{0.95}\text{BO}_3$  composition was studied in the interval 4.2–300 K. The experimental data obtained are described in terms of the model of a dilute magnetic insulator in which atoms of the first coordination sphere provide a major contribution to the hyperfine field at iron nucleus sites. It was found that, at low temperatures, the field  $H_{\text{hf}}$  is generated primarily by the iron ion itself and depends only weakly on substitution. The hyperfine interaction parameters in the discrete configuration series 6Fe, 5Fe1V, 4Fe2V, 3Fe3V, and 2Fe4V were determined. The magnitude of the isomer shift suggests that iron in the crystal resides in the trivalent state. © 2004 MAIK “Nauka/Interperiodica”.

### 1. INTRODUCTION

Transition metal borates with the chemical formula  $\text{MBO}_3$  crystallize in the calcite structure [space group  $R\bar{3}c(D_{3d}^6)$ ]. Strong electronic correlations offer the possibility of observing the rich variety of magnetic structures and electronic properties in this series of compounds governed by the presence of one or another transition metal  $M^{3+} = \text{Fe}, \text{V}, \text{Cr},$  or  $\text{Ti}$ .  $\text{FeBO}_3$  has been a subject of intense interest since the time it was first prepared [1]; studies were made on its optical and magneto-optical properties [2–6], crystal structure [7, 8], magnetic properties [9–11], and NMR [12, 13] and Mössbauer [14, 15] spectra. The  $\text{FeBO}_3$  iron borate is transparent in the visible region, and its magnetic ordering temperature is above room temperature,  $T_N = 348$  K. Unfortunately, experimental information on other representatives of this class of borates is scarce. The isostructural compounds  $\text{VBO}_3$ ,  $\text{CrBO}_3$ , and  $\text{TiBO}_3$  were first synthesized in 1964 [16].  $\text{VBO}_3$  is known to be a ferromagnetic semiconductor with  $T_C = 32$  K, and  $\text{CrBO}_3$  is a low-temperature antiferromagnet with  $T_N = 15$  K and an insulator [17].  $\text{TiBO}_3$  was reported to be a weak ferromagnet ( $T_N = 25$  K) [18]. There are publications on studies of hyperfine interaction in iron borate-based solid solutions  $\text{Fe}_{1-x}M_x\text{BO}_3$ , where the ions  $M = \text{Al}, \text{Ga},$  and  $\text{Cr}$  act as substituting ions [19–21].

A coordinated investigation of the magnetic, electrical, and optical properties of  $\text{Fe}_{1-x}\text{V}_x\text{BO}_3$  solid solutions was performed earlier in [22]. This communication reports on a measurement of the Mössbauer effect in iron-containing samples of  $\text{Fe}_{1-x}\text{V}_x\text{BO}_3$ .

### 2. SAMPLES AND EXPERIMENTAL TECHNIQUES

The  $\text{Fe}_{1-x}\text{V}_x\text{BO}_3$  single crystals under study were grown by spontaneous crystallization from a melt solution [22]. The crystals were hexagonal platelets up to  $4 \times 4$  mm in size and about 0.1 mm thick. The concentration  $x$  quoted in [22] was derived from the content of components in the charge ( $x_{\text{ch}}$ ). The exact amounts of the elements were determined by EDAX ZAF quantification. The values of  $x$  thus obtained are listed in Table 1 together with the earlier  $x_{\text{ch}}$  figures.

Mössbauer measurements were performed on powdered samples of the  $\text{Fe}_{1-x}\text{V}_x\text{BO}_3$  single crystals. The isomer shift  $\delta$  was determined relative to metallic ( $\alpha$ -Fe) iron.

The experiments on the  $\text{Fe}_{1-x}\text{V}_x\text{BO}_3$  samples were carried out at 130 and 300 K with a  $\text{Co}^{57}(\text{Cr})$  source. The optimum sample thickness was calculated with due account of the iron content and the absorption factor and was found to be 5–10 mg Fe/cm<sup>2</sup>. The model spectra were least squares fitted to experimental data under the assumption that the spectral lines have Lorentzian shape. We took as an additional fitting parameter the

**Table 1.** Vanadium concentration in  $\text{Fe}_{1-x}\text{V}_x\text{BO}_3$  solid solutions

$x_{\text{ch}}$	0.25	0.5	0.6	0.75	0.95
$x$	0.02	0.13	0.18	0.3	0.95

Note:  $x_{\text{ch}}$  was derived from the content of components in the charge, and  $x$ , from energy-dispersive analysis of x-rays (EDAX ZAF quantification).



broadening of the outer sextet lines with respect to the inner lines ( $\Gamma_{16}/\Gamma_{34}$ ), which is proportional to the hyperfine field at the nucleus site. Processing of the experimental spectra revealed the presence of an impurity phase,  $\text{Fe}_3\text{BO}_6$ , in the solid solutions, which should be assigned to the crystallization temperatures of these compounds being very similar and was described earlier in [21].

The spectra of the  $\text{Fe}_{0.05}\text{V}_{0.95}\text{BO}_3$  crystal in the range of 4.2 to 300 K were measured with a  $\text{Co}^{57}(\text{Rh})$  source of an initial activity of 25 mCi (925 MBq). The measurements were performed in the transmission geometry. The source was placed inside a  $^4\text{He}$  cryostat close to the sample. The maximum source velocity was

$$V_{\max} = CU_{\text{eff}},$$

where  $U_{\text{eff}}$  is the effective amplitude of the sine signal and  $C$  is the calibration factor, equal to 0.041326 mm/s mV. The measurements were performed on polycrystalline samples containing 1 mg  $\text{Fe}/\text{cm}^2$  that were mixed thoroughly with  $\text{Al}_2\text{O}_3$ .

### 3. EXPERIMENTAL RESULTS

Figure 1 shows Mössbauer spectra of  $\text{Fe}_{1-x}\text{V}_x\text{BO}_3$  solid solutions obtained at room temperature. The  $\text{FeBO}_3$  spectrum is a well-resolved sextet (Fig. 1, *a*). The hyperfine interaction parameters are in agreement with the data from [14]. The spectral line intensities are in the ratio 3 : 2 : 1 : 1 : 2 : 3.

Because of the compositional disorder characteristic of solid solutions, impurity atoms can be considered to be distributed randomly in the matrix. Thus, all the cation states are equivalent and can be occupied by iron and vanadium atoms in random fashion. Because the exchange interactions have short-range character, we analyze experimental spectra in the nearest neighbor approximation. The central iron atom has  $n$  atoms of vanadium and  $(6 - n)$  atoms of iron in its nearest environment. The probability of finding such atomic configurations in a crystal is described by the well-known binomial distribution

$$P_6(n) = \frac{6!}{n!(6-n)!} (1-x)^n x^{6-n},$$

where  $x$  is the vanadium concentration. The local molecular field theory was applied to interpret complex Mössbauer spectra of mixed oxide systems in [23].

Following this assumption, the spectrum of the  $\text{Fe}_{0.98}\text{V}_{0.02}\text{BO}_3$  crystal (Fig. 1, *b*) can be unfolded into two sextets with occupations of 76 and 24%. The former sextet relates to the nearest iron environment consisting of six iron atoms (6Fe), and the latter sextet, to the configuration in which there is one vanadium atom among the nearest neighbors (5Fe1V). The probability distributions of hyperfine fields at the iron nucleus sites and the calculated hyperfine interaction

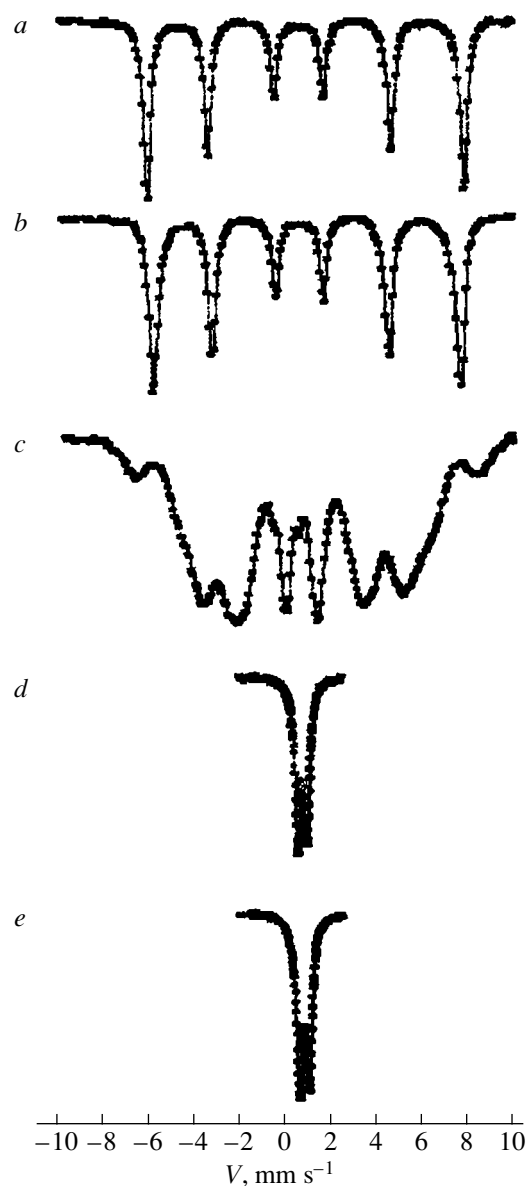


**Fig. 1.** Mössbauer spectra of (a)  $\text{FeBO}_3$ , (b)  $\text{Fe}_{0.98}\text{V}_{0.02}\text{BO}_3$ , (c)  $\text{Fe}_{0.87}\text{V}_{0.13}\text{BO}_3$ , (d)  $\text{Fe}_{0.82}\text{V}_{0.18}\text{BO}_3$ , and (e)  $\text{Fe}_{0.7}\text{V}_{0.3}\text{BO}_3$  obtained at 300 K.

parameters in the solid solutions are displayed in Fig. 2 and listed in Table 2. It is assumed that the hyperfine field in insulators is well described in the nearest neighbor approximation; therefore, the fields of the 6Fe, 5Fe1V, 4Fe2V, etc., configurations are discrete and well resolved and the 6Fe configuration in a substituted crystal has the same hyperfine field as in an unsubstituted one. In our case, while the 5Fe1V configuration ( $H_{\text{hf}} = 323$  kOe) differs noticeably from the 6Fe configuration ( $H_{\text{hf}} = 335$  kOe), the field of 335 kOe is substantially smaller than  $H_{\text{hf}} = 345$  kOe in the unsubstituted borate  $\text{FeBO}_3$ . Quite probably, the hyperfine field at

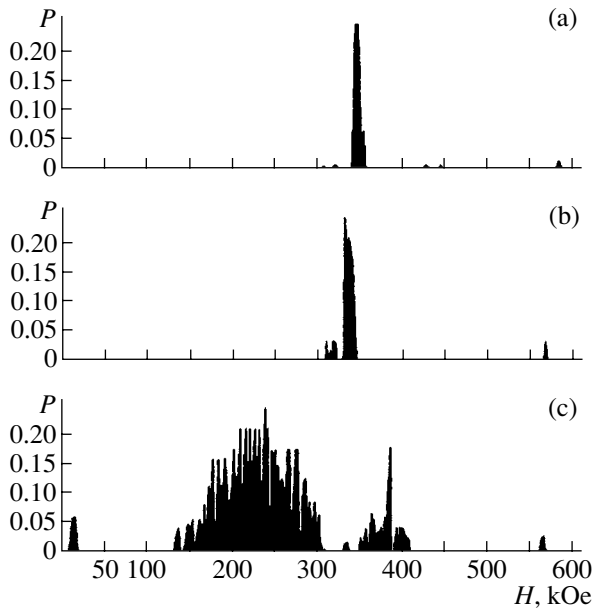


**Fig. 2.** Hyperfine field probability distribution for iron nuclei at 300 K obtained for (a)  $\text{FeBO}_3$ , (b)  $\text{Fe}_{0.98}\text{V}_{0.02}\text{BO}_3$ , and (c)  $\text{Fe}_{0.87}\text{V}_{0.13}\text{BO}_3$ .

iron nucleus sites in  $\text{FeBO}_3$  is contributed to markedly by next-to-nearest neighbors.

The spectrum of the  $\text{Fe}_{0.87}\text{V}_{0.13}\text{BO}_3$  has a complex shape (Fig. 1, *c*). The distribution of the hyperfine field probabilities allows us to isolate three regions (Fig. 2*c*). The region of 350–400 kOe corresponds to fields higher than the field in  $\text{FeBO}_3$  but lower than that in  $\text{Fe}_3\text{BO}_6$ ,  $H_{\text{hf}} = 521$  kOe [24]. This region can be assigned to the vanadium-substituted  $\text{Fe}_3\text{BO}_6$  phase. The broad region of 150–300 kOe can be identified with the  $\text{Fe}_{1-x}\text{V}_x\text{BO}_3$  crystal. The width of the hyperfine field distribution for the  $\text{Fe}_{1-x}\text{V}_x\text{BO}_3$  crystal is larger than that for the substituted  $\text{Fe}_3\text{BO}_6$  phase. This may be explained by the fact that the iron in  $\text{Fe}_3\text{BO}_6$  has a larger number of magnetic bonds (6 for the  $8d$  and 8 for  $4c$  sites, symmetry group  $P_{nma}$ ) [25] compared to  $\text{FeBO}_3$  (6 bonds) and that the number of magnetic bonds is a factor that stabilizes the hyperfine field. Moreover, the Néel temperature of  $\text{FeBO}_3$  (348 K) is substantially lower than that of  $\text{Fe}_3\text{BO}_6$  (508 K) [26]. Note also that the degree of vanadium substitution for the  $\text{FeBO}_3$  crystal is larger than that for  $\text{Fe}_3\text{BO}_6$ . The hyperfine field probability distribution in the 150- to 300-K region is almost symmetrical, with a slight deviation toward higher fields. The experimental spectrum is fitted well by a set of sextets, whose parameters are listed in Table 2. In accordance with the binomial distribution, their assignment is specified by the number of Fe and V neighbors. The weak peak in the hyperfine field probability distribution in the low field region is due to a paramagnetic doublet, which probably belongs

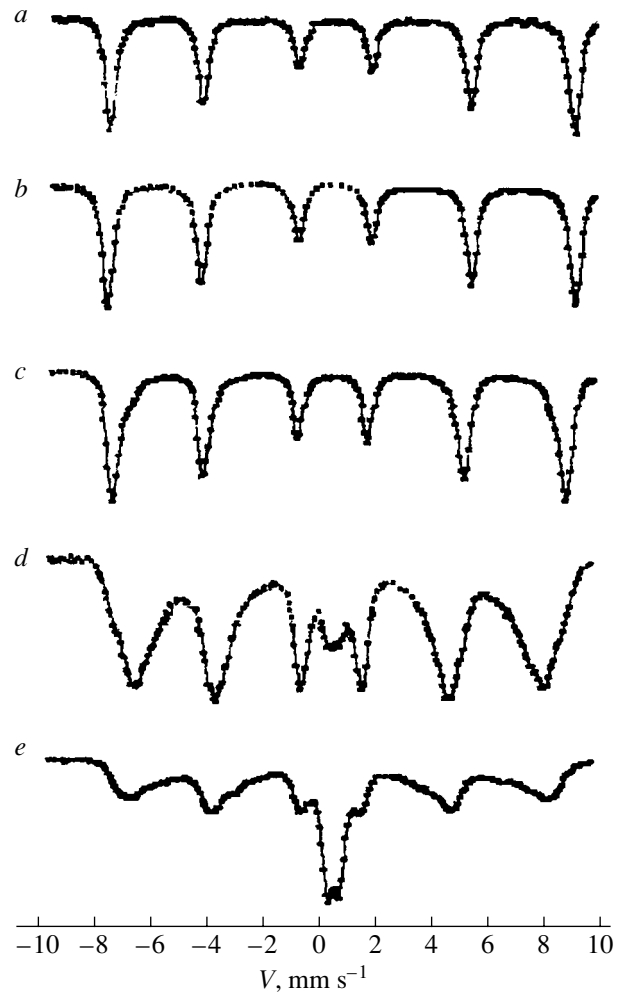


**Fig. 3.** Mössbauer spectra of (a)  $\text{FeBO}_3$ , (b)  $\text{Fe}_{0.98}\text{V}_{0.02}\text{BO}_3$ , (c)  $\text{Fe}_{0.87}\text{V}_{0.13}\text{BO}_3$ , (d)  $\text{Fe}_{0.82}\text{V}_{0.18}\text{BO}_3$ , and (e)  $\text{Fe}_{0.7}\text{V}_{0.3}\text{BO}_3$  obtained at  $T = 130$  K.

to superparamagnetic regions in  $\text{Fe}_{1-x}\text{V}_x\text{BO}_3$  or to the substituted  $\text{Fe}_3\text{BO}_6$ .

The room-temperature spectra of the  $\text{Fe}_{1-x}\text{V}_x\text{BO}_3$  solid solutions with vanadium concentrations  $x = 0.18$ , 0.3, and 0.95 represent quadrupole doublets with asymmetry in the intensities of the  $3/2 \rightarrow 1/2$  and  $1/2 \rightarrow 1/2$  nuclear transitions. This could be assigned to the crystallite  $c$  axes being oriented preferentially parallel to the  $\gamma$ -ray direction; however, we study here powder samples and the observed asymmetry is actually a manifestation of the Gol'danskii–Karyagin effect [27]. This effect is small for monoclinic lattices and, hence, the asymmetry is due to the rhombohedral lattice of the  $\text{Fe}_{1-x}\text{V}_x\text{BO}_3$  crystal. We may thus conclude that each doublet can be unfolded into two doublets, symmetric and asymmetric.

Figures 3 and 4 display the Mössbauer spectra and the distribution functions of the hyperfine field probability at iron nucleus sites, respectively, obtained for the

**Table 2.** Hyperfine interaction parameters in  $\text{Fe}_{1-x}\text{V}_x\text{BO}_3$  solid solutions obtained at 300 K

Compound	$\delta$	$H_{\text{hf}}$	$\Delta E_Q$	$\Gamma_{34}$	$\Gamma_{16}/\Gamma_{34}$	$S$	Assignment
$\text{FeBO}_3$	0.40	345	0.38	0.29	1	1	" $\text{FeBO}_3$ "
$\text{Fe}_{0.98}\text{V}_{0.02}\text{BO}_3$	0.40	335	0.39	0.30	1.04	0.76	6Fe
	0.39	323	0.36	0.30	1.58	0.24	5Fe1V
$\text{Fe}_{0.87}\text{V}_{0.13}\text{BO}_3$	0.39	278	0.41	0.43	1.72	0.20	6Fe
	0.40	251	0.41	0.43	1	0.11	5Fe1V
	0.39	231	0.38	0.41	1	0.14	4Fe2V
	0.39	212	0.36	0.38	1	0.12	3Fe3V
	0.39	189	0.41	0.30	1.91	0.13	2Fe4V
	0.38	159	0.30	0.53	1.58	0.13	1Fe5V
	0.44			1.31		0.06	–
	0.36	375	0.54	0.20	5.26	0.11	" $\text{Fe}_3\text{BO}_6$ "
$\text{Fe}_{0.82}\text{V}_{0.18}\text{BO}_3$	0.42		0.40	0.28		0.70	" $\text{FeBO}_3$ " (GKE = 1.1)
	0.38		0.47	0.32		0.30	" $\text{Fe}_3\text{BO}_6$ "
$\text{Fe}_{0.7}\text{V}_{0.3}\text{BO}_3$	0.41		0.42	0.32		0.71	" $\text{FeBO}_3$ " (GKE = 1.09)
	0.40		0.45	0.30		0.29	" $\text{Fe}_3\text{BO}_6$ "
$\text{Fe}_{0.05}\text{V}_{0.95}\text{BO}_3$	0.42		0.43	0.17		0.43	" $\text{FeBO}_3$ " (GKE = 1.67)
	0.39		0.48	0.39		0.57	

Note:  $\delta$  is the isomer chemical shift relative to metallic iron ( $\alpha\text{Fe}$ ),  $\pm 0.02$  mm/s;  $H_{\text{hf}}$  is the hyperfine field at an iron nucleus site,  $\pm 5$  kOe;  $\Delta E_Q$  is the quadrupole splitting,  $\pm 0.04$  mm/s;  $\Gamma_{34}$  is the FWHM of inner sextet lines,  $\pm 0.02$  mm/s;  $\Gamma_{16}/\Gamma_{34}$  is the ratio of the outer to inner sextet line widths,  $\pm 0.04$  mm/s;  $S$  is the fractional site occupation,  $\pm 0.05$ ; and GKE stands for the Gol'danskii–Karyagin effect.

$\text{Fe}_{1-x}\text{V}_x\text{BO}_3$  solid solutions at 130 K. The temperature dependences of the hyperfine field for  $\text{FeBO}_3$  and  $\text{Fe}_3\text{BO}_6$  are known to cross in the temperature region close to 240 K, and the resolution of the sextets becomes poorer as the temperature is lowered [21]. The hyperfine field probability distribution function does not permit identification of the individual iron positions 6Fe and 5Fe1V (Fig. 4b) for the  $\text{Fe}_{0.98}\text{V}_{0.02}\text{BO}_3$  crystal. Deconvolution into two sextets makes it possible to evaluate the probable occupations of these configurations. For the same reason, one cannot reliably determine the occupations of the inequivalent positions in the  $\text{Fe}_{0.87}\text{V}_{0.13}\text{BO}_3$  composition (Fig. 4c).

The Mössbauer spectra of  $\text{Fe}_{0.82}\text{V}_{0.18}\text{BO}_3$  and  $\text{Fe}_{0.7}\text{V}_{0.3}\text{BO}_3$  samples measured at 130 K are superpositions of several sextets and of a paramagnetic doublet (Figs. 3d, 3e). This complexity of the hyperfine interaction pattern can originate from the nonuniform magnetic state occurring in these crystals. Local deviations from stoichiometry are capable of affecting magnetic order in the sample. The temperature dependence of the magnetization of these solid solutions follows a non-trivial pattern and exhibits two magnetic transitions in the temperature range from 30 to 200 K [22]. The broad hyperfine field distribution observed in the  $\text{Fe}_{0.82}\text{V}_{0.18}\text{BO}_3$  and  $\text{Fe}_{0.7}\text{V}_{0.3}\text{BO}_3$  crystals (Figs. 4d, 4e) allows isolation of a discrete set of the 6Fe, 5Fe1V, 4Fe2V, 3Fe3V, and 2Fe4V configurations, whose hyperfine parameters are listed in Table 3. The binomial

distribution passes through a maximum at the 5Fe1V configuration (17%) for the  $x = 0.18$  composition and at the 6Fe configuration (15%) for the composition with  $x = 0.3$ . The isomer shift is the same for all positions to within experimental error. The spectra obtained suggest the existence of a vanadium-diluted superparamagnetic phase of  $\text{Fe}_3\text{BO}_6$ .

The  $\text{Fe}_{0.05}\text{V}_{0.95}\text{BO}_3$  solid solution remains paramagnetic down to 130 K. To gain deeper insight into the hyperfine interactions in this crystal, we performed Mössbauer studies at temperatures spanning the range from 4.2 to 300 K. The results of calculations and measurements are listed in Table 4 and presented in graphical form in Fig. 5. The spectrum of the  $\text{Fe}_{0.05}\text{V}_{0.95}\text{BO}_3$  composition measured at 4.2 K is a sextet with an admixture of the paramagnetic phase, which adds up to not over 10% of the magnetically ordered phase (Fig. 5a). The relative sextet line intensities are close to 3 : 2 : 1 : 1 : 2 : 3. The hyperfine field  $H_{\text{hf}}$  at iron nucleus sites in this sample is 507 kOe, which is 8.6% lower than that in the unsubstituted  $\text{FeBO}_3$  crystal (555 kOe) measured at the same temperature [14]. The nearest neighbor contribution to the effective hyperfine field at iron nucleus sites in  $\text{FeBO}_3$  is approximately 10% of the ion-core spin polarization. The lower effective field  $H_{\text{hf}}$  in  $\text{Fe}_{0.05}\text{V}_{0.95}\text{BO}_3$  compared to that in  $\text{FeBO}_3$  can be assigned to the perturbation introduced by vanadium impurity atoms.

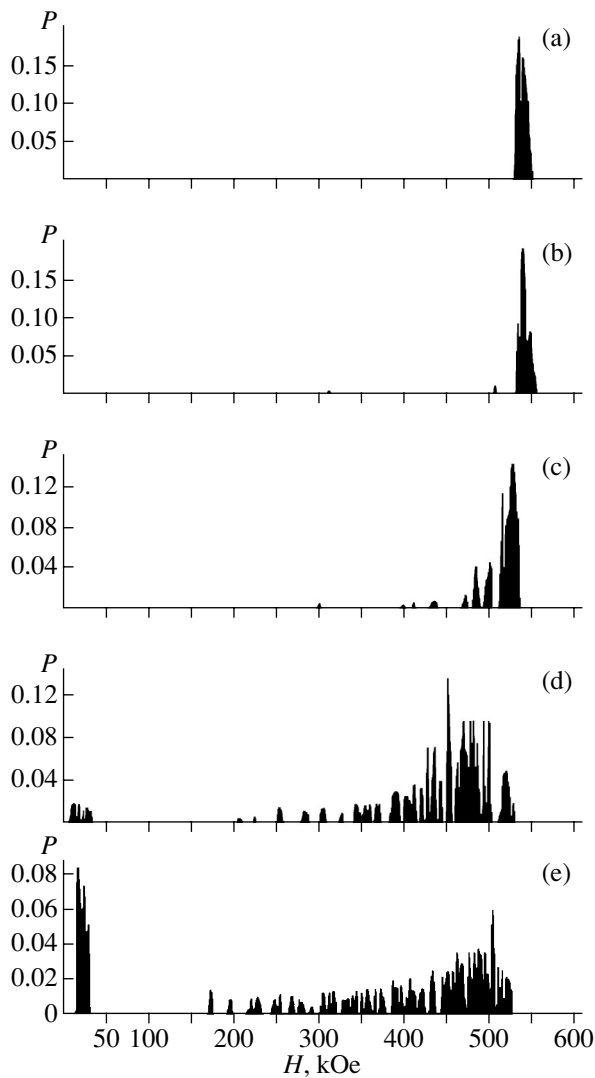


**Fig. 4.** Hyperfine field probability distribution for iron nuclei obtained at  $T = 130$  K for (a)  $\text{FeBO}_3$ , (b)  $\text{Fe}_{0.98}\text{V}_{0.02}\text{BO}_3$ , (c)  $\text{Fe}_{0.87}\text{V}_{0.13}\text{BO}_3$ , (d)  $\text{Fe}_{0.82}\text{V}_{0.18}\text{BO}_3$ , and (e)  $\text{Fe}_{0.7}\text{V}_{0.3}\text{BO}_3$ .

The Mössbauer spectra of the sample obtained at 70 and 130 K are asymmetric doublets characteristic of the paramagnetic state (Figs. 5b, 5c). Each spectrum can be unfolded into doublets relating to different atomic configurations. According to the binomial distribution, for a vanadium concentration  $x = 0.95$ , the probable occupations of the 6V and 1Fe5V configurations acquire maximum values of 76 and 25%, respectively. The two doublets characterizing these configurations are identified in the figures by solid lines. The isomer shifts for these configurations are independent of temperature and are  $\delta = 0.23$  mm/s for iron in the 6V position and  $\delta = 0.29$  mm/s for the 1Fe5V environment. These configurations have a constant quadrupole splitting (Table 4). Unfortunately, the poor resolution of the  $\text{Fe}_{0.05}\text{V}_{0.95}\text{BO}_3$  spectrum does not allow isolation and identification of

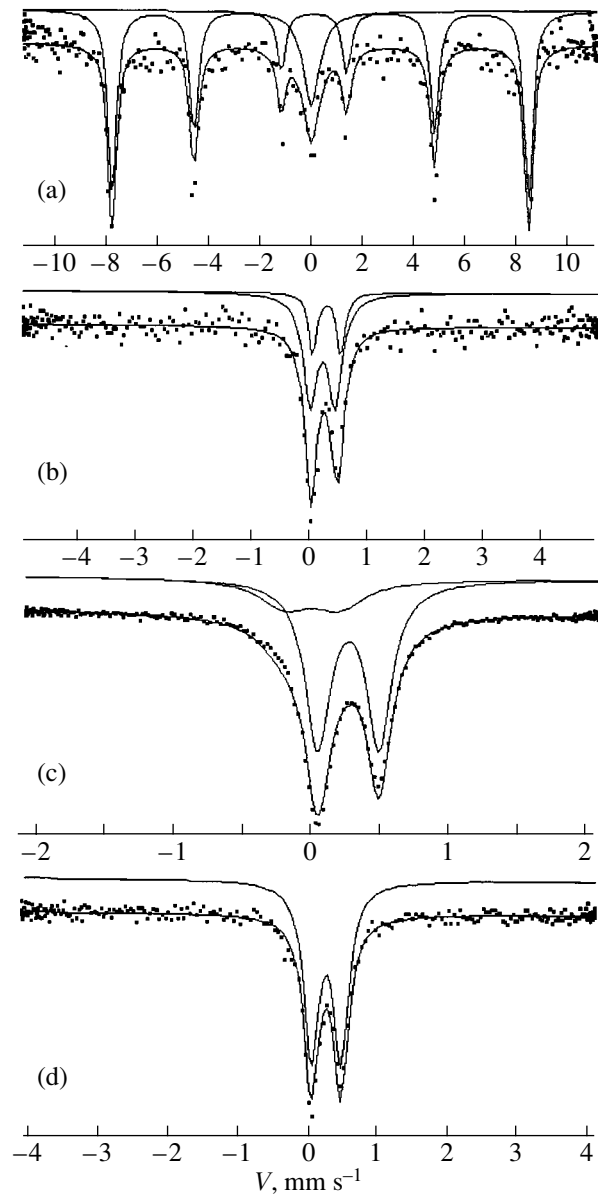


**Fig. 5.** Mössbauer spectra of a  $\text{Fe}_{0.05}\text{V}_{0.95}\text{BO}_3$  crystal obtained at temperatures of (a) 4.2, (b) 70, (c) 130, and (d) 300 K.

the inequivalent iron positions at room temperature (Fig. 5d).

#### 4. DISCUSSION OF THE RESULTS

Thus, deconvolution of solid-solution spectra into constituent spectra of the components of these solutions, which was made under the assumption of a random impurity distribution and of additivity of the contributions due to impurity atoms to  $H_{\text{hf}}$  and  $\delta$  and with due account of the influence of atoms in the first coordination sphere, has permitted us to evaluate the hyperfine parameters for the 6Fe, 5Fe1V, 4Fe2V, 3Fe3V, and

**Table 3.** Hyperfine interaction parameters for  $\text{Fe}_{1-x}\text{V}_x\text{BO}_3$  solid solutions obtained at 130 K

Compound	$\delta$	$H_{\text{hf}}$	$\Delta E_Q$	$\Gamma_{34}$	$\Gamma_{16}/\Gamma_{34}$	$S$	Assignment
$\text{FeBO}_3$	0.50	540	0.46	0.47	1	1	“ $\text{FeBO}_3$ ”
$\text{Fe}_{0.98}\text{V}_{0.02}\text{BO}_3$	0.50	539	0.37	0.44	1	0.87	6Fe
	0.49	528	0.33	0.32	1	0.13	5Fe1V
$\text{Fe}_{0.87}\text{V}_{0.13}\text{BO}_3$	0.50	524	0.39	0.46	1.05	0.76	“ $\text{FeBO}_3$ ”
	0.50	491	0.44	0.51	1.19	0.19	“ $\text{FeBO}_3$ ”
	0.50	425	0.07	0.87	1.01	0.05	“ $\text{Fe}_3\text{BO}_6$ ”
$\text{Fe}_{0.82}\text{V}_{0.18}\text{BO}_3$	0.51	514	0.41	0.28	2.54	0.10	6Fe
	0.51	484	0.44	0.50	1.15	0.17	5Fe1V
	0.51	462	0.45	0.44	1.13	0.14	4Fe2V
	0.51	436	0.43	0.48	1	0.11	3Fe3V
	0.52	403	0.54	0.53	1.11	0.08	2Fe1V
	0.52	351	0.41	0.36	12.3	0.30	“ $\text{Fe}_3\text{BO}_6$ ”
	0.46			1.31		0.1	“ $\text{Fe}_3\text{BO}_6$ ”
	0.51	501	0.41	0.41	1.49	0.15	6Fe
	0.50	471	0.49	0.45	1.40	0.14	5Fe1V
	0.49	430	0.49	0.57	1.94	0.12	4Fe2V
$\text{Fe}_{0.7}\text{V}_{0.3}\text{BO}_3$	0.50	374	0.45	0.56	1.06	0.13	3Fe3V
	0.49	273	0.30	1.77	1.06	0.22	“ $\text{Fe}_3\text{BO}_6$ ”
	0.49		0.43	0.51		0.23	“ $\text{Fe}_3\text{BO}_6$ ”
	0.49			0.48			“ $\text{FeBO}_3$ ”
	0.50						“ $\text{FeBO}_3$ ”

Note:  $\delta$ ,  $\pm 0.02$  mm/s;  $H_{\text{hf}}$ ,  $\pm 5$  kOe;  $\Delta E_Q$ ,  $\pm 0.04$  mm/s;  $\Gamma_{34}$ ,  $\pm 0.02$  mm/s;  $\Gamma_{16}/\Gamma_{34}$ ,  $\pm 0.04$  mm/s; and  $S$ ,  $\pm 0.05$ .

**Table 4.** Hyperfine interaction parameters for a  $\text{Fe}_{0.05}\text{V}_{0.95}\text{BO}_3$  crystal obtained at different temperatures

$T$ , K	$\delta$	$H_{\text{hf}}$	$\Delta E_Q$	$\Gamma_{34}$	$S$	Assignment
4.2	$0.28 \pm 0.005$	$507.2 \pm 0.03$	$0.22 \pm 0.01$	$0.40 \pm 0.02$		
70	$0.23 \pm 0.01$		$0.42 \pm 0.01$	$0.29 \pm 0.023$	0.75	6V
	$0.29 \pm 0.013$		$0.48 \pm 0.016$	$0.16 \pm 0.02$	0.25	1Fe5V
130	$0.23 \pm 0.003$		$0.42 \pm 0.004$	$0.33 \pm 0.007$	0.76	6V
	$0.29 \pm 0.002$		$0.47 \pm 0.003$	$0.14 \pm 0.004$	0.24	1Fe5V
300	$0.27 \pm 0.002$		$0.43 \pm 0.003$	$0.26 \pm 0.005$		

Note:  $\delta$ ,  $\pm 0.01$  mm/s;  $H_{\text{hf}}$ ,  $\pm 0.03$  kOe;  $\Delta E_Q$ ,  $\pm 0.02$  mm/s;  $\Gamma_{34}$ ,  $\pm 0.02$  mm/s; and  $S$ ,  $\pm 0.02$ .

2Fe4V positions in the  $\text{Fe}_{0.87}\text{V}_{0.13}\text{BO}_3$  crystal at room temperature and in the  $\text{Fe}_{0.82}\text{V}_{0.18}\text{BO}_3$  and  $\text{Fe}_{0.7}\text{V}_{0.3}\text{BO}_3$  crystals at a temperature of 130 K. The hyperfine fields at iron nucleus sites decrease monotonically in the series of these configurations in discrete steps of  $\Delta H_{\text{hf}} = 20\text{--}30$  kOe, in full agreement with the usual concepts concerning a dilute magnetic insulator. The chemical isomer shifts for these configurations are the same to within experimental error. The isomer shifts at room temperature,  $\delta = 0.38\text{--}0.40$  mm/s, and at 130 K,  $\delta = 0.51\text{--}0.52$  mm/s, indicate that iron in the  $\text{Fe}_{1-x}\text{V}_x\text{BO}_3$  system is trivalent. Note that the idea of substitution of an average-sized ion used in [28] to interpret Möss-

bauer spectra of the  $(\text{Fe}_{1-x}\text{V}_x)_2\text{O}_3$  system, according to which low vanadium contents are conducive to the formation of  $\text{Fe}^{2+}\text{--V}^{4+}$  ion pairs, did not find support in our studies. This implies that the electronic state of iron does not depend on substitution by vanadium. The iron ion resides in an octahedral environment, and the electric field gradient at iron nucleus sites is directed parallel to the [111] threefold axis. The quadrupole splitting in the  $\text{Fe}_{1-x}\text{V}_x\text{BO}_3$  solid solutions is close in magnitude to  $\Delta E_Q = 0.46$  mm/s, the value for the unsubstituted  $\text{FeBO}_3$  crystal. The small change in the hyperfine field for the  $\text{Fe}_{0.05}\text{V}_{0.95}\text{BO}_3$  sample at 4.2 K compared to that in  $\text{FeBO}_3$  indicates that the  $H_{\text{hf}}$  field in these crystals is

produced primarily by the iron ion itself and depends only weakly on the environment.

#### ACKNOWLEDGMENTS

One of the authors (M.M. A.-E.) would like to thank the Deutsche Forschungsgemeinschaft for financial support (SFB 608).

This study was supported by the Russian Foundation for Basic Research (project no. 03-02-16286) and the federal program "Integration" (project no. B0017).

#### REFERENCES

- I. Bernal, C. W. Struck, and J. G. White, *Acta Crystallogr.* **16**, 849 (1963).
- J. Haisma, H. J. Prins, and K. L. L. van Mierlo, *J. Phys. D: Appl. Phys.* **7**, 162 (1974).
- B. Andlauer, J. Schneider, and W. Wettling, *Appl. Phys.* **10**, 189 (1976).
- R. Wolfe, A. J. Kurtzig, and R. C. LeCraw, *J. Appl. Phys.* **41**, 1218 (1970).
- I. S. Édel'man and A. V. Malakhovskii, *Opt. Spektrosk.* **35**, 959 (1973).
- A. J. Kurtzig, R. Wolfe, R. C. LeCraw, and J. W. Nielsen, *Appl. Phys. Lett.* **14**, 350 (1969).
- R. Diehl, *Solid State Commun.* **17**, 743 (1975).
- M. Pernet, D. Elmaleh, and J.-C. Joubert, *Solid State Commun.* **8**, 1583 (1970).
- J. C. Joubert, T. Shirk, W. B. White, and R. Roy, *Mater. Res. Bull.* **3**, 671 (1968).
- A. S. Kamzin, B. Shtahl, R. Gellert, M. Muller, E. Kankeleit, and D. B. Vcherashniĭ, *Pis'ma Zh. Éksp. Teor. Fiz.* **71**, 197 (2000) [*JETP Lett.* **71**, 134 (2000)].
- A. M. Kodomtseva, R. Z. Levitin, Yu. F. Popov, V. N. Seleznev, and V. V. Uskov, *Fiz. Tverd. Tela (Leningrad)* **14**, 214 (1972) [*Sov. Phys. Solid State* **14**, 172 (1972)].
- M. P. Petrov, G. A. Smolenskii, A. P. Paugurt, S. A. Kizhaev, and M. K. Chizhov, *Fiz. Tverd. Tela (Leningrad)* **14**, 109 (1972) [*Sov. Phys. Solid State* **14**, 87 (1972)].
- L. V. Velikov, E. G. Rudashevskii, and V. N. Seleznev, *Izv. Akad. Nauk SSSR, Ser. Fiz.* **36**, 1531 (1972).
- M. Eibschutz, L. Pfeiffer, and J. W. Nielsen, *J. Appl. Phys.* **41**, 1276 (1970).
- M. Kopcewicz, H. Engelmann, S. Stenger, G. V. Smirnov, U. Gonser, and H. G. Wagner, *Appl. Phys. A* **44**, 131 (1987).
- H. Schmid, *Acta Crystallogr.* **17**, 1080 (1964).
- T. A. Bither, Carol G. Frederick, T. E. Gier, J. F. Weiher, and H. S. Young, *Solid State Commun.* **8**, 109 (1970).
- Xu Ziguang, Matam Mahesh Kumar, and Ye Zuo Guang, in *Proceedings of Annual March Meeting* (Am. Phys. Soc., 2001).
- De Lacklison, J. Chadwick, and J. L. Page, *J. Phys. D: Appl. Phys.* **5**, 810 (1972).
- M. W. Ruckman, R. A. Levy, and R. Chennette, *J. Appl. Phys.* **53**, 1694 (1982).
- O. A. Bayukov, V. P. Ikonnikov, M. I. Petrov, V. V. Rudenko, V. N. Seleznev, and V. V. Uskov, *Tr. MKM-73b* **3**, 313 (1974).
- N. B. Ivanova, V. V. Rudenko, A. D. Balaev, N. V. Kazak, V. V. Markov, S. G. Ovchinnikov, I. S. Édel'man, A. S. Fedorov, and P. V. Avramov, *Zh. Éksp. Teor. Fiz.* **121**, 354 (2002) [*JETP* **94**, 299 (2002)].
- J. M. D. Coey and G. A. Sawatzky, *Phys. Status Solidi B* **44**, 673 (1971).
- A. S. Kamzin and L. A. Grigor'ev, *Zh. Éksp. Teor. Fiz.* **105**, 377 (1994) [*JETP* **78**, 200 (1994)].
- J. G. White, A. Miller, and R. E. Nielsen, *Acta Crystallogr.* **19**, 1060 (1965).
- M. Hirano, T. Okuda, T. Tsushima, S. Umemura, K. Kohn, and S. Nakamura, *Solid State Commun.* **15**, 1129 (1974).
- V. I. Goldanskii, E. F. Markov, and V. V. Karpov, *Phys. Lett.* **3**, 344 (1963).
- G. Shirane, D. E. Cox, and S. L. Ruby, *Phys. Rev.* **125**, 1158 (1962).

*Translated by G. Skrebtsov*

---

## LATTICE DYNAMICS AND PHASE TRANSITIONS

---

# Pretransition State and Structural Transition in a Deformed Crystal

E. E. Slyadnikov

*Institute of Strength Physics and Materials Science, Siberian Division, Russian Academy of Sciences,  
Akademicheskii pr. 8, Tomsk, 634021 Russia*

*e-mail: slyadnik@ngs.ru*

Received June 30, 2003; in final form, August 26, 2003

**Abstract**—It is shown theoretically that a deformed crystal exhibiting structural instability can be treated as a quantum system of pseudospins. The quantum behavior of atoms becomes significant when the characteristic distance between sites of the original crystal lattice and the corresponding sites of the final phase is less than the amplitude of zero-point oscillations of atoms (0.1 Å) and when the area under the barrier separating the two minima of the double-well potential is less than  $aV_2 = 5 \times 10^{-10}$  eV cm. © 2004 MAIK “Nauka/Interperiodica”.

### 1. INTRODUCTION

Certain phenomena that occur during deformation of solids cannot be described in terms of the classical microscopic models of crystals [1]. Among these phenomena are nonlinear elastic effects, pretransition phenomena, and structural transitions that are accompanied by excitation of additional degrees of freedom of the atomic lattice under deformation [2]. Therefore, new microscopic models of crystals are needed to describe such phenomena. In this paper, we propose a microscopic model of a deformed crystal in which an atomic lattice is treated as a quantum system of pseudospins. Within this model, it is shown that the one-particle potential acting on an atom can be approximated by a double-well potential and that the atoms of the lattice of a deformed crystal obey quantum-mechanical laws. The pseudospin model of a crystal allows one to avoid the problem of strong anharmonicity, which always arises near a structural transition.

The conclusion that the one-particle potential acting on an atom can be approximated by a double-well potential can be drawn from the calculated coefficients of expansion of the interatomic pair interaction potential in powers of atomic displacements. According to calculations [3], the anharmonic terms in the pair potential increase sharply near structural transitions and become comparable in magnitude to the harmonic terms. The potential profile changes; more specifically, an infinitely high potential barrier observed far from the transition point is replaced by a barrier of finite height, which is indicative of the existence of another minimum in the interatomic pair interaction potential in the pretransition state [3].

Experimental evidence for the formation of a one-particle double-well potential acting on an atom is the existence of a structural pretransition state to which titanium nickelide transfers with varying temperature

[4] and the  $\gamma \rightarrow \alpha \rightarrow \gamma$  structural transition in austenite steels observed in the region of a stress concentrator [5]. Another prominent example of systems in which an atom moves in a double-well potential is the surface of a crystal. When a crystal is subjected to external fields, its surface undergoes structural phase transformations. Since the crystal surface exhibits structural instability, the surface layer is characterized by two different types of atomic configurations, e.g., the bcc and fcc structures [6].

These specific features of the behavior of a deformed crystal suggest that the one-particle potential in which an atom moves can be represented as a sum of one-particle potentials characterizing the original and final phases (i.e., as an asymmetric double-well potential). In the absence of external fields, the deeper potential well corresponds to the original structure and the shallower well, to the final phase. The configuration in which an atom is located in the deeper well corresponds to the ground state, and the configuration with the atom located in the shallower well corresponds to an excited (virtual) state, because the transfer of the atoms to the virtual state can occur only via a structural (coherent) transition. In this paper, we discuss the possible physical cause of the coherent transition and the physical mechanism through which a pretransition state occurs in a deformed crystal as a superposition of several structures with the formation of new allowed states in the space of interstitial sites [2].

### 2. THE POTENTIAL IN WHICH AN ATOM MOVES IN A DEFORMED CRYSTAL

In order to find the potential acting on an atom, we introduce the atomic density in the crystal:

$$\rho(\mathbf{r}, t) = \sum_i v_i \delta(\mathbf{r}, -\mathbf{r}_i(t)), \quad (1)$$

where  $v_i$  is the volume of the  $i$ th atom. The energy of the atomic system characterized by the atomic density  $\rho(\mathbf{r}, t)$  can be represented in the form of a functional series,

$$E(t) = E_0 + \int V_1(\mathbf{r}, t)\rho(\mathbf{r}, t)d\mathbf{r} + (1/2)\int V_2(\mathbf{r}, \mathbf{r}')\rho(\mathbf{r}, t)\rho(\mathbf{r}', t)d\mathbf{r}d\mathbf{r}' + \dots \quad (2)$$

Here,  $V_k$  is the  $k$ -particle interaction potential between atoms. The one-particle potential acting on an atom at time  $t$  can be found as

$$u(\mathbf{r}, t) = \delta E(t)/\delta\rho(\mathbf{r}, t). \quad (3)$$

Substituting Eq. (2) into Eq. (3) gives

$$u(\mathbf{r}, t) = V_1(\mathbf{r}, t) + \int V_2(\mathbf{r}, \mathbf{r}')\rho(\mathbf{r}', t)d\mathbf{r}' + \dots \quad (4)$$

According to Eq. (4), the potential profile  $u(\mathbf{r}, t)$  depends on  $\rho(\mathbf{r}, t)$ . Therefore, the problem should be solved self-consistently, which can be performed using the pseudopotential theory [7], the electron density functional [8], or computer simulation methods [9].

In considering the macroscopic properties, we should perform averaging over microscopic fluctuations in atomic density  $\rho(\mathbf{r}, t)$ , i.e., over time  $t$ . According to the ergodic hypothesis [10], we can average over an ensemble of effective (smoothed in time) potential profiles  $\{U(\mathbf{r})\}$  rather than average the single potential profile  $u(\mathbf{r}, t)$ . In this case, the average potential profile takes the form of a functional integral,

$$\langle U(\mathbf{r}) \rangle = \int U(\mathbf{r})P\{U(\mathbf{r})\}DU(\mathbf{r}), \quad (5)$$

where  $P\{U(\mathbf{r})\}$  is the probability that the specific profile  $U(\mathbf{r})$  belonging to the ensemble  $\{U(\mathbf{r})\}$  will occur in the crystal. Let us assume that, when the deformed crystal undergoes a structural transition, the potential profiles corresponding to the original and final phases,  $U_M(\mathbf{r})$  and  $U_A(\mathbf{r})$ , respectively, are the most probable. For the sake of simplicity, we also assume that, in the vicinity of the structural transition, the probability  $P\{U(\mathbf{r})\}$  is the sum of  $\delta$  functions

$$P\{U(\mathbf{r})\} = (1/2)\delta[U(\mathbf{r}) - U_A(\mathbf{r})] + (1/2)\delta[U(\mathbf{r}) - U_M(\mathbf{r})]. \quad (6)$$

Substituting Eq. (6) into Eq. (5) gives

$$\langle U(\mathbf{r}) \rangle = (1/2)U_A(\mathbf{r}) + (1/2)U_M(\mathbf{r}). \quad (7)$$

Since the averaged one-particle potential profile is a periodic function of the space coordinates, it will suffice to consider this profile for the unit cell centered at the origin of coordinates. The distance between the potential wells corresponding to the site of the original structure and to the site of the finite phase in the unit cell is equal to  $a \approx 10^{-9}$  cm [5]. If the widths of the local wells of the original structure,  $U_M(\mathbf{r} - \mathbf{a}/2)$  and the final phase,  $U_A(\mathbf{r} + \mathbf{a}/2)$ , centered at  $\mathbf{r} = -\mathbf{a}/2$  and  $\mathbf{r} = \mathbf{a}/2$ ,

respectively, are significantly smaller than the distance between the wells, then the potential  $\langle U(\mathbf{r}) \rangle$  in which an atom moves can be written in the form

$$\langle U(\mathbf{r}) \rangle = -V[\delta(\mathbf{r} + \mathbf{a}/2) + \delta(\mathbf{r} - \mathbf{a}/2)]. \quad (8)$$

It follows from Eq. (8) that the one-particle potential in which an atom moves in a deformed crystal is a double-well potential.

### 3. ATOM IN AN ASYMMETRIC DOUBLE-WELL POTENTIAL

Let us consider a crystal undergoing a structural transition from the original phase to a final phase stimulated by external influences (temperature variations, external forces). In the absence of external influences, the crystal is in the original phase and a lattice atom moves in an asymmetric potential with two local minima differing in depth. The deeper potential well corresponds to the initial structure, and the shallower well corresponds to the final phase. We assume that the minima are located on the  $x$  axis coinciding with the crystallographic axis of the crystal along which the structural transition occurs. In this case, the potential  $U_a(x)$  in which an atom moves can be written as

$$U_a(x) = -V_1b\delta(x + a/2) - V_2b\delta(x - a/2). \quad (9)$$

Here,  $\delta(x)$  is a Dirac function;  $a$  is the distance between the minima of the potential;  $V_1$  and  $V_2$  are the depths of the left-hand (deeper) and the right-hand (shallower) well, respectively ( $V_1 > V_2$ ); and  $b$  is the width of these local wells. We assume that the distance between the local wells is much larger than their width ( $a \gg b$ ). It is convenient to separate the asymmetric potential  $U_a(x)$  into a symmetric part  $U_s(x)$  with local wells of equal depth and a correction  $\Delta U_a(x)$  taking into account the difference in depth (asymmetry) between the local wells:

$$U_a(x) = U_s(x) + \Delta U_a(x), \quad (10)$$

$$U_s(x) = -V_2b\delta(x + a/2) - V_2b\delta(x - a/2),$$

$$\Delta U_a(x) = (V_2 - V_1)b\delta(x + a/2). \quad (11)$$

First, we consider the motion of a lattice atom in the symmetric potential and then take into account the asymmetry of the potential by using perturbation theory under the assumption of smallness of the asymmetric correction,  $(V_1 - V_2)/V_1 \ll 1$ . The motion of an atom in the potential well  $U_s(x)$  is described by the Schrödinger equation [11]

$$[-(\hbar/2m)\partial^2/\partial x^2 + U_s(x)]\Psi(x) = -\varepsilon\Psi(x), \quad (12)$$

where  $\Psi(x)$  is the wave function of the atom and  $-\varepsilon$  is its energy ( $\varepsilon > 0$ ). An atom moving in the symmetric potential  $U_s(x)$  has two equilibrium positions. If the tunneling effect can be ignored, the ground state of the atom in each local well is doubly degenerate; i.e.,  $\varepsilon_+ =$



$\varepsilon_-$  for the even and odd wave functions,  $\Psi_+(x)$  and  $\Psi_-(x)$ , respectively. Allowance for the quantum tunneling of the atom through the potential barrier between the local wells lifts the degeneracy ( $\varepsilon_+ > \varepsilon_-$ ). To find the energy eigenvalues  $\varepsilon_+$  and  $\varepsilon_-$  and the eigenfunctions  $\Psi_+$  and  $\Psi_-$  from Eq. (12), we represent the wave functions  $\Psi_+$  and  $\Psi_-$  in the form (for  $x < -a/2$ )

$$\Psi_{\pm} = A_{\pm} \{ \exp[\kappa_{\pm}(x - a/2)] \pm \exp[\kappa_{\pm}(x + a/2)] \}, \quad (13)$$

$$K_q = (\hbar^2/m)/(V_2 b a).$$

Here,  $\kappa_{\pm}^{-1}$  are the characteristic localization lengths for the even (+) and odd (−) wave functions and  $A_{\pm}$  are the normalization constants. Wave functions (13) must satisfy the corresponding boundary and normalization conditions, from which the quantities  $\kappa_{\pm}$  and  $A_{\pm}$  can be determined.

Solving the Schrödinger equation (12) with the use of Eq. (13), we find

$$(\hbar^2/m)\kappa_{\pm} = V_2 b [1 \pm \exp(-\kappa_{\pm} a)],$$

$$(2A_{\pm}^2/\kappa_{\pm}) [1 \pm (1 + \kappa_{\pm} a) \exp(-\kappa_{\pm} a)] = 1, \quad (14)$$

$$\varepsilon_{\pm} = (\hbar^2/2m)\kappa_{\pm}^2.$$

We calculate the correction  $\hbar\Delta$  to the energy eigenvalues associated with the asymmetry of the potential  $\Delta U_a(x)$  to first order in perturbation theory using the even and odd wave functions (13). The result is

$$\hbar\Delta = \langle \Psi_- | \Delta U_a | \Psi_+ \rangle$$

$$= (V_2 - V_1) b A_+ A_- [1 + \exp(-\kappa_+ a) - \exp(-\kappa_- a) - \exp(-\kappa_+ a - \kappa_- a)]. \quad (15)$$

In the “weak”-tunneling limit  $\kappa_{\pm} a \gg 1$ , it follows from Eqs. (14) and (15) that the splitting of the energy levels of the even and odd states  $\hbar\omega = \varepsilon_+ - \varepsilon_-$  tends to zero and the tunneling effect is practically absent. Let us estimate the quantities in Eqs. (14) and (15) for a typical transition metal. Putting  $V_2 = 4$  eV,  $b = 10^{-10}$  cm,  $a = 10^{-8}$  cm,  $m = 10^{-22}$  g, and  $V_1 - V_2 = 10^{-4}$  eV, we obtain  $K_q^{-1} = 6.4 \times 10^2$ ,  $\kappa_+ \cong \kappa_- = 6.4 \times 10^{10}$  cm $^{-1}$ ,  $\hbar\omega \rightarrow 0$ , and  $\hbar\Delta = 1.6(V_2 - V_1) = -1.6 \times 10^{-4}$  eV. Thus, for the distance  $a = 10^{-8}$  cm, the area under the barrier separating the minima of the double-well potential is  $V_2 a = 4 \times 10^{-8}$  eV cm, quantum tunneling is practically absent, and the potential is highly asymmetric.

In the intermediate case of moderate tunneling,  $\kappa_{\pm} a \approx 1$ , the level splitting  $\hbar\omega$  is nonzero, but the tunneling effect is weak. For  $V_2 = 4 \times 10^{-1}$  eV,  $b = 10^{-10}$  cm,  $a = 10^{-9}$  cm,  $m = 10^{-22}$  g, and  $V_1 - V_2 = 10^{-4}$  eV, Eqs. (14) and (15) give  $K_q^{-1} = 6.4$ ,  $\kappa_+ = 6.40 \times 10^9$  cm $^{-1}$ ,  $\kappa_- = 6.41 \times 10^9$  cm $^{-1}$ ,  $\hbar\omega = 8.8 \times 10^{-4}$  eV, and  $\hbar\Delta = 0.16(V_2 - V_1) = -1.6 \times 10^{-5}$  eV. Thus, for the distance

$a = 10^{-9}$  cm, the area under the barrier is  $V_2 a = 4 \times 10^{-10}$  eV cm, quantum tunneling of an atom is significant (i.e., the quantum properties of atoms of the crystal lattice should be taken into account), and the asymmetry of the potential becomes weaker.

In the limit of intensive tunneling,  $\kappa_{\pm} a \ll 1$ , it follows from Eqs. (14) and (15) that the level splitting  $\hbar\omega$  is large and the tunneling effect is pronounced. For  $V_2 = 1.6 \times 10^{-1}$  eV,  $b = 10^{-10}$  cm,  $a = 4 \times 10^{-10}$  cm,  $m = 10^{-22}$  g, and  $V_1 - V_2 = 10^{-4}$  eV, Eqs. (14) and (15) give  $K_q^{-1} = 1.03$ ,  $\kappa_+ = 3.6 \times 10^9$  cm $^{-1}$ ,  $\kappa_- = 1.5 \times 10^8$  cm $^{-1}$ ,  $\hbar\omega = 4 \times 10^{-2}$  eV, and  $\hbar\Delta = 0.05(V_2 - V_1) = -5 \times 10^{-6}$  eV. Thus, for the distance  $a = 4 \times 10^{-10}$  cm, the area under the barrier is  $V_2 a = 6.4 \times 10^{-11}$  eV cm, quantum tunneling plays a decisive role in the motion of an atom, the atom is highly delocalized in the double-well potential, and the asymmetry of the potential is very weak.

#### 4. PSEUDOSPIN FORMALISM AND THE HAMILTONIAN OF A SYSTEM OF PSEUDOSPINS

The estimates made above show that quantum tunneling of an atom between the related sites of the original and final phases is of importance in a structurally unstable crystal. In other words, in addition to small-amplitude thermal vibrations, an atom in the deeper (left-hand) well of the double-well potential undergoes quantum zero-point oscillations (tunneling) of a certain amplitude along a certain direction, which corresponds to additional discrete degrees of freedom. Therefore, the wave function of the atom depends not only on the continuous space coordinate  $x$  but also on a discrete variable related to the projection of the pseudospin onto the  $z$  axis. For the two-level system at hand, the wave function of an atom has the form of a spinor  $\Psi(x, S^z)$  consisting of two components, namely, the even  $\Psi(x, +1/2) = \Psi_+(x)$  and odd  $\Psi(x, -1/2) = \Psi_-(x)$  coordinate functions corresponding to different values of the  $z$  component of the pseudospin.

In terms of the model considered above, the energy of the system of pseudospins subjected to a mechanical force field is described by the Hamiltonian

$$H = \sum_l H_l^1 + \sum_l H_l^{\text{int}}. \quad (16)$$

In the basis formed by the even and odd wave functions  $\Psi_{\pm}(x)$ , the Hamiltonian  $H_l^1$  has the form

$$H_l^1 = \hbar\omega S_l^z + \hbar\Delta S_l^x, \quad (17)$$

$$\Delta = -(1/2) \sum_k J_{lk} S_k^x - (1/3) \sum_{k,m} I_{lkm} S_k^x S_m^x,$$

where the asymmetry of the double-well potential is associated with two- and three-particle interactions between pseudospins and  $\hbar J_{lk}$  and  $\hbar I_{lkm}$  are the two- and three-particle interaction constants of pseudospins, respectively.

Assuming that the external mechanical force stimulates quantum tunneling and decreases the asymmetry of the double-well potential, we describe the interaction of the pseudospins with the mechanical force field  $\mathbf{\Omega}_l(t) = (\Omega_l^a(t), 0, \Omega_l^t(t))$  by the Hamiltonian

$$H_l^{\text{int}} = \hbar \Omega_l^a(t) S_l^x + \hbar \Omega_l^t(t) S_l^z. \quad (18)$$

Here,  $\Omega_l^t(t) = G^t \mu_l^{xy}$  and  $\Omega_l^a(t) = G^a \mu_l^{yx}$  are the  $z$  and  $x$  components of the mechanical force field, respectively;  $G^t$  and  $G^a$  are positive constants; and  $\mu_l^{yx}$  is the shear component of the stress tensor stimulating the structural transition.

In the basis of the wave functions  $\phi_L$  and  $\phi_R$  localized in the left- and right-hand wells, respectively, the Hamiltonian of the pseudospin system in the mechanical force field has the form

$$\begin{aligned} H = & \sum_l \hbar \omega S_l^x - (1/2) \sum_{l,k} \hbar J_{lk} S_l^z S_k^z \\ & - (1/3) \sum_{l,k,m} \hbar I_{lkm} S_l^z S_k^z S_m^z \\ & + \sum_l (\hbar \Omega_l^a(t) S_l^z + \hbar \Omega_l^t(t) S_l^x). \end{aligned} \quad (19)$$

In the molecular-field approximation [11], the Hamiltonian of the pseudospin system (19) is replaced by the effective Hamiltonian

$$H^M = - \sum_i \mathbf{h}_i \mathbf{S}_i = \sum_i [\partial \langle H \rangle / \partial \langle \mathbf{S}_i \rangle] \mathbf{S}_i, \quad (20)$$

$$\begin{aligned} h_i = & \left( -\hbar \omega_0 - \hbar \Omega_t, 0, -\hbar \Omega_a \right. \\ & \left. + \sum_j \hbar J_{ij} \langle S_j^z \rangle + \sum_{j,m} \hbar I_{ijm} \langle S_j^z \rangle \langle S_m^z \rangle \right). \end{aligned} \quad (21)$$

In this case, the average value of the pseudopotential in the  $i$ th unit cell is defined as

$$\begin{aligned} \langle \mathbf{S}_i \rangle = & \text{Tr}[\mathbf{S}_i \exp(-\beta H_i^M)] / \text{Tr}[\exp(-\beta H_i^M)] \\ = & \partial(\ln Z_i) / \partial(\beta \mathbf{h}_i) = (1/2)(\mathbf{h}_i / h_i) \tanh(\beta h_i / 2), \end{aligned} \quad (22)$$

$$\begin{aligned} h_i = |\mathbf{h}_i| = & \left[ (\hbar \omega_0 + \hbar \Omega_t)^2 + \left( -\hbar \Omega_a + \sum_j \hbar J_{ij} \langle S_j^z \rangle \right. \right. \\ & \left. \left. + \sum_{j,m} \hbar I_{ijm} \langle S_j^z \rangle \langle S_m^z \rangle \right)^2 \right]^{1/2}. \end{aligned} \quad (23)$$

## 5. STATIONARY STATES OF THE PSEUDOSPIN SYSTEM

Let us consider the case where there is no external mechanical force,  $\mathbf{\Omega}_l = \mathbf{\Omega}_a = 0$ . We assume that the structural transition from the initial to the final phase is associated with the ‘‘longitudinal’’ interaction of pseudospins oriented along the  $z$  axis and is characterized by the order parameter  $S^z = \langle S_i^z \rangle$ . Expanding the self-consistency equation (22) in powers of the order parameter  $S^z$  near the structural transition temperature  $T_{MA}$ , we obtain

$$\alpha S^z + \delta (S^z)^2 + \gamma (S^z)^3 = 0, \quad (24)$$

$$\alpha = \hbar J_0 [1 - (J_0/2\omega_0) \tanh(\beta \hbar \omega_0/2)] = \alpha_0 [T - T_c],$$

$$\delta = \delta_0 |T_{MA} - T|^{1/2} \text{sgn}(T_{MA} - T),$$

$$\gamma = \hbar J_0 (J_0^3/4\omega_0^3) [\tanh(\beta \hbar \omega_0/2) \quad (25)$$

$$- (\beta \hbar \omega_0/2) \cosh^{-2}(\beta \hbar \omega_0/2)],$$

$$k_B T_c = (\hbar \omega_0/2) [\text{arctanh}(2\omega_0/J_0)]^{-1},$$

where  $J_0 = \sum_i J_{ij}$ ,  $I_0 = \sum_{i,m} I_{ijm}$ ,  $\alpha_0 = (\hbar^2 J_0^2/4k_B T_c^2) \cosh^{-2}(\hbar \omega_0/2k_B T_c)$ , and  $\delta_0 = 2\hbar I_0 T_{MA}^{-1/2}$ . The coefficients  $\alpha$  and  $\delta$  can change sign, and  $\gamma$  is positive. The corresponding Landau expansion of the free energy near the temperature  $T_{MA}$  has the form

$$\Delta F = \alpha (S^z)^2/2 + \delta (S^z)^3/3 + \gamma (S^z)^4/4. \quad (26)$$

The solution to the self-consistency equation (24) is

$$S^z = [-\delta \pm \sqrt{\delta^2 - 4\alpha\gamma}] / 2\gamma \quad \text{for } \delta^2 \geq |4\alpha\gamma|, \quad (27)$$

$$S^z = 0 \quad \text{for } \delta^2 < |4\alpha\gamma|. \quad (28)$$

It follows from Eq. (27) that there is a temperature range ( $T^+$ ,  $T^-$ ) over which the crystal lattice can be in a pretransition state  $S^z = 0$ . The temperature at which the transition from the original phase to the pretransition state occurs is  $T^+ = T_{MA} + 4\alpha_0\gamma[\delta_0^2 - 4\alpha_0\gamma]^{-1}\Delta T$ , and the temperature at which the crystal undergoes the transition from the pretransition state to the final phase is  $T^- = T_{MA} - 4\alpha_0\gamma[\delta_0^2 + 4\alpha_0\gamma]^{-1}\Delta T$ , where  $\Delta T = T_{MA} - T_c > 0$ .

Let us consider the case of strong interaction between pseudospins ( $\hbar J_0 = 0.4$  eV) and weak tunnel-

ing,  $\hbar\omega_0 \approx 0.0001$  eV. From the condition  $\alpha = 0$ , the temperature of the transition to the pretransition state can be estimated to be  $k_B T_c \approx 0.1$  eV and  $T_c \approx 1000$  K. Therefore, we have  $2\omega_0/J_0 \ll 1$  and  $T_c \gg T_{MA}$ . In the region  $T > T_{MA}$ , Eq. (24) has a nonzero (positive) solution corresponding to the thermodynamically stable original phase. Below the temperature  $T_{MA}$ , Eq. (24) has another nonzero (negative) thermodynamically stable solution. Therefore, in the case of strong interaction between pseudospins and weak tunneling, the crystal bypasses the pretransition state and directly undergoes the transition from the initial to the final phase.

Now, we consider the case of a moderate strength of interaction between pseudospins ( $\hbar J_0 = 0.04$  eV) and of moderate tunneling ( $\hbar\omega_0 \approx 0.001$  eV). From the condition  $\alpha = 0$ , the temperature of the transition to the pretransition state is found to be  $k_B T_c \approx 0.01$  eV and  $T_c \approx 100$  K. Therefore,  $2\omega_0/J_0 < 1$  and  $T_c < T_{MA}$ . Above the transition temperature, in the region  $T_c \gg T_{MA}$ , Eq. (24) has a single nonzero (positive) thermodynamically stable solution, which corresponds to the initial phase. When the temperature  $T_{MA}$  is approached in the region  $T \geq T_{MA} > T_c$ , there is a unique thermodynamically stable solution to Eq. (24),  $S^z = 0$ , which corresponds to the pretransition state of the crystal. Below  $T_c$  (in the region  $T < T_c$ ), Eq. (24) has a nonzero (negative) thermodynamically stable solution. Therefore, in the case of a moderate strength of interaction between pseudospins and of a moderate tunneling intensity, the transformation of the crystal from the initial to the final phase goes through the pretransition state.

Finally, let us consider the case of a moderate strength of interaction between pseudospins ( $\hbar J_0 = 0.04$  eV) and of intensive tunneling ( $\hbar\omega_0 \approx 0.04$  eV). From the self-consistency equation (24), it follows that the structural transition from the pretransition state to the initial (or final) phase can occur if the ‘‘transverse’’ tunneling field  $2\omega_0$  is weaker than the ‘‘longitudinal’’ interaction field of pseudospins  $J_0$ . Indeed, the temperature  $T_c$  is found by linearizing Eq. (24). The linearized equation has a real solution for  $T_c$  only if  $2\omega_0/J_0 \leq 1$ . Therefore, in the case of  $2\omega_0/J_0 \geq 1$ , there is no solution for  $T_c$  and  $S^z = 0$  is a unique thermodynamically stable solution to Eq. (24) at any temperature. Thus, in the case of moderate interaction between pseudospins and intensive tunneling, the crystal can be only in the pretransition state.

Let the crystal be subjected to a mechanical force field with a nonzero component  $\Omega_a$  decreasing the asymmetry of the double-well potential. In this case, the Landau expansion of the thermodynamic potential near the structural transition point has the form [12]

$$\begin{aligned} \Delta\Phi = & \alpha(S^z)^2/2 + \delta(S^z)^3/3 \\ & + \gamma(S^z)^4/4 + \hbar\Omega_a S^z - (1/2)\lambda\Omega_a^2. \end{aligned} \quad (29)$$

The order parameter  $S^z$  is determined from the thermodynamic equilibrium condition

$$\partial\Delta\Phi/\partial S^z = \alpha S^z + \delta(S^z)^2 + \gamma(S^z)^3 + \hbar\Omega_a = 0. \quad (30)$$

It can be seen from Eq. (30) that the solution  $S^z = 0$  exists if  $\hbar\Omega_a = 0$ . This condition is satisfied when there is no external force,  $\sigma = 0$ , and the stress field in the crystal is equal to zero. Another condition under which the solution  $S^z = 0$  exists is the relation  $\hbar\Omega_a \approx S^z$ . This relation takes place in the vicinity of the critical value of the external force  $\sigma = \sigma_c$ , where the component  $\Omega_a$  of the mechanical force field is of a relaxation character due to softening of the elastic constant  $\lambda = \lambda_0(\sigma - \sigma_c)$ . In this case, the thermodynamic equilibrium equation (30) should be supplemented by the equilibrium equation

$$\partial\Delta\Phi/\partial\Omega_a = \hbar S^z - \lambda_0(\sigma_c - \sigma)\Omega_a = 0. \quad (31)$$

This equation relates the component  $\Omega_a$  of the mechanical force field to the order parameter, and the corresponding self-consistency equation takes the form

$$\tilde{\alpha}S^z + \tilde{\delta}(S^z)^2 + \tilde{\gamma}(S^z)^3 = 0, \quad (32)$$

$$\begin{aligned} \tilde{\alpha} = & \alpha\lambda_0(\sigma_c - \sigma)\hbar^{-2} + 1, \quad \tilde{\delta} = \delta\lambda_0(\sigma_c - \sigma)\hbar^{-2}, \\ \tilde{\gamma} = & \gamma\lambda_0(\sigma_c - \sigma)\hbar^{-2}. \end{aligned} \quad (33)$$

Self-consistency equation (32) has a solution

$$S^z = [-\tilde{\delta} \pm \sqrt{\tilde{\delta}^2 - 4\tilde{\alpha}\tilde{\gamma}}]/2\tilde{\gamma} \quad \text{for} \quad \tilde{\delta}^2 \geq |4\tilde{\alpha}\tilde{\gamma}|, \quad (34)$$

$$S^z = 0 \quad \text{for} \quad \tilde{\delta}^2 \leq |4\tilde{\alpha}\tilde{\gamma}|. \quad (35)$$

It can be seen from Eq. (34) that there is a range ( $\sigma^-$ ,  $\sigma^+$ ) for the external force over which the crystal lattice is in the pretransition state. The value of the external force causing the transition from the original phase to the pretransition state is  $\sigma^- = \sigma_c - 4\gamma[\delta^2\lambda_0]^{-1}$ , and the value of the external force causing the transition from the pretransition state to the final phase is  $\sigma^+ = \sigma_c + (4\mu\hbar^6\lambda_0^{-5}\delta^{-2})^{1/5}$ . For the sake of definiteness, we assumed that the coefficient  $\delta$  is negative in the original phase; therefore, when  $\sigma < \sigma_c$ , we have  $S^z > 0$  and the crystal is in the original phase, whereas for  $\sigma > \sigma_c$  we have  $S^z < 0$  and the crystal is in the final phase.

Thus, when the external force is within the range ( $\sigma^-$ ,  $\sigma^+$ ), the thermodynamically stable solution to self-consistency equation (32) is  $S^z = 0$  and, hence, the crystal is in the pretransition state.

## 6. DISCUSSION OF THE RESULTS

Thus, the proposed model describes a deformed crystal as a quantum system of pseudospins. The quantum behavior of lattice atoms becomes significant when

the characteristic distance between the sites of the original structure and the corresponding sites of the final phase is less than the zero-point oscillation amplitude of atoms (0.1 Å) and when the area under the barrier separating the minima of the double-well potential is less than  $aV_2 = 5 \times 10^{-10}$  eV cm.

Near the structural transition from the initial to the final phase stimulated by external influences (temperature variations, external forces), the area under the barrier between the minima of the double-well potential decreases under an external influence. As a result, the quantum-tunneling effects become significant, the asymmetry of the double-well potential decreases, and the initial state of the lattice with the asymmetric double-well potential becomes unstable with respect to the occurrence of the pretransition state of the lattice with a symmetric double-well potential. The pretransition state is taken to mean a condensed state of the crystal in which a lattice atom is completely delocalized in the symmetric double-well potential because of quantum tunneling; i.e., the atom occupies the site of the initial phase and the corresponding site of the final phase with equal probability.

Thus, on the one hand, a crystal exhibiting structural instability transforms into the pretransition state as the temperature is varied near the structural transition temperature  $T_{MA}$ ; on the other hand, the deformed crystal transforms into the pretransition state as an external force varies in the vicinity of the critical value  $\sigma_c$ .

Let us compare the quantum-tunneling frequency and the frequency of thermally assisted hopping of an electron in a double-well potential in the case where the pretransition state occurs at a temperature  $T_n \approx 300$  K. The average thermal energy of an atom is  $k_B T_n \approx 0.02$  eV, and the thermally assisted hopping frequency is  $\omega_n = k_B T_n / \hbar \approx 10^{13}$  s<sup>-1</sup>. In the case where the barrier height between the minima of the double-well potential is  $V_2 = k_B T_n = 0.02$  eV and the distance between a site of the original lattice and the corresponding site of the final lattice is  $a = 10^{-9}$  cm, the quantum-tunneling frequency of an atom is  $\omega_0 \approx 10^{14}$  s<sup>-1</sup>. Therefore, in a crystal exhibiting structural instability at a temperature much lower than room temperature, the quantum-tunneling mechanism is more efficient than the thermally assisted hopping mechanism. Furthermore, if  $V_2 \gg 0.02$  eV at room temperature, the thermally assisted hopping mechanism is also of minor importance in determining the structural transition. The occurrence of

the pretransition state is associated with the fact that the three-particle interatomic interaction responsible for the formation of the original and final phases weakens significantly near the temperature  $T_{MA}$  of the transition from the initial to the final phase, with the consequence that the two-particle interatomic interaction becomes important and takes part in the formation of the pretransition state.

It is reasonable to suggest that quantum tunneling of atoms is the physical basis of the mechanism for the coherent structural transformations occurring in a crystal under loading [4, 5]. Since the wave function of an atom is significantly delocalized because of quantum tunneling, the pretransition state can be considered a superposition of the initial and final structural states of the crystal [2].

## REFERENCES

1. V. E. Panin, *Fiz. Mezomekh.* **1** (1), 5 (1998).
2. V. E. Egorushkin, E. V. Savushkin, V. E. Panin, and Yu. A. Khon, *Izv. Vyssh. Uchebn. Zaved., Fiz.*, No. 1, 9 (1987).
3. É. V. Kozlov, L. L. Meisner, A. A. Klopotov, and A. S. Taihlashev, *Izv. Vyssh. Uchebn. Zaved., Fiz.*, No. 5, 118 (1985).
4. V. G. Pushin, V. V. Kondrat'ev, and V. N. Khachin, *Izv. Vyssh. Uchebn. Zaved., Fiz.*, No. 5, 5 (1985).
5. A. N. Tyumentsev, I. Yu. Litovchenko, Yu. P. Pinzhin, A. D. Korotaev, and N. S. Surikova, *Fiz. Met. Metall-oved.* **95** (2), 86 (2003).
6. V. E. Panin, *Fiz. Mezomekh.* **2** (6), 5 (1999).
7. V. Heine, M. L. Cohen, and D. Weaire, *Solid State Physics*, Ed. by H. Ehrenreich, F. Seitz, and D. Turnbull (Academic, New York, 1970), Vol. 24 [*Theory of Pseudopotential* (Mir, Moscow, 1973)].
8. E. H. Lieb, *Int. J. Quantum Chem.* **34**, 243 (1983).
9. *Monte Carlo Methods in Statistical Physics*, Ed. by K. Binder (Springer, Berlin, 1979; Mir, Moscow, 1982).
10. P. Resibois and M. De Leener, *Classical Kinetic Theory of Fluids* (Wiley, New York, 1977; Mir, Moscow, 1980).
11. L. D. Landau and E. M. Lifshitz, *Course of Theoretical Physics*, Vol. 3: *Quantum Mechanics: Non-Relativistic Theory*, 4th ed. (Nauka, Moscow, 1989; Pergamon, New York, 1977).
12. L. D. Landau and E. M. Lifshitz, *Course of Theoretical Physics*, Vol. 5: *Statistical Physics*, 3rd ed. (Nauka, Moscow, 1976; Pergamon, Oxford, 1980), Part 1.

*Translated by Yu. Epifanov*

---

**LATTICE DYNAMICS  
AND PHASE TRANSITIONS**

---

# Electrostatic Models of Insulator–Metal and Metal–Insulator Concentration Phase Transitions in Ge and Si Crystals Doped by Hydrogen-Like Impurities

N. A. Poklonski\*, S. A. Vyrko\*, and A. G. Zabrodskii\*\*

\*Belarussian State University, pr. F. Skoriny 4, Minsk, 220050 Belarus

e-mail: poklonski@bsu.by

\*\*Ioffe Physicotechnical Institute, Russian Academy of Sciences, Politekhnicheskaya ul. 26, St. Petersburg, 194021 Russia

Received October 29, 2003

**Abstract**—Two electrostatic models have been developed that allow calculation of the critical concentration of hydrogen-like impurities in three-dimensional crystalline semiconductors corresponding to the insulator–metal and metal–insulator transition in the zero temperature limit. The insulator–metal transition manifests itself as a divergence of the static permittivity observed in lightly compensated semiconductors as the concentration of polarizable impurities increases to the critical level. The metal–insulator transition is signaled by the divergence of the dc electrical resistivity in heavily doped semiconductors as the compensation of the majority impurity increases (or its concentration decreases). The critical impurity concentration corresponds to the coincidence of the percolation level for the majority carriers with the Fermi level. The results of the calculations made with these models fit the experimental data obtained for *n*- and *p*-type silicon and germanium within a broad range of their doping levels and impurity compensation. © 2004 MAIK “Nauka/Interperiodica”.

## 1. INTRODUCTION

The critical concentration  $N_c$  of the majority dopant for the insulator–metal (I–M) and metal–insulator (M–I) phase transitions is derived in the zero temperature limit ( $T \rightarrow 0$ ) from low-frequency measurements of the macroscopic permittivity and electrical resistivity, respectively. It is believed that the critical concentrations of the transition determined by these two methods coincide [1]. A relevant review and a comparison of the microscopic models describing the difference between an insulator and a conductor under dc bias can be found in [2]. Performing calculations and making predictions from these models meets, however, with difficulties.

On the insulator side of the I–M transition, increasing the dopant concentration  $N$  up to the critical level  $N_c$  brings about a divergence of the relative permittivity  $\epsilon_r(N)$  of a crystalline sample [3–5]. Quantitative description of the behavior of  $\epsilon_r(N)$  in the vicinity of the I–M transition is, however, lacking (see, e.g., [5]).

On the metallic side, the M–I transition manifests itself experimentally for  $T \rightarrow 0$  as a divergence of the dc electrical resistivity as the concentration of the dopant decreases or as the degree of its compensation increases. On the metallic side of the transition, the majority carrier concentration is  $n_c = (1 - K)N_c$ , where  $K$  is the semiconductor compensation. The critical carrier concentration  $n_c$  for the M–I Anderson transition driven by the introduction of compensating impurities into a heavily doped semiconductor has been experimentally shown [6] to be well described, for high com-

penetration ratios ( $K \rightarrow 1$ ), in terms of percolation theory [7], according to which the transition can be considered a consequence of the Fermi level  $E_F$  becoming equalized with the percolation level  $E_\mu$  in the potential relief of large-scale (non-tunneling) fluctuations. For small compensation ratios (the value  $K = 0$  corresponds to the Mott transition), the fluctuations are not large scale, so the critical concentration  $n_c$  can be described by Mott’s relation [8–12]  $n_c^{1/3} a_B \approx 0.25$ , where  $a_B = 4\pi\epsilon\hbar^2/me^2$  is the Bohr radius for the electron (hole) with an effective mass  $m$  in a lattice with static permittivity  $\epsilon = \epsilon_r\epsilon_0$  ( $\epsilon_0$  is the free-space permittivity). The case of intermediate compensations ( $K \approx 0.5$ ) has been explored to a lesser extent, thus making description of the dependence of the critical carrier concentration  $n_c$  on the compensation of the majority impurity  $K$  at the M–I transition an important problem.

The present communication reports on an analytical description of the I–M and M–I transitions in crystalline semiconductors doped by hydrogen-like impurities. The variation of the macroscopic static permittivity at the I–M transition is treated in terms of the Clausius–Mossotti–Lorentz–Lorenz (CMLL) model. The M–I transition is considered with due account of spatial fluctuations of electrostatic energy in the crystal. Only pure Coulomb interaction among the nearest neighbor charges (the majority carriers and impurity ions) is included.

## 2. THE INSULATOR–METAL TRANSITION

For the sake of definiteness, we consider an  $n$ -type crystalline semiconductor with a concentration of donors  $N = N_0 + N_{+1}$  in charge states (0) and (+1) and with acceptors in the charge state (–1) with concentration  $N_{-1} = KN$ , where  $K$  is the donor compensation ratio. The charge neutrality condition can be written as  $N_{+1} = KN = N_{-1}$ . On the insulator side, at a temperature  $T \rightarrow 0$ , the criterion for the onset of the I–M transition is divergence of the relative permittivity  $\epsilon_r(N)$  of a crystalline sample with the hydrogen-like donor concentration  $N$  increasing to the critical value  $N_c$ .

The permittivity of the material governs the connection between the local electric field  $E_l$  acting on each (native or impurity) polarizable atom and the average macroscopic field  $E_{av}$  [13–15]. This connection is approximated by the CMLL relation. It is usually assumed that the CMLL relation is applicable only to systems made up of single point dipoles. However, in reviews [13, 14], it was shown convincingly that the CMLL relation is also valid for insulators and semiconductors of a fairly general class, including those consisting of atoms or molecules with overlapping electron shells.

In terms of our model [11], with allowance for the superposition of the electric fields of the crystal matrix atoms with a concentration  $N_m$  and polarizability  $\alpha_m$  of a matrix atom and the electric fields of electrically neutral donors with a concentration  $N_0 = (1 - K)N$  and polarizability  $\alpha_0$  of a donor atom, we can write (cf. [16, 17])

$$E_l = E_{av} + \left( \frac{\alpha_m N_m}{\beta_m} + \frac{\alpha_0 N_0}{3} \right) E_l, \quad (1)$$

where  $\beta_m$  is a fitting parameter taking into account the point symmetry of the lattice ( $\beta_m = 3$  corresponds, in accordance with the CMLL model, to the case of the matrix atoms making up a cubic lattice or distributed at random) and  $N_m \gg N_0$ .

The polarizability of a single neutral hydrogen-like donor [18] is  $\alpha_0 = 18\pi a_H^3$ , where  $a_H = e^2/8\pi\epsilon I_d$  is the Bohr orbit radius of the optical electron of a donor with ionization energy  $I_d$ . For  $N < N_c$ , the average radius of the spherical crystal region per neutral donor, which is  $0.62[(1 - K)N]^{-1/3}$ , exceeds  $a_H$  by more than a factor of 2.5 even for  $K \rightarrow 0$  [1, 3, 4]. Therefore, the use of the crystal lattice permittivity  $\epsilon = \epsilon_r \epsilon_0$  in the relation for the Bohr radius  $a_H$  is valid.

The total macroscopic polarization of crystal matrix atoms and neutral donors can be written as [15]

$$(\alpha_m N_m + \alpha_0 N_0) E_l = [\epsilon_r(N_0) - 1] E_{av}, \quad (2)$$

where  $\epsilon_r(N_0)$  is the relative permittivity of the doped semiconductor. For a crystal without impurities ( $N \rightarrow$

0), Eqs. (1) and (2) yield the relative permittivity of the crystal lattice (matrix):

$$\epsilon_r(N_0 \rightarrow 0) = 1 + \frac{\alpha_m N_m}{1 - \alpha_m N_m / \beta_m} = \epsilon_r. \quad (3)$$

Using Eqs. (1)–(3), we obtain the macroscopic relative permittivity of the donor-doped semiconductor:

$$\epsilon_r(N_0) = 1 + \frac{3(\epsilon_r - 1)\beta_m + 3(\epsilon_r - 1 + \beta_m)\alpha_0 N_0}{3\beta_m - (\epsilon_r - 1 + \beta_m)\alpha_0 N_0}; \quad (4)$$

in the absence of neutral donors ( $N_0 \rightarrow 0$ ), we come to  $\epsilon_r(N_0 \rightarrow 0) = \epsilon_r$ .

The criterion  $\epsilon_r(N_0) \rightarrow \infty$  for the onset of the I–M transition for  $N \rightarrow N_c$  or  $N_0 \rightarrow N_{0c} = (1 - K)N_c$  can be used to derive from Eq. (4) the following relation:  $3\beta_m - (\epsilon_r - 1 + \beta_m)(1 - K)\alpha_0 N_c = 0$ . For  $\beta_m = 3$ , we obtain the critical donor concentration

$$N_c = \frac{9}{(1 - K)(\epsilon_r + 2)\alpha_0}, \quad (5)$$

$$N_c^{1/3} a_H = \frac{0.542}{[(1 - K)(\epsilon_r + 2)]^{1/3}},$$

where  $\alpha_0 = 18\pi a_H^3$  is the polarizability of the dopant in charge state (0) and  $a_H = e^2/8\pi\epsilon_r \epsilon_0 I_{d(a)}$  is the electron (hole) orbit radius in a single hydrogen-like donor (acceptor) localized in a crystal lattice with relative permittivity  $\epsilon_r$ .

The  $N_c(a_H)$  relation calculated from Eq. (5) for  $K \rightarrow 0$  is plotted in Fig. 1 by solid lines [(1) for Si with  $\epsilon_r = 11.5$  and (2) for Ge with  $\epsilon_r = 15.4$ ]. Note that the critical concentration  $N_c$  calculated with models [16, 17] for  $\epsilon_r(N_0)$  was found to be  $\epsilon_r(\epsilon_r + 2)/3$  and  $\epsilon_r$  times larger, respectively, than the value obtained using Eq. (5) for the same polarizability  $\alpha_0 = 18\pi a_H^3$  per donor (acceptor).

Equations (4) and (5) yield the dependence of the macroscopic permittivity on the doping level of a crystalline semiconductor (the ratio of the dopant concentration  $N$  on the insulator side to its critical concentration  $N_c$ ):

$$\epsilon_r(N) = \frac{\epsilon_r + 2N/N_c}{1 - N/N_c}, \quad (6)$$

where  $N/N_c = N_0/N_{0c}$ , with  $N_0 = (1 - K)N$  being the concentration of the majority dopant in charge state (0).

The  $\epsilon_r(N)$  relation calculated from Eq. (6) for crystalline silicon is plotted in Fig. 2 together with experimental data. The experimental data [3, 5, 19, 20] were processed using average values of the critical dopant concentrations for  $K \rightarrow 0$  (see the data in Fig. 1):  $N_c(\text{Si} : \text{As}) = 7.8 \times 10^{18} \text{ cm}^{-3}$ ,  $N_c(\text{Si} : \text{P}) = 3.81 \times 10^{18} \text{ cm}^{-3}$ , and  $N_c(\text{Si} : \text{B}) = 4.1 \times 10^{18} \text{ cm}^{-3}$ .

Note that the use of Eqs. (5) and (6) is more appropriate for low compensation ratios of the majority dopant ( $K \ll 1$ ).

### 3. THE METAL-INSULATOR TRANSITION

Taking into account spatial fluctuations of the electrostatic potential, the average electron concentration  $n$  in the conduction band of a degenerate  $n$ -type semiconductor can be described by the relation [7, 21, 22]

$$\begin{aligned} n &= \frac{\nu(2m)^{3/2+\infty}}{2\pi^2\hbar^3} \int_{-\infty}^{+\infty} f dE \int_{-\infty}^{+\infty} (E-U)^{1/2} P(U) dU \\ &= \frac{\nu}{\pi^2} \int_{-\infty}^{+\infty} P(U) dU \int_0^{\infty} f k^2 dk, \end{aligned} \quad (7)$$

where  $\nu$  is the number of valleys, i.e., the energy minima in the band allowed for the majority carriers ( $\nu = 4$  for  $n$ -Ge,  $\nu = 6$  for  $n$ -Si,  $\nu = 1$  for  $p$ -Ge and  $p$ -Si);  $m$  is the effective electron mass in one valley;  $f = [1 + \exp((E - E_F)/k_B T)]^{-1}$  is the Fermi-Dirac function;  $P(U) = (W\sqrt{2\pi})^{-1} \exp(-U^2/2W^2)$  is the Gaussian distribution of fluctuations of the electrostatic electron potential energy  $U$  created by point charges in the crystal (impurity ions and conduction electrons);  $W$  is the rms fluctuation; and the total energy  $E = (\hbar k)^2/2m + U$  of a conduction electron with quasi-momentum  $\hbar k$  is reckoned from the conduction band bottom of the undoped crystal (in the band gap, the electron energy  $E$  is negative).

On the metallic side of the M-I transition, where all impurities are ionized and  $n = (1 - K)N$ , Eq. (7) for temperature  $T \rightarrow 0$  can be recast to [11, 22]

$$\begin{aligned} n &= \frac{\nu}{\pi^2} \int_{-\infty}^{E_F} P(U) dU \int_0^{k_F(U)} k^2 dk \\ &= \frac{\nu}{3\pi^2} \int_{-\infty}^{E_F} [k_F(U)]^3 P(U) dU, \end{aligned} \quad (8)$$

where  $k_F(U) = \hbar^{-1}(2m(E_F - U))^{1/2}$  is the Fermi quasi-wave vector of an electron with kinetic energy  $E_F - U > 0$  in the conduction band. The charge neutrality condition of the crystal can be written as  $n + KN = N$ , where  $N$  is the concentration of donors and  $KN$  is that of acceptors.

Based on Eq. (8) and the condition of equality of the percolation level (mobility edge)  $E_\mu$  under a dc bias and the Fermi level  $E_F$ , the dependence of the critical majority dopant concentration for the onset of the M-I transition,  $N_c = n_c/(1 - K)$ , on the compensation ratio  $K$  for

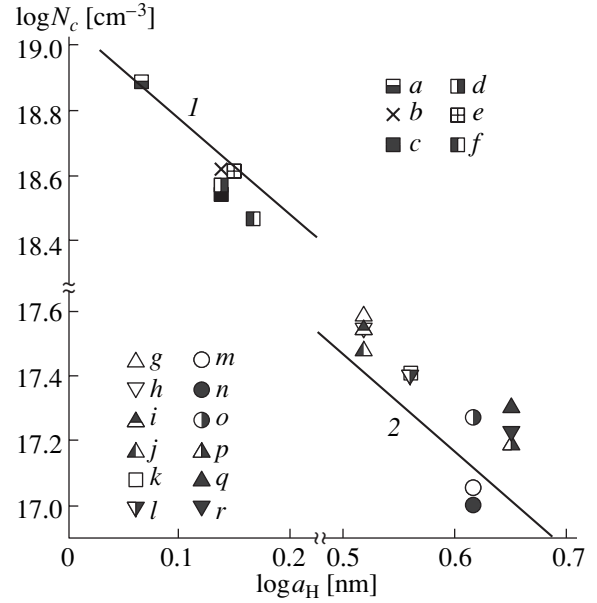


**Fig. 1.** Critical concentration  $N_c$  of hydrogen-like impurities for the onset of the I-M phase transition in Ge and Si plotted vs. Bohr radius  $a_H$  for  $K \leq 0.01$ . Points are experimental data: (a)  $n$ -Si : As [23], (b)  $n$ -Si : P [24], (c)  $n$ -Si : P [25], (d)  $n$ -Si : P [26], (e)  $p$ -Si : B [27], (f)  $n$ -Si : Sb [28], (g)  $n$ -Ge : As [29], (h)  $n$ -Ge : As [30], (i)  $n$ -Ge : As [1, 31], (j)  $n$ -Ge : As [32], (k)  $n$ -Ge : P [29], (l)  $n$ -Ge : P [1, 31], (m)  $p$ -Ge : Ga [29], (n)  $p$ -Ge : Ga [33], (o)  $p$ -Ge : Ga [34], (p)  $n$ -Ge : Sb [29], (q)  $n$ -Ge : Sb [35], and (r)  $n$ -Ge : Sb [36]. Line 1 is  $N_c(a_H)$  for Si calculated from Eq. (5), and line 2 is the same for Ge.

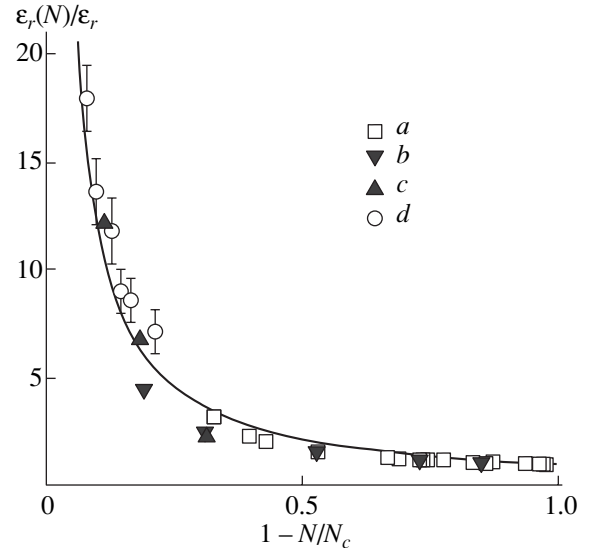


**Fig. 2.** Macroscopic relative permittivity  $\epsilon_r(N)$  of lightly compensated silicon plotted vs. majority dopant concentration  $N$ . Points are experimental data: (a)  $n$ -Si : As [3], (b)  $n$ -Si : P [19], (c)  $n$ -Si : P [20], and (d)  $p$ -Si : B [5]. The curve presents  $\epsilon_r(N)$  calculated from Eq. (6) for  $\epsilon_r = 11.5$ .

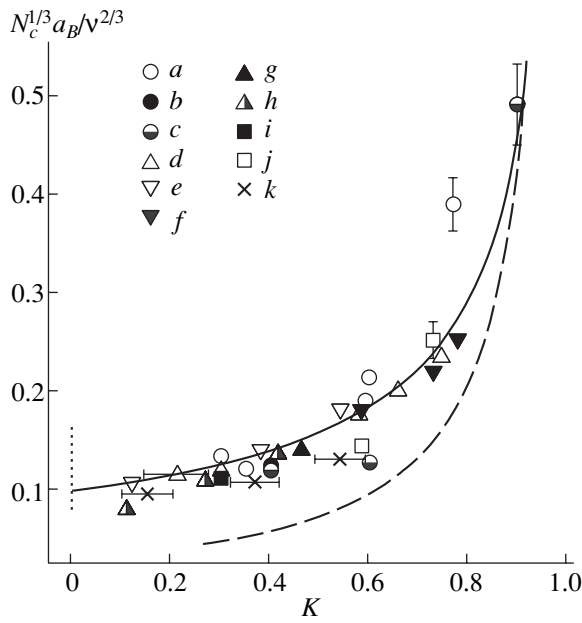


**Fig. 3.** Critical concentration  $N_c$  of donors (acceptors) in Ge and Si plotted vs. their compensation ratio  $K$ . Points are experimental data: (a)  $p$ -Ge : Ga [6, 38, 39], (b)  $p$ -Ge : Ga [33], (c)  $p$ -Ge : Ga [40], (d)  $n$ -Ge : As [6, 29, 41], (e)  $n$ -Ge : As [30], (f)  $n$ -Ge : As [35], (g)  $n$ -Ge : Sb [35], (h)  $n$ -Ge : Sb [29], (i)  $n$ -Ge : Sb [42], (j)  $n$ -Ge : P [6, 29], and (k)  $n$ -Si : P [24]. Solid line is calculated using Eq. (10), and dashed line is calculated within model [7]. Dotted line at  $K = 0$  identifies the range of experimental data on  $N_c$  covered in [1, 23–36] and plotted in Fig. 1 with an average value  $N_c^{1/3} a_B / v^{2/3} = 0.1$ .

this dopant can be presented, according to [11, 22], in the form (cf. [7])

$$N_c^{1/3} a_B = 0.238 \left( \frac{W}{E_B} \right)^{1/2} \times \left[ \frac{v}{1-K} \int_{-\infty}^{E_\mu/W} \left( \frac{E_\mu}{W} - x \right)^{3/2} \exp\left( \frac{-x^2}{2} \right) dx \right]^{1/3}, \quad (9)$$

where  $a_B = 4\pi\epsilon_r\epsilon_0\hbar^2/me^2$  and  $E_B = e^2/8\pi\epsilon_r\epsilon_0 a_B$  are the Bohr radius and energy of an electron (hole), respectively, and  $\epsilon_r\epsilon_0$  is the static permittivity of the undoped crystal.

In the model proposed in [11, 22], the quantity  $W = W_{mn} \approx 1.64(e^2/4\pi\epsilon)(8\pi N_c/3)^{1/3}$  originates from the Coulomb interaction of the nearest neighbor charges (impurity ions, electrons) only. The value  $E_\mu/W_{mn} = -1.15$  is found by fitting equality (9) to experimental data [1, 23–36] for uncompensated semiconductors [ $N_c(K \rightarrow 0)]^{1/3} a_B / v^{2/3} = 0.1$  (Fig. 1). In what follows, we assume that the  $E_\mu/W_{mn}$  ratio is  $-1.15$  for all compensations ( $0 < K < 1$ ). In this case, Eq. (9) yields the dependence of the

critical concentration of the impurity,  $N_c$ , on its compensation  $K$  in the form

$$\frac{N_c^{1/3} a_B}{v^{2/3}} = \frac{0.1}{(1-K)^{2/3}}. \quad (10)$$

The function  $N_c(K)$  calculated from Eq. (10) is plotted in Fig. 3 with a solid line.

The quantity  $W = W_s = [(e^2/4\pi\epsilon)/\sqrt{2}](1 + K)^{2/3}[N_c/(1-K)]^{1/3}$  in model [7] originates from the screening of large-scale dopant-ion concentration fluctuations by electrons.<sup>1</sup> Assuming the critical fractional volume of the semiconductor that contains electrons and corresponds to their percolation level to be 0.17, we obtain  $E_\mu/W_s = -0.675\sqrt{2}$ . The function  $N_c(K)$  calculated within model [7] using Eq. (9) for  $W = W_s$  for a compensated semiconductor is shown in Fig. 3 with a dashed line.

#### 4. RESULTS AND DISCUSSION

The dependences of the critical concentration  $N_c$  for the Mott transition at  $K = 0$  on the Bohr radius  $a_B$ , calculated using the criterion  $\epsilon_r(N_0) \rightarrow \infty$  [see Eq. (5)], are displayed graphically in Fig. 1 for Si and Ge (curves 1 and 2, respectively). The points in Fig. 1 are experimental data for  $n$ - and  $p$ -type germanium and silicon [1, 23–36].

The critical impurity concentration  $N_c$  on the metallic side of the M–I transition is given by Eq. (9) and is a function of the ratio of the Fermi level (equal to the percolation level  $E_\mu$ ) to the impurity band width  $W$ . The parameter  $E_\mu/W$  was found by extrapolating Eq. (9) to the limit  $K = 0$  and by subsequent comparison with experimental data [1, 23–36] available for  $N_c$  for the case of  $K \leq 0.01$  (Fig. 1).

The dependence of the critical concentration  $N_c$  of the majority dopant for the M–I transition on the compensation ratio  $K$  on the metallic side of the transition, calculated using Eq. (10), is plotted by a solid line in Fig. 3, which also displays the available experimental data we are aware of on  $n$ - and  $p$ -Ge [6, 29, 30, 33–35, 38–42] and  $n$ -Si : P [24], with the dashed line showing the prediction made in [7] for  $W = W_s$ . We see that the proposed model fits experimental data well practically throughout the total range of compensations.

A comparison of the experimental data presented in Figs. 1 and 3 with Eq. (9) for  $W = W_{mn}$  shows that the percolation level for a Gaussian distribution of electrostatic potential fluctuations lies within the interval  $-1.5W < E_\mu < -W$  (here, the minus sign means that the percolation level lies in the band gap). This result correlates well with estimates made by other researchers

<sup>1</sup> The temperature dependence of the large-scale potential relief  $W = W_s$  is treated in [37].



[7, 43, 44]. Note that model [7] is valid only for large compensation ratios  $K$ . As seen from Fig. 3, for  $K < 0.5$ , the calculation made with model [7] yields values of  $N_c$  less than the experimental figures.

## 5. CONCLUSIONS

Thus, we have developed models for the I–M and M–I transitions in crystalline covalent semiconductors.

On the insulator side, the transition manifests itself as a divergence of the relative permittivity  $\epsilon_r(N_0)$  of lightly compensated semiconductors, which is due to polarization of neutral impurity atoms as their concentration increases from  $N_0$  to  $N_{0c} = (1 - K)N_c$ . The critical concentration  $N_{0c}$  is expressed through the Bohr radius  $a_H = e^2/8\pi\epsilon I_{d(a)}$  for an electron (hole) on a neutral donor (acceptor) with an ionization energy  $I_{d(a)}$  in a crystal with lattice permittivity  $\epsilon = \epsilon_r\epsilon_0$ . The  $\epsilon_r(N_0)$  dependence is quantitatively described for Si crystals near the I–M transition ( $N_0 \rightarrow N_{0c}$ ).

The M–I transition on the metallic side is observed as a collapse of metallic conduction as the concentration of the dopant atoms is decreased or their compensation ratio is increased. Use is made of the Bohr radius  $a_B = 4\pi\epsilon\hbar^2/me^2$  for the majority carriers, which depends on the effective mass  $m$  of the electron (hole) and the static permittivity  $\epsilon_r\epsilon_0$  of the undoped crystal matrix.<sup>2</sup> It is assumed that the amplitude of electrostatic potential fluctuations is determined by the interaction of the nearest neighbor charges (impurity ions and majority carriers). The dependence of the critical majority dopant concentration  $N_c$  for the onset of the M–I transition on the compensation ratio  $K$  for this dopant was found and compared with the prediction from model [7] and experimental data available for Ge and Si within a broad range of variation of the compensation ratio.

## ACKNOWLEDGMENTS

This study was supported by the Belarussian Foundation for Basic Research (project no. F01-199) and the Russian Foundation for Basic Research (project no. 01-02-17813).

## REFERENCES

1. P. P. Edwards and M. J. Sienko, Phys. Rev. B **17** (6), 2575 (1978).
2. R. Resta, J. Phys.: Condens. Matter **14** (20), R625 (2002).
3. T. G. Castner, Philos. Mag. B **42** (6), 873 (1980).
4. T. G. Castner, N. K. Lee, H. S. Tan, L. Moberly, and O. Symko, J. Low Temp. Phys. **38** (3–4), 447 (1980).
5. M. Lee, J. G. Massey, V. L. Nguyen, and B. I. Shklovskii, Phys. Rev. B **60** (3), 1582 (1999).
6. A. G. Zabrodskii, Fiz. Tekh. Poluprovodn. (Leningrad) **14** (8), 1492 (1980) [Sov. Phys. Semicond. **14**, 886 (1980)].
7. B. I. Shklovskii and A. L. Éfros, *Electronic Properties of Doped Semiconductors* (Nauka, Moscow, 1979; Springer, New York, 1984).
8. V. F. Gantmakher, Usp. Fiz. Nauk **172** (11), 1283 (2002) [Phys. Usp. **45**, 1165 (2002)].
9. A. A. Likal'ter, Usp. Fiz. Nauk **170** (8), 831 (2000) [Phys. Usp. **43**, 777 (2000)].
10. N. Mott, Usp. Fiz. Nauk **105** (2), 321 (1971).
11. N. A. Poklonskiĭ and A. I. Syaglo, Fiz. Tverd. Tela (St. Petersburg) **40** (1), 147 (1998) [Phys. Solid State **40**, 132 (1998)].
12. A. G. Zabrodskii, Philos. Mag. B **81** (9), 1131 (2001).
13. A. P. Vinogradov, Radiotekh. Élektron. (Moscow) **45** (8), 901 (2000).
14. V. L. Ginzburg and E. G. Maksimov, Sverkhprovodimost: Fiz., Khim., Tekh. **5** (9), 1543 (1992).
15. I. E. Tamm, *The Principles of Electricity Theory*, 10th ed. (Nauka, Moscow, 1989).
16. J. Kastellan and F. Seitz, in *Semi-Conducting Materials* (Butterworths, London, 1951; Inostrannaya Literatura, Moscow, 1954).
17. S. Dhar and A. H. Marshak, Solid-State Electron. **28** (8), 763 (1985).
18. L. D. Landau and E. M. Lifshitz, *Course of Theoretical Physics, Vol. 3: Quantum Mechanics: Non-Relativistic Theory*, 3rd ed. (Nauka, Moscow, 1974; Pergamon, New York, 1977).
19. M. Capizzi, G. A. Thomas, F. DeRosa, R. N. Bhatt, and T. M. Rice, Phys. Rev. Lett. **44** (15), 1019 (1980).
20. H. F. Hess, K. DeConde, T. F. Rosenbaum, and G. A. Thomas, Phys. Rev. B **25** (8), 5578 (1982).
21. E. O. Kane, Solid-State Electron. **28** (1/2), 3 (1985).
22. N. A. Poklonskiĭ and S. A. Vyrko, Zh. Prikl. Spektrosk. **69** (3), 375 (2002) [J. Appl. Spectr. (Kluwer) **69** (3), 434 (2002)].
23. P. F. Newman and D. F. Holcomb, Phys. Rev. B **28** (2), 638 (1983).
24. U. Thomanschefsky and D. F. Holcomb, Phys. Rev. B **45** (23), 13356 (1992).
25. P. Dai, Y. Zhang, and M. P. Sarachik, Phys. Rev. B **49** (19), 14039 (1994).
26. G. A. Thomas, M. Paalanen, and T. F. Rosenbaum, Phys. Rev. B **27** (6), 3897 (1983).
27. P. Dai, S. Bogdanovich, Y. Zhang, and M. P. Sarachik, Phys. Rev. B **52** (16), 12439 (1995).
28. A. P. Long, H. V. Myron, and M. Pepper, J. Phys. C **17** (17), L425 (1984).
29. A. G. Zabrodskii, M. V. Alekseenko, A. G. Andreev, and M. P. Timofeev, in *Abstracts of 25th All-Union Meeting on Low-Temperature Physics* (Leningrad, 1988), Part 3, p. 60.
30. R. Rentzsch, M. Müller, Ch. Reich, B. Sandow, A. N. Ionov, P. Fozooni, M. J. Lea, V. Ginodman, and I. Shlimak, Phys. Status Solidi B **218** (1), 233 (2000).
31. M. N. Alexander and D. F. Holcomb, Rev. Mod. Phys. **40** (4), 815 (1968).

<sup>2</sup> For Ge and Si crystals, both  $n$  and  $p$  type,  $a_H \neq a_B$ . Clearly enough, for the hydrogen atom,  $\epsilon_r = 1$ ,  $m = m_0$ , and  $a_H = a_B$ .

32. A. T. Lonchakov, G. A. Matveev, and I. M. Tsidi'kovskii, *Fiz. Tekh. Poluprovodn. (Leningrad)* **22** (8), 1396 (1988) [*Sov. Phys. Semicond.* **22**, 884 (1988)].
33. H. Fritzsche, *Philos. Mag. B* **42** (6), 835 (1980).
34. K. M. Itoh, *Phys. Status Solidi B* **218** (1), 211 (2000).
35. W. Sasaki and C. Yamanouchi, *J. Non-Cryst. Solids* **4**, 183 (1970).
36. S. B. Field and T. F. Rosenbaum, *Phys. Rev. Lett.* **55** (5), 522 (1985).
37. V. G. Karpov, *Fiz. Tekh. Poluprovodn. (Leningrad)* **15** (2), 217 (1981) [*Sov. Phys. Semicond.* **15**, 127 (1981)].
38. A. G. Zabrodskii and A. G. Andreev, *Int. J. Mod. Phys. B* **8** (7), 883 (1994).
39. A. G. Zabrodskii, A. G. Andreev, and S. V. Egorov, *Phys. Status Solidi B* **205** (1), 61 (1998).
40. R. Rentzsch, O. Chiatti, M. Müller, and A. N. Ionov, *Phys. Status Solidi B* **230** (1), 237 (2002).
41. A. G. Zabrodskii and K. N. Zinov'eva, *Zh. Éksp. Teor. Fiz.* **86** (2), 727 (1984) [*Sov. Phys. JETP* **59**, 425 (1984)].
42. F. R. Allen, R. H. Wallis, and C. J. Adkins, in *Proceedings of 5th International Conference on Amorphous and Liquid Semiconductors, Garmisch-Partenkirchen, 1973*, Ed. by J. Stuke and W. Brening (Taylor and Francis, London, 1974), Vol. 2, p. 895.
43. J. M. Ziman, *Models of Disorder: the Theoretical Physics of Homogeneously Disordered Systems* (Cambridge Univ. Press, London, 1979; Mir, Moscow, 1982).
44. V. L. Bonch-Bruевич, *Usp. Fiz. Nauk* **140** (4), 583 (1983) [*Sov. Phys. Usp.* **26**, 664 (1983)].

*Translated by G. Skrebtsov*

## LOW-DIMENSIONAL SYSTEMS AND SURFACE PHYSICS

# Chemisorption on a Quantum-Well Wire

**R. P. Meĭlanov\***, **B. A. Abramova\*\***, **G. M. Musaev\*\***, and **M. M. Gadzhialiev\*\*\***

\* *Institute of Geothermal Problems, Dagestan Scientific Center, Russian Academy of Sciences,  
pr. Kalinina 39a, Makhachkala, 367030 Russia*

*e-mail: lan\_rus@dgu.ru*

\*\* *Dagestan State University, ul. M. Gadzhieva 43a, Makhachkala, 367025 Russia*

\*\*\* *Institute of Physics, Dagestan Scientific Center, Russian Academy of Sciences,  
ul. 26 Bakinskikh Komissarov 94, Makhachkala, 367003 Russia*

Received September 5, 2003

**Abstract**—The specific features of chemisorption on a quantum-well wire are studied. It is shown that the energy of an electron of an adatom chemisorbed on the quantum-well wire changes jumpwise with variations in the wire radius. © 2004 MAIK “Nauka/Interperiodica”.

### 1. INTRODUCTION

Since particular research interest has been expressed in the properties of quantum wires, it is important to investigate the chemisorption on a quantum-well wire. The specific features of chemisorption of an atom are governed by the density of states of the electronic subsystem of the substrate. For a quantum-confined film, it has been demonstrated that the energy of the electronic subsystem of a chemisorbed atom is an oscillating function of the film thickness and external magnetic field [1–5]. This is associated with the fact that the density of states of a quantum-confined metallic film depends on the film thickness and external quantizing magnetic field in a stepwise manner.

In this work, we investigated the case where a quantum-well wire serves as a substrate.

### 2. THEORETICAL BACKGROUND

Theoretical treatment will be performed in the framework of the Anderson–Newns model [6–10] generalized to the case of chemisorption on low-dimensional systems [1–5]. According to the Anderson–Newns model [6–10], the energy of an electron of the adatom can be represented by the relationship  $E_{a,s} = \varepsilon_a + U\langle n \rangle$ , where  $\varepsilon_a$  is the energy of an electron of an isolated atom,  $U$  is the potential of the intra-atomic Coulomb repulsion, and  $\langle n \rangle$  is the perturbation of the electron density of the adatom due to the interaction with the substrate. For the perturbation of the electron density of the adatom  $\langle n \rangle$ , we can write the relationship

$$\langle n \rangle = \int_{-\infty}^{\infty} \frac{d\omega}{\pi} \hat{g}(\omega),$$

where  $\hat{g}$  is the correlation function of the electron of the adatom. Basic relationships for equilibrium correla-

tion functions of electrons of an adatom and a substrate are presented in our previous work [5].

In our case, the electron energy spectrum of a quantum-well wire can be described within the model of an infinitely deep two-dimensional potential well in the following form [11]:

$$E_{np} = \frac{\hbar^2 \alpha_n^2}{2mR^2} + \frac{p_x^2}{2m}. \quad (1)$$

Here,  $R$  is the radius of the quantum-well wire,  $\alpha_n$  are the roots of the Bessel function  $J_l(\alpha_{kl}) = 0$  in ascending order,  $m$  is the electron mass, and  $p_x$  is the electron momentum along the quantum-well wire. In particular, for the first four roots, we have the following values:  $\alpha_1 = \alpha_{10} = 2.42$ ,  $\alpha_2 = \alpha_{11} = 3.835$ ,  $\alpha_3 = \alpha_{21} = 5.14$ , and  $\alpha_4 = \alpha_{12} = 5.5$ .

The density of states of a quantum-well wire takes the form

$$\begin{aligned} \rho(\omega) &= \sum_n \int_{-\infty}^{\infty} \frac{dp_x dx}{2\pi\hbar} \frac{\Gamma_{np}}{(\omega - E_{np_x})^2 + \Gamma_{np}^2} \\ &= (\Gamma \rightarrow 0) = \frac{L_x \sqrt{2m}}{\pi\hbar} \sum_n \frac{\Theta(\omega - \varepsilon_n)}{\sqrt{(\omega - \varepsilon_n)}}. \end{aligned} \quad (2)$$

Here,  $L_x$  is the linear size of the quantum-well wire and  $\Theta(x)$  is the Heaviside step function. The electron concentration can be represented as follows:

$$N = \frac{\sqrt{2m}}{\pi^2 \hbar R^2} \sum_{n=1}^{n_F} \sqrt{\mu - \varepsilon_n}, \quad (3)$$

where  $n_F$  is the number of filled discrete energy levels of the quantum-well wire. Expression (3) relates the chemical potential  $\mu$ , the electron concentration  $N$ , and

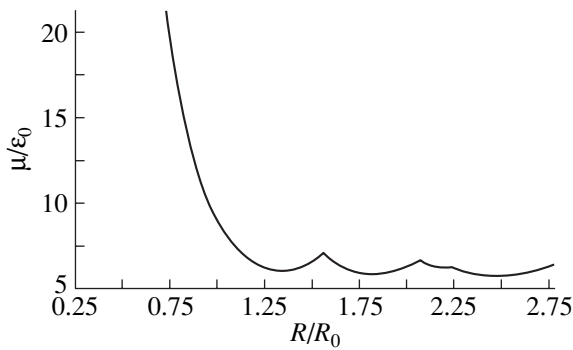


**Fig. 1.** Dependence of the dimensionless chemical potential  $\mu/\varepsilon_0$  on the dimensionless radius  $R/R_0$  of the quantum-well wire.

the radius  $R$  of the quantum-well wire:  $\mu = \mu(R, N)$ . It follows from expression (3) that the chemical potential is an oscillating function of the wire radius. The wire radius at which the next  $n + l$  energy level is filled is determined from the condition  $\mu(R_n, N) = \varepsilon_{n+1}$ . No general expression describing the radius of a quantum-well wire  $R_n$  has been derived to date. For example, for the quantum-wire radii  $R_1$  and  $R_2$ , we have the following expressions:  $R_1 = R_0(\alpha_2^2 - \alpha_1^2)^{1/6}$  and  $R_2 = R_0[2\alpha_3^2 - \alpha_1^2 - \alpha_2^2 + 2\sqrt{\alpha_3^4 + \alpha_1^2\alpha_2^2 - \alpha_3^2(\alpha_1^2 + \alpha_2^2)}]^{1/6}$ . Here,  $R_0 = (\pi^2 N)^{-1/3}$  is the characteristic scale. Figure 1 shows the dependence of the dimensionless chemical potential on the dimensionless radius of the quantum-well wire  $\mu/\varepsilon_0(R/R_0)$  calculated with the use of expression (3). As can be seen from Fig. 1, the dependence  $\mu/\varepsilon_0(R/R_0)$  exhibits an oscillatory behavior.

When calculating the energy of the electron of the adatom  $E_{a,s}$ , we used the expression

$$\langle n \rangle = \frac{1}{2\pi} \int_{-\infty}^{\infty} d\omega \hat{g}(\omega). \quad (4)$$

The correlation function  $\hat{g}(\omega)$  can be written in the following form [5]:

$$\hat{g}(\omega) = g^R(\omega) \hat{\sigma}_a(\omega) g^A(\omega) = |V|^2 f(\omega) a(\omega). \quad (5)$$

Here,  $f(\omega)$  is the Fermi–Dirac distribution function. The spectral function of the adatom  $a(\omega)$  is determined by the relationship

$$a(\omega) = \frac{\sum_{ip} A_{ip}(\omega)}{[\omega - \varepsilon_a - U \langle n \rangle]^2 + |V|^4 \left[ \sum_{ip} A_{ip}(\omega) \right]^2}, \quad (6)$$

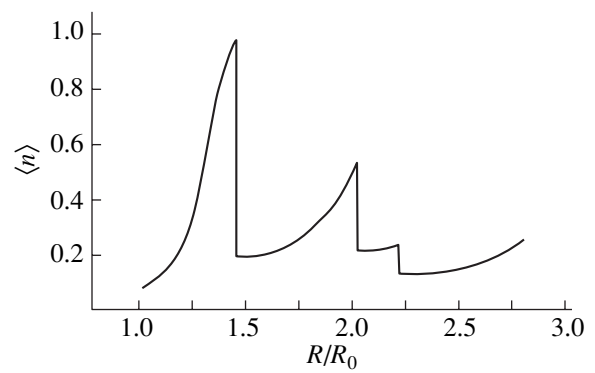


**Fig. 2.** Dependence of the perturbed density of electrons of the adatom  $\langle n \rangle$  on the dimensionless radius  $R/R_0$  of the quantum-well wire.

where the spectral function of the electron of the quantum-well wire is given by the expression

$$A_{ip}(\omega) = \frac{\Gamma_{ip}(\omega)}{(\omega - E_{ip})^2 + \Gamma_{ip}^2(\omega)}. \quad (7)$$

By using the expressions (4)–(7) and taking into account the electron energy spectrum of the quantum-well wire, which is described by relationship (1), we obtain the final expression for the perturbed density of electrons of the adatom:

$$\langle n \rangle = \frac{\rho_0}{2\pi} \sum_{n=0}^{n_F} \int_{\varepsilon_n}^{\mu} d\omega \frac{\sqrt{(\omega - \varepsilon_n)}}{[\omega - \varepsilon_a - U \langle n \rangle]^2 + \left[ \rho_0 \sum_{n=1}^{n_F} \Theta(\omega - \varepsilon_n) \sqrt{\omega - \varepsilon_n} \right]^2}, \quad (8)$$

where  $\rho_0 = |V|^2 L_x \sqrt{2m/\hbar}$ . Figure 2 shows the dependence of the perturbed density of electrons of the adatom on the dimensionless radius of the quantum-well wire  $\langle n \rangle(R/R_0)$  calculated according to expression (8). As follows from the calculations, the perturbed density of electrons of the adatom depends on the film thickness. Specifically, upon filling of the next quantum level of the quantum-well wire, the perturbed density of electrons of the adatom  $\langle n \rangle$  jumpwise increases, which, in turn, leads to a jumpwise change in the chemisorption energy of the adatom. The calculations were performed for the following parameters:  $\rho_0 = 5$ ,  $U/\varepsilon_0 = 7$ , and  $\varepsilon_a/\varepsilon_0 = 0.1$ . Here,  $\varepsilon_0 = \hbar^2/2mR_0^2$  is the characteristic energy.

Experimental observations of the aforementioned effects will make it possible to determine the specific features of the energy characteristics of an adatom and the electronic subsystem of the quantum-well wire. The effect of oscillations in the energy of interaction

between the adatom and the quantum-well wire is of interest from the viewpoint of controlled changes in the electronic properties of quantum-well wires. The condition of observation of oscillations in the interaction energy in a magnetic field has the form  $\Delta\varepsilon_n \gg T, \hbar/\tau$  (where  $T$  is the absolute temperature and  $\tau$  is the relaxation time).

## REFERENCES

1. R. P. Meĭlanov, Fiz. Tverd. Tela (Leningrad) **31** (7), 270 (1989) [Sov. Phys. Solid State **31**, 1254 (1989)].
2. R. P. Meĭlanov, Fiz. Tverd. Tela (Leningrad) **32** (9), 2839 (1990) [Sov. Phys. Solid State **32**, 1649 (1990)].
3. R. P. Meĭlanov, Poverkhnost, No. 6, 37 (1994).
4. R. P. Meĭlanov, Poverkhnost, No. 3, 52 (1999).
5. R. P. Meĭlanov, B. A. Abramova, M. M. Gadzhialiev, and V. V. Dzhabrailov, Fiz. Tverd. Tela (St. Petersburg) **44** (11), 2097 (2002) [Phys. Solid State **44**, 2196 (2002)].
6. P. W. Anderson, Phys. Rev. **124**, 41 (1961).
7. D. M. Newns, Phys. Rev. **178**, 3 (1969).
8. T. Einstein, J. Hertz, and J. Schrieffer, in *Theory of Chemisorption*, Ed. by J. R. Smith (Springer, Berlin, 1980; Mir, Moscow, 1983).
9. S. Yu. Davydov, Fiz. Tverd. Tela (St. Petersburg) **42** (7), 1331 (2000) [Phys. Solid State **42**, 1370 (2000)].
10. S. Yu. Davydov, Fiz. Tverd. Tela (St. Petersburg) **41** (9), 1543 (1999) [Phys. Solid State **41**, 1413 (1999)].
11. V. M. Galitskiĭ, B. M. Karnakov, and V. I. Kogan, *Problems in Quantum Mechanics* (Nauka, Moscow, 1981).

*Translated by I. Volkov*

---

---

**LOW-DIMENSIONAL SYSTEMS  
AND SURFACE PHYSICS**

---

---

## **Hysteretic Galvano-Mechanical Effect on Charging and Discharging Ionistor Structures**

**M. E. Kompan\*, V. P. Kuznetsov\*\*, V. V. Rozanov\*\*\*, and A. V. Yakubovich\*\*\*\***

\* *Ioffe Physicotechnical Institute, Russian Academy of Sciences, Politekhnicheskaya ul. 26, St. Petersburg, 194021 Russia*

\*\* *Girikond Research Institute Open Society, St. Petersburg, 190000 Russia*

\*\*\* *Institute of Analytical Instrumentation, Russian Academy of Sciences, Rizhskii pr. 26, St. Petersburg, 198103 Russia*

\*\*\*\* *Lyceum Physicotechnical School, Physicotechnical Institute, Russian Academy of Sciences,  
St. Petersburg, 194021 Russia*

Received June 30, 2003; in final form, September 23, 2003

**Abstract**—The size of an ionistor capacitor structure is found to change during its charging and discharging. The specific feature of this effect that distinguishes it from other known effects of changing sizes under electric and magnetic fields (the piezoelectric effect and striction) is the complete hysteresis; i.e., the size reached under the exposure remains unchanged after the field is turned off. © 2004 MAIK “Nauka/Interperiodica”.

Submicrometer- and nanometer-scale engineering and technology dictate, among other things, the need for precisely controlled methods and devices for moving instruments and objects in the corresponding spatial scale. Currently, these functions are almost exclusively implemented using piezoelectric movers. In recent decades, their design has been perfected due to the development of scanning probe microscopy techniques (see, e.g., [1]). Alternative techniques for implementing controlled submicrometer-scale displacements can present additional technological possibilities.

In this paper, we report on the detection of the effect of a change in size arising during charging and discharging of capacitor structures based on superionic conductors (ionistors). The effect has a clear physical nature; this effect is observed as low voltages are applied to the ionistor structure and significantly differs from the commonly used piezoelectric effect by the following feature. The size reached under the applied voltage remains unchanged when the power supply (control signal) is removed from the ionistor structures.

An ionistor is a device based on a superionic material, intended for reversible charge accumulation. An ionistor consists of three layers: a composite anode (an activated carbon–superionic interpenetrating composite); a superionic interlayer ( $\text{RbAg}_4\text{I}_5$ ), suppressing the electron current component flowing through the structure; and a metal cathode. During charging, as a voltage of corresponding polarity is applied, silver cations go away from the coal–superionic conductor heterointerface and are reduced to metal silver at the negatively biased cathode [2]. Material deposited on the cathode forms an additional metal interlayer. The anode, from which the cations leave, changes in size only slightly, since, first, the relative change in the cation content in the superionic material remains minor and, second, the

composite anode size is stabilized by the coal skeleton. As a result, the charging (discharging) process should cause an increase (decrease) in the total size. In fact, the mechanical action of the ionistor charging–discharging is caused by the fact that the electric current flowing through the superionics is accompanied by a galvanic mass transfer. After the control current is switched off, the newly formed metal interlayer on the cathode remains unchanged and the structure size remains the same as it was at the instant the current was turned off. As follows from the model of the process, the change in the structure size is formally determined by the charge accumulated by the structure; namely, the change in size is proportional to the integral of the control current. It is this feature that qualitatively distinguishes the ionistor structure as a mover from the known devices based on other effects. Furthermore, in comparison with other possible devices based on the galvanic mass transfer, a device based on solid materials is more convenient and reliable and can operate in a wide temperature range.

In practical implementation of the idea, it was necessary to take into account the fact that the superionic material most used in commercial industry,  $\text{RbAg}_4\text{I}_5$ , is unstable in air under light. For this reason, experiments were performed with ionistor structures encapsulated in a thin metal case similar to that of a watch battery. The height and diameter of the encapsulated element used in the experiment were 3.5 and 23 mm, respectively. The experiments were carried out at room temperature. The change in the size was preliminarily detected by interference measurements. Testing the ability of the ionistor structures to controllably and reversibly provide very small changes in size, as well as the possibility to retain sizes when the power supply is off, was of particular interest. For this reason, most of the experiments were carried out at small control influences. The

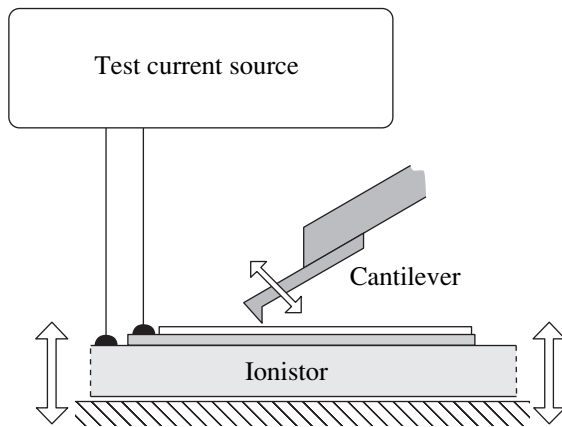


Fig. 1. Experimental layout.

changes in size were measured using an atomic-force microscope (AFM).

The experimental layout is shown in Fig. 1. The SMENA AFM operated in the tapping mode. Since the atomic-force microscope does not operate immediately in the size measurement mode, a charging–discharging current (control influence) was applied during scanning of the top surface of the encapsulated structure. As a result, the microscope recorded a seemingly complex surface profile, which was a reflection of the dynamic change in size. Figure 2 (bottom) shows one of such profiles; the top of the figure shows the surface profile recorded in the absence of control influence. The observed longitudinal depressions in the top profile are methodical distortions caused by the preceding cantilever passage above sizable local hills.

Figure 3 (top) shows a control current series; the bottom of the figure shows the surface section (similar to that shown in Fig. 2) measured during this current action. It is clearly seen that the ionistor structure size is indeed a function of the integral of the control current. It is also seen from Figs. 2 and 3 that the structure size remains unchanged in the absence of a control signal (e.g., portions *A*, *B*). Comparison of Figs. 2 and 3 demonstrates that a certain slope observed in these regions is caused by the initial surface profile.

The samples under study were characterized by a size/charge conversion factor of 200–100 nm/C. We note that the charge/size conversion factor was appreciably higher for small control currents. The measurement accuracy was limited by the SMENA model characteristics and surface roughness. In the first experiments, the capsule material roughness was found not to allow realization of the potential of the AFM. Therefore, further experiments were conducted over the surface of an additional glass coating deposited onto the capsule. We can see from Fig. 2 that surface defects are nevertheless observed; however, sufficiently accurate measurements of changes in size become possible.

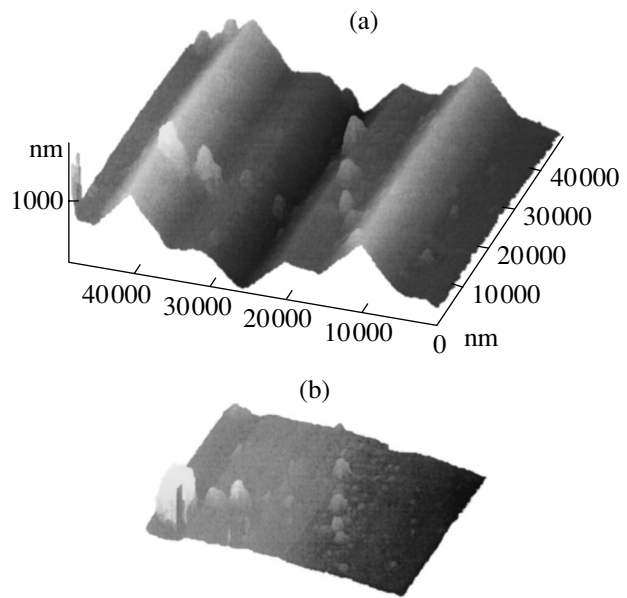


Fig. 2. (a) Surface area scanned by an atomic-force microscope as the control action was applied to the ionistor structure and (b) the actual profile of the same area recorded in the absence of action (demagnified).

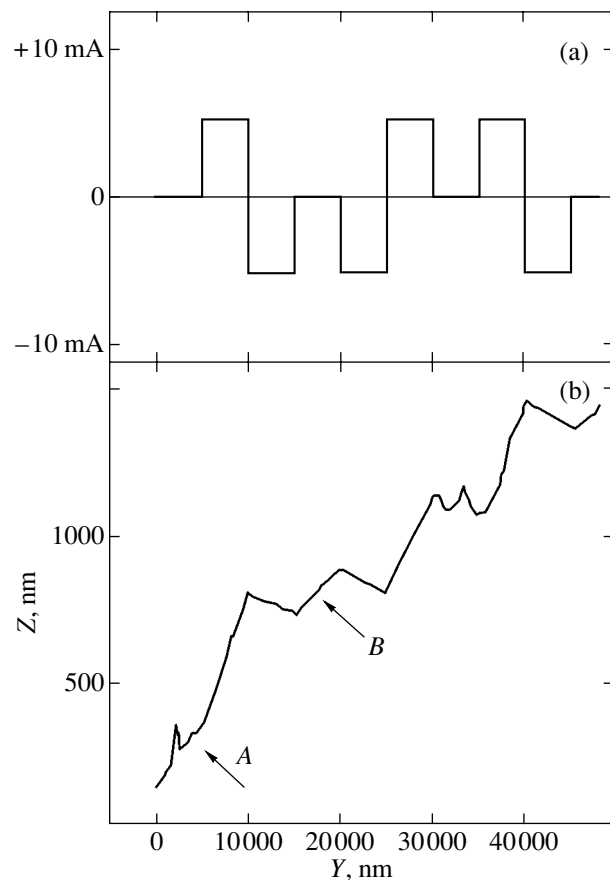


Fig. 3. (a) Test current series used to obtain the relief shown in Fig. 2 and (b) a section of the surface profile shown in Fig. 2; *A* and *B* are the portions corresponding to the absence of control current.

Although the nature of the effect is in general clear, the numerical estimate of the expected effect and the experimentally determined value differ. The chemical type of the released material is beyond question; this material can only be silver, whose ions are charge carriers in  $\text{RbAg}_4\text{I}_5$ . Let us estimate the thickness  $d$  of the newly formed interlayer under the assumption that this layer is formed by ordinary metal silver. Elementary formulas of electrolysis yield

$$d = \mu It / \rho N_a e S, \quad (1)$$

where  $\mu$  is the atomic weight of silver,  $It$  is the charge accumulated in the ionistor,  $\rho$  is the density of metal silver,  $N_a$  is Avogadro's number,  $e$  is the elementary charge, and  $S$  is the cathode area. Substituting numerical values into expression (1) for a cathode of 20 mm in diameter yields the value  $\sim 340$  nm/C. As noted, the experimentally determined numerical value of the charge/size conversion factor is 200–100 nm/C.

This disagreement can be explained as follows. The disagreement means that the mass transfer process in a solid-state composite structure is more complex than in the case described by an elementary model of electrolysis. In the case under consideration, the cause of the slightly smaller effect in comparison with the estimate could be a partial release of metal into micro- and nanopores during its deposition onto the cathode. This behavior of a deposited material in systems similar to that under study is known and has been studied previously [3]. Moreover, to accurately estimate the change

in the ionistor structure size, one should consider the contribution from the decrease in the anode size and the influence of the shell. Details of the effect are of interest for further investigation.

The result of this study is the detection of a change in the ionistor structure size during recharging. A characteristic difference is the strong hysteretic property of the effect, i.e., retention of the structure size when the control voltage is turned off. This hysteretic galvanomechanical effect offers new functionalities for developing nanometer mechanical devices and systems.

#### ACKNOWLEDGMENTS

The authors are grateful to the NT–MDT enterprise for the scanning atomic-force microscope put at the disposal of the laboratory of the Physicotechnical School Lyceum.

#### REFERENCES

1. A. Achuthan, A. K. Keng, and W. C. Ming, *Smart Mater. Struct.* **10** (5), 914 (2001).
2. Yu. Ya. Gurevich and Yu. I. Kharkats, *Superionic Conductors* (Nauka, Moscow, 1982).
3. Yu. M. Gerbshtein, V. P. Kuznetsov, and S. E. Nikitin, *Fiz. Tverd. Tela (Leningrad)* **27** (10), 2996 (1985) [*Sov. Phys. Solid State* **27**, 1799 (1985)].

*Translated by A. Kazantsev*



---

**LOW-DIMENSIONAL SYSTEMS  
AND SURFACE PHYSICS**

---

# Translational–Rotational Interaction in Dynamics and Thermodynamics of a Two-Dimensional Atomic Crystal with Molecular Impurities

**T. N. Antsygina, M. I. Poltavskaya, and K. A. Chishko**

*Verkin Institute of Low-Temperature Physics and Engineering, National Academy of Sciences of Ukraine,  
Kharkov, 61103 Ukraine*

*e-mail: chishko@ilt.kharkov.ua*

Received May 13, 2003; in final form, October 28, 2003

**Abstract**—The interaction between the rotational degrees of freedom of a diatomic impurity molecule and phonon excitations of a two-dimensional atomic matrix commensurate to the substrate is investigated theoretically. It is shown that the translational–rotational interaction leads to renormalization of the crystal field constants and a change in the form of the operator for the rotational kinetic energy as compared to the corresponding expression for a free rotator. The contribution from the rotational degrees of freedom of impurities to the low-temperature heat capacity of a diluted solution of diatomic molecules in the two-dimensional atomic matrix is calculated. The possibility of experimentally observing the predicted effects is discussed. © 2004 MAIK “Nauka/Interperiodica”.

## 1. INTRODUCTION

Investigation of the effects associated with interaction between translational and rotational degrees of freedom in solids is an important problem in the physics of condensed matter [1]. In particular, the inclusion of these effects has made it possible to offer an adequate quantitative interpretation of the low-temperature anomalies in heat capacity due to rotational degrees of freedom of molecular substitutional impurities in three-dimensional atomic cryomatrices [2–7].

In two-dimensional atomic–molecular cryosolutions, the dynamics of an impurity molecule appears to be substantially more complex than that in a three-dimensional system. At present, these objects have not been adequately studied both experimentally and theoretically. Additional factors (such as the type of substrate, coverage, etc.) affecting the physical properties of two-dimensional crystals provide a means for producing (under different conditions) systems with radically different characteristics [8]. As a consequence, these systems can exhibit a wide variety of effects associated with translational–rotational interactions.

In the general case, theoretical analysis of the dynamics of a molecular impurity in an atomic matrix with due regard for the mutual influence of phonon modes of the crystal and rotational modes of the molecular impurity is a sufficiently complex problem [1]. In this respect, in our earlier work [9], we investigated a model in which a diatomic impurity molecule moves in a crystal field induced by the immobile environment and took into account only the effects induced upon interaction between the rotational degrees of freedom

of the molecule and the translations of its center of inertia. However, even such a simplified model provides deeper insight into the basic features in the dynamics of an impurity molecule with a mobile center of inertia in an external crystal field with low symmetry that is characteristic of two-dimensional systems.

The inclusion of phonon degrees of freedom is not only a further step toward generalizing the results obtained previously [9] but is necessary for correct description of the low-temperature thermodynamics of two-dimensional atomic matrices with molecular impurities. It should be noted that, unlike the problem examined in [9], the problem under consideration becomes many-particle and there arises a nontrivial problem of adequate description of the interaction between the rotational degrees of freedom and local (quasi-local) levels in the phonon spectrum of the impure crystal. In the present work, we theoretically analyzed how translational–rotational interaction affects both the rotational dynamics of diatomic impurity molecules in a two-dimensional close-packed atomic matrix and the impurity heat capacity of the system.

## 2. FORMULATION OF THE PROBLEM

Let us consider a diatomic homonuclear molecule with mass  $M$  and internuclear distance  $2d$ , which is a substitutional impurity in a two-dimensional close-packed monoatomic matrix (with the coordination number in the layer  $z_1 = 6$ ) located on a substrate. We examine the case where the matrix and substrate structures are commensurate, so that each atom has  $z_2$  near-

est neighbors in the substrate. The substrate has either a triangular ( $z_2 = 3$ ) or hexagonal ( $z_2 = 6$ ) lattice. For definiteness, we assume that the impurity is located at the origin of the coordinates. The  $OZ$  axis is perpendicular to the layer and is directed away from the substrate. The  $OX$  and  $OY$  axes are oriented along the matrix plane. We will restrict our consideration to the case of an isotopic impurity. The complete Hamiltonian of the system has the form

$$H = H_{\text{rot}} + H_{\text{ph}} + H_1. \quad (1)$$

Here,  $H_{\text{rot}}$  is the kinetic energy of the impurity molecule, which is defined by the relationship

$$H_{\text{rot}} = -B \left[ \frac{1}{\sin \vartheta} \frac{\partial}{\partial \vartheta} \left( \sin \vartheta \frac{\partial}{\partial \vartheta} \right) + \frac{1}{\sin^2 \vartheta} \frac{\partial^2}{\partial \varphi^2} \right], \quad (2)$$

where  $B = \hbar^2/(2I)$  is the rotational constant of the impurity molecule,  $I = Md^2$  is the moment of inertia of the molecule, and  $\vartheta$  and  $\varphi$  are the azimuthal and polar angles specifying the orientation of the molecular axis, respectively. The Hamiltonian of the phonon subsystem  $H_{\text{ph}}$  can be written as

$$H_{\text{ph}} = H_{\text{ph}}^{(0)} + \varepsilon \frac{p_0^2}{2M}, \quad (3)$$

where

$$H_{\text{ph}}^{(0)} = \sum_{\mathbf{f}} \frac{\mathbf{p}_{\mathbf{f}}^2}{2m} + \frac{1}{2} \sum_{\mathbf{f}, \mathbf{f}', i, j} \Lambda_{\mathbf{f}, \mathbf{f}'}^{ij} u_{\mathbf{f}}^i u_{\mathbf{f}'}^j \quad (4)$$

is the phonon Hamiltonian of the impurity-free atomic layer,  $m$  is the mass of the matrix atom,  $\varepsilon = (m - M)/m$  is the mass defect,  $\mathbf{u}_{\mathbf{f}}$  is the displacement of the atom located at the site  $\mathbf{f}$  from the equilibrium position,  $\mathbf{p}_{\mathbf{f}} = -i\hbar \partial / \partial \mathbf{u}_{\mathbf{f}}$ ,  $\Lambda_{\mathbf{f}, \mathbf{f}'}^{ij}$  is the matrix of force constants, and  $i, j = x, y, z$ .

Now, we expand the displacement vectors  $\mathbf{u}_{\mathbf{f}}$  into a series in terms of the polarization unit vectors  $\mathbf{e}_{\mathbf{v}}$  of phonon excitations of the impurity-free layer; that is,

$$\mathbf{u}_{\mathbf{f}} = N^{-1/2} \sum_{\mathbf{v}} \xi_{\mathbf{v}} \mathbf{e}_{\mathbf{v}} \exp(i\mathbf{k}\mathbf{R}_{\mathbf{f}}),$$

where  $\mathbf{v} = (\mathbf{k}, \alpha)$ ;  $\mathbf{k}$  is the two-dimensional wave vector;  $\alpha = l, t, z$  are indices characterizing the polarization of the phonon branch ( $l$  and  $t$  correspond to the longitudinal and transverse modes, respectively, polarized in the layer plane, and  $z$  refers to the mode polarized perpendicularly to the layer);  $\mathbf{R}_{\mathbf{f}}$  is the radius vector of the site  $\mathbf{f}$ ;  $\xi_{\mathbf{v}}$  are the expansion coefficients; and  $N$  is the total

number of particles in the layer. In this case, Hamiltonian (3) takes the form

$$H_{\text{ph}} = \frac{1}{2} \sum_{\mathbf{v}} \left( \frac{|\pi_{\mathbf{v}}|^2}{m} + m\Omega_{\mathbf{v}}^2 |\xi_{\mathbf{v}}|^2 \right) + \frac{\varepsilon}{2MN} \sum_{\mathbf{v}, \mathbf{v}'} (\mathbf{e}_{\mathbf{v}}, \mathbf{e}_{\mathbf{v}'}) \pi_{\mathbf{v}} \pi_{\mathbf{v}'}^*, \quad (5)$$

where  $\pi_{\mathbf{v}} = -i\hbar \partial / \partial \xi_{\mathbf{v}}$  and  $\Omega_{\mathbf{v}}$  are the frequencies of phonon excitations of the impurity-free crystal. For the two-dimensional commensurate structure under consideration, the spectrum of the ideal triangular lattice can be calculated exactly. The appropriate expressions for the three spectral branches  $\Omega_{\mathbf{v}}$  can be represented in the following form [10]:

$$\begin{aligned} \Omega_{l,t}^2(\mathbf{k}) &= \Delta^2 + \frac{4}{3}(\Omega^2 + D) \\ &\times [1 - \cos 2\chi \cos(\chi + \nu) \cos(\chi - \nu)] \\ &\pm \frac{\Omega^2}{3} [(\cos 4\chi - \cos 2\chi \cos 2\nu)^2 \\ &+ 3 \sin^2 2\chi \sin^2 2\nu]^{1/2}, \end{aligned} \quad (6)$$

$$\begin{aligned} \Omega_z^2(\mathbf{k}) &= \Delta_z^2 \\ &+ \frac{4}{3} D [1 - \cos 2\chi \cos(\chi + \nu) \cos(\chi - \nu)], \end{aligned} \quad (7)$$

where

$$\chi = \frac{k_x R_1}{4}, \quad \nu = \frac{\sqrt{3} k_y R_1}{4}, \quad \mathbf{k} = (k_x, k_y).$$

Here,  $\Delta$ ,  $\Delta_z$ ,  $\Omega$ , and  $D$  are the constants expressed through the mass of the lattice atom and parameters of the potentials of the interaction of layer atoms with each other and with the substrate [10] and  $R_1$  is the distance from the matrix atom to the nearest neighbor in the layer. As can be seen from relationships (6) and (7), all branches of the phonon spectrum of the impurity-free commensurate structure are characterized by gaps; in this case,  $\Delta_z > \Delta$  and, as a rule,  $D \ll \Omega^2$ . Therefore, the  $z$  mode is virtually dispersionless. In the presence of an isotopic impurity, the phonon spectrum involves local and quasi-local frequencies [11–13]. When the impurity is light ( $\varepsilon > 0$ ), the local levels  $\omega_{\text{loc}}$  are located above the upper edge of the continuous spectrum. If the impurity is heavy ( $\varepsilon < 0$ ), the frequencies  $\omega_{\text{loc}}$  lie below the lower edge of the continuous spectrum, i.e., in the gap.

The Hamiltonian  $H_1$  involved in expression (1) describes the interaction between the impurity and the environment. This interaction will be taken into

account in the atom-atom potential approximation [14]; that is,

$$H_1 = \sum_{\delta} \{V_1(|\mathbf{r}_{\delta} - \mathbf{r}_a|) + V_1(|\mathbf{r}_{\delta} - \mathbf{r}_b|) - U_1(|\mathbf{r}_{\delta} - \mathbf{u}_0|)\} + \sum_{\Delta} \{V_2(|\mathbf{r}_{\Delta} - \mathbf{r}_a|) + V_2(|\mathbf{r}_{\Delta} - \mathbf{r}_b|) - U_2(|\mathbf{r}_{\Delta} - \mathbf{u}_0|)\}. \tag{8}$$

Here,  $V_1$  is the potential of the interaction between the impurity atom and the matrix atom;  $V_2$  is the potential of the interaction between the impurity atom and the substrate atom;  $U_1$  is the potential of the interaction between the matrix atoms;  $U_2$  is the potential of the interaction between the matrix atom and the substrate atom;  $\mathbf{r}_{a,b} = \mathbf{u}_0 \pm \mathbf{w}d$  are the coordinates of the atoms in the impurity molecule;  $\mathbf{w} = (\sin\vartheta\cos\phi, \sin\vartheta\sin\phi, \cos\vartheta)$  is the unit vector specifying the spatial orientation of the impurity molecule;  $\mathbf{r}_{\delta} = R_1\boldsymbol{\delta} + \mathbf{u}_{\delta}$  is the coordinate of the layer atom of the nearest environment;  $\mathbf{r}_{\Delta} = R_2\boldsymbol{\Delta}$  is the coordinate of the substrate atom of the nearest environment;  $R_2$  is the distance from the matrix atom to the nearest neighbor atom in the substrate;  $\boldsymbol{\delta}$  and  $\boldsymbol{\Delta}$  are the unit vectors specifying the direction to the nearest neighbors in the layer and the substrate, respectively;  $\mathbf{u}_0$  is the displacement of the center of inertia of the molecule from the equilibrium position; and  $\mathbf{u}_{\delta}$  is the displacement of the lattice atom from the equilibrium position.

When writing expression (8), we took into account that the impurity is isotopic (and, hence, the equilibrium position of the center of inertia of the impurity lies in the layer plane) and, moreover, restricted our treatment to the rigid-substrate approximation. Furthermore, it was assumed that the potentials  $V_i(r)$  and  $U_i(r)$  are short-range potentials (which is the case in real systems). Consequently, only the interaction with nearest neighbors was included in Hamiltonian (8). Note also that the theory proposed below is assumed to be valid, in principle, for potentials  $V_i(r)$  and  $U_i(r)$  of arbitrary type. Hence, all further calculations will be carried out without specifying the form of these potentials, except for numerical evaluations in which, for definiteness, the interatomic interaction will be described using the Lennard-Jones potential [14].

By assuming that the displacement of the center of inertia of the impurity molecule from the equilibrium position is small compared to the distances  $R_i$  and allowing for the smallness of the ratios  $d/R_i$ , we expand Hamiltonian (5) into a series in terms of these small parameters [9]. In subsequent calculations, insignificant constants that lead only to a change in the energy origin will be omitted.

The first-order terms do not depend on the orientation of the molecular axis and determine the equilibrium position of the layer with respect to the substrate. In contrast to three-dimensional crystals with cubic

symmetry, in which the crystal field  $H_c$  arises only in the fourth order in  $d/R$  [15], in the system under investigation, these terms appear even in the second order. Nonetheless, we will retain the fourth-order terms in the relationship for the crystal field, because, as will be shown below, the interaction of phonons with the impurity molecule substantially affects these terms. As a result, we have

$$H_c = -\frac{G_0}{2}w_z^2 + \frac{1}{2}[G_1w_z^4 + \Delta_{z_2,3}G_2w_yw_z(w_y^2 - 3w_x^2)]. \tag{9}$$

Here,

$$G_0 = d^2 \left\{ \sum_{i=1,2} z_i \mathcal{M}_i - z_2(1-b^2)[3\mathcal{M}_2 + d^2(5b^2-2)\mathcal{P}_2] \right\},$$

$$G_1 = \frac{d^4}{2} \left[ \sum_{i=1,2} z_i \mathcal{P}_i + \frac{5}{3}z_2(1-b^2)(1-7b^2)\mathcal{P}_2 \right],$$

$$G_2 = \frac{4d^4}{3}z_2b^3\sqrt{1-b^2}\mathcal{P}_2, \tag{10}$$

$$\mathcal{M}_i = A_i + \frac{d^2}{8}R_i \frac{d}{dR_i} \left( \frac{1}{R_i} \frac{dA_i}{dR_i} \right),$$

$$\mathcal{P}_i = \frac{1}{8}R_i \frac{d}{dR_i} \left( R_i^3 \frac{d}{dR_i} \frac{A_i}{R_i^4} \right),$$

$$A_i = R_i \frac{d}{dR_i} \left( \frac{1}{R_i} \frac{dV_i}{dR_i} \right),$$

and the parameters  $b$  for the substrates with the triangular and hexagonal lattices are equal to  $R_1/(\sqrt{3}R_2)$  and  $R_1/(3R_2)$ , respectively. It can be seen from expressions (10) that the interactions of the impurity with the layer and the substrate make additive contributions to the coefficients  $G_{0,1}$ . An analysis of these coefficients demonstrates that the substrate and matrix fields tend to orient the impurity molecule along the layer plane and perpendicular to the substrate, respectively. As a consequence, the equilibrium position of the impurity is governed by the competition between the above two factors. From expression (9), it also follows that the relationships for the crystal field are different for  $z_2 = 6$  and 3. For  $z_2 = 3$ , the crystal field has symmetry group  $S_6$  (sixfold inversion-rotational axis) [16, 17]. The term determining this symmetry is of the order of  $(d/R_i)^4$ , and the coefficient  $G_2$  of this term depends only on the

parameters of the substrate field [see relationships (9), (10)]. For  $z_2 = 6$ , the symmetry of the crystal field should correspond to symmetry group  $C_6$ . However, the corresponding terms arise only in the sixth order in  $d/R_i$ , which is not considered in our work. As a result, the symmetry of the crystal field  $H_c$  at  $z_2 = 6$  corresponds to the continuous two-dimensional rotation group  $C_\infty$ .

The terms describing the interaction of the phonon subsystem with the rotational degrees of freedom of the impurity molecule appear only beginning with the third-order terms [9, 18]. In this approximation, the interaction Hamiltonian under consideration can be written in the form

$$H_{\text{int}} = -\frac{d^2}{2\sqrt{N}} \sum_{\mathbf{v}} (f_{\mathbf{v}}^* \xi_{\mathbf{v}} + \text{c.c.}), \quad (11)$$

$$f_{\mathbf{v}} = \Gamma_{\mathbf{v}}^{\alpha\beta} Q_{\alpha\beta} + C_{\mathbf{v}}.$$

Here, we introduced the following designations:

$$\Gamma_{\mathbf{v}}^{\alpha\beta} = s^{\alpha\beta\gamma}(\mathbf{k}) e_{\mathbf{v}}^{\gamma} + 2h^{\alpha}(\mathbf{k}) e_{\mathbf{v}}^{\beta}, \quad (12)$$

$$C_{\mathbf{v}} = \frac{1}{3} [s^{\alpha\alpha\gamma}(\mathbf{k}) + 5h^{\gamma}(\mathbf{k})] e_{\mathbf{v}}^{\gamma},$$

$$s^{\alpha\beta\gamma}(\mathbf{k}) = \mathcal{H}_1 \sum_{\delta} \delta^{\alpha} \delta^{\beta} \delta^{\gamma} \exp(i\mathbf{k}\delta R_1) + \mathcal{H}_2 \sum_{\Delta} \Delta^{\alpha} \Delta^{\beta} \Delta^{\gamma}, \quad (13)$$

$$h^{\alpha}(\mathbf{k}) = \kappa_1 \sum_{\delta} \delta^{\alpha} \exp(i\mathbf{k}\delta R_1) + \kappa_2 \sum_{\Delta} \Delta^{\alpha}, \quad (14)$$

$$\mathcal{H}_i = R_i^2 \frac{d}{dR_i} \frac{A_i}{R_i^2}, \quad \kappa_i = \frac{A_i}{R_i}, \quad (15)$$

where  $Q_{\alpha\beta} = w_{\alpha} w_{\beta} - \Delta_{\alpha\beta}/3$  is the dimensionless quadrupole moment of the impurity molecule. Therefore, the complete Hamiltonian of the system is the sum of relationships (2), (5), (9), and (11).

### 3. DYNAMICS OF THE IMPURITY MOLECULE

In this section, we analyze how the interaction between the rotational degrees of freedom of the impurity molecule and the matrix phonons affects the rotational motion of the molecule. The magnitudes of the corresponding effects are calculated by functional integration [19]. Within an insignificant normalizing factor, the partition function  $Z$  has the form

$$Z = \int D[\xi(\tau)] D[\mathbf{w}(\tau)] \exp(S/\hbar), \quad (16)$$

$$S = \int_0^{\beta\hbar} d\tau L(\tau), \quad L = L_{\text{ph}} + L_{\text{rot}} + L_{\text{int}} + L_c, \quad (17)$$

$$L_{\text{ph}} = -\frac{m}{2} \sum_{\mathbf{v}} \left[ |\dot{\xi}_{\mathbf{v}}|^2 + \Omega_{\mathbf{v}}^2 |\xi_{\mathbf{v}}|^2 - \frac{\varepsilon}{N} \sum_{\mathbf{v}} (\mathbf{e}_{\mathbf{v}}, \mathbf{e}_{\mathbf{v}}) \dot{\xi}_{\mathbf{v}} \dot{\xi}_{\mathbf{v}}^* \right],$$

$$L_{\text{rot}} = -\frac{I}{2} \left( \frac{\partial \mathbf{w}}{\partial \tau} \right)^2 = -\frac{I}{2} (\dot{\vartheta}^2 + \dot{\varphi}^2 \sin^2 \vartheta),$$

$$L_{\text{int}} + L_c = -(H_{\text{int}} + H_c),$$

where  $\beta = 1/T$  (the Boltzmann constant is taken equal to unity) and  $\tau$  is the imaginary time. The dot denotes differentiation with respect to  $\tau$ . Expression (17) can be represented as the sum of two terms. The first term  $S_0$  depends only on the rotational degrees of freedom of the impurity molecule, and the second term  $S_1$  includes both rotational and phonon variables:

$$S_0 = \int_0^{\beta\hbar} d\tau (L_{\text{rot}} + L_c), \quad S_1 = \int_0^{\beta\hbar} d\tau (L_{\text{ph}} + L_{\text{int}}). \quad (18)$$

Let us now expand the functions  $\xi_{\mathbf{v}}(\tau)$  and  $f_{\mathbf{v}}(\tau)$  (entering into the second term  $S_1$ ) into a series in terms of the Matsubara frequencies:

$$\xi_{\mathbf{v}}(\tau) = \frac{1}{\beta\hbar} \sum_{n=-\infty}^{\infty} \tilde{\xi}_{\mathbf{v}}(\omega_n) \exp(-i\omega_n \tau), \quad \omega_n = \frac{2\pi n}{\beta\hbar}.$$

As a result, the integrand in the partition function (16) transforms into a form that is bilinear in the Fourier amplitudes  $\tilde{\xi}_{\mathbf{v}}$  and  $\tilde{f}_{\mathbf{v}}$ . The bilinear form can be rearranged into diagonal form by changing the variables

$$\tilde{\xi}_{\mathbf{v}}(\omega_n) = \zeta_{\mathbf{v}}(\omega_n) + \Phi_{\mathbf{v}}(\omega_n),$$

$$\Phi_{\mathbf{v}}(\omega_n) = \frac{d^2}{m(\omega_n^2 + \Omega_{\mathbf{v}}^2)} \left[ \tilde{f}_{\mathbf{v}}(\omega_n) + \frac{\varepsilon \omega_n^2}{1 - \varepsilon \omega_n^2 \sigma_{\alpha}} (\mathbf{e}_{\mathbf{v}}, \mathbf{g}) \right], \quad (19)$$

where

$$\mathbf{g} = \frac{1}{N} \sum_{\mathbf{v}} \frac{\tilde{f}_{\mathbf{v}}(\omega_n) \mathbf{e}_{\mathbf{v}}}{\omega_n^2 + \Omega_{\mathbf{v}}^2},$$

$$\sigma_{l,t} \equiv \sigma_{\perp} = \frac{1}{2N} \sum_{\mathbf{k}, \gamma=l,t} \frac{1}{\omega_n^2 + \Omega_{\gamma}^2(\mathbf{k})},$$

$$\sigma_z = \frac{1}{N} \sum_{\mathbf{k}} \frac{1}{\omega_n^2 + \Omega_z^2(\mathbf{k})}.$$

Integration over the phonon variables gives the following expression for the partition function:

$$Z = Z_{\text{ph}} Z_1, \quad Z_1 = \int D[\mathbf{w}(\tau)] \exp\left(\frac{S_0 + \Delta S}{\hbar}\right), \quad (20)$$

$$\begin{aligned} \Delta S = & \frac{d^4}{2m\beta\hbar} \sum_{n=-\infty}^{\infty} \left\{ \frac{1}{N} \sum_{\mathbf{v}} \frac{|\tilde{f}_{\mathbf{v}}(\omega_n)|^2}{\omega_n^2 + \Omega_{\mathbf{v}}^2} \right. \\ & \left. + \varepsilon \omega_n^2 \left[ \frac{|g_z|^2}{1 - \varepsilon \omega_n^2 \sigma_z} + \frac{|g_{\perp}|^2}{1 - \varepsilon \omega_n^2 \sigma_{\perp}} \right] \right\}, \quad (21) \\ & \mathbf{g}_{\perp} = (g_x, g_y, 0). \end{aligned}$$

In expression (20), the factor  $Z_{\text{ph}}$  represents the phonon partition function of the two-dimensional crystal and the quantity  $Z_1$  accounts for the rotational motion of the molecule with due regard for the contribution of the phonon subsystem. As follows from expressions (20) and (21), this interaction leads to the appearance of the additional term  $\Delta S$ . In principle, expression (21) is the solution of the posed problem. This solution will be analyzed with allowance made for the fact that the rotational states for the majority of molecular impurities in two-dimensional atomic lattices are characterized by low energies (the spacing between the ground and first excited rotational levels, as a rule, is less than  $\Delta$  [17]) and, hence, the specific effects due to the rotational excitations manifest themselves only at low temperatures. For this reason, our interest here is in the temperature range  $T \leq \hbar\Delta$  or  $\hbar\omega_{\text{loc}}$ . On this basis, by analogy with the transformations performed in [9, 18, 20], we found that, in the basic approximation in  $T/(\hbar\Delta)$  or  $T/(\hbar\omega_{\text{loc}})$ , the addition  $\Delta S$  is separated into terms of two types. The terms of the first type renormalize the constants of the crystal field; that is,

$$\tilde{H}_c = H_c + \Delta H_c, \quad \Delta H_c = -\frac{d^4}{2mN} \sum_{\mathbf{v}} \frac{|f_{\mathbf{v}}|^2}{\Omega_{\mathbf{v}}^2}. \quad (22)$$

The terms of the second type lead to a change in the form of the kinetic energy:

$$\begin{aligned} \tilde{H}_{\text{rot}} = & H_{\text{rot}} + \Delta H_{\text{rot}}, \\ \Delta H_{\text{rot}} = & \frac{d^4}{2m} \left\{ \frac{1}{N} \sum_{\mathbf{v}} \frac{|f_{\mathbf{v}}|^2}{\Omega_{\mathbf{v}}^4} - \varepsilon \left| \frac{1}{N} \sum_{\mathbf{v}} \frac{f_{\mathbf{v}} \mathbf{e}_{\mathbf{v}}}{\Omega_{\mathbf{v}}^2} \right|^2 \right\}. \quad (23) \end{aligned}$$

Unlike correction (22) to the crystal field, addition (23) to the kinetic energy depends on the mass defect  $\varepsilon$ . This is obvious from the general relationship (21). Indeed, the term dependent on  $\varepsilon$  contains the factor  $\omega_n^2$ ; i.e., it is determined by the derivatives of the dimensionless quadrupole moment and, hence, makes a contribution to the kinetic energy of the system. Note also

that, since  $\varepsilon < 1$  and any function  $F_{\mathbf{v}}$  satisfies the inequality

$$\frac{1}{N} \sum_{\mathbf{v}} |F_{\mathbf{v}}|^2 \geq \left| \frac{1}{N} \sum_{\mathbf{v}} F_{\mathbf{v}} \right|^2, \quad (24)$$

the addition  $\Delta H_{\text{rot}}$  is a nonnegative quantity.

Now, we analyze relationships (22) and (23) with the aim of elucidating the physical effects caused by the additions  $\Delta H_c$  and  $\Delta H_{\text{rot}}$ . First and foremost, it should be noted that the expression for  $f_{\mathbf{v}}$  [see formulas (11)–(14)] involves summation over the nearest neighbors in the layer plane. For lattices with sufficiently large coordination numbers, an efficient method for calculating the corresponding sums consists in replacing the summation over the nearest neighbors by integration over the unit circle [10, 21]. This approximation is justified, because corrections (22) and (23) are integrated characteristics that are weakly sensitive to the dependence of the integrands on the direction of the wave vector. As a result, the sums entering into relationships (12)–(14) take the form

$$\begin{aligned} & \frac{1}{z_1} \sum_{\delta} \delta^{\alpha} \delta^{\beta} (\mathbf{e}_{\mathbf{v}} \delta) \exp(i\mathbf{k}\delta R_1) \\ & \longrightarrow -iJ_3(kR_1) (\mathbf{e}_{\mathbf{v}}, \mathbf{n}_{\mathbf{k}}) n_{\mathbf{k}}^{\alpha} n_{\mathbf{k}}^{\beta} \\ & + \frac{iJ_2(kR_1)}{kR_1} [e_{\mathbf{v}}^{\alpha} n_{\mathbf{k}}^{\beta} + n_{\mathbf{k}}^{\alpha} e_{\mathbf{v}}^{\beta} + (\mathbf{e}_{\mathbf{v}}, \mathbf{n}_{\mathbf{k}}) \Delta_{\alpha, \beta}], \quad (25) \\ & \frac{1}{z_1} \sum_{\delta} \delta^{\alpha} \exp(i\mathbf{k}\delta R_1) \longrightarrow iJ_1(kR_1) n_{\mathbf{k}}^{\alpha}, \end{aligned}$$

where  $J_n(x)$  is the  $n$ th-order Bessel function. Moreover, for convenience of calculation, exact expressions (6) and (7) can be replaced by the approximate relationships for the branches of the phonon spectrum [10, 21], which were derived in the aforementioned approximation:

$$\begin{aligned} \Omega_{l,t}^2(kR_1) = & \Delta^2 + (\Omega^2 + D)[1 - J_0(kR_1)] \pm \Omega^2 J_2(kR_1), \\ \Omega_z^2(kR_1) = & \Delta_z^2 + D[1 - J_0(kR_1)]. \end{aligned}$$

By substituting relationships (11)–(14) into expression (22) and using formula (25), we find that the inclusion of the interaction between the rotational degrees of freedom of the impurity molecule and the phonons does not lead to a change in the general form of expression (9) for the crystal field but results in the renormalization of all the coefficients entering into it; that is,

$$\begin{aligned} H_c \longrightarrow \tilde{H}_c = & -\frac{\tilde{G}_0}{2} w_z^2 \\ & + \frac{1}{2} [\tilde{G}_1 w_z^4 + \Delta_{z,3} \tilde{G}_2 w_y w_z (w_y^2 - 3w_x^2)]. \quad (26) \end{aligned}$$

Here,

$$\tilde{G}_i = G_i + \Delta G_i, \quad \Delta G_i = \Delta G_i^L + \Delta G_i^S, \quad i = 0, 1, 2,$$

where the superscripts  $L$  and  $S$  indicate that the contributions are predominantly made by the interactions of the impurity molecule with the matrix and substrate atoms, respectively. From symmetry considerations, it is *a priori* evident that allowance made for the interaction of the impurity molecule with nearest neighbors in the layer leads only to renormalization of the coefficients  $G_0$  and  $G_1$  and does not affect the last term in formula (26). The corresponding corrections  $\Delta G_{0,1}^L$  can be written as

$$\begin{aligned} \Delta G_0^L &= -\frac{z_1^2 d^4}{6m} (\mathcal{A}_1 + 3\mathcal{B}_1 + \mathcal{C}_1), \\ \Delta G_1^L &= -\frac{z_1^2 d^4}{4m} (\mathcal{A}_1 + \mathcal{B}_1), \end{aligned} \quad (27)$$

where

$$\begin{aligned} \mathcal{A}_m &= \frac{1}{N} \sum_{\mathbf{k}} \frac{\alpha_1^2}{\Omega_l^{2m}}, \\ \mathcal{B}_m &= \frac{1}{8N} \sum_{\mathbf{k}} \left[ \frac{(\alpha_2 - \alpha_3)^2}{\Omega_l^{2m}} + \frac{(\alpha_2 + \alpha_3)^2}{\Omega_l^{2m}} \right], \\ \mathcal{C}_m &= \frac{1}{N} \sum_{\mathbf{k}} \frac{\alpha_1(3\alpha_2 - \alpha_1)}{\Omega_l^{2m}}, \quad \alpha_1 = (\mathcal{H}_1 + 2\kappa_1)J_1(kR_1), \\ \alpha_2 &= (\mathcal{H}_1 + 4\kappa_1)J_1(kR_1), \quad \alpha_3 = \mathcal{H}_1 J_3(kR_1). \end{aligned} \quad (28)$$

From expressions (27) and (28), it follows that the corrections  $\Delta G_0^L$  and  $\Delta G_1^L$  are negative in sign. The additions to the crystal field due to the interaction with the immobile substrate can be represented in the form

$$\begin{aligned} \Delta G_0^S &= \frac{z_2^2 d^4}{2m} [(2K_0^2 - K_2^2 \Delta_{z_2,3})s_{\perp}^{(1)} - K_0 K_1 s_z^{(1)}], \\ \Delta G_1^S &= \frac{z_2^2 d^4}{4m} [(4K_0^2 - K_2^2 \Delta_{z_2,3})s_{\perp}^{(1)} - K_1^2 s_z^{(1)}], \\ \Delta G_2^S &= -\frac{z_2^2 d^4}{m} K_0 K_2 s_{\perp}^{(1)}, \end{aligned} \quad (29)$$

where

$$\begin{aligned} K_0 &= \sqrt{1 - b^2} (b^2 \mathcal{H}_2 + 2\kappa_2), \\ K_1 &= \sqrt{1 - b^2} [(3b^2 - 2)\mathcal{H}_2 - 4\kappa_2], \\ K_2 &= \frac{b^3}{2} \mathcal{H}_2, \end{aligned} \quad (30)$$

$$s_{\perp}^{(m)} = \frac{1}{2N} \sum_{\mathbf{k}, \alpha=l,t} \frac{1}{\Omega_{\alpha}^{2m}}, \quad s_z^{(m)} = \frac{1}{N} \sum_{\mathbf{k}} \frac{1}{\Omega_z^{2m}}. \quad (31)$$

Note that, for short-range potentials (of Lennard-Jones type), the inequalities  $K_0 > 0$ ,  $K_1 < 0$ , and  $|K_2| < K_0$  are satisfied and, hence,  $\Delta G_0^S > 0$ .

The crystal field (9) contains additive contributions associated with the interaction of the impurity molecule with the layer and substrate atoms. An analysis shows that these contributions each decrease in the amplitude owing to additions (27) and (29), respectively, which appear upon the translational-rotational interaction. This result is physically quite obvious. Actually, the rotator moves in the environment of mobile atoms of the matrix and is most strongly affected by the high-frequency phonons that generate the highest strains in the first coordination sphere around the impurity molecule. In this sense, the problem under consideration is similar to the known problem regarding the motion of a particle in a rapidly oscillating field [22], when the averaging over oscillations results in an effective decrease in the depth of the initial potential well.

A different situation is observed for the additions to the kinetic energy. It follows from relationship (23) that the interaction between the rotational degrees of freedom of the impurity molecule and the phonons leads to a substantial change in the form of the Hamiltonian  $H_{\text{rot}}$ . Indeed, after a number of manipulations, the addition  $\Delta H_{\text{rot}}$  can be rewritten in the form

$$\Delta H_{\text{rot}} = \frac{1}{2} (\Delta I_{\perp} \dot{\mathbf{w}}_{\perp}^2 + \Delta I_z \dot{w}_z^2 + \Delta_{z_2,3} \Delta I_{ij} \dot{w}_i \dot{w}_j). \quad (32)$$

Here, the corrections  $\Delta I_{\perp, z}$  to the moment of inertia of the impurity molecule have the following form:

$$\begin{aligned} \Delta I_{\perp, z} &= \Delta I_{\perp, z}^L + \Delta I_{\perp, z}^S, \quad \Delta I_{\perp}^L = \frac{z_1^2 d^4}{m} \mathcal{B}_2 w_{\perp}^2, \\ \Delta I_z^L &= \frac{z_1^2 d^4}{m} \mathcal{A}_2 w_z^2, \\ \Delta I_{\perp}^S &= \frac{z_2^2 d^4}{m} \zeta_{\perp} (K_0^2 w_z^2 + \Delta_{z_2,3} K_2^2 w_{\perp}^2), \\ \Delta I_z^S &= \frac{z_2^2 d^4}{m} [K_0^2 \zeta_{\perp} (1 - 3w_z^2) + K_1^2 \zeta_z w_z^2], \end{aligned} \quad (33)$$

where

$$\zeta_{\perp, z} = s_{\perp, z}^{(2)} - \varepsilon (s_{\perp, z}^{(1)})^2.$$

Furthermore, for substrates with a triangular lattice ( $z_2 = 3$ ), there arises a term containing off-diagonal ele-

ments (with respect to  $\dot{w}_i\dot{w}_j$ ); that is,

$$\Delta I_{ij} = -\frac{z_2^2 d^4}{m} \zeta_{\perp} K_0 K_2 \begin{bmatrix} 2w_y w_z & 2w_x w_z & 2w_x w_y \\ 2w_x w_z & -2w_y w_z & w_x^2 - w_y^2 \\ 2w_x w_y & w_x^2 - w_y^2 & 0 \end{bmatrix}. \quad (34)$$

Therefore, the interaction of the impurity molecule with phonons results in a radical change in its inertial properties; more precisely, the effective kinetic energy of the rotator takes the generalized positively definite quadratic form [see expression (23)] of the components of the angular velocity, which corresponds to the symmetry of the system under investigation ( $C_{\infty}$  or  $S_6$ ). By virtue of the positive definiteness of the addition  $\Delta H_{\text{rot}}$  (32), we can write the condition  $\Delta I_{\perp,z} > 0$ . Actually, since  $\zeta_{\perp,z} \geq 0$  [see inequality (24)], the quantities  $\Delta I_{\perp,z}^L$  and  $\Delta I_{\perp}^S$  are obviously positive. As regards the addition  $\Delta I_z^S$ , this quantity can appear to be negative at specific molecular orientations; however, the total addition  $\Delta I_z$  is always positive. Consequently, the interaction between the rotational degrees of freedom of the impurity molecule and the phonons leads to an increase in the principal moments of inertia of the impurity molecule, i.e., to an increase in its weight.

It should be noted that the separation of the renormalizations of the crystal field and the moments of inertia into the layer and substrate contributions is conventional in a sense. Although each contribution explicitly depends on the parameters of the potential associated with one component of the system (only the substrate or only the matrix), all the contributions, according to expressions (27)–(29) and (33), are functions of the frequencies  $\Omega_v$  of phonon excitations, which characterize the system as a whole.

All the corrections to the crystal field and the moment of inertia are of the order of  $(d/R)^4$ . In explicit form, the corrections expressed through the parameters of the system in the general case are rather complicated [see formulas (27)–(31)]. However, the situation can be simplified in some cases, for example, in the tight-binding limit, when the crystal field is sufficiently strong as compared to the rotational constant of the impurity molecule. If the condition  $G_0 - 2G_1 > 0$  is satisfied, the molecule executes small librations with respect to the equilibrium position at which the molecular axis is perpendicular to the layer. In this case, the off-diagonal elements arising in the inertia tensor due to the translational-rotational interaction prove to be negligible and only the corrections to the diagonal elements make significant contributions. We performed numerical calculations of the renormalizations for a number of systems under the assumption that the interaction of the impurity molecule with atoms of the matrix and the substrate is described by the Lennard-Jones potential with the

parameters corresponding to the interatomic interaction in the gaseous phase [15]. It was found that the maximum relative change in the moment of inertia is approximately equal to 30% and the renormalization of the crystal field amplitudes can be as large as 50–60%. Undeniably, the above estimates are rather crude, because the Lennard-Jones potential used is extremely sensitive to the choice of parameters, whose real values for two-dimensional systems can differ substantially from those for gaseous phases [21]. Nonetheless, we can argue that the renormalization effect associated with the translational-rotational interaction is significant and should be accounted for when discussing physical phenomena in the systems under investigation.

Finally, we should note that, in the limit of the immobile environment, the expressions for the renormalization of the crystal field constants and the additions to the rotational kinetic energy of the impurity molecule transform into the corresponding expressions obtained in our earlier work [9].

#### 4. IMPURITY HEAT CAPACITY

Now, we calculate the contribution made to the low-temperature thermodynamic properties of a two-dimensional atomic crystal by the rotational degrees of freedom of a system formed by noninteracting diatomic impurity molecules with due regard for the translational-rotational interaction. Our treatment will be carried out in the tight-binding limit when a molecule executes small librations with respect to the equilibrium position coinciding with the normal to the layer plane. In this case, the Hamiltonian of the system can be derived under the assumption [20]

$$Q_{\alpha\beta} = \langle Q_{\alpha\beta} \rangle + q_{\alpha\beta}, \quad \xi_v = \langle \xi_v \rangle + \eta_v, \quad (35)$$

where the angle brackets denote the thermodynamic average of the corresponding functions and  $q_{\alpha\beta}$  is a small addition. Only the diagonal elements  $\langle Q_{xv} \rangle = \langle Q_{yv} \rangle = -1/3$  and  $\langle Q_{zv} \rangle = 2/3$  are nonzero. The quantities  $\langle \xi_v \rangle$ , which are nonzero due to the translational-rotational interaction, satisfy the relationship [20]

$$\langle \xi_v \rangle = \frac{d^2 \langle f_v \rangle}{\sqrt{Nm}\Omega_v^2}. \quad (36)$$

The deviation of the rotator axis from the equilibrium position is conveniently described in terms of the variables  $u = \sin\vartheta \cos\varphi$  and  $v = \sin\vartheta \sin\varphi$ , which are small quantities for the system under consideration. Then, the vector  $\mathbf{w}$  takes the form

$$\mathbf{w} = \left( u, v, 1 - \frac{u^2 + v^2}{2} \right). \quad (37)$$

By substituting formulas (35)–(37) into relationships (2), (5), (9), and (11) and retaining the terms up to

the second order, we obtain the Hamiltonian of the system:

$$\mathcal{H} = \mathcal{H}_0 + \mathcal{H}_1, \quad \mathcal{H}_0 = \mathcal{H}_{\text{ph}} + \mathcal{H}_2. \quad (38)$$

Here,  $\mathcal{H}_{\text{ph}}$  is the Hamiltonian of the phonon subsystem,

$$\begin{aligned} \mathcal{H}_{\text{ph}} = & \frac{1}{2} \sum_{\mathbf{v}} \left( \frac{|\pi_{\mathbf{v}}|^2}{m} + m\Omega_{\mathbf{v}}^2 |\eta_{\mathbf{v}}|^2 \right) \\ & + \frac{\varepsilon}{2MN} \sum_{\mathbf{v}, \mathbf{v}'} (\mathbf{e}_{\mathbf{v}}, \mathbf{e}_{\mathbf{v}'}) \pi_{\mathbf{v}} \pi_{\mathbf{v}'}^*, \end{aligned} \quad (39)$$

and  $\mathcal{H}_2$  is the Hamiltonian related to the rotational degrees of freedom of the impurity molecule,

$$\mathcal{H}_2 = \frac{B}{\hbar^2} (P_u^2 + P_v^2) + \kappa(u^2 + v^2). \quad (40)$$

The Hamiltonian  $\mathcal{H}_1$  describing the interaction between the rotational degrees of freedom of the molecule and phonon excitations has the form

$$\mathcal{H}_1 = \frac{1}{2\sqrt{N}} \sum_{\mathbf{v}} (b_{\mathbf{v}} u + c_{\mathbf{v}} v) (\eta_{\mathbf{v}} + \eta_{\mathbf{v}}^*). \quad (41)$$

Here, we introduced the following designations:

$$\begin{aligned} \pi_{\mathbf{v}} = & -i\hbar \partial / \partial \eta_{\mathbf{v}}, \quad P_{u(v)} = -i\hbar \partial / \partial u(v), \\ \kappa = & \frac{B}{4} + \frac{G_0}{2} - G_1 \end{aligned} \quad (42)$$

$$\begin{aligned} & + \frac{d^4}{4m} \left[ z_2^2 K_1 (K_1 - K_0) s_z^{(2)} + \frac{z_1^2}{3} (2\mathcal{A}_2 - \mathcal{C}_2) \right], \\ b_{\mathbf{v}} = & z_2 d^2 K_0 e_{\mathbf{v}}^x, \quad c_{\mathbf{v}} = z_2 d^2 K_0 e_{\mathbf{v}}^y. \end{aligned} \quad (43)$$

Hamiltonian (39) describes the phonon subsystem of a two-dimensional crystal that is located on the substrate and contains an isotopic impurity. It is known that, in the presence of such an impurity, the vibrational spectrum is characterized by local and quasi-local frequencies [11]. Note that, in the spectrum of a three-dimensional cubic crystal, all local frequencies are triply degenerate [11–13]. By contrast, the spectrum of the two-dimensional atomic crystal on the substrate involves a doubly degenerate vibration polarized in the layer plane and a nondegenerate vibration polarized perpendicularly to the layer plane. The corresponding equations for determining the local and quasi-local frequencies have the form [10]

$$\begin{aligned} 1 - \varepsilon \omega^2 S_{\perp}(\omega) = 0, \quad S_{\perp}(\omega) = & \frac{1}{2N} \sum_{\mathbf{k}, \gamma=l,t} \frac{1}{\omega^2 - \Omega_{\gamma}^2(\mathbf{k})}, \\ 1 - \varepsilon \omega^2 \frac{1}{N} \sum_{\mathbf{k}} \frac{1}{\omega^2 - \Omega_z^2(\mathbf{k})} = 0. \end{aligned} \quad (44)$$

One more specific feature of the two-dimensional system (as compared to the three-dimensional case) is that it has no threshold mass defect for localized vibrations; i.e., localized vibrations occur at any  $\varepsilon < 1$ . Note that to every local level there necessarily corresponds a conjugated quasi-local state. These results are similar to those obtained for localized states in the vicinity of a rectilinear dislocation [23]. The translational–rotational interaction leads not only to renormalization of the rotational parameters of the impurity molecule but also to a modification of the vibrational spectrum of the system.

The thermodynamic characteristics of the system described by Hamiltonian (38) will be calculated using the following procedure. The auxiliary numeral factor  $\lambda$  is introduced so that

$$\mathcal{H}_{\lambda} = \mathcal{H}_0 + \lambda \mathcal{H}_1. \quad (45)$$

It is evident that Hamiltonian (45) coincides with Hamiltonian (38) at  $\lambda = 1$ . The free energy corresponding to Hamiltonian (45) obeys the relationship

$$\frac{\partial \mathcal{F}(\lambda)}{\partial \lambda} = \langle \mathcal{H}_1 \rangle_{\lambda}, \quad \langle \mathcal{H}_1 \rangle_{\lambda} = \frac{\text{Sp}[\mathcal{H}_1 \exp(-\beta \mathcal{H}_{\lambda})]}{\text{Sp}[\exp(-\beta \mathcal{H}_{\lambda})]}. \quad (46)$$

Then, the free energy of the system under consideration can be represented in the form

$$\mathcal{F} = \mathcal{F}_0 + \Delta \mathcal{F}, \quad \Delta \mathcal{F} = \int_0^1 \langle \mathcal{H}_1 \rangle_{\lambda} d\lambda, \quad (47)$$

where  $\Delta \mathcal{F}$  is the addition associated with the translational–rotational interaction and  $\mathcal{F}_0$  is the free energy in the absence of this interaction. The latter quantity includes the contributions from the impurity-free layer, local and quasi-local frequencies, and the rotational degrees of freedom of impurities with nonrenormalized parameters.

Therefore, the problem is reduced to calculating the quantity  $\langle \mathcal{H}_1 \rangle_{\lambda}$ . This can be accomplished in terms of two-time Green's functions. The two-time retarded commutator Green's function is defined by the expression [24]

$$\langle \langle \hat{A}(t) | \hat{B}(t') \rangle \rangle = -\frac{i}{\hbar} \Theta(t - t') \langle [\hat{A}(t), \hat{B}(t')] \rangle.$$

The equations for the Fourier components of the Green's function for the system described by Hamiltonian (45) are written as

$$\begin{aligned} i\omega \langle \langle \eta_{\mathbf{v}} | u \rangle \rangle_{\omega} = & \frac{1}{m} \langle \langle \pi_{\mathbf{v}} | u \rangle \rangle_{\omega} + \frac{\varepsilon}{MN} \sum_{\mathbf{v}'} (\mathbf{e}_{\mathbf{v}}, \mathbf{e}_{\mathbf{v}'}) \langle \langle \pi_{\mathbf{v}'} | u \rangle \rangle_{\omega}, \\ i\omega \langle \langle \pi_{\mathbf{v}} | u \rangle \rangle_{\omega} = & -m\Omega_{\mathbf{v}}^2 \langle \langle \eta_{\mathbf{v}} | u \rangle \rangle_{\omega} - \lambda b_{\mathbf{v}} \langle \langle u | u \rangle \rangle_{\omega}, \\ i\omega \langle \langle u | u \rangle \rangle_{\omega} = & \frac{2B}{\hbar^2} \langle \langle P_u | u \rangle \rangle_{\omega}, \end{aligned} \quad (48)$$



$$i\omega \langle \langle P_u | u \rangle \rangle_\omega = -2\kappa \langle \langle u | u \rangle \rangle_\omega - \lambda \sum_v b_v \langle \langle \eta_v | u \rangle \rangle_\omega - 1.$$

The equations for the Green's functions with the variable  $v$  have a similar form. After eliminating the functions  $\langle \langle \pi_v | u \rangle \rangle_\omega$  and  $\langle \langle P_u | u \rangle \rangle_\omega$ , Eqs. (48) are reduced to a system of integral equations with degenerate kernels whose solution can be found in an explicit form. As a result, for the Green's function under consideration

$$\mathcal{G}_\lambda(\omega) = \frac{1}{\sqrt{N}} \sum_v (b_v \langle \langle \eta_v | u \rangle \rangle_\omega + c_v \langle \langle \eta_v | v \rangle \rangle_\omega), \quad (49)$$

we obtain

$$\mathcal{G}_\lambda(\omega) = \frac{2\lambda\Phi}{1 - \lambda^2\Phi}. \quad (50)$$

Here,

$$\Phi = \frac{aS_\perp(\omega)}{(\omega^2 - \omega_0^2)[1 - \varepsilon\omega^2 S_\perp(\omega)]}, \quad (51)$$

where  $\omega_0 = 2\sqrt{\kappa B}/\hbar$  is the frequency of rotator librations in the absence of the translational–rotational interaction and  $a = 2z_2^2 d^4 K_0^2 B / (m\hbar^2)$  is the parameter characterizing this interaction. It follows from expressions (44) and (51) that, within our approximation, displacements of the center of inertia of the impurity molecule along the  $OZ$  axis do not affect the rotational motion of the molecule. This is obvious even from the form of relationship (41), which contains only the in-plane components of the displacement of the center of inertia of the rotator in the monolayer.

By using the spectral representation for the Green's function [24]

$$\langle \mathcal{H}_l \rangle_\lambda = \frac{i\hbar}{2\pi\delta} \lim_{\delta \rightarrow 0} \int_{-\infty}^{\infty} \frac{\mathcal{G}_\lambda(\omega + i\delta) - \mathcal{G}_\lambda(\omega - i\delta)}{\exp(\beta\hbar\omega) - 1} d\omega \quad (52)$$

and expression (47), after integration over  $\lambda$ , we derive the following relationship for the addition to the free energy:

$$\Delta\mathcal{F} = -\frac{i\hbar}{2\pi\delta} \lim_{\delta \rightarrow 0} \int_{-\infty}^{\infty} \frac{d\omega}{\exp(\beta\hbar\omega) - 1} \quad (53)$$

$$\times \{ \ln[1 - \Phi(\omega + i\delta)] - \ln[1 - \Phi(\omega - i\delta)] \}.$$

After substituting expression (51) into relationship (53) and a number of transformations, the addition  $\Delta\mathcal{F}$  can be represented as the sum of three terms. Two terms cancel out both the contribution made to the free energy  $\mathcal{F}_0$  by the rotational degrees of freedom of the rotator with the nonrenormalized parameters and the contributions from the local and quasi-local states (polarized in the layer plane) of the phonon spectrum. The third term

is the part of the impurity contribution that is modified through the translational–rotational interaction. This last term, which involves the contributions from the rotational and translational degrees of freedom of the impurity, can be written in the form

$$\Delta\tilde{\mathcal{F}} = \frac{\hbar}{\pi\delta} \lim_{\delta \rightarrow 0} \int_0^{\infty} d\omega \coth \frac{\beta\hbar\omega}{2} \phi(\omega, \delta), \quad (54)$$

$$\phi(\omega, \delta) = \arctan \left( \frac{P(\omega, \delta)}{R(\omega)} \right).$$

Here,

$$P(\omega, \delta) = 2\omega\delta[1 - \varepsilon\rho(\omega)(2\omega^2 - \omega_0^2)] - \mu(\omega)[\varepsilon\omega^2(\omega^2 - \omega_0^2) + a], \quad (55)$$

$$R(\omega) = (\omega^2 - \omega_0^2)[1 - \varepsilon\omega^2\rho(\omega)] - a\rho(\omega), \quad (56)$$

$$S_\perp(\omega + i\delta) = \rho(\omega) + i\mu(\omega).$$

The procedure for calculating integral (54) depends on the location of the librational frequency  $\omega_0$  with respect to the lower edge  $\Delta$  of the continuous spectrum (hereinafter, the continuous spectrum will be considered to mean only excitations belonging to the  $l$  and  $t$  modes of the impurity-free monolayer).

For the majority of real systems, the librational frequency  $\omega_0$  of the nonrenormalized rotator is low compared to the upper edge  $\Omega_{\max}$  of the continuous spectrum of the impurity-free two-dimensional crystal. This implies that the librational frequency  $\omega_0$  lies either in the gap ( $\omega_0 < \Delta$ ) or in the range of the continuous spectrum in the vicinity of the lower edge. It is these low frequencies  $\omega_0$  that are of interest from the standpoint of the possibility of observing effects due to the rotational heat capacity in experiments. Indeed, in the impurity system, apart from the contribution of the rotational degrees of freedom, there are contributions from translational excitations (associated with both the continuous spectrum and the local and quasi-local states). Therefore, the lower the frequency  $\omega_0$  and the lower the temperature, the simpler the separation of the rotational contribution to the heat capacity against the background of the translational contribution.

Initially, we consider the systems for which the librational frequency  $\omega_0$  lies in the gap of the phonon spectrum ( $\omega_0 < \Delta$ ). For a light impurity ( $\varepsilon > 0$ ), local and quasi-local translational levels of the impurity molecule are located in the vicinity of the upper edge  $\Omega_{\max}$  and their influence on the low-temperature thermodynamic characteristics of the system can be ignored. According to relationships (54)–(56), the contributions made to the free energy and the heat capacity (per par-

title) by the rotational degrees of freedom have the form

$$\begin{aligned}\Delta\tilde{\mathcal{F}}_{\text{rot}} &= 2T \ln \left( 2 \sinh \frac{\hbar\tilde{\omega}_0}{2T} \right), \\ \Delta C &= 2 \left( \frac{\hbar\tilde{\omega}_0}{2T} \operatorname{arcsinh} \frac{\hbar\tilde{\omega}_0}{2T} \right)^2,\end{aligned}\quad (57)$$

where  $\tilde{\omega}_0$  is the smallest root of the equation

$$R(\omega) = 0. \quad (58)$$

This root is given by the formula

$$\tilde{\omega}_0^2 = \omega_0^2 [1 - a\zeta_{\perp}] - as_{\perp}^{(1)}. \quad (59)$$

In the absence of the translational–rotational interaction, the frequency  $\tilde{\omega}_0$  coincides with the frequency  $\omega_0$  of unperturbed librations. Expression (57) describes the heat capacity of a two-dimensional Einstein oscillator with the renormalized librational frequency  $\tilde{\omega}_0$ . It is easy to verify that formula (59) coincides with the corresponding formula derived from relationships (27), (29), (33), and (34) in the tight-binding limit. As could be expected, the renormalization of the parameters of the rotational motion leads to an effective decrease in the frequency  $\omega_0$  and, hence, to an increase in the relative fraction of the rotational degrees of freedom in the low-temperature heat capacity of the system.

In the case of a heavy impurity ( $\varepsilon < 0$ ), apart from the frequency  $\omega_0$ , there is a local vibrational level at  $\omega_{\text{loc}} < \Delta$  in the gap. The contribution from this level to the thermodynamic functions can be comparable to that from the rotational degrees of freedom. Note that the main contribution made by the impurity to the free energy and the heat capacity consists of two terms defined by formulas similar to expression (57) with frequencies determined as the roots of Eq. (58), which can be conveniently represented in the form

$$(\omega^2 - \omega_0^2)(\omega^2 - \omega_{\text{loc}}^2) - a\omega_{\text{loc}}^2(s_{\perp}^{(1)} + \omega^2 s_{\perp}^{(2)}) = 0. \quad (60)$$

In the case when the difference between the unperturbed frequencies  $\omega_{\text{loc}}$  and  $\omega_0$  is large compared to the parameter  $a$  of the translational–rotational interaction, i.e., when the inequality  $a \ll (\omega_{\text{loc}}^2 - \omega_0^2)^2$  is satisfied, the excitations under consideration, as before, can be treated as librational and local excitations with the renormalized frequencies

$$\begin{aligned}\tilde{\omega}_0^2 &= \omega_0^2 [1 - af(\omega_0, \omega_{\text{loc}})] - as_{\perp}^{(1)}, \\ \tilde{\omega}_{\text{loc}}^2 &= \omega_0^2 [1 + af(\omega_0, \omega_{\text{loc}})], \\ f(\omega_0, \omega_{\text{loc}}) &= \frac{s_{\perp}^{(1)} + \omega_{\text{loc}}^2 s_{\perp}^{(2)}}{\omega_{\text{loc}}^2 - \omega_0^2}.\end{aligned}\quad (61)$$

As follows from relationships (61), irrespective of the mutual arrangement of the nonrenormalized librational and local levels, the translational–rotational interaction leads to a decrease in the free energy and, hence, to an increase in the heat capacity of the system at low temperatures. It is easy to see that, at  $\omega_{\text{loc}} \gg \omega_0$ , relationship (61) for  $\tilde{\omega}_0$  coincides with formula (59).

If the parameter  $a$  of the translational–rotational interaction is comparable to or exceeds the spacing between the rotational and local levels, i.e., at  $a \geq (\omega_{\text{loc}}^2 - \omega_0^2)^2$ , the frequencies are mixed. As a result, molecular librations and local vibrations cease to be well-defined eigenstates of the system.

A more complex situation is observed in the case when the librational frequency is located in the range of the continuous spectrum of phonon excitations in the vicinity of the lower edge ( $\omega_0 > \Delta$ ) [12, 20]. For a heavy impurity ( $\omega_{\text{loc}} < \Delta$ ), the contribution from the rotational degrees of freedom to the thermodynamic functions of the system is small compared to that from the local frequencies. Therefore, we dwell on the more interesting case of a light impurity. In order to derive the contribution from the rotational degrees of freedom to the free energy, we rewrite relationship (54) in the following form:

$$\Delta\tilde{\mathcal{F}} = -\frac{2T}{\pi} \lim_{\delta \rightarrow 0} \int_{\Delta}^{\infty} d\omega \ln 2 \sinh \left( \frac{\hbar\omega}{2T} \right) \frac{\partial\phi(\omega, \delta)}{\partial\omega}. \quad (62)$$

The analytical and numerical treatment demonstrated that the function  $\partial\phi/\partial\omega$  exhibits a sharp maximum at the frequency  $\tilde{\omega}_0$  and rapidly decays away from this frequency. The frequency  $\tilde{\omega}_0$  coincides to high accuracy with the frequency determined from relationship (59). This agreement is explained by the fact that the density of phonon states in the system under consideration drastically increases at  $\omega \rightarrow \Omega_{\text{max}}$ . Therefore, at  $\omega_0 - \Delta \ll \Delta$ , the main contribution to the renormalization of the rotational frequency of the impurity molecule is made by high-frequency phonons.

By approximating the function  $\partial\phi/\partial\omega$  in the vicinity of the maximum, we obtain the contribution from the rotational motion of the molecule to the free energy:

$$\Delta\tilde{\mathcal{F}} = \frac{2T}{\pi} \int_{\Delta}^{\Omega_{\text{max}}} d\omega \ln 2 \sinh \left( \frac{\hbar\omega}{2T} \right) \frac{\gamma_0}{(\omega - \tilde{\omega}_0)^2 + \gamma_0^2}, \quad (63)$$

where  $\gamma_0 = -a\mu(\tilde{\omega}_0)/(2\tilde{\omega}_0)$  is the half-width of the Lorentzian peak of the integrand in the vicinity of the frequency  $\tilde{\omega}_0$ . It should be emphasized that approximation (63) holds true if the frequency  $\omega_0$  is not too close to the lower edge of the continuous spectrum, i.e., if the inequality  $\omega_0 - \Delta \gg \gamma_0$  is satisfied.

The integrand in expression (63) has the form of a standard dispersion relation in which the half-width  $\gamma_0$  is proportional to the interaction parameter  $a$ . Physically, this result can be explained as follows: the phonon subsystem is excited by the rotator and, in turn, has an effect on the rotator state. This effect, as in any distributed system, is characterized by a retardation determined by the response function of the system. Actually, the quantity  $\gamma_0$  includes the interaction parameter  $a$  and the characteristics of the phonon subsystem.

Since the half-width  $\gamma_0$  is small, the contribution from the rotational degrees of freedom of the impurity molecule to the heat capacity can be approximately represented by expression (57). Therefore, the rotational part of the heat capacity at low temperatures has an exponential form,

$$\Delta C = 2 \left( \frac{\hbar \tilde{\omega}_0}{T} \right)^2 \exp \left( -\frac{\hbar \tilde{\omega}_0}{T} \right), \quad (64)$$

whereas the corresponding dependence for three-dimensional crystals is described by a power function [20]. The result obtained is explained by the gap character of the phonon spectrum of the two-dimensional atomic crystal commensurate to the substrate [8, 21]. In this respect, we recall that the heat capacity of the matrix also has an exponential form [8, 21],

$$C_{\text{ph}} \sim \frac{\Delta}{T} \exp \left( -\frac{\Delta}{T} \right).$$

The above dependence of the heat capacity on the temperature differs from that represented by relationship (64) in terms of the preexponential factor. This circumstance can appear to be useful in separating the rotational contribution from the total experimentally measured heat capacity of the system, especially in the case when  $\omega_0$  and  $\Delta$  are close in magnitude.

## 5. CONCLUSIONS

The behavior of a diatomic impurity molecule in a two-dimensional atomic matrix located on a substrate turns out to be considerably more complex than that in a three-dimensional atomic matrix with cubic symmetry [18, 20]. In a three-dimensional system, owing to the high symmetry of the environment, the interaction of the rotator with phonons leads only to an increase in its moment of inertia without changing the character of the rotational motion. In a two-dimensional system, which is characterized by the anisotropy due to a preferential direction (perpendicular to the layer plane), the interaction of the rotator with phonons brings about substantial changes: the inertia tensor components become dependent on the orientation of the axis of the impurity molecule. In this case, the inertia tensor remains diagonal when the substrate atoms form a hexagonal structure and has off-diagonal components for substrates with triangular lattices. Therefore, the impu-

rity molecule in the two-dimensional matrix located on the substrate represents a parametric rotator whose dynamics significantly differs from the behavior of both a free rotator and a rotator in a three-dimensional cubic lattice.

Upon introduction of molecular impurities into the two-dimensional atomic lattice, the low-temperature heat capacity of the system is characterized by an additional contribution that is associated with the rotational degrees of freedom of the impurity molecule and can be observed experimentally. For commensurate structures, two-dimensional solutions of light impurities are experimentally simpler, because the contribution made to the heat capacity by local translational frequencies does not affect the contribution from the rotational degrees of freedom. The case of a heavy impurity is theoretically more interesting and, at the same time, is more complex for experimental investigations. This is explained by the difficulties encountered in correct separation of the contributions from the localized and rotational states.

Thus, the results obtained in the present work demonstrated that the inclusion of the translational–rotational interactions is of considerable importance in analyzing and interpreting the dynamics and thermodynamics of molecular impurities in two-dimensional crystals.

## REFERENCES

1. R. M. Lynden-Bell and K. H. Michel, *Rev. Mod. Phys.* **66** (3), 721 (1994).
2. A. I. Krivchikov, M. I. Bagatskiĭ, V. G. Manzheliĭ, *et al.*, *Fiz. Nizk. Temp.* **14** (11), 1208 (1988) [*Sov. J. Low Temp. Phys.* **14**, 667 (1988)].
3. P. I. Muromtsev, M. I. Bagatskiĭ, V. G. Manzheliĭ, *et al.*, *Fiz. Nizk. Temp.* **16** (8), 1058 (1990) [*Sov. J. Low Temp. Phys.* **16**, 616 (1990)].
4. P. I. Muromtsev, M. I. Bagatskiĭ, V. G. Manzheliĭ, and I. Ya. Minchina, *Fiz. Nizk. Temp.* **20** (3), 247 (1994) [*Low Temp. Phys.* **20**, 195 (1994)].
5. V. G. Manzheliĭ, E. A. Kosobutskaya, V. V. Sumarov, *et al.*, *Fiz. Nizk. Temp.* **12** (2), 151 (1986) [*Sov. J. Low Temp. Phys.* **12**, 86 (1986)].
6. T. N. Antsygina and V. A. Slyusarev, *Fiz. Nizk. Temp.* **19** (1), 102 (1993) [*Low Temp. Phys.* **19**, 73 (1993)].
7. T. N. Antsygina and V. A. Slyusarev, *Fiz. Nizk. Temp.* **20** (3), 255 (1994) [*Low Temp. Phys.* **20**, 202 (1994)].
8. J. G. Dash, *Fiz. Nizk. Temp.* **1** (7), 839 (1975) [*Sov. J. Low Temp. Phys.* **1**, 401 (1975)].
9. T. N. Antsygina, M. I. Poltavskaya, and K. A. Chishko, *Fiz. Tverd. Tela (St. Petersburg)* **44** (7), 1215 (2002) [*Phys. Solid State* **44**, 1268 (2002)].
10. T. N. Antsygina, K. A. Chishko, and I. I. Poltavsky, *J. Low Temp. Phys.* **126** (1/2), 15 (2002).
11. I. M. Lifshits and A. M. Kosevich, *Rep. Prog. Phys.* **29**, 217 (1966).
12. Yu. Kagan and Ya. Iosilevskii, *Zh. Éksp. Teor. Fiz.* **45** (3), 819 (1963) [*Sov. Phys. JETP* **18**, 562 (1963)].

13. H. Bottger, *Principles of the Theory of Lattice Dynamics* (Physik, Weinheim, 1983; Mir, Moscow, 1986).
14. A. I. Kitaigorodskii, *Molecular Crystals* (Nauka, Moscow, 1972).
15. *Cryocrystals*, Ed. by B. I. Verkin and A. F. Prikhot'ko (Naukova Dumka, Kiev, 1983).
16. M. I. Poltavskaya and K. A. Chishko, *Fiz. Nizk. Temp.* **26** (4), 394 (2000) [*Low Temp. Phys.* **26**, 289 (2000)].
17. M. I. Poltavskaya and K. A. Chishko, *Fiz. Nizk. Temp.* **26** (8), 837 (2000) [*Low Temp. Phys.* **26**, 615 (2000)].
18. N. Antsygina, K. A. Chishko, and V. A. Slusarev, *Phys. Rev. B* **55** (6), 3548 (1997).
19. R. P. Feynman and A. R. Hibbs, *Quantum Mechanics and Path Integrals* (McGraw-Hill, New York, 1965; Mir, Moscow, 1968).
20. T. N. Antsygina and V. A. Slyusarev, *Teor. Mat. Fiz.* **77** (2), 234 (1988).
21. T. N. Antsygina, I. I. Poltavskii, M. I. Poltavskaya, and K. A. Chishko, *Fiz. Nizk. Temp.* **28** (6), 621 (2002) [*Low Temp. Phys.* **28**, 442 (2002)].
22. L. D. Landau and E. M. Lifshitz, *Course of Theoretical Physics, Vol. 1: Mechanics*, 2nd ed. (Nauka, Moscow, 1963; Pergamon, Oxford, 1965).
23. A. M. Kosevich, *The Theory of Crystal Lattice* (Vishcha Shkola, Kharkov, 1988).
24. D. N. Zubarev, *Nonequilibrium Statistical Thermodynamics* (Nauka, Moscow, 1971; Consultants Bureau, New York, 1974).

*Translated by O. Borovik-Romanova*

# Photoinduced Ion Transfer in Heterojunctions Based on Solid Electrolytes with a Mixed Ionic–Electronic (Hole) Conductivity

A. I. Stetsun

*Institute of Semiconductor Physics, National Academy of Sciences of Ukraine, Kiev, 03028 Ukraine*

Received May 19, 2003; in final form, August 26, 2003

**Abstract**—The concept of photoinduced ion transfer in heterojunctions based on solid electrolytes with a mixed ionic–electronic (hole) conductivity is justified. This concept is confirmed by the experiments on photo-deposition of a metal in a heterojunction based on a solid electrolyte with a mixed conductivity. The possibility of using heterojunctions based on a solid electrolyte layer with a mixed ionic–electronic (hole) conductivity for optical recording of information is considered. © 2004 MAIK “Nauka/Interperiodica”.

## 1. INTRODUCTION

Since the advent of heterojunctions and, especially, with the advance of their technology and theory, heterojunctions have been widely used in fabricating diodes, transistors, photodiodes, solar cells, light-emitting diodes, semiconductor lasers, etc. [1–3]. Despite the extensive application in many fields, the possibility of using heterojunctions for optical recording of information has not been adequately studied. In this respect, the present work is devoted to the design and investigation of specific heterojunctions intended for optical recording of information.

It is known that one of the applications of heterojunctions is based on the generation of a photovoltage under illumination [4, 5]. The generation of a photovoltage is associated with the fact that electron–hole pairs excited by light in both parts of the heterojunction are separated by an electric field in space-charge regions of the heterojunction. The photovoltage can be determined from the relationship [4]

$$\begin{aligned} V = & \int \left( \frac{\Delta\sigma_n + \Delta\sigma_p}{\sigma} \right) \xi_0 dx - \int \left( \frac{\Delta\sigma_n}{\sigma} \right) \left( \frac{d\chi}{dx} \right) dx \\ & - \int \left( \frac{\Delta\sigma_p}{\sigma} \right) \left( \frac{d\chi}{dx} + \frac{dE_g}{dx} \right) dx \\ & + kT \int \left[ \left( \frac{\Delta\sigma_p}{\sigma} \right) \frac{d}{dx} (\ln N_v) - \left( \frac{\Delta\sigma_n}{\sigma} \right) \frac{d}{dx} (\ln N_c) \right] dx, \end{aligned} \quad (1)$$

where  $\sigma$  is the conductivity induced under illumination,  $\Delta\sigma$  is the photoconductivity,  $\chi$  is the electron affinity,  $N_c$  is the density of states in the conduction band,  $N_v$  is the density of states in the valence band,  $\xi_0$  is the strength of the electric field in the heterojunction, and  $E_g$  is the band gap.

The electric field induced by separated electrons and holes is opposed to the electric field generated in the space-charge regions of the heterojunction. The strength of the photoinduced field can be defined as

$$E = \frac{V}{\Delta x}, \quad (2)$$

where  $\Delta x$  is the distance between electrons and holes separated by the heterojunction. Under exposure of the heterojunction to light, the electric field is induced both in the space-charge regions of the heterojunction and in the quasi-neutral region.

Let us now assume that charged particles (differing from electrons and holes), such as ions with a particular charge and mobility, are placed in either of two parts of the photoelectric heterojunction. In this case, the electric field arising upon generating a photovoltage should initiate ion migration across one of the parts of the heterojunction. Therefore, illumination of the heterojunction, which induces the photovoltage, should also stimulate an ion mass transfer. Correspondingly, the difference in the concentration distribution of ions over the thickness in one of the parts of the heterojunction before and after exposure to light can be used for optical recording of information.

Since mobile charges of two types, namely, ions and electrons (or holes), reside in solid electrolytes with a mixed ionic–electronic (hole) conductivity, it is possible to fabricate a specific heterojunction between a conventional semiconductor with electronic (or hole) conductivity and a solid electrolyte (whose illumination generates a photovoltage) with a mixed conductivity. This heterojunction is characterized by the photoinduced ion transfer across one of the two parts of the heterojunction.

The interface between two materials with different bond lengths contains a large number of defects in the

**Table 1.** Characteristics of electrical conductivity of  $\text{As}_2\text{S}_3$  films photodoped with silver at different contents (temperature, 300 K) [7]

$C_{\text{Ag}}$ , at. %	$\sigma_i$ , $\Omega^{-1} \text{ cm}^{-1}$	$\sigma_p$ , $10^{-5} \Omega^{-1} \text{ cm}^{-1}$	$\eta_i$
20	$7.6 \times 10^{-8}$	0.17	0.04
25	$8.2 \times 10^{-6}$	2.8	0.23
29	$3.5 \times 10^{-5}$	4.7	0.43
32	$3.0 \times 10^{-4}$	6.3	0.83

Note:  $C_{\text{Ag}}$  is the silver content,  $\sigma_i$  is the ionic conductivity,  $\sigma_p$  is the hole conductivity, and  $\eta_i$  is the transport number.

form of dangling bonds [3]. Dangling bonds can serve both as electron trapping centers and as recombination centers. The recombination of electrons and ions at the interface formed by two parts of the heterojunction brings about the photodeposition of a chemical element responsible for ionic conductivity in the solid electrolyte.

For the purpose of experimentally verifying the possibility of photoinducing mass transfer of ions across the layer of a solid electrolyte with mixed conductivity in a heterojunction, we investigated how illumination affects the properties of heterojunctions between  $\text{A}^{\text{IV}}\text{B}^{\text{VI}}$  semiconductors and vitreous  $\text{As}_2\text{S}_3$  layers photodoped with silver at a content of 2–32 at. %.

The choice of the  $\text{A}^{\text{IV}}\text{B}^{\text{VI}}$  semiconductor material as a constituent of a heterojunction was made for the reason that these materials are characterized by a high photovoltage [6].

Silver-photodoped  $\text{As}_2\text{S}_3$  layers are solid electrolytes with a mixed (ionic and hole) conductivity [7–9]. Photodoping allows one to vary the metal content in a semiconductor layer over a wide range and, thus, to control the ionic and hole conductivities (Table 1). In turn, this makes it possible to vary substantially the conditions of experimental investigations into the properties of heterojunctions with solid electrolytes.

The photoinduced transfer of silver ions and the photodeposition of silver in a heterojunction were found experimentally in  $\text{CdSe-As}_2\text{S}_3\text{Ag}_x$  ( $x = 0.9\text{--}2.4$ ) heterojunctions. The experimental results obtained in this work proved that heterojunctions with mixed ionic–electronic (hole) conductors can be used for optical recording of information.

The main objective of the present work was to justify the concept of photoinduced ion transfer and to reveal experimentally the photoinduced transfer of silver ions across one of the parts of the heterojunction with a solid electrolyte under illumination.

## 2. EXPERIMENTAL TECHNIQUE

Photoinduced changes in heterojunctions were initiated under exposure to light of a KG-220-500 halogen

lamp at different illuminances. In the course of illumination, the sample was cooled with an air stream produced by a fan.

After exposure to light, the samples were examined under a Biolam optical microscope. The concentration distribution of the metal over the thickness of a solid electrolyte layer was investigated on a JAMP-10S Auger analyzer.

Heterojunctions were prepared through thermal evaporation under vacuum with the use of a VUP-5 vacuum setup. During evaporation, the residual pressure was no less than  $10^{-3}$  Pa.

Photodoping of  $\text{As}_2\text{S}_3$  layers with silver was carried out according to the procedure described in [10, 11]. After deposition of a silver-photodoped  $\text{As}_2\text{S}_3$  layer on a quartz or silicon substrate, this layer was coated with a CdSe layer through thermal evaporation.

The optical reflectance and transmittance spectra of the heterojunctions before and after illumination were recorded on a KSVU-23 spectrophotometer in the wavelength range 200–1200 nm.

The photovoltage was measured with the use of a V7-45 voltmeter. The internal resistance of the voltmeter was equal to  $10^{16} \Omega$ .

## 3. EXPERIMENTAL RESULTS

The heterojunctions studied in this work contained 400- to 500-nm-thick  $\text{As}_2\text{S}_3$  layers photodoped with silver and 200- to 500-nm-thick CdSe layers.

At the first stage of our investigation, we examined heterojunctions between a CdSe layer and a silver-photodoped  $\text{As}_2\text{S}_3$  layer without exposure to light. Initially, these unexposed heterojunctions were studied using an optical microscope. No inhomogeneities, precipitates, or clusters were found in the heterojunction structure.

The unexposed heterojunctions were subjected to chemical treatment. The CdSe layer was removed by chemical etching in a mixture of  $\text{HNO}_3$  and HCl acids. The remaining  $\text{As}_2\text{S}_3$  layer photodoped with silver was examined with the use of an electron microscope from the Auger analyzer. This examination also did not reveal precipitates or clusters in the silver-photodoped layer. The results of Auger spectroscopy demonstrated that the silver content in the surface region of the  $\text{As}_2\text{S}_3$  layer photodoped with silver at a content of 25 at. % differs from this value by no more than 1 at. %.

At the second stage of the investigation, the heterojunctions were exposed to light.

For heterojunctions between a CdSe layer and an  $\text{As}_2\text{S}_3$  layer photodoped with silver at a content of 15–32 at. % (the chemical composition corresponds to the formula  $\text{As}_2\text{S}_3\text{Ag}_x$  at  $x = 0.9\text{--}2.4$ ), exposure from the side of the photodoped layer to light of a KG-220-500 halogen lamp at an illuminance of  $8 \times 10^4$  lx for 2 h

leads to the formation of silver precipitates of two types, namely, small-sized and large-sized precipitates, in the heterojunction. The precipitates are formed in the photodoped layer in the vicinity of the interface. The characteristic sizes of the precipitates are equal to 0.2–0.5 (smaller precipitates) and 2–5  $\mu\text{m}$  (larger precipitates).

According to the results of Auger spectroscopy, the exposure of the heterojunctions to light results in an increase in the content of silver ions in the vicinity of the interface between the layers. These experiments were performed as follows. A CdSe–As<sub>2</sub>S<sub>3</sub> heterojunction photodoped with silver at a content of 25 at. % (the chemical composition corresponds to the formula As<sub>2</sub>S<sub>3</sub>Ag<sub>1.67</sub>) was exposed to light of the halogen lamp at an illuminance of  $8 \times 10^4$  lx for 20 min in the chamber of the Auger analyzer. Then, under exposure of the sample at the same illuminance for 20 min, the CdSe layer was etched away with an argon ion beam. Exposure under these conditions brought about the formation of precipitates 0.2–0.3  $\mu\text{m}$  in size in the surface region of the photodoped layer. In the regions free of precipitates, the silver content in the surface region of the photodoped layer increased by 5 at. % as compared to that in the bulk of the photodoped layer.

Moreover, the CdSe–As<sub>2</sub>S<sub>3</sub>Ag<sub>1.67</sub> heterojunction was exposed and etched under the same conditions but at an illuminance of  $2 \times 10^4$  lx. In this case, no formation of photoprecipitates was observed and the silver content in the surface region of the As<sub>2</sub>S<sub>3</sub>Ag<sub>1.67</sub> layer increased by 3 at. %.

The size of the photoprecipitates formed under exposure of the CdSe–As<sub>2</sub>S<sub>3</sub>Ag<sub>1.67</sub> heterojunction to light depends on the illuminance and exposure time. The exposure of the heterojunction to light at an illuminance of  $8 \times 10^4$  lx for 2 h leads to saturation of the photodeposition of silver, i.e., to the formation of large-sized silver photoprecipitates whose height is equal to the thickness of the photodoped layer.

Similar results were obtained for the CdSe–As<sub>2</sub>S<sub>3</sub>Ag<sub>x</sub> ( $x = 0.9$ – $2.4$ ) heterojunctions exposed from the side of the CdSe layer.

In the heterojunctions under investigation, we measured a dark voltage with a positive potential at the CdSe layer. However, under exposure of the heterojunction to light, we revealed a photovoltage with a negative potential at the CdSe layer.

For example, in the CdSe–As<sub>2</sub>S<sub>3</sub>Ag<sub>1.67</sub> heterojunction between a CdSe layer 200 nm thick and an As<sub>2</sub>S<sub>3</sub>Ag<sub>1.67</sub> layer 430 nm thick, the dark voltage with a positive potential at the CdSe layer is equal to 105 mV. The exposure of this heterojunction to light at an illuminance of  $8 \times 10^4$  lx induces a photovoltage of 90 mV with a negative potential at the CdSe layer. Upon generation of the photovoltage with this sign, the electric field induced in the layer of the solid electrolyte is

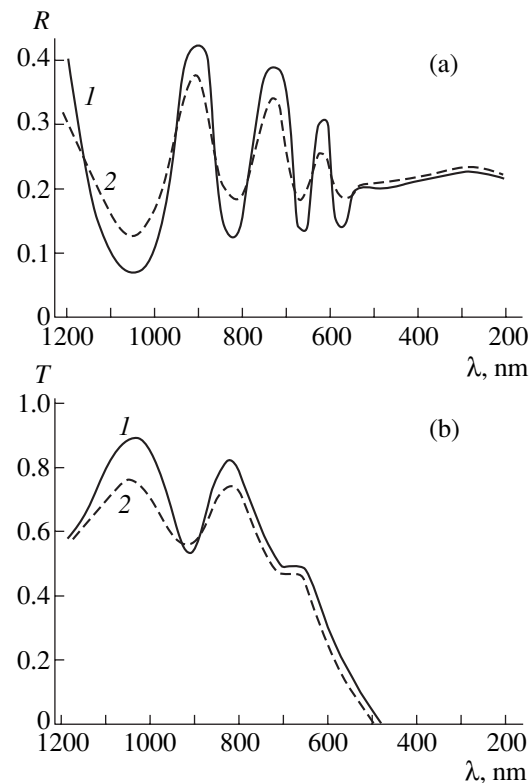


Fig. 1. (a) Reflectance ( $R$ ) and (b) transmittance ( $T$ ) spectra of the CdSe–As<sub>2</sub>S<sub>3</sub>Ag<sub>1.67</sub> heterojunction (1) before and (2) after exposure to light.

directed such that it initiates the migration of positive silver ions toward the interface.

The reflectance and transmittance spectra of the initial and exposed CdSe–As<sub>2</sub>S<sub>3</sub>Ag<sub>1.67</sub> heterojunctions are depicted in Fig. 1. The exposure of the As<sub>2</sub>S<sub>3</sub>Ag<sub>1.67</sub> heterojunction to light results in a decrease in the amplitude of interference oscillations, which indicates an increase in the absorption by the photoinduced layer. As was shown in our earlier work [12], an increase in the silver content in the photodoped As<sub>2</sub>S<sub>3</sub> layer leads to a shift in the absorption edge toward the long-wavelength range and to an increase in the absorption in the layer. Therefore, the observed decrease in the amplitude of interference oscillations can be associated with an increase in the silver content in photodoped layer regions of different thicknesses.

The photosensitivity of the CdSe–As<sub>2</sub>S<sub>3</sub>Ag<sub>1.67</sub> heterojunction was calculated from the spectral dependence of the reflectance. The photosensitivity  $S$  was defined as the reciprocal of the radiant exposure responsible for the relative change in the reflectance  $R$ , that is,

$$S = \frac{A}{Et}, \quad (3)$$

**Table 2.** Photosensitivities of the CdSe–As<sub>2</sub>S<sub>3</sub>Ag<sub>1.67</sub> heterojunction at different wavelengths

$\lambda$ , nm	$S$ , $10^{-9} \text{ lx}^{-1} \text{ s}^{-1}$
1200	0.30
1180	0.35
1140	0.20
1100	1.10
1060	1.20
1020	0.30
980	0.10
940	0.14
900	0.20
860	0.21
820	0.70
780	0.10
740	0.30
700	0.20
660	0.70
620	0.40
580	0.50
540	0.01

where  $E$  is the illuminance,  $t$  is the exposure time, and

$$A = \frac{\Delta R}{R}. \quad (4)$$

The photosensitivities of the CdSe–As<sub>2</sub>S<sub>3</sub>Ag<sub>1.67</sub> bilayer structure at different wavelengths are presented in Table 2.

#### 4. DISCUSSION

The observed increase in the content of silver ions in the vicinity of the interface formed by the heterojunction layers and the formation of photoprecipitates at the interface under exposure of the heterojunction to light have demonstrated that the illumination of the hetero-

junction leads to photoinduced mass transfer of silver ions to the interface between the layers. This mass transfer is induced by an electric field arising upon generation of a photovoltage. Thus, the experimental results obtained confirm the concept of photoinduced ion transfer in a heterojunction with a solid electrolyte, which was proposed in formulating the problem to be solved in this work.

The photoinduced processes occurring in a heterojunction that contains a solid electrolyte with a mixed ionic–electronic (hole) conductivity can be explained in terms of the energy band diagram of the heterojunction. For this purpose, we will consider the formation of a heterojunction between a CdSe layer and an As<sub>2</sub>S<sub>3</sub> layer doped with silver at a content of 25 at. %.

The electron affinity of silver-doped As<sub>2</sub>S<sub>3</sub> exceeds the electron affinity of CdSe by 0.3 eV [13]. As a consequence, when CdSe is thermally evaporated onto the As<sub>2</sub>S<sub>3</sub>Ag<sub>1.67</sub> layer, electrons diffuse from CdSe into the As<sub>2</sub>S<sub>3</sub>Ag<sub>1.67</sub> layer and recombine with holes. These processes bring about the formation of a positively charged region in the CdSe layer and a negatively charged region in the As<sub>2</sub>S<sub>3</sub>Ag<sub>1.67</sub> layer.

The formation of the space-charge regions in the heterojunction that contains the solid electrolyte with mixed conductivity results in two competing processes of ion migration.

First, the ions involved in the space-charge region of the solid electrolyte are expelled from this region under the action of an electric field induced by the space-charge regions.

Second, the ion migration can be initiated by the interaction between the charges that form the positively and negatively charged regions in the heterojunction with positive ions located in the bulk of the solid electrolyte layer. If the charges distributed in the positively and negatively charged regions in the heterojunction induce a dipole field at distances considerably larger than their sizes, the positive ions should be attracted to the negatively charged region of depletion of the heterojunction.

These two processes of ion migration result in the formation of a close-packed layer of ions after the space-charge region of the solid electrolyte. The existence of such close-packed layers of ions is characteristic of interfaces between solid electrolytes and other materials, in particular, in double electrical layers [14].

In the heterojunction with a solid electrolyte, the ion migration occurs until the sum of forces acting on each ion from the space-charge regions and other particles becomes equal to zero.

The band diagram thus obtained for the CdSe–As<sub>2</sub>S<sub>3</sub>Ag<sub>1.67</sub> heterojunction is shown in Fig. 2. This diagram was constructed without regard for the migration of ions from deep within the solid electrolyte layer to the space-charge region, because the strength of the electric field of the space dipole is substantially weaker

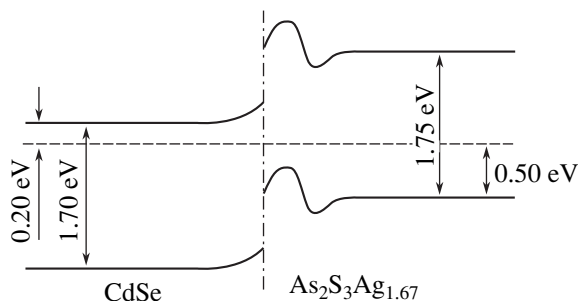


**Fig. 2.** Band diagram of the CdSe–As<sub>2</sub>S<sub>3</sub>Ag<sub>1.67</sub> heterojunction. The parameters of the material are taken from [6, 10].



than that inside the space-charge region of the solid electrolyte.

The above band diagram is similar to the band diagram of a graded-gap heterojunction [15].

The illumination of the CdSe-As<sub>2</sub>S<sub>3</sub>Ag<sub>1.67</sub> heterojunction leads to the generation of electron-hole pairs that are separated by the electric field in the space-charge regions of the heterojunction. The potential barrier on the side of the As<sub>2</sub>S<sub>3</sub>Ag<sub>1.67</sub> layer can be overcome by electrons through injection, injection with preliminary thermalization, and tunneling. As follows from the results of investigations of the CdSe-As<sub>2</sub>S<sub>3</sub>Ag<sub>2.4</sub> heterojunction [16], the injection is the most important mechanism of overcoming the potential barrier by electrons. Owing to these processes, electrons are accumulated in quasi-neutral regions of the CdSe layer, whereas holes are concentrated in quasi-neutral regions of the As<sub>2</sub>S<sub>3</sub>Ag<sub>1.67</sub> photodoped layer.

The schematic drawing of the space-charge regions in the CdSe-As<sub>2</sub>S<sub>3</sub>Ag<sub>1.67</sub> heterojunction is presented in Fig. 3. The concentration distributions of photoexcited electrons and holes separated by the electric field of the heterojunction are also schematically shown in this figure. The distributions of photoexcited electrons and holes are given according to the data taken from [3].

Under exposure of the heterojunction to light, the electric field induced in the region between photoexcited electrons and holes separated by the electric field of the heterojunction (Fig. 3) acts on positive Ag<sup>+</sup> ions and thus induces mass transfer of silver ions toward the interface. The former field affects both the quasi-neutral region of the solid electrolyte layer and the space-charge region.

Owing to the spatial distribution of the electric field induced by photoexcited carriers and the electric field of the heterojunction, the most intensive mass transfer of ions occurs from the quasi-neutral region to the depletion region of the solid electrolyte. This can be explained by the fact that the strength of the electric field in the quasi-neutral region is relatively high and is directed toward the interface between the layers, whereas the field strength of the heterojunction in the space-charge region is opposite in direction (i.e., it is opposed to the electric field of separated electron-hole pairs).

After the ion transfer from the quasi-neutral region to the space-charge region, silver ions diffuse in the space-charge region of the solid electrolyte toward the interface between the layers. This diffusion becomes possible under exposure of the heterojunction to light, because the electric field of separated electron-hole pairs reduces the strength of the electric field of the heterojunction and, in the limiting case at high illuminances, can provide the band alignment of the heterojunction. Furthermore, silver ions are entrained by electrons that moves in response to the electric field of the

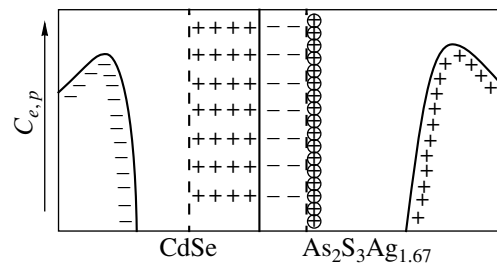


**Fig. 3.** Schematic drawing of the space-charge regions in the CdSe-As<sub>2</sub>S<sub>3</sub>Ag<sub>1.67</sub> heterojunction and the concentration distributions of photoexcited electrons and holes separated by the electric field of the heterojunction over its thickness.

heterojunction toward the CdSe layer (the electron wind effect [17]).

The interface between the CdSe and As<sub>2</sub>S<sub>3</sub>Ag<sub>1.67</sub> layers is a boundary between polycrystalline and amorphous materials with different bond lengths. Therefore, this interface contains a large number of defects in the form of dangling bonds. It is known that dangling bonds can serve both as electron trapping centers and as recombination centers [2, 3]. As a consequence, the photodeposition of silver occurs through the recombination of an electron and an ion at the interface. The precipitates can grow either through the same process (the capture of an electron by a dangling bond and recombination of this electron with another ion, followed by binding of both ions) or through the capture of an electron upon the photodeposition of silver and recombination of the next ion with this electron. When multiply repeated, these processes provide the growth of precipitates.

The theoretical analysis of the photoinduced processes observed in heterojunctions based on mixed ionic-electronic (hole) conductors and the analysis of the experimental results obtained have demonstrated that, depending on the conditions of illumination of the heterojunction with a solid electrolyte, there are two variants of photoinduced ion transfer: (1) photoinduced ion transfer with subsequent photodeposition of the chemical element responsible for the ionic conductivity and (2) photoinduced ion transfer without photodeposition.

The second variant is observed under exposure of the heterojunction to light at lower illuminances when the electric field induced upon the generation of a photovoltage cannot ensure mass transfer of ions to the space-charge region of the solid electrolyte toward the interface between the layers.

The analysis of the results obtained in the present work allowed us to propose a new method of designing a medium for optical recording of information. This medium can be prepared in the form of a bilayer or multilayer thin-film structure in which heterojunctions capable of generating a photovoltage are formed

between layers of a solid electrolyte with mixed conductivity and layers of other materials with electronic or hole conductivity. Exposure of the heterostructure to light leads to photoinduced transfer of ions across the layer of the solid electrolyte. Moreover, depending on the conditions of illumination of the heterojunction and the properties of the constituent materials, there can occur photodeposition of the chemical element responsible for the ionic conductivity in the solid electrolyte. In this medium, the data recording is based on the difference between the reflectances (or transmittances) in exposed and unexposed regions.

The proposed method makes it possible to prepare media for optical recording of information from numerous combinations of solid electrolytes (possessing a mixed conductivity) with semiconductors, dielectrics, and metals. Consequently, heterostructures based on solid electrolytes with mixed conductivity can be expected to differ substantially in terms of their physical properties. In this case, the possibility of producing heterojunctions with band diagrams of different types has assumed a particular importance. Furthermore, solid electrolytes differ in the type and magnitude of conductivity. For example, the conductivity of  $\text{As}_2\text{S}_3\text{Ag}_x$  ( $x = 0.9\text{--}2.4$ ) glasses falls in the range from  $7.6 \times 10^{-8}$  to  $3.08 \times 10^{-4} \Omega^{-1} \text{cm}^{-1}$  [7], whereas the ionic conductivity of the  $(\text{Ag}_2\text{GeS}_3)_{48}(\text{AgI})_{52}$  glass is equal to  $6 \times 10^{-3} \Omega^{-1} \text{cm}^{-1}$  [18].

It should be noted that the ionic conductivities of  $\text{Cu}_4\text{RbCl}_3\text{I}_2$  and  $\text{Ag}_4\text{RbI}_5$  crystals are considerably higher ( $0.5$  and  $0.3 \Omega^{-1} \text{cm}^{-1}$ , respectively) [19].

If the electronic (hole) component of the conductivity is provided in the aforementioned materials either through doping with impurities or by other methods and the materials thus modified are used to prepare heterojunctions capable of generating a photovoltage, it can be expected that the time of data recording with these heterojunctions will be several orders of magnitude shorter than that for the  $\text{CdSe-As}_2\text{S}_3\text{Ag}_x$  ( $x = 0.9\text{--}2.4$ ) heterostructures.

## 5. CONCLUSIONS

Thus, the results obtained in this work demonstrated that a necessary condition for photoinduced mass transfer of ions in a heterojunction that contains a solid electrolyte with a mixed ionic–electronic (hole) conductivity is the generation of a photovoltage.

Depending on the conditions of illumination of the heterojunction and the properties of the constituent materials, there are two variants of photoinduced ion transfer: (1) photoinduced ion transfer with subsequent photodeposition of the chemical element responsible for the ionic conductivity and (2) photoinduced ion transfer without photodeposition.

The analysis of the photoinduced processes occurring in heterojunctions based on solid electrolytes with mixed conductivity showed that, depending on the type of band diagram of the heterojunction and the type of conductivity of the constituent materials, the photoinduced ion transfer can occur in two directions. This process can proceed from deep within the solid electrolyte layer to the interface between the layers or in the opposite direction (from the interface between the layers to the surface of the solid electrolyte layer).

## REFERENCES

1. A. G. Milnes and D. L. Feucht, *Heterojunctions and Metal–Semiconductor Junctions* (Academic, New York, 1972; Mir, Moscow, 1975).
2. B. L. Sharma and R. K. Purohit, *Semiconductor Heterojunctions* (Pergamon, Oxford, 1974; Sovetskoe Radio, Moscow, 1979).
3. A. L. Fahrenbruch and R. H. Bube, *Fundamentals of Solar Cells* (Academic, New York, 1987; Énergoatomizdat, Moscow, 1987).
4. *Current Topics in Photovoltaic*, Ed. by T. G. Coutts and J. D. Meakin (Academic, London, 1972; Mir, Moscow, 1988), p. 25.
5. A. van der Ziel, *Solid State Physical Electronics* (Prentice Hall, Englewood Cliffs, 1957), p. 284.
6. K. L. Chopra and S. R. Das, *Thin Film Solar Cells* (Plenum, New York, 1983; Mir, Moscow, 1986).
7. V. A. Dan'ko, I. Z. Indutnyi, and V. I. Min'ko, *Fiz. Khim. Stekla* **18**, 128 (1992).
8. I. Z. Indutnyi, *Zh. Nauchn. Prikl. Fotogr.* **39**, 65 (1994).
9. K. Tanaka, *J. Non-Cryst. Solids* **137–138**, 1021 (1991).
10. I. Z. Indutnyi, M. T. Kostyshin, O. P. Kosyurum, V. I. Min'ko, E. V. Mikhailovskaya, and P. F. Romanenko, *Photoinduced Interactions in Metal–Semiconductor Structures* (Naukova Dumka, Kiev, 1992).
11. A. I. Stetsun, I. Z. Indutnyi, and V. G. Kravets, *J. Non-Cryst. Solids* **202**, 113 (1996).
12. I. Z. Indutnyi, A. I. Stetsun, M. V. Sopinskiĭ, and V. D. Nechiporuk, *Optoelektron. Poluprovodn. Tekh.* **30**, 42 (1995).
13. V. S. Fomenko, *Emission Properties of Materials* (Naukova Dumka, Kiev, 1981), p. 184.
14. V. M. Arutyunyan, *Usp. Fiz. Nauk* **158**, 255 (1989) [*Sov. Phys. Usp.* **32**, 521 (1989)].
15. W. G. Oldham and A. G. Milnes, *Solid State Electron.* **6**, 121 (1963).
16. A. I. Stetsun, *Fiz. Tekh. Poluprovodn. (St. Petersburg)* **37**, 1197 (2003) [*Semiconductors* **37**, 1169 (2003)].
17. V. B. Fiks, *Ionic Conductivity in Metals and Semiconductors* (Nauka, Moscow, 1983), pp. 108–123.
18. A. Feltz, *J. Non-Cryst. Solids* **90**, 545 (1987).
19. Yu. Ya. Gurevich, *Solid Electrolytes* (Nauka, Moscow, 1986).

Translated by O. Borovik-Romanova

---

---

**LOW-DIMENSIONAL SYSTEMS  
AND SURFACE PHYSICS**

---

---

# Electron Localization in Conducting Langmuir–Blodgett Films

L. A. Galchenkov, S. N. Ivanov, and I. I. Pyataikin

*Institute of Radio Engineering and Electronics, Russian Academy of Sciences, Mokhovaya ul. 11, Moscow, 125009 Russia*

*e-mail: iip@mail.cplire.ru*

Received October 14, 2003

**Abstract**—The temperature dependence of the intracrystallite conductivity of Langmuir–Blodgett films of the  $(C_{16}H_{33}\text{--TCNQ})_{0.4}(C_{17}H_{35}\text{--DMTTF})_{0.6}$  charge-transfer complex (CTC) is studied by measuring the surface acoustic wave attenuation in a piezoelectric delay line coated with such a film.  $(C_{16}H_{33}\text{--TCNQ})_{0.4}(C_{17}H_{35}\text{--DMTTF})_{0.6}$  is a surface-active CTC made from a 1.5 : 1 mixture of heptadecyl-dimethyltetrathiafulvalene ( $C_{17}H_{35}\text{--DMTTF}$ ) and hexadecyl-tetracyanoquinodimethane ( $C_{16}H_{33}\text{--TCNQ}$ ). The temperature dependence of the intracrystallite conductivity is found to have a maximum at  $T_{MD} = 193.5$  K. Above  $T_{MD}$ , the conductivity of the films is metallic ( $\partial\sigma/\partial T < 0$ ), while below this temperature it obeys a law that is close to the one-dimensional Mott law. The decrease in the conductivity with decreasing temperature at  $T < T_{MD}$  is shown to be related to the localization of electron states in the quasi-one-dimensional system under study and to be caused by the presence of impurities and defects in the TCNQ chains, along which a charge is transferred. The detected variation in the conductivity with temperature below  $T_{MD}$  is found to qualitatively and quantitatively agree with the model of localization in a weakly disordered quasi-one-dimensional system proposed earlier by Nakhmedov, Prigodin, and Samukhin. Fitting the experimental results to the theoretical dependences obtained in the framework of this model allows us to find the electron–phonon and electron–impurity scattering times. The structural parameters of the conducting layer are used to estimate the density of states at the Fermi level and the Fermi velocity in the films. With these values, the mean free path and the localization length in the films under study are determined.  
© 2004 MAIK “Nauka/Interperiodica”.

## 1. INTRODUCTION

Conducting Langmuir–Blodgett (LB) films based on surface-active charge-transfer complexes (CTCs) are being intensively studied now because of their potential application in molecular electronics (ME) [1]. The LB technology makes it possible to fabricate homogeneous conducting films having a nanometer-scale thickness and stable properties from CTC molecules, which opens up broad fields for their application in thin-film ME devices [2].

In the last decade, substantial progress has been achieved in producing LB structures with increasing conductivity. Among CTC-based LB films, the maximum conductivity has been reached in systems based on bis(ethylenedioxy)tetrathiafulvalene (BEDO–TTF) with various acceptors. For example, films made from a mixture of  $(BEDO\text{--}TTF)_{0.71}(C_{10}H_{21}\text{--TCNQ})_{0.29}$  with arachidic acid have a conductivity  $\sigma$  of about 10 S/cm at room temperature [3], whereas LB films made from a mixture of BEDO–TTF with behenic acid exhibit a record room-temperature value  $\sigma \approx 40$  S/cm [4]. It should be noted that the conductivities of LB systems are several times lower than those of the corresponding bulk organic-conductor crystals.<sup>1</sup> This circumstance narrows the area of application of LB films in ME.

<sup>1</sup> For example,  $(BEDO\text{--}TTF)ReO_4 \cdot H_2O$  crystals have  $\sigma \approx 147$  S/cm at room temperature [5].

Two main causes of the decreased electrical conductivity of LB films are currently known: first, their polycrystalline structure and, as a result, the presence of intercrystallite potential barriers causing thermally activated transport through them, and, second, the significant difference in the mechanism of intracrystallite conductivity in the films, compared to that in the bulk parent crystals. It is obvious that a detailed study of electron transport in crystallites might contribute to improving the conductivity of such films as a whole. Moreover, such studies could reveal new physical phenomena, since the conductivity mechanism in LB systems can have unique features that are absent in bulk crystals because of the low dimensionality of these systems.

Electron transport in individual crystallites of LB films was first investigated in [6] using a microwave-cavity perturbation technique that had been successfully applied earlier for studying the conductivity of bulk crystals of organic conductors [7, 8]. However, the application of this technique for examining LB systems encounters difficulties, since it is impossible to separate such films from the substrates. The microwave field perturbation caused by a substrate with thickness of about 0.5 mm is many orders of magnitude higher than the perturbation caused by an LB film with thickness of 300–500 Å. Therefore, to ensure the required measurement accuracy, it is necessary to provide a stable driving-oscillator frequency and stable parameters of the

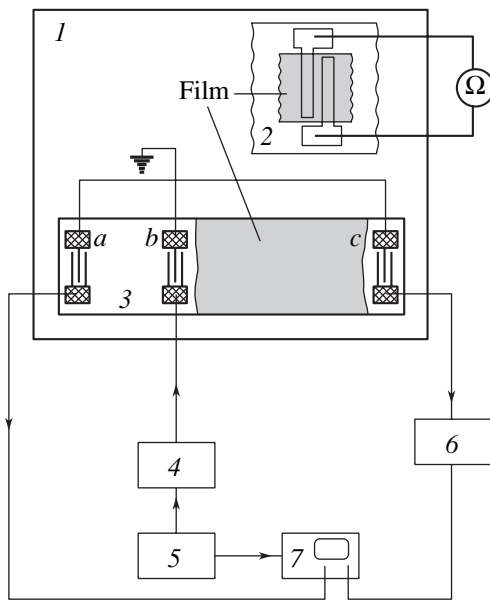


**Fig. 1.** Schematic diagram of the experimental setup: (1) cryostat cold finger, (2) sapphire substrate with sputtered Au electrodes for measuring the conductivity by the two-probe method, (3) delay line, (4) high-frequency oscillator, (5) pulse oscillator, (6) precision attenuator, and (7) oscilloscope.

experimental device used during measurement. These circumstances determine the measurement accuracy and the accessible temperature range. Earlier [9], we proposed another approach for studying the temperature dependence of the intracrystallite conductivity of films, which was based on measuring the attenuation of surface acoustic waves (SAWs) in piezoelectric delay lines coated with an LB film. In that work, we showed that the SAW attenuation is mainly determined by the film conductivity and is directly proportional to the acoustic-wave frequency. Moreover, the film-induced attenuation is higher by 1–1.5 order of magnitude (depending on the SAW frequency) than the attenuation induced by the losses due to the divergence of a SAW beam and dissipative processes that are unrelated to conductivity (losses in the material delay lines and the attenuation caused by the film viscosity). Therefore, the studying of electron transport in crystallites with this technique is much simpler and not a less accurate procedure than using the microwave technique.

In this work, we measured the temperature dependences of the intracrystallite conductivity of  $(C_{16}H_{33}-TCNQ)_{0.4}(C_{17}H_{35}-DMTTF)_{0.6}$  films using the acoustic technique developed in [9]. The temperature dependence of the intracrystallite conductivity is found to have a maximum at  $T_{MD} = 193.5$  K. Above  $T_{MD}$ , the conductivity of the films exhibits metallic behavior ( $\partial\sigma/\partial T < 0$ ), whereas below this temperature it follows a close-to-Mott law. We show that the conductivity decreases with decreasing temperature at  $T < T_{MD}$

because of the localization of electron states in the quasi-one-dimensional system under study and that the metallic behavior of conductivity at  $T > T_{MD}$  is caused by the suppression of the localization effects by inelastic electron-phonon scattering, which becomes significant at high temperatures. It should be noted that the structure of the films under study and the conductivity mechanism in them are typical of conducting LB systems based on quasi-one-dimensional CTCs. Therefore, all the conductivity mechanism features caused by one-dimensional localization that are discussed here are common for this class of conducting LB films.

## 2. EXPERIMENTAL TECHNIQUE

Figure 1 shows the measurement circuit. As SAW delay lines, we used substrates of lithium niobate ( $LiNbO_3$ ,  $Y + 128^\circ$  cut) with three groups of interdigital transducers (IDTs) photolithographically patterned onto the substrate surface. A pulse-modulated signal with a high-frequency component was applied to the central IDT group from a high-frequency oscillator. Thus, this group was the source of SAWs and the two other transducer groups were receivers. The film studied was deposited between IDT groups *b* and *c* (Fig. 1), and the space between groups *a* and *b* remained clear. This measurement circuit allowed us to eliminate systematic errors related to random spontaneous changes in the output power of the driving oscillator. Signals from IDT groups *a* and *c* were fed to a two-channel high-frequency oscilloscope, and the readout of the signal levels was performed visually. To increase the sensitivity, a precision attenuator was built in one of the receiving paths.

Before the deposition of the LB film, the surface of the delay line was carefully cleaned chemically and treated in an oxygen plasma. Then, two layers of stearic acid were deposited in the gap between groups *b* and *c* for hydrophobization of the surface. They were coated with 18–20 layers of the film under study by the vertical-lifting LB technique. The deposition of the film onto a sapphire substrate with contacts for two-probe dc conductivity measurements (Fig. 1) was performed simultaneously with the film deposition onto the delay line. Then, the delay line and the sample for two-probe measurement were glued to the cold finger of the insert of an evacuated cryostat, which was used to measure the temperature dependence of the acoustic-wave attenuation.

As shown in [9], the main cause of SAW attenuation is the interaction of the field of an acoustic wave with charge carriers in the film. The alternating electric field with the SAW frequency that accompanies a strain wave in the piezoelectric substrate induces electric currents in the deposited film and, hence, Joule's losses. As a result of this interaction, the wave power is absorbed. However, this source of attenuation is not the only one, since the wave also loses its energy due to the viscosity

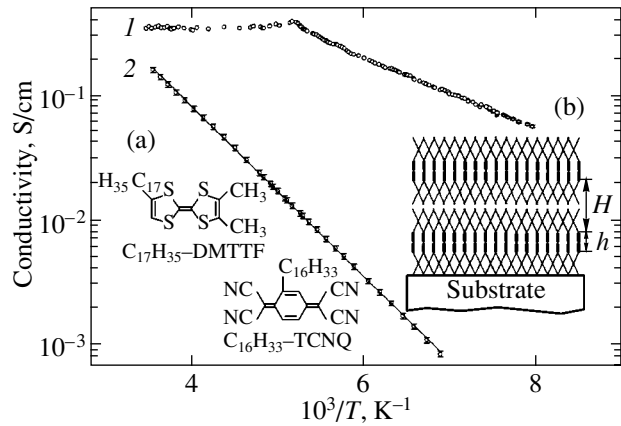
of the film and dissipative processes occurring in the material of the delay line. To exclude the contributions from these sources, we performed the following check experiment. The insert with the glued samples was removed from the cryostat and placed inside a quartz tube, which was then filled with nitrogen. Then, the samples were irradiated with light from a DRT 125-1 mercury ultraviolet lamp located at a distance of 7–8 cm from the sample for 200 h (the radiation intensity was about  $100 \mu\text{W}/\text{cm}^2$ ); as a result, the film became nonconducting. Then, the insert was again placed in the cryostat and we measured the temperature dependence of the attenuation caused by the nonconducting film. The results of these measurements were subtracted from the data obtained in the experiments performed on the conducting film. The thus-determined attenuation (per unit length) was then used to calculate the film conductivity from the Adler formula [9], whose temperature dependence is discussed in this work.

We measured several delay lines with IDTs having resonance frequencies in the range 200–400 MHz and obtained similar results. Here, we present the data obtained on the typical sample with fundamental frequency  $f_0 = 355.6$  MHz.

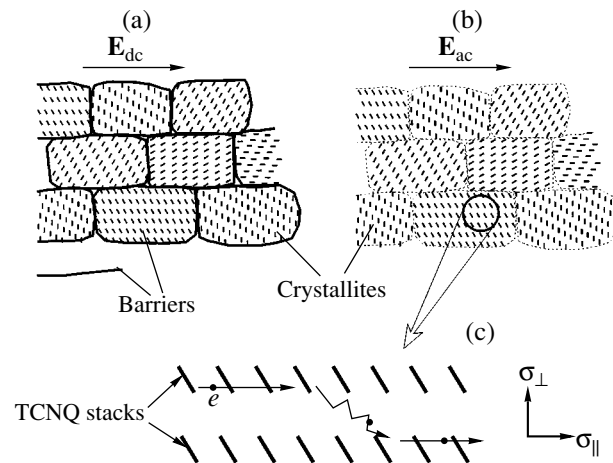
### 3. RESULTS AND DISCUSSION

Figure 2 shows the temperature dependences of the conductivity of the film found using the acoustic and usual dc techniques (curves 1 and 2, respectively). The temperature dependence measured from the SAW attenuation is seen to have a characteristic feature at  $T_{\text{MD}} = 193.5$  K; above  $T_{\text{MD}}$ , the conductivity of the film is metallic ( $\partial\sigma/\partial T < 0$ ), whereas below this temperature it varies according to the law  $\ln\sigma \propto -1/T^\gamma$  (where  $0 < \gamma < 1$ ). At the same time, the measured dc conductivity of the film decreases with decreasing temperature according to the Arrhenius law  $\sigma \propto \exp(-T_a/T)$ , where  $T_a \approx 1393$  K. This temperature dependence is monotonic and has no characteristic features at  $T_{\text{MD}}$ . Note that the activation energy  $k_B T_a$  of the dc conductivity measured in this work (0.12 eV) coincides with the value measured earlier in [10] with the four-probe method.

It is generally accepted [1] that the activation character of the dc conductivity of the LB film is caused by its polycrystalline structure, because the film consists of randomly oriented two-dimensional (2D) crystallites (Fig. 3a); therefore, charge carriers need to overcome intercrystallite potential barriers, whose height determines the activation energy  $k_B T_a$ . The regions adjacent to grain boundaries make a dominant contribution to the resistivity of the film; the variation of the electric potential within crystallites is small as compared to its jump at the boundaries. Therefore, the temperature dependence of the dc conductivity mainly characterizes the properties of the intercrystallite barriers. Information on the electron transport within crystallites of the



**Fig. 2.** Temperature dependences of the conductivity of the LB film measured with (1) the acoustic technique and (2) the dc two-probe method. The temperature dependence of the dc conductivity is fitted to the function  $\sigma \propto \exp(-T_a/T)$ , where  $T_a \approx 1393$  K. Inset (a) shows the structural formulas of the molecules forming the film. Inset (b) schematically shows the cross section of the LB system consisting of four monolayers. The conducting bilayers of thickness  $h \approx 10$  Å are formed by the –TCNQ and –DMTTF head groups, and the dielectric bilayers of thickness  $H \approx 25$  Å are formed by the – $\text{C}_{16}\text{H}_{33}$  and – $\text{C}_{17}\text{H}_{35}$  side groups.



**Fig. 3.** Two-dimensional polycrystalline structure of the conducting bilayer: (a) dc conductivity (determined by intercrystallite barriers) and (b) transport in the high-frequency field of an acoustic wave. Within a half-period of field oscillations, there is no time for charge to accumulate at grain boundaries; therefore, the applied electric field is not shielded by the space charge. Thus, the effect of intercrystallite barriers on the conductivity is eliminated. (c) Transport at the microscopic level (schematic); electrons move along the TCNQ stacks, jumping from one stack to the similar nearest neighbor stack from time to time.

film turns out to be masked, and it is virtually impossible to extract it from the results of such measurements.

Unlike the dc measurements, the acoustic technique measures a quantity that is related closely to the intrac-

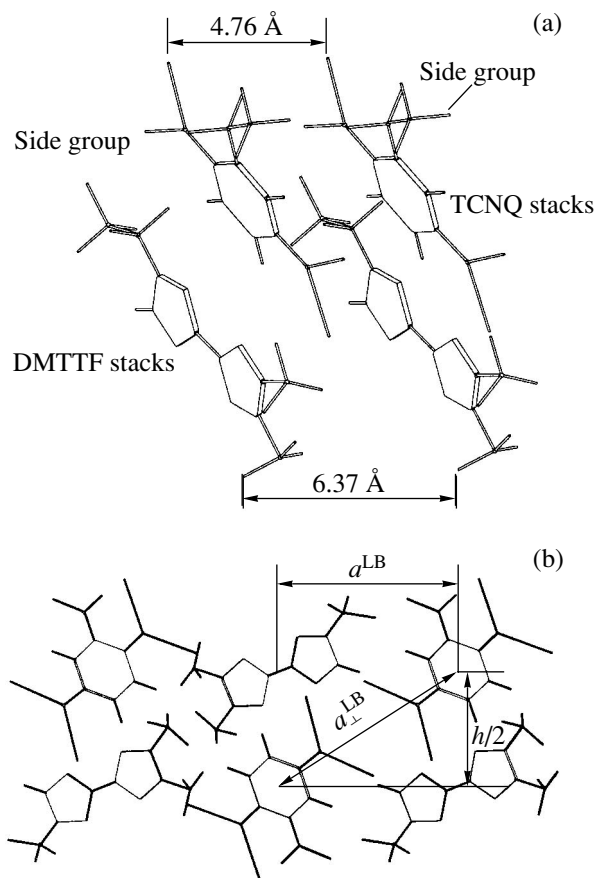


**Fig. 4.** (a) Schematic representation of the conducting monolayer structure (according to data from [13]); for simplicity, only the first two  $-\text{CH}_2-$  links of the side groups ( $-\text{C}_n\text{H}_{2n+1}$ ,  $n = 16, 17$ ) are shown. (b) Structure of the conducting bilayer; the axes of the TCNQ and DMTTF stacks are normal to the sketch plane.  $a^{LB} \approx 7.65 \text{ \AA}$  [13],  $h/2 \approx 5 \text{ \AA}$ , and  $a_{\perp}^{LB} = \sqrt{(h/2)^2 + (a^{LB})^2} \approx 9.2 \text{ \AA}$ .

crystallite conductivity. Indeed, as noted above, the SAW attenuation in delay lines coated with a conducting Langmuir film is determined by the ohmic losses caused by the coupling of the high-frequency ( $10^7$ – $10^9$  Hz) electric field of an acoustic wave with charge carriers in the film. The non-Arrhenius temperature behavior of the film conductivity measured with the SAW technique suggests that charge carriers do not accumulate at grain boundaries at such high frequencies; therefore, the shielding of the applied electric field of the acoustic wave by the space charge is insignificant. Thus, electron transport in a field of such a high frequency is insensitive to intercrystallite barriers and the ohmic losses are completely determined by the conductivity mechanism within the crystallites. Actually, with the SAW technique, we measure the conductivity  $\sigma(\omega, T)$  of the polycrystal formed by randomly oriented 2D crystallites with short-circuited intercrystallite barriers (Fig. 3b). The conductivity  $\sigma(\omega, T)$  can be repre-

sented in the form  $\sigma(\omega, T) = \langle \sigma(T) \rangle + \sigma_{ac}(\omega, T)$ , where  $\langle \sigma(T) \rangle$  is the dc conductivity of the 2D polycrystal with short-circuited intercrystallite barriers and  $\sigma_{ac}(\omega, T)$  is its ac conductivity, which is an isotropic quantity. The problem of finding  $\langle \sigma \rangle$  was solved by Dykhne [11]:  $\langle \sigma \rangle = \sqrt{\sigma_{11}\sigma_{22}}$ , where  $\sigma_{11}$  and  $\sigma_{22}$  are the principal values of the intracrystallite conductivity tensor. As will be shown below,  $\sigma_{ac}$  is several times smaller than  $\langle \sigma \rangle$  at frequencies of several hundreds of megahertz. As a result, it is the intracrystallite conductivity averaged over all possible crystallite orientations that is measured using the acoustic technique. Hence, the temperature dependences of the conductivity measured with this technique (Fig. 2, data set 1) reflect the features inherent in the electron transport within crystallites.

Below, we will consider the microscopic structure of the films, the mechanism of charge transfer within crystallites, and the related theoretical models. This consideration will allow us to choose expressions for  $\sigma_{11}$ ,  $\sigma_{22}$ , and  $\sigma_{ac}$ , which will be used for fitting the experimental data to the function  $\sigma(2\pi f_0, T) = \sqrt{\sigma_{11}(T)\sigma_{22}(T)} + \sigma_{ac}(2\pi f_0, T)$  and finding the quantities that characterize the electron transport in the films.

### 3.1. The Structure of the Films and a Model of Electron Transport in Them

Inset b in Fig. 2 schematically shows the cross section of the LB system consisting of four monolayers formed by CTC molecules (Fig. 2, inset a). The thicknesses of the dielectric ( $H \approx 25 \text{ \AA}$ ) and conducting ( $h \approx 10 \text{ \AA}$ ) bilayers were determined by small-angle x-ray diffraction [12]. The structure of the conducting layer was schematically presented in [13] (Fig. 4a). Based on those data, we show the detailed structure of the conducting bilayer in Fig. 4b. It is seen that the head groups ( $-\text{DMTTF}$  and  $-\text{TCNQ}$ ) in the film are arranged in separate stacks (chains), similarly to the molecular packing in bulk TTF–TCNQ crystals. However, the distance between the neighboring DMTTF and TCNQ stacks in the layer is  $a^{LB} \approx 7.65 \text{ \AA}$  and the lattice parameter along the TCNQ chains is  $b^{LB} \approx 4.76 \text{ \AA}$ , whereas the corresponding distances in TTF–TCNQ crystals are equal to  $a^{\text{cryst}}/2 \approx 6.8 \text{ \AA}$  and  $b^{\text{cryst}} \approx 3.8 \text{ \AA}$ , respectively [14]. Charge carriers in the bilayer move mainly along the DMTTF and TCNQ stacks, just as in the case of bulk crystals. From time to time, the carriers jump between similar nearest neighbor chains. In other words, the system is quasi-one-dimensional. The negative sign of the Hall coefficient detected in our films in [15] indicates that, just as in the crystals, the films exhibit electronic conductivity and that a charge is mainly transferred along the acceptor TCNQ stacks. Note that the distance between the nearest neighbor TCNQ chains in the bilayer is  $a_{\perp}^{LB} = \sqrt{(h/2)^2 + (a^{LB})^2} \approx 9.2 \text{ \AA}$  (Fig. 4b), which virtually coincides with the distance between the

nearest neighbor TCNQ stacks in the bulk crystals ( $a_{\perp}^{\text{cryst}} = c^{\text{cryst}}/2 \approx 9.1 \text{ \AA}$ ) [14].

As noted above, the dc conductivity within the 2D crystallite of the film is characterized by a  $2 \times 2$  tensor  $\sigma_{ij}$ . One of the principal axes of this tensor is parallel to the TCNQ stacks, and the other axis is orthogonal to them (Fig. 3c). In the principal axes frame, we have  $\sigma_{ij} = \sigma_{ik}\delta_{kj}$ , where  $\delta_{kj}$  is the unit tensor and  $\sigma_{11} = \sigma_{\parallel}$  and  $\sigma_{22} = \sigma_{\perp}$  are the conductivities along the TCNQ stacks (longitudinal conductivity) and along the orthogonal direction to them (transverse conductivity), respectively. Impurities and defects in the TCNQ chains, along which a charge moves, cause electron-wave scattering, whose intensity is characterized by the electron-impurity scattering time  $\tau$ . The quantum interference of scattered electron waves leads to the localization of electronic states, thereby changing the conductivity in character and decreasing its magnitude. On the contrary, the interaction between individual TCNQ chains, which is characterized by the interchain transfer integral  $t_{\perp}$ , favors delocalization. The presence of these two opposite tendencies results in the possibility of the quasi-one-dimensional disordered system being in either metallic and dielectric state, depending on the relation between the values of  $t_{\perp}$  and  $\hbar/\tau$ . Note that the inelastic scattering of electrons by phonons with sufficiently high energy dispersion (the intensity of this process is characterized by the electron-phonon scattering time  $\tau_{\text{in}}$ ) also weakens the localization and, at  $\tau_{\text{in}} \ll \tau$ , completely suppresses it [16]. It was found in [17] that, at  $t_{\perp}\tau/\hbar = 0.3$ , the quasi-one-dimensional disordered system at hand undergoes a metal-insulator transition (the system is in the insulator state at  $t_{\perp} < 0.3\hbar/\tau$  and in the metallic state at  $t_{\perp} > 0.3\hbar/\tau$ ). The frequency and temperature dependences of the conductivity of this system at various relations between  $t_{\perp}$  and  $\hbar/\tau$  were analyzed in [18], where the cases  $t_{\perp} \equiv t_c = 0.3\hbar/\tau$  (the system is near the metal-insulator transition) and  $t_{\perp} \ll t_c$  (the system is characterized by a weak transverse overlapping and is far from the transition) were considered. In what follows, the expressions derived in that work for  $\sigma_{\parallel}(T)$ ,  $\sigma_{\perp}(T)$ , and  $\sigma_{\text{ac}}(\omega, T)$  will be used for fitting the experimental temperature dependence of the conductivity to the function  $\sigma(2\pi f_0, T) = \sqrt{\sigma_{\parallel}(T)\sigma_{\perp}(T)} + \sigma_{\text{ac}}(2\pi f_0, T)$  in order to determine the parameters characterizing the electron transport within the crystallites.

The experimental temperature dependence (Fig. 2, data set I) shows that our films belong to systems with weak interchain overlapping ( $t_{\perp} \ll t_c$ ), where, according to [18], the conductivity is nonmetallic in the temperature range corresponding to the inequality  $\tau < \tau_{\text{in}}(T)$ . In this range, three characteristic regions (modes I, II, III) in the temperature dependence of the conductivity can be distinguished (see [18, Fig. 2]).

In the range  $T_1 < T < T_0$  (mode I), the transverse conductivity is described by the Mott-type relation<sup>2</sup>

$$\sigma_{\perp} = 2e^2 g(\epsilon_F) a_{\perp}^2 v_{\text{ph}} (t_{\perp} \tau / \hbar)^2 \exp[-2(2T_0/Tz)^{1/2}], \quad (1)$$

and the longitudinal conductivity obeys the Arrhenius law

$$\sigma_{\parallel} = 2e^2 g(\epsilon_F) v_{\text{ph}} \xi_{\parallel}^2 / (2\sqrt{\pi}) \sqrt{T_0/(2T)} \times \exp[-T_0/(2T)], \quad (2)$$

where  $T_0 = \pi\hbar/(4k_B\tau)$ ,  $e$  is the electron charge,  $g(\epsilon_F) = 1/(\pi\hbar v_F a_{\perp}^2)$  is the density of states (per spin) at the Fermi level,  $v_F$  is the Fermi velocity,  $a_{\perp}$  is the distance between nearest chains,  $T_1 = 3T_0/(4\kappa)$ ,  $\kappa = \ln[4k_B T_0/(\pi t_{\perp})]$ ,  $z$  is the number of nearest neighbor chains (in the two-dimensional case in question,  $z = 2$ ; Fig. 4b),  $\xi_{\parallel} = 4v_F\tau$ , and  $v_{\text{ph}} = \tau_{\text{in}}^{-1}$ .

In the range  $T_2 < T < T_1$ , where  $T_2 = T_0/(2\kappa^2)$  (mode II), the transverse conductivity is still described by Eq. (1), but the longitudinal conductivity is determined by Eqs. (68)–(71) from [18].<sup>3</sup> Finally, at  $T \ll T_2$  (mode III), the temperature dependences of the longitudinal and transverse conductivities are determined by Eqs. (77)–(80) from [18].<sup>4</sup> As shown in [18],  $\sigma_{\text{ac}}$  manifests itself at frequencies  $\omega \geq \omega_1 = v_{\text{ph}} \exp[-3T_0/(2T)]$ ; more specifically,  $\sigma_{\text{ac}}(\omega, T) = 0$  at  $\omega < \omega_1$  and  $\sigma_{\text{ac}}(\omega, T) \propto \omega^{s(\omega, T)}$  at  $\omega_1 \leq \omega \leq \omega_2 = v_{\text{ph}} \exp[-2(2T_0/T)^{1/2}]$ , where  $s(\omega, T) \rightarrow 1$  at  $\omega \rightarrow \omega_2$ . At higher frequencies ( $\omega > \omega_2$ ), the ac conductivity should be calculated within the pair approximation. Therefore, we have  $\sigma_{\text{ac}}(\omega, T) = \sigma_p(\omega, T)$ , where

$$\sigma_p = \frac{(4v_F\tau)^3 e^2 N(\epsilon_F)^2}{96} a_{\perp}^2 k_B T \omega \ln^2(v_{\text{ph}}/\omega), \quad (3)$$

in accordance with [19], where  $N(\epsilon_F) = 2g(\epsilon_F)$ . The expressions describing the frequency dependence of the conductivity in the different  $\omega$  ranges transform continuously into one another. Below, we will find which of the modes of the dc and ac conductivities describes our experimental data at  $T < T_{\text{MD}}$  most adequately.

### 3.2. Determination of $g(\epsilon_F)$ , $t_{\perp}$ , and the Form of $v_{\text{ph}}(T)$

The relations given for  $\sigma_{\parallel}(T)$ ,  $\sigma_{\perp}(T)$ , and  $\sigma_{\text{ac}}(\omega, T)$  are seen to depend on four parameters:  $v_{\text{ph}}$ ,  $T_0$ ,  $g(\epsilon_F)$ , and  $t_{\perp}$ . The density of states  $g(\epsilon_F)$  and the interchain transfer integral  $t_{\perp}$  can be estimated from the structural

<sup>2</sup> Equations (48) and (63) in [18], describing  $\sigma_{\parallel}$  and  $\sigma_{\perp}$  in the range  $T_1 < T < T_0$ , contain misprints and, hence, somewhat differ from Eqs. (1) and (2) in this work.

<sup>3</sup> Equation (68) in [18] contains an incorrect sign in the exponent.

<sup>4</sup> In Eqs. (77)–(79) from [18],  $T_2$  should be replaced by  $T_0$ .



data given in Fig. 4. In turn, the fitting of the measured temperature dependences (Fig. 2, data set 1) to a function  $\sigma(2\pi f_0, T)$  allows us to determine  $v_{\text{ph}}$  and  $T_0$  and, hence, to find the electron–phonon and electron–impurity scattering times. Using these values and  $g(\epsilon_F)$ , we will find the mean free path and the localization length in the films.

The interchain transfer integral  $t_{\perp}$  characterizes the intensity of electron tunneling between neighboring TCNQ chains and decreases exponentially with increasing interchain distance  $a_{\perp}$ . As noted above, this distance in the film bilayer,  $a_{\perp}^{\text{LB}}$ , virtually coincides with the distance between TCNQ chains in the bulk crystals,  $a_{\perp}^{\text{cryst}}$ ; therefore,  $t_{\perp}^{\text{LB}}$  in the films should coincide with  $t_{\perp}^{\text{cryst}}$ . The latter quantity is known to be  $t_{\perp}^{\text{cryst}} \approx 5$  meV [20]. This value of  $t_{\perp}^{\text{cryst}}$  is confirmed by modern quantum-chemical Hartree–Fock calculations [21, 22]. Thus, we have  $t_{\perp}^{\text{LB}} \approx 5$  meV.

Based on the structural parameters of the bilayer shown in Fig. 4, we can find the value of  $v_F$  in the film and determine the value of  $g(\epsilon_F)$ . Indeed, since  $v_F \propto b t_{\parallel}$  (where  $t_{\parallel}$  is the intrachain transfer integral and  $b$  is the translation period along a chain), we obtain  $v_F^{\text{cryst}}/v_F^{\text{LB}} = b^{\text{cryst}} t_{\parallel}^{\text{cryst}}/(b^{\text{LB}} t_{\parallel}^{\text{LB}})$ . The value of  $t_{\parallel}^{\text{cryst}}$  is known to be 135 meV [20], and the values of  $b^{\text{cryst}}$  and  $b^{\text{LB}}$  are given above; therefore, we only have to calculate  $t_{\parallel}^{\text{LB}}$ . Similarly to  $t_{\perp}$ ,  $t_{\parallel}$  also decreases exponentially with increasing distance  $u$  between the neighboring TCNQ molecules in the stack and can be represented in the form  $t_{\parallel} = A u \exp(-u/r_0)$  [19]. The constants  $A$  and  $r_0$  can be determined from the condition  $t_{\parallel}|_{u=u^{\text{cryst}}} = t_{\parallel}^{\text{cryst}}$  and  $\partial t_{\parallel}/\partial u|_{u=u^{\text{cryst}}} = -0.20$  eV/Å [23] (here,  $u^{\text{cryst}} = b^{\text{cryst}} \cos \theta = 3.17$  Å [14], where  $\theta$  is the angle between the stack axis and the normal to the plane of the TCNQ molecule). Assuming that  $\theta$  in our films has the same value as in TTF–TCNQ crystals, we obtain  $u^{\text{LB}} = b^{\text{LB}} \cos \theta = 3.95$  Å. After simple calculations, we arrive at  $t_{\parallel}^{\text{cryst}}/t_{\parallel}^{\text{LB}} \approx 3.18$ , whence it follows that  $t_{\parallel}^{\text{LB}} \approx 42.5$  meV and  $v_F^{\text{cryst}}/v_F^{\text{LB}} \approx 2.55$ . The Fermi velocity in TTF–TCNQ crystals is known to be  $v_F^{\text{cryst}} \approx 1.2 \times 10^7$  cm/s [23]; therefore, we have  $v_F^{\text{LB}} \approx 4.7 \times 10^6$  cm/s. Taking into account  $a_{\perp}^{\text{LB}} \approx a_{\perp}^{\text{cryst}}$ , we calculate the ratio of the density of states at the Fermi level in the films and the crystals:  $g^{\text{LB}}(\epsilon_F)/g^{\text{cryst}}(\epsilon_F) \approx v_F^{\text{cryst}}/v_F^{\text{LB}} \approx 2.55$ . The value of  $g^{\text{cryst}}(\epsilon_F)$  is known to be  $4.7 \times 10^{21}$  eV<sup>-1</sup> cm<sup>-3</sup> [24], whence it follows that  $g^{\text{LB}}(\epsilon_F) \approx 1.2 \times 10^{22}$  eV<sup>-1</sup> cm<sup>-3</sup>.

As noted in [16, 18], the  $v_{\text{ph}}(T) = \tau_{\text{in}}^{-1}(T)$  dependence is different in temperature ranges above the Debye temperature  $\Theta_D$  of the system under study and below it. At  $T > \Theta_D$ , we have  $\tau_{\text{in}}^{-1} \propto T$ , and, at  $T < \Theta_D$ ,  $\tau_{\text{in}}^{-1} \propto T^3$ . The Debye temperature of DMTTF–TCNQ crystals was found to be  $\Theta_D^{\text{cryst}} \approx 85$  K [25]. Let us show that, in LB films,  $\Theta_D^{\text{LB}} \leq \Theta_D^{\text{cryst}}$ . Indeed, as noted above, the distance between the neighboring DMTTF and TCNQ chains in the film and the distance between the nearest neighbor molecules in the chain are greater than the respective distances in the crystals. Therefore, the bonding forces between individual molecules in the chain and between chains in the monolayer are weaker than the corresponding forces in the crystals. Moreover, the insulator layers (Fig. 2, inset b) formed by the hydrocarbon side groups ( $-\text{C}_n\text{H}_{2n+1}$ ,  $n = 16, 17$ ) weaken the interaction between the conducting bilayers of the film. As a result, the LB structures turn out to be “softer” systems than the crystals, which results in the inequality  $\Theta_D^{\text{LB}} \leq \Theta_D^{\text{cryst}}$ . Hence, we should assume that  $v_{\text{ph}} = \tau_{\text{in}}^{-1} \propto T$  over the whole temperature range under study ( $125 < T < 300$  K).

To quantitatively describe the temperature dependence of  $\tau_{\text{in}}^{-1}$  in TTF–TCNQ crystals, Bright *et al.* [26] proposed using the Hopfield relation  $\tau_{\text{in}}^{-1}(T) = 2\pi k_B T \lambda / \hbar$ , where  $\lambda$  is the dimensionless electron–phonon interaction constant (according to [27],  $\lambda \approx 0.23$  in TTF–TCNQ). When fitting our experimental data to the dependence  $\sigma(2\pi f_0, T)$ , we also assume that  $v_{\text{ph}}(T) = 2\pi k_B T \lambda / \hbar$ . Since the electron–phonon interaction constant in the LB films under study is unknown, the parameter  $\lambda$  is taken to be free and adjusted during fitting.

Finally, the quantity  $T_0$ , which enters into Eqs. (1) and (2) and is related to the electron–impurity scattering time, is also taken to be a free parameter and is determined by fitting.

### 3.3. Fitting the Experimental Data at $T < T_{\text{MD}}$

Before processing the experimental data, let us consider the second term in the expression  $\sigma(2\pi f_0, T) = \sqrt{\sigma_{\parallel}(T)\sigma_{\perp}(T)} + \sigma_{\text{ac}}(2\pi f_0, T)$ . As seen from Eq. (3),  $\sigma_{\text{ac}}(2\pi f_0, T)$  decreases almost linearly with decreasing temperature, whereas at  $T < T_{\text{MD}}$  the experimental dependence (Fig. 2, data set 1) most likely decrease exponentially with decreasing temperature. Therefore, we can conclude that, in the temperature range under study, the ac contribution to the conductivity at the given frequency  $f_0 = 355.6$  MHz is much lower than the dc contribution. Hence, as a fitting function, we can



simply use  $\sqrt{\sigma_{\parallel}(T)\sigma_{\perp}(T)}$  instead of  $\sigma(2\pi f_0, T)$ . After  $T_0$  and  $\lambda$  have been determined, we can calculate  $\sigma_{ac}(2\pi f_0, T)$  and check the validity of neglecting this term in  $\sigma(2\pi f_0, T)$ .

Assuming  $t_{\perp} = 5$  meV and  $g(\epsilon_F) = 1.2 \times 10^{22}$  eV $^{-1}$  cm $^{-3}$  and varying  $T_0$  and  $\lambda$ , we fit the experimental data (Fig. 2, data set 1,  $T < T_{MD}$ ) to the  $\sqrt{\sigma_{\perp}(T)\sigma_{\parallel}(T)}$  dependence, whose components are determined from Eqs. (1) and (2), respectively.<sup>5</sup> As a result, we find that  $T_0 = 1344 \pm 4$  K and  $\lambda = 0.26 \pm 0.01$ . As noted above, the expressions for  $\sigma_{\perp}(T)$  and  $\sigma_{\parallel}(T)$  in mode I are valid in the temperature range  $T_1 < T < T_0$  however, the calculated value of  $T_0$  leads to  $T_1 = 298$  K  $> T_{MD}$ . Whence it follows that Eqs. (1) and (2) cannot be applied for describing our results at  $T < T_{MD}$ .

The expressions for the longitudinal and transverse conductivities in mode III also cannot be used to explain our data. Indeed, these expressions are valid at  $T \ll T_2$ . Therefore, for them to describe the experimental data over the whole range  $T < T_{MD}$ , at least the condition  $T_2 > T_{MD}$  must be satisfied. At  $T_{MD} = 193.5$  K, the latter inequality results in  $T_0 > 12\,500$  K. However, the calculation by Eqs. (77)–(80) from [18] at such a high value of  $T_0$  and reasonable values of  $\lambda$  ( $\lambda < 3$  [28]) gives values of the conductivity that are eight orders of magnitude smaller than the experimental values.

Our experimental data can adequately be described by the expressions for conductivities in mode II. Fitting the data in Fig. 2 (data set 1,  $T < T_{MD}$ ) to the  $\sqrt{\sigma_{\perp}(T)\sigma_{\parallel}(T)}$  dependence, where  $\sigma_{\perp}$  is described by Eq. (1) and  $\sigma_{\parallel}$  by Eqs. (68)–(71) from [18], we obtain  $T_0 = 1317 \pm 6$  K and  $\lambda = 0.11 \pm 0.01$ .<sup>6</sup> The fitting results are shown in Fig. 5, curve 3. Using the known value of  $T_0$ , the temperatures  $T_1$  and  $T_2$  (which determine the limits of applicability of the mode II formulas) are found to be  $T_1 = 294$  K and  $T_2 = 58$  K. It is seen that the temperature range under study ( $125$  K  $< T < T_{MD}$ ) falls in this range.

Now, having the values of  $T_0$  and  $\lambda$ , let us return to the problem of estimating  $\sigma_{ac}(2\pi f_0, T)$ . Curve 4 in Fig. 5 shows the  $\sigma_p(2\pi f_0, T)$  dependence calculated by Eq. (3) using the values of  $T_0$  and  $\lambda$  obtained. Comparing  $2\pi f_0$  with the values of  $\omega_1$  and  $\omega_2$  introduced above,

<sup>5</sup> Fitting was performed using the nonlinear Levenberg–Marquardt least squares method, which is available in the Origin software package intended for numerical data processing and visualization. The final values of  $T_0$  and  $\lambda$  thus obtained are insensitive to the choice of their initial values.

<sup>6</sup> Recent electronic band structure calculations for TTF–TCNQ crystals using a modification of the pseudopotential method [29] give values of  $t_{\perp}$  that are, on average, three times greater than the generally accepted value  $t_{\perp} = 5$  meV [20]. Fitting our data at  $t_{\perp} = 15$  meV and  $g(\epsilon_F) = 1.2 \times 10^{22}$  eV $^{-1}$  cm $^{-3}$  gives  $T_0 = 1609 \pm 7$  K and  $\lambda = 0.11 \pm 0.01$ .

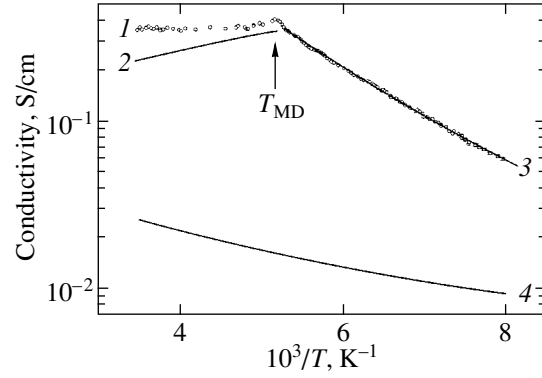


**Fig. 5.** Temperature dependences of the conductivity obtained using different approximations: (1) the experimental data determined with the acoustic technique (Fig. 2); (2) the temperature dependence of the conductivity of the type  $\sigma \propto T^{-1}$  constructed according to [18] at  $T > T_{MD}$ ; and (3) the best fit to the experimental results at  $T < T_{MD}$  with the dependence  $\sqrt{\sigma_{\parallel}(T)\sigma_{\perp}(T)}$ , where  $\sigma_{\parallel}(T)$  and  $\sigma_{\perp}(T)$  are the mode II longitudinal and transverse conductivities, respectively. The best fit to the experimental points is achieved at  $T_0 = 1317 \pm 6$  K and  $\lambda = 0.11 \pm 0.01$ . (4) The temperature dependence of  $\sigma_p(2\pi f_0, T)$  calculated by Eq. (3) using the determined values of  $T_0$  and  $\lambda$ ;  $f_0 = 355.6$  MHz.

we find that, at  $T < 141$  K,  $\sigma_{ac}(2\pi f_0, T) = \sigma_p(2\pi f_0, T)$  (Fig. 5). At temperatures  $T > 217$  K,  $\sigma_{ac}(2\pi f_0, T) = 0$ , and the range  $141 < T < 217$  K corresponds to the transition range where  $\sigma_{ac}$  increases monotonically from 0 to  $\sigma_p$ . Therefore, in the range  $141 < T < 300$  K, curve 4 in Fig. 5 is the upper estimate for  $\sigma_{ac}(2\pi f_0, T)$ . The ac component of the conductivity is seen to be far less than the dc component,  $\sigma_{ac}(2\pi f_0, T) \ll \langle \sigma(T) \rangle$ , over the whole temperature range under study, which supports our assumption that the contribution of  $\sigma_{ac}(2\pi f_0, T)$  to  $\sigma(2\pi f_0, T)$  can be neglected.

Using the calculated value of  $T_0$ , we determine the electron–impurity scattering time  $\tau = \pi\hbar/(4k_B T_0) \approx 4.6 \times 10^{-15}$  s. With this time and the value of  $v_F^{LB}$  calculated above, we can determine the mean free path  $l = v_F^{LB} \tau$  and the localization length  $l_{loc} = 4l$  [16] in the film; they are  $l \approx 0.45b^{LB}$  and  $l_{loc} = 4v_F^{LB} \tau \approx 8.6$  Å. The value of  $l_{loc}$  is seen to be smaller than the double lattice parameter along the TCNQ chains.

Let us compare the obtained values of  $\tau$  and  $l$  with analogous parameters in other disordered quasi-one-dimensional systems in which the effects of electron localization are also important. The best known examples of such systems are conducting polymers and disordered 1 : 2 complexes of quinolinium (Qn) and acridinium (Ad) with TCNQ [Qn(TCNQ) $_2$  and Ad(TCNQ) $_2$ , respectively]. In [30], the values of  $\tau$  and

$l$  in polypyrrole (PPy) doped with hexafluorophosphate ( $\text{PF}_6$ ) were found to be  $5.5 \times 10^{-16}$  s and  $0.85a$ , respectively ( $a$  is the length of the repeated polymer structural unit). The corresponding parameters of  $\text{Qn}(\text{TCNQ})_2$  were found to be  $1.3 \times 10^{-14}$  s and  $2.5b$ , respectively [31] ( $b$  is the lattice parameter along the TCNQ stacks). It is seen that our LB films are intermediate in degree of electron localization between the conducting polymers and TCNQ salts with asymmetric cations.

In the literature, the degree of electron localization is estimated by comparing the value of  $k_{\text{F}}l$  with unity ( $k_{\text{F}}$  is the Fermi wave vector). If  $k_{\text{F}}l \leq 1$ , the localization is strong (Anderson localization); otherwise ( $k_{\text{F}}l \gg 1$ ), the localization is weak. In our films, we have  $k_{\text{F}}l = \pi\rho l/b^{\text{LB}}$ , where  $\rho$  is the degree of charge transfer from donor to acceptor. Assuming that the value of  $\rho$  in our films is identical to that in TTF–TCNQ bulk crystals ( $\rho \approx 0.6$  [20]), we obtain  $k_{\text{F}}l \approx 0.85$ , which indicates strong electron localization in them.

As noted above, LB films based on a mixture of BEDO–TTF with fatty acids have the highest conductivity among CTC films. Recently, negative magnetoresistance was detected in films prepared from a mixture of BEDO–TTF with stearic acid (SA) [32]; this fact was explained in that work in terms of weak electron localization. Note that the localization in our films is much stronger than in the BEDO–TTF + SA films, whose conductivity is metallic down to 120 K and decreases weakly (logarithmically) with decreasing temperature in the range  $15 < T < 120$  K. This fact is explained by a strong interaction between the chains of BEDO–TTF molecules in the conducting bilayers of such films, which results in the formation of a quasi-two-dimensional electron system. In other words, charge carriers in the films studied in [32] move along conducting planes rather than along quasi-one-dimensional chains, as in our case. It is known that, at the same defect concentration, localization effects in a quasi-one-dimensional system are much more pronounced than in a quasi-two-dimensional system.

Thus, the temperature dependence of the intracrystallite conductivity of the films under study at  $T < T_{\text{MD}}$  agrees with the model of electron-state localization in a disordered quasi-one-dimensional system [18]. Fitting the experimental data to the relations from that work leads to reasonable values of the electron–phonon and electron–impurity scattering times, as well as the mean free path and the localization length.

### 3.4. Metallic Conductivity at $T > T_{\text{MD}}$

We now consider the temperature range  $T > T_{\text{MD}}$ , where the conductivity has metallic behavior ( $\partial\sigma/\partial T < 0$ ). In terms of the electron localization described above, the change in the character of conductivity at  $T > T_{\text{MD}}$  is explained by the fact that the quantum interference of scattered electron waves is suppressed by the

inelastic electron–phonon interaction, which becomes substantial at sufficiently high temperatures (when the inequality  $\tau_{\text{in}} \ll \tau$  is satisfied). In this case, the longitudinal and transverse conductivities are given by Eqs. (28) in [18]. According to those equations, the temperature dependences of the conductivities are fully determined by the inelastic-relaxation rate  $\tau_{\text{in}}^{-1}(T)$ , which reflects the specific features of the phonon subsystem of quasi-one-dimensional materials. As noted above, at high temperatures ( $T > \Theta_{\text{D}}$ ), we have  $\tau_{\text{in}}^{-1} \propto T$ ; therefore, according to [18], we can expect  $\sigma_{\perp}(T)$ ,  $\sigma_{\parallel}(T) \propto T^{-1}$  at  $T > T_{\text{MD}}$ . The conductivity  $\langle\sigma(T)\rangle$  measured in our experiments should also obey this law, namely,  $\langle\sigma(T)\rangle = \sqrt{\sigma_{\perp}(T)\sigma_{\parallel}(T)} \propto T^{-1}$ . However, Fig. 5 shows that the temperature variation of the curve is much weaker. This discrepancy can be due to the simplified approach used to describe the  $\tau_{\text{in}}^{-1}(T)$  dependence. Indeed, the properties of the phonon subsystem of low-dimensional organic materials are specific: at high temperatures, one has to take into account intramolecular phonon excitations in addition to lattice phonons. Gor'kov *et al.* [33] tried to describe the temperature dependence of  $\tau_{\text{in}}^{-1}$  in such systems; however, they considered only the case of low temperatures ( $T \ll \Theta_{\text{D}}$ ). At high temperatures, a large number of phonon modes is excited and the situation becomes very complex. Therefore, the description of  $\tau_{\text{in}}^{-1}(T)$  with the Hopfield relation, which is justified at not very high temperatures above the Debye temperature, can be too rough an approximation at  $T > 200$  K. The situation is also complicated by the fact that, at sufficiently high temperatures, thermally excited phonons contribute to the random potential [31], which leads to additional electron localization.

Note that the crystals of the  $\text{Qn}(\text{TCNQ})_2$  salts with a weak intrinsic structural disorder caused by a random orientation of asymmetric Qn cations also exhibit a change in the character of conductivity from semiconducting ( $\partial\sigma/\partial T > 0$ ) to metallic at 240 K, which is caused by suppression of the localization by inelastic electron–phonon scattering. The mechanisms of electron transport and localization in this compound can be explained in the same way as in the case described above for films. However, the temperature dependence of the conductivity of these crystals also deviates from the law  $\sigma \propto T^{-1}$ ; namely, at  $T > 240$  K,  $\sigma \propto T^{-n}$ , where  $n = 1.5\text{--}2$  [7].

However, the most serious discrepancy between the predictions made in [18] and the experimental data [which indicates that the approximation used for  $\tau_{\text{in}}^{-1}(T)$  becomes rough at high temperatures] manifests itself when the temperature of the conductivity maximum  $T_{\text{MD}}^*$  is estimated. In terms of the model developed in

[18],  $T_{MD}^*$  can be found from the condition that, at this temperature, the inelastic electron–phonon scattering time becomes equal to the electron–impurity scattering time, i.e.,  $\tau = (2\pi k_B T_{MD}^* \lambda / \hbar)^{-1}$ . Whence it follows that  $T_{MD}^* = \hbar / (2\pi k_B \lambda \tau) = 2426$  K, which exceeds the experimental value of  $T_{MD}$  by an order of magnitude. Similar estimations for  $\text{Qn}(\text{TCNQ})_2$  lead to  $T_{MD}^* = 406$  K.<sup>7</sup> This value also differs from the experimental temperature of the conductivity maximum (240 K), although this discrepancy is not as high as in the case of the films.

The fact that using the Hopfield relation for describing  $\tau_{in}^{-1}(T)$  at high temperatures causes problems was noted long ago. For example, Bright *et al.* [26] established that the experimental room-temperature values of  $\tau_{in}^{-1}$  in TTF–TCNQ crystals correspond to  $\lambda$  equal to approximately 1.3 in the Hopfield relation.<sup>8</sup> However, as mentioned in review [20], this high value of  $\lambda$  is about an order of magnitude greater than the value required for correct description of the whole spectrum of the magnetic and structural properties of these crystals. Due to the reasons given above, the problem of finding the form of  $\tau_{in}^{-1}(T)$  in quasi-one-dimensional organic materials at high temperatures has not yet been solved, and this circumstance hinders comparing the results from [18] with the experimental data at  $T > T_{MD}$ . At the same time, as shown above, the Hopfield relation is a valid approximation for  $\tau_{in}^{-1}$  in the temperature range  $\Theta_D < T < 200$  K and its using leads to reasonable values for  $\lambda$  in the films.

#### 4. CONCLUSIONS

We have presented the results of studying the temperature dependence of the intracrystallite conductivity of the LB films of  $(\text{C}_{16}\text{H}_{33}\text{–TCNQ})_{0.4}(\text{C}_{17}\text{H}_{35}\text{–DMTTF})_{0.6}$  measured with the acoustic technique proposed by us in [9]. We have found that the temperature dependence of the conductivity has a characteristic feature at  $T_{MD} = 193.5$  K; more specifically, the conductivity of the films above  $T_{MD}$  is metallic ( $\partial\sigma/\partial T < 0$ ), whereas below this temperature it obeys the law  $\sigma(T) = \sigma_0(T) \exp[-(8T_0/Tz)^{1/2}]$ , where  $\sigma_0(T)$  varies with temperature more slowly than the exponential factor. We believe that the nonmetallic behavior of the conductivity at  $T < T_{MD}$  is related to the localization of electron states in the quasi-one-dimensional system under study

<sup>7</sup> When calculating  $T_{MD}^*$ , we assumed that the electron–phonon interaction constant  $\lambda$  in  $\text{Qn}(\text{TCNQ})_2$  is the same as that in TTF–TCNQ crystals,  $\lambda \approx 0.23$  [27].

<sup>8</sup> Note that calculating  $T_{MD}^*$  in the films at  $\lambda = 1.3$  gives  $T_{MD}^* = 205$  K, which is close to the experimental value  $T_{MD} = 193.5$  K.

and is caused by the presence of impurities, defects, and distortions in the linear conducting chains of TCNQ molecules, along which charges are transferred. The observed temperature dependence of the conductivity agrees qualitatively and quantitatively with the model of electron localization in a weakly disordered quasi-one-dimensional system [18]. Fitting the experimental results to the theoretical dependences taken from [18] allowed us to evaluate the electron–phonon [ $\tau_{in}(193.5 \text{ K}) = 6 \times 10^{-14}$  s] and electron–impurity ( $\tau = 4.6 \times 10^{-15}$  s) scattering times. Based on the structural parameters of the conducting layer, we estimated the density of states at the Fermi level ( $g^{\text{LB}}(\epsilon_F) \approx 1.2 \times 10^{22} \text{ eV}^{-1} \text{ cm}^{-3}$ ) and the Fermi velocity ( $v_F^{\text{LB}} \approx 4.7 \times 10^6 \text{ cm/s}$ ) in the films under study, which allowed us to determine the mean free path  $l$  and the localization length  $l_{\text{loc}} = 4v_F^{\text{LB}}\tau \approx 8.6 \text{ \AA}$  in the films. Our estimations show that a strong (Anderson) localization mode ( $k_F l \leq 1$ ) is realized in the films.

The metallic temperature behavior of the conductivity at  $T > T_{MD}$  is caused by suppression of the localization effects by inelastic electron–phonon scattering, which becomes substantial at high temperatures, when the inequality  $\tau_{in} \ll \tau$  is satisfied. The experimental temperature dependence of the film conductivity at  $T > T_{MD}$  differs from that predicted in [18]. Moreover, the estimates of  $T_{MD}$  based on the results of that work are an order of magnitude higher than the experimental values. We believe that these discrepancies can be explained by the imperfection of the approximation used for  $\tau_{in}^{-1}(T)$ , whose roughness becomes more pronounced at high temperatures. In concluding, it should be noted that the problem of finding the form of  $\tau_{in}^{-1}(T)$  in quasi-one-dimensional organic materials at high temperatures has remained unsolved for more than thirty years [20, 26].

#### ACKNOWLEDGMENTS

This work was supported by the Russian Foundation for Basic Research (project nos. 01-02-16068, 03-02-22001) and the federal program of support for leading scientific schools (project no. NSh 1391.2003.2).

#### REFERENCES

1. P. Delhaés and V. M. Yartsev, in *Spectroscopy of New Materials*, Ed. by R. J. H. Clark and R. E. Hester (Wiley, Chichester, 1993), Vol. 22, p. 199.
2. S. N. Ivanov, L. A. Galchenkov, and F. Ya. Nad', *Radiotekh. Élektron. (Moscow)* **38** (12), 2249 (1993).
3. T. Nakamura, G. Yunome, R. Azumi, M. Tanaka, H. Tachibana, M. Matsumoto, S. Horiuchi, H. Yamochi, and G. Saito, *J. Phys. Chem.* **98** (7), 1882 (1994).

4. H. Ohnuki, T. Noda, M. Izumi, T. Imakubo, and R. Kato, *Phys. Rev. B* **55** (16), R10225 (1997).
5. S. Kahlich, D. Schweitzer, I. Heinen, S. E. Lan, B. Nuber, H. J. Keller, K. Winzer, and H. W. Helberg, *Solid State Commun.* **80** (3), 191 (1991).
6. J. Richard, M. Vandevyver, P. Lesieur, A. Barraud, and K. Holczer, *J. Phys. D: Appl. Phys.* **19** (12), 2421 (1986).
7. I. F. Shchegolev, *Phys. Status Solidi A* **12** (1), 9 (1972).
8. H. W. Helberg and M. Dressel, *J. Phys. I (France)* **6** (12), 1683 (1996).
9. V. Chernov, L. Galchenkov, S. Ivanov, P. Monceau, I. Pyataikin, and M. Saint-Paul, *Solid State Commun.* **97** (1), 49 (1996).
10. L. A. Galchenkov, S. N. Ivanov, F. Ya. Nad', V. P. Chernov, T. S. Berzina, and V. I. Troitskiĭ, *Biol. Membr.* **7** (10), 1105 (1990).
11. A. M. Dykhne, *Zh. Éksp. Teor. Fiz.* **59** (1), 110 (1970) [*Sov. Phys. JETP* **32**, 63 (1971)].
12. O. V. Konovalov and I. I. Pyataikin, unpublished.
13. F. Rustichelli, S. Dante, P. Mariani, I. V. Myagkov, and V. I. Troitsky, *Thin Solid Films* **242** (1–2), 267 (1994).
14. T. J. Kistenmacher, T. E. Phillips, and D. O. Cowan, *Acta Crystallogr. B* **30** (3), 763 (1974).
15. L. A. Galchenkov, S. N. Ivanov, F. Ya. Nad', V. P. Chernov, T. S. Berzina, and V. I. Troitsky, *Synth. Met.* **42** (1–2), 1471 (1991).
16. A. A. Gogolin, V. I. Mel'nikov, and É. I. Rashba, *Zh. Éksp. Teor. Fiz.* **69** (1), 327 (1975) [*Sov. Phys. JETP* **42**, 168 (1975)].
17. V. N. Prigodin and Yu. A. Firsov, *Pis'ma Zh. Éksp. Teor. Fiz.* **38** (5), 241 (1983) [*JETP Lett.* **38**, 284 (1983)].
18. É. P. Nakhmedov, V. N. Prigodin, and A. N. Samukhin, *Fiz. Tverd. Tela (Leningrad)* **31** (3), 31 (1989) [*Sov. Phys. Solid State* **31**, 368 (1989)].
19. Z. H. Wang, A. Ray, A. G. MacDiarmid, and A. J. Epstein, *Phys. Rev. B* **43** (5), 4373 (1991).
20. D. Jérôme and H. J. Schulz, *Adv. Phys.* **31** (4), 299 (1982).
21. E. B. Starikov, *Int. J. Quantum Chem.* **66** (1), 47 (1998).
22. E. B. Starikov, private communication.
23. E. M. Conwell, *Phys. Rev. B* **22** (4), 1761 (1980).
24. S. K. Khanna, E. Ehrenfreund, A. F. Garito, and A. J. Heeger, *Phys. Rev. B* **10** (6), 2205 (1974).
25. T. Wei, P. S. Kalyanaraman, K. D. Singer, and A. F. Garito, *Phys. Rev. B* **20** (12), 5090 (1979).
26. A. A. Bright, A. F. Garito, and A. J. Heeger, *Phys. Rev. B* **10** (4), 1328 (1974).
27. A. J. Berlinsky, *Contemp. Phys.* **17** (4), 331 (1976).
28. L. N. Bulaevskiĭ, V. L. Ginzburg, G. F. Zharkov, D. A. Kirzhnits, Yu. V. Kopaev, E. G. Maksimov, and D. I. Khomskiĭ, in *Problem of High-Temperature Superconductivity*, Ed. by V. L. Ginzburg and D. A. Kirzhnits (Nauka, Moscow, 1977).
29. S. Ishibashi and M. Kohyama, *Phys. Rev. B* **62** (12), 7839 (2000).
30. K. Lee, R. Menon, C. O. Yoon, and A. J. Heeger, *Phys. Rev. B* **52** (7), 4779 (1995).
31. A. A. Gogolin, S. P. Zolotukhin, V. I. Mel'nikov, É. I. Rashba, and I. F. Shchegolev, *Pis'ma Zh. Éksp. Teor. Fiz.* **22** (11), 564 (1975) [*JETP Lett.* **22**, 278 (1975)].
32. Y. Ishizaki, M. Izumi, H. Ohnuki, K. Kalita-Lipinska, T. Imakubo, and K. Kobayashi, *Phys. Rev. B* **63** (13), 134201 (2001).
33. L. P. Gor'kov, O. N. Dorokhov, and F. V. Prigara, *Zh. Éksp. Teor. Fiz.* **85** (4), 1470 (1983) [*Sov. Phys. JETP* **58**, 852 (1983)].

*Translated by K. Shakhlevich*

## LOW-DIMENSIONAL SYSTEMS AND SURFACE PHYSICS

# Adsorption of Barium and Rare-Earth Metals on Silicon

S. Yu. Davydov

Ioffe Physicotechnical Institute, Russian Academy of Sciences, Politekhnicheskaya ul. 26, St. Petersburg, 194021 Russia  
e-mail: sergei.davydov@ioffe.mail.ru

Received September 8, 2003

**Abstract**—The change in the work function of the Si(111) surface caused by deposition of a submonolayer film of barium has been calculated with due account of dipole–dipole adatom repulsion and metallization effects. The results of the calculations agree satisfactorily with experimental data. The character of the variation in the model parameters in the Ba–Sm–Eu–Yb series is discussed. The electron tunneling probability from an adatom quasi-level to the substrate conduction band and the energy barrier for interatomic transitions of electrons in an adlayer were estimated. © 2004 MAIK “Nauka/Interperiodica”.

1. Submonolayer films of alkali (AM) and alkaline-earth metal (AEM) atoms have been intensely used in emission electronics to lower the work function of high-melting thermionic cathodes; as a result, the AM and AEM interaction with metallic substrates has been studied fairly well [1, 2]. AM films on semiconductor substrates have been explored to a much lesser extent, because such adsorption systems undergo structural rearrangement and feature metal–semiconductor electronic transitions (see, e.g., [3] and references therein). As for AEM films on semiconductors, their investigation is only at the earliest stage.

A scanning tunneling microscopy study [4] explored the effect of a barium film deposited on a Si(111)-(7 × 7) surface on the variation of the work function  $\Delta\phi(\Theta)$  of the adsystem, where  $\Theta = N/N_{\text{ML}}$  is the coverage ( $N$  is the concentration of adatoms and  $N_{\text{ML}}$  is the concentration of adatoms in a monolayer). It was established that an increase in  $\Theta$  brings about a lowering of the work function of the system and rearrangement of the silicon (111) surface from the (7 × 7) structure to (3 × 1) → (5 × 1) → (2 × 8). This communication reports on a calculation of  $\Delta\phi(\Theta)$  in the Ba/Si(111)-(7 × 7) system carried out within the model developed in [5] for describing the adsorption of rare-earth metals (REM) on semiconductors.

2. To describe AM adsorption on semiconductor substrates, a model was proposed in [6, 7] based on the Anderson–Newns Hamiltonian [2]. This model takes into account the dipole–dipole adatom repulsion and the metallization effects associated with electron exchange among atoms in the adlayer. The model disregarded the specific adlayer structure, which made it possible to describe the  $\Delta\phi(\Theta)$  relation for AM adsorption on silicon [6] and rutile [7] fairly simply (and satisfactorily). This model was subsequently extended to cover REM adsorption on Si(111) [5]. Considered in terms of the Anderson–Newns Hamiltonian, the difference between the AM and REM adsorption is that, in

the former case, the adsorbed atom has one electron in the outer  $s$  shell, while in the latter, the  $s$  shell contains two electrons. Because the barium 6s shell also contains two electrons, it appears only natural to use here the results obtained in [5].

In accordance with [5], the adatom charge  $Z$  is

$$Z(\Theta) = \frac{2}{\pi} \arctan \frac{\Omega - \xi \Theta^{3/2} Z(\Theta)}{\Gamma(\Theta)}, \quad (1)$$

$$\xi = 2e^2 \lambda^2 N_{\text{ML}}^{3/2} A, \quad \Gamma = \Gamma_0(1 + \gamma\Theta).$$

Here,  $\xi$  is the adatom dipole–dipole repulsion constant,  $e$  is the positronic charge,  $2\lambda$  is the adsorption bond length (which is equal to the thickness of the double electric layer),  $A = 10$  is a dimensionless coefficient that depends weakly on the adatom array geometry,  $\Omega = (I - \phi + \Delta)$  is the position of the adatom quasi-level relative to the substrate Fermi level,  $I$  is the  $s$ -shell ionization energy,  $\phi$  is the substrate work function,  $\Delta = e^2/4\lambda$  is the Coulomb shift of the level of the adatom caused by the interaction of its electron with the substrate electrons,  $\Gamma_0$  is the quasi-level half-width of a single adatom, and  $\gamma$  is a dimensionless parameter taking into account the broadening of the adatom quasi-level into a two-dimensional band, i.e., the metallization effects.

The change in the work function  $\Delta\phi(\Theta)$  resulting from adsorption is given by

$$\Delta\phi(\Theta) = -\Phi\Theta Z(\Theta), \quad (2)$$
$$\Phi = 4\pi e^2 N_{\text{ML}} \lambda.$$

3. Prior to continuing our calculations, we have first to specify the model parameters. The value of  $N_{\text{ML}}$  can be derived from the distance between the nearest neighbors in bulk barium samples,  $d = 4.35 \text{ \AA}$  [8]. As in [5], we set  $\lambda = 0.7r_a$ , where  $r_a = 2.24 \text{ \AA}$  is the atomic radius of barium [9]. As in [4], we assume the silicon work function  $\phi$  to be 4.8 eV and the barium ionization

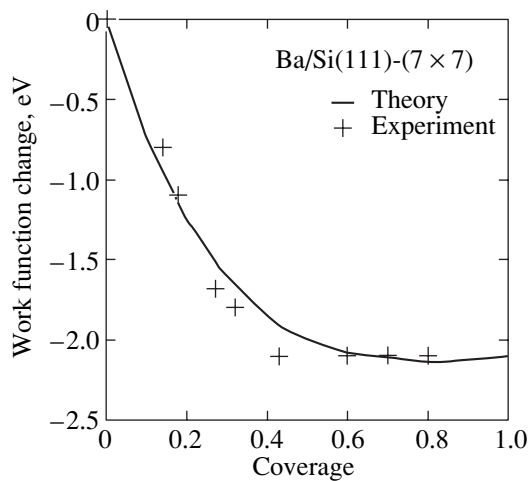
**Table 1.** Model parameters

Film	$\Omega$ , eV	$\Gamma_0$ , eV	$\Phi$ , eV	$\xi$ , eV	$\gamma$	$N_{ML}$ , $10^{14}$ atoms/cm <sup>2</sup>	$\lambda$ , Å	$Z_0$	$Z_{ML}$
Ba	1.88	1.88	15.1	8.7	0.575	5.3	1.6	0.50	0.14
Sm	1.725	2.55	17.6	10.0	1.87	7.5	1.3	0.38	0.08
Eu	1.50	1.87	15.5	8.6	0.45	6.0	1.4	0.43	0.12
Yb	1.12	1.37	15.3	8.1	0.10	6.5	1.3	0.44	0.11

energy to be  $I = 5.21$  eV. To find  $\Gamma_0$  and  $\gamma$ , we make use of the scheme proposed in [6, 7] based on fitting the values of  $(d\Delta\phi/d\Theta)_{\Theta \rightarrow 0}$  and  $\Delta\phi_{ML} \equiv \Delta\phi(\Theta = 1)$  to experimental data. Note that, for the work function of the monolayer coverage, we took the value corresponding to the intensity of the Auger signal equal to unity [4, Fig. 2]. The model parameters found for Ba are presented in Table 1, which also lists the parameters for REMs for comparison.

The calculated  $\Delta\phi(\Theta)$  data are compared with the experimental data in the figure. The agreement between the calculations and experiment is seen to be quite satisfactory. Note that not all of the available experimental data are displayed in the figure. The reason for this is that the values of  $\Delta\phi$  for the coverage region  $\Theta \approx 0.15$  quoted in [4] have a large scatter and vary from 0.2 to 0.8 eV [4, Fig. 2]. The figure shows  $\Delta\phi(0.15) = 0.8$  eV, the value closest to the calculation. (Note that, at larger coverages, the experimental scatter is also quite large.)

The agreement between the calculated and experimental data permits us to interpret the change in the work function differently from what was accepted in [4], where the reduction of the work function was believed to be a consequence of a rearrangement of the silicon surface caused by barium adsorption. Our model, disregarding reconstruction of both the substrate and the adlayer, assigns the  $\Delta\phi(\Theta)$  dependence to



Variation of the work function plotted vs. Si(111) coverage by barium atoms.

adatom depolarization through the dipole–dipole and exchange interactions, i.e., through the same effects that are significant in adsorption on metals [2]. This does not come as a surprise. Indeed, the electron affinity for silicon is  $\chi = 3.99$  eV and the band gap is  $E_g = 1.11$  eV [10]; therefore, the adatom quasi-level, which for zero coverage is at an energy  $\Omega = 1.88$  eV, overlaps the silicon conduction band, a typical “metallic” situation.<sup>1</sup> For monolayer coverage, where  $\Omega_{ML} = \Omega - \xi Z_{ML} = 0.66$  eV, the situation for the silicon substrate possessing intrinsic or electronic conduction (the material used in [4] is *n*-Si) does not change. Thus, we believe that structural rearrangement of the silicon surface is not the primary reason for the decrease in the work function; rather, both the decrease in  $\phi$  and the reconstruction of the silicon surface are a consequence of a change in the electronic structure of the adlayer (see, e.g., [11] and references therein).

**4.** Consider the variation of the model fitting parameters  $\Gamma_0$  and  $\gamma$  in the adsorbate series Ba–Sm–Eu–Yb (Table 1). Such a consideration is appropriate for two reasons. First, all these atoms have a filled outer *6s* shell, and second, barium is a model atom for calculating the REM cohesion energy [12] and the REM adsorption energy on *d* metals [13].

In the Anderson–Newns model, the quasi-level half-width is  $\Gamma_0 = \pi\rho_s V^2$ , where  $\rho_s$  is the substrate density of states (in our particular case, the density of states in the conduction band), which for the sake of simplicity is assumed to be constant, and  $V$  is the matrix element of the adatom–substrate interaction representing a two-center tunneling integral between the states of the adatom  $|a\rangle$  and of the substrate  $|s\rangle$  [14]. According to [15], the matrix element  $V$  squared can be presented in the form

$$V^2 \sim \rho_s^{-1} \rho_a^{-1} D_s, \quad (3)$$

where  $\rho_{s(a)}$  is the density of states of the substrate (adatom) and  $D_s$  is the probability of electron tunneling through the energy barrier separating the adatom from the substrate. The probability of an electron having an energy  $E = \chi - I + \Delta$  (the energy is reckoned from the

<sup>1</sup> The metallic situation is identified in this case with the possibility of direct electron tunneling from the adatom quasi-level to free substrate states.

**Table 2.** Probability of adatom electron tunneling  $D_s$  into the substrate

Parameter	Ba	Sm	Eu	Yb
$D_s$	0.13	0.22	0.145	0.09
$D_s/\rho_a$ , eV	1.52	2.57	1.40	0.65
$U_a$ , eV	3.78	1.69	4.33	6.41

Note: The ratio  $D_s/\rho_a$  is proportional to the half-width of the single adatom quasi-level  $\Gamma_0$ ;  $U_a$  is the barrier height for electron tunneling from the adatom quasi-level into the adlayer.

conduction band bottom) to cross a barrier of height  $\chi$  and width  $b$  is [16]

$$D_s = \frac{4k_1^2\kappa_2^2}{(k_1^2 + \kappa_2^2)^2 \sinh^2(\kappa_2 b) + 4k_1^2\kappa_2^2}, \quad (4)$$

where  $\hbar k_1 = \sqrt{2mE}$  and  $\hbar \kappa_2 = \sqrt{2m(\chi - E)}$ .

We set the barrier width  $b$  equal to the half-sum of the atomic radii of silicon and of the adsorbed atom. Because  $\Gamma_0 = \pi\rho_s V^2$ , we have, in accordance with Eq. (3),

$$\Gamma_0 \sim D_s/\rho_a, \quad (5)$$

where the density of states for the adatom is  $\rho_a = \Gamma_0/\pi(\Omega^2 + \Gamma_0^2)$ . The calculated tunneling probability  $D_s$  and the  $D_s/\rho_a$  ratio are listed in Table 2, from which it is seen that the value of the ratio  $D_s/\rho_a$  correlates well with the value of  $\Gamma_0$  for Ba, Sm, and Eu, whereas for Yb the agreement is not as good.

Consider now the parameter  $\gamma$ . If one takes into account only direct electron exchange between the nearest neighbor adatoms,  $\gamma$  can be shown to have the form [17]

$$\gamma = T^2/(\Omega^2 + \Gamma_0^2), \quad T^2 \equiv z_{n.n.} t_{ML}^2, \quad (6)$$

where  $z_{n.n.}$  is the number of nearest neighbors in a monolayer and  $t_{ML}$  is the electron transfer integral between the nearest neighbor adatoms in a monolayer. Equation (6) can be recast as

$$\gamma = \Gamma_a/\Gamma_0, \quad \Gamma_a = \pi\rho_a T^2. \quad (7)$$

We have introduced here the half-width of the adatom quasi-level  $\Gamma_a$  related to the possibility of electron tunneling in the adlayer. We can thus set

$$\gamma = D_a/D_s, \quad (8)$$

where  $D_a$  is the probability of an electron tunneling into the adlayer by crossing a barrier of height  $U_a$  and width  $d/2$ . Hence, parameter  $\gamma$  determines the probability ratio for an adatom electron to tunnel into the adlayer and into the substrate.

The probability  $D_a$  is calculated from Eq. (4), with the electron affinity  $\chi$  replaced by  $U_a$  and  $a$  replaced by  $d/2$ . Equating  $D_a$  to the product  $\gamma D_s$  calculated from the

data in Tables 1 and 2, we obtain the values of  $U_a$  listed in Table 2. The values of  $U_a$  for Ba, Sm, and Eu appear quite reasonable, whereas for ytterbium the barrier height is obviously a gross overestimate, which is a consequence of the extreme smallness of the corresponding parameter  $\gamma = 0.1$ . (In this connection, it should be stressed that the magnitude of the fitting parameter  $\gamma$  derived from [6, Eq. (6)] or [7, Eq. (4)], is extremely sensitive to variation of the adatom charge in the monolayer,  $Z_{ML}$ , which is small. Indeed, a decrease in  $Z_{ML}$  for Yb by one one-hundredth brings about a two-fold increase in the parameter  $\gamma$ .<sup>2</sup>)

To sum up, we have shown that, first, the model proposed originally for describing the adsorption of alkali metal atoms on semiconductors has a broader area of application. Second, we have demonstrated that the fitting parameters of the proposed model are quite reasonable. From this it follows that the major factor governing structural transitions in the substrate, which were pointed out in [4], is the depolarization of the adatoms, which grows in significance as their concentration increases.

## REFERENCES

1. L. A. Bol'shov, A. P. Napartovich, A. G. Naumovets, and A. G. Fedorus, *Usp. Fiz. Nauk* **122** (1), 125 (1977) [*Sov. Phys. Usp.* **20**, 432 (1977)].
2. O. M. Braun and V. K. Medvedev, *Usp. Fiz. Nauk* **157** (4), 631 (1989) [*Sov. Phys. Usp.* **32**, 328 (1989)].
3. S. Yu. Davydov, *Fiz. Tverd. Tela (St. Petersburg)* **42** (6), 1129 (2000) [*Phys. Solid State* **42**, 1164 (2000)].
4. M. Komani, M. Sasaki, R. Ozawa, and S. Yamamoto, *Appl. Surf. Sci.* **146** (1), 158 (1999).
5. S. Yu. Davydov and A. V. Pavlyk, *Fiz. Tverd. Tela (St. Petersburg)* **45** (7), 1325 (2003) [*Phys. Solid State* **45**, 1388 (2003)].
6. S. Yu. Davydov and A. V. Pavlyk, *Fiz. Tekh. Poluprovodn. (St. Petersburg)* **35** (7), 796 (2001) [*Semiconductors* **35**, 796 (2001)].
7. S. Yu. Davydov and I. V. Noskov, *Pis'ma Zh. Tekh. Fiz.* **27** (20), 1 (2001) [*Tech. Phys. Lett.* **27**, 844 (2001)].

<sup>2</sup>For such a small variation in the parameter  $\gamma$ , the  $\Delta\phi(\Theta)$  function changes only insignificantly.

8. C. Kittel, *Introduction to Solid State Physics*, 5th ed. (Wiley, New York, 1976; Nauka, Moscow, 1978).
9. *Physical Quantities. Handbook*, Ed. by I. S. Grigor'ev and E. Z. Meilikhov (Énergoatomizdat, Moscow, 1991).
10. T. Bechshedt and R. Enderlein, *Semiconductor Surfaces and Interfaces. Their Atomic and Electronic Structures* (Academie, Berlin, 1988; Mir, Moscow, 1990).
11. S. Yu. Davydov, *Fiz. Tverd. Tela (Leningrad)* **21** (8), 2283 (1979) [*Sov. Phys. Solid State* **21**, 1314 (1979)].
12. J. M. Wills and W. A. Harrison, *Phys. Rev. B* **29** (10), 5486 (1984).
13. S. Yu. Davydov and S. K. Tikhonov, *Surf. Sci.* **371** (1–3), 157 (1997).
14. C. Kittel, *Quantum Theory of Solids* (Wiley, New York, 1963; Nauka, Moscow, 1967), Chap. 18.
15. J. R. Schrieffer, *Theory of Superconductivity* (Benjamin, New York, 1964; Nauka, Moscow, 1970), Chap. 3.
16. L. D. Landau and E. M. Lifshitz, *Course of Theoretical Physics, Vol. 3: Quantum Mechanics: Non-Relativistic Theory*, 3rd ed. (Nauka, Moscow, 1974; Pergamon, New York, 1977).
17. S. Yu. Davydov, *Surf. Sci.* **411** (1–3), L878 (1998).

*Translated by G. Skrebtsov*



---

LOW-DIMENSIONAL SYSTEMS  
AND SURFACE PHYSICS

---

## X-ray Spectral Analysis of the Interface of a Thin Al<sub>2</sub>O<sub>3</sub> Film Prepared on Silicon by Atomic Layer Deposition

A. S. Shulakov, A. P. Braiko, S. V. Bukin, and V. E. Drozd

*Fock Institute of Physics, St. Petersburg State University, ul. Ul'yanovskaya 1, Petrodvorets, St. Petersburg, 198504 Russia*

*e-mail: shulak@paloma.spbu.ru*

Received October 23, 2003

**Abstract**—The extent and phase chemical composition of the interface forming under atomic layer deposition (ALD) of a 6-nm-thick Al<sub>2</sub>O<sub>3</sub> film on the surface of crystalline silicon (c-Si) has been studied by depth-resolved, ultrasoft x-ray emission spectroscopy. ALD is shown to produce a layer of mixed Al<sub>2</sub>O<sub>3</sub> and SiO<sub>2</sub> oxides about 6–8 nm thick, in which silicon dioxide is present even on the sample surface and its concentration increases as one approaches the interface with the substrate. It is assumed that such a complex structure of the layer is the result of interdiffusion of oxygen into the layer and of silicon from the substrate to the surface over grain boundaries of polycrystalline Al<sub>2</sub>O<sub>3</sub>, followed by silicon oxidation. Neither the formation of clusters of metallic aluminum near the boundary with c-Si nor aluminum diffusion into the substrate was revealed. It was established that ALD-deposited Al<sub>2</sub>O<sub>3</sub> layers with a thickness up to 60 nm have similar structure. © 2004 MAIK “Nauka/Interperiodica”.

The method of atomic layer deposition (ALD) has recently been attracting increasing interest as a promising means of forming heterostructures for the development of modern micro- and nanoelectronics devices. In view of the extremely small size of the nanostructures, their formation requires the control of the growth process at the monatomic layer. To solve this problem, one has to apply to the surface of one compound very thin perfect layers of other compounds in a given order and of a predetermined thickness. The principles underlying the ALD method are outlined in [1].

In this study, we used the ALD process to deposit the oxide Al<sub>2</sub>O<sub>3</sub> on the Si(100) surface layers. Because aluminum oxide has a considerably higher value of dielectric permittivity  $k$  than silicon oxide, this structure is considered a promising material for microelectronics (the so-called high- $k$  material). Obviously enough, the electrophysical properties of the heterostructure are determined not only by the characteristics of the thin Al<sub>2</sub>O<sub>3</sub> layer but also by the characteristics of the interface with silicon. The present study addresses this issue. We are interested here in the phase chemical composition of the Al<sub>2</sub>O<sub>3</sub>/Si interface and its extent (thickness).

Considerable attention has been focused recently on the analysis of the properties of Al<sub>2</sub>O<sub>3</sub> films fabricated by ALD [2–8]. The formation of the structure of thin ALD-deposited Al<sub>2</sub>O<sub>3</sub> films and the underlying processes have been studied primarily by electron (x-ray photoelectron and Auger electron) spectroscopy, secondary ion mass spectrometry, recording the elastic recoil of light atoms upon scattering of heavy atoms, etc. However, the results obtained in such studies

remain contradictory in many respects. This is apparently associated with the application of destructive methods to a depth-resolved analysis of the structure and chemical composition of films. These methods also do not permit one to study thick coatings.

The present communication reports on a study of interfaces using a nondestructive method of probing the phase chemical composition, namely, depth-resolved ultrasoft x-ray emission spectroscopy [9, 10]. This method makes use of the dependence of the depth of escape of characteristic x-ray radiation on the primary electron energy. The characteristic x-ray emission bands are created by valence band electrons spontaneously filling the vacancies produced by electron impact in the inner atomic shells. The dependence of the shape of the x-ray emission bands on the chemical state of the emitting atom permits reliable determination of the phase chemical composition of a sample.

Silicon plates were preliminarily exposed to hydrofluoric acid vapor and a glow discharge plasma in the presence of water vapor at a temperature of 200–300°C under reduced pressure. The actual atomic layer deposition process consisted of the following cycles. The reactor was filled by vapors of trimethyl aluminum (TMA) for a few tenths of a second, with subsequent evacuation of the reagent and admission of water vapor to the reactor, which prepared the surface for the next ALD cycle. These cycles were repeated the required number of times. Samples with Al<sub>2</sub>O<sub>3</sub> layer thicknesses varying from a few nanometers to a few hundreds of nanometers were prepared. X-ray spectroscopy showed the interfaces of thin films, with thicknesses of up to about 60 nm, to have similar properties, which vary with increasing coating thickness (i.e., interface depth).

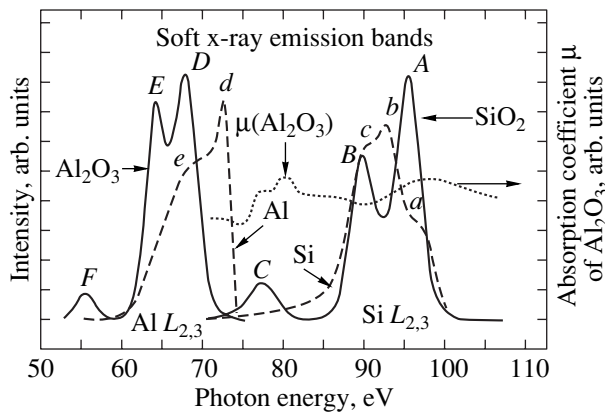


**Fig. 1.** Ultrasoft x-ray  $L_{2,3}$  emission bands of crystalline aluminum and silicon (solid lines) and the emission bands of these atoms in stoichiometric oxides (dashed lines);  $\mu(\text{Al}_2\text{O}_3)$  is the  $\text{Al}_2\text{O}_3$  absorption coefficient (dotted line).

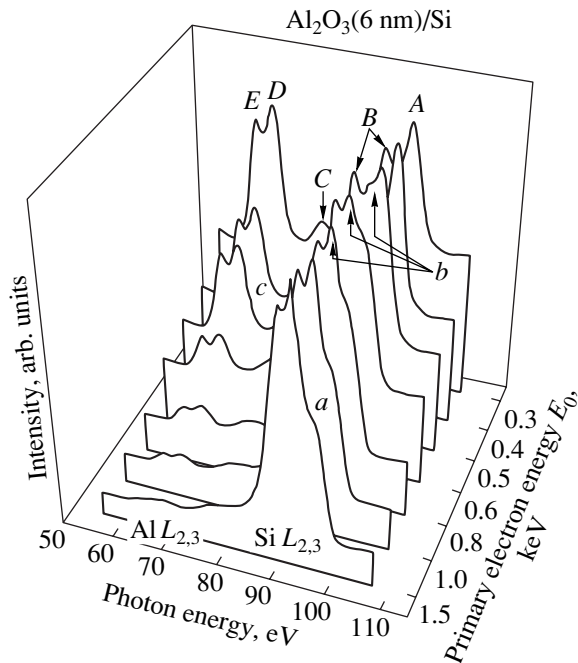


**Fig. 2.** Variation in the shape of x-ray emission spectra with primary electron energy for a sample consisting of a 6-nm-thick  $\text{Al}_2\text{O}_3$  layer prepared by ALD on the Si(100) surface. The silicon  $L_{2,3}$  bands are normalized in intensity.

Because the amount of the data obtained is too large to be presented in one publication, we describe only the results of a study of thin coatings using the example of a 6-nm-thick layer. The studies of deeper lying  $\text{Al}_2\text{O}_3/\text{Si}$  interfaces will be reported later.

We studied the dependence of the shape of the aluminum and silicon  $L_{2,3}$  x-ray emission bands on the primary electron energy  $E_0$ . The measurements were conducted on an RSL-1500 ultrasoft x-ray spectrometer [11]. The spectra in the range 50–110 eV were obtained

with a wavelength resolution of 0.2 nm. The primary electron current did not exceed 1 mA, and the reproducibility of the results and the constancy of the electro-physical parameters of the structures were monitored periodically.

Figure 1 shows  $L_{2,3}$  x-ray emission bands of pure crystalline aluminum and silicon (c-Si) and the bands of the same atoms in stoichiometric oxides. These bands will be used as references when analyzing the emission spectra of an ALD-deposited  $\text{Al}_2\text{O}_3/\text{Si}$  film. Figure 1 also shows the spectral response of the absorption coefficient of x-ray radiation by an  $\text{Al}_2\text{O}_3$  film. The fine structure of the absorption spectrum near the  $L_{2,3}$  absorption edge may distort the spectral shape of the silicon radiation passing through the film, and this effect should be taken into account in analyzing the shape of the spectra. This effect (self-absorption of escaping radiation) was found to be small for the thin coatings studied here and could not produce noticeable distortions in the spectral shape.

Figure 2 displays x-ray emission spectra of a sample with the silicon surface coated by a 6-nm-thick  $\text{Al}_2\text{O}_3$  layer ( $\text{Al}_2\text{O}_3(6 \text{ nm})/\text{Si}$ ) that demonstrate the dependence of the spectral shape on  $E_0$  in the range including Al and Si  $L_{2,3}$  bands. The labeling of the maxima of the spectra is the same as that in Fig. 1, and the spectra are normalized against the intensity of the Si  $L_{2,3}$  band.

The spectra obtained at the minimum primary electron energy (0.3 keV) are seen to contain  $L_{2,3}$  bands of the Al and Si atoms entering into  $\text{Al}_2\text{O}_3$  and  $\text{SiO}_2$ , respectively (maxima A, B, C, D, E). After  $E_0$  has been increased to 0.5 keV, a maximum *b* appears in the silicon spectrum. As  $E_0$  is increased still further, maxima *a* and *c* become evident and the silicon spectrum practically coincides with the c-Si spectrum (Fig. 1). The shape of the Al  $L_{2,3}$  band is independent of  $E_0$ , with only its relative intensity changing. At  $E_0 = 1.5$  keV, the contribution from the aluminum band intensity to the total intensity of recorded radiation becomes negligible.

The explanation for the observed variations is straightforward. Indeed, at the lowest energy  $E_0 = 0.3$  keV, the sample layer responsible for the x-ray emission bands does not exceed the  $\text{Al}_2\text{O}_3$  coating in thickness and contains, in addition to the aluminum oxide, oxidized silicon atoms in the coordination characteristic of  $\text{SiO}_2$ . As  $E_0$  increases, the lower boundary of the emitting layer shifts away from the surface to cross the substrate interface and its contribution to the spectrum increases (the c-Si  $L_{2,3}$  band in pure silicon, maxima *a*, *b*, and *c*) and quickly becomes dominant.

Analysis of the band shape evolution with increasing  $E_0$  suggests the obvious conclusion that ALD of  $\text{Al}_2\text{O}_3$  on an oxide-free surface of a silicon single crystal produces an interface containing, nevertheless, a considerable amount of the silicon oxide  $\text{SiO}_2$ . This conclusion can be supported in a more revealing way.

Figure 3 shows deconvolution of an experimental silicon spectrum into constituents for two values of  $E_0$ . For constituents, we chose only the  $\text{Si}L_{2,3}$  bands in c-Si and  $\text{SiO}_2$  (Fig. 1). The fit to the experimental spectrum unfolded into constituents by the standard least squares procedure turned out to be very good. This shows that, in the region of the interface, silicon atoms are coordinated either as in c-Si (the substrate) or as in  $\text{SiO}_2$  (the coating). Figure 3 identifies the fine structure in the experimental spectra in the notation used in Fig. 1.

While the above analysis provides evidence for the presence of not only aluminum oxide but also a substantial amount of  $\text{SiO}_2$  (in a concentration comparable to that of  $\text{Al}_2\text{O}_3$ ) in the surface layer, it does not offer insight into the silicon oxide distribution in depth. This information can be extracted from data on the dependence of the relative band intensities on  $E_0$ . Figure 4 displays the behavior of the integrated intensities of the  $\text{Si}L_{2,3}$  bands in  $\text{SiO}_2$  and c-Si obtained from unfolded spectra and normalized against the  $\text{Al}L_{2,3}$  band intensity in  $\text{Al}_2\text{O}_3$  (Fig. 2). The relative intensity of the c-Si spectrum grows rapidly, which reflects the shift of the center of gravity of the excitation into the substrate with increasing  $E_0$ . Obviously enough, excitation of the c-Si band starts when the energy  $E_0$  reaches a value close to 0.3 keV. This means that the c-Si interface is overlaid and, in order for the electrons crossing the layer to be able to ionize the Si  $2p$  shell, their energy has to exceed the binding energy of the electrons in this shell (99.8 eV) by approximately 200 eV.

The  $E_0$  dependence for the  $\text{SiO}_2$  band is more complex; its relative intensity increases and saturates at  $E_0 = 0.8$  keV. Extrapolating this graph to zero through the first three points shows that the  $\text{SiO}_2$  spectrum appears when  $E_0$  enters the region of  $100.0 \pm 0.5$  eV, which includes the binding energy of the Si  $2p$  electrons in  $\text{SiO}_2$  (104.1 eV). The matching (to within experimental error) of the extrapolation point to the binding energy of the scanning  $2p$  level means that silicon oxides are not only present in the synthesized  $\text{Al}_2\text{O}_3$  film but emerge onto its surface as well. Let us estimate the pattern of the silicon dioxide distribution across the coating thickness. In our case, where the atomic numbers of the elements and the ionization energies of the scanning  $2p$  shells are similar and the film thickness is small, it can be shown that the dependence of the intensity ratio of the Si and Al  $L_{2,3}$  spectra on  $E_0$  should be determined primarily by the ratio of the  $2p$ -shell electron-impact ionization cross sections,  $\sigma_{\text{Si}}(E_0)/\sigma_{\text{Al}}(E_0)$ . This ratio was calculated using the Grynskiy formula for the cross sections of  $np$  shell ionization by electron impact [12] and is shown in Fig. 4 by circles (the experimental and theoretical curves are matched in magnitude at the 0.8-keV point). The cross-section ratio also grows with  $E_0$ , but substantially faster than the experimental intensity ratio. For  $E_0 \geq 0.8$  keV, the graphs become identical in shape. The

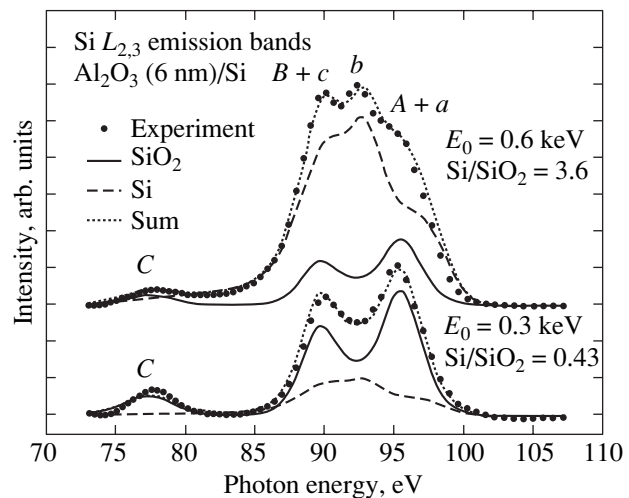


**Fig. 3.** Deconvolution of experimental silicon  $L_{2,3}$  spectra into the constituent  $L_{2,3}$  bands of Si in  $\text{SiO}_2$  (solid lines) and in c-Si (dashed lines) plotted for  $E_0 = 0.3$  and 0.6 keV. The notation of the maxima is the same as that in Fig. 1.

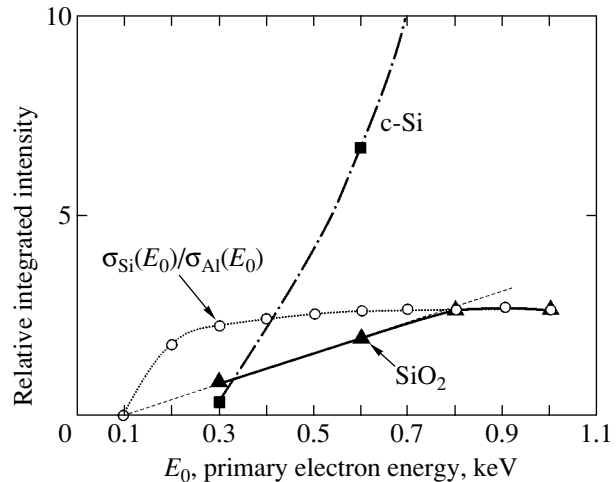


**Fig. 4.** Relative integrated intensities of Si  $L_{2,3}$  bands in  $\text{SiO}_2$  (solid line) and in Si (dash-dotted line) plotted vs. primary electron energy  $E_0$ . The spectra are normalized against the Al  $L_{2,3}$  band intensity in  $\text{Al}_2\text{O}_3$ . Dashed line is extrapolation of the dependence for  $\text{SiO}_2$  to zero. Circles are the ionization cross-section ratios of the Si and Al  $2p$  levels calculated from the Grynskiy relation [12].

observed difference in shape between the experimental and theoretical curves can be accounted for as follows. The theoretical graph is constructed under the assumption that the Al and Si atoms are present in equal concentrations (the cross sections are given per atom); therefore, by varying the scale of the  $\sigma_{\text{Si}}(E_0)/\sigma_{\text{Al}}(E_0)$  curve, we vary, as it were, the relative concentration of the Si and Al atoms. Far from the thresholds, the cross sections follow the same course and, therefore, their ratio saturates. This corresponds obviously to about

0.8 keV (Fig. 4). The relative intensity of the  $\text{Si}L_{2,3}$  band should also reach saturation with increasing  $E_0$ , because at high enough values of  $E_0$  the conditions of excitation of Si and Al spectra in a thin near-surface film become practically the same, irrespective of the relative concentration distributions. The same reason accounts for the saturation in the theoretical relation; thus, there is nothing strange in the fact that the saturation starts in both cases at the same point (0.8 keV). Thus, by normalizing the theoretical and experimental relations in this region, we reduce the relative, layer-averaged atomic concentrations in the theoretical curve to the experimental value. After this procedure, the theoretical curve provides an estimate of the relative Si radiation intensity for a certain constant average silicon concentration. As seen from Fig. 4, for any  $E_0$ , the ordinates of the experimental curve lie below the theoretical values, but the difference between them decreases with increasing  $E_0$ . This fact is a direct indication of the Si atom concentration (in the  $\text{SiO}_2$  coordination) increasing as one approaches the interface.

Let us estimate the thickness of the surface layer coating the silicon substrate. For this purpose, we can use the empirical relation describing the behavior of the maximum escape depth from which the Si  $L_{2,3}$  radiation emerges from  $\text{SiO}_2$  [9] by properly changing the layer density. The coating density should apparently be an average between the densities of  $\text{SiO}_2$  and  $\text{Al}_2\text{O}_3$ , i.e., approximately  $3\text{--}4\text{ g/cm}^3$ , in which case the layer thickness is  $6\text{--}8\text{ nm}$ . If we take into account that ALD is capable of depositing  $\text{Al}_2\text{O}_3$  layers  $6\text{ nm}$  thick with a high accuracy, this estimate appears reasonable. Indeed, the presence of  $\text{SiO}_2$  in noticeable amounts, irrespective of its location, should bring about film swelling.

As follows from an analysis of our results, ALD of a thin  $\text{Al}_2\text{O}_3$  layer on a c-Si surface freed of its native oxide is a complex process. It gives rise to the formation of a  $6\text{--}8\text{-nm}$ -thick layer of mixed  $\text{Al}_2\text{O}_3$  and  $\text{SiO}_2$  oxides, in which silicon dioxide is present even on the surface of the structure and its concentration increases as one approaches the c-Si substrate interface. Strictly speaking, the  $\text{Al}_2\text{O}_3/\text{Si}$  interface does not form, with a more complex  $\text{Al}_2\text{O}_3\text{--SiO}_2/\text{Si}$  boundary appearing in its place. Clusters of metallic aluminum were reported to have been observed to form in the vicinity of the interface [2–4]. No such clusters at the thin film interface were found by us within the limits of sensitivity of our measurements (less than 0.5 wt %) for a thickness of the emitting layer of about  $6\text{--}8\text{ nm}$ .

Noticeable oxygen diffusion was found to occur through the  $\text{Al}_2\text{O}_3$  layer in the course of ALD [6–8], and silicon was observed to diffuse from the substrate to the surface during the ALD and annealing [8]. Our results corroborate the findings reported in [6–8]. Indeed, the most probable mechanism for the formation, in the  $\text{Al}_2\text{O}_3$  film, of the  $\text{SiO}_2$  oxide, whose concentration increases as one approaches the substrate, is interdiffu-

sion of the oxygen and silicon, followed by silicon oxidation. One could agree with the suggestion from [8] that oxygen diffuses most probably over grain boundaries of the  $\text{Al}_2\text{O}_3$  polycrystalline layer, although this requires supporting evidence. The distributions of elements in depth presented in [8] indicate that Al atoms penetrate deep into the substrate. Our results indicate that the boundary between the c-Si substrate and the variable-composition  $\text{Al}_2\text{O}_3\text{--SiO}_2$  layer is sharp, with no Al diffusion into the c-Si observed.

Our study has demonstrated a high efficiency of ultrasoft x-ray emission spectroscopy in investigating thin surface layers, and our data offer the possibility of examining the results obtained by traditional methods from a different standpoint.

#### ACKNOWLEDGMENTS

This study was supported by the Russian Foundation for Basic Research, project no. 01-03-32771.

#### REFERENCES

1. V. B. Aleskovskii and V. E. Drozd, *Acta Polytech. Scand., Chem. Technol. Ser.* **195**, 155 (1990).
2. Y. K. Kim, S. H. Lee, S. J. Choi, H. B. Park, Y. D. Seo, K. H. Chin, D. Kim, J. S. Lim, W. D. Kim, K. J. Nam, M.-H. Cho, K. H. Hwang, and Y. S. Kim, in *Proceedings of the International Electron Devices Meeting* (San Francisco, CA, 2000).
3. W. S. Yang, U. K. Kim, S.-Y. Yang, J. H. Choi, H. B. Park, S. I. Lee, and J.-B. Yoo, *Surf. Coat. Technol.* **131**, 79 (2000).
4. J. Kim, D. Kwong, K. Chakrabarti, C. Lee, K. Oh, and J. Lee, *J. Appl. Phys.* **92** (11), 6739 (2002).
5. V. Consier, H. Bender, M. Caumax, J. Chen, T. Conard, H. Nohira, O. Richard, W. Tsai, W. Vandervorst, E. Young, C. Zhao, S. D. Gendt, M. Heyns, J. W. H. Maes, M. Tuominen, C. Rochart, M. Oliver, and A. Chabli, in *Proceedings of the International Workshop on Gate Insulator (IWGI)* (Japan, 2001).
6. M. Kadoshima, T. Nabatame, T. Yasuda, M. Nishizawa, M. Ikeda, T. Horikawa, and A. Toriumi, in *Proceedings of Atomic Layer Deposition Conference* (Seoul, 2002).
7. G. Parson, D. Niu, T. Gougoushi, M. J. Kelly, and T. Abatemarco, in *Proceedings of Atomic Layer Deposition Conference* (Seoul, 2002).
8. S. Jakschik, U. Schroeder, T. Hecht, D. Krueger, G. Dollinger, A. Bergmaier, C. Luhmann, and J. W. Bartha, *Appl. Surf. Sci.* **211**, 352 (2003).
9. A. S. Shulakov, *Cryst. Res. Technol.* **23**, 835 (1988).
10. A. Zimina, A. S. Shulakov, S. Eizebitt, and W. Eberhardt, *Surf. Sci. Lett.* **9** (1), 461 (2002).
11. A. P. Lukirskii, V. A. Fomichev, and A. V. Rudnev, *Appar. Metody Rentgen. Anal.* **9**, 89 (1970).
12. M. Grynskiy, *Phys. Rev.* **138**, A305 (1965); *Phys. Rev.* **138**, A322 (1965).

*Translated by G. Skrebtsov*

POLYMERS  
AND LIQUID CRYSTALS

Correlation between Characteristics of Thermal  
and Stress Reversible Deformations in Solids  
with Different Structures

L. A. Laius<sup>†</sup>\*, A. I. Slutsker\*\*, I. V. Gofman\*, and V. L. Gilyarov\*\*

\* Institute of Macromolecular Compounds, Russian Academy of Sciences,  
Bol'shoi pr. 31, St. Petersburg, 199004 Russia

\*\* Ioffe Physicotechnical Institute, Russian Academy of Sciences,  
Politekhnikeskaya ul. 26, St. Petersburg, 194021 Russia

e-mail: Alexander.Slutsker@mail.ioffe.ru

Received August 25, 2003

**Abstract**—The dependences of the coefficients of reversible thermal expansion on the tensile stress and the temperature dependences of the elastic modulus are measured for solids with different structures, such as a metal, rigid-chain oriented polymers, and a flexible-chain oriented polymer—poly(ethylene) in the devitrified state. For these materials, the elastic moduli differ by several orders of magnitude, whereas the thermal expansion coefficients can differ not only in magnitude but also in sign. It is found that, for a solid, the derivative of the thermal expansion coefficient with respect to the stress is close to the derivative of the reciprocal of the elastic modulus with respect to the temperature. The inference is made that these parameters do not depend on the specific features of the solids under investigation. Calculations are performed for several mechanisms of thermal and stress deformations of solids with different structures. The results of these calculations are in reasonable agreement with experimental data. © 2004 MAIK “Nauka/Interperiodica”.

1. INTRODUCTION

Thermal and stress reversible deformations of solids have different origins.

Reversible thermal deformation (thermal expansion) is caused by a change in the temperature  $T$  and is characterized by the thermal expansion coefficient  $\alpha = \frac{\partial \epsilon}{\partial T}$ , where  $\partial \epsilon = \frac{\partial l}{l}$  is the relative change in the size of a solid.

Reversible stress deformation (elastic deformation) is caused by a change in the mechanical stress  $\sigma$  and is characterized by the elastic modulus  $E = \frac{\partial \sigma}{\partial \epsilon}$  or the reciprocal of this quantity, i.e., the elastic compliance  $E^{-1} = \frac{\partial \epsilon}{\partial \sigma}$ .

The quantities  $\alpha$  and  $E^{-1}$  have different dimensions ( $\text{K}^{-1}$  and  $\text{Pa}^{-1}$ , respectively) and, therefore, cannot be quantitatively compared for a particular solid.

At the same time, the thermal expansion coefficient and the elastic compliance  $E^{-1}$  for a solid are not constants and depend on the stress and the temperature. For the stress-dependent thermal expansion coefficient  $\alpha(\sigma)$  and the temperature-dependent elastic modulus or

temperature-dependent elastic compliance  $E^{-1}(T)$ , we can write the following relationship:

$$\frac{\partial \alpha}{\partial \sigma} = \frac{\partial(E^{-1})}{\partial T} = \frac{\partial^2 \epsilon}{\partial \sigma \partial T}. \quad (1)$$

Therefore, the derivative of the thermal expansion coefficient with respect to the stress and the derivative of the reciprocal of the elastic modulus with respect to the temperature have identical dimensions ( $\text{Pa}^{-1} \text{K}^{-1}$ ) and coincide in magnitude (i.e., there is a peculiar invariant). Relationship (1) is general and, hence, should be satisfied for any solid.

Moreover, solids with different structures exhibit a great variety of mechanisms of thermal expansion and elastic deformation and differ substantially in terms of the thermal expansion coefficients (and even in their sign) and elastic moduli.

A considerable amount of data is available in the literature on the temperature dependence of the elastic modulus for low-molecular crystalline materials (predominantly, metals) [1] and polymers [2]. There are only a few works concerned with the stress dependence of the thermal expansion coefficient for metals [3, 4] that provide a means for verifying relationships (1). However, there is virtually no data on the stress dependence of the thermal expansion coefficient for polymers (it is these polymers that can have negative coefficients of thermal expansion).

<sup>†</sup> Deceased.

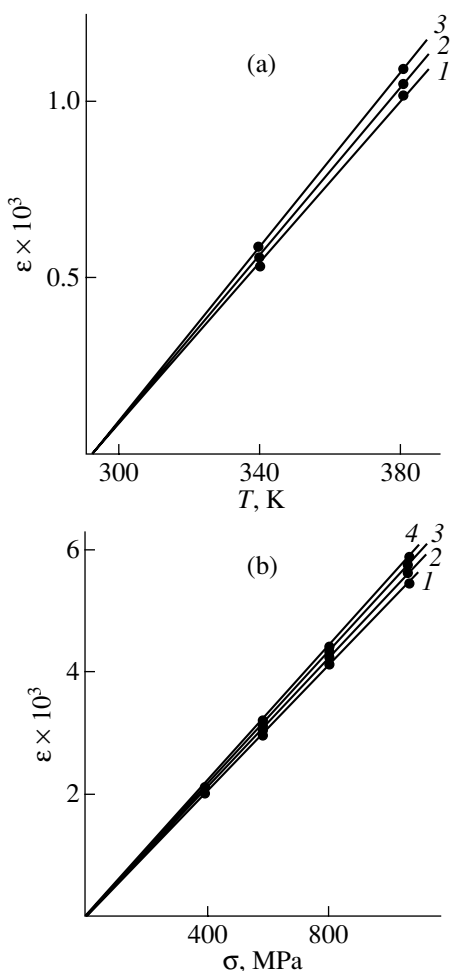


**Fig. 1.** (a) Temperature and (b) stress dependences of the recoverable strain of the steel wire. (a) Tensile stress  $\sigma$ : (1) 303, (2) 730, and (3) 1090 MPa. (b) Temperature  $T$ : (1) 293, (2) 323, (3) 353, and (4) 381 K.

In the present work, we measured the thermal deformation with a variation in the stress and the stress deformation with a variation in the temperature for metals and polymers. The stress derivatives of the thermal expansion coefficient were compared with the temperature derivatives of the elastic modulus. The ratios of the experimentally obtained derivatives of these quantities were interpreted in terms of several mechanisms of thermal expansion and elastic deformation of solids with different structures.

## 2. EXPERIMENTAL TECHNIQUE AND OBJECTS OF INVESTIGATION

The thermal and stress deformations were investigated using rodlike samples with an operating length of 100 mm. The deformation of samples was measured with an accuracy of 3  $\mu\text{m}$ . The temperature was kept constant to within 0.5 K. The tensile stress was controlled to within 2%.

The stress dependence of the thermal expansion coefficient was measured as follows: the sample at the initial temperature was subjected to a number of specified stresses; under each stress, the sample was heated at different temperatures; and the thermal strain of the sample upon heating at these temperatures was measured.

The temperature dependence of the elastic modulus was measured as follows: the sample was thermostated at several specified temperatures; at each temperature, the sample was subjected to a number of different stresses; and the stress strain of the sample under these stresses was measured.

During measurements, the temperature and stress were varied over sufficiently narrow ranges; as a result, the thermal and stress strains were virtually recoverable (i.e., plastic and shrinkage deformations were absent).

The experiments were performed with a metal sample and several polymer samples.

### 2.1. Metal

The high-elasticity steel wire used as a metal sample was 0.4 mm in diameter and possessed a positive coefficient of thermal expansion.

### 2.2. Polymers

Highly oriented fibers (10–12  $\mu\text{m}$  in diameter) from rigid-chain polymers, namely, poly(4,4'-oxydiphenylene pyromellitic imide) (PM), poly(*p*-phenylene terephthalamide) (Kevlar-49, K-49), and poly(amido-benzimidazole) (synthetic high-polymer material, SHPM), had a negative coefficient of thermal expansion along the axis.

Oriented rods (~1 mm in diameter) from a flexible-chain polymer, namely, poly(ethylene) (PE), had a large negative coefficient of thermal expansion along the axis.

## 3. RESULTS AND DISCUSSION

### 3.1. Metal

The temperature dependences of the recoverable strain of the steel wire under different tensile stresses are shown in Fig. 1a. The stress dependences of the recoverable strain of the steel wire at different temperatures are depicted in Fig. 1b. Since the thermal strains are positive, we deal with a conventional thermal expansion. As can be seen from these figures, the thermal expansion of the sample increases under tensile stresses (Fig. 1a), whereas an increase in the temperature leads to an increase in the elastic elongation (Fig. 1b).

It can be seen from Fig. 1 that the temperature and stress dependences of the recoverable strain exhibit an almost linear behavior. From the slopes of these dependences, we can determine the thermal expansion coef-

coefficients  $\alpha = \Delta\varepsilon/\Delta T$  at different stresses  $\sigma$  and the values of the reciprocal of the elastic modulus  $E^{-1} = \Delta\varepsilon/\Delta\sigma$  at different temperatures  $T$ . The stress dependence of the thermal expansion coefficient  $\alpha(\sigma)$  and the temperature dependence of the reciprocal of the elastic modulus  $E^{-1}(T)$  for the steel wire are plotted in Figs. 2a and 2b, respectively. After linear approximation of these dependences, we determined the quantities  $\Delta\alpha/\Delta\sigma$  and  $\Delta(E^{-1})/\Delta T$ , which are given in the table. The thermal expansion coefficients  $\alpha$  at  $T = 293$  K and  $\sigma = 0$  and the elastic moduli  $E$  at  $T = 293$  K are also listed in the table. Moreover, the table presents the characteristics of thermal and stress deformations for metallic copper [4, 5].

As follows from the table, the quantities  $\Delta\alpha/\Delta\sigma$  and  $\Delta(E^{-1})/\Delta T$  are close to each other (especially for copper). The small difference between these quantities for the steel can be associated with the errors in the measurements, because, as can be seen from Fig. 1, the effects of the stress  $\sigma$  on  $\varepsilon(T)$  and the temperature  $T$  on  $\varepsilon(\sigma)$  are insignificant.

Let us consider the factors responsible for the close values of  $\Delta\alpha/\Delta\sigma$  and  $\Delta(E^{-1})/\Delta T$  and determine the magnitudes of these derivatives for metals. It should be noted that, in this case, the dominant role is played by the anharmonicity of the interatomic interaction. It is this factor that governs not only the thermal expansion but also the stress dependence of the thermal expansion coefficient and the temperature dependence of the elastic modulus.

In the simplest model of a solid (a diatomic molecule with an anharmonic bond), the potential of the interatomic interaction can be represented by an approximate expression, that is,

$$U(r) \approx -D + \frac{1}{2}f(r-a)^2 - \frac{1}{3}g(r-a)^3, \quad (2)$$

where  $D$  is the dissociation energy,  $f$  is the coefficient of linear elasticity,  $g$  is the anharmonicity coefficient, and  $a$  is the equilibrium interatomic distance.

According to [6], from expression (2), we derive an approximate relationship for the elastic modulus,

$$E \approx \frac{f}{a}, \quad (3)$$

$$\alpha \approx \frac{gk}{f^2 a}, \quad (4)$$

where  $K$  is the Boltzmann constant.

The elongation of the anharmonic bond by  $\Delta l$  leads to a change (a decrease) in the bond rigidity, i.e., the coefficient  $f$ , which can be represented as follows:

$$f \approx f_0 \left( 1 - \frac{2g}{f_0} \Delta l \right), \quad (5)$$

where  $f_0$  is the initial value of  $f$  (at  $\Delta l = 0$ ).

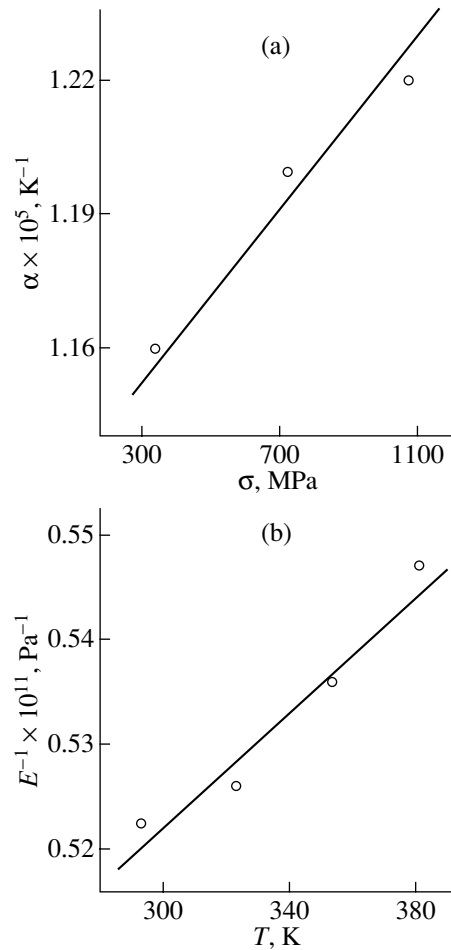


Fig. 2. (a) Stress dependence of the thermal expansion coefficient and (b) temperature dependence of the reciprocal of the elastic modulus for the steel wire.

Then, from relationships (3) and (4) for small  $\Delta l$ , we obtain

$$\alpha \approx \alpha_0 \left( 1 + 4 \frac{\alpha_0 E_0 a^2}{k} \Delta l \right), \quad (6)$$

$$E^{-1} \approx E_0^{-1} \left( 1 + 2 \frac{\alpha_0 E_0 a^2}{k} \Delta l \right), \quad (7)$$

$$\alpha_0 = \frac{gk}{f_0^2 a}, \quad E_0 = \frac{f_0}{a}.$$

An analysis of expressions (6) and (7) shows that the thermal expansion coefficient and the elastic modulus depend on the bond elongation, which, in turn, can be caused by both the stress  $\sigma$  and heating (thermal expansion). Therefore, the thermal expansion coefficient  $\alpha$  and the elastic modulus  $E$  depend on the stress  $\sigma$  and the temperature  $T$ . Consequently, upon heating of the loaded sample (when measuring the dependence of the thermal expansion coefficient on the stress), the strain is determined not only by the thermal expansion but



## Characteristics of thermal and stress deformations

Material		$\alpha, K^{-1}$ (at 293 K, $\sigma = 0$ )	$E, Pa$ (at 293 K)	$\Delta\alpha/\Delta\sigma,$ $Pa^{-1} K^{-1}$	$\Delta(E^{-1})/\Delta T,$ $Pa^{-1} K^{-1}$	Calculation
						$\Delta\alpha/\Delta\sigma$ $= \Delta(E^{-1})/\Delta T, Pa^{-1} K^{-1}$
Metals	Steel	$1.12 \times 10^{-5}$	$1.9 \times 10^{11}$	$0.9 \times 10^{-15}$	$2.7 \times 10^{-15}$	$(0.6-1.3) \times 10^{-15}$
	Copper [4, 5]	$1.65 \times 10^{-5}$	$1.2 \times 10^{11}$	$2.9 \times 10^{-15}$	$3.1 \times 10^{-15}$	
Polymers	PM	$-0.66 \times 10^{-5}$	$1.1 \times 10^{11}$	$6 \times 10^{-15}$	$7 \times 10^{-15}$	$\sim 5 \times 10^{-15}$
	K-49	$-0.53 \times 10^{-5}$	$1.2 \times 10^{11}$	$3 \times 10^{-15}$	$6 \times 10^{-15}$	
	SHPM	$-0.75 \times 10^{-5}$	$1.2 \times 10^{11}$	$4 \times 10^{-15}$	$4 \times 10^{-15}$	
	PE	$-34 \times 10^{-5}$	$0.7 \times 10^9$	$0.6 \times 10^{-11}$	$2.2 \times 10^{-11}$	

also has a stress component due to the change in the elastic modulus with variations in temperature. Correspondingly, upon loading of the heated sample (when measuring the dependence of the elastic modulus on the temperature), the strain is governed not only by the elastic elongation but also has a thermal expansion component associated with the change in the thermal expansion coefficient under a stress. Thus, the thermal expansion coefficient and the elastic modulus, which are defined as derivatives of the strain with respect to the temperature and stress, respectively, turn out to be more complex functions.

Making allowance for the combined character of the bond elongation involving the stress component  $\Delta l_\sigma = a(E^{-1})\Delta\sigma$  and the thermal component  $\Delta l_T = a\alpha\Delta T$ , we obtain the expression

$$\frac{\Delta\alpha}{\Delta\sigma} = \frac{\Delta(E^{-1})}{\Delta T} \approx 6 \frac{\alpha_0^2}{k} a^3. \quad (8)$$

Therefore, the analysis of the diatomic model confirms the validity of the general relationship (1), i.e., the equality of the cross derivatives.

Now, we quantitatively estimate the magnitude of the “invariant.” According to the data presented in the table, the thermal expansion coefficient can be estimated as  $\alpha_0 \approx (1.1-1.6) \times 10^{-5} K^{-1}$ . The atomic volume can be taken as  $a^3 \approx V_a$  or  $V_a \approx \frac{A}{N_A \rho}$ , where  $A$  is the atomic mass,  $\rho$  is the density, and  $N_A$  is the Avogadro number. For iron and copper, we have  $V_a \approx 1.2 \times 10^{-2} nm^3$ . As a result, from expression (8), we obtain

$$6 \frac{\alpha_0^2}{k} a^3 \approx (0.6-1.3) \times 10^{-15} Pa^{-1} K^{-1}.$$

We can assert that the calculations in the framework of a rather crude model of a solid lead to a quantitative result that is in close agreement with the experimental data.

Thus, for low-molecular materials with a conventional positive coefficient of thermal expansion, the

invariant is explained in terms of the anharmonicity of the interatomic interaction.

### 3.2. Rigid-Chain Oriented Polymers

Rigid-chain polymers are polymers whose skeletons contain ring groups that prevent conformational transitions and, thus, provide a straightened form of chain molecules in the polymer material. In oriented polymers, the axes of chain molecules are predominantly aligned along the axis of the orientation of the polymer (fiber axes).

In this work, the thermal expansion coefficients and elastic moduli were measured in the longitudinal direction under tensile stresses applied along the fiber axis.

Figure 3 shows the temperature dependences of the recoverable longitudinal strain at different tensile stresses (Fig. 3a) and the stress dependences of the recoverable longitudinal strain at different temperatures (Fig. 3b) for a rigid-chain oriented polymer—polyimide PM.

First and foremost, it can be seen from Fig. 3a that the longitudinal thermal expansion of the fiber is negative. The tensile stress leads to a decrease in the magnitude of the negative expansion (contraction).

The stress strain of the fiber is positive (Fig. 3b). An increase in the temperature results in an increase in the stress strain.

Consequently, the stress strain and the temperature dependence of the stress strain for the fiber are similar to those for the metals, whereas the thermal strain and the stress dependence of the magnitude of the thermal strain for the fiber are opposite in sign to those for the metals (cf. Figs. 3, 1). As can be seen from Fig. 3, the temperature and stress dependences of the recoverable longitudinal strain exhibit an almost linear behavior. From the slopes of these dependences, we can determine the thermal expansion coefficients  $\alpha = \Delta\varepsilon/\Delta T$  at different stresses  $\sigma$  (from Fig. 3a) and the elastic moduli  $E = \Delta\sigma/\Delta\varepsilon$  at different temperatures  $T$  (from Fig. 3b). The thermal expansion coefficients  $\alpha$  at  $\sigma = 0$  and the elastic moduli  $E$  at  $T = 293 K$  are presented in the table. As can be seen, the elastic modulus  $E$  for



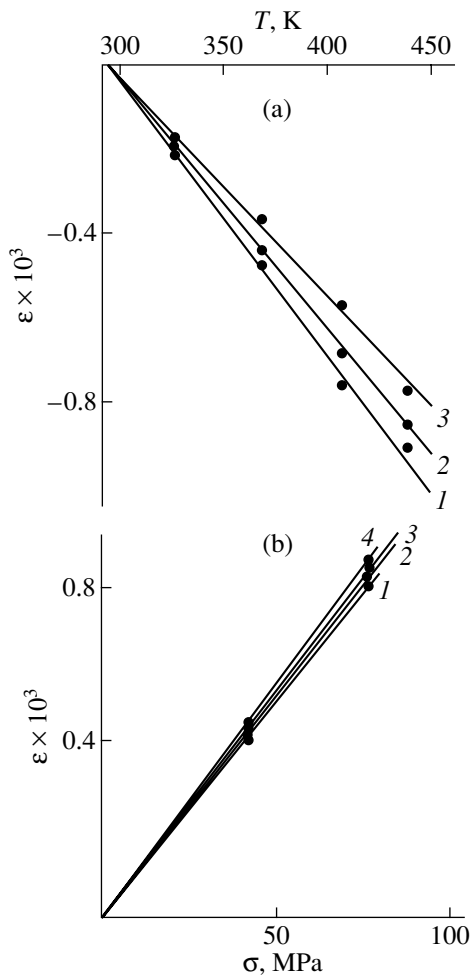


**Fig. 3.** (a) Temperature and (b) stress dependences of the recoverable longitudinal strain for a rigid-chain oriented polymer—polyimide PM. (a) Tensile stress  $\sigma$ : (1) 2, (2) 126, and (3) 253 MPa. (b) Temperature  $T$ : (1) 293, (2) 323, (3) 353, and (4) 381 K.

polyimide PM is close in magnitude but opposite in sign to the elastic moduli  $E$  for steel and copper.

The stress dependence of the longitudinal thermal expansion coefficient  $\alpha(\sigma)$  and the temperature dependence of the reciprocal of the longitudinal elastic modulus  $E^{-1}(T)$  for polyimide PM are depicted in Figs. 4a and 4b, respectively. The table presents the quantities  $\Delta\alpha/\Delta\sigma$  and  $\Delta(E^{-1})/\Delta T$ , which were determined from the slopes of the linear approximations of the dependences  $\alpha(\sigma)$  and  $E^{-1}(T)$  shown in Figs. 4a and 4b.

The results of similar measurements for other rigid-chain oriented polymers (K-49, SHPM) are also given in the table. It can be seen from the table that the values of each parameter ( $\alpha$ ,  $E$ ,  $\Delta\alpha/\Delta\sigma$ , or  $\Delta(E^{-1})/\Delta T$ ) for different rigid-chain polymers are close to each other.

We call the reader's attention to the main result of these investigations: the close values of  $\Delta\alpha/\Delta\sigma$  and  $\Delta(E^{-1})/\Delta T$  for different rigid-chain polymers are consis-

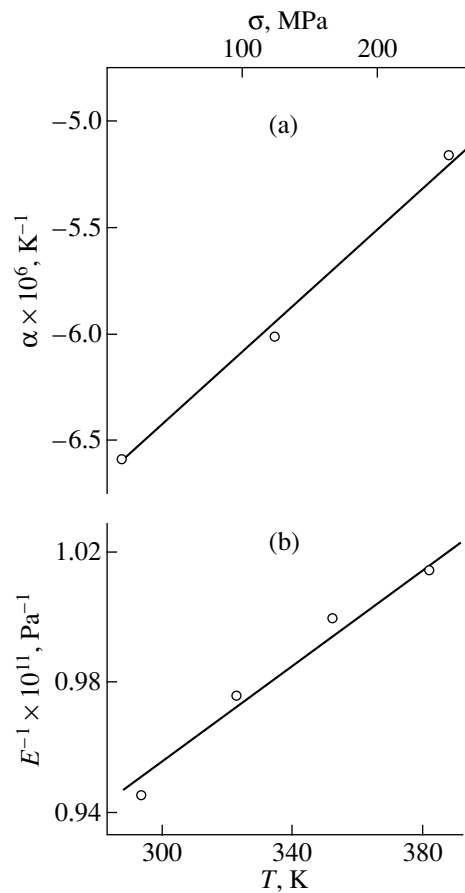


**Fig. 4.** (a) Stress dependence of the longitudinal thermal expansion coefficient and (b) temperature dependence of the reciprocal of the longitudinal elastic modulus for polyimide PM.

tent with the general relationship (1), as is the case with negative coefficients of thermal expansion.

Let us now analyze the mechanism ensuring the validity of this relationship for rigid-chain polymers. This mechanism is associated with the specific features of the molecular dynamics in these polymers, which are primarily responsible for the negative sign of the longitudinal thermal expansion coefficient. The skeleton of chain polymer molecules has a high longitudinal rigidity due to the rigidity of covalent interatomic bonds. As a consequence, the characteristic temperature of longitudinal vibrations of polymer molecules is relatively high (1000–1500 K [2]); hence, virtually no longitudinal vibrations are excited at room temperature. The characteristic temperature of transverse vibrations is considerably lower (200–400 K [2]). It is these transverse vibrations that bring about the so-called membrane effect [7] or, more specifically, a decrease in the projection of the molecular skeleton contour onto the molecular axis, i.e., a decrease in the axial length of the molecule with an increase in the temperature (negative coefficient of longitudinal thermal expansion). The theory of negative longitudinal expansion in crystals and

vitrified oriented polymers was developed in [8, 9]. This analysis did not include the effect of stresses on the thermal expansion coefficient.

In our calculations, we used the model allowing for the transverse vibrations, which was proposed earlier in [9], and additionally took into account the effect of the longitudinal stress  $\sigma$  on the sample. As a result, we derived the following expression for the negative longitudinal strain in a sample due to the combined effect of temperature and longitudinal stress (to the first order in  $T$  and  $\sigma$ ):

$$\varepsilon(T, \sigma) \approx -\frac{1}{3} \frac{k}{f_{\perp} a_{\parallel}} T + \frac{S_m}{f_{\parallel} a_{\parallel}} \sigma + q \frac{S_m k}{f_{\perp}^2 a_{\parallel}^3} \sigma T, \quad (9)$$

where  $f_{\parallel}$  and  $f_{\perp}$  are the longitudinal and transverse rigidities of the polymer molecule, respectively;  $S_m$  is the cross-sectional area of the molecule;  $a_{\parallel}$  is the length of the interatomic bond in the molecular skeleton; and  $q$  is a coefficient of the order of unity.

From formula (9), we obtain the relationships for the longitudinal thermal expansion coefficient and the longitudinal elastic modulus:

$$\alpha = \frac{\partial \varepsilon}{\partial T} = -\frac{1}{3} \frac{k}{f_{\perp} a_{\parallel}} + q \frac{S_m k}{f_{\perp}^2 a_{\parallel}^3} \sigma, \quad (10)$$

$$E^{-1} = \frac{\partial \varepsilon}{\partial \sigma} = \frac{S_m}{f_{\parallel} a_{\parallel}} + q \frac{S_m k}{f_{\perp}^2 a_{\parallel}^3} T. \quad (11)$$

According to relationship (10), the thermal expansion coefficient  $\alpha$  is negative at  $\sigma = 0$  and decreases in magnitude with an increase in the longitudinal stress  $\sigma$ , which is actually observed in the experiment.

As follows from expression (11), the quantity  $E^{-1}$  should increase with an increase in the temperature. This behavior is also in agreement with the experimental data.

An analysis of relationships (10) and (11) shows that the aforementioned properties of the thermal expansion coefficient and the elastic modulus are associated with the transverse vibrations. This can be judged from the coefficient  $f_{\perp}$  (the rigidity of transverse vibrations) involved in these formulas.

The main result following from relationships (10) and (11) can be represented as

$$\frac{\partial \alpha}{\partial \sigma} = \frac{\partial(E^{-1})}{\partial T} = \frac{\partial^2 \varepsilon}{\partial \sigma \partial T} = q \frac{S_m k}{f_{\perp}^2 a_{\parallel}^3}. \quad (12)$$

This means that the processes under consideration are consistent with the general relationship (1) (invariant).

The quantitative estimates were made for the following parameters: the longitudinal rigidity of the carbon-chain molecular skeleton  $f_{\parallel} \approx 400 \text{ N m}^{-1}$  [10], the transverse rigidity of the molecular skeleton  $f_{\perp} \approx 20 \text{ N m}^{-1}$  [10], the projection of the C–C bond onto the molecular

axis  $a_{\parallel} \approx 0.13 \text{ nm}$  [11], and the cross-sectional area of the molecule  $S_m \sim 0.3 \text{ nm}^2$  [11].

Upon substituting the above parameters into relationships (10)–(12), we obtain the longitudinal thermal expansion coefficient  $\alpha \approx -1 \times 10^{-5} \text{ K}^{-1}$  at  $\sigma = 0$ , the longitudinal elastic modulus  $E \cong 1.5 \times 10^{11} \text{ Pa}$  at  $T = 293 \text{ K}$ , and the derivatives  $d\alpha/d\sigma = d(E^{-1})/dT \approx 5 \times 10^{-15} \text{ Pa}^{-1} \text{ K}^{-1}$ .

The results of these calculations are in reasonable agreement with the experimental data for rigid-chain polymers (see table).

Thus, for rigid-chain oriented polymers with specific negative coefficients of thermal expansion, the invariant is explained in terms of the anisotropy of the molecular dynamics.

### 3.3. A Flexible-Chain Oriented Polymer—Poly(ethylene)

Flexible-chain polymers are polymers with simple “one-dimensional” molecular skeletons of the –C–C–C– type, which can twist upon devitrification due to conformational transitions [2].

The temperature dependences of the recoverable longitudinal strain at different tensile stresses for a flexible-chain oriented polymer—poly(ethylene) are shown in Fig. 5a. The stress dependences of the recoverable longitudinal strain at different temperatures for the flexible-chain oriented poly(ethylene) are depicted in Fig. 5b.

As can be seen from Fig. 5, the behavior of the flexible-chain oriented poly(ethylene) is qualitatively similar to that of the rigid-chain oriented polymers. Indeed, the longitudinal thermal expansion of poly(ethylene) is also negative and the tensile stress leads to a decrease in the magnitude of the thermal expansion (Fig. 5a). The stress strain of poly(ethylene) also increases with an increase in the temperature (Fig. 5b). However, quantitatively, the thermal expansion coefficients and elastic moduli of the flexible-chain oriented poly(ethylene) differ substantially from those of the rigid-chain oriented polymers (see below).

It is worth noting that the temperature dependences of the recoverable longitudinal strain  $\varepsilon(T)$  (Fig. 5a) are nonlinear (this inconstancy of the thermal expansion coefficient with a variation in the temperature is in agreement with the data obtained for oriented poly(ethylene) in [12]). In order to elucidate the character of the stress dependence of the thermal expansion coefficient, we analyzed the values of  $\alpha(\sigma) = \partial \varepsilon / \partial T$  in the vicinity of only one temperature (300 K). The thermal expansion coefficient  $\alpha$  for the flexible-chain oriented poly(ethylene) at  $\sigma = 0$  is given in the table, and the stress dependence of the longitudinal thermal expansion coefficient  $\alpha(\sigma)$  is plotted in Fig. 6a.

The stress dependences of the recoverable longitudinal strain  $\varepsilon(\sigma)$  are approximately linear (Fig. 5b). The

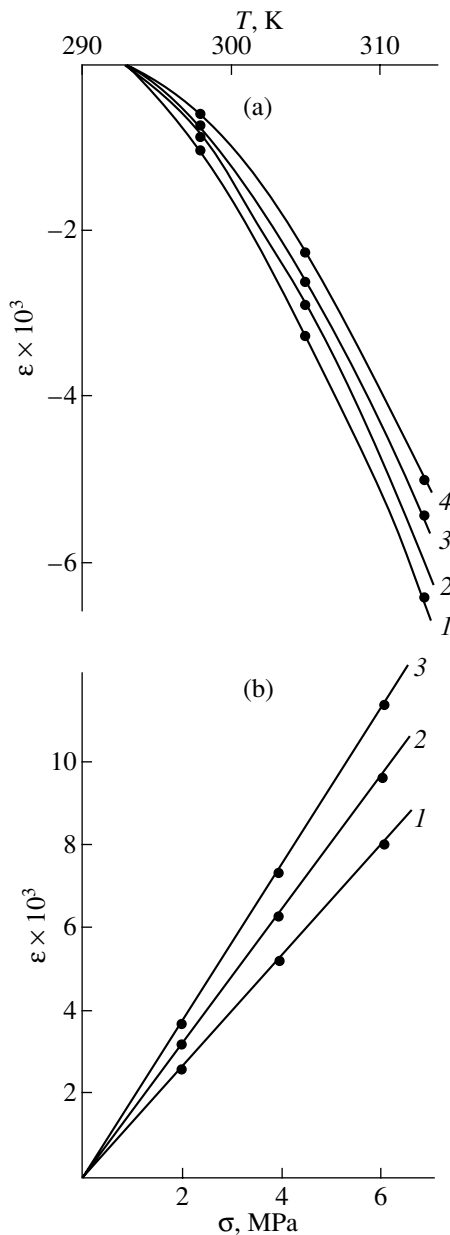


**Fig. 5.** (a) Temperature and (b) stress dependences of the recoverable longitudinal strain for a flexible-chain oriented polymer—poly(ethylene). (a) Tensile stress  $\sigma$ : (1) 5, (2) 10, (3) 15, and (4) 20 MPa. (b) Temperature  $T$ : (1) 293, (2) 305, and (3) 311 K.

elastic modulus  $E = \partial\sigma/\partial\epsilon$  for poly(ethylene) at  $T = 293$  K is presented in the table, and the temperature dependence of the reciprocal of the longitudinal elastic modulus  $E^{-1}(T)$  is shown in Fig. 6b.

The table also presents the quantities  $\Delta\alpha/\Delta\sigma$  and  $\Delta(E^{-1})/\Delta T$ , which were determined from the slopes of the linear approximations of the dependences  $\alpha(\sigma)$  and  $E^{-1}(T)$  depicted in Figs. 6a and 6b.

As follows from the table, the quantities  $\Delta\alpha/\Delta\sigma$  and  $\Delta(E^{-1})/\Delta T$  are in satisfactory agreement. This implies

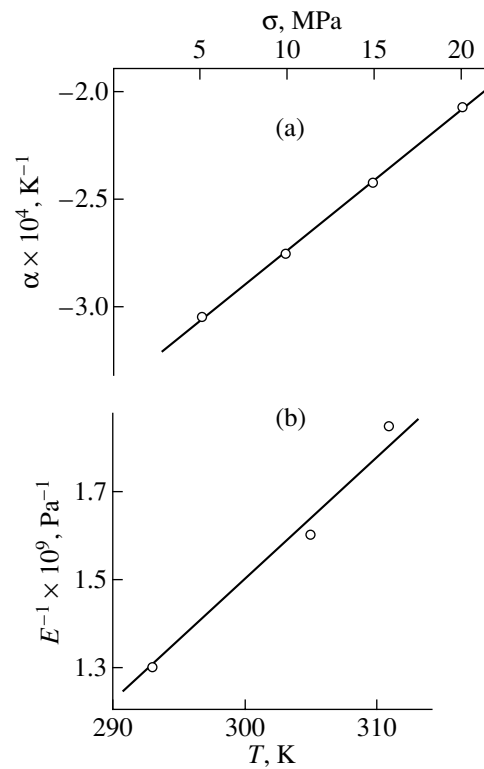


**Fig. 6.** (a) Stress dependence of the longitudinal thermal expansion coefficient and (b) temperature dependence of the reciprocal of the longitudinal elastic modulus for poly(ethylene).

that the general relationship (1) is satisfied for the flexible-chain oriented poly(ethylene), as is the case with metals and rigid-chain oriented polymers.

However, quantitatively, the characteristics of poly(ethylene) and rigid-chain polymers differ significantly. For poly(ethylene), the negative coefficient of longitudinal thermal expansion is approximately one and a half orders of magnitude larger, the longitudinal elastic modulus is nearly two orders of magnitude smaller, and the temperature–stress invariant [ $\Delta\alpha/\Delta\sigma = \Delta(E^{-1})/\Delta T$ ] is almost four orders of magnitude greater than those for the rigid-chain polymers.

These differences suggest that the data obtained for poly(ethylene) cannot be interpreted within the model proposed for rigid-chain polymers. Actually, the extremely small elastic modulus of poly(ethylene) indicates that the stress strain is inconsistent with the elongation of covalent bonds in the polymer skeleton. Correspondingly, the large negative coefficient of thermal expansion has defied description in the framework of the membrane mechanism. It is evident that, in the flexible-chain oriented poly(ethylene), the thermal and stress deformations occur through a different mechanism.

In poly(ethylene), the thermal and stress deformation processes proceed through the conformational

mechanism. This mechanism involves local conformational transitions of fragments in the chain molecule that lead to a change in the axial length of the molecule (projection of the molecular skeleton contour onto the molecular axis) [13].

The polymer molecule can be considered as a sequence of *trans* conformers (straightened fragments) and *gauche* conformers (bent fragments). The conformers can transform from one type into the other type, which results in a change in the axial length of the molecule. These transitions are accompanied by overcoming the potential barrier due to local fluctuations of the thermal energy [13]. The difference between the potential energies of the conformers leads to an increase in the equilibrium concentration of *gauche* conformers with an increase in the temperature [13] and, hence, to a negative longitudinal expansion. Under longitudinal tensile stresses, the difference between the energies of the *gauche* and *trans* conformers increases. This leads to a decrease in the equilibrium concentration (at a given temperature) of *gauche* conformers and, correspondingly, to an increase in the axial length of the molecule (i.e., to an elongation of the oriented polymer).

Therefore, in amorphous (noncrystalline) regions of a flexible-chain devitrified oriented polymer, the thermal and stress deformations occur through the mechanism of conformational transitions. The approximate calculations of the longitudinal strain of the devitrified (i.e., at temperatures above the glass transition point) oriented polymer due to conformational transitions were carried out in our previous works [9, 14].

The expressions derived for the quantities under investigation are as follows.

The longitudinal thermal expansion coefficient is determined by the formula

$$\alpha = \frac{\Delta \varepsilon}{\Delta T} \approx -(1 - \chi) \frac{\delta l}{l_t} \frac{1}{kT^2} \exp\left(-\frac{\Delta U}{kT}\right) \times \left[ \Delta U - \delta l S_m \sigma \left( \frac{\Delta U}{kT} - 1 \right) \right]. \quad (13)$$

The reciprocal of the elastic modulus has the form

$$E^{-1} = \frac{\Delta \varepsilon}{\Delta \sigma} \approx (1 - \chi) \frac{\delta l}{l_t} \frac{1}{kT} \exp\left(-\frac{\Delta U}{kT}\right) \delta l S_m. \quad (14)$$

From relationships (13) and (14), we obtain

$$\frac{\partial \alpha}{\partial \sigma} = \frac{\partial (E^{-1})}{\partial T} \approx (1 - \chi) \frac{\delta l^2 S_m}{l_t k} \frac{1}{T^2} \exp\left(-\frac{\Delta U}{kT}\right) \left( \frac{\Delta U}{kT} - 1 \right), \quad (15)$$

where  $l_t$  is the axial length of the *trans* conformer,  $\delta l$  is the difference between the axial lengths of the *trans* and *gauche* conformers,  $\Delta U$  is the initial difference between the potential energies of the *gauche* and *trans*

conformers,  $S_m$  is the cross-sectional area of the molecule, and  $\chi$  is the degree of crystallinity (volume fraction of crystallites).

Thus, the general relationship (1), i.e., the equality of the derivatives, is satisfied for poly(ethylene).

Now, we perform a number for quantitative estimations.

Poly(ethylene) is an amorphous–crystalline polymer. The glass transition temperature of poly(ethylene) is approximately equal to 240 K. At higher temperatures ( $T > 240$  K), poly(ethylene) is in the devitrified state. For oriented poly(ethylene) samples, the degree of crystallinity is estimated as  $\chi \approx 0.4$ . An elementary conformer in poly(ethylene) involves four  $\text{CH}_2$  groups. The length of the elementary *trans* conformer is approximately equal to 0.5 nm, whereas the length of the elementary *gauche* conformer is approximately equal to 0.3 nm. The difference between the potential energies of the *trans* and *gauche* conformers is estimated as  $\Delta U_e \approx 2.3 \times 10^{-2}$  eV [2].

A single conformational transition of an elementary conformer in a long-chain molecule is virtually impossible. Such transitions occur with the participation of several (three or four) conformers [2, 13]. Hence, the calculations were performed for the following parameters:  $l_t \approx (1.5\text{--}2.0)$  nm,  $\delta l \approx (0.6\text{--}0.8)$  nm,  $\Delta U \approx (7\text{--}10) \times 10^{-2}$  eV, and  $S_m \approx 0.3$  nm<sup>2</sup>.

Then, from relationships (13)–(15), we found  $\alpha \approx -20 \times 10^{-5}$  K<sup>-1</sup> at  $\sigma = 0$ ,  $E \approx 1 \times 10^9$  Pa at  $T = 293$  K, and  $\partial \alpha / \partial \sigma = \partial (E^{-1}) / \partial T \approx 0.5 \times 10^{-11}$  Pa<sup>-1</sup> K<sup>-1</sup>.

With due regard for the roughness of the calculations and the errors in the measurements, the calculated and experimental data (see table) are in reasonable agreement.

#### 4. CONCLUSIONS

The thermal expansion of solids proceeds through different mechanisms. These are the vibrational–anharmonic mechanism (due to the anharmonic interatomic interaction) in low-molecular solids, the vibrational–anisotropic (membrane) mechanism in polymer crystals and oriented polymers in the vitreous state (without participation of the anharmonic interatomic interaction), and the conformational mechanism (associated with the jumpwise fluctuation dynamics) in polymers in the devitrified state. As a result, the thermal expansion coefficients of solids can differ not only by several orders of magnitude but also in sign.

It should be noted that solids undergo elastic deformation also through different mechanisms, such as stress elongation (contraction) of interatomic bonds in low-molecular materials and polymers in the vitreous state and conformational transitions in polymers in the devitrified state. In these cases, the elastic moduli of different solids are always positive but can differ by several orders of magnitude.

All the above mechanisms were revealed in the materials studied in this work (see table).

The results obtained in the above investigation demonstrated that, although solids involved in the processes under consideration can exhibit quite different thermal and stress behaviors, all materials share a number of traits. In particular, the thermal expansion coefficient depends on the mechanical stress; however, tensile stress can lead to an increase in the thermal expansion coefficient for metals and a decrease in the (negative!) coefficient of thermal expansion for polymers. The elastic modulus for all materials depends on the temperature in a similar manner: i.e., it decreases with an increase in the temperature. The equality between the temperature and stress derivatives  $\partial\alpha/\partial\sigma = \partial(E^{-1})/\partial T$  holds good for all solids (with allowance made for inadvertent errors in the measurements). This implies that the general relationship (1) (thermodynamically independent of the specific properties of different solids) is valid for all solids.

The results of the approximate calculations performed in this work are in reasonable agreement with the experimental data. These results confirm and justify the concept regarding different mechanisms of thermal and stress deformations of solids with different structures.

Moreover, the values of the invariant  $\partial\alpha/\partial\sigma = \partial(E^{-1})/\partial T$ , which can differ by several orders of magnitude for solids (see table), correspond to different mechanisms of thermal and stress deformations of solids with different structures.

#### ACKNOWLEDGMENTS

This work was supported by the Russian Foundation for Basic Research, project no. 00-03-33064.

#### REFERENCES

1. *Physical Quantities: A Handbook*, Ed. by I. S. Grigor'ev and E. Z. Meĭlikhov (Énergoatomizdat, Moscow, 1991).
2. Yu. K. Godovskii, *Thermal Physics of Polymers* (Khimiya, Moscow, 1982).
3. S. I. Novikova, *Thermal Expansion of Solids* (Nauka, Moscow, 1974).
4. N. F. Kunin and V. N. Kunin, *Fiz. Met. Metalloved.* **5** (1), 173 (1957).
5. A. Nadai, *Theory of Flow and Fracture of Solids*, 2nd ed. (McGraw-Hill, New York, 1963; Mir, Moscow, 1969), Vol. 2.
6. Ya. I. Frenkel, *Introduction to the Theory of Metals* (GITTL, Moscow, 1948).
7. I. M. Lifshitz, *Zh. Éksp. Teor. Fiz.* **22** (4), 475 (1952).
8. F. C. Chen, C. L. Choy, and K. Young, *J. Polym. Sci., Polym. Phys. Ed.* **19** (12), 2313 (1980).
9. A. I. Slutsker, V. L. Gilyarov, G. Dadobaev, L. A. Laĭus, I. V. Gofman, and Yu. I. Polikarpov, *Fiz. Tverd. Tela* (St. Petersburg) **44** (5), 923 (2002) [*Phys. Solid State* **44**, 964 (2002)].
10. L. R. G. Treloar, *Polymer*, No. 1, 95 (1960).
11. K. Bunn, *Trans. Faraday Soc.*, No. 35, 482 (1939).
12. F. C. Chen, C. L. Choy, and K. Young, *J. Polym. Sci., Polym. Phys. Ed.* **19** (2), 335 (1981).
13. M. V. Vol'kenshtein, *Configurational Statistics of Polymeric Chains* (Akad. Nauk SSSR, Moscow, 1959; Interscience, New York, 1963).
14. A. I. Slutsker, V. L. Gilyarov, L. A. Laĭus, I. V. Gofman, Yu. I. Polikarpov, and B. A. Averkin, in *Nonlinear Problems in Mechanics and Physics of Strained Solids* (S.-Peterb. Gos. Univ., St. Petersburg, 2002), No. 5.

*Translated by O. Borovik-Romanova*

---

**POLYMERS  
AND LIQUID CRYSTALS**

---

## **Thermal Fluctuations in Smectic-A Films on the Surface of Solid Substrates**

**L. V. Mirantsev**

*Institute for Problems of Mechanical Engineering, Russian Academy of Sciences,  
Bol'shoi pr. 61, Vasil'evskii Ostrov, St. Petersburg, 199178 Russia  
e-mail: miran@microm.ipme.ru*

Received September 18, 2003; in final form, November 10, 2003

**Abstract**—The static and dynamic characteristics of layer displacement fluctuations in smectic-A films supported on the surface of a solid substrate are calculated with due regard for the profiles of the flexural and tensile (compressive) moduli of smectic layers. The difference in the surfaces bounding the film and the asymmetry of the profiles of the elastic moduli with respect to the central layer of the film are taken into account. The profiles of fluctuations of smectic-layer displacements and the correlations between these fluctuations are determined for the films formed by liquid-crystal compounds that can undergo a bulk smectic-A–nematic phase transition. The dynamic correlation functions derived for these fluctuations are used for calculating the correlations between the intensities of x-ray scattering by a film at different instants of time. It is demonstrated that, in smectic-A films supported on the surface of a solid substrate, unlike free-standing smectic-A films, the effect of temperature on the dynamics of layer displacement fluctuations can be observed in experiments on dynamic x-ray scattering from films that are not very thick (the number of layers  $N \sim 20$ ) and at considerably smaller recoil-momentum components in the film plane. © 2004 MAIK “Nauka/Interperiodica”.

### 1. INTRODUCTION

Smectic liquid crystals have a one-dimensional layered structure [1] and, consequently, can form free-standing films with a macroscopic area ( $\sim \text{cm}^2$ ) [2] and a thickness that can be varied from several hundreds to two smectic layers or even to one layer [3, 4]. In this respect, smectic liquid crystals are the most appropriate model objects for use in studying the physics of two-dimensional systems. Moreover, in thin free-standing smectic films, the effects associated with their microscopic thickness are combined with surface effects. As a result, these films exhibit effects and phenomena that are not observed in the bulk phase of liquid crystals [5–9]. For this reason, over the last 20–25 years, free-standing smectic films have been extensively studied both experimentally and theoretically.

In recent years, considerable interest has been expressed by researchers in smectic films supported on the surface of a solid substrate [10–15]. These systems, like free-standing smectic films, have been predominantly studied using specular and diffuse (nonspecular) small-angle x-ray scattering, as well as neutron scattering. The aforementioned scattering methods provide a means for determining the equilibrium characteristics of smectic liquid-crystal films (such as the number of smectic layers, the layer thickness, and the type of molecular packing in a layer) and reliable data on thermal fluctuations in films. Over the last decade, experiments on diffuse x-ray scattering have revealed useful information about defects on the surface of a solid substrate that induce distortions in layers of the film over-

lying the substrate [10–12, 15]. In particular, de Boer [16] showed that, for these films, the correlation functions of layer displacement fluctuations, which determine the intensity of diffuse x-ray scattering, can be separated into two components. One component is governed by the thermal fluctuations of smectic-layer displacements, and the other component is determined by the defects on the substrate surface. Therefore, the adequate theoretical description of thermal fluctuations of layer displacements in a smectic liquid-crystal film offers possibilities for using x-ray scattering as an efficient tool for obtaining information on both thermal fluctuations in the film and defects on the surface of a substrate.

The thermal fluctuations of layer displacements in smectic-A (*SmA*) films supported on the surface of a solid substrate were theoretically described by de Boer [16] and Romanov and Ul'yanov [17]. In these works, the thermal fluctuations of layer displacements were treated in the framework of the well-known discrete model (Holyst model) [18–20] proposed for describing the layer displacement fluctuations in free-standing smectic-A films. Within this model, the smectic-A film is considered to be spatially homogeneous and characterized by the following parameters: the number  $N$  of smectic layers, the surface tension coefficient  $\gamma$  of the free surface (note that, in [16], the surface tension coefficient of the film–substrate interface was treated as infinitely large, whereas in [17], the equivalent assumption was made that the smectic layer at the boundary with the substrate is fixed), and the flexural modulus  $K$

and tensile (compressive) modulus  $B$  of the smectic layers. The last two quantities are considered to be identical for all layers in the film irrespective of their location and are taken equal to the corresponding elastic modulus in the bulk of the smectic- $A$  phase. In my previous works [21–23], it was noted that, even for free-standing smectic- $A$  films, the above assumption is physically justified only at temperatures substantially lower than the temperatures of the  $SmA$ –nematic ( $SmA$ – $N$ ) or  $SmA$ –isotropic ( $SmA$ – $I$ ) phase transitions in the bulk of liquid crystals. In this case, the film has a pronounced smectic- $A$  structure throughout the volume and the orientational and translational orders of molecules and, hence, the elastic characteristics of the inner and surface layers of the film only slightly differ from each other. However, thin smectic layers of particular liquid crystals can exist at temperatures considerably higher than the temperatures at which the smectic order in the bulk of mesogens disappears [5–9]. The microscopic model proposed in [24–27] for free-standing smectic- $A$  films describes the behavior of these films upon heating above the temperatures of the  $SmA$ –nematic and  $SmA$ –isotropic phase transitions rather well. According to the predictions of this model, both the orientational and translational orders in inner layers of the film at these temperatures can be substantially less pronounced than those in the vicinity of the free bounding surfaces. This theoretical result was experimentally confirmed in studies of the optical transmission spectra of free-standing smectic- $A$  films [28] and the specular x-ray reflectivity of smectic- $A$  films above the temperature of the  $SmA$ –nematic phase transition in the bulk of liquid crystals [9]. It is well known [1] that, in the bulk of liquid crystals, the flexural modulus  $K$  is proportional to the square of the orientational order parameter  $p$  and the tensile (compressive) modulus  $B$  of smectic layers is proportional to the square of the translational order parameter  $s$ . Under the assumption that these relationships are also valid for liquid-crystal films, the elastic moduli of the smectic layers at temperatures higher than the temperatures of the  $SmA$ –nematic or  $SmA$ –isotropic phase transitions in the bulk of liquid crystals should decrease with an increase in the distance to the free surface and reach minimum values at the center of the film. Since this profile of the elastic moduli is completely ignored in the model proposed in [18–20], the model at the aforementioned temperatures should incorrectly predict the fluctuations of smectic-layer displacements and correlations between these fluctuations. The influence of spatial inhomogeneity of the free-standing smectic- $A$  films on the thermal fluctuations of layer displacements was theoretically analyzed in [21–23]. It turned out that the results obtained differ significantly from the data predicted by the Holyst model at the highest temperatures of existence of free-standing smectic- $A$  films with a specified thickness. However, it should be noted that the assumption regarding the spatial homogeneity of the smectic film supported on the surface of a substrate can also be invalid at lower tem-

peratures. This is associated with the fact that the surfaces bounding the film (i.e., the free surface and the film–substrate interface) are not equivalent and can have different orienting effects on molecules in the film. As a result, the film has no symmetry with respect to the central layer, which is inconsistent with the assumption of spatial homogeneity. This indicates that the theoretical approach used in [16, 17] for describing the thermal fluctuations of layer displacements is inadequate for the films under consideration.

Although the static properties of thermal fluctuations of layer displacements in free-standing smectic films have already long been investigated, their dynamics has come under the scrutiny of science only in recent years. The dynamics of thermal fluctuations of layer displacements has been experimentally investigated using coherent soft [29] and hard [30] x-ray dynamic scattering. The experimental results obtained were theoretically interpreted in [31–34]. The theoretical interpretation was based on the linearized hydrodynamic equations for the smectic- $A$  phase and the aforementioned Holyst model [18–20] for the energy of layer displacement fluctuations in free-standing smectic- $A$  films. The models proposed in [31–34] make it possible to determine the dynamic correlation functions for layer displacement fluctuations in films and then to use these functions for calculating the correlations between the intensities of x-ray scattering by films at different instants of time. The predictions of these models are in qualitative agreement with the experimental data on coherent x-ray dynamic scattering in free-standing smectic- $A$  films with different thicknesses [29, 30]. The dynamics of thermal fluctuations of layer displacements in smectic- $A$  films supported on the surface of a solid substrate has not been experimentally studied to date. However, this dynamics was theoretically analyzed in [17] within the Holyst model [18–20], according to which the spatial inhomogeneity of the smectic- $A$  films is disregarded. As a consequence, the results obtained in [17] turned out to be independent of the temperature, because the above assumption leads to complete disregard of the temperature dependence of the viscoelastic parameters for layers of the film.

The influence of the profiles of the flexural modulus  $K$  and the tensile (compressive) modulus  $B$  of smectic layers and, hence, the temperature on the dynamics of thermal fluctuations of layer displacements in free-standing smectic- $A$  films was theoretically treated in my recent work [35]. It was demonstrated that this effect can be revealed in experiments on x-ray dynamic scattering in sufficiently thick films ( $N \geq 100$ ) and at large recoil-momentum components in the film plane ( $\geq 10^6 \text{ cm}^{-1}$ ). In films with a smaller thickness and at smaller recoil-momentum components in the film plane, the dominant role in the dynamics of thermal fluctuations of layer displacements in free-standing smectic- $A$  films is played by the so-called acoustic

mode [31, 32] with a virtually temperature-independent relaxation time,

$$\tau^{(1)} = Nd_{\text{in}}\eta_3/2\gamma, \quad (1)$$

where  $d_{\text{in}}$  is the interlayer spacing and  $\eta_3$  is the viscosity coefficient of interlayer sliding. This mode corresponds to the motion of the film during which the interlayer spacing remains constant, and, hence, the motion does not depend on the profiles of the elastic moduli  $K$  and  $B$ . However, the acoustic mode is absent in smectic films supported on the surface of a solid substrate [17]. Therefore, thermal fluctuations of layer displacements in the smectic film are always accompanied by a change in the interlayer spacing and the dynamic characteristics of thermal fluctuations should depend on the profiles of the elastic moduli  $K$  and  $B$  and, consequently, on the temperature even for not very thick films and at not very large recoil-momentum components in the film plane. To put it differently, the thermal fluctuations of layer displacements in the smectic films supported on the substrate surface should be affected by the spatial inhomogeneity to a greater extent than those in free-standing smectic- $A$  films.

In this work, the static and dynamic characteristics of layer displacement fluctuations in smectic- $A$  films supported on the surface of a solid substrate were calculated with due regard for the dependences of the flexural modulus  $K$  and the tensile (compressive) modulus  $B$  of smectic layers on the distance to the surfaces bounding the film. The computational procedure was similar to that used in [21–23, 35] for calculating the thermal fluctuations in free-standing smectic- $A$  films but also took into account the difference in the surfaces bounding the film (the surface tension coefficient  $\gamma$  was taken to be finite for the free surface and infinitely large for the film–substrate interface) and the asymmetry of the profiles of the elastic moduli  $K$  and  $B$  with respect to the central layer of the film. The elastic modulus profiles were determined in terms of the microscopic model proposed in [24–27] with allowance made for different orienting effects of the bounding surfaces on molecules in the film. The profiles of smectic-layer displacement fluctuations and correlations between these fluctuations were calculated for the films formed by liquid-crystal compounds that can undergo a bulk  $SmA$ –nematic phase transition. The calculations were performed both at temperatures considerably below the temperature of the phase transition in the bulk of liquid crystals and at the highest temperatures of existence of films with a specified thickness. It was shown that, at temperatures below the temperature at which the smectic order disappears in the bulk of liquid crystals, the inclusion of the profiles of the elastic moduli  $K$  and  $B$  does not lead to disagreement with the data obtained within the Holyst model [16, 17]. However, at temperatures considerably above the temperature of the bulk phase transition, this inclusion can result in substantial deviations from the predictions of the Holyst model,

especially when the orienting effect of the solid substrate on liquid-crystal molecules is appreciably weaker than that of the free surface of the film. Moreover, the dynamic correlation functions derived for the layer displacement fluctuations were used to calculate the correlations between the intensities of x-ray scattering by the film at different instants of time. It was demonstrated that, in smectic- $A$  films supported on the surface of a solid substrate, unlike free-standing smectic- $A$  films, the effect of temperature on the dynamics of layer displacement fluctuations can be observed in experiments on dynamic x-ray scattering from not very thick films ( $N \sim 20$ ) and at considerably smaller recoil-momentum components ( $\leq 10^5 \text{ cm}^{-1}$ ) in the film plane.

## 2. FLUCTUATIONS OF LAYER DISPLACEMENTS IN A SMECTIC- $A$ FILM ON THE SURFACE OF A SOLID SUBSTRATE AND FLUCTUATION CORRELATIONS

In [16, 17], it was shown that thermal fluctuations of smectic-layer displacements from equilibrium positions in a smectic- $A$  film supported on the surface of a solid substrate can be described in the framework of the discrete model proposed in [18–20] for calculating thermal fluctuations of layer displacements in free-standing smectic- $A$  films. We will consider a smectic- $A$  film that is supported on the surface of a substrate and consists of  $N$  discrete layers. Let  $u_n(x, y)$  be fluctuation displacements of layers from the equilibrium positions  $z_n = (n - 1)d$  along the  $z$  axis perpendicular to the layer plane, where  $d$  is the thickness of the smectic layer and  $n$  is the number of the smectic layer. These displacements are characterized by the excess free energy  $F$ , which involves the bulk contribution  $F_B$  described by Eqs. (2) and (3) from [21] and the surface contribution  $F_S$ . According to [16], the surface contribution  $F_S$  can be written in the form

$$F_S = \frac{1}{2} \int [\gamma_1 |\nabla_{\perp} u_1(\mathbf{R})|^2 + \gamma_N |\nabla_{\perp} u_N(\mathbf{R})|^2] d\mathbf{R}. \quad (2)$$

Here,  $\gamma_1$  is the surface tension coefficient of the free surface of the film,  $\gamma_N$  is the surface tension coefficient of the film–substrate interface,  $\mathbf{R}$  is the radius vector in the plane of smectic layers ( $R^2 = x^2 + y^2$ ), and  $\nabla_{\perp}$  is the projection of the operator  $\nabla$  onto the  $(x, y)$  plane.

With the use of the continuous Fourier transform

$$u_n(\mathbf{R}) = (2\pi)^{-2} \int u_n(\mathbf{q}_{\perp}) \exp(i\mathbf{q}_{\perp} \mathbf{R}) d\mathbf{q}_{\perp}, \quad (3)$$

we obtain a simple expression for the excess free energy  $F$ :

$$F = \frac{1}{2} \sum_{k, n=1}^N \int u_k(\mathbf{q}_{\perp}) M_{kn} u_n(-\mathbf{q}_{\perp}) d\mathbf{q}_{\perp}, \quad (4)$$

where  $M_{kn}$  are the elements of the banded matrix. In this matrix, only the diagonal and first adjacent elements



are nonzero. The latter elements are defined by the following formulas:

$$M_{11} = \gamma_1 q_{\perp}^2 + K_1 d q_{\perp}^4 + (B_1 + B_2)/2d = b_1, \quad (5)$$

$$M_{NN} = \gamma_N q_{\perp}^2 + K_N d q_{\perp}^4 + (B_{N-1} + B_N)/2d = b_N, \quad (6)$$

$$M_{nn} = K_n d q_{\perp}^4 + (B_{n-1} + 2B_n + B_{n+1})/2d = b_n, \quad (7)$$

$$n = 2, \quad N-1,$$

$$M_{n+1n} = M_{nn+1} = -(B_n + B_{n+1})/2d = c_n, \quad (8)$$

$$n = 1, \quad N-1,$$

where  $K_n$  is the flexural modulus of the  $n$ th layer of the film and  $B_n$  is the tensile (compressive) modulus of the  $n$ th layer. When the elastic moduli  $K$  and  $B$  in the bulk of the smectic- $A$  phase of a liquid crystal are known at a temperature  $T_0$  [ $K(T_0) \equiv K_0$ ,  $B(T_0) \equiv B_0$ ], which is lower than the temperature of the  $SmA$ -isotropic or  $SmA$ -nematic phase transition, the elastic moduli  $K_n$  and  $B_n$  for any liquid-crystal film with a specified thickness at arbitrary temperature  $T$  (at which the film exists) can be determined using the microscopic model proposed in [24–27] for a thin liquid-crystal layer with two bounding surfaces. The algorithm for calculating these moduli was described in detail in my previous works [21, 23].

Knowing the elements  $M_{kn}$  of the direct matrix, we can determine the elements  $(M^{-1})_{kn}$  of the inverse matrix. Then, the latter elements can be used to calculate the mean fluctuations of layer displacements in the film  $\sigma_n = \langle u_n^2(0) \rangle^{1/2}$  and the correlations between the fluctuations  $g_{k,n}(R) = \langle u_k(\mathbf{R})u_n(0) \rangle / (\sigma_k \sigma_n)$ . According to [18, 19], we have

$$\sigma_n^2 = \langle u_n^2(0) \rangle = \frac{k_B T}{(2\pi)^2} \int (M^{-1})_{nn} d\mathbf{q}_{\perp}, \quad (9)$$

$$\langle u_k(\mathbf{R})u_n(0) \rangle = \frac{k_B T}{(2\pi)^2} \int (M^{-1})_{kn} \exp(i\mathbf{q}_{\perp} \mathbf{R}) d\mathbf{q}_{\perp}, \quad (10)$$

where  $k_B$  is the Boltzmann constant. On the right-hand side of relationships (9) and (10), the lower limits of integration are determined by the transverse sizes  $L$  of the film and the upper limits of integration are determined by the molecular diameter  $a$  ( $2\pi/L \leq |q_{\perp}| \leq 2\pi/a$ ). If the transverse sizes of the film are macroscopic ( $L \sim \text{cm}$ ), the lower limits of integration in relationships (9) and (10) can be set equal to zero.

The fluctuations of smectic layer displacements  $\sigma_n$  and correlations  $g_{k,n}(R)$  were numerically calculated for the smectic- $A$  film supported on the surface of a solid substrate and consisting of  $N = 24$  layers. It was assumed that the film is formed by a liquid crystal that can undergo a weak first-order  $SmA$ -nematic phase transition. According to the McMillan model [36] for a bulk smectic- $A$  phase and the model developed in [24–

27] for a thin liquid-crystal layer with two bounding surfaces, the above situation can be described by the model parameter  $\alpha = 2 \exp[-(\pi r_0/d)^2] \leq 0.98$ , where  $r_0$  is the characteristic radius of interaction for the model pair intermolecular potential used in the McMillan theory. As in [21–23], the calculations were performed at  $\alpha = 0.871$ . The thermal fluctuations of layer displacements in the film and the correlations between these fluctuations were calculated at two temperatures: the first temperature  $T_1$  was considerably lower than the temperature of the  $SmA$ -nematic phase transition in the bulk of the liquid crystal, whereas the second temperature  $T_2$  was only slightly below the limiting temperature at which the film with a specified thickness can exist. According to [24–27], the limiting temperature is the temperature at which the smectic order in the bulk of the film disappears almost completely ( $s \rightarrow 0$ ). As in [21–23], the first temperature was taken as  $T_1 = 0.204(V_0/k_B)$  [in [36], the temperature of the  $SmA$ -nematic phase transition in the bulk of the liquid crystal at  $\alpha = 0.871$  was determined to be  $T_{AN} = 0.2091(V_0/k_B)$ ], where  $V_0$  is the intermolecular interaction constant in the McMillan theory. In the framework of the model developed in [24–27], the second temperature  $T_2$  is governed by the orienting effect of the surfaces bounding the film on liquid-crystal molecules. This effect is simulated by the effective external fields, whose strengths are proportional to the interaction constants  $W_1$  (the free surface of the film) and  $W_N$  (the film-substrate interface). As in my previous works [21–23], the ratio of the constant  $W_1$  to the intermolecular interaction constant  $V_0$  was taken equal to 1.6. As regards the constant  $W_N$ , we considered three cases. In the first case, the constant  $W_N$  was equal to  $W_1$  (the orienting effects of bounding surfaces on molecules in the film are identical). In the second case, we set  $W_N = 5W_1$  (the profound orienting effect of the film-substrate interface). In the third case, the calculations were carried out at  $W_N = W_1/5$  (the orienting effect of the film-substrate interface is weaker than that of the free surface). As a result, the second temperatures were as follows:  $T_2 = 0.21035(V_0/k_B)$  in the first case (as in [21–23]),  $T_2 = 0.21039(V_0/k_B)$  in the second case, and  $T_2 = 0.2093(V_0/k_B)$  in the third case. As in [21–23], the flexural modulus  $K_0$  and the tensile (compressive) modulus  $B_0$  of smectic layers for the bulk liquid-crystal phase at the temperature  $T_1$  lower than the phase transition temperature  $T_{AN}$  were assumed to be  $K_0 = 10^{-6}$  dyn and  $B_0 = 10^8$  dyn/cm<sup>2</sup> (typical values for the majority of liquid crystals [1]). The surface tension coefficient  $\gamma_1$  for the free surface was equal to 25 dyn/cm (taken from [9]), and the surface tension coefficient  $\gamma_N$  (by analogy with [16]) was assumed to be infinitely large ( $\gamma_N = 1000\gamma_1$ ). The thickness of the smectic layers in the film did not depend on the temperature and was taken equal to the molecular length  $l = 30$  Å, and the molecular diameter

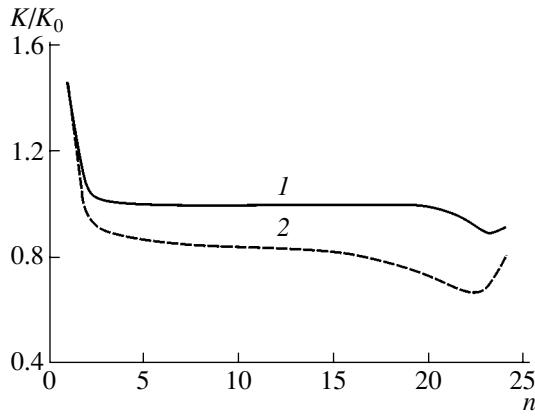


**Fig. 1.** Profiles of the flexural modulus  $K$  in a smectic-A film supported on the surface of a solid substrate: (1) at temperature  $T_1$  below the temperature of the  $SmA$ -nematic phase transition and (2) at the highest temperature  $T_2$  of existence of the film.  $N = 24$ ,  $\alpha = 0.871$ ,  $W_1/V_0 = 1.6$ ,  $W_N = W_1/5$ ,  $T_1 = 0.204(V_0/k_B)$ , and  $T_2 = 0.2093(V_0/k_B)$ .

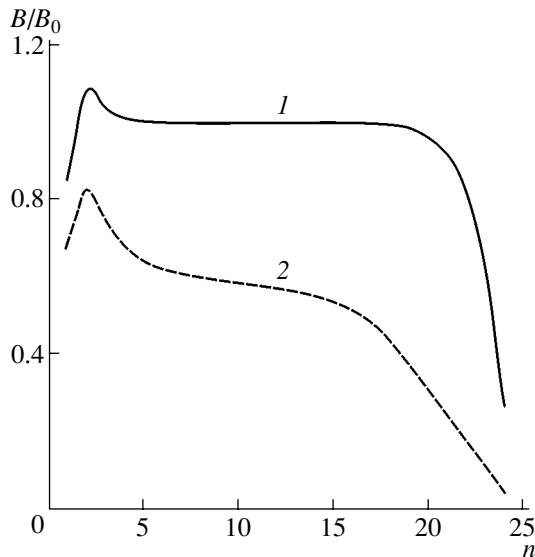


**Fig. 2.** Profiles of the tensile (compressive) modulus  $B$  in a smectic-A film supported on the surface of a solid substrate: (1) at temperature  $T_1$  below the temperature of the  $SmA$ -nematic phase transition and (2) at the highest temperature  $T_2$  of existence of the film. The parameters are the same as in Fig. 1.

$a$  was equal to  $4 \text{ \AA}$  (which are typical sizes for liquid-crystal molecules [1]).

First and foremost, the profiles of the elastic moduli  $K$  and  $B$  for the aforementioned ratios between the orienting effects of the surfaces bounding the film were calculated with the use of the model developed in [24–27]. As could be expected, in the first case, the calculated profiles completely coincide with similar profiles obtained in my earlier works, in which the thermal fluc-

tuations of smectic layer displacements were considered in free-standing smectic-A films (see Figs. 1, 2 in [21, 23]). The profiles determined in the second case ( $W_N = 5W_1$ ) are also almost identical to the profiles calculated in the first case, even though the values of  $K/K_0$  and  $B/B_0$  for the  $N$ th layer of the film are slightly larger than those in the first case. However, in the third case ( $W_N = W_1/5$ ), the profiles for  $K/K_0$  (Fig. 1) and  $B/B_0$  (Fig. 2) differ substantially from the corresponding profiles obtained in [21, 23]. First, as would be expected, these profiles are not symmetric with respect to the center of the film. Second, the minimum elastic moduli (this is especially true for the moduli  $B$ ) are observed not in the central part of the film but in the layer adjacent to the surface of the solid substrate. It should also be noted that, at the low temperature  $T_1$ , the profiles of the elastic moduli  $K$  and  $B$  (curves 1 in Figs. 1, 2; Figs. 1, 2 in [21, 23]) in all three cases are characterized by a rather extended plateau in the central part of the film, in which the moduli are nearly constant and close in magnitude to the bulk values  $K_0$  and  $B_0$ , respectively. At the same time, it can be seen that this plateau is absent at the highest temperature  $T_2$  of existence of the film (curves 2 in Figs. 1, 2; Figs. 1, 2 in [21, 23]). Consequently, at the temperature  $T_1$ , the major part of the smectic-A film on the surface of the solid substrate is actually spatially homogeneous (or almost homogeneous) and the Holyst model [18–20] used in [16, 17] should lead to results that differ very little from our data. However, in the vicinity of the limiting temperature at which the film with a specified thickness can exist ( $T = T_2$ ), the film in all three cases under consideration is spatially inhomogeneous (curves 2 in Figs. 1, 2; Figs. 1, 2 in [21, 23]). Moreover, in the third case, the film is not symmetric with respect to its center and the elastic moduli  $K$  and  $B$  in the layers adjacent to the substrate surface are considerably smaller than those in the layers near the free surface. It is in this case that the results obtained in [16, 17] within the Holyst model should differ most significantly from our data.

Then, the determined profiles of the elastic moduli  $K$  and  $B$  were used to calculate the profiles of the layer displacement fluctuations  $\sigma_n$  in the smectic-A film (consisting of 24 layers) supported on the surface of a solid substrate at the low temperature  $T_1$  and the highest temperature  $T_2$  of existence of the film. The results of these calculations for the first ( $W_N = W_1$ ) and third ( $W_N = W_1/5$ ) cases are presented in Fig. 3 (the profiles for the second case at  $W_N = 5W_1$  differ only slightly from the profiles at  $W_N = W_1$ ). The profile of the displacement fluctuations  $\sigma_n$  calculated within the Holyst model [18, 20] is also shown by the dashed line in Fig. 3. As could be expected, at  $T = T_1$ , our results do not differ greatly from those obtained in terms of this model. However, in the vicinity of the limiting temperature of existence of the film ( $T = T_2$ ), the inclusion of the profiles of the elastic moduli  $K$  and  $B$  leads to a substantial deviation from

the predictions of the Holyst model [18, 20]. Indeed, in the first case, the maximum value of layer displacement fluctuations  $\sigma_n$  calculated with due regard for these profiles at the temperature  $T_2 = 0.21035(V_0/k_B)$  is approximately half the maximum value of  $\sigma_n$  at the temperature  $T_1$ . Furthermore, the maximum of the  $\sigma_n$  profile is shifted to the center of the film, where the moduli  $K$  and  $B$  have minimum values. At the same time, according to the calculations carried out in terms of the Holyst model, this increase in the temperature weakly affects the profile of these fluctuations. In the third case, an increase in the temperature from  $T_1$  to  $T_2 = 0.2093(V_0/k_B)$  leads to a more radical change in the profile of the fluctuations  $\sigma_n$ . At  $T = T_1$ , the fluctuations  $\sigma_n$  only slightly depend on the number of the layer (except for a drastic decrease in  $\sigma_n$  to zero at  $n = 24$ ). On the other hand, at the limiting temperature of existence of the film,  $T = T_2$ , the fluctuations  $\sigma_n$  considerably increase (by a factor of approximately two) with an increase in  $n$  to the penultimate layer of the film and sharply decrease to zero at  $n = 24$ . Therefore, the  $\sigma_n$  profile exhibits a maximum in the vicinity of the surface of the solid substrate, i.e., in the region where the elastic moduli  $K$  and  $B$  have minimum values (Figs. 1, 2). In other words, in all cases under consideration, the thermal fluctuations of layer displacements are maximum in the region where the smectic layer structure is less pronounced. Note that the profile of the fluctuations is determined by the orienting effect of the bounding surfaces on molecules in the film.

We also calculated the correlations  $g_{k,n}(R)$  between displacement fluctuations of different layers in the smectic-A films on the surface of the solid substrate. The results of these calculations for the correlations between the displacement fluctuations of the central layer ( $k = 12$ ) and the other layers ( $n = 1-24$ ) at  $\mathbf{R} = 0$  and  $W_N = W_1$  are presented in Fig. 4. At temperatures ( $T = T_1$ ) below the temperature at which the smectic order disappears in the bulk of the liquid crystal, the results of the calculations are very close to those obtained within the Holyst model [18–20] (the dashed line in Fig. 4). The correlation  $g_{12,n}(0)$  substantially decreases with an increase in the magnitude of the difference between the number  $n$  and 12. However, as would be expected, the dependences obtained are asymmetric with respect to the center of the film. The decay of the correlation  $g_{12,n}(0)$  toward the free surface of the film occurs more slowly than that toward the surface of the solid substrate. The correlation  $g_{12,n}(0)$  in the vicinity of the free surface ( $n = 1$ ) is larger than 0.2, whereas the value of  $g_{12,n}(0)$  for the penultimate film layer ( $n = 23$ ) near the substrate is close to zero. This difference between the correlations is caused by the fact that the layers located near the free surface of the film can be displaced (from their equilibrium positions) synchronously with the central layers. At the same time, the film layers adjacent to the last layer are rigidly fixed

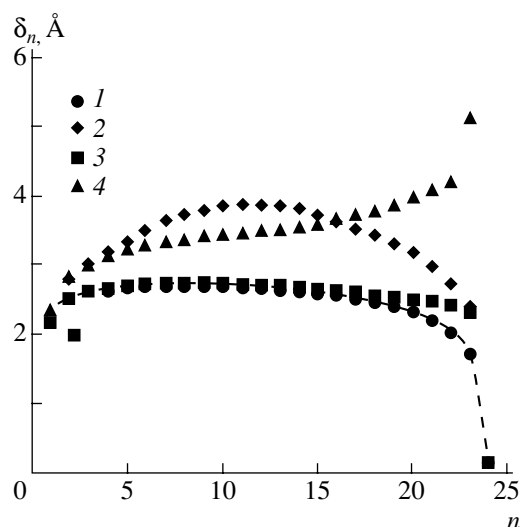


**Fig. 3.** Calculated profiles of layer displacement fluctuations in a smectic-A film supported on the surface of a solid substrate. The calculations were performed with due regard for the profiles of the moduli  $K$  and  $B$  for parameters (1)  $W_N = W_1$  and  $T = T_1 = 0.204(V_0/k_B)$ , (2)  $W_N = W_1$  and  $T = T_2 = 0.21035(V_0/k_B)$ , (3)  $W_N = W_1/5$  and  $T = T_1 = 0.204(V_0/k_B)$ , and (4)  $W_N = W_1/5$  and  $T = T_2 = 0.2093(V_0/k_B)$ .  $W_1/V_0 = 1.6$ ,  $K_0 = 10^{-6}$  dyn,  $B_0 = 10^8$  dyn/cm<sup>2</sup>, and  $\gamma_1 = 25$  dyn/cm. The dashed line represents the results obtained in the framework of the Holyst model [18–20].

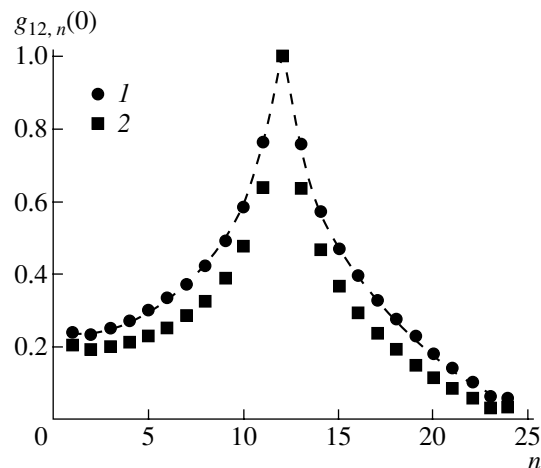


**Fig. 4.** Correlations  $g_{12,n}(0)$  between the displacement fluctuations of the twelfth layer and the other layers ( $n = 1-24$ ) in a smectic-A film supported on the surface of a solid substrate at temperatures (1)  $T = T_1 = 0.204(V_0/k_B)$  and (2)  $T = T_2 = 0.21035(V_0/k_B)$ .  $W_N = W_1$ . The parameters  $N$ ,  $\alpha$ ,  $W_1$ ,  $K_0$ ,  $B_0$ , and  $\gamma_1$  are the same as in Fig. 3. The dashed line represents the results obtained in the framework of the Holyst model.

on the surface of the solid substrate and cannot be involved in a similar process due to high energy expenditures to tensile (compressive) deformation of these layers.

Our calculations also demonstrate that, upon heating of the smectic-A films supported on the surface of a solid substrate to the limiting temperature of their existence  $T_2$ , the change in the correlations  $g_{k,n}(0)$  between the displacement fluctuations of film layers is less pronounced than that in the profiles of these fluctuations (Fig. 4). It should be noted that these changes are completely determined by the orienting effect of the bounding surfaces on molecules in the film. When the orienting effect of the film–substrate interface is equal to the orienting effect of the free surface of the film ( $W_N = W_1$ ) or exceeds it ( $W_N = 5W_1$ ), an increase in the temperature leads to a weakening of the correlations  $g_{12,n}(0)$  (Fig. 4), as is the case with free-standing smectic-A films. If the orienting effect of the film–substrate interface is weaker than that of the free surface of the film ( $W_N = W_1/5$ ), an increase in the temperature results in an enhancement of these correlations  $g_{12,n}(0)$ . This behavior can be easily explained from the physical standpoint. In the first two cases ( $W_N = W_1$ ,  $W_N = 5W_1$ ), heating of the smectic-A film supported on the surface of a solid substrate to the limiting temperature  $T_2$  of its existence leads to a substantial decrease in the elastic moduli  $K$  and  $B$  in the central part of the film, whereas these moduli in the surface layers remain virtually unchanged. As was noted above, the profiles of the moduli  $K$  and  $B$  in these cases are almost identical to the analogous profiles for free-standing smectic-A films (see Figs. 1, 2 in [21, 23]). Since the fluctuation displacements of the central smectic layers of the film are imparted to other layers through the layers adjacent to the central layers, a considerable decrease in their rigidity should result in a weakening of the correlations  $g_{12,n}(0)$  between the fluctuation displacements of the central layers and the other layers of the film. In the third case ( $W_N = W_1/5$ ), an increase in the temperature to the limiting temperature  $T_2$  leads not only to a decrease in the rigidity of the central part of the film but also to a more substantial decrease in the rigidity of the smectic layers adjacent to the surface of the solid substrate (Figs. 1, 2, curves 2), whose fixation hinders synchronous fluctuation displacements of the film layers. Therefore, in this case, heating of the film, for the most part, lifts a barrier to these synchronous fluctuation displacements and, hence, should result in an enhancement of the correlations  $g_{12,n}(0)$ .

### 3. DYNAMICS OF FLUCTUATIONS OF LAYER DISPLACEMENTS IN A SMECTIC-A FILM ON THE SURFACE OF A SOLID SUBSTRATE

According to the model proposed in [31, 32], the time dependence of the fluctuation displacements  $u_n(x, y)$  of layers from their equilibrium positions in

the smectic-A film is described by the equations of motion

$$\rho_0 \frac{\partial^2 u_n}{\partial t^2} = -\eta_3 \Delta_{\perp} \frac{\partial u_n}{\partial t} - \frac{1}{d} \delta F / \delta u_n. \quad (11)$$

Here,  $\rho_0$  is the mean density of the liquid crystal forming the film,  $t$  is the time, and  $F$  is the excess free energy associated with these fluctuation displacements in the film. By taking the continuous Fourier transform (3) of Eqs. (11) and introducing the dimensionless variables  $t' = [(K_0 B_0)^{1/2} / (d \eta_3)] t$  and  $q' = q_{\perp} / q_0$  (where  $q_0^2 = [B_0 / K_0 d^2]^{1/2}$ ), we obtain a system of equations that can be written in the following compact matrix form:

$$(\rho_0 K_0 / \eta_3^2) \frac{\partial^2 u_n}{\partial t'^2} = -q'^2 \frac{\partial u_n}{\partial t'} - M'_{nm} u_m. \quad (12)$$

Here,  $M'_{nm}$  are elements of the banded matrix similar to the matrix  $M_{nm}$  introduced above. For the smectic-A film supported on the surface of a solid substrate, the nonzero elements can be defined by formulas (11)–(15) from my earlier work [35] (devoted to the dynamics of layer displacement fluctuations in free-standing smectic-A films) if the dimensionless surface tension coefficient  $\bar{\gamma} = \gamma (K_0 B_0)^{-1/2}$  in Eqs. (11) and (12) from [35] is replaced by  $\bar{\gamma}_1 = \gamma_1 (K_0 B_0)^{-1/2}$  and  $\bar{\gamma}_N = \gamma_N (K_0 B_0)^{-1/2}$ , respectively.

As in [31, 32, 35], the solution  $u_n(q', t')$  of the system of equations (12) is represented in the form of an expansion

$$u_n(q', t') = \sum_{k=1}^N u_n^{(k)}(q', t') v_n^{(k)}(q') \quad (13)$$

in terms of the eigenvectors  $v_n^{(k)}(q')$  of the matrix  $M'_{nm}(q')$ . The time dependence of the  $k$ th normal mode  $u_n^{(k)}(q', t')$  is described by the relationship

$$u_n^{(k)}(q', t') = u_{n+}^{(k)}(q') \exp[\beta_+^{(k)}(q') t'] + u_{n-}^{(k)}(q') \exp[\beta_-^{(k)}(q') t'], \quad (14)$$

in which the exponents  $\beta_{\pm}^{(k)}(q')$  are expressed through the relaxation times  $\tau_{\pm}^{(k)}(q')$  and the frequencies  $\omega^{(k)}(q')$  with the use of relationships (18)–(21) from [35]. Knowing the time dependences of the normal modes  $u_n^{(k)}(q', t')$ , we can calculate the dynamic correlation functions of layer displacements in the film. In the Fourier representation, these functions are defined as follows [31, 32]:

$$C_{m,n}(q', t') = \langle u_m(q', t') u_n(-q', 0) \rangle. \quad (15)$$

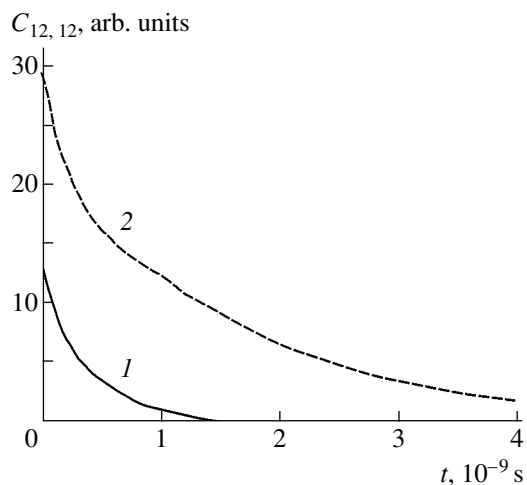


**Fig. 5.** Time dependences of the dynamic correlation function  $C_{12,12}$  at temperatures (1)  $T = T_1 = 0.204(V_0/k_B)$  and (2)  $T = T_2 = 0.21035(V_0/k_B)$ .  $W_N = W_1$  and  $q_{\perp} = 10^5 \text{ cm}^{-1}$ .

With knowledge of the dynamic correlation functions  $C_{m,n}(q', t')$ , we can calculate the correlation  $\langle I(q, t)I(q, 0) \rangle$  between the intensities of x-ray scattering by the film at different instants of time (at  $t = 0$  and  $t$ ). The quantity  $\langle I(q, t)I(q, 0) \rangle / I^2(q, 0)$  is expressed in terms of the correlation functions  $C_{m,n}(q', t')$  with the use of relationships (27) and (28) taken from [35].

The dynamic correlation functions  $C_{m,n}(q_{\perp}, t)$  and the correlations  $\langle I(q, t)I(q, 0) \rangle$  between the intensities of x-ray scattering at different instants of time from the smectic-A film supported on the surface of a solid substrate were numerically calculated for films consisting of 24 layers with the same model parameters used for calculating the profiles of the layer displacement fluctuations and the correlations between them. The viscosity coefficient of interlayer sliding was taken equal to  $\eta_3 = 0.4 \text{ g}/(\text{cm s})$ , which is typical of smectic liquid crystals. The calculations were performed for the aforementioned three ratios between the orienting effects of the bounding surfaces on liquid-crystal molecules in the film at temperatures  $T_1$  and  $T_2$ .

First, we analyze how the temperature affects the dynamic correlation functions. In [35], it was demonstrated that this effect in free-standing smectic-A films can be observed in sufficiently thick films ( $N \geq 100$ ) and at large recoil-momentum components in the film plane ( $\geq 10^6 \text{ cm}^{-1}$ ) (see Figs. 3, 4 in [3, 5]). However, for the smectic-A films supported on the surface of a solid substrate under consideration, this effect is well pronounced in films with a smaller thickness and at substantially smaller recoil-momentum components. This is illustrated in Fig. 5, which shows the time dependences of the dynamic correlation function  $C_{12,12}$  calculated for the film consisting of 24 layers at  $q_{\perp} = 10^5 \text{ cm}^{-1}$ ,  $W_N = W_1$ , and temperatures  $T_1$  (Fig. 5, curve 1)

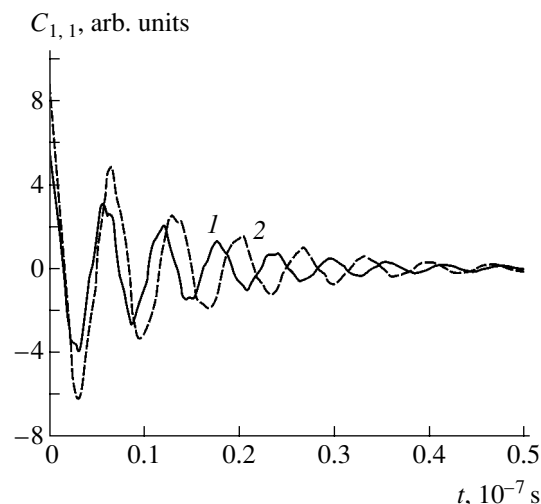


**Fig. 6.** The same as in Fig. 5, but for the dynamic correlation function  $C_{1,1}$  at  $q_{\perp} = 2 \times 10^4 \text{ cm}^{-1}$ .

and  $T_2$  (Fig. 5, curve 2). It can be seen from this figure that, at  $t = 0$ , the magnitude of the correlation function  $C_{12,12}$  at the limiting temperature  $T_2$  of existence of the film is approximately two times larger than that at the lower temperature  $T_1$ . Furthermore, this correlation function at  $T = T_2$  decays considerably more slowly with time as compared to that at  $T = T_1$ . The dependences of the other dynamic correlation functions ( $C_{1,1}$ ,  $C_{1,12}$ , etc.) exhibit a similar behavior. These dynamic correlation functions for free-standing smectic-A films at the same values of  $N$  and  $q_{\perp}$  are entirely independent of the temperature. The difference in the behavior of the smectic-A films supported on the surface of a solid substrate and free-standing smectic-A films is explained by the fact that, in not very thick ( $N \leq 100$ ) free-standing smectic-A films and at  $q_{\perp} \leq 10^6 \text{ cm}^{-1}$ , the dominant role in the dynamics of thermal fluctuations of layer displacements is played by the so-called acoustic mode [31, 32]. This mode corresponds to motion of the film during which the interlayer spacing remains constant, and, hence, the relaxation time does not depend on the profiles of the elastic moduli  $K$  and  $B$ . However, the acoustic mode is absent in the smectic-A films supported on the surface of solid substrates [17] and thermal fluctuations of layer displacements in the film are always accompanied by a change in the interlayer spacing. Consequently, the relaxation times  $\tau_{\pm}^{(k)}(q')$ , which determine the time dependences of the dynamic correlation functions, should depend on the profiles of the elastic moduli  $K$  and  $B$  and, hence, on the temperature already for films that are not very thick ( $N \leq 100$ ) and at values of  $q_{\perp}$  that are not large. It should be noted that, for the smectic-A films supported on the surface of a solid substrate, the temperature dependence of these correlation functions manifests itself for even smaller

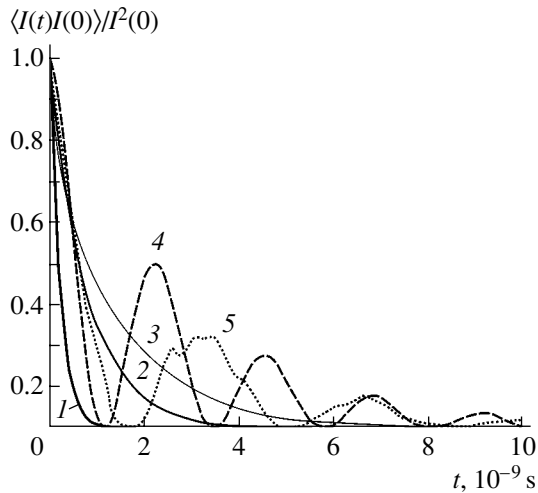


**Fig. 7.** Time dependences of the correlation function  $\langle I(q, t)I(q, 0) \rangle$  at  $W_N = (1, 2) W_1$  and  $(3-5) W_1/5$ ;  $q_{\perp} = (1-3) 10^5$  and  $(4, 5) 3 \times 10^4 \text{ cm}^{-1}$ ; and  $T = (1, 4) 0.204(V_0/k_B)$ ,  $(2) 0.21035(V_0/k_B)$ , and  $(3, 5) 0.2093(V_0/k_B)$ .

recoil-momentum components in the film plane. This is illustrated in Fig. 6, which depicts the time dependences of the dynamic correlation function  $C_{1,1}$  at  $q_{\perp} = 2 \times 10^4 \text{ cm}^{-1}$  and temperatures  $T_1$  (Fig. 6, curve 1) and  $T_2$  (Fig. 6, curve 2). At such a small value of  $q_{\perp}$ , both dependences exhibit an oscillatory behavior; however, the oscillations substantially differ from each other.

Then, the correlation functions  $\langle I(q, t)I(q, 0) \rangle$  were calculated for the smectic-A film comprised of 24 layers and supported on the surface of a solid substrate. The results of the calculations for coherent diffuse x-ray scattering in the vicinity of the main Bragg peak ( $q_z = 2\pi/d$ ) for the recoil-momentum component in the film plane  $q_{\perp} = 10^5 \text{ cm}^{-1}$  and  $W_N = W_1$  are presented in Fig. 7. In this figure, curve 1 corresponds to the temperature  $T_1$  lower than the temperature of the SmA–nematic phase transition in the bulk of the liquid crystal and curve 2 represents the calculated data at the temperature  $T_2$  close to the limiting temperature of existence of the film. It can be seen from Fig. 7 that, upon heating of the film, the correlation function  $\langle I(q, t)I(q, 0) \rangle$  decays more slowly with time. This effect is most pronounced at  $t \sim 10^{-9}$  s. It should also be noted that the results of the calculations carried out in the case of a profound orienting effect of the film–substrate interface on molecules in the film ( $W_N = 5W_1$ ) do not differ greatly from the above data. However, when the orienting effect of the interface is weaker than that of the free surface of the film ( $W_N = W_1/5$ ), the correlation function  $\langle I(q, t)I(q, 0) \rangle$  at the limiting temperature  $T_2$  of existence of the film decays even more slowly with time (Fig. 7, curve 3). Moreover, the calculations performed demonstrate that the effect of temperature on the time dependence of the correlation function  $\langle I(q, t)I(q, 0) \rangle$  is

observed even for smaller recoil-momentum components in the film plane ( $q_{\perp} = 3 \times 10^4 \text{ cm}^{-1}$ ) at which the dependence exhibits a pronounced oscillatory behavior (Fig. 7, curves 4, 5). At similar values of  $q_{\perp}$ , this correlation function for free-standing smectic-A films is entirely independent of the temperature of the film. Thus, compared to free-standing smectic-A films, in the smectic-A films supported on the surface of a solid substrate, the dynamics of layer displacement fluctuations is considerably more sensitive to temperature-induced changes in the internal structure. Experimental investigation into this dynamics can provide valuable structural information.

#### ACKNOWLEDGMENTS

This work was supported by the Russian Foundation for Basic Research, project no. 01-03-32084.

#### REFERENCES

1. P. de Gennes, *The Physics of Liquid Crystals* (Clarendon, Oxford, 1974; Mir, Moscow, 1977).
2. P. Pieranski, L. Beliard, J. P. Tournellec, *et al.*, *Physica A* (Amsterdam) **194** (1–4), 364 (1993).
3. C. Rosenblatt, R. Pindak, N. A. Clark, and R. B. Meyer, *Phys. Rev. Lett.* **42** (18), 1220 (1979).
4. M. Veum, C. C. Huang, C. F. Chou, and V. Surendranath, *Phys. Rev. E* **56** (2), 2298 (1997).
5. T. Stoebe, P. Mach, and C. C. Huang, *Phys. Rev. Lett.* **73** (10), 1384 (1994).
6. E. I. Demikhov, V. K. Dolganov, and K. P. Meletov, *Phys. Rev. E* **52** (2), R1285 (1995).
7. V. K. Dolganov, E. I. Demikhov, R. Fouret, and C. Gors, *Phys. Lett. A* **220**, 242 (1996).
8. P. Johnson, P. Mach, E. D. Wedell, *et al.*, *Phys. Rev. E* **55** (4), 4386 (1997).
9. E. A. L. Mol, G. C. L. Wong, J. M. Petit, *et al.*, *Physica B* (Amsterdam) **248** (1–4), 191 (1998).
10. R. E. Geer, R. Shashidar, A. F. Thibodeaux, and R. S. Duran, *Phys. Rev. Lett.* **71** (9), 1391 (1993).
11. R. E. Geer and R. Shashidar, *Phys. Rev. E* **51** (1), R8 (1995).
12. R. E. Geer, S. B. Qadri, R. Shashidar, *et al.*, *Phys. Rev. E* **52** (1), 671 (1995).
13. G. Henn, M. Stamm, H. Roths, *et al.*, *Physica B* (Amsterdam) **221** (1–3), 174 (1996).
14. M. W. J. van der Wielen, M. A. Cohen Stuart, G. J. Fleer, *et al.*, *Langmuir* **13**, 4762 (1992).
15. T. Salditt, C. Munster, J. Lu, *et al.*, *Phys. Rev. E* **60** (6), 7285 (1999).
16. D. K. G. de Boer, *Phys. Rev. E* **59** (2), 1880 (1999).
17. V. P. Romanov and S. V. Ul'yanov, *Phys. Rev. E* **66**, 061701 (2002).
18. R. Holyst and D. J. Tweet, *Phys. Rev. Lett.* **65** (17), 2153 (1990).
19. R. Holyst, *Phys. Rev. A* **44** (6), 3692 (1991).
20. A. Poniewerski and R. Holyst, *Phys. Rev. B* **47** (15), 9840 (1993).

21. L. V. Mirantsev, Fiz. Tverd. Tela (St. Petersburg) **41** (10), 1882 (1999) [Phys. Solid State **41**, 1729 (1999)].
22. L. V. Mirantsev, Fiz. Tverd. Tela (St. Petersburg) **42** (8), 1511 (2000) [Phys. Solid State **42**, 1554 (2000)].
23. L. V. Mirantsev, Phys. Rev. E **62** (1), 647 (2000).
24. L. V. Mirantsev, Phys. Lett. A **205**, 412 (1995).
25. L. V. Mirantsev, Liq. Cryst. **20** (4), 417 (1996).
26. L. V. Mirantsev, Phys. Rev. E **55** (4), 4816 (1997).
27. L. V. Mirantsev, Liq. Cryst. **27**, 491 (2000).
28. V. K. Dolganov, V. M. Zhilin, and K. P. Meletov, Zh. Éksp. Teor. Fiz. **115** (5), 1833 (1999) [JETP **88**, 1005 (1999)].
29. A. C. Price, L. B. Sorensen, S. D. Kevan, *et al.*, Phys. Rev. Lett. **82** (4), 755 (1999).
30. A. Fera, I. P. Dolbnya, G. Grubel, *et al.*, Phys. Rev. Lett. **85** (11), 2316 (2000).
31. A. Poniewierski, R. Holyst, A. C. Price, *et al.*, Phys. Rev. E **58** (2), 2027 (1998).
32. A. Poniewierski, R. Holyst, A. C. Price, and L. B. Sorensen, Phys. Rev. E **59** (3), 3048 (1999).
33. A. N. Shalaginov and D. E. Sullivan, Phys. Rev. E **62** (1), 699 (2000).
34. V. P. Romanov and S. V. Ul'yanov, Phys. Rev. E **65** (2), 021706 (2002).
35. L. V. Mirantsev, Kristallografiya **48** (4), 745 (2003) [Crystallogr. Rep. **48**, 693 (2003)].
36. W. L. McMillan, Phys. Rev. A **4** (3), 1238 (1971).

*Translated by O. Borovik-Romanova*

---

**FULLERENES  
AND ATOMIC CLUSTERS**

---

## Effect of Carbon Network Defects on the Electronic Structure of Semiconductor Single-Wall Carbon Nanotubes

P. V. Avramov<sup>1,2</sup>, B. I. Yakobson<sup>2</sup>, and G. E. Scuseria<sup>2</sup>

<sup>1</sup> Kirensky Institute of Physics, Siberian Division, Russian Academy of Sciences,  
Akademgorodok, Krasnoyarsk, 660036 Russia

<sup>2</sup> Center for Biological and Environmental Nanotechnology, Rice University, Houston, Texas, 77005-1892 USA

Received September 26, 2003

**Abstract**—For a single-wall (14, 0) carbon nanotube, the total density of electronic states of the ideal structure and of some possible defect structures is calculated in the framework of the band theory approach using Gaussian-type orbitals and the approximation of the generalized density gradient. It is shown that allowance for defects of the atomic structure of a nanotube makes it possible to adequately describe the existing experimental data on nanotube electronic structure. In the framework of the same approach, the total density of electronic states is calculated for an intermolecular contact of (5, 5) and (10, 0) single-wall carbon nanotubes formed due to the creation of a 5–7 defect. It is shown that the electronic states related to the contact region and the 5–7 defect lie in vicinity of the Fermi level. © 2004 MAIK “Nauka/Interperiodica”.

Atomic and electronic structures of a defect (13, 13) carbon nanotube and of an intermolecular contact between the (21, –2) and (22, –5) carbon nanotubes formed by introducing a 5–7 defect were studied using scanning tunneling microscopy (STM) and scanning tunneling spectroscopy (STS) in [1–3]. In those studies, it was shown that a defect introduced into an ideal atomic network of a (13, 13) metal nanotube generates a number of spectroscopic features located between the first Van Hove singularities [1, 3] and that the energy position and intensity of the new spectroscopic features depend on the distance from the defect for which the scanning tunneling spectrum is measured. In [1, 3], the observed oscillations were interpreted in terms of resonant backscattering of the incident electron plane wave by quasibound electronic states of the defect. Experimental STS spectra of the (21, –2)/(22, –5) intermolecular contact measured in the vicinity of the structural defect have shown that the electronic states of the metallic (22, –5) structure and the semiconductor (21, –2) structure are mixed. The relative weights of the spectral features depend on the position of the measurement point with respect to the contact. It has also been shown that the features caused by the contact decay over a distance of several nanometers. Local variations in the densities of states for single-wall nanotubes were experimentally measured in [2] and qualitatively interpreted as interference between the incident and reflected electron waves. The dispersion law in single-wall nanotubes with defects has been interpreted in terms of quantum interference of electrons scattered by defects [1].

Another type of defects in semiconductor carbon nanotubes caused by adsorption of O<sub>2</sub> and NO<sub>2</sub> molecules by the carbon network of these objects was experimentally studied in [4, 5]. Both chemical agents increased the density of electronic states at the Fermi level and converted semiconductor nanotubes into metal nanotubes. On the basis of nonempirical calculations of the electronic structure [6] of a chemisorbed O<sub>2</sub> molecule, these experimental results have been interpreted in terms of extra charge carriers (holes) at the Fermi level and closing of the band gap in semiconductor *p*-type nanotubes.

In the theoretical study performed in [7], on the basis of calculations of the electronic structure of single-wall semiconductor nanotubes performed within the tight-binding model and the local density functional approximation, it was predicted that a 5–7 defect (a Stone–Wales defect) should also result in closing of the band gap in semiconductor nanotubes.

The tight-binding method was also used to calculate a number of intermolecular contacts between nanotubes [8]. These theoretical results have qualitatively confirmed the experimental observations reported in [3].

Nevertheless, correct interpretation of some experimental data even for nonchiral single-wall nanotubes [9] is still lacking. The simplest example is sample no. 7 investigated in the pioneering work [9], where, in particular, the STM spectra of single-wall nanotubes were measured for the first time. According to [9], this sample (of diameter  $d = 1.1$  nm with chiral angle  $\phi = 30^\circ$ ) was a (14, 0) nanotube, which, according to [10], had to have semiconductor properties. Nevertheless, in the



experiment in [9], this sample had metallic properties. In our opinion, the presence of defects in the structure of the carbon (14, 0) nanotube would provide the most reasonable interpretation of such fundamental differences between theory and experiment.

In order to check this assumption, we calculated the electronic structure of an ideal (14, 0) carbon nanotube and a (14, 0) carbon nanotube with different defects [a Stone–Wales defect, double vacancy in the carbon network (2V defect), a defect produced by embedding two additional carbon atoms into the carbon network (an *ad dimmer* defect), and two defects produced by saturating one of the double carbon bonds by the OH and H groups (2OH and 2H defects)]. All calculations were performed using the approximation of a generalized density gradient (the Perdew–Burke–Ernzerhof (PBE) potential) [11] and the band theory approach using Gaussian-type orbitals in the 3–21G, 6–31G, and 6–31G\* bases [12]. To correctly describe the electronic structure of isolated defects, the length of the unit cell was taken to be 20 Å. When modeling the variation in the defect density in the atomic network, the length of the unit cell (and, accordingly, the number of carbon atoms in it) was varied. To study the electronic structure of an intermolecular contact, we chose the structure formed by the contact of a metal (5, 5) and semiconductor (10, 0) nanotubes. The intermolecular contact considered is formed by introducing one pentagon and one heptagon into the (5, 5) or (10, 0) nanotube. To model noninteracting contacts, the length of the unit cell was increased to 40 Å.

Optimization of the geometry of defect structures was performed using the method of the analytical gradient of the potential energy surface and the PBE functional [11] in the 3–21G basis. The number of atoms per unit cell was varied from 226 for 2H and 2OH defects (carbon–carbon bonds saturated by two atoms of hydrogen or two functional groups, 2020 functions in the 6–31G basis) to 334 for a 2V defect (3006 functions in the 6–31G basis). The electronic structure of all objects was calculated using 128 points of  $\mathbf{k}$  space in the Brillouin zone. The electronic structure of the ideal (14, 0) nanotube was calculated using both the PBE functional [11] and the hybrid PBE0 functional [13], whose distinctive feature is the admixture of 25% of the exact Hartree–Fock exchange to the pure PBE potential of the density functional theory; this approach makes it possible to take into account electronic correlations in the system more fully. It is believed that this approach [13] is equivalent to the Møller–Plesset fourth-order perturbation theory. The PBE0 functional was shown to provide much better agreement between the total theoretical electronic densities of states (DOS) and the experimental STS spectra of semiconductor nanotubes [14].

The unit cell of the intermolecular (5, 5)/(10, 0) contact contains 360 carbon atoms (3240 functions in the 3–21G basis). The length of the unit cell for this struc-

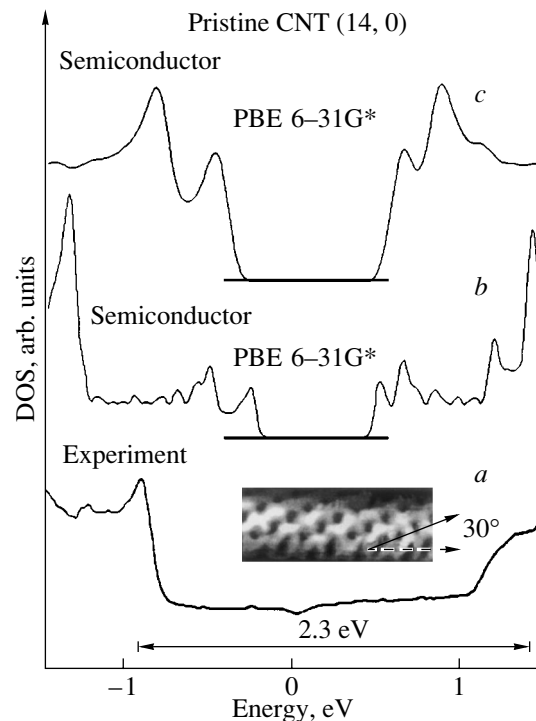


**Fig. 1.** (a) Experimental STS spectra [9] and the theoretical (b) PBE and (c) PBE0 densities of states (DOS) for semiconductor zigzag (14, 0) carbon nanotubes. The inset shows a photograph of the structure obtained with a scanning tunneling microscope [9]. It is clearly seen that the nanotube has a zigzag structure.

ture is 40 Å. Optimization of the geometry was performed using the semiempirical quantum-chemical PM3 method (for a cluster containing three unit cells) and the analytical gradient of the potential energy. To calculate the electronic structure, 64 points were taken in  $\mathbf{k}$  space in the Brillouin zone. For interpretation of the data on the electronic structure of the intermolecular contact, band calculations for ideal (10, 0) and (5, 5) nanotubes were performed using the PBE potential and 128 points in  $\mathbf{k}$  space.

Figure 1 shows the experimental STS spectra (Fig. 1, a [9]) and the theoretical densities of electronic states calculated using the PBE (Fig. 1b) and PBE0 (Fig. 1, c) potentials for the ideal semiconductor (14, 0) nanotube. It is seen from Fig. 1 that the experimental spectra exhibit metallic conductivity, which is in disagreement with the previous theoretical prediction [10]. In contrast to the experimental spectrum, the theoretical densities of states obtained using both the PBE and PBE0 potentials agree with the results from [10] and are characterized by the presence of a band gap with a width of about 1 eV (Fig. 1).

Figure 2 shows the experimental spectrum [9] (Fig. 2, a) and a set of theoretical spectra for the structures with a Stone–Wales defect (Fig. 2, b) and 2H (Fig. 2, c), 2OH (Fig. 2d), *ad dimmer* (Fig. 2, e), and 2V

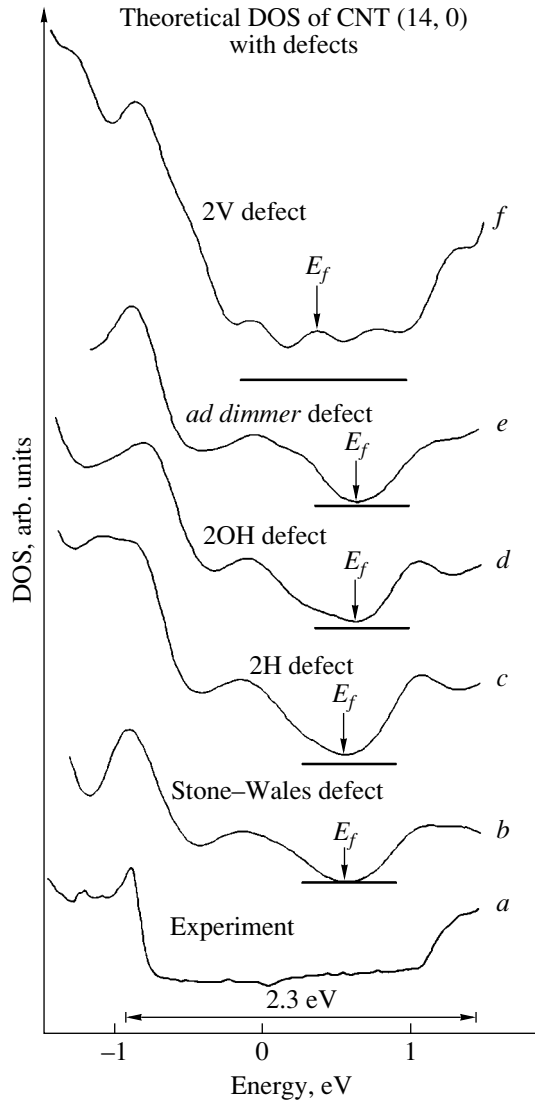


**Fig. 2.** (a) Experimental STS spectrum of a (14, 0) carbon nanotube (CNT) [9], (b) theoretical PBE 6–31G density of states for a (14, 0) nanotube with a Stone–Wales defect (the unit cell contains 226 carbon atoms), (c) theoretical PBE 6–31G densities of states for a (14, 0) nanotube with a 2H defect (the unit cell contains 226 carbon atoms), (d) theoretical PBE 6–31G density of states for a (14, 0) nanotube with a 2OH defect (the unit cell contains 226 carbon atoms), (e) theoretical PBE 6–31G density of states for a (14, 0) nanotube with an *ad dimmer* defect created by sorption of a  $C_2$  fragment at the carbon wall (the unit cell contains 282 carbon atoms), and (f) theoretical density of states  $T^R$  obtained for a rigid band of a 2V defect using the total PBE 6–31G densities of states calculated for 2V defect densities of 0.3 and 0.6% per unit cell (the unit cell contains 334 and 332 carbon atoms, respectively).

defects (Fig. 2, f). Introducing structural defects into the ideal graphite network results in the appearance of states in the band gap. In all cases, the main features of the experimental densities of states at energies of approximately  $-0.9$  and  $1.4$  eV are described ade-

quately. There is a gap in the density of states only for the structure with a Stone–Wales defect (Fig. 2, b); all other defects produce metallic-type densities of states.

Characteristic energy-dependent oscillations in the density of states were simulated in [15] by using 1D plane waves  $\exp(ikx)$ , where  $x$  is the space coordinate. The incident plane wave can be resonantly reflected from a quasibound defect state with reflection coefficient  $|R|^2$  [ $R = |R|\exp(-i(kx + \delta))$ ], where  $\delta$  is the phase shift]. The corresponding standing wave can be written as  $\psi(k, x) = \exp(ikx) + |R|\exp(-i(kx + \delta))$ , which corresponds to spatial oscillations in the densities of states  $\rho(k, x) = |\psi(k, x)|^2 = 1 + |R|^2 + 2|R|\cos(2kx + \delta)$  [15].

In order to simulate the effect of the defect density on the electronic structure of nanotubes, we performed calculations of the band structure for a 2V defect with two different cells. The first cell contained one defect per unit cell (334 atoms, which corresponds to a defect density of 0.3%), whereas the second cell had two defects (the unit cell was the same; both defects were placed on opposite ends and opposite faces of the unit cell; the defect density was 0.6%). The translation vector for both unit cells was  $25 \text{ \AA}$ .

Using this special choice of the unit cells, we can write  $\mathbf{k}^1x \sim \mathbf{k}^2x$  ( $\mathbf{k}^1$  is the wave vector of the defect state with the former density and  $\mathbf{k}^2$  is that for the defect state with the latter density); therefore, we can obtain the energy positions of the density-of-states oscillations for both unit cells.

For systems with low defect densities, we can use the model of independent centers [16] (assuming that defects do not interact with each other) and the models of rigid bands and impurity bands (a rigid band does not depend on the occupation numbers, whereas the nature of an impurity band is fully determined by the type and density of the impurity). Application of these two models means that we can distinguish between the two independent electronic subsystems of the system (naturally, in narrow intervals of defect densities), namely, the subsystem of defect states  $T^D$  and the subsystem  $T^R$  formed by the other states with occupation numbers  $x$  and  $(1 - x)$ , respectively.

In terms of these two models, we can write two linear equations

$$T_1^T = x_1 T^D + (1 - x_1) T^R,$$

$$T_2^T = x_2 T^D + (1 - x_2) T^R,$$

where  $T_1^T$  and  $T_2^T$  are the total densities of states for the systems with different defect densities.

For systems with a significant number of noninteracting defects uniformly distributed over the entire atomic network, we can extract the quantity  $T^R$ , since different defects can mutually suppress oscillations in the densities of states due to interference effects. Most

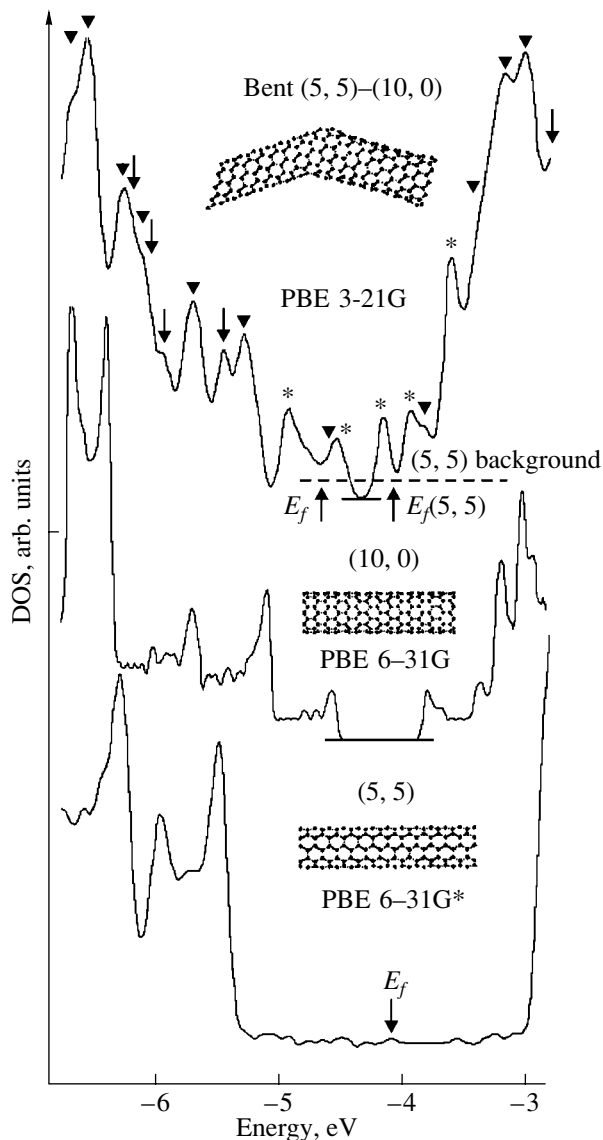


**Fig. 3.** The total densities of states for the (5, 5) and (10, 0) nanotubes and for the (5, 5)/(10, 0) intermolecular contact. Arrows indicate the features related to the (5, 5) structure, triangles indicate the features related to the (10, 0) structure, and asterisks denote the features related to the intermolecular contact itself. The (5, 5), (10, 0), and (5, 5)/(10, 0) structures are shown in the insets.

likely,  $T^R$  can be seen in spectroscopic experiments for such systems.

Figure 2,  $f$  shows  $T^R$  obtained by using the theoretical densities of states for unit cells with 2V-defect densities of 0.3 and 0.6%. It is clearly seen that such an approach provides an opportunity to quantitatively describe the experimental density of states obtained in [9] for a (14, 0) nanotube.

The calculations described above show the high quality of the results obtained for defect 1D carbon

nanostructures; thus, we may hope for a qualitative description of the electronic structure of the (5, 5)/(10, 0) intermolecular contact (Fig. 3). The length of the unit cell ( $\sim 40$  Å) was chosen to be sufficiently large to avoid significant interaction between the defects. By applying the translational symmetry to the unit cell, we can construct an infinite zigzag structure in which the sections with (5, 5) and (10, 0) structures are separated by the structures containing five- and seven-membered rings (the upper inset in Fig. 3).

Figure 3 shows the densities of states for the (5, 5) and (10, 0) nanotubes and for the (5, 5)/(10, 0) intermolecular contact. According to our nonempirical calculations, the intermolecular contact is metallic with a non-zero density of electronic states at the Fermi level, whose energy position is  $-4.7$  eV. The features near the Fermi level are produced by the electronic states corresponding to the 5–7 defect, whereas the spectral features below and above the Fermi level originate from either (5, 5) or (10, 0) structures.

Comparison of the experimental STS spectra and theoretical electronic densities of states calculated using the band theory approach, Gaussian-type orbitals, and the PBE potential of the approximation of the generalized density gradient shows that the method described above can be successfully applied to calculate the electronic structure of semiconductor single-wall nanotubes with defects. Noticeable differences in the densities of states of ideal nanotubes and nanotubes with defects can serve as an elementary test of the imperfection of the atomic structure of this type of object.

#### ACKNOWLEDGMENTS

This study was supported by the Nanoscale Science and Engineering Initiative of the National Science Foundation, award number EEC-0118007 (Rice CBEN), and by the Welch Foundation.

#### REFERENCES

1. M. Ouyang, J.-L. Huang, and C. M. Lieber, *Phys. Rev. Lett.* **88**, 066804 (2002).
2. M. Ouyang, J.-L. Huang, C. L. Cheung, and C. M. Lieber, *Science* **291**, 97 (2001).
3. M. Ouyang, J.-L. Huang, and C. M. Lieber, *Annu. Rev. Phys. Chem.* **53**, 201 (2002).
4. P. G. Collins, K. Bradley, M. Ishigami, and A. Zettl, *Science* **287**, 1801 (2000).
5. J. Kong, N. R. Franklin, C. Zhou, M. G. Chapline, S. Peng, K. Cho, and H. Dai, *Science* **287**, 622 (2000).
6. S.-H. Jhi, S. G. Louie, and M. L. Cohen, *Phys. Rev. Lett.* **85**, 1710 (2000).
7. V. H. Crespi and M. L. Cohen, *Phys. Rev. Lett.* **79**, 2093 (1997).

8. S. G. Louie, *Top. Appl. Phys.* **80**, 113 (2001).
9. J. W. G. Wildöer, L. C. Venema, A. G. Rinzler, R. E. Smalley, and C. Dekker, *Nature* **391**, 59 (1998).
10. J. W. Mintmire, B. I. Dunlop, and C. T. White, *Phys. Rev. Lett.* **68**, 631 (1992).
11. J. P. Perdew, K. Burke, and M. Ernzerhof, *Phys. Rev. Lett.* **77**, 3865 (1996); *Phys. Rev. Lett.* **78**, 1396(E) (1997).
12. M. J. Frisch, G. W. Trucks, H. B. Schlegel, *et al.*, *GAUSSIAN 01. Development Version* (Gaussian, Pittsburgh, PA, 2001).
13. M. Ernzerhof and G. E. Scuseria, *J. Chem. Phys.* **110**, 5029 (1999); C. Adamo and V. Barone, *J. Chem. Phys.* **110**, 6158 (1999).
14. P. V. Avramov, K. N. Kudin, and G. E. Scuseria, *Chem. Phys. Lett.* **370**, 597 (2003).
15. M. Ouyang, J.-L. Huang, and C. M. Lieber, *Annu. Rev. Phys. Chem.* **53**, 201 (2002).
16. P. V. Avramov and S. G. Ovchinnikov, *Fiz. Tverd. Tela (St. Petersburg)* **37**, 2559 (1995) [*Phys. Solid State* **37**, 1405 (1995)].

*Translated by I. Zvyagin*

---

## FULLERENES AND ATOMIC CLUSTERS

---

# Electronic Structure of Carbon Nanotubes Modified by Alkali Metal Atoms

I. V. Zaporotzkova\*, N. G. Lebedev\*, and L. A. Chernozatonskii\*\*

\*Volgograd State University, Volgograd, 400062 Russia

\*\*Institute of Biochemical Physics, Russian Academy of Sciences, Moscow, 117334 Russia

e-mail: cherno@sky.chph.ras.ru

Received July 1, 2003; in final form, November 3, 2003

**Abstract**—The electronic structure and parameters of the energy band structure of  $(n, 0)$ -type nanotubes modified by alkali metal atoms (Li, Na) and intercalated by potassium atoms are studied. The quantum-chemical semiempirical MNDO method and a model of the covalent cyclic cluster built in via ionic bonding are used to model infinitely long nanotubes. The electronic density of states of modified nanotubes is found. It is shown that semiconductor–metal transitions can occur in semiconductor nanotubes and that semimetal nanotubes can undergo metal–metal transitions. © 2004 MAIK “Nauka/Interperiodica”.

## 1. INTRODUCTION

A lot of attention is currently being paid to the experimental and theoretical study of a recently discovered form of open-surface carbon called nanotubes (NTs) [1–10]. In the course of partial thermal destruction of graphite layers, not only fullerene molecules but also long tubes are formed, whose surface consists of regular hexagons. These tubes are up to several microns long and several nanometers in diameter, can consist of one or several layers (depending on the preparation conditions), and have open or closed ends. The methods of NT fabrication are explicitly described in reviews [6, 7]. The NT structures can be classified using the symbols  $(n, m)$ , as suggested by Hamada *et al.* [4]. An  $(n, m)$  NT is obtained by rolling a graphite fragment so that one hexagon is located above another with the shift  $m\mathbf{A}_1 + n\mathbf{A}_2$ , where  $\mathbf{A}_1$  and  $\mathbf{A}_2$  are primitive translation vectors for the graphite fragment. Among the NTs (tubelens) with cylindrical symmetry,  $(n, n)$  NTs are said to be of the “armchair” type and  $(n, 0)$  NTs are said to be of the “zigzag” type. At present, it is possible to prepare and study the structure, elastic properties, and conductivity of separate single-wall and multi-wall NTs and of bundles of single-wall tubes ~1 nm in diameter [6, 7, 10–12].

One of the interesting aspects of the study of carbon NTs is the possibility of fabricating structures having new mechanical, electronic, or optical properties through doping or modification by other atoms. Immediately after the discovery of carbon NTs, the problem of filling and modifying NTs by various materials arose. In particular, an NT filled by conductor, semiconductor, or superconductor material can be used in modern microelectronics as a miniature device [6–8]. Theoretical study of the mechanisms of formation of filled and modified NTs makes it possible to understand

the synthesis mechanisms and to develop new experimental methods of NT fabrication. In this study, we present the results of our investigations into the electronic structure and energy spectrum parameters of small-diameter carbon NTs modified and intercalated by alkali metal atoms (Li, Na, K); these investigations were started as early as in the middle of the 1990s [13–19].

We discuss the results from calculating two possible alternatives for modifying zigzag-type  $(n, 0)$  carbon NTs: (1) regular adsorption of alkali metal atoms on the external surface of an NT (surface modification) and (2) introduction of alkali metal atoms into the NT cavity (intercalation).

## 2. SURFACE MODIFICATION OF CARBON NANOTUBES

A model of a covalent cyclic cluster built in via ionic bonding [20], adapted to calculations for crystals and polymers in the framework of the semiempirical quantum-chemical MNDO calculation procedure [21], was applied to calculate the electronic structure and energy band structure parameters for  $(6, 0)$ ,  $(8, 0)$ , and  $(12, 0)$  NTs modified by Li and Na atoms. The extended unit cells (EUCs) of the tubes under study contained three layers with 6, 8, and 12 carbon hexagons in each layer and 6, 8, and 12 alkali metal atoms, respectively, located above the surface hexagons. The distance between the nearest neighbor carbon atoms was taken to be 1.4 Å. An example of EUCs for a  $(6, 0)$  NT modified by Na atoms is shown in Fig. 1. Cyclic boundary conditions for molecular orbitals (MOs) of a cylindrical EUC were imposed in the direction of the NT axis. Two possible positions of metal atoms above the tube surface were considered: (I) metal atoms were located above the hexagon centers along the tubelene circle

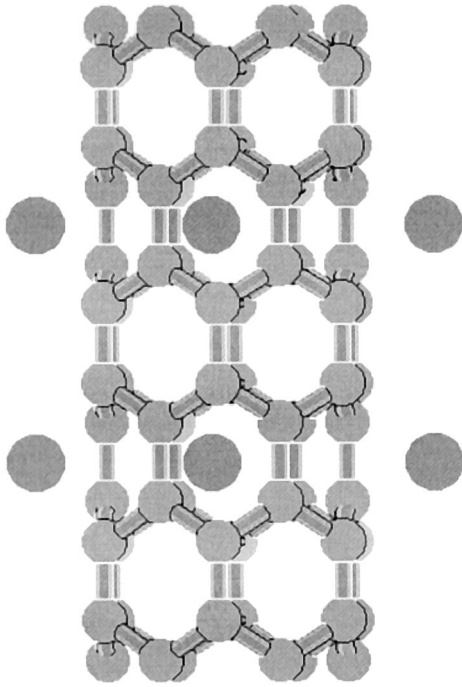


**Fig. 1.** Extended unit cell of a (6, 0) nanotube modified by Na atoms.

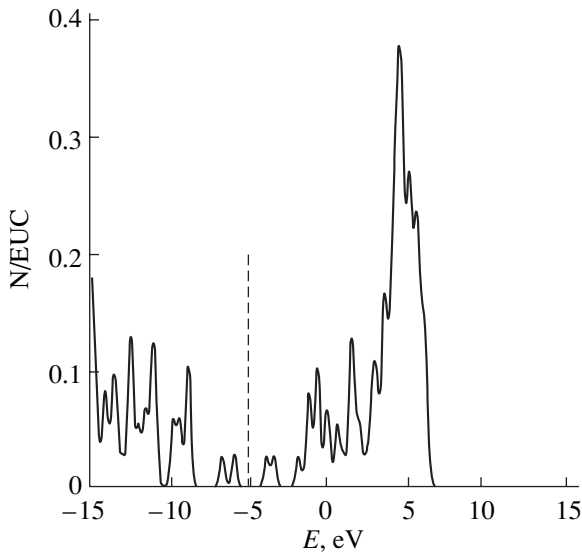


**Fig. 2.** Density of electronic states of a (8, 0) carbon nanotube normalized to an extended unit cell (EUC) and calculated using the method of covalent cyclic cluster built in via ionic bonding; the dashed line indicates the position of the Fermi level (approximately  $-5\text{eV}$ ).

forming two “rings” not shifted with respect to each other (a rectangular superlattice) (Fig. 1) and (II) the metal atoms of one ring were shifted with respect to the atoms of the other ring by one hexagon (a rhombic superlattice). One ring contained three, four, and six

metal atoms for (6, 0), (8, 0), and (12, 0) NTs, respectively. The geometrical parameters of the rings of alkali metal atoms were optimized in quantum-chemical calculations; for NTs, the rigid lattice approximation was used. The calculated energy structure parameters for modifications I and II of NTs are given in Table 1.

Analysis of these results shows that modification I is energetically more favorable and, therefore, more stable in all cases. As the NT diameter increases, the difference in the specific energy (i.e., the energy per hexagon) between the two modifications  $\Delta = E_{\text{II}} - E_{\text{I}}$  decreases from 0.46 [for the (6, 0) tube] to 0.06 eV [for the (12, 0) tube] in the case of Li and from 0.42 to 0.04 eV for Na. This difference in specific energy approaches values of 0.05 and 0.02 eV, respectively, obtained in the case of the same modifications I and II with the same atoms for a single-layer  $C_{72}$  graphite cluster (this is actually the limiting case of an NT of infinite diameter; see Table 1).

Analysis of the calculated electronic structure of modified NTs shows that the molecular orbitals (MOs) are grouped into energy bands. The  $2s$ - and  $2p$ -atomic orbitals (AO) of carbon atoms contribute to the molecular orbitals corresponding to the states of the valence band. The MOs corresponding to the bottom of the conduction band are constructed from the  $2p$  AOs of carbon atoms and  $2s$  and  $2p$  AOs of Li atoms or  $3s$  and  $3p$  AOs of Na atoms. Calculations reveal the presence of metallic conductivity (the band gap  $\Delta E_g = 0$ ) in the systems under study and the appearance of minibands of unoccupied levels in the energy spectrum corresponding to the AOs of alkali metal and C atoms. These features are a consequence of the appearance of a superlattice of metal atoms and indirectly confirm the correctness of the above results. Due to the presence of defects (atoms of the superlattice), the band of the crystal splits into minibands. Figure 2 shows the density of electronic states in a pure ( $n, 0$ ) carbon tubulene with  $n = 8$ . The density of states for the (8, 0) NT has a gap of about 2 eV near the Fermi level, thus indicating the semiconductor properties of the tube. Figure 3 shows the density of states for modification I with Li atoms. Comparison with the case of a pure carbon NT clearly shows an increase in the peak amplitudes corresponding to minibands near the Fermi level  $E_F$  (the main contribution to the minibands comes from the alkali metal atoms). Generally, for the ( $n, 0$ ) tubes, the modification by alkali metal atoms results in the appearance of minibands in the band gap and, therefore, in the disappearance of the energy gap, which indicates the onset of metallic conductivity in such NTs.

We calculated the Li and Na atom adsorption energies for both surface modifications using the formula

$$E_{ad} = \frac{(E_t + NE_{me}) - E_{mt}}{N}, \quad (1)$$

where  $N$  is the number of metal atoms per EUC,  $E_t$  is the total energy of a pure carbon ( $n, 0$ ) NT,  $E_{me}$  is the

**Table 1.** Energy structure parameters of modified ( $n, 0$ ) nanotubes ( $n = 6, 8, 12$ )

$d_t, \text{\AA}$	Atom	Modification	$r, \text{\AA}$	$Q$	$E, \text{eV}$	$\Delta E_g, \text{eV}$	$\Delta E_v, \text{eV}$	$\Delta, \text{eV}$	$E_{ad}, \text{eV}$
(6, 0)									
4.6	Li	I	1.6	0.68	-509.96	0.0	50.60	0.46	3.7
		II	1.6	0.67	-509.50	0.0	49.52		2.3
	Na	I	1.7	0.65	-510.04	0.0	50.94	0.42	3.9
		II	1.7	0.65	-509.62	0.0	49.74		2.7
(8, 0)									
6.2	Li	I	1.6	0.68	-511.54	0.0	50.10	0.24	3.4
		II	1.6	0.66	-511.30	0.0	49.31		2.7
	Na	I	1.7	0.65	-511.66	0.0	50.28	0.22	3.7
		II	1.7	0.65	-511.44	0.0	49.49		3.0
(12, 0)									
9.3	Li	I	1.7	0.68	-521.66	0.0	50.88	0.06	3.5
		II	1.7	0.67	-521.60	0.0	49.90		2.5
	Na	I	1.8	0.65	-522.32	0.0	51.02	0.04	3.6
		II	1.8	0.65	-522.28	0.0	50.10		2.8
Graphite $C_{72}$									
$\infty$	Li	I	1.7	0.62	-504.21	0.0	50.51	0.05	-
		II	1.7	0.63	-504.16	0.0	50.40		-
	Na	I	1.8	0.60	-504.16	0.0	50.50	0.02	-
		II	1.8	0.60	-504.14	0.0	50.45		-

Note: I and II are the modification types,  $r$  is the optimum distance between the metal atoms and the centers of carbon hexagons at the surface, and  $Q$  is the charge on a metal atom;  $E$  is the energy of the system per hexagon,  $\Delta = E_{II} - E_I$ ,  $d_t$  is the tubelene diameter,  $\Delta E_g$  is the band gap, and  $\Delta E_v$  is the valence band width.

**Table 2.** Adsorption energies (in electronvolts) of Li and Na atoms for the two modifications of ( $n, 0$ ) nanotubes with  $n = 6, 8$ , and 12

Nanotube type	(6, 0)				(8, 0)				(12, 0)			
	Li		Na		Li		Na		Li		Na	
Modification	I	II	I	II	I	II	I	II	I	II	I	II
	3.7	2.3	3.9	2.7	3.4	2.7	3.7	3.0	3.5	2.5	3.6	2.8

metal atom energy (Li or Na), and  $E_{mt}$  is the total energy of the modified NT. The results of the calculation are given in Table 2.

It is seen from Table 2 that, for a rectangular superlattice, the adsorption energy is greater than for a rhombic superlattice. Thus, modification I actually turns out to be energetically more favorable than modification II.

The geometrical parameters of the rings of alkali metals vary only slightly as the NT diameter is increased (Table 1). For (6, 0) and (8, 0) NTs, all adsorbed Li atoms are at a distance of 1.6 Å from the tube surface for both superlattice modifications and the Na atoms are at a distance of 1.7 Å. Only for a substantially increased NT diameter [in the case of a (12, 0) NT] do the adsorption lengths change to 1.7 and 1.8 Å,

respectively. A further increase in diameter does not change these quantities appreciably.

The charge distribution over the metal atoms of the superlattices indicates that electron transfer to carbon NTs takes place, which increases the number of majority charge carriers in the NTs; as a result, the semiconductor tubes [e.g., (8, 0) NTs] begin to take on semimetal properties and the conductivity of metal NTs [e.g., (6, 0) and (12, 0) tubes] increases. In our case, the superlattice parameter exceeds 4 Å for the chosen configuration of alkali metal atoms (Fig. 1). The lattice parameters of bcc alkali metal crystals are 3.5 Å (Li) and 4.2 Å (Na) [22] and are comparable to the respective values for the superlattices under study. Moreover, as noted above, the distance between the metal atoms and the tubes is 1.6–1.7 Å in most cases. All these facts indicate that, in an NT modified by alkali metals, there

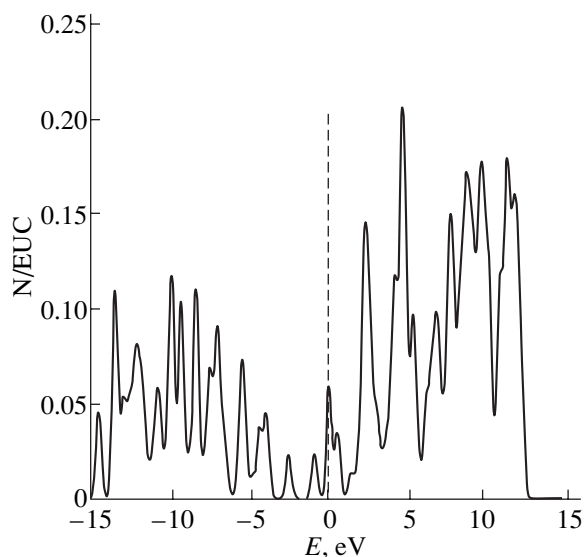


**Fig. 3.** Density of electronic states of a (6, 0) nanotube modified by Li atoms (modification I); the density is normalized to an extended unit cell. The dashed line indicates the position of the Fermi level ( $\sim 0$  eV).

are two types of conducting channels, namely, the metal superlattice and the carbon NT itself. However, the alkali metal atoms are monovalent and have one electron in their valence electron shell; according to calculations, the electron is transferred to the NT. Therefore, in our opinion, the greater contribution to the conductivity of our NTs comes from the second channel, namely, the carbon NT itself.

Thus, our calculations show once again that the surface modification of NTs by metal atoms results in the occurrence of a semiconductor–metal transition in semiconductor NTs and a metal–semiconductor transition in semimetal NTs. Therefore, by introducing, e.g., metal atoms between the layers of multilayer tubulenes, it is possible to create hollow alternating metal superlattices and NT conductors in a semiconducting carbon shell that have new conducting, magnetic, and electrical properties.

### 3. INTERCALATION OF CARBON NANOTUBES

In addition to surface modification of carbon NTs, we used the method of covalent-cyclic cluster built in via ionic bonding in the framework of the MNDO approach to calculate the electronic structures of ( $n$ , 0) NTs ( $n = 6, 8$ ) with potassium atoms introduced into the tube cavity. Two ways of intercalating carbon NTs were considered: one or two K atoms were placed at the center of an NT. The EUC of such a system consists of three layers containing six or eight carbon hexagons each and of one or two K atoms inside the NT that lie on the symmetry axis joining the centers of the opposite hexagons (Fig. 4). The distances between the nearest neighbor C atoms were chosen to be the same as those

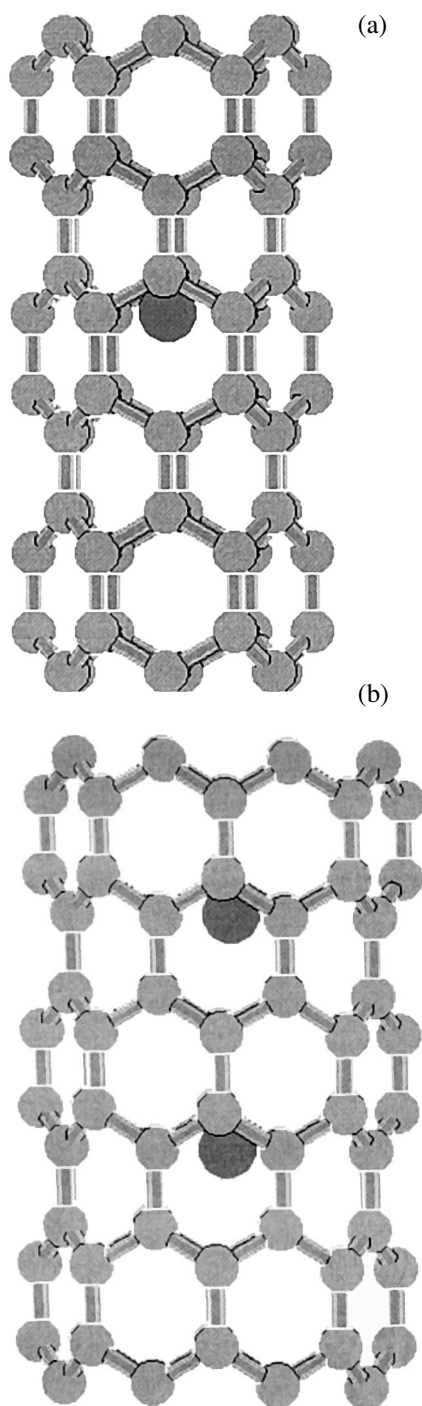


**Fig. 4.** Extended unit cell (a) of a (6, 0) nanotube with an intercalated potassium atom and (b) of a (8, 0) nanotube with two intercalated potassium atoms.

in graphite, i.e., 1.4 Å. In the case where two K atoms were intercalated, the distance between them was chosen to be  $\sim 4.5$  Å (the minimum interatomic distance in the crystal). Application of the cyclic model (with the cyclic boundary conditions) makes it possible to cor-



**Table 3.** Energy parameters of  $(n, 0)$  nanotubes ( $n = 6, 8$ ) intercalated by potassium atoms

Nanotube type	Number of K atoms	$Q$	$\Delta E_g$ , eV	$\Delta E_v$ , eV
(6, 0)	1	0.32	0.00	48.51
	2	0.32	0.00	49.53
(8, 0)	1	0.84	0.00	47.00
	2	0.84	0.00	47.23

Note:  $Q$  is the charge on a K atom,  $\Delta E_g$  is the band gap, and  $\Delta E_v$  is the valence band width.

rectly describe a special type of filled (endohedral) NTs called quantum nanowires.

Analysis of the electronic structure of the above systems shows that intercalation of an NT by K atoms produces a sharp decrease in the band gap  $\Delta E_g$ , to the point of its disappearance, which corresponds to the onset of metallic conduction in the system (Table 3). In this case, the semiconductor–metal transition is observed. This transition occurs because of the appearance of energy levels in the band gap characteristic of empty NTs; the energy levels are mainly due to the potassium AOs. The electronic density of states in an intercalated (6, 0) tubelene with one potassium atom per EUC is similar to that for a modified (6, 0) tube (Fig. 3) and obviously exhibits peaks at the Fermi level, i.e., in the region of  $-4.9\text{eV}$ ; these peaks generally result in the disappearance of the band gap characteristic of carbon NTs of this type. A similar situation is observed for semiconductor (8, 0) NTs as well.

The charge distribution over the potassium atoms also indicates the electron transfer to the NT surface; just as in the case of surface modification, the charge transfer increases the number of majority carriers in NTs and, therefore, leads to semimetal properties in semiconductor NTs [e.g., of the (8, 0) type] and to an increase in the conductivity of metal NTs [e.g., of the (6, 0) type].

#### 4. CONCLUSIONS

Thus, our calculations have shown that internal (intercalation) and surface modifications result in internal or external metallization of carbon NTs and to the occurrence of the semiconductor–metal transition in semiconductor NTs and the metal–metal transition in semimetal NTs. To date, a number of researchers have succeeded in experimentally producing carbon NTs intercalated by atoms of various metals: potassium, platinum, zirconium, chromium, silver, gold, palladium [23–27], etc. In particular, the suggested experimental methods of opening multilayer carbon NTs, filling them with metal atoms, and then closing them are described in detail in [27]. In this way, new carbon NT–based composite materials (quantum nanowires) are obtained. It should be noted that the nanometer system

size gives rise to new magnetic and electric quantum-confinement effects that can find numerous applications in modern microelectronics and nanoelectronics, which have been rapidly developing in recent years.

Our results agree well with previous quantum-chemical nonempirical studies of carbon NTs filled by transition metal atoms [28–30]. Using modifications of the linear augmented plane wave method (the linear augmented cylindrical wave method), a detailed analysis of the variation in the energy band structure of NTs after filling with various intercalants has been performed. On the whole, the conclusion was drawn that the density of states at the Fermi level increases for both metal and semiconductor NTs intercalated by various transition metals.

#### ACKNOWLEDGMENTS

The authors thank A.O. Litinskiĭ (Volgograd State Technical University) for useful discussions of the results and for valuable advice.

This study was supported in part by the Russian Foundation for Basic Research (project no. 02-03-81008) and INTAS (grant no. 00-237).

#### REFERENCES

1. S. Iijima, *Nature* **354**, 56 (1991).
2. T. W. Ebbesen and P. M. Ajayan, *Nature* **358**, 220 (1992).
3. Z. Ya. Kosakovskaya, L. A. Chernozatonskiĭ, and E. A. Fedorov, *Pis'ma Zh. Éksp. Teor. Fiz.* **56**, 26 (1992) [*JETP Lett.* **56**, 26 (1992)].
4. N. Hamada, S. Samada, and A. Oshiyama, *Phys. Rev. Lett.* **68**, 1579 (1992).
5. J. W. Mintmire and C. T. White, *Carbon* **33**, 893 (1995).
6. M. S. Dresselhaus, G. Dresselhaus, and P. C. Eklund, *Science of Fullerenes and Carbon Nanotubes* (Academic, New York, 1996).
7. A. L. Ivanovskii, *Quantum Chemistry in Materials Science: Nanotube Forms of Substance* (Ural. Otd. Ross. Akad. Nauk, Yekaterinburg, 1999).
8. Yu. E. Lozovik and A. M. Popov, *Usp. Fiz. Nauk* **167**, 752 (1997) [*Phys. Usp.* **40**, 717 (1997)].
9. A. V. Eletskiĭ, *Usp. Fiz. Nauk* **170**, 113 (2000) [*Phys. Usp.* **43**, 111 (2000)].
10. A. V. Eletskiĭ, *Usp. Fiz. Nauk* **172**, 401 (2002) [*Phys. Usp.* **45**, 369 (2002)].
11. M. M. J. Treacy, T. W. Ebbesen, and J. M. Gibson, *Nature* **381**, 678 (1996).
12. A. M. Rao, P. C. Eklund, S. Bandow, A. Thess, and R. E. Smalley, *Nature* **386**, 377 (1997).
13. E. G. Gal'pern, I. V. Stankevich, A. L. Chistyakov, and L. A. Chernozatonskiĭ, *Chem. Phys. Lett.* **214** (1–2), 345 (1993).
14. I. V. Zaporotskova, Candidate's Dissertation (Volgogr. Gos. Univ., Volgograd, 1997).
15. I. V. Zaporotskova, A. O. Litinskiĭ, and L. A. Chernozatonskiĭ, *Pis'ma Zh. Éksp. Teor. Fiz.* **66**, 799 (1997) [*JETP Lett.* **66**, 841 (1997)].

16. N. G. Lebedev, I. V. Zaporotskova, A. O. Litinsky, and L. A. Chernozatonsky, *Aerosols* **4c**, 143 (1998).
17. E. G. Gal'pern, I. V. Stankevich, A. L. Chistyakov, and L. A. Chernozatonskii, *Izv. Ross. Akad. Nauk, Ser. Fiz.* **11**, 2061 (1999).
18. L. A. Chernozatonsky, N. G. Lebedev, I. V. Zaporotskova, A. O. Litinskii, E. G. Gal'pern, I. V. Stankevich, and A. L. Chistyakov, in *Proceedings of the Second Pacific Basin Conference on Adsorption Science and Technology*, Ed. by D. Duong (Brisbane, 2000), p. 125.
19. I. V. Zaporotskova, N. G. Lebedev, and L. A. Chernozatonski, in *Abstracts of Invited Lectures and Contributed Papers on Fullerenes and Atomic Clusters* (St. Petersburg, Russia, 2001), p. 325.
20. A. O. Litinskii, N. G. Lebedev, and I. V. Zaporotskova, *Zh. Fiz. Khim.* **69** (1), 215 (1995).
21. M. J. S. Dewar and W. Thiel, *J. Am. Chem. Soc.* **99**, 4899 (1977).
22. T. Penkalya, *Zarys Krystalochemii* (Pa'nstwowe Wydawn. Naukowe, Warszawa, 1972; Khimiya, Leningrad, 1974).
23. M. Baxendale, V. Z. Mordkovich, and S. Yoshimura, *Phys. Rev. B* **56**, 2161 (1997).
24. T. Kyotani, L.-F. Tsai, and A. Tomita, *Chem. Commun.*, 701 (1997).
25. C. N. R. Rao, B. C. Satiskumar, and A. Govindaraj, *Chem. Commun.*, 1581 (1997).
26. F. Okuyama and I. Ogasawara, *Appl. Phys. Lett.* **71** (5), 623 (1997).
27. B. C. Satiskumar, A. Govindaraj, J. Mofokeng, G. N. Subbanna, and C. N. R. Rao, *J. Phys. B* **29**, 4925 (1996).
28. P. N. D'yachkov and D. V. Kirin, *Dokl. Akad. Nauk* **369** (5), 639 (1999).
29. D. V. Kirin and P. N. D'yachkov, *Dokl. Akad. Nauk* **374** (1), 68 (2000).
30. P. N. D'yachkov, *Zh. Neorg. Khim.* **46** (1), 101 (2001).

*Translated by I. Zvyagin*

---

## FULLERENES AND ATOMIC CLUSTERS

---

# Correlation of the Chemical Properties of Carbon Nanotubes with Their Atomic and Electronic Structures

F. N. Tomilin<sup>1,2</sup>, P. V. Avramov<sup>2,4</sup>, A. A. Kuzubov<sup>2,3</sup>, S. G. Ovchinnikov<sup>2,4</sup>, and G. L. Pashkov<sup>1</sup>

<sup>1</sup> Institute of Chemistry and Chemical Technology, Siberian Division, Russian Academy of Sciences,  
Krasnoyarsk, 660041 Russia

<sup>2</sup> Kirensky Institute of Physics, Siberian Division, Russian Academy of Sciences, Akademgorodok,  
Krasnoyarsk, 660036 Russia

<sup>3</sup> Siberian State Technological University, Krasnoyarsk, 660041 Russia

<sup>4</sup> Krasnoyarsk State University, Krasnoyarsk, 660079 Russia

e-mail: felix@iph.krasn.ru

Received September 4, 2003

**Abstract**—The nature of chemical bonding in carbon nanoclusters is investigated by the PM3 semiempirical quantum-chemical method. The influence of the atomic structure on the electronic characteristics and chemical properties of nanoclusters is analyzed. A  $\sigma$ - $\pi$  model is proposed for the chemical bonding in nanotubes. It is shown that, in the framework of the proposed model, nanotubes are objects characterized by a small contribution of  $\pi$  states to the valence band top. © 2004 MAIK “Nauka/Interperiodica”.

### 1. CHOICE OF THE OBJECTS FOR INVESTIGATION

The specific feature of elemental carbon is its ability to form a great variety of complex spatial structures consisting of polygons. Nanotubes were theoretically predicted by Kornilov [1, 2] in 1977 and Chernozatonskii [3] in 1991 and were found experimentally by Ijima [4] in 1991. To date, nanotubes have been used as materials for designing macromolecular structures up to hundreds of nanometers in size. The discovery of nanotubes has attracted considerable attention due to the possibility of preparing materials with unusual physicochemical properties.

In this work, we investigated the nature of chemical bonding in carbon nanoclusters and analyzed how their atomic structure affects the electronic characteristics. For model calculations, we chose two structures with the same set of atoms located in a circle of a carbon cylinder. These were zigzag (10, 0) and armchair (5, 5) nanotubes, which differ in terms of the mutual arrangement of hexagons (with respect to the longitudinal axis of the tube) and radii. The choice of the tube sizes was limited by the computational power. In particular, the number of atoms in nanotubes was varied from 150 to 250 and the tube length was varied from 15 to 25 nm. Dangling chemical bonds at the ends of carbon nanoclusters were terminated by hydrogen.

Calculations of the nanotubes were performed by the PM3 semiempirical method [5] with the GAMESS program package [6]. Semiempirical methods offer an adequate description of both the atomic structure (bond lengths, bond angles) and electronic structure (photoelectron spectra), which has been confirmed in a num-

ber of works (see, for example, [7, 8]). Moreover, the PM3 method makes it possible to calculate the electronic and atomic structures of sufficiently large-sized clusters.

### 2. CALCULATION OF THE ELECTRON DENSITIES OF STATES

The electronic structure was analyzed in terms of densities of states. We constructed an energy spectrum of a molecule in which each molecular orbital was represented by one line. The intensities of all lines were taken equal to unity. Then, each line was replaced by a Gaussian distribution whose half-width at half-maximum was equal to 0.1 eV. The intensities of all the distributions at each energy were summarized.

When constructing the partial densities of states of atomic orbitals  $x$ , the intensity of each line corresponding to the molecular orbital  $y$  was taken equal to the sum of the squares of the coefficients of the atomic orbitals  $x$  in the LCAO MO expansion of the orbital  $y$ . Then, the partial density of states was constructed by the algorithm used to construct the total density of states.

In standard quantum-chemical programs, the wave functions of the  $P$  orbitals for each atom are oriented in a global coordinate system. In order to interpret the partial densities of states for molecules with spherical and cylindrical symmetry, the basis set calculated for each carbon atom is sometimes transformed from the global coordinate system into a local coordinate system through the Euler transformation. In the case of nanotubes, this is a cylindrical transformation with respect

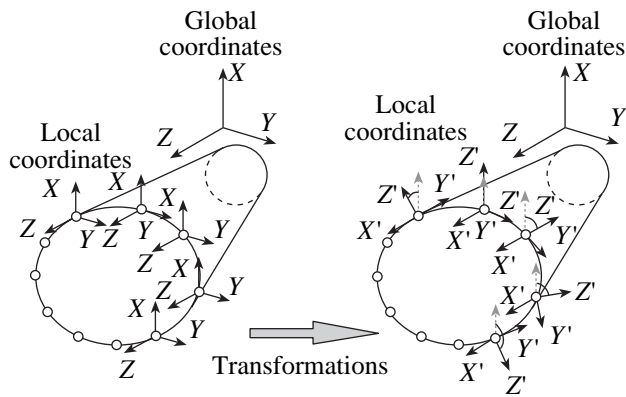


**Fig. 1.** Transformation of the  $P$  wave functions of carbon from a global coordinate system into a local coordinate system for nanotubes.

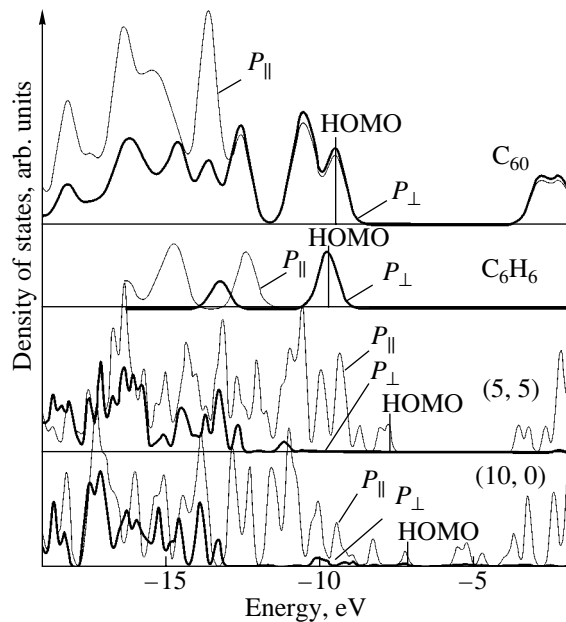


**Fig. 2.** Partial densities of  $P_{\parallel}$  and  $P_{\perp}$  states for carbon nanostructures.

to the longitudinal axis of the tube, when one of the  $P$  orbitals of a carbon atom is oriented normally to the tube surface (Fig. 1). The transformation of the basis set results in a set of orbitals oriented normally ( $P_{\perp}$ ) and tangentially ( $P_{\parallel}$ ) to the tube surface.

### 3. RESULTS OF CALCULATIONS OF NANOCCLUSERS

The nature of chemical bonding was investigated by comparing the electron densities of states. The densities of states were compared for the  $P$  orbitals directed both tangentially to the molecular plane ( $P_{\parallel}$ ,  $\sigma$  bonding) and normally to the tube surface ( $P_{\perp}$ ,  $\pi$  bonding) (Fig. 2).

When investigating nanotubes, it is of interest to compare the electronic structures of fullerenes (with a spherical structure) and benzene (with a planar structure) (Fig. 2). It can be seen from Fig. 2 that the upper levels in the valence band of benzene are characterized only by the  $\pi$  ( $P_{\perp}$ ) bonding, whereas the  $P_{\parallel}$  and  $P_{\perp}$  states are mixed (with approximately equal contributions) for  $C_{60}$  fullerene [9]. The benzene molecule has the shape of a regular hexagon, the  $\sigma$  ( $P_{\parallel}$ ) and  $\pi$  ( $P_z$  or  $P_{\perp}$ ) bonds differ in energy, and the upper orbitals consist only of the  $P_z$  ( $P_{\perp}$ ) orbitals. The  $C_{60}$  fullerene molecule is icosahedral in shape, and undistorted hexagons form faces of the structure. The curvature of the surface leads to mixing of the  $P_z$  ( $P_{\perp}$ ),  $P_x$  ( $P_{\parallel}$ ), and  $P_y$  ( $P_{\parallel}$ ) orbitals, and the upper valence levels are composed of the  $P_{\perp}$  and  $P_{\parallel}$  states.

Figure 2 shows the partial densities of  $P_{\parallel}$  and  $P_{\perp}$  states for the calculated carbon nanotubes. As can be seen from Fig. 2, the electron wave functions that are aligned normally and tangentially to the surface of the structure and, correspondingly, determine the  $\sigma$  ( $P_{\parallel}$ ) and  $\pi$  ( $P_{\perp}$ ) bonding appear to be mixed as a result of the surface curvature of the carbon nanotube. The nature of chemical bonding in nanotubes is governed by the ratio of the contributions from these wave functions to the molecular orbitals. The upper filled levels in the valence band of nanotubes involve, for the most part, the  $P_{\parallel}$  states and a small number of the  $P_{\perp}$  states. The nanotubes have a cylindrical structure. Hence, from general considerations, the ratio of the contributions from the  $P_{\perp}$  and  $P_{\parallel}$  wave functions to the valence band top should be intermediate between the corresponding ratios for benzene and fullerenes. Let us discuss why this is not the case.

First, we analyze the nature of chemical bonding in the (5, 5) and (10, 0) nanotubes. A comparison of the partial densities of states for the (5, 5) and (10, 0) tubes shows that the contribution from the  $P_{\perp}$  bonding is somewhat larger in the electronic structure of the (10, 0) tube. This can be explained by the larger diameter and, hence, by the smaller surface curvature of the tube, which leads to a larger overlap between the  $P_{\perp}$  orbitals and an increase in the contribution of the  $P_{\perp}$  orbitals to the upper occupied molecular orbital (the valence band top). However, the aforesaid does not explain the small contribution of the  $P_{\perp}$  bonding to the valence band top, even though these nanotubes are comparable in diameter to  $C_{60}$  fullerene [ $d(n, n) < d(2n, 0)$ ,  $d(5, 5) = 6.78 \text{ \AA}$ ,  $d(10, 0) = 7.83 \text{ \AA}$ ,  $d(C_{60}) = 7.09 \text{ \AA}$ ].

### 4. DISCUSSION

As was noted above, compared to fullerenes, nanotubes should possess a sufficiently high density of  $P_{\perp}$  states at the valence band top. Carbon nanotubes are intermediate in structure between planar benzene (and graphite) and ideally spherical fullerene  $C_{60}$  (symmetry

$I_h$ ). The large scatter in the diameters of nanotubes leads to mixing of the  $P_z$  ( $P_\perp$ ),  $P_x$  ( $P_\parallel$ ), and  $P_y$  ( $P_\parallel$ ) orbitals in the valence band, as is the case with fullerenes. However, the contribution from the  $P_z$  ( $P_\perp$ ) orbitals to the top of the valence band is smaller in nanotubes.

In order to answer the question as to why the electronic structure of nanotubes possesses such specific properties, it is necessary to change over from considering their geometric structure (tube radius, tube length) to a detailed analysis of the atomic structure of hexagons forming a carbon skeleton of the tube.

The bond angles in hexagons of all the structures remain constant throughout the tube and are approximately equal to  $120^\circ$  (typical angle for the  $sp^2$  hybridization), as is the case in benzene, graphite, and fullerene hexagons. The scatter of internuclear distances in nanotubes also slightly differs from the scatter characteristic of fullerene molecules and, hence, like the bond angle, does not affect the redistribution of the  $P_\parallel$  and  $P_\perp$  bonding.

An analysis of the torsion (dihedral) angles (Fig. 3) describing polygon distortions (deviations from the planarity) revealed an interesting regularity. In all nanotubes, the structure of all polygons is strongly distorted.

In the structure of the (10, 0) tube, the torsion angle in hexagons (angle between the planes formed by 1–2–3–4 and 4–5–6–1 carbon atoms; see Fig. 3a) is approximately equal to  $18^\circ$ . The hexagon plane is folded so that the fold line is parallel to the tube axis. In the structure of the (5, 5) tube, the torsion angle in the hexagon is approximately equal to  $24^\circ$ . The hexagon plane is folded, and the fold line in the hexagon is perpendicular to the tube axis (Fig. 3b).

The torsion angle in the (5, 5) structure is, on the average,  $6^\circ$  larger than that in the (10, 0) structure. The hexagon structure in the former nanotubes is formed by two well-defined planes. In the (10, 0) nanotubes, two less pronounced planes can also be distinguished in the distorted structure of hexagons. It can be seen from Fig. 2 that the density of  $P_\perp$  states at the valence band top is higher for the (10, 0) nanotube characterized by a smaller distortion of the hexagon structure, and vice versa.

Therefore, the smaller the distortion of hexagons in the structure of the carbon nanotube, the larger the overlap of the  $P_\perp$  orbitals, which, in turn, results in an increase in the density of  $P_\perp$  states at the valence band top. As a consequence, strong distortions of carbon hexagons lead to a change in the character and energy of overlap between the  $P_\perp$  orbitals and to an increase in the contribution of the  $\sigma$  bonding.

Owing to specific features in the geometry, the hexagons forming the surface of carbon nanostructures are distorted in the vast majority of carbon nanoobjects. These spatial distortions are responsible for the substantial differences in the electronic structure.

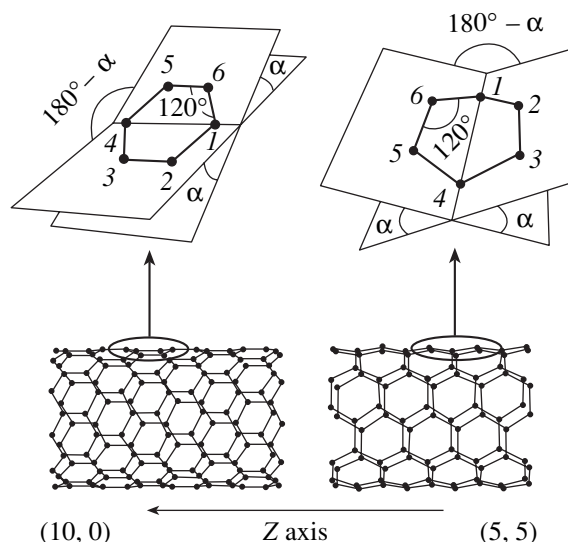


Fig. 3. Torsion angles of (a) (10, 0) and (b) (5, 5) carbon nanotubes.

In the case of planar molecules (benzene, graphite), the overlap between the  $P_z$  orbitals leads to the formation of typical  $\pi$  bonds. Since the fullerene molecule is spherical in shape, the overlap of the  $P_z$  orbitals above the molecular plane is not equivalent to that below the molecular plane. This gives rise to mixed states formed by  $\sigma$  and  $\pi$  bonds. The distortion of nanotube hexagons results in a shift of the overlap between the  $P_z$  orbitals toward the low-energy range, and, hence, the contribution of the  $P_z$  orbitals to the valence band top for nanotubes is small. The above analysis of the electronic structure permits us to elucidate particular chemical properties of carbon nanoclusters.

Fullerene molecules possess an electron affinity and act as weak oxidants in chemical reactions. This can be observed, for example, in the hydrogenation of  $C_{60}$  fullerene with the formation of  $C_{60}H_{36}$  as the reaction product [10]. At room temperature,  $C_{60}$  fullerene oxidizes only under irradiation with photons, which is explained by the formation of negative  $O_2^-$  ions with a high reactivity [10]. The composition of the products of fullerene fluorination substantially depends on the reaction conditions. The reaction of  $C_{60}$  with NaF at  $T = 500\text{--}550$  K predominantly leads to the formation of  $C_{60}F_{46}$  (with addition of 10–15%  $C_{60}F_{48}$ ). Chlorination of  $C_{60}$ , as a rule, results in the formation of compounds containing either 12 or 24 chlorine atoms. Moreover, fullerene participates in addition reactions with the formation of products involving hydrogen radicals, phosphorus, halogens, metals and their oxides, benzene rings and their derivatives,  $NO_2$ , alkyl radicals, etc. [10].

As a rule, approximately 5–8% of carbon atoms in nanotubes undergo chemical transformation under soft conditions depending on the type of carbon structures

and reactants. Usually, these atoms belong to defects in the nanostructure. In this case, the terminal atoms have a higher reactivity as compared to atoms located on the nanotube surface. Under sufficiently severe conditions (strong acids, high temperatures, plasma activation, etc.), more than 50% of carbon atoms undergo chemical transformation. This leads to a change in the properties of nanotubes, in particular, to a decrease in the stability [11–16].

Owing to formally identical  $sp^2$  hybridization, the same type of carbon–carbon bonds, and the predominance of hexagons in all structures, fullerenes and nanotubes should resemble graphite in terms of their chemical properties. Actually, nanotubes (compared to fullerenes) are similar in terms of their chemical properties to graphite, because they are rather inactive in reactions.

The chemical properties of fullerenes can be explained by the difference in the overlap of the  $P_{\perp}$  orbitals above and below the molecular plane due to the sphericity of the molecule. The overlap density above the fullerene surface is lower. As a result, the corresponding orbitals are more susceptible to attacks by electrophilic agents. For this reason, fullerene more easily enters into chemical reactions as compared to graphite, in which the overlap densities of the  $P_{\perp}$  orbitals above and below the plane are identical to each other. For benzene, the configuration of the  $P_{\perp}$  orbitals is the same as for graphite. As a consequence, reactions of substitution for hydrogen rather than reactions of electrophilic addition to the  $\pi$  cloud are characteristic of benzene.

All the aforementioned features of fullerene molecules allow us to draw the conclusion that nanotubes should also readily enter into addition reactions. Since the geometry of nanotubes is similar to that of fullerenes, the overlap of the  $P_{\perp}$  orbitals above and below the tube surface should also be similar to the overlap in fullerene. However, this is not the case, because all hexagons in nanotubes are strongly distorted. As a result, the contribution of the  $\pi$  states to the valence band top is small, since these states are shifted to the low-energy range. Therefore, the reactivity of nanotubes is considerably lower than that of fullerenes.

## 5. CONCLUSIONS

Thus, the electronic structure of carbon nanotubes was investigated in the framework of the  $\sigma$ – $\pi$  model. It was shown that carbon nanotubes are objects characterized by a small contribution of the  $\pi$  states to the valence band top. The surface curvature of carbon nanostructures leads to mixing of the atomic orbitals aligned tangentially and normally to the surface. The ratio of the contributions from these wave functions determines the nature of chemical bonding in the nanostructures. Owing to specific features in the geometry, all hexagons forming the tube wall are strongly distorted in all carbon nanotubes. These spatial distortions of hexagons are responsible for the substantial differ-

ences in the electronic structure. The distortion affects the character and energy of overlap between the  $P_z$  orbitals, which leads to an increase in the contribution of  $\sigma$  bonding and, correspondingly, to a decrease in the contribution of  $\pi$  bonding to the upper occupied orbitals. Therefore, the smaller the distortion of hexagons in the structure of carbon nanotubes, the larger the overlap of the  $P_{\perp}$  orbitals.

## ACKNOWLEDGMENTS

This work was performed at the “Quantum-Chemical Calculations of Nanoclusters” Collective Use Center of the Krasnoyarsk Center of Science and Education in High Technology, which is supported by the Russian State Federal Program “Integration of Higher Education and Fundamental Science” (projects nos. 31 and 69) and the 6th Competition of Research Projects of Young Scientists of the Russian Academy of Sciences (project no. 155).

## REFERENCES

1. M. Yu. Kornilov, Dokl. Akad. Nauk Ukr. SSR, Ser. B: Geol. Khim. Biol. Nauki **12**, 1097 (1977).
2. M. Yu. Kornilov, Khim. Zhizn', No. 8, 22 (1985).
3. L. A. Chernozatonskii, Phys. Lett. A **160** (4), 392 (1991).
4. S. Iijima, Nature **354**, 56 (1991).
5. J. J. Stewart, J. Comput. Chem. **10** (2), 209 (1989).
6. M. W. Shmidt, K. K. Baldrige, J. A. Boatz, *et al.*, J. Comput. Chem. **14**, 1347 (1993).
7. S. A. Varganov, P. V. Avramov, and S. G. Ovchinnikov, Fiz. Tverd. Tela (St. Petersburg) **42** (11), 2103 (2000) [Phys. Solid State **42**, 2168 (2000)].
8. L. G. Bulusheva, A. V. Okotrub, D. A. Romanov, and D. Tomanek, Phys. Low-Dimens. Semicond. Struct., No. 3–4, 107 (1998).
9. A. A. Kuzubov, P. V. Avramov, S. G. Ovchinnikov, *et al.*, Fiz. Tverd. Tela (St. Petersburg) **43** (9), 1721 (2001) [Phys. Solid State **43**, 1794 (2001)].
10. A. V. Eletskiĭ and B. M. Smirnov, Usp. Fiz. Nauk **165**, 977 (1995) [Phys. Usp. **38**, 935 (1995)].
11. A. Hirsch, Angew. Chem. Int. Ed. Engl. **41** (11), 1853 (2002).
12. A. Kuznetsova, I. Popova, J. T. Yates, Jr., *et al.*, J. Am. Chem. Soc. **43**, 10699 (2001).
13. T. W. Odom, J.-L. Huang, P. Kim, and C. M. Lieber, J. Phys. Chem. B **104**, 2794 (2000).
14. J. Liu, A. G. Rinzler, H. Dai, *et al.*, Science **280**, 1253 (1998).
15. J. Chen, M. A. Hamon, H. Hu, *et al.*, Science **282**, 95 (1998).
16. M. Monthieux, B. W. Smith, B. Bouteaux, *et al.*, Carbon **39**, 1251 (2001).

*Translated by N. Korovin*



**METALS  
AND SUPERCONDUCTORS**

# Kinetics of Interatomic Correlations in a Ni–11.8 at. % Mo Alloy

**S. M. Bokoch and N. P. Kulish**

Shevchenko National University, Vladimirskaya ul. 64, Kiev, 01033 Ukraine

e-mail: srg@univ.kiev.ua

Received August 18, 2003

**Abstract**—The kinetics of interatomic correlations in low-concentration Ni–Mo (8–18 at. % Mo) alloys is studied on the basis of the data on residual-resistivity measurements upon isothermal and isochronous annealings, as well as using x-ray diffuse scattering. The atomic ordering kinetics studied at low temperatures (~373 K) suggests the coexistence of clusters of various ordered structures, which transform in a complex fashion depending on the fixed short-range order structure in various temperature ranges. For example, spinodal ordering of  $N_2M_2$ -,  $N_3M$ -, and  $N_4M$ -type structures is observed in low-concentration Ni–Mo alloys. © 2004 MAIK “Nauka/Interperiodica”.

## 1. INTRODUCTION

As follows from the phase state diagram, several equilibrium ordered phases, namely,  $\beta$ -Ni<sub>4</sub>Mo ( $D1_a$ ),  $\gamma$ -Ni<sub>3</sub>Mo ( $DO_{22}$ ), and  $\delta$ -NiMo ( $P2_12_12_1$ ) containing 20, 25, and 50 at. % Mo, respectively, are formed in Ni–Mo alloys. In this system, ordering processes were studied in most detail for stoichiometric and close-to-stoichiometric compositions [1–6]. A specific feature of these alloys in the concentration range 8–33 at. %, as well as of some other alloys (Au<sub>4</sub>V, Au<sub>4</sub>Fe, Au<sub>4</sub>Mn, Au<sub>4</sub>Cr) is

the presence of  $\left\{1\frac{1}{2}0\right\}$ -type x-ray diffuse scattering

maxima in samples quenched from the disordered fcc phase region. Figure 1 shows that the positions of these maxima differ from the arrangement of superstructural reflections corresponding to long-range order equilibrium phases (the superstructure peaks of the  $DO_{22}$  phase

are at the  $\frac{1}{5}\{420\}$  and  $\frac{1}{3}\{420\}$  sites). In Ni–Mo alloys, ordering processes are accompanied by nucleation and competition between a number of long-range order structures. All these superstructures [Ni<sub>4</sub>Mo ( $D1_1$ ), Ni<sub>3</sub>Mo ( $DO_{22}$ ), Ni<sub>2</sub>Mo ( $Pt_2Mo$ ), Ni<sub>2</sub>Mo<sub>2</sub> ( $I4_1/amd$ )] can be described using static concentration waves [7], whose amplitude is related to the long-range order parameters. In the atomic representation, these structures are characterized by a certain filling of the  $\{420\}$ -family planes with Ni and Mo atoms (Fig. 2).

Depending on the alloy stoichiometry, the transition from the quenched state, to which the diffuse maxima

at  $\left\{1\frac{1}{2}0\right\}$ -type sites correspond, to the long-range order state is accompanied by the formation and development of various intermediate structures. For example, it is assumed that the  $M_2N_2$ -to- $D1_a$  transformation takes place in a Ni<sub>4</sub>Mo alloy, reasoning from the contin-

uous intensity transfer from the special points  $\left\{1\frac{1}{2}0\right\}$

to the  $\frac{1}{5}\{420\}$  sites observed upon low-temperature

annealing. This transformation corresponds to a continuous transition, which, at the first stage, can promote the development of the  $M_2N_2$  structure accompanied by

an increase in the intensity of the  $\left\{1\frac{1}{2}0\right\}$  diffuse maxima, followed by their decay and the generation of a

$\frac{1}{5}\{420\}$  concentration wave. Annealing at temperatures close to the order–disorder transition temperature

$T_C$  causes a first-order phase transition, at which the

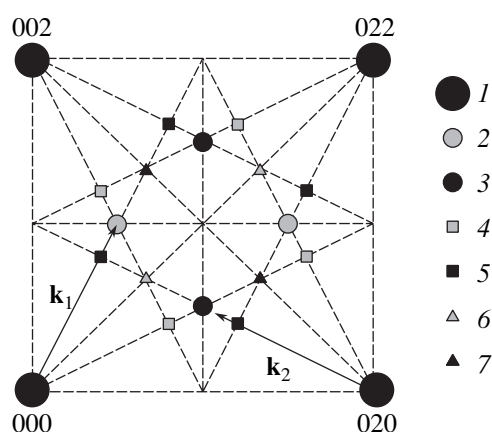


**Fig. 1.** Arrangement of the sites, superlattice reflections, and diffuse maxima in the (001)\* plane of the reciprocal lattice: (1) fcc lattice sites, (2, 3)  $\left\{1\frac{1}{2}0\right\}$  sites, (4, 5)  $\frac{1}{5}\{420\}$   $D1_a$  sites, and (6, 7)  $\frac{1}{3}\{420\}$   $Pt_2Mo$  sites.

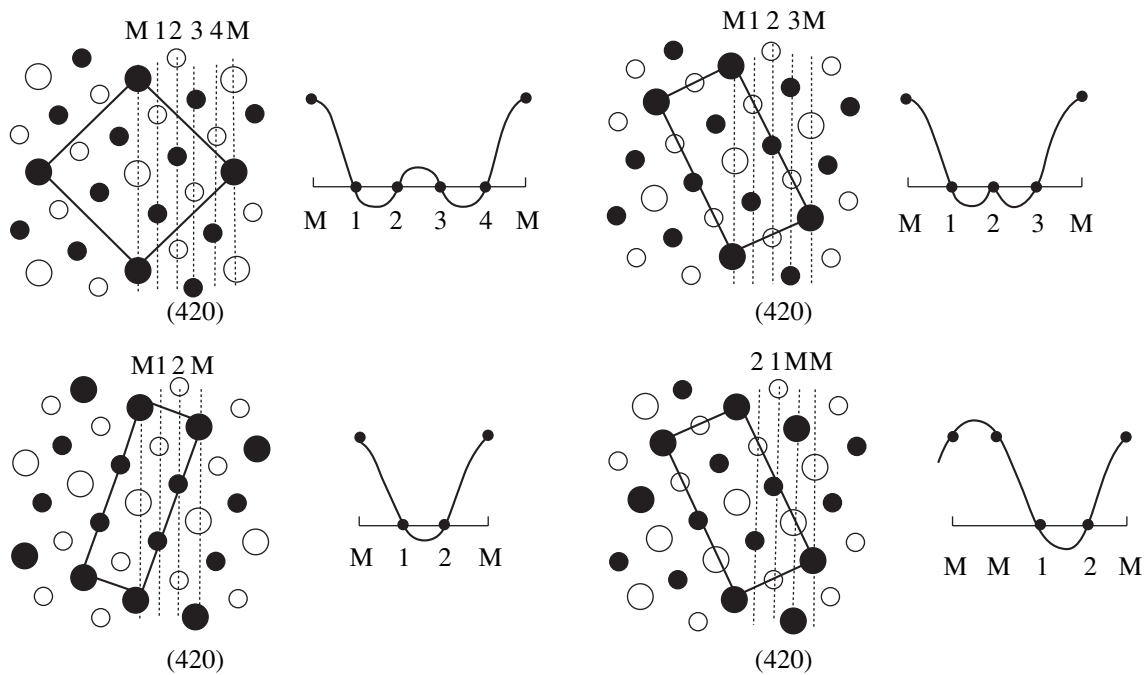


**Fig. 2.** Filling of the  $\{420\}$  planes, with static concentration waves of subcell clusters for various superstructures observed in Ni–Mo alloys ( $[001]$  projection).

nucleation and growth of  $D1_a$ -structure particles are observed, accompanied by the initiation of superstructure reflections  $\frac{1}{5}\{420\}$ .

The transition from the quenched state to the equilibrium ordered state in a  $\text{Ni}_3\text{Mo}$  alloy is more complex and is associated with the short-range order structure to which the  $\left\{1\frac{1}{2}0\right\}$  diffuse maxima correspond. According to the model developed in [8, 9], the short-range order state that arises during quenching is a result of the initiation and amplification of concentration waves characterized by the wave vectors  $\mathbf{k}$  at special high-symmetry points  $\left\{1\frac{1}{2}0\right\}$  of the fcc structure.

These waves are caused by instabilities of the fcc phase with respect to such waves and occur below the instability temperature  $T_i$ . Concentration waves of the  $\left\{1\frac{1}{2}0\right\}$  type correspond to a coherent  $\text{Ni}_2\text{Mo}_2$  structure, whose development is caused by spinodal ordering and represents an order–disorder transition of second order. The preferred instability of the fcc phase with respect to the ordered  $\text{Ni}_2\text{Mo}_2$  structure in comparison with other possible ordered structures is confirmed by calculations of the free energy  $F(\eta)$  of various structures. This energy was determined by appropriately selecting the pair interaction energies for the three nearest coordination shells [2], as well as using *ab initio* cal-

culated concentration-dependent values of these energies for the first four coordination shells [4]. In addition to thermodynamic factors, the generation of an ordered  $\text{Ni}_2\text{Mo}_2$  structure is also facilitated by the largest amplification rate of the concentration wave inherent to this structure. This rate is determined by the second derivative of the free energy  $F''_{\text{Ni}_2\text{Mo}_2}$  for the long-range order parameter  $\eta = 0$ , i.e., by the curvature of the  $F(\eta)|_{\eta=0}$  curve.

However, in contrast to  $\text{Ni}_4\text{Mo}$  alloys, which are characterized by the transformation of only one  $\left\{1\frac{1}{2}0\right\}$ -type concentration wave,  $\text{Ni}_3\text{Mo}$  alloys feature secondary ordering as a result of instability of the formed nonstoichiometric, partially ordered  $\text{Ni}_2\text{Mo}_2$  structure at  $T \rightarrow 0$  K. The secondary ordering in this  $\text{Ni}_2\text{Mo}_2$  structure can be accompanied by the development of long-wavelength concentration waves with the wave vector  $\mathbf{k}\langle 000\rangle$ , which results in decay of the structure into a phase mixture containing a disordered solid solution and a stoichiometric ordered  $\text{Ni}_2\text{Mo}_2$  structure. Another type of secondary ordering is the formation of concentration wave  $\langle 100\rangle$ , which gives rise to the  $D0_{22}$  structure. In the third case of secondary ordering, there appears a wave analogous to the concentration wave  $\left\{1\frac{1}{2}0\right\}$  generating the nonstoichiometric  $\text{Ni}_2\text{Mo}_2$  structure but with a wave vector  $\mathbf{k}_2$  perpendicular to the primary-wave direction with vector  $\mathbf{k}_1$ . The



interaction between these waves gives rise to the  $N_3M$  structure. Thus, at the initial stage, ordering in a quenched sample arises as a result of instability with respect to the formation of the  $Ni_2Mo_2$  structure and subsequent annealing at various temperatures brings about the formation of various structures caused by secondary ordering [3].

The above concepts regarding the initial stage of transformations from short-range order to equilibrium long-range order in Ni–Mo alloys were developed using the results of electron-microscopy studies of stoichiometric samples. Such studies do not allow quantitative description of the short-range order structure in the generated structures. This circumstance is especially important in the case of low-concentration alloys far from stoichiometry. Taking into account the spinodal ordering dynamics of these structures, which should be observed in a wide concentration range, one would expect, on the one hand, the formation of concentration waves similar to those described above and, on the other hand, the absence of certain competing structures associated with equilibrium intermetallic ordered phases. A comparison of the ordering processes in  $Ni_4Mo$  and  $Ni_3Mo$  alloys occurring at the initial stage shows that they differ substantially. Hence, it is impossible to predict the short-range order structure at alloy concentrations below the region of existence of the ordered  $Ni_4Mo$  phase.

This study is devoted to the transformation of the short-range order structure in low-concentration Ni–Mo alloys. We took samples containing 8, 11.8, 14, and 18 at. % molybdenum. The short-range order structure was approximated by studying the isochronous and isothermal dependences of the residual resistivity. The quantitative characteristics were determined using x-ray diffuse scattering.

It should be noted that, in the absence of structural changes in the solid-solution region, the residual resistivity is very sensitive to evolution of the short-range order structure [10]. However, since this effect is integral (as in the case of electron diffraction studies), it is impossible to obtain a detailed description of changes in the behavior of interatomic correlations by measuring the residual resistivity. The short-range order kinetics can be uniquely described only by studying x-ray diffuse scattering (or elastic incoherent scattering of thermal neutrons).

## 2. RESIDUAL RESISTIVITY OF Ni–Mo ALLOYS

Ni–Mo alloy samples were prepared differently for various studies. To measure the residual resistivity, polycrystalline samples of all compositions indicated above were used. The samples were obtained by smelting a charge that contained vacuum-remelted Ni of 99.95% purity and Mo of 99.99% purity in a high-frequency induction furnace in an alumina crucible in

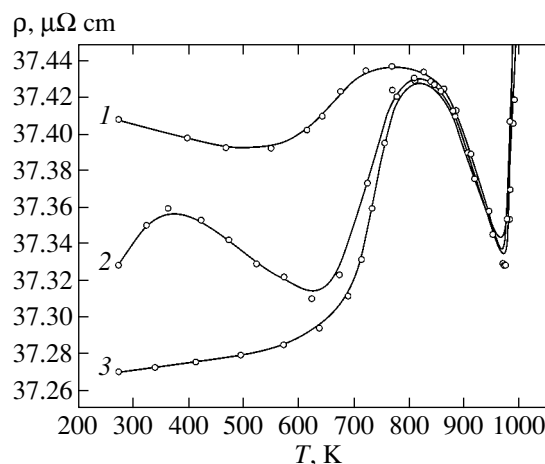


Fig. 3. Isochronous dependences of the residual resistivity in a Ni–11.8 at. % Mo alloy for (1) the annealed, (2) quenched, and (3) deformed initial states.

purified argon. The casts were homogenized at a temperature of 1123 K for 75 h. Then, the casts were used to obtain rods, which were stretched into wire and rolled into strips ~0.1 mm thick. The room-temperature plastic deformation exceeded 1000%. Such an initial state of the sample corresponds to a deformed state. Then, samples deformed in such a way were annealed at a temperature of 1273 K for 2 h in vacuum and slowly cooled (at a rate of 2 K/min) to room temperature. Such processing yields another (in comparison with deformation) initial state of the short-range order, which corresponds to the annealed state. A third initial state of the short-range order was obtained by 1-h annealing of a deformed sample at 1223 K in vacuum, followed by room-temperature quenching in a 10 wt % NaOH solution in water in a special setup.

All samples in each of the initial states were isochronously annealed. Such annealing was carried out in the temperature range 323–1073 K in steps of 30 K. After 10-min annealings at each temperature in vacuum, the samples were quenched. The residual resistivity was measured in liquid nitrogen using the four-probe potentiometric method. The accuracy of determining the relative residual resistivity,  $\Delta\rho/\rho$ , was 0.001%. The kinetics of the residual resistivity for annealed, and quenched samples was studied upon isothermal annealing at the temperature  $T_a = 323$  and 373 K.

Figure 3 shows the isochronous curves of the residual resistivity for a Ni–11.8 at. % Mo alloy in the three initial states indicated above. For the other concentrations, the same features in the behavior of the residual resistivity are observed, which suggests that the ordering processes in the Ni–Mo composition range under study are similar.

We can see that the residual resistivities in the initial state differ significantly. In the annealed state, the resid-

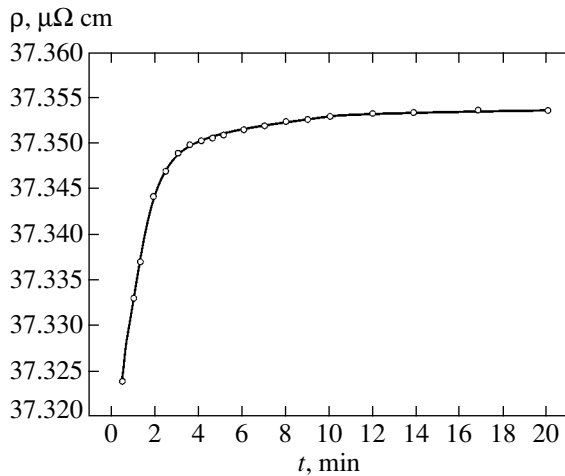


**Fig. 4.** Kinetics of the residual resistivity of a Ni–11.8 at. % Mo alloy quenched at  $T_q = 1223$  K.

ual resistivity is larger than that for the other treatments. Obviously, the defect structure is different in all the initial states; however, the differences observed in the residual resistivity are so significant that they cannot be explained by electron scattering at defects. Therefore, it can be assumed that these differences are caused by the difference in the short-range order structure of the solid solution that takes place in each initial state. As the isochronous annealing temperature increases, i.e., for values of the residual resistivity measured in the states that arise in alloys at various temperatures, the behavior of the resistivity depends on the initial state (up to  $T = 773$  K for a Ni–11.8 at. % Mo alloy; see Fig. 3).

For example, the residual resistivity of annealed samples (curve 1) decreases at low temperatures, in contrast to that of quenched (curve 2) and deformed (curve 3) samples.

For the deformed state, the resistivity increases upon isochronous annealing, whereas it passes through a maximum after quenching.

At higher temperatures of isochronous annealing, beginning from  $T \approx 573$ – $623$  K, the resistivity increases for all initial states, although its values differ. For annealing temperatures above  $T \approx 773$  K, the residual resistivities sharply decrease and are identical for all initial treatments.

Figure 4 shows the evolution of the residual resistivity measured upon isothermal annealing of the quenched sample. The annealing temperature  $T = 373$  K corresponds to the first maximum of the isochronous curve measured after the sample quenching (curve 2 in Fig. 3). We can see that a sharp increase in the resistivity is initially observed, which is then slowed down and tends to flatten out.

The isochronous and isothermal curves of the residual resistivity suggest the complexity of the ordering processes occurring in low-concentration Ni–Mo alloys at various temperatures and durations of annealing.

### 3. SHORT-RANGE ORDER STRUCTURE IN A Ni–11.8 AT. % Mo ALLOY: RESULTS AND DISCUSSION

The short-range order structure was studied using x-ray diffuse scattering in a Ni–11.8 at. % Mo single crystal  $2.5 \times 6 \times 6$  mm in size grown in argon in an alundum crucible with a conic seed region. An outer facet of the sample under study was cut parallel to the (100) plane. The sample was studied in the annealed and quenched initial states. Both initial states were obtained similarly to the states of the samples used for measuring the residual resistivity. To study the intensity kinetics associated with the short-range order, the quenched sample was isothermally annealed at  $T_a = 373$  K; this was carried out in the same way as in the study of the residual resistivity.

X-ray diffuse scattering was measured using hard  $\text{MoK}_\alpha$  radiation, which made it possible to separate high harmonics and the fluorescent component from the spectrum of x-rays monochromatized by a one-dimensionally bent LiF crystal through selecting the operating conditions of the setup [11]. The use of obliquely incident hard x-rays in diffractometry of the samples and the use of low-absorbing fused quartz as a reference for measuring the intensities in absolute electronic units require corrections for the angular dependence of absorption [12]. Taking into account these corrections, the diffuse scattering intensity  $I_{sp}(\theta)$  from a sample in electronic units expressed in terms of the intensity from the reference at an angle  $\theta_0$  is given by

$$I_{sp}(\theta) = I_{st}(\theta_0) \frac{I_{sp}(\theta_0)(n/2\mu L)_{sp}}{I_{st}(\theta_0)(n/2\mu L)_{st}} \times \frac{1 + \gamma' \cos^2 2\theta_M \cos^2 2\theta_0}{1 + \gamma' \cos^2 2\theta_M \cos^2 2\theta}, \quad (1)$$

where  $I_{st}(\theta_0)$  is the experimentally measured scattering intensity from fused quartz and  $L_{st}$  and  $L_{sp}$  are the corrections to the absorptance  $\mu$  for the reference and the sample, respectively. The monochromator imperfection is taken into account by the parameter  $\gamma'$ , which is close to unity for the LiF crystal used.

The intensity components associated with the short-range order and static and dynamic distortions, which modulate diffuse scattering in alloys [13–15], were separated using the Cohen–Georgopoulos method [16–18]. This separation is based on the difference in the symmetry of diffuse background modulation in the reciprocal space between these scattering components. The intensities of two-phonon and multiphonon thermal diffuse scattering were calculated using the technique described in [11]. The distribution of the x-ray diffuse scattering intensity was studied at the positions

equivalent to the points  $\frac{1}{4}(420)$  ( $\text{Ni}_2\text{Mo}_2$ ),  $\frac{1}{5}(420)$  ( $\text{Ni}_4\text{Mo}$ ), and  $\frac{1}{3}(420)$  ( $\text{Ni}_2\text{Mo}$ ) and in their vicinity cov-

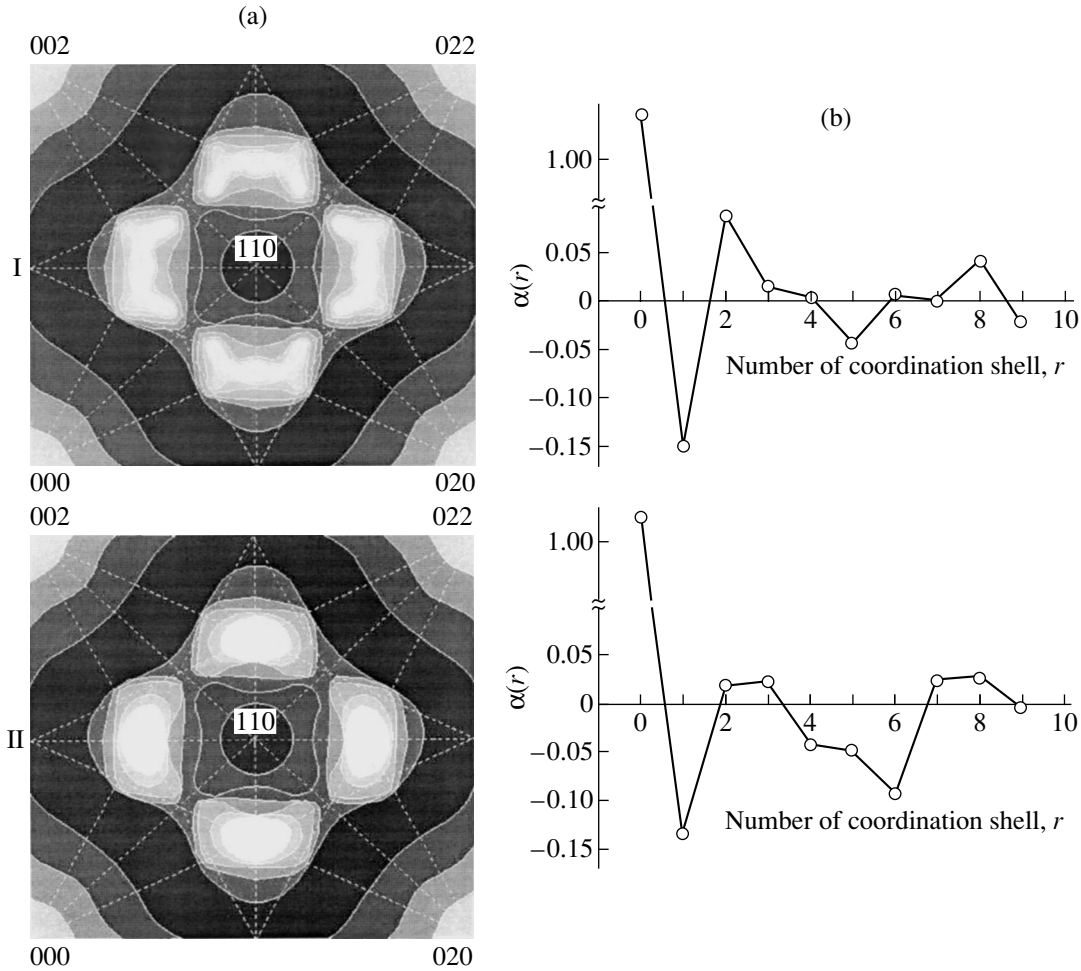


**Fig. 5.** (a) Distribution of the short-range order scattering intensity  $I_{\text{SRO}}(h_1, h_2, h_3)$  in the  $(001)^*$  plane and (b) the short-range order parameters  $\alpha(r)$  for (I) annealed and (II) quenched states of a Ni–11.8 at. % Mo alloy.

ering the part of the irreducible Brillouin zone in the  $(001)^*$  plane of the reciprocal space.

The Warren–Cowley short-range order parameters  $\alpha_{lmn}$  for atomic positions with coordinates  $lmn$  were calculated by taking the inverse Fourier transform of the determined intensities of the short-range order  $I_{\text{SRO}}(h_1, h_2, h_3)$  at a given point in reciprocal space with coordinates  $h_1 h_2 h_3$  according to the expression

$$\alpha_{lmn} = k \sum_{h_1, h_2, h_3=0}^1 I_{\text{SRO}}(h_1, h_2, h_3) \cos(\pi h_1 l) \times \cos(\pi h_2 m) \cos(\pi h_3 n), \quad (2)$$

where  $k$  is the normalizing factor, which depends on the position of the atom.

A study of the short-range order structure of the Ni–11.8 at. % Mo alloy in the initial annealed state shows that the intensity  $I_{\text{SRO}}(h_1, h_2, h_3)$  is mostly concentrated

at the  $\left\{1\frac{1}{2}0\right\}$  and  $\frac{1}{5}\{420\}$  sites and in their vicinities, in particular, along the  $[210]$  direction. At the point  $\frac{1}{3}\{420\}$ , the short-range order intensity is low (Fig. 5a, panel D). The short-range order parameters  $\alpha(lmn)$  are shown in Fig. 5b, panel I. Despite the smallness of the reciprocal space volume in which the intensities  $I_{\text{SRO}}(h_1, h_2, h_3)$  used for calculating  $\alpha(lmn)$  were separated, these parameters are in good agreement with those previously determined with a large number of points  $h_1 h_2 h_3$  for the same initial state [19–21].

Comparison of these parameters  $\alpha(lmn)$  with the short-range order parameters for the  $D1_a$ ,  $DO_{22}$ ,  $N_3M$ , and  $N_2M_2$  structures suggests that the short-range order related to the  $D1_a$  type is dominant in this initial state.

The rather intense diffuse maxima at the  $\left\{1\frac{1}{2}0\right\}$  sites show that the short-range order structure is more com-

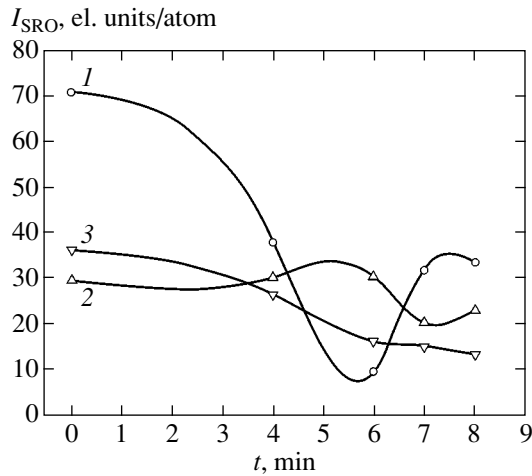


Fig. 6. Kinetics of the short-range order scattering intensity  $I_{\text{SRO}}$  at the positions (1)  $N_2M_2$ , (2)  $N_4M$ , and (3)  $N_2M$ .

plex and represents a mixed state that also includes the  $N_2M_2$ -type short-range order.

When a sample is quenched from 1223 K, the distribution of diffuse scattering associated with the short-range order changes abruptly. The intensity  $I_{\text{SRO}}(h_1, h_2, h_3)$  at the  $\left\{1\frac{1}{2}0\right\}$  sites and neighboring points increases by several times. For example, the intensity at this position is 31.4 and 70.9 el. units/atom for the annealed and quenched states, respectively. The intensity at the  $\frac{1}{3}\{420\}$  sites and their vicinities also increases (Fig. 5a, panel II). The predominance of the  $N_2M_2$  structure is also confirmed by the calculated parameters  $\alpha(lmn)$  (Fig. 5b, panel II). It is worth noting that the parameter  $\alpha(lmn)$  for the sixth shell appreciably increases, which is inherent to the  $N_2M_2$  structure. However, in this case, we cannot argue that only the  $N_2M_2$  short-range order exclusively exists.

The distribution of the short-range scattering intensity suggests that the short-range order structure in the quenched state corresponds to the coexistence of spinodal-ordered  $N_2M_2$ ,  $N_2M$ , and  $N_4M$  structures. A comparison of the data on spinodal ordering with the data on residual resistivity in the annealed and quenched initial states shows that the predominant  $D1_a$  short-range order in the annealed alloy samples causes an increase in their resistivity. The preferential formation of the  $N_2M_2$  short-range order in the quenched state causes a decrease in resistivity.

Isothermal annealing of the quenched sample for 4 min at 373 K results in a sharp decrease in the intensity  $I_{\text{SRO}}(h_1, h_2, h_3)$  at the point  $\left\{1\frac{1}{2}0\right\}$ , while the intensities at the two other points remain almost unchanged

(Fig. 6). At the same time, the intensity increases in strands directed from the point  $\left\{1\frac{1}{2}0\right\}$  to the positions  $\frac{1}{3}\{420\}$  and  $\frac{1}{5}\{420\}$ . These intensities, especially near the point  $\frac{1}{3}\{420\}$ , even exceed  $I_{\text{SRO}}(h_1, h_2, h_3)$  at the positions of the  $D1_a$  and  $N_2M_2$  superstructures (Fig. 7a, panel I).

Thus, the destruction of the ordered  $N_2M_2$  structure described by the unit concentration wave  $\left\{1\frac{1}{2}0\right\}$  is accompanied (as noted for the initial stages of  $\text{Ni}_3\text{Mo}$  alloy ordering [2, 3]) by secondary ordering caused by interference from mutually perpendicular  $\left\{1\frac{1}{2}0\right\}$  concentration waves, i.e., by the nucleation of the  $N_3M$  structure. Despite the fact that the short-range order parameters  $\alpha(lmn)$  (Fig. 7b, panel I) still correspond to the  $N_2M_2$  structure, their behavior differs from that of  $\alpha(lmn)$  for the initial state. It is worth noting the smallness of the parameter for the fourth coordination shell and the relative values of the parameters for other shells, whose behavior is similar to that of the Warren-Cowley parameters for an ordered  $D0_{22}$  structure. It is reasonable to expect that the destruction of the ordered  $N_2M_2$  structure will be accompanied by an increase in the residual resistivity, which does actually take place at this stage of the ordering kinetics of the quenched sample (Figs. 3, 4).

Further isothermal annealing for 6 min is accompanied by a change in the short-range order, which affects the  $I_{\text{SRO}}(h_1, h_2, h_3)$  distribution (Fig. 7a, panel II). A specific feature of this distribution is the appreciable decrease in intensity at points  $\left\{1\frac{1}{2}0\right\}$  and a certain increase in intensity at the position  $\frac{1}{5}\{420\}$  (Fig. 6). The intensity at points  $\frac{1}{3}\{420\}$  and  $\frac{1}{5}\{420\}$  exceeds the intensity at  $\left\{1\frac{1}{2}0\right\}$ , although their difference is not as distinct as that for the initial quenched state.

The intensity of the strands in the directions from  $\left\{1\frac{1}{2}0\right\}$  to  $\frac{1}{3}\{420\}$  and  $\frac{1}{5}\{420\}$  exceeds the intensity at the point  $\left\{1\frac{1}{2}0\right\}$  itself. The most significant increase is observed near the latter two positions. The change in the short-range order parameters (Fig. 7b, panel II) suggests preferential formation of the  $N_3M$  structure.

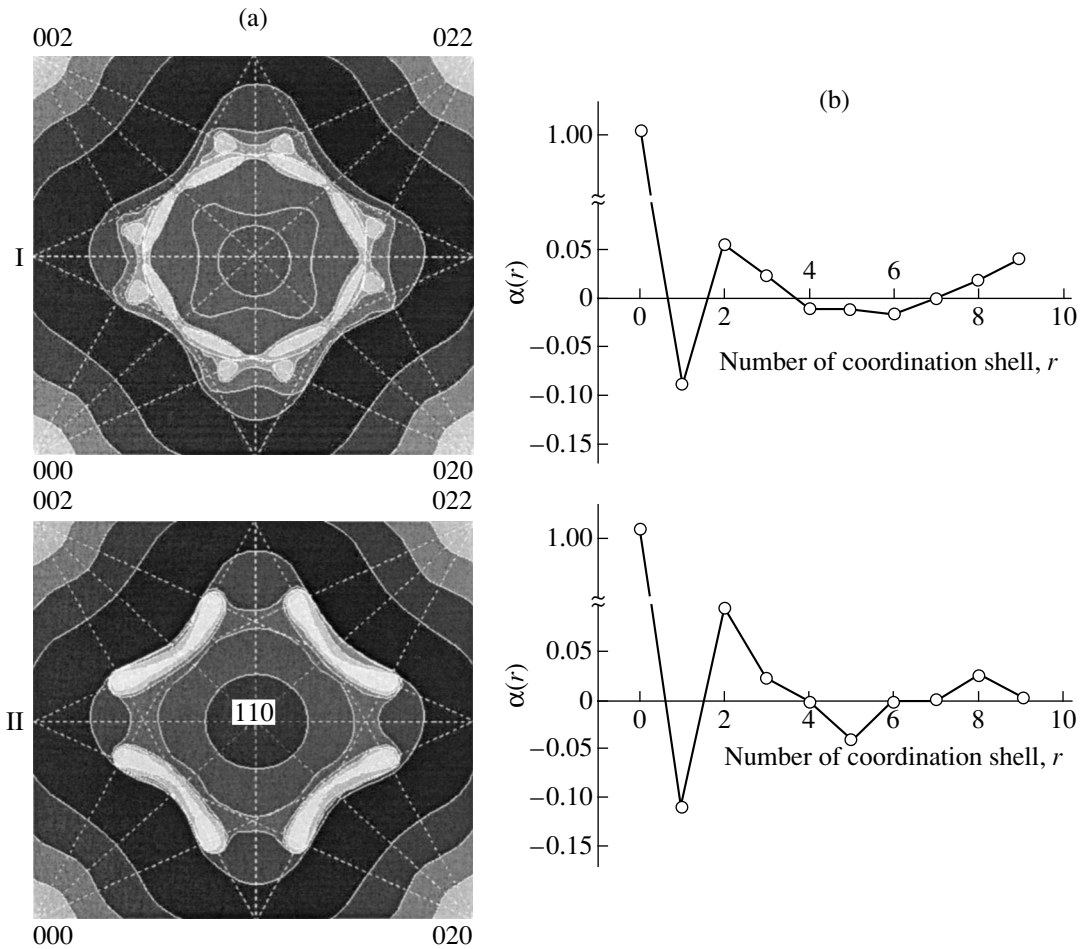


**Fig. 7.** (a) Distribution of the short-range order scattering intensity  $I_{\text{SRO}}(h_1, h_2, h_3)$  in the  $(001)^*$  plane and (b) the short-range order parameters  $\alpha(r)$  for quenched Ni–11.8 at. % Mo alloy samples isothermally annealed at  $T_a = 373$  K for (I) 4 and (II) 6 min.

Thus, as time passes, the  $N_3M$  structure is formed in the quenched sample at 373 K due to secondary ordering. This structure is a mixture of clusters [2, 3] corresponding to the  $N_4M$  and  $N_2M$  structures. The formation of this structure is accompanied by a decrease in the residual resistivity, which results in a change in slope of the kinetic curve (Fig. 4). Upon isochronous annealing (Fig. 3), the resistivity decreases in the temperature ranges  $\sim 323$ – $573$  and  $\sim 373$ – $623$  K for annealed and quenched samples, respectively. It is reasonable to assume that such a decrease in the residual resistivity is also caused by interference from concentration waves  $\left\{1\frac{1}{2}0\right\}$ , i.e., by the nucleation of the  $N_3M$  structure. From the fact that ordering with the formation of clusters of the  $\text{Ni}_4\text{Mo}$  structure results in an increase in the resistivity, it follows that the increase in  $\rho$  (observed from the isochronous curves) at  $\sim 573$ – $773$  and  $\sim 623$ – $773$  K for annealed and quenched samples, respectively, arises from the solid-solution instability with

respect to concentration waves  $\frac{1}{5}\{420\}$ . At higher temperatures, the resistivity decreases (Fig. 3), which indicates disordering, i.e., the formation of an ordinary disordered fcc structure that is stable to the generation of various concentration waves.

This scheme of spinodal ordering is confirmed by the behavior of the isothermal residual resistivity in the case of quenching of isochronously annealed samples (for both initial states) from 573 and 673 K. As before, isothermal annealing was carried out at  $T_a = 373$  K (Fig. 8). We can see that the kinetic curves measured at these quenching temperatures significantly differ, which indicates that the short-range order structures are different at these temperatures.

Indeed, as noted above, isochronous annealing temperatures of 573 and 673 K (curves 1, 2 in Fig. 3) correspond to the existence of the  $N_3M$  and  $N_4M$  structures, respectively. In the former case (curve 1 in Fig. 8), the resistivity slowly increases, while in the latter case (curve 2 in Fig. 8) the  $\varphi(t)$  dependence is complex. It is clear that annealing at  $T_a = 373$  K of the sample

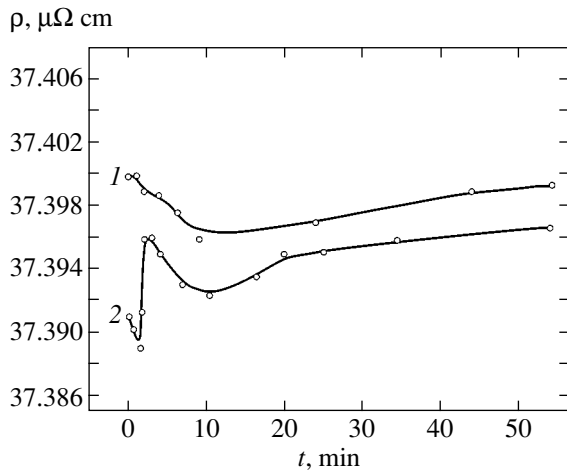


**Fig. 8.** Kinetics of the residual resistivity at  $T_a = 373$  K for isochronously annealed samples quenched at (1)  $T_q = 573$  and (2) 673 K.

quenched from  $T_q = 573$  K causes destruction of the  $N_3M$  structure and that the  $N_2M_2$  structure prevails, although its content seems to be lower than in the initial quenched state. In the case of quenching from  $T_q = 673$  K followed by annealing at  $T_a = 373$  K, the short-range order with the  $N_4M$  structure is initially destroyed, which decreases the resistivity. Then,  $N_3M$  is destroyed, which increases  $\rho(t)$ . This  $N_3M$  destruction can be considered a result of the disappearance of the

interaction between concentration waves  $\left\{1 \frac{1}{2} 0\right\}$  at low temperatures, i.e., the formation of solitary waves. In this case, the nucleation of the  $N_2M_2$  structure is accompanied by a decrease in the residual resistivity. The content of the  $N_2M_2$  structure formed at this temperature is not optimal; therefore, this structure is partially destroyed and  $\rho(t)$  increases. As the duration of annealing increases, the residual resistivity tends to an equilibrium value, which seems to correspond to a mixed state of short-range order involving the  $N_2M_2$  and  $N_3M$  structures.

#### 4. CONCLUSIONS

Thus, spinodal ordering of the  $N_2M_2$ ,  $N_3M$ , and  $N_4M$  structures takes place in low-concentration Ni–Mo (8–18 at. %) alloys, which is also observed at the initial ordering stages in quenched samples of Ni–Mo alloys with stoichiometric compositions. Moreover, the ordering process scheme is simpler in this case, as it excludes the nucleation of  $N_2M$ - and  $DO_{22}$ -structure clusters [2, 3]. Study of the low-temperature ordering kinetics suggests the coexistence of clusters of various structures, which are transformed in a complex fashion depending on the short-range order structure observed in various temperature ranges. Based on the isochronous and iso-

thermal dependences of the residual resistivity and the distribution of x-ray diffuse scattering intensity in low-concentration Ni–Mo alloys, the temperature ranges where clusters of various ordered structures exist can be determined.

#### REFERENCES

1. S. Banerjee, K. Urban, and M. Wilknes, *Acta Metall.* **32** (3), 299 (1984).
2. U. D. Kulkarni and S. Banerjee, *Acta Metall.* **36** (2), 413 (1988).
3. S. Banerjee, U. D. Kulkarni, and K. Urban, *Acta Metall.* **37** (1), 35 (1989).
4. A. Arya, S. Banerjee, G. P. Das, I. Dasgupta, T. Saha-Dasgupta, and A. Mookerjee, *Acta Mater.* **49**, 3575 (2001).
5. S. Hata, S. Matsumura, N. Kuwano, and K. Oki, *Acta Mater.* **46** (3), 881 (1998).
6. S. Hata, T. Mitute, N. Kuwano, S. Matsumura, D. Shindo, and K. Oki, *Mater. Sci. Eng. A* **312**, 160 (2001).
7. A. G. Khachatryan, *Theory of Structural Transformations in Solids* (Wiley, New York, 1983).
8. D. de Fontaine, *Acta Metall.* **23** (4), 553 (1975).
9. D. de Fontaine, *Solid State Phys.* **34**, 73 (1979).
10. P. L. Rossiter and P. Wolls, *J. Phys. C: Solid State Phys.* **4**, 354 (1971).
11. N. P. Kulish, N. A. Mel'nikova, P. V. Petrenko, V. G. Poroshin, and N. L. Zyuganov, *Izv. Vyssh. Uchebn. Zaved., Fiz.* **32** (2), 82 (1989).
12. V. G. Poroshin and N. P. Kulish, *Metallfiz. Noveishie Tekhnol.* **21**, 75 (1999).
13. M. A. Krivoglaz, *Theory of X-ray and Thermal Neutron Scattering by Real Crystals* (Nauka, Moscow, 1967; Plenum, New York, 1969).
14. M. A. Krivoglaz, *Diffuse Scattering of X-ray and Neutrons by Fluctuations in Solids* (Naukova Dumka, Kiev, 1984; Springer, Berlin, 1996).
15. C. J. Sparks and B. Borie, *Local Atomic Arrangements Studied by X-ray Diffraction*, Ed. by J. B. Cohen and J. E. Hilliard (Gordon and Breach, New York, 1966).
16. P. Georgopoulos and J. B. Cohen, *J. Phys. (Paris)* **38** (12), 7191 (1977).
17. P. Georgopoulos and J. B. Cohen, *Acta Metall.* **29**, 1535 (1981).
18. J. B. Cohen, *Solid State Phys.* **39**, 131 (1986).
19. V. G. Poroshin, N. P. Kulish, P. V. Petrenko, N. A. Mel'nikova, and S. P. Repetskiĭ, *Fiz. Met. Metall-oved.* **87** (2), 145 (1999).
20. V. G. Poroshin, N. P. Kulish, P. V. Petrenko, and N. A. Mel'nikova, *Fiz. Tverd. Tela (St. Petersburg)* **41** (12), 2121 (1999) [*Phys. Solid State* **41**, 1945 (1999)].
21. N. P. Kulish, N. A. Melnikova, P. V. Petrenko, and V. G. Poroshin, *Met. Phys. Adv. Technol.* **19**, 1147 (2001).

*Translated by A. Kazantsev*

METALS  
AND SUPERCONDUCTORS

# Hyperfine Nuclear Interaction at Copper Lattice Sites of High-Temperature Superconductors Studied by $^{61}\text{Cu}$ ( $^{61}\text{Ni}$ ) Mössbauer Emission Spectroscopy

S. A. Nemov\*, P. P. Seregin\*, N. P. Seregin\*\*, and A. V. Davydov\*\*\*

\*St. Petersburg State Polytechnical University, Politekhnikeskaya ul. 25, St. Petersburg, 195251 Russia

\*\*Institute of Analytical Instrumentation, Russian Academy of Sciences, St. Petersburg, 198103 Russia

\*\*\*Ioffe Physicotechnical Institute, Russian Academy of Sciences,  
Politekhnikeskaya ul. 26, St. Petersburg, 194021 Russia

Received October 30, 2003

**Abstract**—Mössbauer emission spectroscopy on the  $^{61}\text{Cu}$ ( $^{61}\text{Ni}$ ) isotope has been used to determine the quadrupole coupling constant  $C(\text{Ni})$  and magnetic induction  $B(\text{Ni})$  for the  $^{61}\text{Ni}^{2+}$  probe at copper sites in  $\text{Cu}_2\text{O}$ ,  $\text{CuO}$ ,  $\text{La}_{2-x}\text{Ba}_x\text{CuO}_4$ ,  $\text{Nd}_{2-x}\text{Ce}_x\text{CuO}_4$ ,  $\text{RBA}_2\text{Cu}_3\text{O}_6$ , and  $\text{RBA}_2\text{Cu}_3\text{O}_7$  ( $R = \text{Y, Nd, Gd, Yb}$ ). The compounds containing divalent copper were found to exhibit linear  $C(\text{Ni})$  vs.  $C(\text{Cu})$  and  $B(\text{Ni})$  vs.  $B(\text{Cu})$  relations [ $C(\text{Cu})$  and  $B(\text{Cu})$  are the quadrupole coupling constant and magnetic induction for the  $^{63}\text{Cu}$  probe, respectively, found by NMR], which is interpreted as an argument for the copper being in divalent state. The deviation of the data points corresponding to the  $\text{Cu}(1)$  sites in  $\text{RBA}_2\text{Cu}_3\text{O}_6$  and  $\text{RBA}_2\text{Cu}_3\text{O}_7$  from the  $C(\text{Ni})$  vs.  $C(\text{Cu})$  straight line may be due either to the copper valence being other than  $2+$  (in the  $\text{RBA}_2\text{Cu}_3\text{O}_6$  compounds) or to the principal axes of the total and valence electric field gradient being differently oriented (in the  $\text{RBA}_2\text{Cu}_3\text{O}_7$  compounds).  
© 2004 MAIK “Nauka/Interperiodica”.

Mössbauer spectroscopy is widely used in studies of nuclear quadrupole interactions in high-temperature superconductors; by comparing experimentally determined parameters with calculated parameters of the electric field gradient (EFG) tensor, one can, in principle, determine the spatial distribution of electronic defects and the effective charges of atoms [1].

These studies acquire particular significance in cases where the Mössbauer probe occupies a copper site, and this is why the version of Mössbauer emission spectroscopy (MES) involving the  $^{67}\text{Cu}$ ( $^{67}\text{Zn}$ ) isotope was proposed and realized [2]. However, determination of the parameters of nuclear quadrupole coupling in magnetically ordered lattices using  $^{67}\text{Cu}$ ( $^{67}\text{Zn}$ ) Mössbauer spectroscopy did not meet with success for a number of technical reasons [2]. This communication reports on an investigation into the nuclear hyperfine interaction at copper sites in  $\text{Cu}_2\text{O}$ ,  $\text{CuO}$ ,  $\text{La}_{2-x}\text{Ba}_x\text{CuO}_4$ ,  $\text{Nd}_{2-x}\text{Ce}_x\text{CuO}_4$  ( $x = 0, 0.15$ ),  $\text{RBA}_2\text{Cu}_3\text{O}_6$ , and  $\text{RBA}_2\text{Cu}_3\text{O}_7$  ( $R = \text{Y, Nd, Gd, Yb}$ ) using MES on the  $^{61}\text{Cu}$ ( $^{61}\text{Ni}$ ) isotope; the  $^{61}\text{Ni}^{2+}$  Mössbauer probe forming in the decay of  $^{61}\text{Cu}$  is localized in the copper sites, and the nuclear and atomic parameters of this probe are appropriate for determining the parameters of the combined hyperfine interaction at these sites [3]. Quadrupole splitting of the  $^{61}\text{Ni}$  Mössbauer spectrum gives rise to the appearance of five components with an intensity ratio of  $10 : 8 : 1 : 6 : 9$ , and the mag-

netic field completely lifts the degeneracy of the  $^{61}\text{Ni}$  nuclear levels, to make the  $^{61}\text{Ni}$  Mössbauer spectrum a superposition of 12 lines with a theoretical intensity ratio of  $10 : 4 : 1 : 6 : 6 : 3 : 3 : 6 : 6 : 1 : 4 : 10$ .

Samples were prepared by sintering the corresponding oxides, and x-ray diffraction showed them to be single phase. All the starting samples were single phase. The  $\text{La}_{2-x}(\text{Sr,Ba})_x\text{CuO}_4$  compounds studied for  $x = 0.1, 0.15, 0.20$ , and  $0.30$  yielded  $T_c = 25, 37, 27$ , and  $<4.2$  K, respectively. The  $\text{Nd}_{2-x}\text{Ce}_x\text{CuO}_4$  composition with  $x = 0$  did not become superconducting down to  $4.2$  K, and the composition with  $x = 0.15$  yielded  $T_c = 22$  K. For  $\text{YBa}_2\text{Cu}_3\text{O}_{6.9}$ , we obtained  $T_c = 90$  K, and for the  $\text{RBA}_2\text{Cu}_3\text{O}_7$  compounds  $T_c$  varied from  $83$  to  $90$  K. The samples of  $\text{RBA}_2\text{Cu}_3\text{O}_6$  did not cross over to the superconducting state down to  $4.2$  K. Mössbauer sources were prepared through diffusion of the short-lived isotope  $^{61}\text{Cu}$  into the prefabricated ceramic at temperatures ranging from  $773$  to  $923$  K for two hours in an oxygen environment. Annealing of check samples in similar conditions did not affect the values of  $T_c$ . Four to six samples were employed to measure an experimental spectrum.  $^{61}\text{Cu}$ ( $^{61}\text{Ni}$ ) Mössbauer emission spectra were measured on a commercial spectrometer at  $80$  K with a  $\text{Ni}_{0.86}\text{V}_{0.14}$  alloy used as an absorber.

To compare the possibilities offered by MES on the  $^{67}\text{Cu}$ ( $^{67}\text{Zn}$ ) and  $^{61}\text{Cu}$ ( $^{61}\text{Ni}$ ) isotopes, Figs. 1 and 2

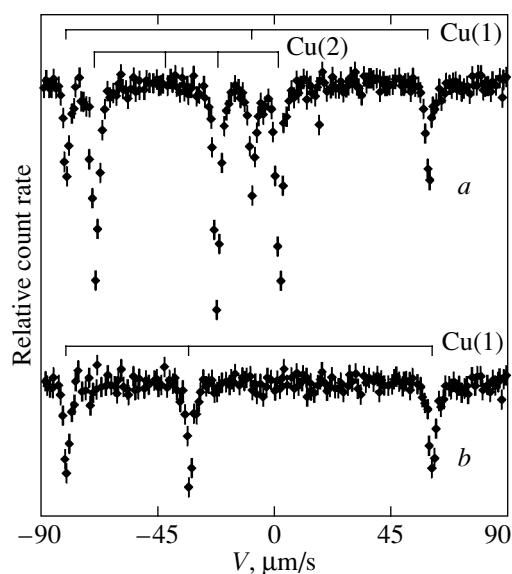


**Fig. 1.**  $^{67}\text{Cu}(^{67}\text{Zn})$  Mössbauer spectra of (a)  $\text{YBa}_2\text{Cu}_3\text{O}_7$  and (b)  $\text{YBa}_2\text{Cu}_3\text{O}_6$  measured at 4.2 K. The positions of the quadrupole triplet components for the Cu(1) and Cu(2) sites are specified.

present  $^{67}\text{Cu}(^{67}\text{Zn})$  and  $^{61}\text{Cu}(^{61}\text{Ni})$  spectra of the  $\text{YBa}_2\text{Cu}_3\text{O}_7$  and  $\text{YBa}_2\text{Cu}_3\text{O}_6$  compounds [the  $^{67}\text{Cu}(^{67}\text{Zn})$  Mössbauer sources were prepared through diffusion doping of the above compounds with the  $^{67}\text{Cu}$  radioactive isotope,  $^{67}\text{ZnS}$  served as an absorber when measuring the  $^{67}\text{Cu}(^{67}\text{Zn})$  spectra, and the spectra were taken at 4.2 K]. In crystal fields with a symmetry lower than cubic, the Mössbauer spectrum splits into three components of equal intensity. As is evident from Fig. 1, the  $^{67}\text{Cu}(^{67}\text{Zn})$  spectrum of  $\text{YBa}_2\text{Cu}_3\text{O}_7$  is a superposition of two quadrupole triplets with an intensity ratio of 1 : 2. Based on the x-ray diffraction data, the weaker triplet should be assigned to  $^{67}\text{Zn}^{2+}$  centers in the Cu(1) sites and the stronger one, to the  $^{67}\text{Zn}^{2+}$  centers occupying the Cu(2) sites. The  $^{67}\text{Cu}(^{67}\text{Zn})$  spectrum of  $\text{YBa}_2\text{Cu}_3\text{O}_6$  is a quadrupole triplet, although copper in this compound also occupies two structurally inequivalent positions. The experimental spectrum relates to the  $^{67}\text{Zn}^{2+}$  centers in the Cu(1) sites, whereas the spectrum due to the  $^{67}\text{Zn}^{2+}$  centers in the Cu(2) sites is split by magnetic interaction and is not seen in the experimental spectrum (its observation would require higher Doppler velocities that could not be reached with the spectrometer at our disposal).

As seen from Fig. 2, however, both copper states in the  $\text{YBa}_2\text{Cu}_3\text{O}_7$  and  $\text{YBa}_2\text{Cu}_3\text{O}_6$  lattices manifest themselves in the  $^{61}\text{Cu}(^{61}\text{Ni})$  spectra. The spectrum of  $\text{YBa}_2\text{Cu}_3\text{O}_7$  is actually a superposition of two quadrupole multiplets; based on the relative intensities of the constituents of the spectrum, the spectrum with the smaller  $eQU_{zz}$  should be assigned to  $^{61}\text{Ni}^{2+}$  centers in

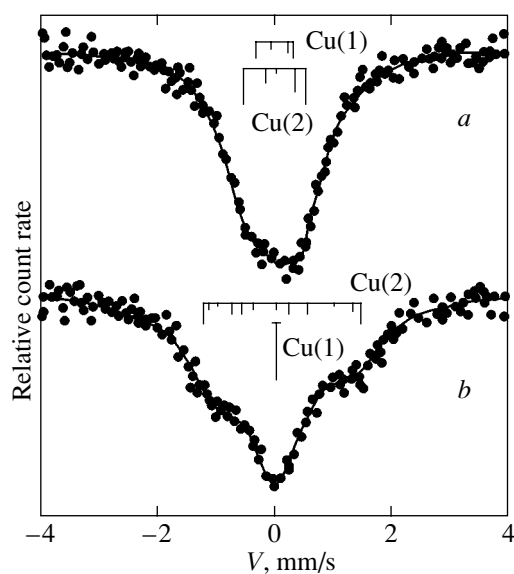


**Fig. 2.**  $^{61}\text{Cu}(^{61}\text{Ni})$  Mössbauer spectra of (a)  $\text{YBa}_2\text{Cu}_3\text{O}_7$  and (b)  $\text{YBa}_2\text{Cu}_3\text{O}_6$  measured at 80 K. The positions of the quadrupole and Zeeman multiplet components for the Cu(1) and Cu(2) sites are specified.

the Cu(1) sites and the spectrum with the larger  $eQU_{zz}$ , to  $^{61}\text{Ni}^{2+}$  centers in the Cu(2) sites. The Cu(2) sublattice in  $\text{YBa}_2\text{Cu}_3\text{O}_6$  is magnetically ordered; therefore, the spectrum of this sample may be considered a superposition of a magnetic multiplet [ $^{61}\text{Ni}^{2+}$  centers in the Cu(2) sites] and a broadened singlet [ $^{61}\text{Ni}^{2+}$  centers in the Cu(1) sites].

The nuclear hyperfine interaction parameters for the  $^{61}\text{Ni}$  probe [the quadrupole coupling constant  $C(\text{Ni})$  and the magnetic induction  $B(\text{Ni})$ ] are displayed in Figs. 3 and 4.

The quadrupole coupling constant  $C(\text{Cu})$  was measured for the  $^{63}\text{Cu}$  probe in cuprous oxides by NMR [4–11], which permits one to check the correlation between the  $^{61}\text{Cu}(^{61}\text{Ni})$  MES data and  $^{63}\text{Cu}$  NMR measurements. Figure 3 presents a  $|C(\text{Ni})|$  vs.  $|C(\text{Cu})|$  graph for the divalent-copper compounds  $\text{La}_2\text{CuO}_4$ ,  $\text{La}_{1.85}\text{Sr}_{0.15}\text{CuO}_4$ ,  $\text{Nd}_2\text{CuO}_4$ ,  $\text{Nd}_{1.85}\text{Ce}_{0.15}\text{CuO}_4$ , and  $\text{CuO}$ . We readily see that the experimental points fit a straight line. This linear dependence can be understood if we recall that the EFG at nucleus sites for the  $\text{Ni}^{2+}$  and  $\text{Cu}^{2+}$  centers is generated both by the lattice ions (the crystal field EFG) and by the nonspherical valence shell of the ion itself (the valence EFG), so the quadrupole coupling constant for the probe can be cast as

$$C = eQ(1 - \gamma)V_{zz} + eQ(1 - R_0)W_{zz},$$

where  $eQ$  is the quadrupole moment of the probe nucleus;  $V_{zz}$  and  $W_{zz}$  are the principal components of the crystal and valence EFG tensors, respectively; and



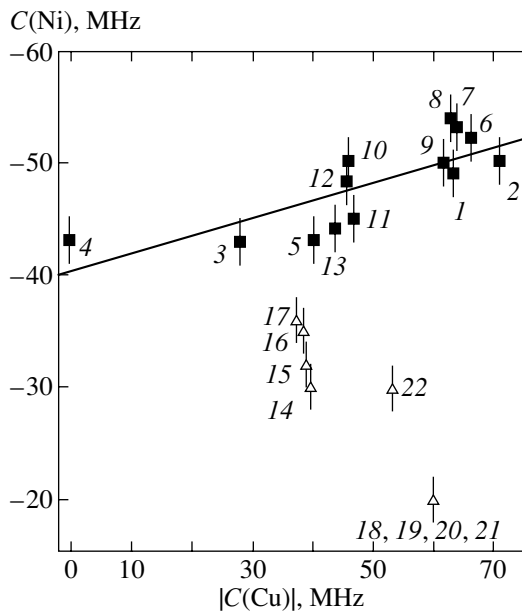


**Fig. 3.**  $|C(\text{Ni})|$  vs.  $|C(\text{Cu})|$  diagram for (1)  $\text{La}_2\text{CuO}_4$  [4], (2)  $\text{La}_{1.85}\text{Sr}_{0.15}\text{CuO}_4$  [5], (3)  $\text{Nd}_2\text{CuO}_4$  [6], (4)  $\text{Nd}_{1.85}\text{Ce}_{0.15}\text{CuO}_4$  [6], (5)  $\text{CuO}$  [4], (6)  $\text{Cu}(2)$  in  $\text{NdBa}_2\text{Cu}_3\text{O}_7$  [7], (7)  $\text{Cu}(2)$  in  $\text{GdBa}_2\text{Cu}_3\text{O}_7$  [7], (8)  $\text{Cu}(2)$  in  $\text{YBa}_2\text{Cu}_3\text{O}_7$  [8], (9)  $\text{Cu}(2)$  in  $\text{YBa}_2\text{Cu}_3\text{O}_7$  [7], (10)  $\text{Cu}(2)$  in  $\text{NdBa}_2\text{Cu}_3\text{O}_6$  [7], (11)  $\text{Cu}(2)$  in  $\text{GdBa}_2\text{Cu}_3\text{O}_6$  [9], (12)  $\text{Cu}(2)$  in  $\text{YBa}_2\text{Cu}_3\text{O}_6$  [10], (13)  $\text{Cu}(2)$  in  $\text{YbBa}_2\text{Cu}_3\text{O}_6$  [9], (14)  $\text{Cu}(1)$  in  $\text{NdBa}_2\text{Cu}_3\text{O}_7$  [9], (15)  $\text{Cu}(1)$  in  $\text{GdBa}_2\text{Cu}_3\text{O}_7$  [9], (16)  $\text{Cu}(1)$  in  $\text{YBa}_2\text{Cu}_3\text{O}_7$  [8], (17)  $\text{Cu}(1)$  in  $\text{YbBa}_2\text{Cu}_3\text{O}_7$  [9], (18)  $\text{Cu}(1)$  in  $\text{NdBa}_2\text{Cu}_3\text{O}_6$  [9], (19)  $\text{Cu}(1)$  in  $\text{GdBa}_2\text{Cu}_3\text{O}_6$  [9], (20)  $\text{Cu}(1)$  in  $\text{YBa}_2\text{Cu}_3\text{O}_6$  [10], (21)  $\text{Cu}(1)$  in  $\text{YbBa}_2\text{Cu}_3\text{O}_6$  [9], and (22)  $\text{Cu}_2\text{O}$  [11]. The straight line is a least squares fit through points 1–13 corresponding to divalent copper. The references concern  $^{63}\text{Cu}$  NMR data.

$\gamma$  and  $R_0$  are the Sternheimer coefficients for the probe used.

The linear relation  $|C(\text{Ni})|$  vs.  $|C(\text{Cu})|$  is actually a consequence of the linear relations  $C(\text{Ni})$  vs.  $V_{zz}$  and  $C(\text{Cu})$  vs.  $V_{zz}$ , which were observed [12] for compounds of divalent copper. Because the data obtained for the  $\text{Cu}(2)$  sites in the  $\text{RBa}_2\text{Cu}_3\text{O}_7$  and  $\text{RBa}_2\text{Cu}_3\text{O}_6$  compounds fall onto the above straight line, one may conclude that copper in these sites is in the divalent state.

As seen from Fig. 3, the points obtained for the copper sites in  $\text{Cu}_2\text{O}$  and for the  $\text{Cu}(1)$  sites in  $\text{RBa}_2\text{Cu}_3\text{O}_6$  and  $\text{RBa}_2\text{Cu}_3\text{O}_7$  deviate from a linear relationship. There are two reasons for this deviation, namely, the copper valence state being other than  $2+$  and different orientations of the total and valence EFG axes for the  $^{61}\text{Ni}^{2+}$  and  $^{63}\text{Cu}^{2+}$  probes. The first reason is valid for the  $\text{Cu}(1)$  sites in  $\text{RBa}_2\text{Cu}_3\text{O}_6$  and for the copper sites in  $\text{Cu}_2\text{O}$  [the copper in  $\text{Cu}_2\text{O}$  and in the  $\text{Cu}(1)$  sites of the

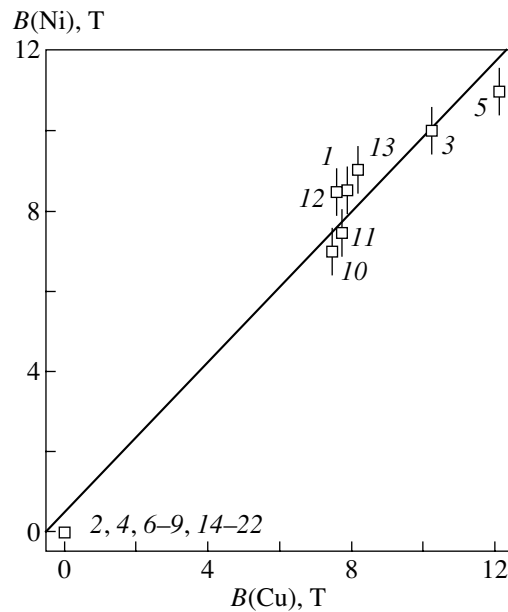


**Fig. 4.**  $B(\text{Ni})$  vs.  $B(\text{Cu})$  diagram. The data points are denoted as in Fig. 3. The straight line is a least squares fit through all points.

$\text{RBa}_2\text{Cu}_3\text{O}_6$  compounds is univalent], and the second applies to the  $\text{Cu}(1)$  sites in the  $\text{RBa}_2\text{Cu}_3\text{O}_7$  compounds [it is known that, at least for the  $\text{Cu}(1)$  sites in  $\text{YBa}_2\text{Cu}_3\text{O}_7$ , the  $z$  axis of the total EFG tensor is directed along the  $b$  crystallographic axis, whereas the  $z$  axis of the crystal-field EFG is aligned with the  $a$  crystallographic axis [13]].

Magnetic induction at the copper sites,  $B(\text{Cu})$ , was measured for the  $^{63}\text{Cu}$  probe in cuprous oxides by NMR [4–11]. As is evident from Fig. 4, the  $^{61}\text{Cu}(^{61}\text{Ni})$  MES data are linearly related to the  $^{63}\text{Cu}$  NMR data for all the compounds studied. This is obviously the result of the probe occupying the copper sites in the lattice.

#### ACKNOWLEDGMENTS

This study was supported by the Russian Foundation for Basic Research, project no. 02-02-17306.

#### REFERENCES

1. V. F. Masterov, F. S. Nasredinov, and P. P. Seregin, *Fiz. Tverd. Tela* (St. Petersburg) **37** (5), 1265 (1995) [*Phys. Solid State* **37**, 687 (1995)].
2. V. F. Masterov, F. S. Nasredinov, N. P. Seregin, and P. P. Seregin, *Yad. Fiz.* **58** (9), 1554 (1995) [*Phys. At. Nucl.* **58**, 1467 (1995)].
3. F. S. Nasredinov, P. P. Seregin, V. F. Masterov, N. P. Seregin, O. A. Prikhodko, and M. A. Sagatov, *J. Phys.: Condens. Matter* **7** (11), 2339 (1995).
4. T. Tsuda, T. Shimizu, H. Yasuoka, K. Kishio, and K. Kitazawa, *J. Phys. Soc. Jpn.* **57** (9), 2908 (1988).

5. S. Ohsugi, Y. Kitaoka, K. Ishida, and K. Asayama, *J. Phys. Soc. Jpn.* **60**, 7, 2351 (1991); S. Ohsugi, Y. Kitaoka, K. Ishida, G. Zheng, and K. Asayama, *J. Phys. Soc. Jpn.* **63** (2), 700 (1994).
6. K. Kumagai, M. Abe, S. Tanaka, Y. Maeno, and T. Fujita, *J. Magn. Magn. Mater.* **90–91**, 675 (1990).
7. M. Itoh, K. Karashima, M. Kyogoku, and I. Aoki, *Physica C (Amsterdam)* **160** (1), 177 (1989).
8. C. H. Pennington, D. J. Durand, C. P. Slichter, J. P. Rice, E. D. Bukowski, and D. M. Ginsberg, *Phys. Rev. B* **39** (4), 2902 (1989).
9. T. Takatsuka, K. Kumagai, H. Nakajima, and A. Yamanaka, *Physica C (Amsterdam)* **185–189**, 1071 (1991).
10. H. Yasuoka, T. Shimizu, T. Imai, S. Sasaki, Y. Ueda, and K. Kosuge, *Hyperfine Interact.* **49** (1), 167 (1989).
11. H. Kruger and U. Meyer-Berkhout, *Z. Phys.* **132** (1), 171 (1952).
12. P. P. Seregin, V. F. Masterov, F. S. Nasredinov, and N. P. Seregin, *Phys. Status Solidi B* **201** (1), 269 (1997).
13. V. F. Masterov, F. S. Nasredinov, N. P. Seregin, and P. P. Seregin, *Fiz. Tverd. Tela (St. Petersburg)* **39** (12), 2118 (1997) [*Phys. Solid State* **39**, 1895 (1997)].

*Translated by G. Skrebtsov*